UNIVERSITY OF Southampton

University of Southampton Research Repository

Copyright © and Moral Rights for this thesis and, where applicable, any accompanying data are retained by the author and/or other copyright owners. A copy can be downloaded for personal non-commercial research or study, without prior permission or charge. This thesis and the accompanying data cannot be reproduced or quoted extensively from without first obtaining permission in writing from the copyright holder/s. The content of the thesis and accompanying research data (where applicable) must not be changed in any way or sold commercially in any format or medium without the formal permission of the copyright holder/s.

When referring to this thesis and any accompanying data, full bibliographic details must be given, e.g.

Thesis: Author (Year of Submission) "Full thesis title", University of Southampton, name of the University Faculty or School or Department, PhD Thesis, pagination.

Data: Author (Year) Title. URI [dataset]

University of Southampton

Faculty of Environmental and Life Sciences

School of Ocean and Earth Science

Serpentinisation of the Troodos Massif, Cyprus

by

Aled Dafydd Evans
MESci

ORCID ID: https://orcid.org/0000-0003-3252-5998

Thesis for the degree of Doctor of Philosophy

May 2022

University of Southampton

Abstract

Faculty of Environmental and Life Sciences

School of Ocean and Earth Science

Doctor of Philosophy

Serpentinisation of the Troodos Massif, Cyprus

by

Aled Dafydd Evans

The interaction between ultramafic rocks and water, a process termed serpentinisation, plays a critical role within the wider Earth system, aiding plate tectonics, influencing geochemical cycles, and may be instrumental in the origin of life. Recovered serpentinised mantle rocks, both on land and in the oceans, typically reflect multiple overprinting serpentinisation events. To date, the conditions of distinct serpentinisation episodes are generally poorly constrained since mantle rocks generally reveal complex geological histories. This thesis integrates field observations, physical properties, elemental concentrations and isotope compositions of sampled waters, precipitates, and variably serpentinised mantle rocks to unravel the progressive sequence of overprinting fluid rock interaction events that have resulted in the occurrence of mantle rocks forming the highest elevations of the Troodos ophiolite, Cyprus.

In the Troodos Mantle Sequence, different serpentinisation styles have resulted in contrasting nested serpentinite diapirs formed due to differing extents of serpentinisation and density reduction. Mechanistic isostatic and differential erosional modelling show that the Troodos Mountains can form within the geologically constrained uplift time frame (~5.5 Myr) exclusively through partial serpentinisation reactions. Serpentinisation-induced differential uplift and exhumation have decoupled the two serpentinite diapirs from the originally overlying ocean crustal rocks. Incursion of meteoric water resulted in further serpentinisation, generating a second decoupling between the contrasting serpentinite diapirs resulting in localised differential uplift and exhumation and the extrusion of deep materials.

Sr, B, O, and H isotopes and equilibrium modelling coupled with a Bayesian inversion engine are consistent with a progressive sequence of overprinting serpentinisation events: (i) A localised serpentinisation episode by Cretaceous hydrothermal fluids, limited to the crust-mantle transition zone soon after formation at the spreading ridge; (ii) A pervasive serpentinisation event by Cyprus slab-derived fluids focussed underneath the differentially uplifted Mount Olympus, inducing serpentinisation of the Troodos Mantle Sequence by up to 66 % reaction extent; (iii) A pervasive serpentinisation event by meteoric waters that interacted with previously overlying submarine sediments and Messinian evaporites, resulting in further serpentinisation of up to 33 %; (iv) Once at high altitudes continued incursion of meteoric water locally reinforced serpentine alteration through coupled deformation-alteration-recrystallisation processes that manifest as a low density serpentinite breccia end member. The alteration of serpentine forms hyperalkaline high pH >11.5 meteoric-derived waters emanating from portions of the Troodos Massif. In addition to these high pH waters, contrasting meteoric-derived lower pH <10 surficial waters reflect variable proportions of remobilised geochemical and isotopic signals from previous serpentinisation events.

Some, but not all, of the observed change in the physical properties of variably serpentinised mantle rocks can be explained by serpentinisation hydration reactions. To reconcile this difference, ongoing serpentine alteration processes are proposed to modify mantle rock physical properties further, resulting in contrasting but parallel mantle rock alteration pathways. Consequently, in addition to serpentinisation hydration reactions, ongoing serpentine alteration, carbonation, and oxidation are also instrumental processes that can induce serpentinite diapirism, generate hyperalkaline waters, and produce significant changes to physical and hydraulic properties of serpentinised mantle rocks.

Table of Contents

Table of Contents ..... **i**
Table of Tables ..... **vii**
Table of Figures ..... **ix**
Research Thesis: Declaration of Authorship ..... **xxix**
Acknowledgements ..... **xxxi**
Definitions and Abbreviations ..... **xxxiii**
Chapter 1 Introduction **1**

1.1 Rationale 1
1.2 Serpentinisation and its wider importance in the Earth system 2
1.3 Where does serpentinisation occur? 9
1.4 When does serpentinisation occur? 13
1.5 Serpentinite Alteration 16
1.6 Aims of the Thesis 18
1.7 Thesis outline 19

Chapter 2 Geological Setting **21**

2.1 The Troodos ophiolite 21
2.2 The Troodos Massif Mantle Sequence 25
2.3 Uplift Trajectories 29

Chapter 3 Uplift and Exposure of Serpentinised Massifs: Modelling Differential Serpentinite Diapirism and Exhumation of the Troodos Mantle Sequence, Cyprus **33**

3.1 Introduction 34
3.2 Mantle peridotite massifs and serpentinite diapirism 35
3.2.1 Examples of serpentinite diapirism associated with isostatic uplift 36
3.2.2 Examples of serpentinite diapirism not associated with isostatic uplift 37
3.3 Structure of the Troodos Mantle Sequence 38
3.3.1 Structure of the Olympus domain 38
3.3.2 Structure of the Artemis domain 47
3.4 Contrasting properties within the Troodos Mantle Sequence 50
3.4.1 Contrasting Mineralogy 50

3.4.2 Contrasting serpentine oxygen and hydrogen stable isotope values .. 54
3.4.3 Contrasting bulk densities 55
3.5 Mechanistic Uplift Modelling 57
3.5.1 Model parameters..... 57
3.5.2 Uplift Modelling Results 63
3.6 Discussion 64
3.6.1 Serpentinite Diapirism of the Troodos Mantle Sequence 64
3.6.2 Previous uplift mechanisms attributed to the Troodos Mantle Sequence 66
3.6.3 A unified model for the uplift of the Troodos Mantle Sequence..... 67
3.7 Application of the mechanistic uplift model to other settings 69
3.7.1 St. Peter and St. Paul Rocks 70
3.7.2 New Idria serpentinite diapir 71
3.7.3 ODP Leg 103 Site 637 72
3.7.4 Macquarie Island 73
3.7.5 Wider implications of the mechanistic uplift model 75
3.8 Conclusions 75

Chapter 4 Serpentine alteration produces high pH >11.5 hyperalkaline waters: Insights from the Troodos Massif, Cyprus..... 77

4.1 Introduction 78
4.2 Geological Setting..... 79
4.2.1 The Troodos Mantle Sequence 79
4.2.2 Precipitates from the Troodos Mantle Sequence modern meteoric waters 84
4.3 Methods 93
4.3.1 Field sampling 93
4.3.2 Sample Preparation..... 93
4.3.3 Elemental Analyses 94
4.3.3.1 Waters and Precipitates..... 94
4.3.3.2 Artemis Diapir rocks..... 99
4.3.4 $^{87}Sr/^{86}Sr$ determination 104

4.3.5 Stable isotope determination 104
4.4 Results 105
4.4.1 Composition of waters 105
4.4.2 Precipitates and Artemis Diapir rocks 130
4.4.3 Summary 171
4.5 Discussion 171
4.5.1 Origin of the Troodos Mantle Sequence waters 171
4.5.2 Origin of salinity and high fluid-mobile elemental concentrations in hyperalkaline waters 174
4.5.3 Contrasting Sr reservoirs in sampled waters of the Troodos Mantle Sequence 176
4.5.4 Evolution of the Troodos Mantle Sequence waters 178
4.5.4.1 Evolution of the low pH surficial waters 179
4.5.4.2 Increased fluid-rock interaction within mine tailings 181
4.5.4.3 Evolution of the high pH hyperalkaline waters 181
4.6 Conclusions 185

Chapter 5 Unravelling a progressive serpentinisation-alteration history: Geochemical and isotopic fingerprinting within the Troodos Mantle Sequence, Cyprus 187

5.1 Introduction 188
5.2 Geological Setting 189
5.3 Methods 193
5.3.1 Field sampling and sample preparation 193
5.3.2 Major and Trace Elements 193
5.3.3 $^{87}Sr/^{86}Sr$ determination 194
5.3.4 *In situ* $\delta^{11}B$ determination 194
5.3.5 *In situ* B concentration determination and elemental mapping 197
5.4 Analytical Results 198
5.4.1 Radiogenic strontium isotopic compositions 242
5.4.2 Trace element ratios 248
5.4.3 Boron isotopic composition and concentration 250
5.5 Comparison with previous serpentine geochemical and isotopic data 261

5.5.1 Isotope values 261
5.5.2 Trace element ratios 264
5.6 Cretaceous seafloor serpentinisation 269
5.6.1 $^{87}Sr/^{86}Sr$ Constraints 269
5.6.2 Oxygen and Hydrogen Isotopic Constraints 276
5.6.3 Boron Isotope Constraints 277
5.6.3.1 Boron Isotopes Systematics 277
5.6.3.2 Serpentinisation of the Troodos Mantle Sequence by a seawater-derived hydrothermal fluid 279
5.6.4 Summary 281
5.7 Miocene Slab-derived Serpentinisation of the Troodos Mantle Sequence 282
5.7.1 $\delta^{18}O$ and δD 285
5.7.2 $^{87}Sr/^{86}Sr$ Constraints 289
5.7.3 $\delta^{11}B$ constraints 289
5.7.4 Mass Balance Calculation 296
5.8 Sediment-derived meteoric serpentinisation 302
5.8.1 $^{87}Sr/^{86}Sr$ Constraints 303
5.8.2 $\delta^{18}O$ and δD 303
5.8.3 $\delta^{11}B$ 304
5.9 Modern serpentinisation-alteration exchange with meteoric water 306
5.10 A serpentinisation history of the Troodos Mantle Sequence 307

Chapter 6 Serpentinzation-induced mantle rock alteration pathways: Insights from the evolving physical properties of the Troodos Mantle Sequence, Cyprus 311

6.1 Introduction 312
6.2 Geological setting 313
6.3 Methods 319
6.3.1 Sample Preparation 319
6.3.2 Experimental setup 319
6.3.3 Experimental Procedure 327
6.4 Results 327

6.5 Discussion 335
6.5.1 Comparison with other recovered serpentinised and altered mantle peridotite settings 335
6.5.1.1 Bulk density and porosity 345
6.5.1.2 V_p and V_s 345
6.5.1.3 Resistivity and permeability 347
6.5.2 Mantle Rock Alteration Pathways 348
6.5.3 Implications of contrasting mantle rock alteration pathways 352
6.6 Conclusions 352

Chapter 7 Summary and Conclusions 355

7.1 Summary 355
7.2 Conclusions 355
7.2.1 Serpentinisation-induced uplift 355
7.2.2 High pH >11.5 hyperalkaline waters emanating from the completely serpentinised Artemis Diapir and remobilisation of previous geochemical and isotopic signals of previous serpentinisation events 356
7.2.3 Multiple overprinting serpentinisation events 357
7.2.4 Physical properties of altered mantle rocks 358
7.3 Further work 359

Appendix A Boron equilibrium model 361

A.1.1 Model output with synthetic data 369

Appendix B 371
Appendix C 397
References 411

Table of Tables

Table 3.1: Contrasting characteristics, properties and serpentinisation styles exhibited by the proposed Olympus and Artemis domains of the Troodos Mantle Sequence. 50

Table 3.2: New density measurements with estimated primary and secondary modal mineral assemblages. DSDP Leg 37 average density of serpentinised peridotite from Hyndman and Drury (1976). Average density of unserpentinised mantle peridotite from Birch (1961). Calculated errors for differing proportions of Artemis clast and gouge are also shown. 55

Table 3.3: Model parameters for the Olympus and Artemis domains used in the mechanistical uplift modelling. 59

Table 3.4. Summary table of parameters utilised in the application of the mechanistic uplift model to other settings. 69

Table 4.1: Sampled Troodos Massif analytical results table; $CBE\ \% = 100 \cdot \Sigma cations - \Sigma anions \Sigma cations + \Sigma anions$ 95

Table 4.2 (A): Table of precision and accuracy for ICP-MS. Certified values are compiled from GeoReM (Jochum et al., 2005) 100

Table 4.3: Summary table of results. 106

Table 4.4: Table of Troodos Massif waters analytical results. 110

Table 4.5: Elemental ratios summary table (molar). 120

Table 4.6: Elemental summary table. 122

Table 4.7: Table of Troodos Mantle Sequence precipitates analytical results. 131

Table 4.8: Table of Artemis Diapir whole rock analytical results. 140

Table 4.9: 10 % Acetic Leachates 158

Table 4.10: 3M HCl Table. 161

Table 4.11: Bulk Rock Residue. 164

Table 4.12: Mass balance calculation of meteoric water infiltration. 174

Table 5.1: *$\delta^{11}B$ Precision and accuracy table for LA-MC-ICP-MS and LA-ICP-MS* 196

Table of Tables

Table 5.2: Analytical results of whole-rocks, serpentine veins, cohesive fault rocks, and incohesive serpentinite breccias. 199

Table 5.3: Progressive leaching experiments analytical results – 10% Acetic Acid Leachate. 224

Table 5.4: Progressive leaching experiments analytical results – 3M HCl Leachate. .229

Table 5.5: Progressive leaching experiments analytical results – Bulk Residue. 236

Table 5.6: Summary Table. 240

Table 5.7: $\delta^{11}B$ (LA-MC-ICP-MS) and B (LA-ICP-MS) concentration analytical result table 252

Table 5.8: Trace element ratio summary table. 266

Table 5.9: Isotope Summary Table. 270

Table 5.10: Cyprus subduction zone characteristics. 284

Table 5.11: Estimated Cyprus slab-derived fluid isotope compositions. Smectite oxygen-water fractionation factor (Savin and Lee, 1988); Smectite hydrogen-water fractionation factor (Yeh, 1980). Phyllosilicate boron fractionation factor (Boschi et al., 2008; Liu and Tossell, 2005). Oxygen calcite-water fractionation factor (Zheng, 1999). 287

Table 5.12: Boron equilibrium model coupled with a Bayesian inversion engine prior likelihoods table ('hydrothermal' conditions >50°C to <500°C). 291

Table 5.13: Boron equilibrium model coupled with a Bayesian inversion engine prior likelihoods table ('seawater' conditions >0°C to <50°C). 293

Table 5.14: Troodos ophiolite lavas geochemical and isotopic characteristics. 294

Table 5.15: Mass Balance Calculation. 299

Table 6.1: Table of experimental results on samples from the Troodos Massif. V_p, V_s, Q_p^{-1}, Q_s^{-1}, electrical resistivity, permeability, and the permeability error are shown at differing differential pressures. $P_{Diff} = P_c - P_F$; P_F = 5 MPa. 321

Table 6.2: Table compiling reported data of physical and hydraulic properties from a range of serpentinising settings, both on land and in the oceans. 343

Table of Figures

Figure 1.1: Serpentine pressure-temperature dependent diagram (Guillot et al., 2015) from petrological observations and experimental data of serpentinites. (I) Refers to the onset destabilisation of lizardite to antigorite (Evans, 2004). (II) Refers to the stability limit of lizardite (Schwartz et al., 2013). (III) Refers to dehydration of serpentine (Perrillat et al., 2005). (IV) Refers to the stability limit of antigorite (Wunder and Schreyer, 1997). (V) Refers to the breakdown of antigorite (Ulmer and Trommsdorff, 1995). Metamorphic facies boundaries and the cold subduction gradient are also shown (Guillot et al., 2015; Liou et al., 2000). Lz is lizardite, Ctl is chrysotile, Atg is antigorite, Tc is talc, Ol is olivine, En is Enstatite. 5

Figure 1.2: Map of serpentinite occurrences on land and in the oceans (from Guillot et al., 2015; Guillot and Hattori, 2013). Global seafloor spreading rates are mapped with black lines denoting spreading ridge axes (Cannat et al., 2010). Major seafloor occurrences of serpentinite are denoted by yellow circles with green outlines denoting continental serpentinites (Coleman, 1971). 10

Figure 1.3: Respective range of $\delta^{18}O_{Serpentine}$ and $\delta D_{Serpentine}$ values of previous serpentine isotope measurements are shown (adapted from Sheppard, 1980; Wenner and Taylor, 1973). Global meteoric water line is also plotted (Craig, 1961). The range of oxygen and hydrogen stable isotope values from the Troodos Mantle Sequence are shown (Heaton, 1976; Magaritz and Taylor, 1974; Nuriel et al., 2009) and other occurrences of serpentine both on land and in the oceans (Sheppard, 1980; Sheppard and Epstein, 1970; Wenner, 1971; Wenner and Taylor, 1974, 1973, 1971). 15

Figure 2.1: Geological map of the Troodos ophiolite with the bullseye geometry of the Mantle Sequence highlighted along with the Limassol Forest Complex terrane, the Cyprus arc and northernmost portion of the Eratosthenes Seamount. 22

Figure 2.2: Troodos ophiolite crustal ophiolite stratigraphy adapted from Malpas et al., (1989). Thickness of the ophiolite is estimated by stacking drillholes CY-1, CY-1A, CY-2, CY-2A, and CY-4 from the Cyprus Crustal Study Project. 23

Figure 2.3: Geological map of the Troodos Mantle Sequence, adapted and updated from Wilson (1959). X to X' shows line of cross-section. 26

Table of Figures

Figure 2.4: Geological cross-section of the Troodos Mantle Sequence and associated ocean crustal rocks. 27

Figure 2.5: (a) 3D gravity map covering Cyprus, data sourced from Gass and Masson-Smith (1963). (b) Gravity cross-section along line Y-Y' again using data of Gass and Masson-Smith (1963), cross-section highlights the asymmetric nature of the Mount Olympus anomaly with the gravity low centred broadly on the former chrysotile asbestos mine of Pano Amiantos. 29

Figure 2.6: Summary table of the circum-Troodos sedimentary sequences. 31

Figure 3.1: (A) Geological map of the Troodos ophiolite with the bullseye geometry of the Mantle Sequence highlighted along with the Limassol Forest Complex terrane, the Cyprus arc and northernmost portion of the Eratosthenes Seamount. (B) Geological map of the Troodos Mantle Sequence, adapted and updated from Wilson (1959). X to X' shows line of cross-section (Fig. 2.3; Fig. 2.4). Density sample locations shown as are sample locations for published oxygen and hydrogen stable isotope analyses by Magaritz and Taylor (1974); Heaton (1976); Nuriel et al. (2009). 35

Figure 3.2: Aerial imagery map of the Troodos Mantle Sequence with locations of field pictures, tectonic foliation measurements are from Wilson (1959). 39

Figure 3.3: (A) Typical outcrop of partly serpentinised mantle peridoties from the Olympus domain with near horizontal, narrow shear zones orientated 120° apart, that form laterally continuous ~100 m lensoidal geometries. (B) Massive Olympus domain dunite displaying the common hard, blocky, cohesive, partially serpentinised mantle peridotite outcrop pattern. (C) Olympus domain outer boundary highlighting a zone of intensely deformed peridotite and intercalated blocks of overturned layered gabbro. 40

Figure 3.4: (A) Unannotated and annotated field picture pair within the Olympus Domain. A moderately dipping brittle-plastic shear zone is shown. Deformation is concentrated within a zone ~1.5 m in thickness. S C fabrics are observed within the shear zone with competent lozenges exhibiting predominantly asymmetric morphologies. Outside of the main deformation band, shear surfaces separate the rock into separate generally underformed partially serpentinised lozenges of varying symmetries. Subsequent brittle fracturing has resulted in a complex extensional fracture (joint) pattern. Person for scale. (B) Sub-horizontal conjugate brittle-plastic shear zone shown with generally symmetrical and undeformed lozenges forming in

between the shear surfaces. These interconnected shear surfaces intersect at 120° (red lines) and are generally interpreted as examples of conjugate shear zones that have undergone coaxial deformation (e.g., Ramsay, 1980; Fossen and Cavalcante, 2017). The implication of the geometry is that the undeformed lozenges exhibit 'internal boudinage' (i.e., boudinage not related to competence contrasts; Ramsay, 1980) and in this case have extended in the ~horizontal direction and likely flattened in the ~vertical direction. Subsequent brittle fracturing (black lines) occurs within these undeformed, symmetrical, massive, partially serpentinised lozenges. These low-angle conjugate shears are prevalent in road cuttings on the road to the summit of Mount Olympus and are continuous over ~100 m in distance. Away from the summit the general dip angle of these conjugate shear zones increases from low angles (<30°) to moderate-high angles (~60° to <90°; (C)), with a general increase in the asymmetry of the lozenges (e.g., Fig. 3.5). Hammer for scale. (C) A shear zone array orientated at moderate dip angles is shown. Shear surfaces are generally orientated 120° and their geometries are more asymmetric relative to the lozenges of B. Domain sub-division occurs where, within larger ~2 m lozenges, smaller lozenges are bounded by shear surfaces forming an intricated, anastomosing shear zone array across differing domain scales. Person for scale. 41

Figure 3.5: Field picture of the Artemis / Olympus northern boundary. A complex high angle, ~NW dipping, shear zone array occurs. Asymmetric lozenge geometries occur, and shear surfaces are inferred across a range of scales (red lines), highlighting domain sub-division into increasing smaller asymmetric lozenges that are bounded by brittle-plastic shear surfaces. Despite the substantial internal deformation of the Olympus domain, deformation within the Artemis domain is greater than the Olympus domain. Deformation within the Olympus domain results in a cohesive, blocky outcrop pattern, with development of serpentinite breccias localised to outcrop scales where strain has localised between less deformed lozenges. In contrast, in the Artemis domain, entire hillslopes are composed of serpentinite breccia (e.g., Fig. 3.4 (C)). 42

Figure 3.6: (A) SE boundary between the Olympus Domain Transition Zone and lower ocean crust cumulate ultramafic rocks and gabbro. This boundary is interpreted as a complex fault zone composed (here at this locality) of primarily Olympus Domain dunites intercalated with lower ocean crust

cumulate ultramafic rocks and gabbros. Discontinuous surfaces are inferred (red lines) and highlight a complex array of structures. The prime structure is the ~W-E orientated structure and is inferred as a high-angle reverse fault. The intensity of deformation varies spatially across the Olympus Transition Zone. The western margin of the uplifted mantle peridotites is less deformed (e.g., B) relative to the intensely deformed SE portion (e.g., A). 44

Figure 3.7: A) A variably serpentinised massive pyroxenite body is wrapped by a matrix composed of a variably serpentinised foliated 'scaly' fabric. 46

Figure 3.8: (A) 3D satellite-terrain hybrid image of the Troodos Mantle Sequence, highlighting the extent and differences in terrain and geomorphology between the Olympus and Artemis domains. Locations of inset images (B to E) shown. (B) Artemis domain serpentine gouge displaying the complex and intricate structure within recrystallised serpentine breccia-gouge. Hammer for scale. (C) Competent serpentinite block-clast with mutually cross-cutting orthogonally orientated serpentine veins, that is surrounded by highly comminuted serpentine cataclasite and localised serpentine gouge. (D) Artemis domain clast-gouge mountainside structure, highlighting the complex domain-wide network of isolated competent serpentinised block-clasts surrounded by weaker serpentine breccia-gouge. Viewing platform overlooking the former Amiantos asbestos mine for scale. (E) Actively collapsing Artemis domain hillslopes due to high proportions of weak, friable, serpentine gouge. 48

Figure 3.9: (A) Foliated serpentine gouge orientated 290/42 SW at the A locality. Hammer for scale. (B) Typical Artemis domain block-clast-breccia-gouge assemblage with clasts of Competent Serpentinised Peridotite and Lower Crustal and Cumulate Ultramafic Rocks. Foliated gouge wraps around competent clasts. Hammer for scale. (C) NE boundary of the Artemis domain highlights the chaotic nature of the Artemis domain. The general orientation of the structure is of a low dipping angle. 49

Figure 3.10: (A) Scanning electron microscope back-scattered electron (BSE) image of the partly serpentinised Olympus domain with the olivine-serpentine mesh interface highlighted. Common micro-fracturing associated with the dissolution and transformation of primary olivine to secondary serpentine through the serpentinisation style of partial serpentinisation hydration reactions. (B) Cross-polarised light photomicrograph of a typical Artemis

domain completely serpentinised competent clast with variable dynamically recrystallised serpentine and associated cataclastic deformation. (C) Oxygen and hydrogen stable isotope plot of published serpentine measurements (Heaton, 1976; Magaritz and Taylor, 1974; Nuriel et al., 2009). Troodos Mantle Sequence values are separated based on sample location either from the Olympus or Artemis domain. Calculated serpentine oxygen and hydrogen stable isotope values in equilibrium with Cyprus meteoric water ($\delta^{18}O$ -7 ‰, δD -35 ‰; e.g., Boronina et al., 2005), Cretaceous seawater ($\delta^{18}O$ -1 ‰, δD -7 ‰; e.g., Heaton and Sheppard, 1977), and slab-derived metamorphic water ($\delta^{18}O$ +7.8 ‰, δD -15 ‰; e.g., Alt and Shanks, 2006) are shown. Triangles represent calculated serpentine values in equilibrium using empirical oxygen isotope fractionation factors from Wenner and Taylor (1971) and hydrogen isotope fractionation factors from Saccocia et al., (2009b). Squares represent calculated serpentine values in equilibrium using semi-empirical oxygen isotope fractionation factors from Zheng (1993) and empirical hydrogen isotope fractionation factors from Saccocia et al. (2009). 54

Figure 3.11: (A) Uplift model set up. One-dimensional horizontally confined model where elevation is determined by subtracting erosion from the isostatic uplift in response to an advancing average serpentinisation transformation front. Model is repeated over a number of iterative steps from an initial elevation of 0 m for a total run time of 5.5 Myr. Differing parameters are utilised for each domain (see Table 3.3). (B) Olympus domain isostatic uplift output shown with no erosion applied. Output highlights the theoretical maximum surface uplift that can be generated through an advancing average serpentinisation transformation front. (C) Olympus domain elevation model output shown, where differential erosional parameters are applied to the uplift model, generating an elevation value through subtracting erosion from surface uplift. Artemis domain total elevation output is also shown in dashed. Inflection point at 4.4 Myr highlights the change in parameterisation from Olympus to Artemis (Table 3.3). (D) Olympus domain evolving thickness output shown highlights the interplay between erosion and the advancing serpentinisation front in producing the thickness of the domain. (E) Olympus domain exhumation total is shown along with the Artemis domain exhumation total (in dashed). Inflection

point at 4.4 Myr represents the activation of Artemis parameters (see Table 3.3). 60

Figure 3.12: Serpentine dissolution time vs particle size under varying pH conditions log-log plot (see main text for details). Serpentine dissolution rate from Thom et al., (2013). 62

Figure 3.13: A schematic illustration of our uplift model for the Troodos Mantle Sequence Model highlights the temporal evolution within the Troodos Mantle Sequence culminating in differential serpentinite diapirism and exhumation resulting from contrasting serpentinisation styles between both diapiric domains. 68

Figure 3.14: Output from the mechanistic uplift model applied to the St. Peter and St. Paul Rocks. 71

Figure 3.15: Output from the mechanistic uplift model applied to the New Idria Serpentinite Diapir....72

Figure 3.16: Output from the mechanistic uplift model applied to Macquarie Island. 74

Figure 4.1: (A) Geological map of the Troodos ophiolite with the bullseye geometry of the Mantle Sequence highlighted along with the Limassol Forest Complex terrane, the Cyprus Arc, and northernmost portion of the Eratosthenes Seamount. (B) Geological map of the Troodos Mantle Sequence, adapted and updated from Wilson (1959). Water sample, Precipitate sample, and Artemis Bulk Rock sample locations are shown. Shaded area shows the abandoned Amiantos asbestos mine. Location of the Allas spring is shown (Rizoulis et al., 2016). 80

Figure 4.2: Compilation of $^{87}Sr/^{86}Sr$ of published data from sedimentary subbasins of the Mediterranean. Plot is from (Schildgen et al., 2014). Data is sourced from Schildgen et al. (2014; and references therein) 83

Figure 4.3: (A) Artemis Diapir serpentinite breccia sample DJ1 is shown with aragonite carbonate infilling matrix porosity. Sample shows serpentine vein hosted within the infilling aragonite carbonate. (B) A more competent completely serpentinised clast within the Artemis Diapir yielding a complex hierarchical mutually cross-cutting serpentine and carbonate veinset. Carbonate veins commonly cross-cut most serpentine veins, but in rare occurrences serpentine veins cross-cut carbonate veins. (C) Serpentine-magnesite clast-matrix assemblage. (D) Small hyperalkaline pH >11 seep

in the Artemis Diapir associated pyroaurite with precipitation of brucite with minor calcite and halite.....85

Figure 4.4: (A) TRAV1 travertine deposit highlighting multiple layers of precipitation. Material composed of calcite, aragonite, brucite, halite, and detrital serpentine. Hammer for scale. (B) A portion of the TRAV2 deposit hosted in a crack-seal serpentine-carbonate vein assemblage. Centre of the crack-seal syntaxial vein is composed of calcite displaying multiple episodes of precipitation. Variable recrystallisation of the wall rock is also indicated. (C) TRAV3 travertine deposit highlighting successive travertine precipitation episodes. Hyperalkaline pH 11.5 water seep is shown emanating from the Artemis serpentinite breccia. Hammer for scale. .87

Figure 4.5: Artemis' Tears spring site is shown. High pH >11.5 hyperalkaline waters emanate from five discrete seeps (shaded dark blue). Precipitates composed of a harder carbonated material (shaded cream) and a softer brucite-dominated material (shaded grey) are associated with hyperalkaline water discharge. Lower pH 8 waters emanate from a shallow drainage channel forming a creek, waters flow downhill and mix with emanating hyperalkaline waters, precipitating softer brucite-dominated material. 89

Figure 4.6: Time series of annotated field pictures is shown over a 10-month period (May 2019 – March 2020). (A) & (B) May 2019 field image showing the respective outlines of softer brucite-dominated material and harder carbonated travertine material and sites of hyperalkaline water seeps. (C) July 2019 – softer brucite-dominated and harder carbonated travertine deposits have partially dried up. Hyperalkaline water seep MM2 was actively discharging water and was sampled. Other hyperalkaline seeps had mostly dried up. (D) March 2020 – continuation of hyperalkaline water discharge and precipitation of both harder carbonated travertine deposits and softer-brucite dominated deposits. A new deposit of harder travertine carbonated materials had formed from hyperalkaline water discharge. March 2020 yields marked lower amounts of softer brucite-dominated material relative to May 2019.....90

Figure 4.7: Close up field picture showing the pool of high pH >11.5 hyperalkaline water (BX1) associated with soft material primarily composed of brucite with minor calcite, aragonite, halite, and detrital serpentine. Harder material is

primarily composed of calcite and aragonite with minor brucite, halite, and detrital serpentine. 91

Figure 4.8: (A) Annotated field picture looking downhill into the river, distance from BX3 to BX7 is ~25 m. Dark blue shading denotes seep localities. Purple dots reflect precipitate sampling points. (B) Alternative view of the Artemis' Tears site, highlighting where initial precipitation of softer brucite-dominated material occurs at the point where lower pH 8 surficial stream waters mix with high pH >11.5 waters. (C) Field picture of the Artemis' Tears spring site showing greater context of site location that is located at the floor of a valley, which drains the completely serpentinised mantle rocks (up to 1750 m asl) of the Artemis Diapir. 92

Figure 4.9: Plots of Ca, Na, Mg, and Si (log scale) vs pH. Scales are equal in all subplots. Circles reflect data from this study. Squares reflect data from (Neal and Shand, 2002) and diamonds reflect data from (Rizoulis et al., 2016).115

Figure 4.10: (A) Cl vs Na plot of Troodos Mantle Sequence waters, dashed line reflects a 1:1 molar ratio, which in this case denotes a halite dissolution line. Dashed and dotted line reflets the seawater dilution line. Lower pH <10 waters yield low Na and Cl concentrations. (B) SO_4 vs Ca plot. Dashed 1:1 molar line in this case reflects the gypsum dilution line. (C) SO_4 vs Cl plot. (D) Cl vs K plot. (E) SO4 vs B. (F) SO_4 vs Li. (G) SO_4 vs Cs. (H) SO_4 vs Ba. 117

Figure 4.11: A) Plot of Mg/Ca (mol/mol) and pH. (B) Plot of Sr/Ca (µmol/mmol) and pH. Clear distinction between lower pH <10 waters and high pH >11.5 waters is shown. Mg/Ca (mol/mol) of modern seawater is ~5.2 (e.g., Coggon et al., 2010) and Sr/Ca (µmol/mmol) is ~8.5 (e.g., Coggon et al., 2010). Cretaceous ~90 Ma seawater Mg/Ca (mol/mol) is ~1.5 and Sr/Ca (µmol/mmol) is ~2 (Coggon et al., 2010). 123

Figure 4.12: Plot of Na/Cl (mol/mol) and Ca/SO_4 (mol/mol). Ca/SO_4 is log scale. 1:1 Molar ratio line refers to the respective halite and gypsum dissolution line. 124

Figure 4.13: (A) Plot of Mg and Na concentrations in Troodos Massif waters from this study and others. Waters from the Samail ophiolite, Oman are also shown. (B) Plot of Mg and Si concentrations in Troodos Massif waters from this study and others. Waters from the Samail ophiolite, Oman are also shown. (C) Plot of Ca and Cl concentrations in Troodos Massif

waters from this study and others. Waters from the Samail ophiolite, Oman are also shown. 126

Figure 4.14: Plot of sampled waters and their respective groups $^{87}Sr/^{86}Sr$ vs pH. Boundaries of Troodos volcanic glasses (Rautenschlein et al., 1985), Troodos hydrothermally altered rock (Bickle and Teagle, 1992), Cretaceous ~90 Ma and modern day seawater (McArthur et al., 2012), and Cyprus Messinian evaporites (Flecker and Ellam, 2006; McCulloch and Deckker, 1989; Müller and Mueller, 1991) are shown. 127

Figure 4.15: Plot of $^{87}Sr/^{86}Sr$ and Sr/Ca (ng/g/µg/g) of Troodos Mantle Sequence waters, Artemis bulk rock, Artemis 10% acetic leachate, Artemis bulk rock residue, Artemis travertine, Artemis calcite vein, Artemis aragonite vein. Messinian evaporite compositions are from ODP Leg 107 (Müller et al., 1990). High pH >11.5 waters reflect variable mixing of contrasting Sr reservoirs located in trace carbonates and rock. Lower pH <10 waters likely reflect relative mixing of three distinct solid Sr reservoirs. See text for details. 128

Figure 4.16: Plot of $\delta^{18}O_{Water}$ and δD_{Water} values of sampled Troodos Mantle Sequence waters. Global meteoric water line (GMWL) is plotted (Craig, 1961). The local Cyprus meteoric water line is also plotted (Boronina et al., 2005). Shaded area reflects a closed system water-rock equilibrium model (Taylor, 1977) with differing proportions of W/R shown. 129

Figure 4.17: Plot of $^{87}Sr/^{86}Sr$ and $\delta^{18}O$ of sampled waters and precipitates. Calculated $\delta^{18}O_{Water}$ values in equilibrium with carbonates (calcite and aragonite) at temperatures of 5°C to 25°C are shaded in grey. Calcite and aragonite fractionation factors of Zheng (1999) were used. 136

Figure 4.18: Oxygen stable isotope values of precipitates sampled within the Troodos Mantle Sequence. Precipitates are grouped into Travertine, Magnesite, Calcite veins and Aragonite veins. Calculated ranges of oxygen stable isotope values in equilibrium with lower pH <10 water ($\delta^{18}O$ -7.6 ‰) and high pH >11.5 hyperalkaline water ($\delta^{18}O$ -3.5 ‰) at temperatures between 0 and 25°C are shown. Respective magnesite, calcite, and aragonite fractionation factors of Zheng (1999) were used. 137

Figure 4.19: $\delta^{13}C_{(VPDB)}$ Caltech plot of precipitates sampled within the Troodos Mantle Sequence. Boundaries of Atmospheric $\delta^{13}C_{(VPDB)}$ composition (Keeling, 1958) and Mantle $\delta^{13}C_{(VPDB)}$ composition (Rollinson, 2014) are shown. 138

Table of Figures

Figure 4.20: (A) $^{87}Sr/^{86}Sr$ Caltech plot of progressive leaching results of completely serpentinised whole rocks sampled within the Artemis Diapir. Boundaries of Troodos volcanic glasses (Rautenschlein et al., 1985), Troodos hydrothermally altered rock (Bickle and Teagle, 1992), Cretaceous ~90 Ma and modern day seawater (McArthur et al., 2012), and Cyprus Messinian evaporites (Flecker and Ellam, 2006; McCulloch and Deckker, 1989; Müller and Mueller, 1991) are shown. (B) Sr (ng/g) concentration Caltech plot of progressive leaching results of whole rocks. 167

Figure 4.21: Caltech plot of Li (µg/g) concentration (log scale) in different rock types within the completely serpentinised Artemis Diapir. 168

Figure 4.22: Completely serpentinised mantle rock block within the Artemis Diapir. Sample AR1 surrounds the margin of the block and yields more radiogenic $^{87}Sr/^{86}Sr$ ratios and lower Sr (ng/g) concentrations relative to the centre of the block (sample AR2). Filled squares reflect $^{87}Sr/^{86}Sr$ ratios. Empty squares reflect Sr (ng/g) concentration. Each colour reflects a progressive leaching step. Each leaching step balances against the bulk rock value. 169

Figure 4.23: Sample CU unannotated and annotated image pairs. Progressive leaching analytical results ($^{87}Sr/^{86}Sr$ and Sr (ng/g) concentration) are shown. Star reflects chrysotile vein CY3. Respective colours reflect each leaching step. Filled squares/star reflect $^{87}Sr/^{86}Sr$ ratios and empty squares/star reflect Sr (ng/g). CU1, CU2, CU4 yield differing serpentine textures at the outcrop scale, but similar $^{87}Sr/^{86}Sr$ values and Sr (ng/g) concentrations. Progressive leaching results show contrasting $^{87}Sr/^{86}Sr$ reservoirs (~0.705-6 and ~0.7087) are preserved, culminating in a mixed whole rock $^{87}Sr/^{86}Sr$ signal (~0.7073). The serpentine vein CU5 sample yields more radiogenic $^{87}Sr/^{86}Sr$ values, but lower Sr (ng/g) concentrations. 170

Figure 4.24. A schematic illustration of the Troodos Mantle Sequence highlighting the temporal evolution of contrasting Sr reservoirs reflected in the whole rock samples. A pre-Messinian pervasive serpentinisation event modifies the radiogenic Sr isotope composition of the Troodos Mantle Sequence from assumed mantle values of ~0.7037 (Rautenschlein et al., 1985) to 0.705-6. Subsequent serpentinisation by waters with a Messinian evaporite $^{87}Sr/^{86}Sr$ signal of ~0.7086-89 contaminates the underlying mantle rocks. Once mantle rocks are exhumed, the infiltration of meteoric water is inevitable. This results in the remobilisation and redistribution of

geochemical and isotopic signals from previous serpentinisation events, culminating in mixing of these distinct reservoirs as reflected in the whole rocks of the Artemis Diapir. 178

Figure 4.25: Schematic diagram of the Artemis Diapir, Cyprus, highlighting how contrasting fluid evolution pathways result in hyperalkaline pH >11.5 waters (red), lower pH <10 surficial waters (blue), and lower pH <10 Amiantos mine waters (green) emanating from the Artemis Diapir. .. 184

Figure 5.1: (A) Geological map of the Troodos ophiolite with the bullseye geometry of the Mantle Sequence highlighted along with the Limassol Forest Complex terrane, the Cyprus Arc, and northernmost portion of the Eratosthenes Seamount. (B) Geological map of the Troodos Mantle Sequence, adapted and updated from Wilson (1959). Bulk Rock sample locations are shown. 190

Figure 5.2: Oxygen and hydrogen stable isotope plot of published serpentine measurements (Heaton, 1976; Magaritz and Taylor, 1974; Nuriel et al., 2009). Troodos Mantle Sequence values are separated based on sample location either from the Artemis or Olympus Diapirs. Calculated serpentine oxygen and hydrogen stable isotope values in equilibrium with Cyprus meteoric water ($\delta^{18}O$ -7 ‰; δD -35 ‰; e.g., Boronina et al., 2005), Cretaceous seawater ($\delta^{18}O$ -1 ‰; δD -7 ‰; e.g., Heaton and Sheppard, 1977), and Messinian brine water ($\delta^{18}O$ +0.6 ‰; δD +1.1 ‰; e.g., Evans et al., 2015) are shown. Triangles represent calculated serpentine values in equilibrium using empirical oxygen isotope fractionation factors from Wenner and Taylor (1971) and hydrogen isotope fractionation factors from Saccocia et al. (2009b). Squares represent calculated serpentine values in equilibrium using semi-empirical oxygen isotope fractionation factors from Zheng (1993) and empirical hydrogen isotope fractionation factors from Saccocia et al. (2009). 192

Figure 5.3: (Left) Plot of Bulk Rock $^{87}Sr/^{86}Sr$ and Bulk Density (kg/m^3) of samples from the Troodos Mantle Sequence. A least squares regression through samples from the Olympus Diapir has a R^2 value of 0.96. (Middle) Plot of $^{87}Sr/^{86}Sr$ vs Sr (ng/g) concentration of Bulk Rock samples located within the Olympus Diapir, Artemis Diapir, and Limassol Forest Complex. (Right) Plot of $^{87}Sr/^{86}Sr$ vs Sr (ng/g) concentration of 10% Acetic Acid Leachates and Bulk Residue samples located within the Olympus Diapir, Artemis Diapir, and Limassol Forest Complex. Boundaries of Troodos volcanic

glasses (Rautenschlein et al., 1985), Troodos hydrothermally altered rock (Bickle and Teagle, 1992), Cretaceous ~90 Ma and modern day seawater (McArthur et al., 2012), and Cyprus Messinian evaporites (Flecker and Ellam, 2006; McCulloch and Deckker, 1989; Müller and Mueller, 1991) are shown.....243

Figure 5.4: A series of Caltech plots of determined $^{87}Sr/^{86}Sr$ ratios from progressive leaching step results of respective sample types within the Troodos Massif and Limassol Forest Complex. Boundaries of Troodos volcanic glasses (Rautenschlein et al., 1985), Troodos hydrothermally altered rock (Bickle and Teagle, 1992), Cretaceous ~90 Ma and modern day seawater (McArthur et al., 2012), and Cyprus Messinian evaporites (Flecker and Ellam, 2006; McCulloch and Deckker, 1989; Müller and Mueller, 1991) are shown.....244

Figure 5.5: A series of Caltech plots of Sr (ng/g) concentrations from progressive leaching step results of respective sample types within the Troodos Massif and Limassol Forest Complex. 246

Figure 5.6: (A) Plot of $^{87}Sr/^{86}Sr$ and Li (ng/g) of Bulk Rocks with a parallel plot of progressive leaching steps 10% Acetic Leachate, 3M HCl Leachate, and Bulk Residue. (B) Plot of $^{87}Sr/^{86}Sr$ and Li (ng/g) of Bulk Rocks with a parallel plot of progressive leaching steps 10% Acetic Leachate, 3M HCl Leachate, and Bulk Residue. (C) Plot of $^{87}Sr/^{86}Sr$ and Li (ng/g) of Bulk Rocks with a parallel plot of progressive leaching steps 10% Acetic Leachate, 3M HCl Leachate, and Bulk Residue. (D) Plot of $^{87}Sr/^{86}Sr$ and Li (ng/g) of Bulk Rocks with a parallel plot of progressive leaching steps 10 % Acetic Leachate, 3M HCl Leachate, and Bulk Residue. Boundaries of Troodos volcanic glasses (Rautenschlein et al., 1985), Troodos hydrothermally altered rock (Bickle and Teagle, 1992), Cretaceous ~90 Ma and modern day seawater (McArthur et al., 2012), and Cyprus Messinian evaporites (Flecker and Ellam, 2006; McCulloch and Deckker, 1989; Müller and Mueller, 1991) are shown.....247

Figure 5.7: Primitive mantle normalised trace element plots using primitive mantle values from Palme and O'Neill (2014). (A) Refers to whole rock samples from the Olympus Diapir and (B) whole rock samples from the Artemis Diapir.248

Figure 5.8: Plots of $^{87}Sr/^{86}Sr$ and Rb/K (ng/g/µg/g), Rb/Cs and K/Cs. Previously published serpentine ratio values are also shown as shaded areas. Shaded areas reflect the reported range, which typically spans several orders of

magnitude (e.g., Peters et al. (2017) and references therein). In addition, Troodos volcanic glasses, Marine sediment, and Troodos Altered Ocean Crust values are also shown (Elliott et al., 1997; Patten et al., 2017; Woelki et al., 2020). 249

Figure 5.9: (A) Plot of δ^{11}B and B (µg/g) of *in situ* LA-MC-ICP-MS and LA-ICP-MS data. Error bars are ±2SE of the mean of 100 integration cycles. Most symbols are larger than the ±2SE of the analysis. (B) Plot of $^{87}Sr/^{86}Sr$ and B (µg/g) is shown. 10% Acetic Leachates were measured by ICP-MS and rock samples were prepared as pressed powder pellets and measured by LA-ICP-MS. (C) Plot of $^{87}Sr/^{86}Sr$ and δ^{11}B. Troodos Fresh Volcanic Glass values (Fonseca et al., 2017) are shown and error bars are equivalent to ±2σ of the mean of reported values. Seawater values (Foster et al., 2010; Spivack et al., 1987) and primitive mantle values (Chaussidon and Jambon, 1994) are also shown.....257

Figure 5.10: A series of Caltech plots showing δ^{11}B and B (µg/g) concentration data from LA-MC-ICP-MS on samples from the Olympus Diapir, Artemis Diapir, and Limassol Forest Complex. Boundaries of δ^{11}B of Troodos volcanic glasses (Fonseca et al., 2017), Messinian evaporites (Paris et al., 2010), modern day seawater (Foster et al., 2010), and primitive mantle (Chaussidon and Jambon, 1994) are shown. Boundaries of B (µg/g) of Troodos volcanic glasses (Fonseca et al., 2017), modern day seawater (Spivack et al., 1987), and primitive mantle (Chaussidon and Jambon, 1994) are also shown. Shading is equivalent to 2σ of the reported value. 258

Figure 5.11: A series of Caltech plots showing B (µg/g) concentration data from LA-MC-ICP-MS on pressed powder pellets and 10% Acetic leachate ICP-MS data from the Olympus Diapir, Artemis Diapir, and Limassol Forest Complex. Boundaries of B (µg/g) of Troodos volcanic glasses (Fonseca et al., 2017), modern day seawater (Spivack et al., 1987), and primitive mantle (Chaussidon and Jambon, 1994) are also shown. Shading is equivalent to 2σ of the reported value.....259

Figure 5.12: *In situ* Boron element map of a completely serpentinised sample from within the Artemis Diapir. Boron data is plotted as counts per second and the relative differences are colour mapped accordingly. Three distinct B phases are reflected within the map. 260

Table of Figures

Figure 5.13: Plots of $\delta^{11}B$ and B (µg/g) of published serpentine and ocean crust values. Errors bars are equivalent to ±2SE of the mean and most error bars are smaller than markers. Plots are divided into groupings of showing all serpentine and ocean crust values, all ocean crust data, all Troodos and Limassol Forest Complex data, and all serpentine data (Benton et al., 2001; Boschi et al., 2008; Fonseca et al., 2017; Foster et al., 2010; Harvey et al., 2014; Ishikawa and Nakamura, 1992; Marschall et al., 2017; Martin et al., 2016; Smith et al., 1995; Spivack and Edmond, 1987; Vils et al., 2009; Yamaoka et al., 2012, 2015a). 263

Figure 5.14: Troodos ophiolite isotope-depth plot of ocean crustal rocks and Troodos Mantle Sequence. Troodos ophiolite crustal stratigraphy is adapted from Malpas et al. (1989). Depths of samples have been scaled accordingly to the stacked crustal stratigraphy of Malpas et al. (1989). Troodos ocean crust $\delta^{11}B$ data (Yamaoka et al., 2015b), $\delta^{18}O$ (Gillis and Robinson, 1990; Heaton and Sheppard, 1977; Rautenschlein et al., 1985; Rommel et al., 1987; Schiffman and Smith, 1988; Spooner et al., 1977, 1974; Vibetti, 1993, 1987), $^{87}Sr/^{86}Sr$ (Bickle and Teagle, 1992; Chapman and Spooner, 1977; Gillis and Robinson, 1990; Kawahata and Scott, 1990; Rautenschlein et al., 1985; Rommel et al., 1987; Spooner et al., 1977) are plotted with depth. In the $\delta^{11}B$-depth plot, black squares reflect $\delta^{11}B_{Fluid}$ values calculated in equilibrium from measured rock $\delta^{11}B$ values using the boron equilibrium model coupled with a Bayesian inversion engine (Appendix A) using reasonable priors (Table 5.12), error bars are equivalent to ±2σ error. The $\delta^{11}B_{Fluid}$ values in equilibrium with Troodos Mantle Sequence serpentinites is also shown with respective minimum, mean, and maximum measured serpentine values inverted to yield estimated $\delta^{11}B_{Fluid}$ values, error bars are equivalent to ±2σ error. The range of calculated $\delta^{18}O_{Serp}$ values in equilibrium with Troodos hydrothermal fluid ($\delta^{18}O_{HydrothermalFluid}$ +2 to +3.5 ‰; Turchyn et al., 2013) is shown. Previously published serpentine $\delta^{18}O$ published isotope values are shown (Heaton, 1976; Magaritz and Taylor, 1974; Nuriel et al., 2009). A LOWESS (Locally weighted scatterplot smoothing; Cleveland, 1979) is a non-parametric fitting technique and was applied to measured rock isotope values (yellow, red, blue) and calculated fluid isotope values (black), with shading equivalent to ±2σ error. Boundaries of respective $\delta^{11}B$ signatures of Troodos volcanic glasses (Fonseca et al., 2017), Messinian evaporites (Paris et al., 2010), and modern day seawater

(Foster et al., 2010) are shown. Boundaries of respective $\delta^{18}O$ signatures of mantle values (Mattey et al., 1994), Cretaceous seawater (Heaton and Sheppard, 1977), Troodos hydrothermal fluid (Turchyn et al., 2013) are shown. Boundaries of respective $^{87}Sr/^{86}Sr$ signatures of Troodos volcanic glasses (Rautenschlein et al., 1985), Troodos hydrothermal fluid (Bickle and Teagle, 1992), Cretaceous seawater (McArthur et al., 2012); Cyprus Messinian evaporites (Flecker and Ellam, 2006; McCulloch and Deckker, 1989; Müller and Mueller, 1991) are shown. 274

Figure 5.15: Plot of $\delta^{11}B$ and B (µg/g) and $B_{Seawater}/B_{VentFluid}$ with previously published hydrothermal vent fluid data. A least squares regression through the Back-arc hydrothermal vent fluids and the East Pacific Rise fluids yields an R^2 value of 0.88. The Cretaceous Troodos hydrothermal fluid $\delta^{11}B$ endmember is also shown and is estimated through the boron equilibrium model (see Appendix A). Seawater values are from Foster et al. (2010; Spivack et al., 1987). Primitive Mantle values are from Chaussidon and Jambon (1994). Troodos Basaltic Glass values are from Fonseca et al. (2017) and error bars reflect 2σ of the mean value. 278

Figure 5.16: (A) Cross-section of the present-day scenario of the current geometry of the Cyprus Arc subduction zone. (B) Cross-section of the Troodos Mantle Sequence and estimated location of the slab beneath the Mount Olympus region. Scale is 1:1. 285

Figure 5.17: Oxygen and hydrogen stable isotope plot of published serpentine measurements (Heaton, 1976; Magaritz and Taylor, 1974; Nuriel et al., 2009). Troodos Mantle Sequence values are separated based on sample location either from the Artemis or Olympus Diapirs. Calculated serpentine oxygen and hydrogen stable isotope values in equilibrium with Cyprus meteoric water ($\delta^{18}O$ -7 ‰; δD -35 ‰; e.g., Boronina et al., 2005); hyperalkaline high pH >11.5 waters ($\delta^{18}O$ -3.5 ‰; δD -28 ‰; Chapter 4); Cyprus slab-derived fluid ($\delta^{18}O$ +4 ‰; δD -23 ‰; this study), and Messinian brine water ($\delta^{18}O$ +0.6 ‰; δD +1.1 ‰; e.g., Evans et al., 2015)) are shown. Triangles represent calculated serpentine values in equilibrium using empirical oxygen isotope fractionation factors from (Wenner and Taylor, 1971) and hydrogen isotope fractionation factors from Saccocia et al. (2009b). Squares represent calculated serpentine values in equilibrium using semi-empirical oxygen isotope fractionation factors from Zheng (1993) and empirical hydrogen isotope fractionation factors from Saccocia

et al. (2009). Fluid mixing trajectories at constant temperatures between Cyprus meteoric water and Messinian brine water is shown. 288

Figure 5.18: Temperature-$\delta^{11}B_{Fluid}$ density hexbin plot with marginal posterior probability distributions from the Bayesian inversion boron equilibrium model (Appendix A). (A) Plot reflects an inversion output of a $\delta^{11}B_{Serp}$ value of +7 ± 1 ‰ (lowest $\delta^{11}B_{Serp}$ value; Table 5.7) with Cyprus slab-derived fluid priors (Table 5.12). (B) Plot reflects an inversion output of a $\delta^{11}B_{Serp}$ value of +12.5 ± 3.2 ‰ (average value of Troodos Mantle Sequence $\delta^{11}B_{Serp}$ data; 1σ; n = 48; Table 5.7) with Cyprus slab-derived fluid priors (Table 5.12). (C) Plot reflects an inversion output of a $\delta^{11}B_{Rock}$ value of +2.5 ± 2.5 ‰ (estimated composition of slab-derived smectite; Yamaoka et al., 2015b) with Cyprus slab-derived fluid priors (Table 5.12). (D) Plot reflects an inversion output of a $\delta^{11}B_{Serp}$ value of +18.4 ± 1 ‰ (highest $\delta^{11}B_{Serp}$ value; Table 5.7) with Cyprus slab-derived fluid priors (Table 5.12). Note: Estimated $\delta^{11}B_{Fluid}$ compositions of (B) and (C) are similar. 295

Figure 5.19: Illustration of the set up for the mass balance calculation. The assumed proportions of the Troodos Mantle Sequence and the respective volume of dehydrating and dewatering downgoing Cyprus slab required to harvest H_2O and focus into the Mount Olympus region are shown. Orange denotes 1 wt.% H_2O and a volume of 100 x 150 x 2 km. Blue denotes 3 wt.% H_2O and a volume of 80 x 60 x 2 km. Green denotes 6 wt.% H_2O and a volume of 40 x 60 x 2 km. Illustration not to scale. See text for full details.....301

Figure 5.20: Temperature-$\delta^{11}B_{Fluid}$ density hexbin plot with marginal posterior probability distributions from the Bayesian inversion boron equilibrium model (Appendix A). (A) Plot reflects an inversion output of a $\delta^{11}B_{Serp}$ value of +12.5 ± 3.2 ‰ with Messinian meteoric water priors (Table 5.12). (B) Plot reflects an inversion output of a $\delta^{11}B_{Serp}$ value of +12.5 ± 3.2 ‰ with low temperature <50°C priors (Table 5.13). 305

Figure 5.21: Schematic illustration of the Cyprus Arc at differing stages in its evolution from: (A) Mid-Miocene subduction, where dewatering and dehydration reactions in the downgoing slab are insufficient to induce serpentinite diapirism; (B) the Messinian salinity crisis results in uplifted localised evaporite basins, where meteoric water interacts with overlying Troodos sediments and serpentinises the underlying mantle rocks; the approach of

the Eratosthenes seamount induces fluid focussing of the dewatering and dehydrating Cyprus slab underneath the Mount Olympus region; (C) Pliocene-Pleistocene, Eratosthenes seamount stalls the Cyprus Arc subduction zone, where prolonged fluid focussing has resulted in serpentinisation-induced differential uplift and exhumation forming the Olympus Diapir; (D) Late-Pleistocene to Holocene, meteoric water infiltration results in ongoing serpentine alteration mechanisms that manifest as coupled deformation-alteration-recrystallisation processes that result in the differential exhumation of the completely serpentinised Artemis Diapir. 308

Figure 6.1: (A) Geological map of the Troodos ophiolite with the bullseye geometry of the Mantle Sequence highlighted along with the Limassol Forest Complex terrane, the Cyprus Arc, and northernmost portion of the Eratosthenes Seamount. (B) Geological map of the Troodos Mantle Sequence, adapted and updated from Wilson (1959). X-X' shows line of cross-section (Fig. 2.4). Bulk density sample locations shown. 314

Figure 6.2: (A) Field pictures of the cohesive and competent outcrop pattern of the Olympus Diapir. (B) Photomicrograph in PPL and XPL of Olympus Diapir sample AH1. (C) Photomicrograph in PPL and XPL of Olympus Diapir sample AH2. (D) Photomicrograph in PPL and XPL of Olympus Diapir sample AJ2. (B-D) Show a general decrease in bulk density (kg/m^3), increasing serpentinisation extent, increase in whole-rock $^{87}Sr/^{86}Sr$ and decreasing Sr (ng/g) concentration. PPL and XPL photomicrographs show a general increase in recrystallised serpentine manifested as irregular black serpentine veins. Serpentinisation extent is calculated using the equation of Miller and Christensen (1997). 316

Figure 6.3: (A) Field picture of the Artemis Diapir highlighting the incompetent and incohesive outcrop pattern composed of variable proportions of a completely serpentinised blocks-clasts-breccia-gouge assemblage (Evans et al., 2021). (B) Field picture of a more competent and cohesive completely serpentinised block within the Artemis Diapir with corresponding XPL and PPL photomicrographs. Hammer for scale. (C) Field pictures of coherent completely serpentinised clasts with a progressive cataclasite matrix. Hammer for scale. (D) Field pictures showing the Artemis Diapir periphery serpentinite breccia with a greater extent of cataclasite and an increased component of clay-sized gouge. Hammer for scale. (B-D) Shows a general increase in the extent of

serpentine alteration through coupling of deformation-alteration-recrystallisation processes, culminating in the evolution from more competent blocks to a low-density serpentinite breccia endmember (e.g., Evans et al., 2021). 318

Figure 6.4: Schematic diagram of the experimental rig with ultrasonic pulse-echo (P- & S-wave) and electrical resistivity tomography systems with pore fluid and confining pressure control systems. Figure is from Falcon-Suarez et al. (2017).....320

Figure 6.5: Caltech plots showing physical properties Bulk Density (kg/m^3) and Porosity (%). The expected contribution of serpentinisation hydration reactions (blue arrow) and serpentine alteration processes (red arrow) to the overall change in physical properties values is also shown. 328

Figure 6.6: Caltech plots showing physical properties V_p (km/s), V_s (km/s) and their attenuations (inverse quality factors, Q_p^{-1} and Q_s^{-1}). The expected values of unaltered mantle peridotites are also shown. 330

Figure 6.7: Plots of V_p and V_s variation with differential stress (P_{Diff}). Solid lines reflect loading stress and dashed lines reflect unloading stress conditions. 331

Figure 6.8: Plots of Resistivity and Permeability variation with differential stress (P_{Diff}). Solid lines reflect loading stress and dashed lines reflect unloading stress conditions. 333

Figure 6.9: Caltech plots of physical properties parameters resistivity (Ω m) and permeability (m^2). 334

Figure 6.10: Summary figure of physical and hydraulic properties measured in the Troodos Mantle Sequence. 336

Figure 6.11. Caltech plot of reported Bulk Density (kg/m^3) of serpentinised mantle rocks from a range serpentinisation settings on land and in the oceans. See Table 6.2 for references. Arrows reflect reported range. Squares reflect average values with error bars equivalent to 2σ of the mean. 337

Figure 6.12: Caltech plot of reported V_p (km/s) of serpentinised mantle rocks from a range serpentinisation settings on land and in the oceans. See Table 6.2 for references. Arrows reflect reported range. Squares reflect average values with error bars equivalent to 2σ of the mean. 338

Figure 6.13: Caltech plot of reported V_s (km/s) of serpentinised mantle rocks from a range serpentinisation settings on land and in the oceans. See Table 6.2 for references. Arrows reflect reported range. Squares reflect average values with error bars equivalent to 2σ of the mean. 339

Figure 6.14: Caltech plot of reported electrical resistivity (Ω m) of serpentinised mantle rocks from a range serpentinisation settings on land and in the oceans. See Table 6.2 for references. Arrows reflect reported range. Squares reflect average values with error bars equivalent to 2σ of the mean. 340

Figure 6.15: Caltech plot of reported Porosity (%) of serpentinised mantle rocks from a range serpentinisation settings on land and in the oceans. See Table 6.2 for references. Arrows reflect reported range. Squares reflect average values with error bars equivalent to 2σ of the mean. 341

Figure 6.16: Caltech plot of reported Permeability (m^2) of serpentinised mantle rocks from a range serpentinisation settings on land and in the oceans. See Table 6.2 for references. Arrows reflect reported range. Squares reflect average values with error bars equivalent to 2σ of the mean. 342

Figure 6.17: Schematic diagram highlighting the relative measured range in physical properties between differing sites of serpentinisation. 349

Research Thesis: Declaration of Authorship

Print name: Aled Dafydd Evans

Title of thesis: Serpentinisation of the Troodos Massif, Cyprus

I declare that this thesis and the work presented in it are my own and has been generated by me as the result of my own original research.

I confirm that:

1. This work was done wholly or mainly while in candidature for a research degree at this University;
2. Where any part of this thesis has previously been submitted for a degree or any other qualification at this University or any other institution, this has been clearly stated;
3. Where I have consulted the published work of others, this is always clearly attributed;
4. Where I have quoted from the work of others, the source is always given. With the exception of such quotations, this thesis is entirely my own work;
5. I have acknowledged all main sources of help;
6. Where the thesis is based on work done by myself jointly with others, I have made clear exactly what was done by others and what I have contributed myself;
7. Parts of this work have been published as:

Evans, A.D., Teagle, D.A.H., Craw, D., Henstock, T.J., Falcon-Suarez, I.H., 2021. Uplift and exposure of serpentinized massifs: Modeling differential serpentinite diapirism and exhumation of the troodos mantle sequence, Cyprus. J. Geophys. Res. [Solid Earth] 126. https://doi.org/10.1029/2020jb021079

Signature: ..... Date: 6/5/2022

Acknowledgements

In completing this thesis, an enormous amount gratitude is placed to my supervisor, Damon Teagle, for his support, encouragement, mentorship, and conception of this project. Also, thank you for acquiring every opportunity on my behalf, reading and editing this thesis, and sustaining my ambition and motivation throughout these four years.

A huge amount of thanks is also placed to Dave Craw for his support, encouragement, and who was always willing to be the world's most overqualified field assistant. Thank you for our long conversations discussing all things serpentine whilst sipping lattes, and for disseminating the Craw methodology.

I would like to thank all at the Cyprus Geological Survey Department with a special mention to the director Christodoulos Hadjigeorgiou for facilitating access to resources and samples. The undertaking of this project in Cyprus has been a privilege that I will carry for the rest of my days.

I would also like to thank my other supervisors, Rachael James and Gavin Foster, for their time, patience, and knowledge. A huge thanks also to Ismael Falcon-Suarez for his knowledge of all thing's rock physics and for his aid in developing the physical properties dataset. Tim Henstock is thanked for his help and supervision in conceptualising serpentinisation modelling approaches, the first-hand experience of developing a model from concept to completion has been a privilege. I am also indebted to Juerg Matter for your time and knowledge and especially for the additional work of reopening the geochemistry labs during the ongoing pandemic.

A special thanks to Catriona Menzies, for not only interviewing me, but also for the support, encouragement, and help over the years. I have now passed the rock crushing methodology onto the next student. Thank you to Roz Coggon for always having time to talk about my data, its implications, and all things science. A thank you to present and past members of our wider research group who I have interacted with over the last four years: Michelle Harris, Jude Coggon, Tom Belgrano, Liam Bullock, Barbara Zihlmann, Francesca Rotondo, Lewis Grant, and Marta Grabowska.

I would especially like to thank Grace Andrews for the opportunity of being her research assistant on our days off from the Oman Drilling Project. Your introduction to aqueous geochemistry and sample collection techniques inspired me to undertake a water sampling project as part of this thesis.

Acknowledgements

A special thanks and gratitude are placed to Matt Cooper for not only teaching me but also his time and patience in collecting the stream geochemical data during this thesis. Andy Milton is thanked for keeping the various mass spectrometers in line and well behaved, especially when the laser ablation system was connected. Matt and Andy are especially thanked for all the additional work that was involved in keeping the geochemistry labs open and safe during the pandemic. Chris Standish is thanked for his patience, time, and help in developing and acquiring the laser ablation boron isotope data in this thesis.

Agnes Michalik is thanked for her help and support in the clean labs. Richard Pearce is thanked for assistance with XRD analyses and SEM work. Matt Beverley-Smith and Dan Doran are thanked for the never ending list of thin section work. Anita Flohr and Cynthia Dumousseaud are thanked for their assistance with DIC measurements. Adrian Boyce is thanked for oxygen and hydrogen stable isotope analyses of waters. Heather Goring-Harford is thanked for boron isotope analyses. Kate Peel is also thanked for aid in anion measurements. Scott Smith and Matthew Tarling are thanked for their hospitality whilst visiting the University of Otago and for use of the Raman Spectrometer.

Benoit Ildenfonse is also thanked for hunting down an elusive paper hidden away. I would like to thank the following for various conversations on all things serpentine over the last four years: Peter Kelemen, Greg Hirth, Bethany Ehlmann, Chris MacLeod, Julian Pearce, Andy McCaig, Tony Morris, Alastair Robertson, Gretchen Früh-Green, Susan Lang, Billy Brazelton, Dave Butterfield, Mike Cheadle, Ian Bastow, and Chris Ogden.

Thank you to my officemates Tanya Beattie and Callum Fry for keeping every day different and constant support.

Thank you to the entire NOCS Estates Team for all their work, especially during the pandemic in minimising risk for all those present on site during the various lockdowns. This is also extended to those in leadership roles in both the University of Southampton and NOCS in keeping the site open and functioning despite difficulties caused by COVID-19.

A special thank you to Abbie, during this thesis your support, care, and most of all patience has sustained me during these years. Finally, Mam thank you for everything and your sacrifices that have given me the privilege to be able to undertake this thesis.

Diolch am bopeth.

Definitions and Abbreviations

DIC ..... Dissolved Inorganic Carbon

DSDP ..... Deep Sea Drilling Program

DSW ..... Distilled Seawater

DW ..... Distilled Water

EC ..... Electrical Conductivity

EKS ..... East Kilbride Snow

GMWL ..... Global Meteoric Water Line

ICDP ..... International Continental Drilling Program

IODP ..... International Ocean Drilling/Discovery Program

LFC ..... Limassol Forest Complex

MORB ..... Mid-Ocean Ridge Basalt

NOCS ..... National Oceanography Centre Southampton

ODP ..... Ocean Drilling Program

PPL ..... Plain Polarised Light

PPT ..... Parts per thousand

QQQ ..... Triple Quadrupole

SEM ..... Scanning Electron Microscope

SUERC ..... Scottish Universities Environmental Research Centre

TDS ..... Total Dissolved Solids

VSMOW ..... Vienna Standard Mean Ocean Water

XPL ..... Cross Polarised Light

MB ..... Mass Balance

Chapter 1 Introduction

1.1 Rationale

Mantle rocks are the most common rock type on Earth, but surface exposures of mantle rocks are generally rare and when they do occur these ultramafic rocks are generally strongly to completely altered (Guillot et al., 2015; Kelemen et al., 2011). This alteration is predominantly manifest as a secondary hydrated magnesium silicate mineral – serpentine (e.g., Evans et al., 2013). Serpentine is a product of the interaction between primary minerals such as olivine and pyroxene with water, a process termed serpentinisation. Serpentinisation transforms dense, anhydrous, mechanically strong mantle peridotites into weak, low-density, hydrated serpentinites containing up to 13.5 % water. As a result, serpentinisation is considered a chemical and physical process, inducing up to 40 % volume expansion, due to a significant decrease in bulk density from 3,300 kg/m^3 to 2,550 kg/m^3 (Macdonald and Fyfe, 1985; Toft et al., 1990). These dramatic serpentinisation-induced physicochemical transformations of mantle rocks consequently play critical roles in the Earth system (e.g., Kerrick, 2002) by aiding plate tectonics (Hirth and Guillot, 2013), providing energy for microbial communities (e.g., Schrenk et al., 2013; Sleep et al., 2004), and acting as a geological sponge for fluid-mobile elements (e.g., Alt et al., 2013; Früh-Green et al., 2004).

In addition to serpentinisation hydration reactions, subsequent deformation-alteration-recrystallisation of serpentine further modifies the physicochemical characteristics of altered mantle rocks (Evans et al., 2021; Klein et al., 2020, 2017; Milliken et al., 1996; Snow and Dick, 1995). Altered mantle rocks recovered from the seafloor and on land reflect variable proportions of serpentinisation hydration reactions and the ongoing alteration, oxidation, and carbonation of mantle rocks. These contrasting styles of mantle rock alteration occur as a progressive series of fluid rock interaction events. Consequently, subsequent serpentine alteration events may obscure and overprint earlier serpentinisation events, inhibiting the identification of the conditions of distinct serpentinisation episodes. In this thesis, I focus on the variably altered mantle rocks of the Troodos ophiolite, Cyprus, that display evidence of both serpentinisation hydration reactions and serpentine alteration processes (Evans et al., 2021; Gass and Masson-Smith, 1963; Wilson, 1959). My aim is to unravel the progressive sequence of fluid rock interaction events that have resulted in the occurrence of mantle rocks forming the highest elevations of Cyprus.

1.2 Serpentinisation and its wider importance in the Earth system

Serpentinisation and its resulting reaction pathways are invariably complex and despite the generally limited number of reactants and products, serpentinisation refers to a series of reactions rather than a single reaction (e.g., Bach et al., 2006, 2004; Frost and Beard, 2007; Klein et al., 2013; Leong and Shock, 2020; McCollom et al., 2016; McCollom and Bach, 2009; Palandri and Reed, 2004; Toft et al., 1990) and can be expressed as the following reactions (Eq. 1.1; Eq. 1.2):

$$2Mg_2SiO_4 + 3H_2O \rightarrow Mg_3Si_2O_5(OH)_4 + Mg(OH)_2$$

$$Olivine\ (Fosterite) + Water \rightarrow Serpentine + Brucite \quad (1.1)$$

$$3MgSiO_3 + 2H_2O \rightarrow Mg_3Si_2O_5(OH)_4 + SiO_{2\,(aq)}$$

$$Orthopyroxene\ (Enstatite) + Water \rightarrow Serpentine + Aqueous\ Silica \quad (1.2)$$

These reactions produce brucite and aqueous silica that drive additional hydration reactions and serpentine formation (Eq. 1.3; Eq. 1.4; Eq. 1.5):

$$3Mg_2SiO_4 + 2SiO_2 + 4H_2O \rightarrow 2Mg_3Si_2O_5(OH)_4$$

$$Olivine(Fosterite) + Aqueous\ Silica + Water \rightarrow Serpentine \quad (1.3)$$

$$Mg_2SiO_4 + 4Mg(OH)_2 + 3SiO_2 \rightarrow 2Mg_3Si_2O_5(OH)_4$$

$$Olivine(Fosterite) + Brucite + Aqueous\ Silica \rightarrow Serpentine \quad (1.4)$$

$$3Mg(OH)_2 + 2SiO_{2\,(aq)} \rightarrow Mg_3Si_2O_5(OH)_4 + H_2O$$

$$Brucite + Aqueous\ Silica \rightarrow Serpentine + Water \quad (1.5)$$

As a result, in dunites, brucite is expected to be prevalent, but in harzburgites isochemical hydration of olivine and orthopyroxene results in the formation of serpentine without brucite (Eq. 1.6):

$$Mg_2SiO_4 + MgSiO_3 + 2H_2O \rightarrow Mg_3Si_2O_5(OH)_4$$

$$Olivine(Fosterite) + Orthopyroxene(Enstatite) + Water \rightarrow Serpentine$$

(1.6)

These reactions consume H^+, resulting in the progressive increase of fluid pH. Serpentinising fluids are characterised as both high pH (up to ~13) and reduced (low Eh) (e.g., Barnes et al., 1967; Barnes and O'Neil, 1969; Mottl et al., 2004; Neal and Stanger, 1985; Sleep et al., 2004). To generate high pH >11, additional reactions likely occur such as the dissolution of brucite in the weathering environment (Eq. 1.7; Eq. 1.8):

$$Mg(OH)_2 + 2CO_2 \longrightarrow Mg^{2+} + 2HCO_3^-$$

$$Brucite + Carbon\ Dioxide \longrightarrow Magnesium + Bicarbonate$$

(1.7)

$$Mg(OH)_2 \longrightarrow Mg^{2+} + 2OH^-$$

$$Brucite \longrightarrow Magnesium + Hydroxide$$

(1.8)

Some serpentinising fluids within the Mariana Forearc are characterised as high pH 12.5, low H_2, high CH_4, and high alkalinity. To account for such fluids, abiotic formation of methane from bicarbonate is proposed to occur (e.g., Eq. 1.9; Menzies et al., 2022; Mottl et al., 2004; Wheat et al., 2020):

$$4H_2 + HCO_3^- \longrightarrow CH_4 + 2H_2O + OH^-$$

$$Hydrogen + Bicarbonate \longrightarrow Methane + Water + Hydroxide$$

(1.9)

This reaction conserves alkalinity, but replaces bicarbonate alkalinity with hydroxide alkalinity, which results in an increase in pH. H_2 can be generated through serpentinisation by oxidation reactions, producing reduced fluids, a characteristic of serpentinisation (e.g., Eq. 1.10; Chavagnac et al., 2013; McCollom and Seewald, 2013; Sleep et al., 2004):

$$2Fe^{II}O + H_2O \longrightarrow {Fe^{III}}_2O_3 + H_2$$

$$Ferrous\ Iron\ + Water\ \longrightarrow Ferric\ Iron + Hydrogen$$

(1.10)

Iron is sourced from iron-bearing minerals such as olivine, orthopyroxene, clinopyroxene, and serpentine. In addition, formation of magnetite an abiotic hydrogen is proposed to occur through the hydration-oxidation of fayalite (Eq. 1.11):

$$3Fe_2SiO_4 + 2H_2O \longrightarrow 3SiO_2 + 2Fe_3O_4 + 2H_2$$

$$Olivine(Fayalite) + Water\ \longrightarrow Quartz + Magnetite + Hydrogen$$

(1.11)

Magnetite formation is favoured at higher temperatures of serpentinisation (~>250°C; Klein et al., 2009; McCollom et al., 2016). At lower reaction temperatures iron is favoured to partition into Fe-brucite (~<250°C) and can react to form Fe^{3+}-serpentine and H_2 (Eq. 1.12; Klein et al., 2009; McCollom et al., 2016):

$$2Fe(OH)_2 + 2SiO_{2\,(aq)} + H_2O \longrightarrow Fe^{III}{}_2Si_2O_5(OH)_4 + H_2$$

$$Fe\text{-}Brucite + Aqueous\ Silica + Water\ \longrightarrow Serpentine + Hydrogen$$

(1.12)

Oxidation reactions during have been proposed as an additional source of hydroxide alkalinity resulting in high pH and reduced fluids (Eq. 1.13; Chavagnac et al., 2013):

$$Fe^{II} + 2H_2O \longrightarrow Fe^{III} + H_2 + 2OH^-$$

$$Ferrous\ Iron + Water\ \longrightarrow Ferric\ Iron + Hydrogen + Hydroxide$$

(1.13)

The progressive set of reactions outlined above results in the serpentinisation of ultramafic rocks and culminates in reduced and high pH serpentinising fluids.

Although serpentinisation can occur at temperatures below <700°C (Fig. 1.1), where olivine becomes unstable in the presence of fluid (Evans, 2004; Evans et al., 2013; Guillot et al., 2015), serpentinisation reactions predominantly occur at temperatures of <400°C involving lower temperature serpentine polymorphs lizardite and chrysotile (Evans, 2004; Mével, 2003). Lizardite, chrysotile, and the higher temperature polymorph antigorite are the most common serpentine minerals and their structures are composed of 1:1 layers of a tetrahedral Si_2O_5 and an octahedral $Mg_3O_2(OH)_4$ sheet with variations between serpentine types resulting from the consequences of sheet attachment (Evans, 2004). In lizardite, the

layers are flat, forming platy or elongate crystals that in mesh-textured serpentinite are typically less than 2-3 μm in cross-section, but wider, up to 2 mm crystal size in discrete lizardite veins (Evans, 2004; Mével, 2003). In contrast, chrysotile yields a fibrous texture composed of hollow nanotubes, occurring at similar thermodynamic conditions as lizardite (Fig. 1.1) and is common as late-stage cross-cutting veins (Andreani et al., 2007; Evans, 2004; Evans et al., 2013; Guillot et al., 2015; O'Hanley, 1991; Wilson, 1959). Additionally, antigorite yields corrugated layers forming flaky crystals that typically form a schistose texture (Evans, 2004; Mével, 2003) and has previously been considered a higher temperature serpentine mineral (~>250°C; Fig. 1.1; Evans, 2004). However, recent petrographic investigations show compelling evidence that antigorite does not necessarily equate to higher temperatures of serpentinisation and may form at lower temperatures (Rouméjon et al., 2019).

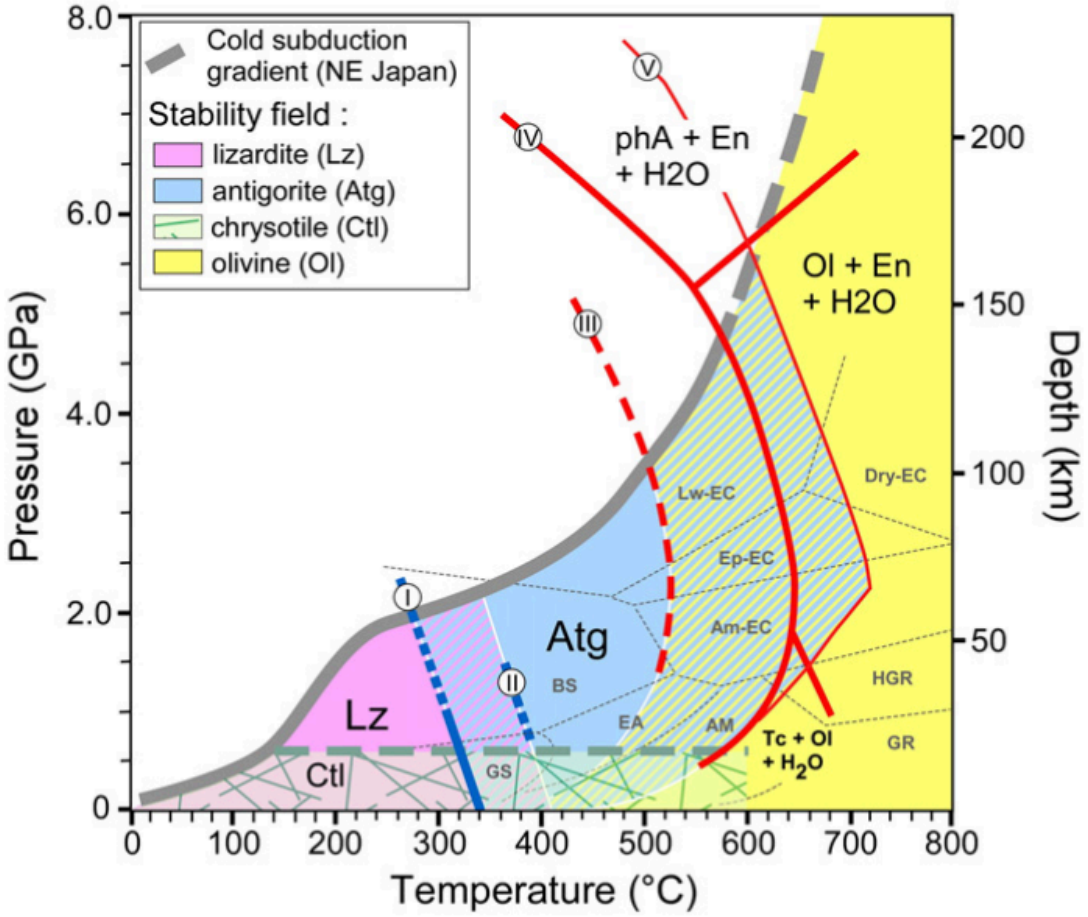

Figure 1.1: Serpentine pressure-temperature dependent diagram (Guillot et al., 2015) from petrological observations and experimental data of serpentinites. (I) Refers to the onset destabilisation of lizardite to antigorite (Evans, 2004). (II) Refers to the stability limit of lizardite (Schwartz et al., 2013). (III) Refers to dehydration of serpentine (Perrillat et al., 2005). (IV) Refers to the stability limit of antigorite (Wunder and Schreyer, 1997). (V) Refers to the breakdown of antigorite (Ulmer and Trommsdorff, 1995). Metamorphic facies boundaries and the cold subduction gradient are also shown (Guillot et al., 2015; Liou et al., 2000). Lz is lizardite, Ctl is chrysotile, Atg is antigorite, Tc is talc, Ol is olivine, En is Enstatite.

The frictional and rheological properties of serpentinites are in great contrast to mantle peridotites, which are mechanically strong (e.g., Escartin et al., 2001; Escartín et al., 1997; Hirth, 2002; Hirth and Guillot, 2013). Serpentine is inherently weak, as highlighted by experimentally-determined internal friction coefficients (μ) that vary from fibrous chrysotile serpentine values of $\mu = 0.15$ to antigorite serpentine values of $\mu = 0.53$ (Tesei et al., 2018; Viti et al., 2018) and are significantly lower than quartz-dominated crustal rocks of $\mu = 0.6$ to 0.85 (Byerlee, 1978). In addition, experimental studies propose that minimally (10 to 15 %) serpentinised mantle rocks yield similar strengths as pure serpentinites (Escartin et al., 2001), indicating that relatively low extents of serpentinisation may induce significant weakness and localise deformation along discrete zones of serpentinisation (Escartin et al., 2001; Guillot et al., 2015; Hirth and Guillot, 2013). As a result, due to the rheological properties of serpentinites, it is proposed that serpentine acts as a lubricant, inducing weakness, and consequently plays critical roles along tectonic plate boundaries, aiding plate tectonics (e.g., Cann et al., 1997; Guillot et al., 2015; Guillot and Hattori, 2013; Hilairet et al., 2007; Hirth and Guillot, 2013; Moore and Lockner, 2013).

During subduction, serpentine can be transported in the downgoing slab resulting in serpentinite dehydration reactions, which are proposed to result in the chemical and isotopic modification of hydrous melts (e.g., Cooper et al., 2020; Jones et al., 2014). Recently, combined geochemical and geophysical investigations within the Lesser Antilles volcanic arc propose dehydration of serpentine as the dominant supplier of water to the arc system (Cooper et al., 2020). Consequently, the serpentinisation extent of a subducting plate is directly connected to the evolution of the arc, including the supply of magma, earthquakes, formation of arc crust, and mineral resources (Cooper et al., 2020).

Serpentine has distinct affinities for fluid-mobile elements and consequently serpentinisation processes can have impacts on planetary geochemical budgets for many elements and molecules, such as water, carbon, sulphur, chlorine, boron, and lithium (Alt et al., 2013; Boschi et al., 2008; Früh-Green et al., 2004; Hacker, 2008; Kelemen et al., 2011; Kelemen and Manning, 2015; Seyfried et al., 1984; Sharp and Barnes, 2004). However, the quantification of the role of serpentinites in planetary geochemical budgets is generally inhibited due to unknowns in the abundance of serpentine throughout the Earth system and the relative importance between distinct episodes of serpentinisation (e.g., Alt et al., 2013; Kelemen et al., 2011; Kelemen and Manning, 2015). As such, large uncertainties of up to several orders of magnitude are reported in current geochemical budgets (e.g., Kelemen and Manning, 2015).

The influence of serpentinisation on biogeochemical cycles is now becoming apparent with serpentinisation reactions producing abiotic hydrogen (Eq. 1.10; Eq. 1.11) and organic compounds such as methane (e.g., Eq. 1.9), formate, and acetate, key for microbial communities and biogeochemical cycles (e.g., Brazelton et al., 2006; Lang et al., 2018, 2010; Schrenk et al., 2013). The formation of abiotic hydrogen provides a ubiquitous energy source in serpentinising environments, where oxidation of hydrogen under either aerobic or anaerobic conditions provides metabolic energy to local communities (Lang et al., 2021; McCollom and Seewald, 2013, 2007; Schrenk et al., 2013; Sleep et al., 2004). This energy source can then be utilised to generate organic compounds abiotically (e.g., Eq. 1.9; Eq. Eq. 1.10), providing fuel for microbial communities (Brazelton et al., 2006; Lang et al., 2010; Lang and Brazelton, 2020; Schrenk et al., 2013). As serpentinisation is the inevitable consequence of interactions between ultramafic rock and water, serpentinisation has been proposed as instrumental in the origin of life (Martin et al., 2008; Russell et al., 2010; Schrenk et al., 2013).

Mantle peridotite carbonation has previously been proposed as a mechanism for the permanent storage of CO_2 by sequestering atmospheric carbon into carbonate veins and surficial travertine terraces (Kelemen et al., 2011; Kelemen and Matter, 2008; Matter and Kelemen, 2009). In the natural system, the drawdown of atmospheric-derived carbon into carbonate veins and travertine terraces is proposed to occur from active and ongoing serpentinisation reactions with meteoric-derived water (Eq. 1.14; Eq. 1.15; Eq. 1.16; Eq. 1.17; Eq. 1.18; Eq. 1.19; Dichicco et al., 2015; Kelemen et al., 2011; Kelemen and Matter, 2008; Neal and Stanger, 1985):

$$2Mg_2SiO_4 + 2CO_2 \longrightarrow 2MgCO_3 + SiO_2$$

$$Olivine(Fosterite) + Carbon\ Dioxide \longrightarrow Magnesite + Quartz$$

(1.14)

$$Mg_2SiO_4 + MgCaSi_2O_6 + 2CO_2 + 2H_2O \longrightarrow Mg_3Si_2O_5(OH)_4 + CaCO_3 + MgCO_3$$

$$Olivine(Fosterite) + Clinopyroxene(Diopside) + Carbon\ Dioxide + Water \longrightarrow Serpentine + Calcite + Magnesite$$

(1.15)

$$4Mg_2SiO_4 + MgCaSi_2O_6 + 7H_2O \longrightarrow 3Mg_3Si_2O_5(OH)_4 + Ca^{2+} + 2OH^-$$

$$Olivine(Fosterite) + Clinopyroxene(Diopside) \longrightarrow Serpentine + Calcium + Hydroxide$$

(1.16)

$$Ca^{2+} + 2OH^{-} + CO_2 \longrightarrow CaCO_3 + H_2O$$

$$Calcium + Hydroxide + Carbon\ Dioxide \longrightarrow Calcite + Water$$

(1.17)

$$Ca^{2+} + 2HCO_3^{-} \longrightarrow CaCO_3 + CO_2 + H_2O$$

$$Calcium + Bicarbonate \longrightarrow Calcite + Carbon\ Dioxide + Water$$

(1.18)

$$Mg_3Si_2O_5(OH)_4 + 3CO_2 \longrightarrow 3MgCO_3 + 2SiO_{2\,(aq)} + 2H_2O$$

$$Serpentine + Carbon\ Dioxide \longrightarrow Magnesite + Aqueous\ Silica + Water$$

(1.19)

These serpentinisation-carbonation reactions are proposed to result in the modification of the water, forming calcium hydroxide high pH >11 hyperalkaline waters (Barnes et al., 1967; Barnes and O'Neil, 1969; Kelemen et al., 2011; Neal and Stanger, 1985). Despite the generally low abundance of Ca in ultramafic rocks (e.g., Niu, 2004), the source of calcium within calcites, precipitated from high pH >11 hyperalkaline waters, are proposed to be derived from the ultramafic rock, which would require very low water/rock ratios (Kelemen et al., 2011). However, recent studies have proposed external sources of calcium, derived from overlying marine sediments, have contaminated the underlying carbonated and serpentinised mantle peridotites (de Obeso and Kelemen, 2018).

Upon discharge at surface spring sites, hyperalkaline waters either mix with surficial lower pH magnesium bicarbonate waters or interact with atmospheric CO_2, inducing precipitation of carbonate minerals in veins, travertines, and cements (Barnes and O'Neil, 1969; Kelemen and Matter, 2008; Neal and Stanger, 1985). It is estimated that in the natural system ~10^4 to 10^5 T/yr of atmospheric CO_2 are converted to carbonate minerals in the Samail Ophiolite, Oman and proposed enhanced engineering solutions may increase the drawdown potential to 10^9 T/yr in Oman alone, possibly providing an effective method to capture and store CO_2 long-term (Kelemen et al., 2011; Kelemen and Matter, 2008; Matter and Kelemen, 2009).

1.3 Where does serpentinisation occur?

a) Mid-ocean Ridges

Serpentinisation can occur at Mid-Ocean Ridges, where serpentinised mantle peridotites form a component of the oceanic crust. At slow-spreading ridges, mantle rocks become serpentinised during exhumation and unroofing along detachment faults (Andreani et al., 2007; Blackman et al., 1998; Cann et al., 1997; Dick et al., 2008; MacLeod et al., 2002; Smith et al., 2006). Several sites of serpentinites are associated with ultramafic-hosted high-temperature hydrothermal vents such as the Rainbow (Allen and Seyfried, 2004; Andreani et al., 2014; Charlou et al., 2002; Lowell and Rona, 2002) and Logachev sites (Schmidt et al., 2007). In addition, low-temperature ~100°C hyperalkaline pH >11 ultramafic-hosted vent sites such as Lost City, which sits near the summit of the ~4000 m high Atlantis Massif at 30°N of the Mid-Atlantic Ridge, occur at slow-spreading ridges (Kelley et al., 2001a). Serpentinised mantle peridotites also occur at ultraslow spreading ridges such the Gakkel Ridge, Arctic and the Southwest Indian Ridge, where mantle rocks are typically exhumed at the seafloor symmetrically along the spreading axes (Alt et al., 2013; Cannat et al., 2006; Dick et al., 2003; Grevemeyer et al., 2018a; Michael et al., 2003). In intermediate and fast-spreading crust, the extent of serpentine in ocean crust and associated lithospheric mantle is inferred to be low (Grevemeyer et al., 2018b). However, in these settings serpentinised mantle rocks are exhumed locally at propagating rifts, in fracture zones, and in rare tectonic windows such as Hess or Pito Deep (Francheteau et al., 1990; Früh-Green et al., 1996; Hekinian et al., 1996, 1993; Karson et al., 2002). Additionally, serpentinisation is associated with isolated sub-aerial mantle peridotite massifs, located away from Mid-Ocean Ridges, and are partly composed of serpentine, such as the St. Paul and St. Peter's Rocks archipelago (Darwin, 1835; Melson et al., 1972; Campos et al., 2010).

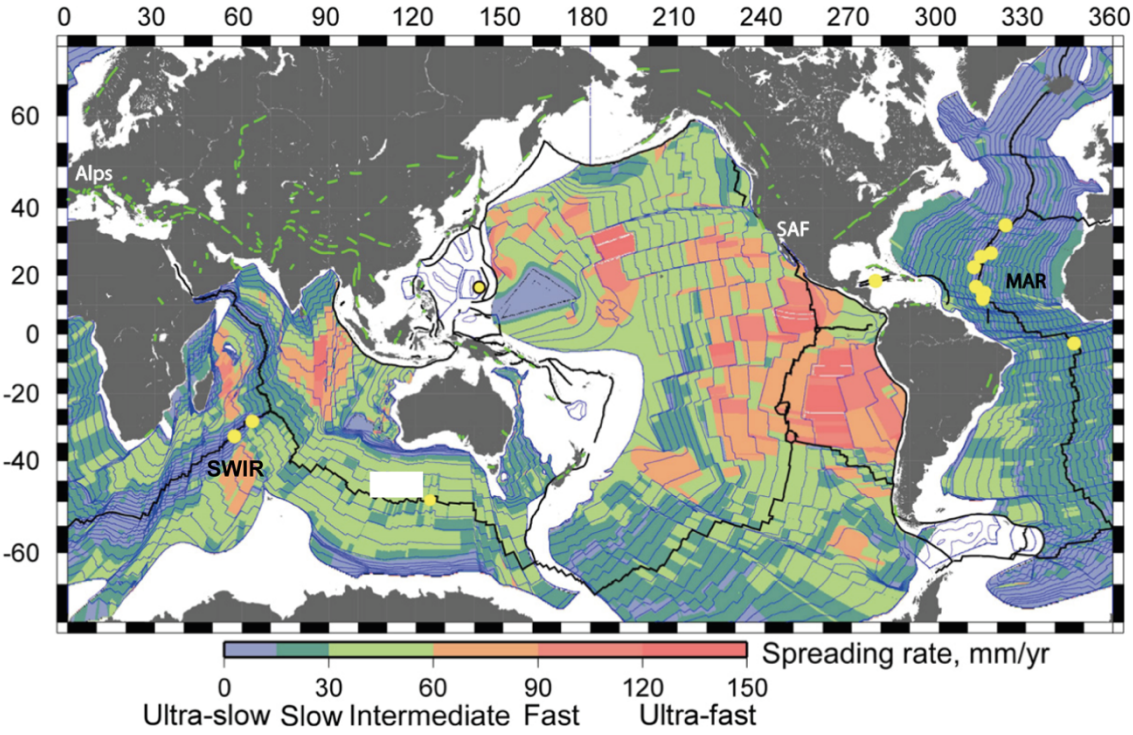

Figure 1.2: Map of serpentinite occurrences on land and in the oceans (from Guillot et al., 2015; Guillot and Hattori, 2013). Global seafloor spreading rates are mapped with black lines denoting spreading ridge axes (Cannat et al., 2010). Major seafloor occurrences of serpentinite are denoted by yellow circles with green outlines denoting continental serpentinites (Coleman, 1971).

b) Bent Faults

Prior to entering the subduction channel, normal stresses are exerted on the incoming plate, resulting in bending-related extensional faulting (Ranero et al., 2003). Lower than expected seismic wave velocities inferred from geophysical imaging offshore Central America indicates bend faults of up to 50 km in length that penetrate up to 20 km down into the incoming plate, in places more than 10 km into the mantle region (Ranero et al., 2003). This suggests bend-related faulting generates pathways for seawater to penetrate through the ocean crust into the mantle of a downgoing slab, providing the opportunity for pervasive serpentinisation reactions between the mantle and seawater. Consequently, significant amounts of water, carbon, sulphur, boron, and other fluid-mobile geochemical tracers formed during bend-fault induced serpentinisation may be transported into the mantle along the subduction conveyor belt into the mantle (Hatakeyama et al., 2017; Park et al., 2021; Ranero et al., 2003)

c) Mantle Wedge slab-derived serpentinisation

During subduction, hydrated and altered ocean crust and sediments progressively dewater and dehydrate from the downgoing slab, and these liberated slab-derived fluids can pervasively serpentinises peridotites in the overlying mantle wedge. A type example of this occurrence are the submerged serpentinite mud volcanoes of the Mariana Forearc, where evidence of slab-derived mantle wedge serpentinisation reactions is recorded in the clasts of strongly serpentinised mantle peridotite (Albers et al., 2020; Alt and Shanks, 2006; Fryer et al., 1985; Kahl et al., 2015; Mottl et al., 2003; Savov et al., 2007) and other exotic subduction related xenoliths.

d) Crustal scale Strike-slip faults

At large plate boundary strike slip faults such as the San Andreas Fault, California, and the Alpine Fault, New Zealand, localised discrete bodies of serpentinised mantle rocks occur. Along an active trace of the San Andreas Fault, serpentinite gouge was recovered by the San Andreas Fault Observatory at Depth (SAFOD) drilling project (Moore and Rymer, 2012, 2007; Morrow et al., 2014). In addition to localised occurrences of serpentinites along fault planes, large exhumed completely serpentinised serpentinite bodies such as the ~5 km^2 Table Mountain and ~100 km^2 New Idria Massif occur near the San Andreas Fault. Magnetic (~210 nT; Byerly, 1966; McPhee et al., 2004) and gravity (-35 to -55 mGal; Byerly, 1966) anomalies are associated with the New Idria serpentinite massif, which is interpreted to reflect a dome-like body that only extends to ~4 km in depth. These serpentinite bodies are associated with moderate relief (>1000 m) and high uplift rates, which are significantly greater relative to the regional uplift rate (Coleman, 1996; Page et al., 1998). Consequently, recent isostatic uplift modelling (Evans et al., 2021) has suggested that to maintain relief of such shallow serpentinite bodies for a sustained time period of ~12 Myr (Casey and Dickinson, 1976; Coleman, 1996; Vermeesch et al., 2006), ongoing serpentinisation-alteration reactions may be occurring, producing serpentinite diapirism and continued exhumation of the New Idria Massif (Tsujimori et al., 2007).

e) Rifted margin ocean-continent transition

Along the Iberian Margin, exhumed mantle peridotites occur along an inferred ~70 km wide, ~250 km long peridotite ridge, organised into a series of broadly N-S orientated margin parallel segments, some of which extend over tens of kilometres, and generally denote the ocean-continental crust boundary (Beslier et al., 1993; Henning et al., 2004; Minshull et al., 2014). Based on seismic imaging and samples recovered by scientific ocean drilling (ODP Leg 103, 149, 173; Boillot et al., 1987; Sawyer et al., 1994; Whitmarsh et al., 1998) the

exhumed mantle peridotites are inferred to be strongly to completely serpentinised on top of the basement with the serpentinisation extent decreasing to <25 % ~2 km below (Minshull et al., 2014). In addition, at the conjugate Newfoundland Rifted Margin, ODP (Ocean Drilling Program) Leg 210 recovered strongly to completely serpentinised mantle peridotites (Site 1277, Shipboard Science Party, 2004). The implication of exhumed serpentinised mantle rocks on both sides of the Atlantic is that subcontinental mantle is exhumed from depth during continental break-up, providing significant amounts (as wide as 150 to 180 km; Robertson et al., 2007) of mantle rock available for subsequent pervasive serpentinisation.

f) Sub-aerial ongoing meteoric serpentinisation

The occurrence of hyperalkaline high pH >11 fluids emanating from continental serpentinised massifs have long been proposed to reflect active and ongoing low temperature serpentinisation by meteoric waters (Barnes et al., 1967; Barnes and O'Neil, 1969; Neal and Stanger, 1985). Such fluids have been reported from numerous serpentinised massifs including the Samail Ophiolite, Oman (Barnes et al., 1978; Leong et al., 2021; Leong and Shock, 2020; Neal and Stanger, 1985), New Caledonia (Monnin et al., 2014), Liguria (Boschetti et al., 2013; Chavagnac et al., 2013), California (Barnes et al., 1967; Barnes and O'Neil, 1969; Boschetti et al., 2017), Troodos Ophiolite, Cyprus (Neal and Shand, 2002; Rizoulis et al., 2016), Dun Mountain Ophiolite Belt, New Zealand (Menzies, 2012), and the Ronda Massif, Spain (Giampouras et al., 2019). In addition to hyperalkaline waters, evidence of low-temperature serpentinisation by meteoric waters is presented by stable oxygen and hydrogen isotopic compositions of measured serpentinites (Magaritz and Taylor, 1976, 1974; Wenner and Taylor, 1974, 1973, 1971).

g) Other planetary bodies

Serpentinisation is inferred to occur on other planetary bodies besides Earth. For example, serpentine deposits have been inferred to occur on the surface of Mars from near-infrared spectral imaging data (Ehlmann et al., 2009; Ehlmann and Mustard, 2010). In addition, H_2, a product of serpentinisation reactions (Eq. 1.10; Eq. 1.11; Sleep et al., 2004), has been detected in the hydrothermal jet plumes emitted into space from Enceladus, an icy rocky moon of Saturn with a saline ocean (Waite et al., 2017). It is proposed that H_2 may be generated by ongoing serpentinisation reactions beneath the icy surface between the rocky core and liquid saline ocean that yields an estimated pH of 11 to 12 (Glein et al., 2015), similar to measured high pH >11 hyperalkaline waters emanating from continental serpentinised massifs (Barnes et al., 1967; Barnes and O'Neil, 1969).

1.4 When does serpentinisation occur?

Determining when, where, and with what fluids serpentinisation reactions occur has been a long standing motivation for investigation (e.g., Barnes and O'Neil, 1969; Coleman and Keith, 1971; Früh-Green et al., 1990; Kelemen et al., 2011; Merrill, 1899; O'Hanley and Offler, 1992; Wenner and Taylor, 1973). Previous studies that have investigated the serpentinisation history of altered mantle rocks propose serpentinisation reactions occurred as a progressive series of discrete serpentinisation episodes, typically culminating in multiple fluid-rock interaction events (e.g., Agrinier et al., 1996; Alt and Shanks, 2006; Andreani et al., 2007; Bach et al., 2006; Burkhard and O'Neil, 1988; Coleman and Keith, 1971; Cooperdock and Stockli, 2016; Coulton et al., 1995; Früh-Green et al., 1990; Hostetler et al., 1966; Kahl et al., 2015; Kodolányi and Pettke, 2011; Kyser et al., 1999; Nuriel et al., 2009; O'Hanley et al., 1992; O'Hanley and Offler, 1992; Peacock, 1987; Peters et al., 2020; Schwarzenbach et al., 2012; Ulrich et al., 2020; Wenner and Taylor, 1974, 1973, 1971). However, establishing the conditions of distinct serpentinisation episodes remains challenging, especially as mantle rocks typically reveal complex geological histories.

Serpentinised mantle rocks that crop out in ophiolites are generally partially to completely serpentinised and have complex geological histories, from their formation at some form of ocean spreading ridge, aging on the ocean floor, through to their to obduction and emplacement on a continental margin, and subsequent unroofing (e.g., Gass, 1977). It has been suggested that stable oxygen and hydrogen isotope values of serpentinites from ophiolites indicate that serpentinisation reactions predominantly occurred at low temperatures (<200°C) with meteoric waters, forming a serpentine assemblage mainly composed of lizardite and chrysotile (Wenner, 1971; Wenner and Taylor, 1974, 1973, 1971). An initial, limited, serpentinisation event forming rare antigorite serpentine at higher temperatures of >200°C with 'metamorphic water', rather than seawater or meteoric water has also been interpreted to occur in mantle sequences of ophiolites by these authors (Fig. 1.3; Wenner, 1971; Wenner and Taylor, 1974, 1973, 1971). Consequently, the contrasting relative proportions of lizardite and chrysotile versus antigorite in ophiolitic serpentinites is inferred as evidence of serpentinization reactions occurring predominantly with meteoric water at low temperatures and after obduction and emplacement (Wenner and Taylor, 1973). Additional evidence of active, ongoing serpentinisation reactions in ophiolites is proposed from the observation of hyperalkaline pH >11 waters emanating from the mantle portions of many ophiolites (Barnes et al., 1978, 1967; Barnes and O'Neil, 1969; Leong et al., 2021; Neal and Stanger, 1985). These hyperalkaline waters are proposed to occur from low temperature serpentinisation reactions with meteoric water, forming serpentine and modifying the fluid composition of meteoric water to hyperalkaline compositions (Eq. 1.1-

Eq. 1.8; Barnes et al., 1978, 1967; Barnes and O'Neil, 1969; Leong et al., 2021; Neal and Stanger, 1985).

Serpentinised mantle rocks recovered from the seafloor are commonly partially to completely serpentinised and stable oxygen and hydrogen isotope values typically have lower $\delta^{18}O$ values and higher δD values (Fig. 1.3), in contrast with ophiolite serpentinites (Wenner and Taylor, 1974, 1973, 1971). In general, stable oxygen and hydrogen isotope values of seafloor serpentinites reflect initial serpentinisation, likely with modified seawater, at moderate temperatures (>150°C to <500°C) and subsequent exchange with seawater at lower temperatures <200 °C (Alt and Shanks, 2006; Früh-Green et al., 1996; Wenner and Taylor, 1974, 1973). This subsequent exchange is commonly recorded by serpentine veins and some whole rock samples that have higher $\delta^{18}O$ values and lower δD values (e.g., Alt and Shanks, 2006; Wenner and Taylor, 1973). In addition, seafloor antigorite serpentine separates generally yield lower $\delta^{18}O$ values and higher δD values relative to seafloor chrysotile and lizardite serpentine samples, indicating formation at higher temperatures and indicate multiple serpentinisation episodes (Alt and Shanks, 2006; Früh-Green et al., 1996; Wenner and Taylor, 1973).

Differences in stable oxygen and hydrogen serpentine isotope values between the serpentine polymorphs of chrysotile-lizardite and antigorite have been proposed to reflect contrasting extents of isotopic overprinting (e.g., Kyser et al., 1999; Kyser and Kerrich, 1991; O'Hanley, 1991; O'Hanley and Offler, 1992; Wenner, 1971). It is suggested that since antigorite is coarser-grained and generally does not display textural evidence of recrystallisation, it is more resistant to isotopic overprinting by subsequent fluid-rock interaction events than chrysotile and lizardite, and consequently reflects initial formation temperatures (e.g., Kyser et al., 1999; Kyser and Kerrich, 1991; O'Hanley, 1991; O'Hanley and Offler, 1992; Wenner, 1971). In contrast, chrysotile and lizardite serpentine polymorphs may reflect conditions of subsequent fluid-rock interaction events rather than the initial serpentinisation conditions (Kyser et al., 1999; Kyser and Kerrich, 1991; O'Hanley, 1991; O'Hanley and Offler, 1992; Wenner, 1971).

As serpentine stable oxygen and hydrogen isotope values may reflect varying extents of isotopic overprinting, to constrain the serpentinisation history of a mantle rock, additional geochemical and isotopic investigations must be undertaken and combined with detailed understanding of cross-cutting relationships for the various serpentine phases. In combination with traditional $\delta^{18}O$ and δD systems, detailed trace element geochemistry and isotopic investigations using $^{87}Sr/^{86}Sr$ ratios and novel stable isotope systems such as $\delta^{11}B$, $\delta^{7}Li$, $\delta^{34}S$, $\delta^{37}Cl$ have been utilised, and have identified distinct serpentinisation episodes within serpentinised mantle rocks (Alt et al., 2012; Alt and Shanks, 2006; Barnes et al.,

2009; Barnes and Sharp, 2006; Boschi et al., 2008; Kodolányi and Pettke, 2011; McCaig et al., 2010; Peters et al., 2017, 2020; Scott et al., 2019; Vils et al., 2009).

However, to date, few detailed multi-isotope studies that utilise both traditional and novel isotope systems, in parallel with trace element concentrations and detailed field observations, have occurred in settings where serpentinised mantle rocks yield complex geological histories, such as ophiolites.

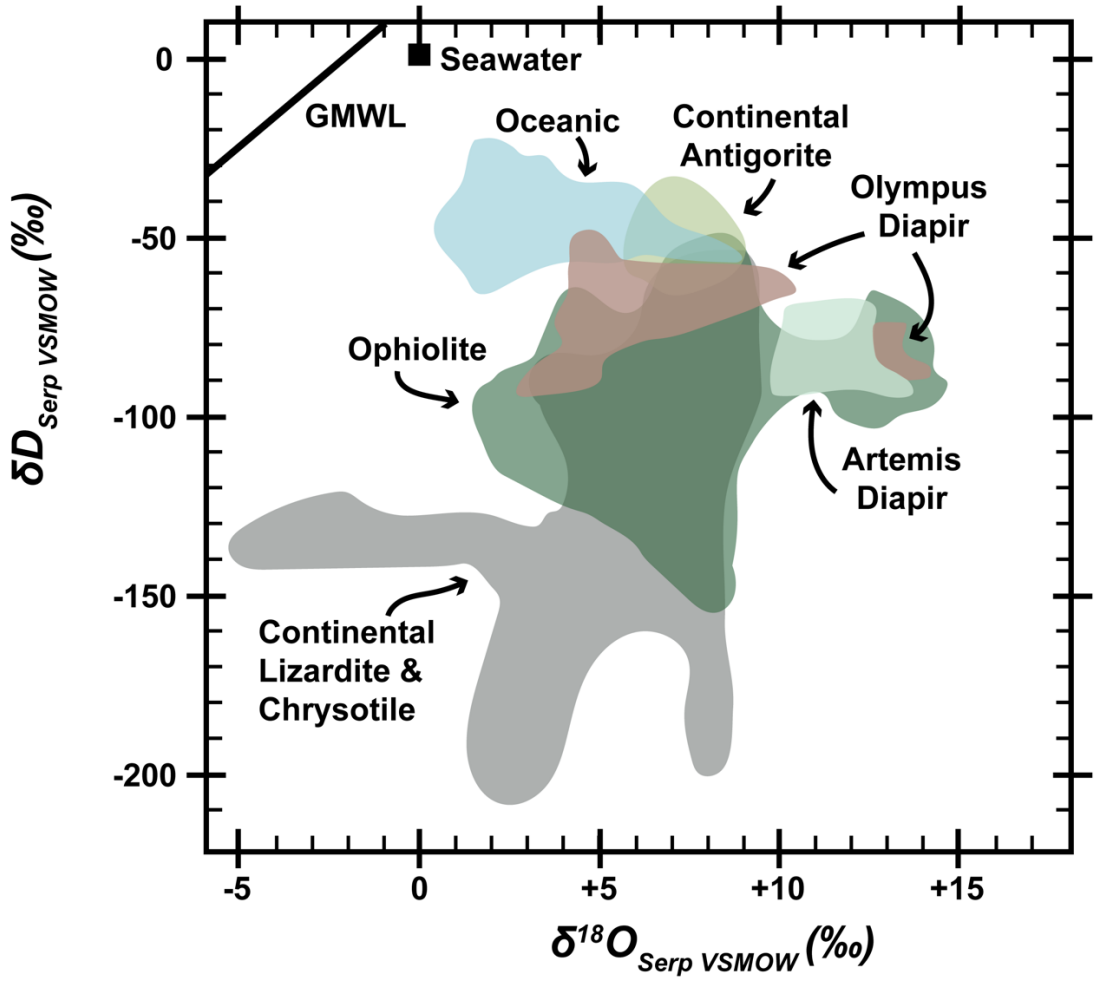

Figure 1.3: Respective range of $\delta^{18}O_{Serpentine}$ and $\delta D_{Serpentine}$ values of previous serpentine isotope measurements are shown (adapted from Sheppard, 1980; Wenner and Taylor, 1973). Global meteoric water line is also plotted (Craig, 1961). The range of oxygen and hydrogen stable isotope values from the Troodos Mantle Sequence are shown (Heaton, 1976; Magaritz and Taylor, 1974; Nuriel et al., 2009) and other occurrences of serpentine both on land and in the oceans (Sheppard, 1980; Sheppard and Epstein, 1970; Wenner, 1971; Wenner and Taylor, 1974, 1973, 1971).

1.5 Serpentinite Alteration

Serpentine alteration refers to the interaction between serpentine and water. The alteration of serpentine is proposed to modify major and trace element concentrations (Kodolányi and Pettke, 2011; Niu, 2004; Snow and Dick, 1995), isotopic compositions (Geilert et al., 2020; Kyser et al., 1999; Kyser and Kerrich, 1991; O'Hanley, 1991; Wenner, 1971), mineralogy and physical properties of serpentinised mantle rocks (Albers et al., 2021; Evans et al., 2021; Klein et al., 2020, 2017; Milliken et al., 1996), and may contribute to global geochemical cycles (Geilert et al., 2020). Despite the apparent importance of serpentine alteration in modifying the bulk chemical and physical characteristics of serpentinised mantle rocks, to date, few investigations into the alteration of serpentine have occurred relative to studies of serpentinisation hydration reactions (Geilert et al., 2020).

The contribution of serpentinite alteration to the overall physicochemical evolution of mantle peridotites is highlighted by inferred differences in whole rock chemistry. Serpentinisation hydration reactions are commonly invoked as a volume increasing (up to 40%; Klein and Le Roux, 2020; Macdonald and Fyfe, 1985) isochemical process, except for the addition of water and fluid-mobile trace elements and apparent loss of calcium (e.g., Coleman and Keith, 1971). In contrast, some studies propose that extensive mass transfer occurs during serpentinisation hydration reactions (Malvoisin, 2015; Thayer, 1966), which would inhibit volume expansion requirements. These previous studies that invoke serpentinisation-induced mass transfer fail to account for the geological context of recovered serpentinised mantle rocks, which are typically on or near the seafloor or sub-aerial surface, and have likely undergone post-serpentinisation alteration with seawater or meteoric water. Such a scenario is inferred from lower than expected MgO/SiO_2 ratios from recovered mid-ocean ridge serpentinised mantle peridotites (Klein et al., 2020; Niu, 2004; Snow and Dick, 1995). This change in bulk rock MgO/SiO_2 ratios is inferred due to either the loss of Mg (de Obeso and Kelemen, 2020), likely from dissolution of brucite (Jöns et al., 2017; Klein et al., 2020), or the gain of silica (e.g., de Obeso and Kelemen, 2018), or a combination of both (de Obeso et al., 2021). This indicates that changes in the bulk chemistries of altered mantle rocks occurs during serpentine alteration. Such changes are proposed to occur through a generalised serpentine dissolution reaction that is also referred to as a serpentine hydration reaction (e.g., Frost and Beard, 2007; Milliken et al., 1996):

$$Mg_3Si_2O_5(OH)_4 + H_2O \longrightarrow 3Mg(OH)_2 + 2SiO_2$$

$$Serpentine + Water \longrightarrow Brucite + Aqueous\ Silica$$

(1.20)

$$Mg_3Si_2O_5(OH)_4 + 5H_2O \longrightarrow 3Mg^{2+} + 2H_4SiO_4 + 6OH^-$$

$$Serpentine + Water \longrightarrow Magnesium + Silicic\ acid + Hydroxide$$

(1.21)

In addition to these serpentine alteration reactions, the dissolution of brucite (e.g., Eq. 1.7; Eq. 1.8) is proposed to occur (e.g., Klein et al., 2020; Snow and Dick, 1995).

In samples where dissolution of serpentine occurs, precipitation of other alteration minerals such as saponite, Mg-hydroxides, carbonates, palygorskite, andradite, and quartz are inferred to occur, forming a complex sequence of dissolution-precipitation reactions (Albers et al., 2021; Beard and Hopkinson, 2000; Klein et al., 2017; Milliken et al., 1996). These serpentine alteration related mineral assemblages typically occur in completely serpentinised rocks with extensive evidence of fracturing and cataclasis that form serpentinite breccia assemblages (Evans et al., 2021; Milliken et al., 1996; Robertson, 2007).

Contrasting serpentine recrystallisation textural relationships of recovered serpentinites have been proposed to reflect varying proportions of serpentine alteration (Bach et al., 2004; Brindley and Hayami, 1963; Evans et al., 2021; Hopkinson et al., 2004; O'Hanley, 1991; O'Hanley and Offler, 1992; Pabst et al., 2011; Picazo et al., 2013; Roumejon et al., 2015; Rouméjon et al., 2018b; Rumori et al., 2004; Wicks and O'Hanley, 1988; Wicks and Plant, 1979). Stable oxygen and hydrogen isotope values of recrystallised serpentinites typically yield higher δ^{18}O and lower δD values relative to less altered and recrystallised serpentinites (Kyser and Kerrich, 1991; O'Hanley, 1991; O'Hanley et al., 1992; Rouméjon et al., 2018b; Wenner, 1971). For example, in the completely serpentinised serpentinite breccias of ODP Site 897 and 899 at the Iberian Margin, stable oxygen isotope values indicate isotopic exchange occurred with seawater at low temperatures (<100°C) due to high δ^{18}O values of >+10 ‰ (Agrinier et al., 1996). However, an initial hydration alteration event composed of secondary chlorite and tremolite is inferred to have occurred at temperatures between >350°C to <500°C, apparently without inducing serpentinisation hydration reactions (Agrinier et al., 1996). Since the serpentine of ODP Sites 879 and 899 are extensively recrystallised (e.g., Milliken et al., 1996), the apparent decoupling in measured stable oxygen isotope values may instead reflect ongoing serpentine alteration. Consequently, in this context, measured serpentine stable oxygen and hydrogen isotope values likely reflect conditions of isotopic exchange during serpentine alteration, and not earlier serpentinisation conditions. In addition, stable δ^{18}O and δ^{13}C values of corresponding carbonate minerals hosted in the serpentinite breccias of ODP Sites 897 and 899 indicate precipitation at low temperatures ~10 to 25°C from seawater. This indicates that serpentine

alteration is an ongoing process, occurring at low temperatures, modifying the chemical and physical compositions of serpentinised mantle rocks, in addition to serpentinisation hydration reactions. Yet, the relative contributions of serpentinisation hydration and serpentine alteration processes to the overall alteration of mantle rocks are poorly constrained. Additional investigations are required to determine the role of serpentine alteration in the overall alteration of mantle rocks and the wider Earth system.

1.6 Aims of the Thesis

The research presented in this thesis was undertaken in the Troodos ophiolite, Cyprus with the aims of:

1) Determine whether serpentinisation can generate enough surface uplift to produce significant relief within a constrained timeframe, by developing a mechanistic serpentinisation-induced isostatic uplift model and applying it to the Troodos Mantle Sequence and other occurrences of exhumed serpentinised mantle peridotite massifs.
2) Document the fluid type(s) and resulting precipitates currently occurring in the modern meteoric regime within the Troodos Mantle Sequence and determine their composition(s), genesis, and fluid pathway evolution.
3) Establish if a progressive sequence of serpentinisation events is recorded in the serpentinised mantle rocks of the Troodos Mantle Sequence, by determining the fluid source(s) through geochemical and isotopic fingerprinting, using both traditional ($\delta^{18}O$, δD, $^{87}Sr/^{86}Sr$) and novel ($\delta^{11}B$) isotope systems.
4) Develop a new methodology to determine $^{87}Sr/^{86}Sr$ ratios in serpentinites at low Sr (<1 ug/g) concentrations.
5) Develop a new methodology to determine *in situ* $\delta^{11}B$ of serpentinites using LA-MC-ICP-MS methods.
6) Develop a new methodology to produce *in situ* elemental LA-QQQ-ICP-MS count maps of B in serpentinites.
7) Measure the physical and hydraulic properties of the mantle rocks and establish whether changes are the result of serpentinisation reactions alone or additional processes are required.

1.7 Thesis outline

Chapter 2 provides a brief outline of the Troodos ophiolite, the Troodos Mantle Sequence, and the uplift history of the ophiolite.

Chapter 3 integrates field observations, new density measurements, and mechanistic isostatic uplift and differential erosional modelling to show the Troodos Mountains can form exclusively by partial serpentinisation reactions within the constrained time frame of 5.5 ~Myr.

Chapter 4 combines elemental and molecular concentrations and isotope compositions of sampled waters, precipitates, leachates and bulk rocks occurring within the Troodos Mantle Sequence to yield insights into the modern meteoric water regime. Contrasting water types emanate from the Troodos Mantle Sequence, reflecting differing fluid rock reaction pathways and remobilisation of geochemical and isotopic signals of previous serpentinisation events.

Chapter 5 unravels the progressive sequence of overprinting serpentinisation events that have occurred in the Troodos Mantle Sequence. This was achieved by novel (B) with traditional (Sr, O, H) isotope analyses in combination with equilibrium modelling coupled to a Bayesian inversion engine. A mass balance calculation was undertaken to estimate the potential of each serpentinization event to contribute to the overall serpentinization budget.

Chapter 6 utilises a new physical properties dataset on the variably serpentinised mantle rocks of the Troodos Mantle Sequence and compares with previously published physical properties datasets on similar serpentinised mantle rocks. As the observed range in physical properties cannot be explained be serpentinisation reactions alone, additional reactions are proposed to explain this discrepancy.

Chapter 7 summarises and presents the main conclusions of this thesis.

Appendix A presents the boron equilibrium model outline coupled with the novel Bayesian inversion approach.

Appendix B presents Evans et al. (2021)

Appendix C presents the supplementary material of Evans et al. (2021)

Chapter 2 Geological Setting

Parts of this chapter are based on the following paper:

Evans, A.D., Teagle, D.A.H., Craw, D., Henstock, T.J., Falcon-Suarez, I.H., 2021. Uplift and exposure of serpentinized massifs: Modeling differential serpentinite diapirism and exhumation of the troodos mantle sequence, Cyprus. J. Geophys. Res. [Solid Earth] 126. https://doi.org/10.1029/2020jb021079

2.1 The Troodos ophiolite

The Troodos Massif is one of the world's best-preserved, least deformed, and most complete ophiolites (Gass, 1968). The Troodos mountains expose ocean crust and upper mantle rocks that formed ~90 to 92 Ma at some form of supra-subduction zone spreading ridge in the Neo-Tethyan Ocean (Moores et al., 1984; Moores and Vine, 1971; Mukasa and Ludden, 1987; Pearce et al., 1984). The ~90 km-long and ~30 km-wide ophiolitic sequence crops out as an elliptical bullseye-patterned welt (Fig. 2.1), with the stratigraphically deepest rocks, partially serpentinised mantle peridotites, forming the highest elevation of the Troodos mountains (Mount Olympus, 1952 m asl). This Mantle Sequence is surrounded by an eroded anticlinal dome comprising concentric annuli of gabbroic and ultramafic cumulate rocks, sheeted dykes, lavas, and submarine sediments that crop out at progressively lower altitudes around the slopes of the massif (Fig. 2.2).

Although not the focus of this thesis, the Limassol Forest Complex terrane (Fig. 2.1) is an area of ~400 km^2 located to the SE of the Troodos mountains and yields a contrasting magmatic and deformation history relative to the Troodos Massif (e.g., MacLeod et al., 1990; MacLeod and Murton, 1993; Moores and Vine, 1971; Murton, 1986). The Limassol Forest Complex is interpreted to reflect a Cretaceous dextral oceanic transform fault zone (e.g., MacLeod et al., 1990; MacLeod and Murton, 1993; Moores and Vine, 1971; Murton, 1986). In contrast to the Troodos Massif, there is compelling evidence in the Limassol Forest Complex for the Cretaceous seafloor exhumation of mantle rocks (e.g., MacLeod, 1988; MacLeod et al., 1990; Murton, 1986).

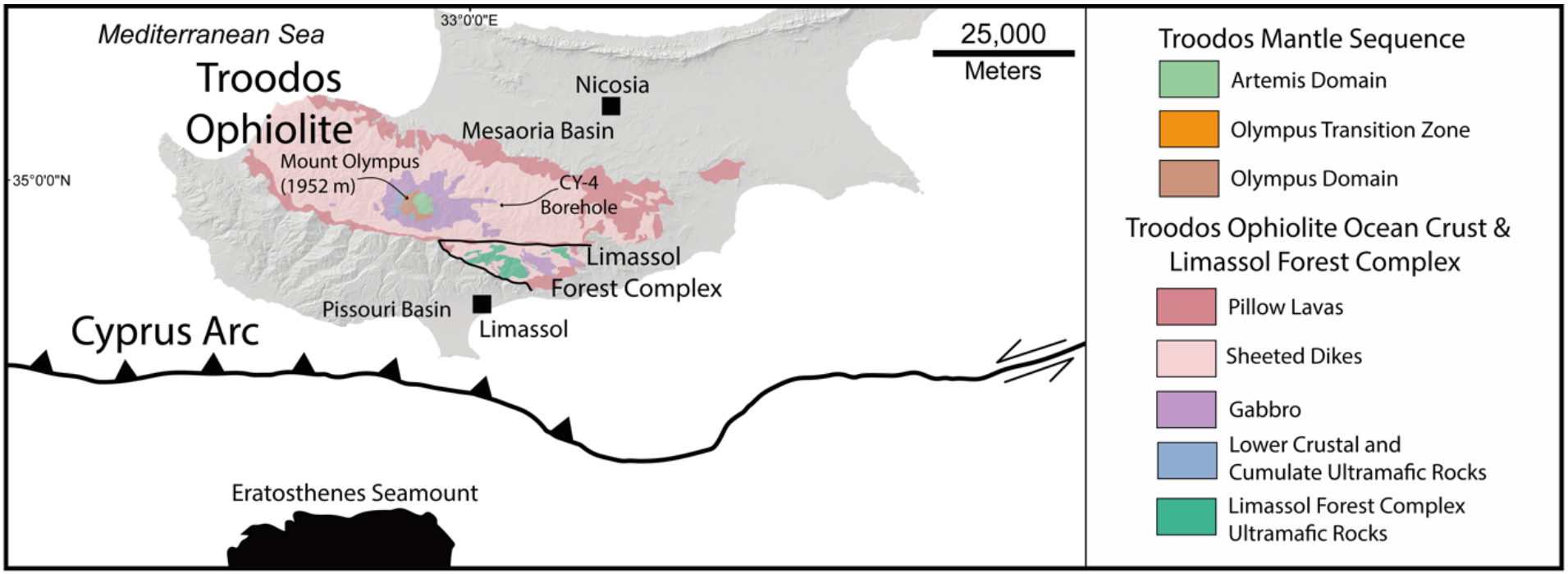

Figure 2.1: Geological map of the Troodos ophiolite with the bullseye geometry of the Mantle Sequence highlighted along with the Limassol Forest Complex terrane, the Cyprus arc and northernmost portion of the Eratosthenes Seamount.

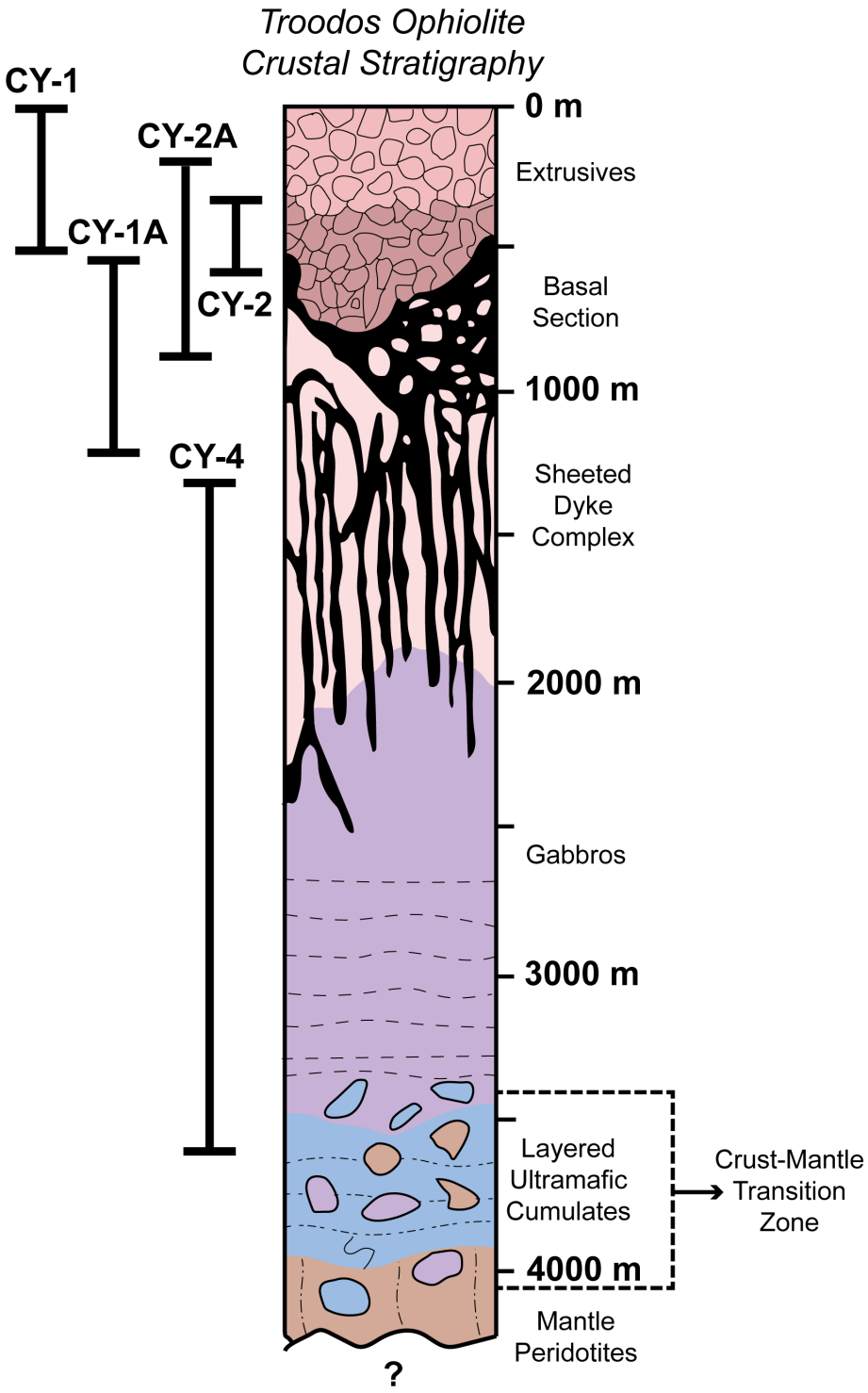

Figure 2.2: Troodos ophiolite crustal ophiolite stratigraphy adapted from Malpas et al., (1989). Thickness of the ophiolite is estimated by stacking drillholes CY-1, CY-1A, CY-2, CY-2A, and CY-4 from the Cyprus Crustal Study Project.

Unlike other ophiolites, such as the Samail ophiolite of Oman (e.g., Hacker et al., 1996; Searle and Cox, 1999), the Troodos ophiolite was not obducted onto a continental margin soon after its formation and there is no metamorphic sole to the massif. In contrast, significant uplift of the Troodos ophiolite has occurred since 5.5 Ma (e.g., McCallum, 1989; Poole and Robertson, 1998, 1991; Robertson, 1977; Rouchy et al., 2001; Stow et al., 1995) and it is qualitatively inferred that the exposure of the Troodos massif results from the serpentinisation of peridotites from the mantle below the ocean crustal rocks of the ophiolite (Gass and Masson-Smith, 1963; Moores and Vine, 1971; Robertson, 1977; Robertson, 1998a, 1998b).

The initial serpentinisation of the Troodos Mantle Sequence is commonly invoked to have occurred due to the collision of the Eratosthenes Seamount continental block with the Cyprean trench to the south of Cyprus that has stalled the northward subduction of the African plate (Ergün et al., 2005; Robertson, 1998a, 1998b). It is proposed that this has resulted in the focussed upwelling into the overlying mantle wedge of hydrous fluids generated by the dewatering of partially subducted marine sediments and ocean lithosphere, inducing and focussing serpentinite diapirism onto the Mount Olympus region (Moores and Vine, 1971; Robertson, 1977; Gass, 1977; Robertson, 1998a, 1998b). The best estimates for the dip of the subducting plate in the Cyprean arc are between ~13° to ~33° (Feld et al., 2017; Mackenzie et al., 2006) with the top of the down-going slab lying between ~13 and ~40 km below Mount Olympus. Oxygen and hydrogen isotopic measurements of the Troodos Mantle Sequence indicate that discrete portions of the Mantle Sequence have interacted with both ‘oceanic-like’ and meteoric waters (Magaritz and Taylor, 1974; Nuriel et al., 2009), suggesting the progressive and episodic serpentinisation of the Mantle Sequence is likely on-going.

Other mechanisms have also been suggested to explain the geometry of the Troodos Massif including Cretaceous ridge-related serpentine diapirism (Schuiling, 2011) and Cretaceous ridge-related detachment faulting (Nuriel et al., 2009). Recent regional structural analysis downplays the importance of serpentinisation and suggests uplift can be generated solely by Miocene to present-day convergence across the Cyprean subduction zone (Ring and Pantazides, 2019).

2.2 The Troodos Massif Mantle Sequence

The highest part of the Troodos Massif (Fig. 2.3) comprises a ~200 km^2 central region at moderate altitude (>1200 m) made up of a zone of mantle peridotite outcrops surrounded by gabbroic rocks, characterised by gentle hillslopes and relatively wide, shallow valleys, although the boundary between the gabbros and peridotites is commonly faulted with steep relief in places. In contrast, the surrounding Sheeted Dyke Complex is exposed in steep-sided ridges up to ~1000 m altitude that are deeply incised, with the encompassing Extrusive Sequences and circum-Troodos sediments occurring at lower altitudes in gently dipping outcrops best exposed in river canyons.

The Mantle Sequence of the Troodos Massif can be sub-divided into two discrete regions (Fig. 2.3): (1) an arcuate western zone of partially (~50 to ~70%) serpentinised tectonised harzburgites with minor dunites, referred to here as the Olympus domain, juxtaposed by faults against (2) an eastern ~5 km diameter, sub-circular region of completely serpentinised peridotite blocks in a sheared matrix of serpentine breccia (Fig. 2.4), here named the Artemis domain. The Artemis domain rocks have previously been referred to as the Smash zone (Wilson, 1959) or The Serpentine (Gass and Masson-Smith, 1963), or the remobilised serpentinite plug (Moores and Vine, 1971).

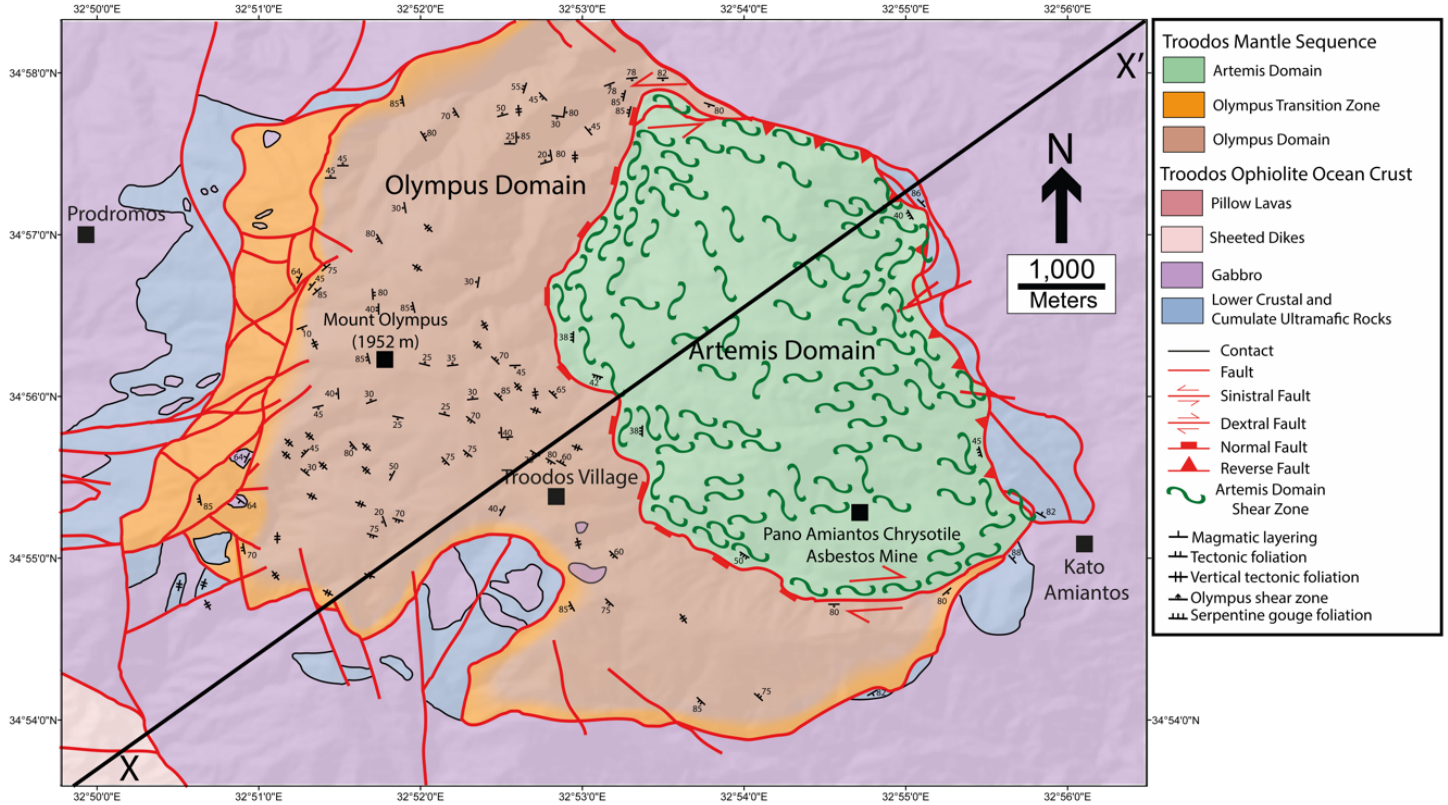

Figure 2.3: Geological map of the Troodos Mantle Sequence, adapted and updated from Wilson (1959). X to X' shows line of cross-section.

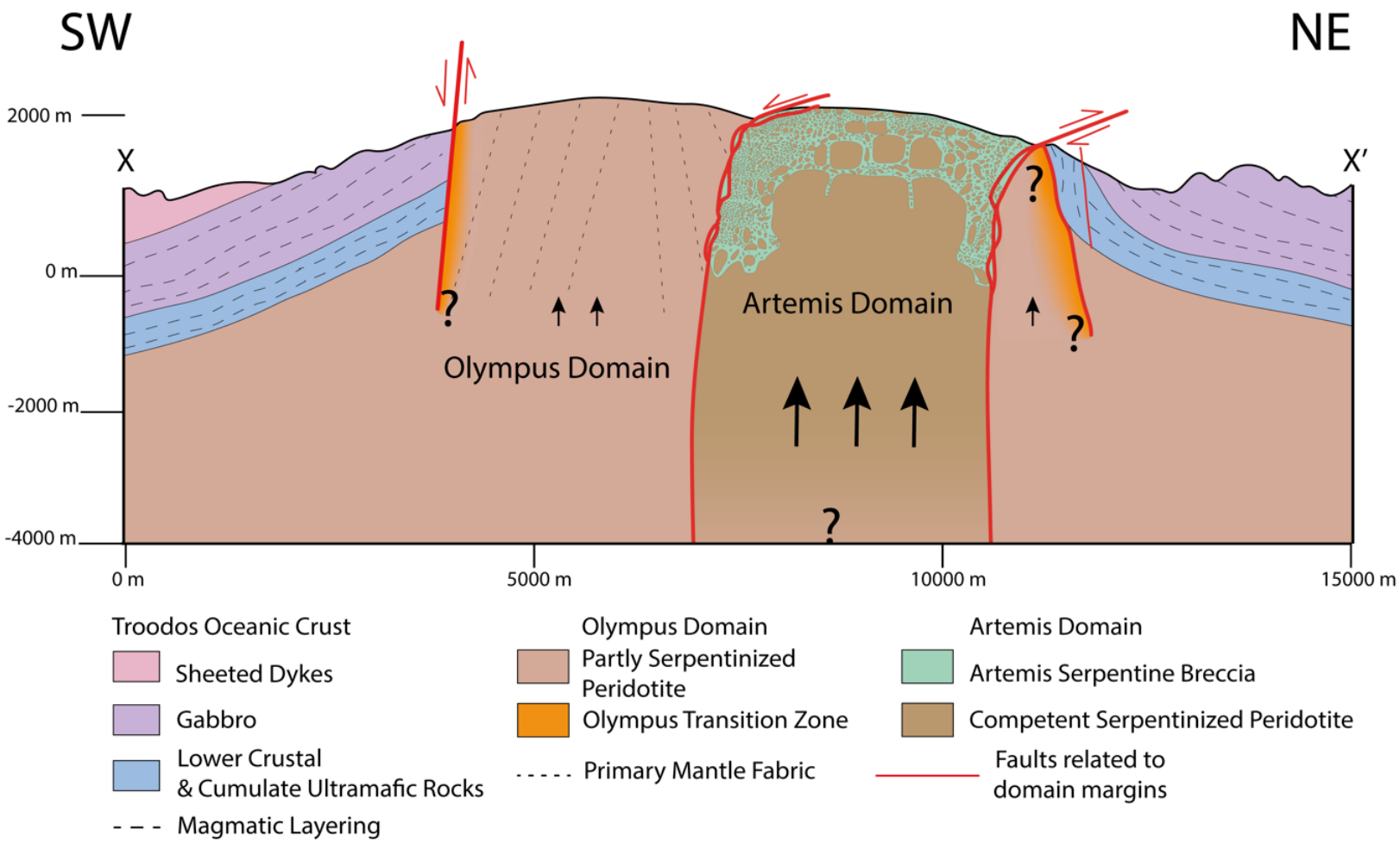

Figure 2.4: Geological cross-section of the Troodos Mantle Sequence and associated ocean crustal rocks.

The Cr-number (Cr/Cr+Al) of chrome spinels is a commonly used parameter to identify the tectonic setting of residual mantle peridotites (e.g., Arai, 1994; Dick and Bullen, 1984; Parkinson and Pearce, 1998), and contrasting Cr-numbers of Troodos Mantle Sequence chrome spinel (Batanova and Sobolev, 2000) indicate that the completely serpentinised peridotites of the Artemis domain originate from a region of fertile mantle lherzolite (Cr# 0.22 to 0.28) that has been exhumed from depth and juxtaposed against the refractory shallow mantle harzburgites (Cr# 0.51 to 0.70) of the Olympus domain.

A regional (200 x 100 km) oblong positive Bouguer gravity anomaly between +100 to +250 mGal coincides with the Troodos ophiolite (Fig. 2.5; Gass and Masson-Smith, 1963). This regional positive anomaly generally decreases from west to east across the ophiolite (Fig. 2.5), with smaller localised anomalies superimposed onto this regional trend (Fig. 2.5). The variably serpentinised outcrops of the Troodos Mantle Sequence spatially coincide with a large negative gravity anomaly relative to the regional trend (Fig. 2.5; 80 mGal to 120 mGal; Gass and Masson-Smith,1963; Shelton, 1993). This superimposed negative gravity anomaly is broadly centred on the abandoned chrysotile asbestos mine at Pano Amiantos (Fig. 2.3; Gass and Masson-Smith, 1963; Shelton, 1993). In published studies, this negative gravity anomaly is best represented as a vertical, cylindrical body of lower density serpentinised peridotite (2670 kg/m^3) extending ~11 km deep, within a higher density background of unserpentinised mantle (3300 kg/m^3; Gass and Masson-Smith, 1963; Shelton, 1993).

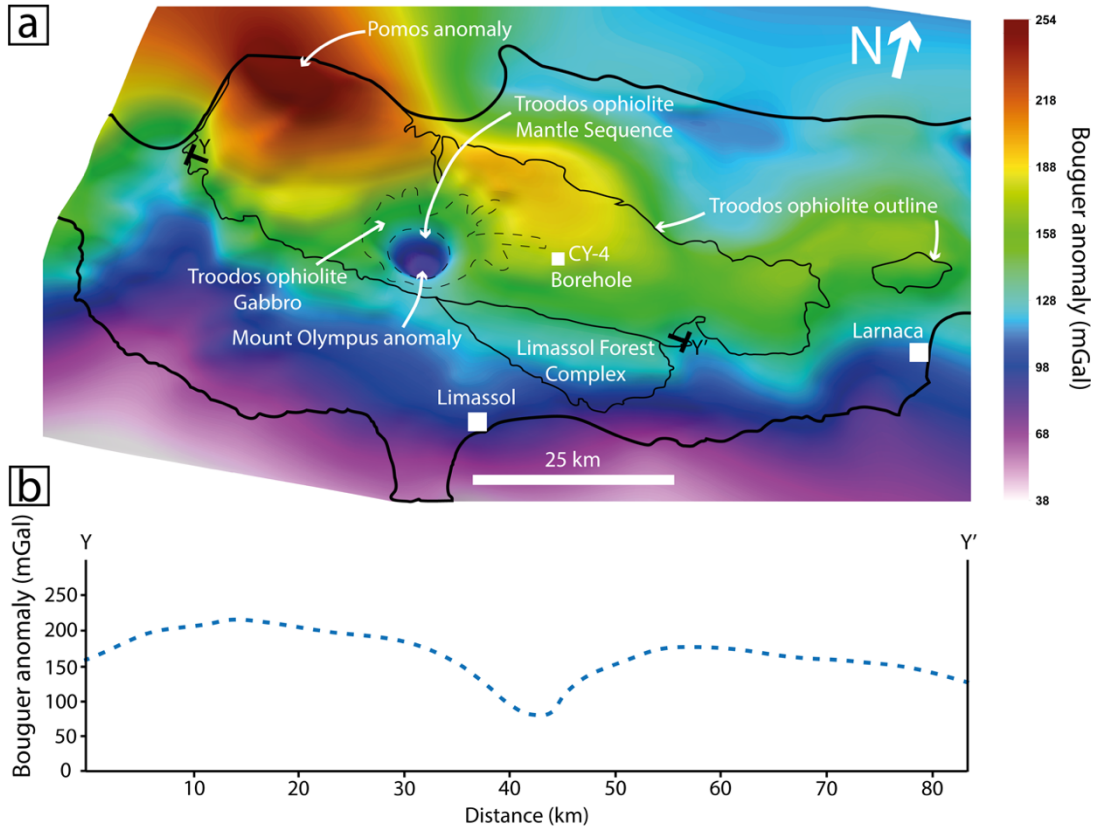

Figure 2.5: (a) 3D gravity map covering Cyprus, data sourced from Gass and Masson-Smith (1963). (b) Gravity cross-section along line Y-Y' again using data of Gass and Masson-Smith (1963), cross-section highlights the asymmetric nature of the Mount Olympus anomaly with the gravity low centred broadly on the former chrysotile asbestos mine of Pano Amiantos.

2.3 Uplift Trajectories

The Troodos ocean crust is relatively thin, only ~4 km thick from the top of the extrusive rocks to the uppermost mantle peridotites (Malpas, 1989; Fig. 2.2), relative to typical ocean crust that is 6 to 7 km thick. However, this still requires that a minimum of ~4000 m of exhumation must have occurred since the initial sub-aerial emergence of the Troodos ophiolite. The circum-Troodos sediments in the Mesaoria and Pissouri basins surrounding the Troodos Ophiolite (Fig. 2.1) preserve stratigraphic records of the unroofing and erosion of progressively deeper levels of the Troodos ophiolite (Follows, 1990; McCallum, 1989; Poole and Robertson, 1998, 1991; Robertson, 1977; Rouchy et al., 2001; Stow et al., 1995) (Fig. 2.6). Significant amounts of Troodos-derived diabase and lava clasts occur in latest Messinian / Early Pliocene (~5.5 Ma) strata indicating significant subaerial relief and exposure of the uppermost Troodos crust by this time (McCallum, 1989; Stow et al., 1995; Rouchy et al., 2001). Gabbroic clasts are first recorded in the Late Pliocene (McCallum, 1989; Stow et al., 1995). The proportion of gabbroic clasts is significantly greater in the Pleistocene Fanglomerates than the Pliocene successions

(McCallum, 1989; Poole and Robertson, 1991; Poole and Robertson, 1998). The first occurrence of ultramafic clasts is recorded within the Lower Pleistocene (<2.58 Ma) sequence (Wilson, 1959; Poole and Robertson, 1991; Stow et al., 1995; Poole and Robertson, 1998). The abundance of ultramafic clasts progressively increases within the Pleistocene Fanglomerate sequences (2.58 – 0.0117 Ma) (Poole and Robertson, 1991; Poole and Robertson, 1998). The Plio-Pleistocene sedimentary sequences have been interpreted to record pulses of uplift focussed on Mount Olympus (e.g., Robertson, 1977; McCallum, 1989; Poole and Robertson, 1991; Poole and Robertson, 1998b), with the intensity of the uplift episodes having waned from the Late Pleistocene to the present day (Poole and Robertson, 1998).

Low-temperature (U-Th)/He thermochronology on plutonic rocks from the Troodos Massif suggests an exhumation rate of 0.86 mm/yr with the onset of uplift at 6 ± 2 Ma (Morag et al., 2016). This rate broadly agrees with the uplift trajectory compiled from clast occurrences in the circum-Troodos sedimentary sequences (McCallum, 1989; Poole and Robertson, 1991; Poole and Robertson, 1998; Stow et al., 1995; Rouchy et al., 2001).

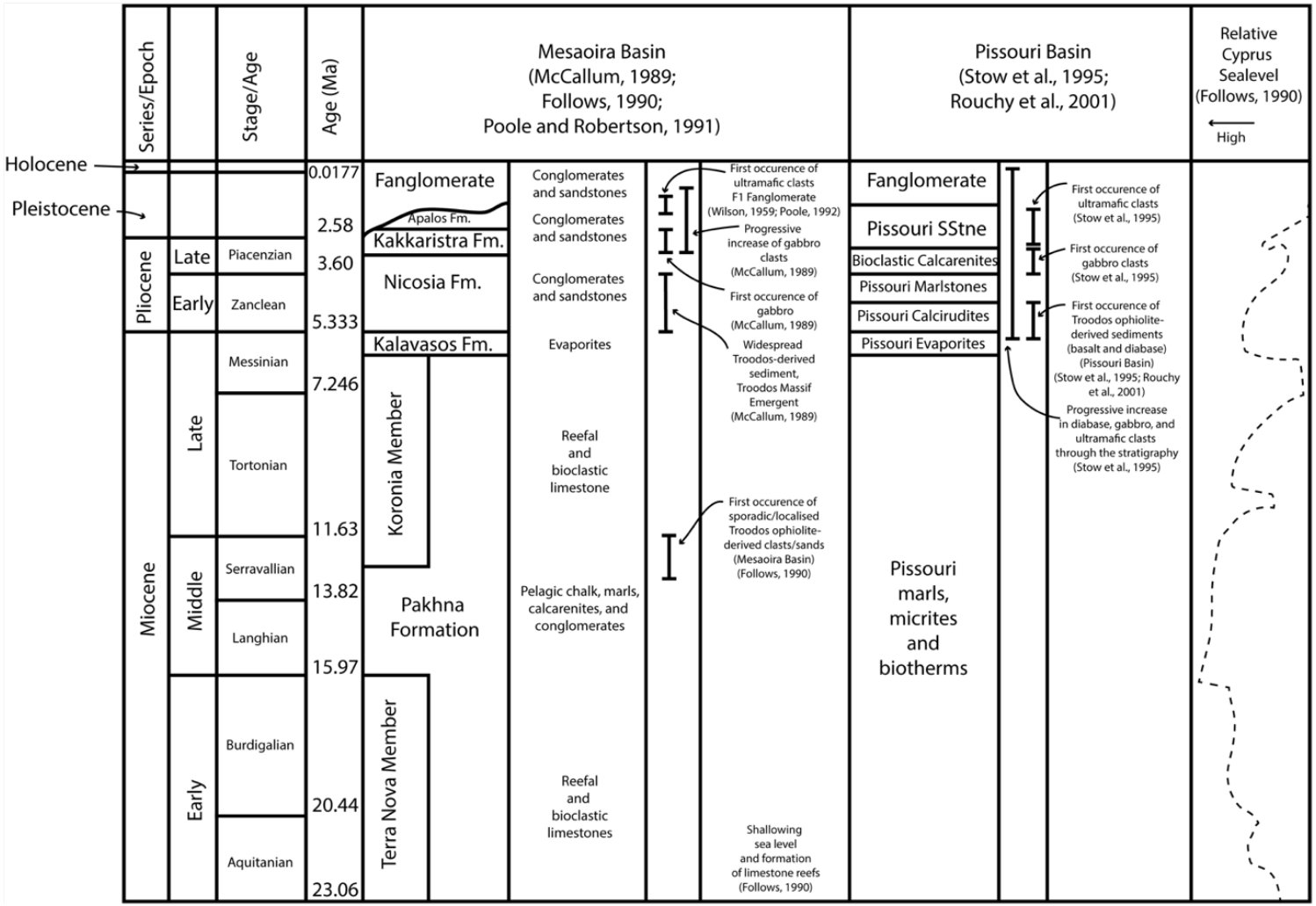

Figure 2.6: Summary table of the circum-Troodos sedimentary sequences.

Chapter 3 Uplift and Exposure of Serpentinised Massifs: Modelling Differential Serpentinite Diapirism and Exhumation of the Troodos Mantle Sequence, Cyprus

Parts of this chapter are based on the following paper:

Evans, A.D., Teagle, D.A.H., Craw, D., Henstock, T.J., Falcon-Suarez, I.H., 2021. Uplift and exposure of serpentinized massifs: Modeling differential serpentinite diapirism and exhumation of the troodos mantle sequence, Cyprus. J. Geophys. Res. [Solid Earth] 126. https://doi.org/10.1029/2020jb021079

Abstract

Serpentinised mantle peridotites form prominent mountains, including the highest elevations of the Troodos ophiolite in Cyprus (Mount Olympus, 1952 m), but to date only qualitative mechanisms have been proposed to explain the uplift of mantle rocks to high altitudes. Serpentinisation reactions between mantle rocks and water result in profound changes to the rheology and physical properties of peridotites including significant density reduction (~900 kg/m^3). Field observations, density measurements, and isostatic uplift and erosional modelling provide new constraints on the contribution of serpentinisation to the uplift of the Troodos Mantle Sequence. Different serpentinisation styles have resulted in two distinct serpentinite domains with contrasting densities. Our modelling shows that the Troodos Mountains can form within the geologically constrained uplift time frame (~5.5 Myr) exclusively through partial serpentinisation reactions. We interpret the serpentinite domains as two nested diapirs that formed due to different extents of serpentinisation and density reduction. Differential uplift and exhumation has decoupled the two serpentinite diapirs from the originally overlying ocean crustal rocks. Once at high altitudes the incursion of meteoric water reinforced coupled deformation-alteration-recrystallisation processes in the shallow sub-subsurface producing a localised low density completely serpentinised diapir. A second decoupling between the contrasting serpentinite diapirs results in localised differential uplift and exhumation, extruding deep materials to the east of Mount Olympus. Application of our modelling to other serpentinite massifs (e.g., St. Peter and St. Paul Rocks, New Idria*, California) highlights the contribution of isostasy to the uplift of serpentinised massifs.*

3.1 Introduction

Partially serpentinised mantle rocks form prominent topographic features in numerous locations on Earth, both on land and in the oceans, for example Ronda Massif, Spain, Dun Mountain, New Zealand, and the Atlantis Massif on the Mid-Atlantic Ridge. Although some of these exposures can be explained by dynamic tectonics, other features require different explanations.

Serpentinisation reactions between water and mantle rocks dramatically change high density (3300 kg/m^3), relatively strong, anhydrous, low permeability, mantle peridotites into low density (2400 kg/m^3), weak serpentinites, inducing up to 40% volume expansion (Macdonald and Fyfe, 1985; Toft et al., 1990). The reduction in bulk density results in isostatic uplift, that together with serpentinite diapirism, has been proposed to have led to the exposure of serpentinised mantle peridotites at moderate to high altitudes on land in the Troodos Massif, Cyprus (Fig. 3.1; e.g., Gass and Masson-Smith,1963; Moores and Vine, 1971; Gass, 1977) and the New Idria Massif, California (e.g., Coleman, 1996; Tsujimori et al., 2007), and in the oceans forming the emergent St. Peter and St. Paul Rocks (e.g., Campos et al., 2010).

Here we investigate the uplift and exposure of the Troodos Massif of Cyprus and combine field observations with new density measurements and isostatic and differential erosion rate calculations to test whether serpentinisation can form the Troodos Massif. We document the contrasting manifestations of serpentinisation in the exhumed Mantle Sequence and calculate whether the isostatic consequences of the density and rheological differences can develop the distinctive but hitherto poorly explained outcrop pattern of this iconic geological terrane. We further apply our mechanistic uplift model to other settings and demonstrate the universality of our approach.

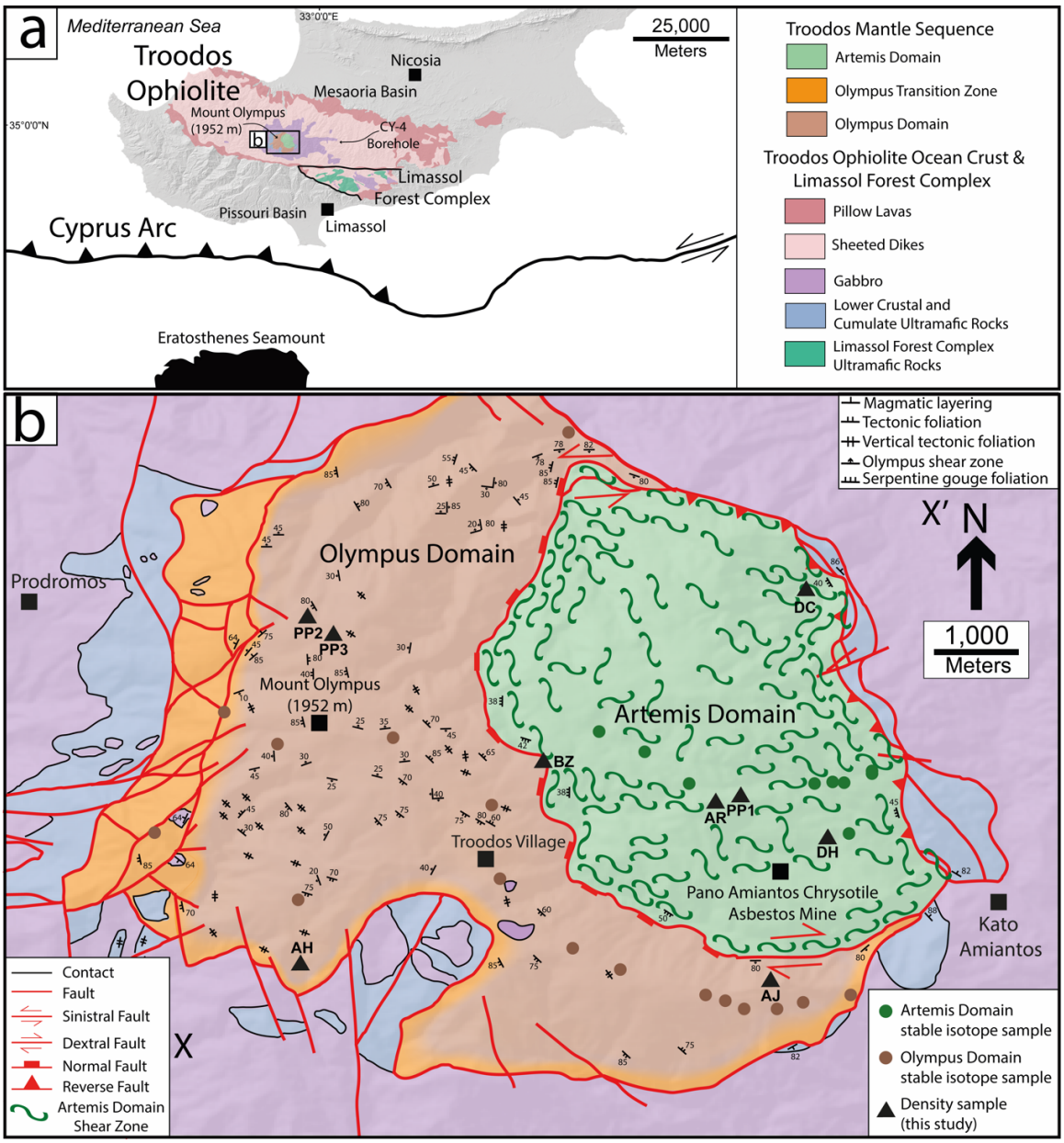

Figure 3.1: (A) Geological map of the Troodos ophiolite with the bullseye geometry of the Mantle Sequence highlighted along with the Limassol Forest Complex terrane, the Cyprus arc and northernmost portion of the Eratosthenes Seamount. (B) Geological map of the Troodos Mantle Sequence, adapted and updated from Wilson (1959). X to X' shows line of cross-section (Fig. 2.3; Fig. 2.4). Density sample locations shown as are sample locations for published oxygen and hydrogen stable isotope analyses by Magaritz and Taylor (1974); Heaton (1976); Nuriel et al. (2009).

3.2 Mantle peridotite massifs and serpentinite diapirism

Although mantle peridotite is the most common rock-type on Earth, surface exposures of mantle rocks are relatively rare and predominantly strongly to completely altered by serpentinzation reactions (e.g., Kelemen et al., 2011). Major outcrops of mantle peridotites are generally limited to ophiolites and oceanic core-complexes. A component of isostasy is

an inevitable consequence of serpentinisation reactions, but serpentinite diapirism is not ubiquitously invoked in every manifestation of serpentinisation. It is unclear whether serpentinite diapirism is overlooked or if subsequent deformation has obliterated geological evidence (e.g., Gass, 1977). Previously reported occurrences of serpentinite diapirism indicate a diverse spectrum of diapiric modes rather than a single mechanism. Here, we briefly outline some previously reported examples of serpentinite diapirism that represent this spectrum of occurrence.

3.2.1 Examples of serpentinite diapirism associated with isostatic uplift

Partially serpentinised serpentinite diapirs

Isolated mantle peridotite massifs have long been associated with variable extents of serpentinisation (e.g., Darwin, 1835), and their differential uplift relative to the surrounding seafloor has been proposed to occur due to the lower density of serpentine (e.g., Boillot et al., 1980; Bonatti, 1976; Hess, 1954). Isostatic uplift as a result of density-reduction from partial serpentinisation reactions, in combination with transpressional tectonics, has been previously invoked to explain isolated mantle peridotite massifs along oceanic fracture zones (e.g., Bonatti, 1978; Campos et al., 2010; Kil et al., 2010). For example, associated with the St Paul and St Peter Fracture Zones (0.6 and 2.5°N) in the equatorial Atlantic, the St. Peter and St. Paul Rocks archipelago (Campos et al., 2010) is primarily composed of variably serpentinised mylonitised mantle peridotite (e.g., Melson et al., 1972; Hekinian et al., 2000; Campos et al., 2005; Campos et al., 2010). These islands are only the emergent portion of the much larger (~90 km x ~20 km at 3000 m bsl) submerged variably serpentinised North Ridge mantle peridotite massif that rises from abyssal depths (~4000 mbsl, Campos et al., 2010; Hekinian et al., 2000; Maia et al., 2016). Radiometric dating suggests that the archipelago only became emergent in the past ~6500 years, with uplift on-going at a minimum uplift rate of >1.5 mm/yr (Campos et al., 2010).

Completely serpentinised serpentinite diapirs

Discrete occurrences of completely serpentinised mantle peridotities have previously been interpreted as distinct serpentinite diapirs. A key characteristic and composition of these surficial serpentinite extrusions is a low-density, mélange-like serpentinite breccia assemblage, where strongly altered and completely serpentinised peridotite clasts are hosted in a finely comminuted serpentinite gouge. These easily erodible materials are commonly associated with elevated topography, and consequently high uplift rates are often inferred to maintain the high relief of these easily erodible serpentinite extrusions. Examples occur near the San Andreas Fault, California include the ~5 km^2 1027 m-high

Table Mountain (Dickinson, 1966; Moore and Rymer, 2007) and the ~100 km^2 New Idria massif (1605 m, Coleman, 1996; Tsujimori et al., 2007). Both features are interpreted as completely serpentinised serpentinite diapirs. A rapid uplift rate of ~4 mm/yr is estimated from the relative displacement of sedimentary indicators (Coleman, 1996). This rapid uplift rate is balanced by an inferred high erosion rate of ~4 mm/yr that indicates ~17 km^3 has been removed from the New Idria serpentinite diapir (Coleman, 1996; Mumpton and Thompson, 1975). The rapid uplift rate (~4 mm/yr) is significantly greater than the estimated regional uplift rate for the Coast Ranges (~1 mm/yr; Page et al., 1998), implying differential uplift and exhumation between the New Idria serpentinite diapir and surrounding area simultaneously producing and maintaining ~1000 m of elevated relief.

3.2.2 Examples of serpentinite diapirism not associated with isostatic uplift

The large (~30 km in diameter, ~2 km high) submerged serpentinite mud volcanoes of the Mariana forearc have previously been referred to as examples of serpentinite diapirism (e.g., Fryer et al., 1985; Ishii et al., 1992; Fryer et al., 1992). Although these features contain clasts of strongly serpentinised mantle peridotite and metabasalts, some with sub-blueschist assemblages, these mud volcanoes are predominantly built from multiple effusions of unconsolidated serpentinite muds. These muds are, inferred to be produced by progressive interactions between serpentinised peridotites from the mantle wedge of the upper plate and subducting slab-derived fluids. Over-pressured mud-rich fluids then rise up steeply dipping faults before episodically erupting onto the seafloor (e.g., Mottl et al., 2004; Fryer, 2012). Fluid mass transfer resulting in multiple episodes of mud-eruption have built up these serpentinite seamounts (Fryer, 2012) as opposed to isostatic responses resulting directly from serpentinisation reactions. These mud volcanoes therefore differ from other completely serpentinised peridotite diapirs as they are not associated with surface uplift.

3.3 Structure of the Troodos Mantle Sequence

3.3.1 Structure of the Olympus domain

The rocks of the Olympus domain exhibit a steeply dipping ~NW-SE orientated primary tectonic fabric (Fig. 3.2) of elongated orthopyroxene grains, in some places isoclinally folded, that is interpreted as Cretaceous ridge-related high-temperature deformation (Moores and Vine, 1971). Overlaying this primary tectonic foliation are conjugate brittle-plastic shear zones (following Fossen and Cavalcante, 2017; Ramsay, 1980), which in the Olympus domain are thin, localised shear surfaces (~5 cm wide) and laterally continuous for ~100 m (Fig. 3.3; Fig. 3.4). These shear surfaces intersect and are orientated ~120° to each other (Fig. 3.3; Fig. 3.4), forming generally undeformed elongated lozenges of partially serpentinised Olympus domain mantle peridotite encompassed by shear surfaces (Fig. 3.3; Fig. 3.4). Surrounding the summit region of Mount Olympus, conjugate shear zones are orientated at low dip angles and in general progressively steepen away from the summit region to moderate-high dip angles at the margins of the Olympus domain (Fig. 3.3; Fig. 3.4; Fig 3.5). Fracturing at the outcrop scale is minor and manifests as joints and along shear surfaces (Fig. 3.3; Fig. 3.4). The Olympus domain displays a distinctive, cohesive, blocky, and competent outcrop pattern (Fig. 3.3; Fig. 3.4).

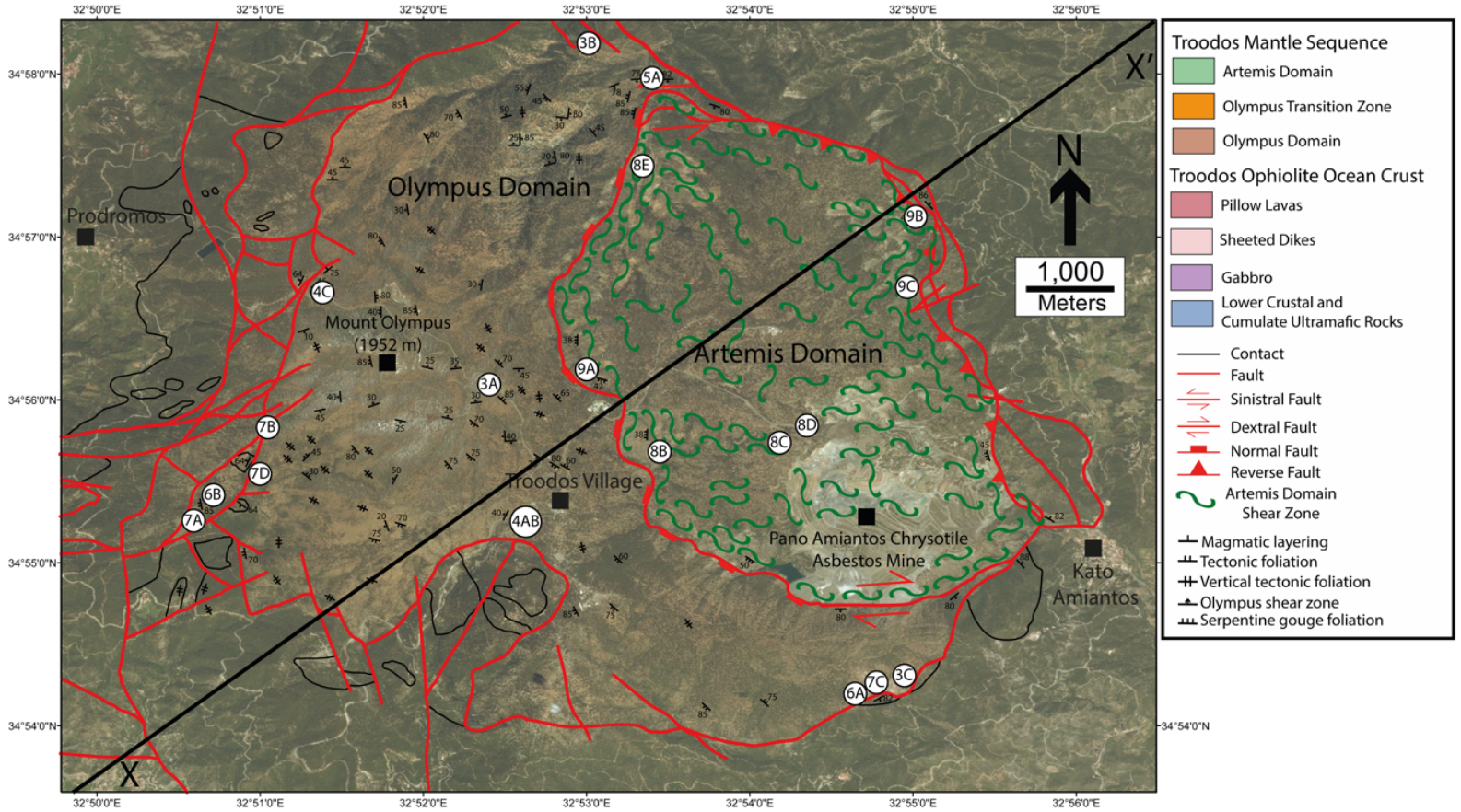

Figure 3.2: Aerial imagery map of the Troodos Mantle Sequence with locations of field pictures, tectonic foliation measurements are from Wilson (1959).

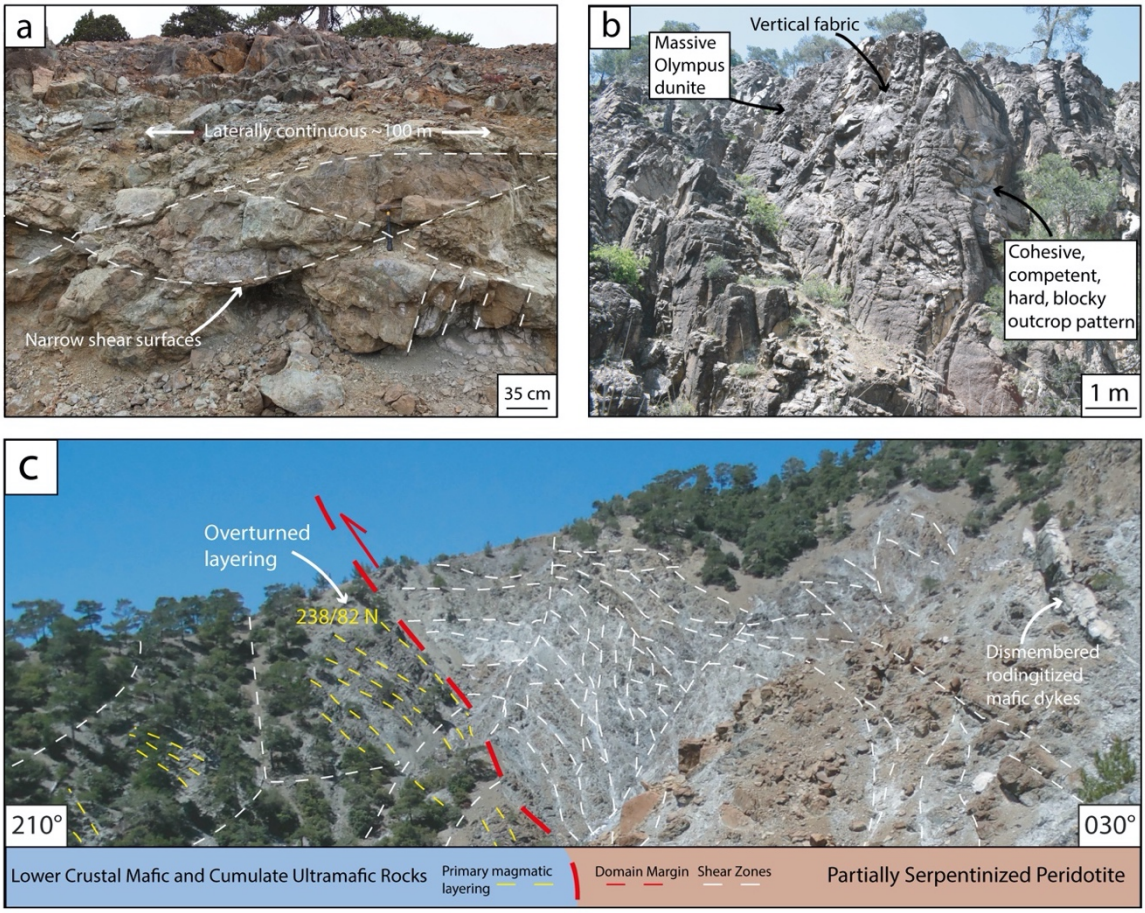

Figure 3.3: (A) Typical outcrop of partly serpentinised mantle peridoties from the Olympus domain with near horizontal, narrow shear zones orientated 120° apart, that form laterally continuous ~100 m lensoidal geometries. (B) Massive Olympus domain dunite displaying the common hard, blocky, cohesive, partially serpentinised mantle peridotite outcrop pattern. (C) Olympus domain outer boundary highlighting a zone of intensely deformed peridotite and intercalated blocks of overturned layered gabbro.

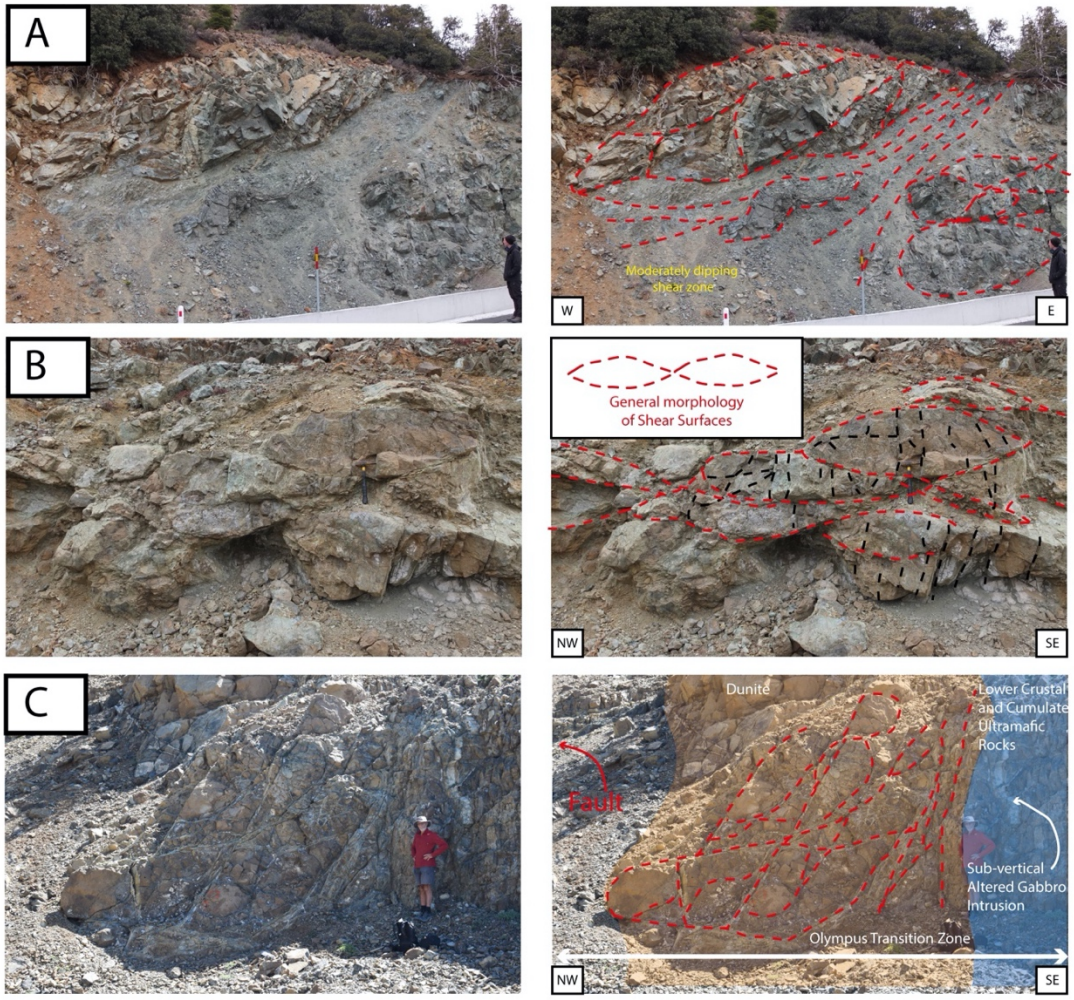

Figure 3.4: (A) Unannotated and annotated field picture pair within the Olympus Domain. A moderately dipping brittle-plastic shear zone is shown. Deformation is concentrated within a zone ~1.5 m in thickness. S C fabrics are observed within the shear zone with competent lozenges exhibiting predominantly asymmetric morphologies. Outside of the main deformation band, shear surfaces separate the rock into separate generally underformed partially serpentinised lozenges of varying symmetries. Subsequent brittle fracturing has resulted in a complex extensional fracture (joint) pattern. Person for scale. (B) Sub-horizontal conjugate brittle-plastic shear zone shown with generally symmetrical and undeformed lozenges forming in between the shear surfaces. These interconnected shear surfaces intersect at 120° (red lines) and are generally interpreted as examples of conjugate shear zones that have undergone coaxial deformation (e.g., Ramsay, 1980; Fossen and Cavalcante, 2017). The implication of the geometry is that the undeformed lozenges exhibit 'internal boudinage' (i.e., boudinage not related to competence contrasts; Ramsay, 1980) and in this case have extended in the ~horizontal direction and likely flattened in the ~vertical direction. Subsequent brittle fracturing (black lines) occurs within these undeformed, symmetrical, massive, partially serpentinised lozenges. These low-angle conjugate shears are prevalent in road cuttings on the road to the summit of Mount Olympus and are continuous over ~100 m in distance. Away from the summit the general dip angle of these conjugate shear zones increases from low angles (<30°) to moderate-high angles (~60° to <90°; (C)), with a general increase in the asymmetry of the lozenges (e.g., Fig. 3.5). Hammer for scale. (C) A shear zone array orientated at moderate dip angles is shown. Shear surfaces are generally orientated 120° and their geometries are more asymmetric relative to the lozenges of B. Domain sub-division occurs where, within larger ~2 m lozenges, smaller lozenges are bounded by shear surfaces forming an intricated, anastomosing shear zone array across differing domain scales. Person for scale.

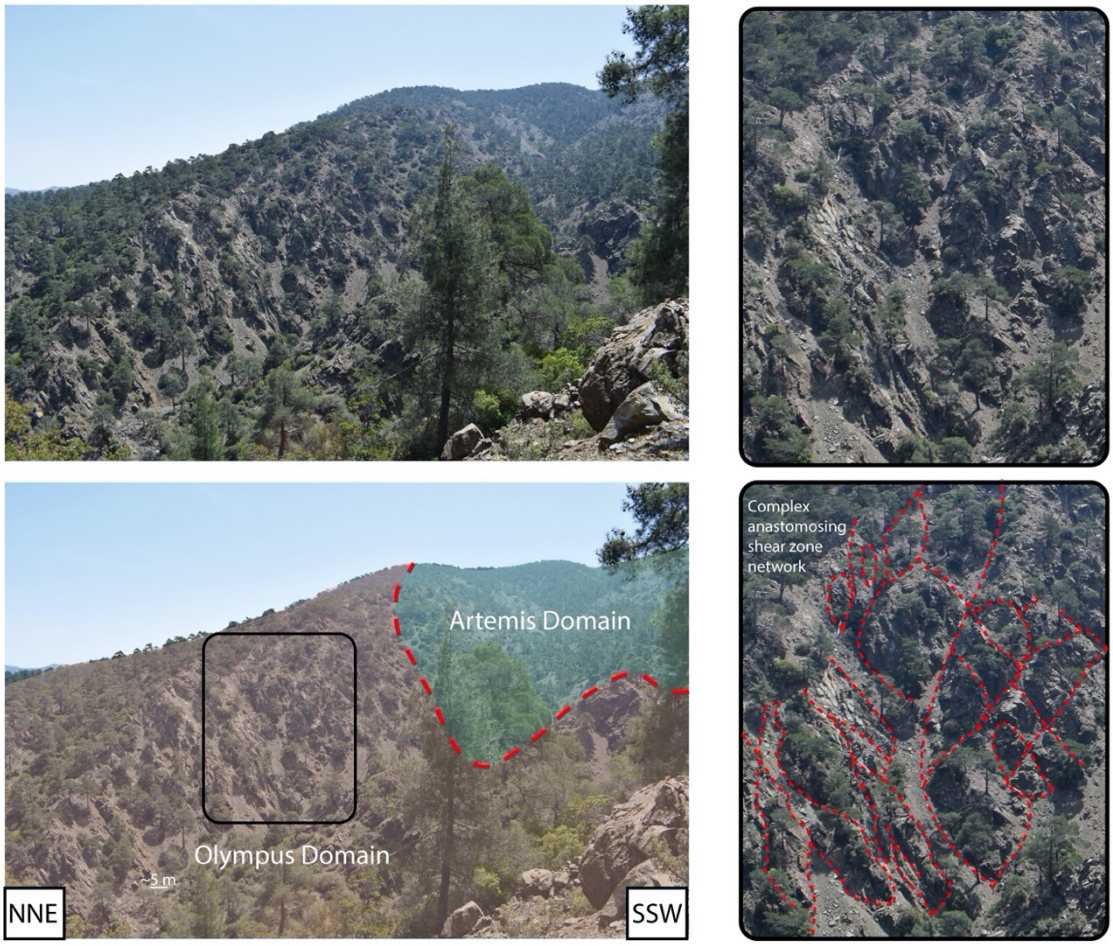

Figure 3.5: Field picture of the Artemis / Olympus northern boundary. A complex high angle, ~NW dipping, shear zone array occurs. Asymmetric lozenge geometries occur, and shear surfaces are inferred across a range of scales (red lines), highlighting domain sub-division into increasing smaller asymmetric lozenges that are bounded by brittle-plastic shear surfaces. Despite the substantial internal deformation of the Olympus domain, deformation within the Artemis domain is greater than the Olympus domain. Deformation within the Olympus domain results in a cohesive, blocky outcrop pattern, with development of serpentinite breccias localised to outcrop scales where strain has localised between less deformed lozenges. In contrast, in the Artemis domain, entire hillslopes are composed of serpentinite breccia (e.g., Fig. 3.4 (C)).

There is a complex marginal boundary between the Olympus domain and the encircling plutonic crustal rocks (Fig. 3.5; Fig. 3.6; Fig. 3.7), which we term here as the Olympus Transition Zone. This zone is of variable width, up to ~1 km at its widest extent, and comprises a generalised transition from predominantly lower ocean crustal cumulate rocks intercalated with localised bodies of dunite and pyroxenite to predominantly mantle rocks of the Olympus domain, principally harzburgites and dunites with intercalated localised bodies of lower ocean crustal mafic and ultramafic cumulate rocks (Fig. 3.6; Fig. 3.7). Deformation is distributed throughout the Olympus Transition Zone but is mostly localised to an encircling array of steeply dipping interconnected fault-zones that isolate and juxtapose regions of

undeformed and massive partially serpentinised bodies with moderately to steeply dipping (60° to >90°) layered gabbros that in places are locally overturned (Fig. 3.3; Fig.3.4; Fig. 3.6; Fig. 3.7). This structural style occurs across differing scales from outcrop to hillslope (Fig. 3.1; Fig. 3.4; Fig. 3.6), consequently producing a complex structural unit that anastomoses irregularly around the arcuate periphery of the Olympus domain (Fig. 3.1). Although on the western slopes of Mount Olympus, some rare, small, fault-isolated regions preserve igneous boundaries between cumulate to mantle rocks, at a larger scale, faults always separate the main Olympus domain from the continuous sequences of ultramafic cumulate rocks and gabbros of the lower Troodos ocean crust (Wilson, 1959).

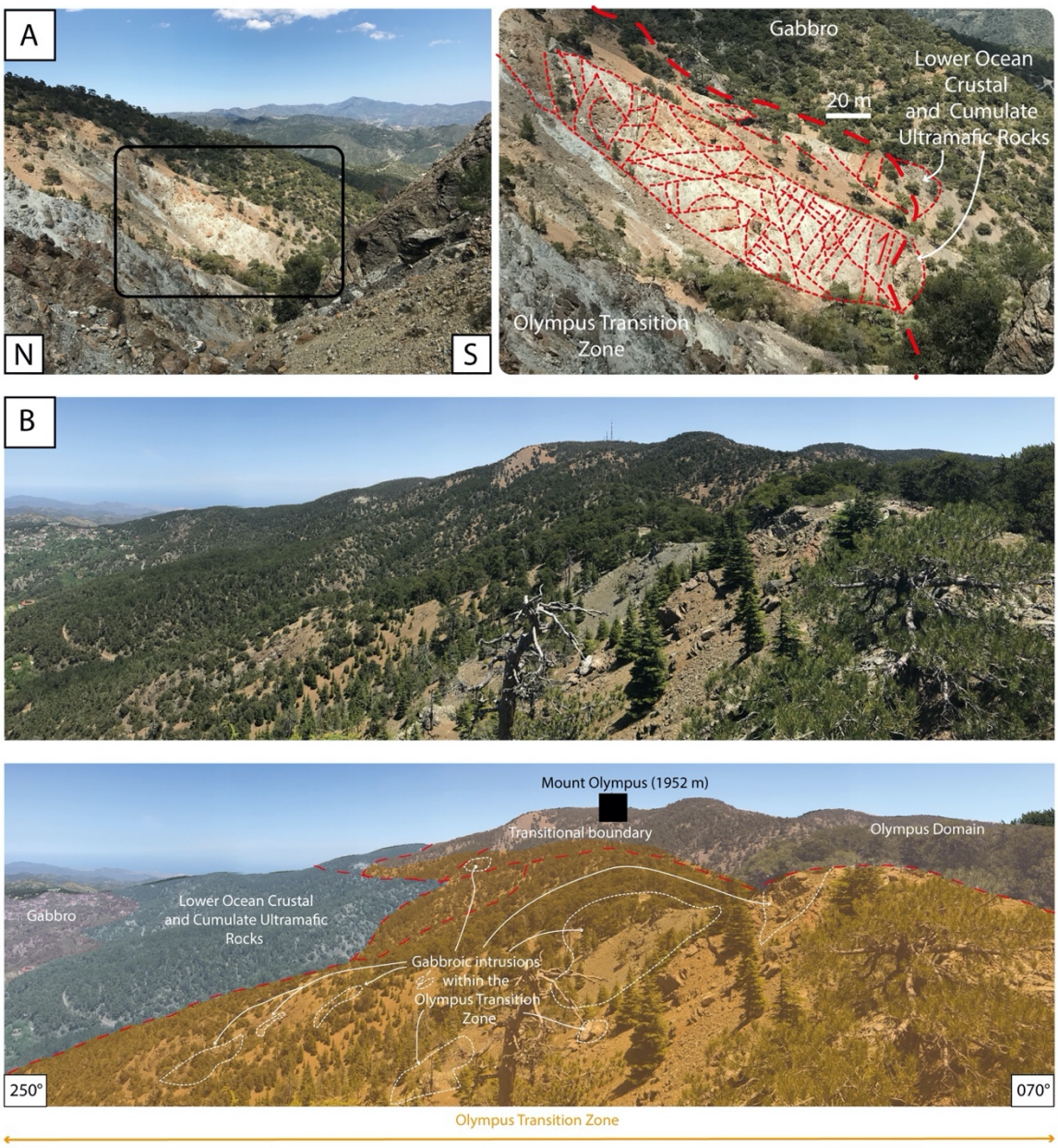

Figure 3.6: (A) SE boundary between the Olympus Domain Transition Zone and lower ocean crust cumulate ultramafic rocks and gabbro. This boundary is interpreted as a complex fault zone composed (here at this locality) of primarily Olympus Domain dunites intercalated with lower ocean crust cumulate ultramafic rocks and gabbros. Discontinuous surfaces are inferred (red lines) and highlight a complex array of structures. The prime structure is the ~W-E orientated structure and is inferred as a high-angle reverse fault. The intensity of deformation varies spatially across the Olympus Transition Zone. The western margin of the uplifted mantle peridotites is less deformed (e.g., B) relative to the intensely deformed SE portion (e.g., A).

(B) Field picture looking ~N towards the summit of Mount Olympus, highlighting the complex boundary between the differentially uplifted mantle peridotites and stratigraphically higher but topographically lower ocean crustal rocks. This differential uplift is evident and has been accommodated by a distributed ~500 m to ~1000 m wide zone of variable deformation presented here as the Olympus Transition Zone. The Olympus Transition Zone is a structural unit composed primarily of Olympus Domain dunites with of varying proportions of lower ocean crust cumulate ultramafic rocks and intrusive gabbroic bodies. A transition occurs within the Olympus Transition Zone from predominantly lower ocean crustal units with localised intercalated bodies of dunite and pyroxenite to predominantly Olympus

Domain dunites with localised intercalated bodies of gabbro and lower ocean crustal mafic and ultramafic rocks.

Earlier mapping (Wilson, 1959) has inferred that the Previously, ~N-S orientated segment of this western boundary have been inferred as a continuous and conformable boundary with discontinuous oblique faults mapped as offsetting these otherwise conformable boundaries (e.g., Wilson, 1959). We propose that these ~N-S orientated contacts are not discrete lithological contacts but are discontinuous, and likely form part of a complex array of faults that have resulted in distributed deformation across the Olympus Transition Zone.

The western contact of the Olympus Transition Zone is inferred as a faulted contact and is generally denoted by: The occurrence of dunitic bodies; geomorphological changes such as a break in slope and development of valley lows; a sharp reduction in the density of vegetation; and a change in the colour of float from white/grey to orange as highlighted in aerial photographs (Fig. 3.2). Whereas the eastern contact of the Olympus Transition Zone is transitional and is generally denoted as where outcrops are less deformed, generally massive, and composed of Olympus Domain partially serpentinised dunite and harzburgite.

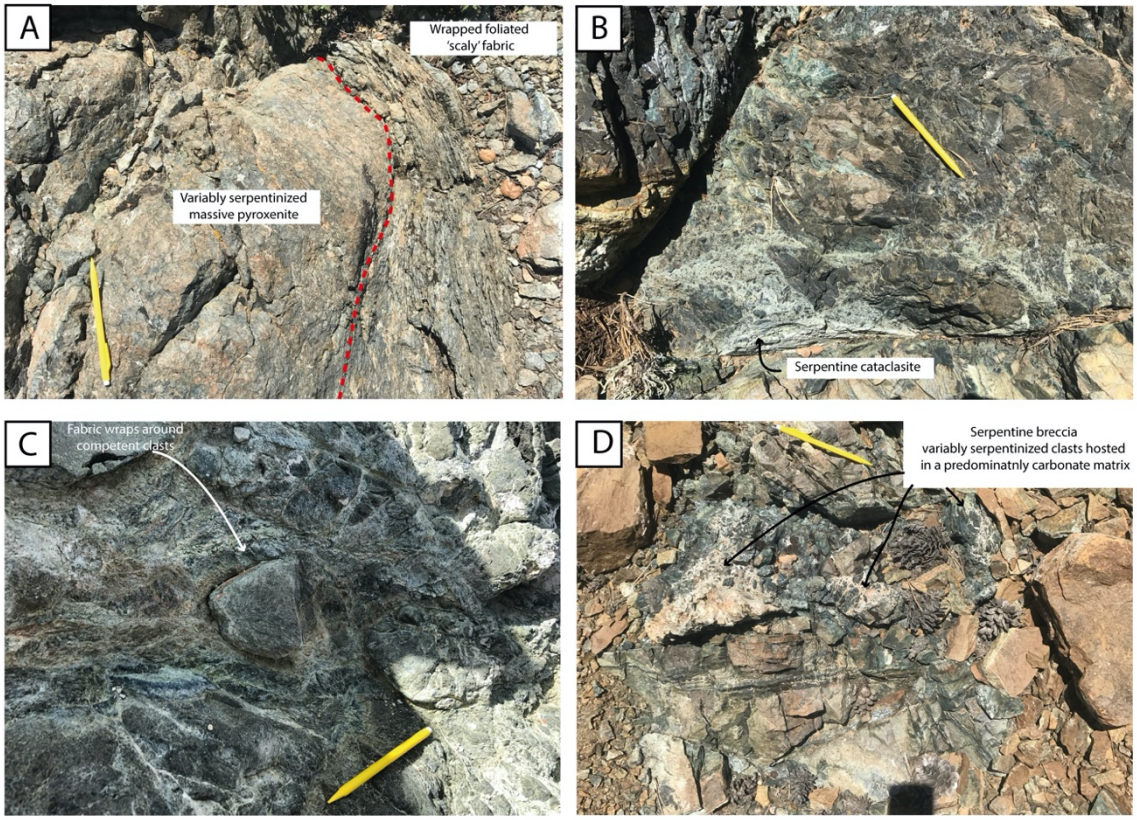

Figure 3.7: A) A variably serpentinised massive pyroxenite body is wrapped by a matrix composed of a variably serpentinised foliated 'scaly' fabric.

(B) Serpentine cataclasite located within the Olympus Transition Zone, composed of a cohesive cataclasite composed of variably serpentinised clasts hosted in a fine-grained comminuted serpentine gouge. This Olympus Transition Zone cataclasite is not equivalent to the Artemis serpentine breccia as it is cohesive and competent. The Olympus Transition Zone cataclasite is not ubiquitous, it is generally located where strain has localised between bodies of less deformed competent partially serpentinised peridotites.

(C) A clast-breccia-gouge assemblage of the Olympus Transition Zone is shown. The assemblage is generally incohesive. The foliated gouge wraps around the competent undeformed clast.

(D) Serpentine breccia located within the Olympus domain, nearby to the transitional boundary between the Olympus Transition Zone and the Olympus Domain. Deformation is expressed through brecciation with partially serpentinised angular clasts hosted in a predominantly carbonate matrix.

(A-D) This image plate highlights a general transition in deformation mechanisms from predominantly brittle-plastic shear zones that wrap around more massive and undeformed clasts (A) to predominantly brittle deformation mechanisms generally cohesive cataclasis (B) to then generally incohesive gouge and breccia development (C) likely overprinting earlier brittle-ductile deformation similar to A. Finally, an incohesive serpentinite breccia with a carbonate matrix and variably serpentinised clasts (D). These rocks are likely recording the deformation resulting in the progressive exhumation of mantle peridotites.

3.3.2 Structure of the Artemis domain

To the east of Mount Olympus is the sub-circular Artemis domain that comprises a heterogenous assemblages of highly serpentinised blocks and clasts and serpentine gouge, which is juxtaposed by faults against the massive peridotites of the Olympus domain (Fig. 3.8). The Artemis domain is generally at lower altitude than (>1200 to ~1700 m) the Olympus domain (>1200 to 1952 m) (Fig. 3.8). Within the Artemis domain coherent blocks and clasts (>100 m to dm) are completely serpentinised and occur within a friable matrix of highly comminuted serpentine cataclasite and serpentine clay gouge. In some zones the serpentine gouges have developed a well-defined secondary foliation fabric (Fig. 3.8; Fig. 3.9) that anastomoses around the more competent clasts (Fig. 3.8, Fig. 3.9). Within the more competent clasts, fibrous asbestiform chrysotile and crack-seal serpentine veining is common on scales from 0.5 mm to ~10 m, forming abundant mutually cross-cutting orthogonal, concentric, and oblique veinsets (Fig. 3.8). In rare occurrences serpentine veins cross-cut the Artemis serpentine gouge. Variable proportions and extents of recrystallisation occur throughout the Artemis domain (e.g., Fig. 3.8), with the greatest concentration along localised zones of high strain.

Overall, the Artemis domain comprises an approximately 50:50 mixture of serpentine breccia and gouge to competent serpentinised clasts, although the relative proportions are spatially variable (Fig. 3.8). The highest proportion of serpentine breccia-gouge to block-clasts is around the sub-circular margin of the Artemis domain (~80:20 respectively) with localised regions of 100% recrystallised serpentine gouge (Fig. 3.8; Fig. 3.9). These areas typically exhibit poorly consolidated steep slopes with active mass wasting and gravity-driven slumping in deeply incised valleys around the periphery of the Artemis domain (Fig. 3.8; Fig. 3.9).

In contrast, in the central zone of the Artemis domain, the ratio of blocks-clasts to serpentine breccia-gouge is reversed, with large (>100 m) blocks of strongly altered peridotite separated by complex networks of relatively narrow (~10 m) serpentine breccia (Fig. 2.4).

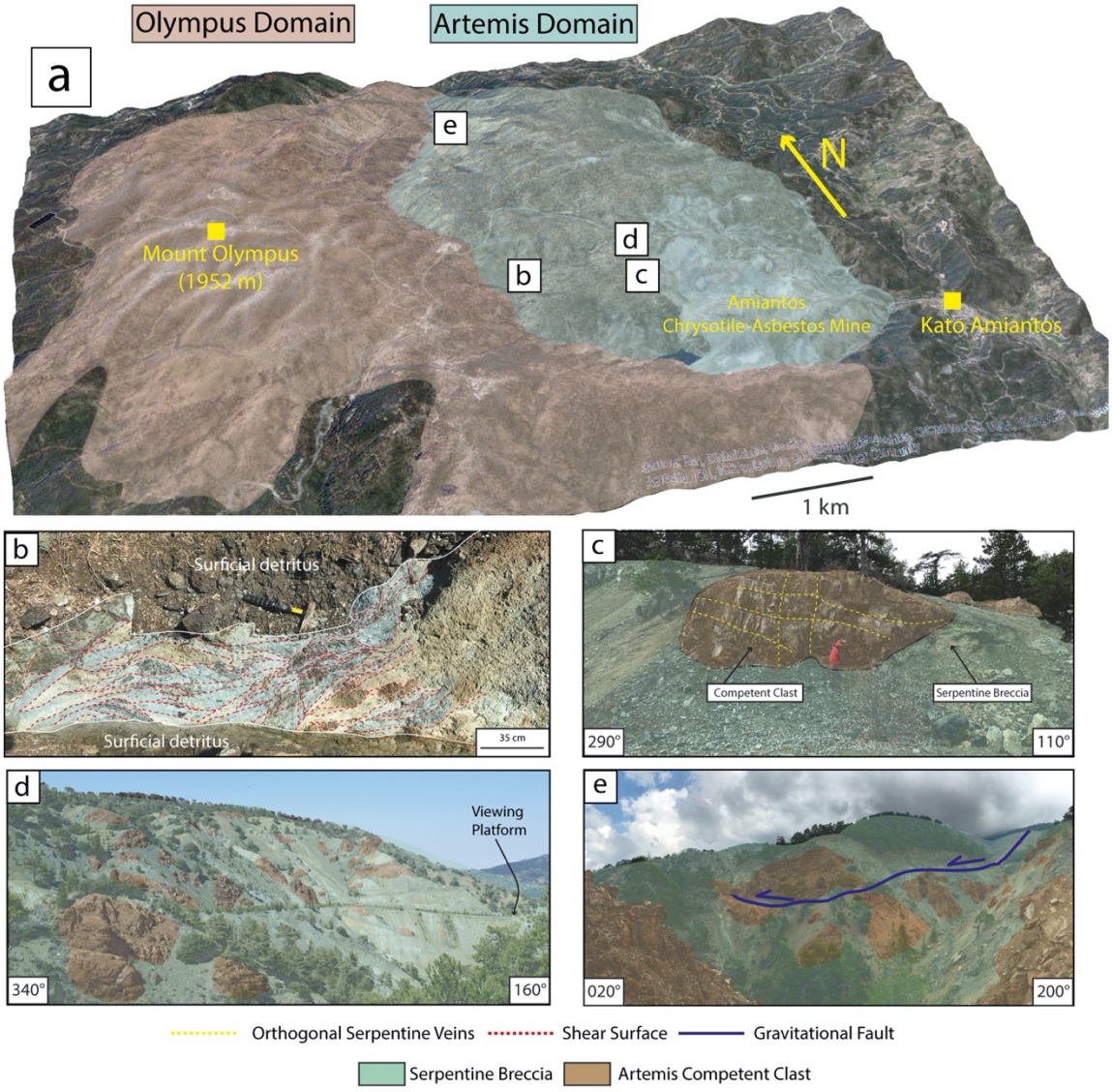

Figure 3.8: (A) 3D satellite-terrain hybrid image of the Troodos Mantle Sequence, highlighting the extent and differences in terrain and geomorphology between the Olympus and Artemis domains. Locations of inset images (B to E) shown. (B) Artemis domain serpentine gouge displaying the complex and intricate structure within recrystallised serpentine breccia-gouge. Hammer for scale. (C) Competent serpentinite block-clast with mutually cross-cutting orthogonally orientated serpentine veins, that is surrounded by highly comminuted serpentine cataclasite and localised serpentine gouge. (D) Artemis domain clast-gouge mountainside structure, highlighting the complex domain-wide network of isolated competent serpentinised block-clasts surrounded by weaker serpentine breccia-gouge. Viewing platform overlooking the former Amiantos asbestos mine for scale. (E) Actively collapsing Artemis domain hillslopes due to high proportions of weak, friable, serpentine gouge.

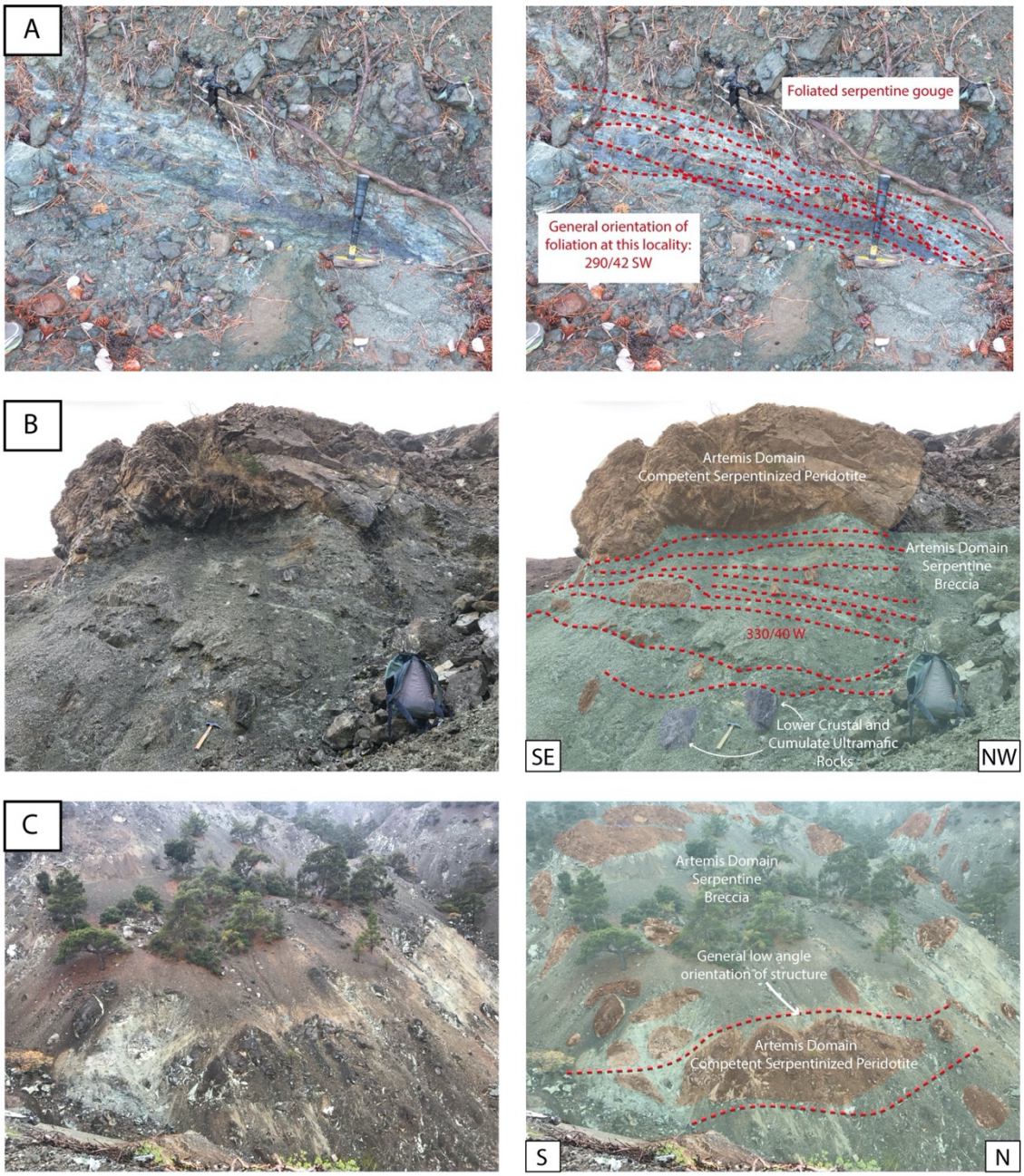

Figure 3.9: (A) Foliated serpentine gouge orientated 290/42 SW at the A locality. Hammer for scale. (B) Typical Artemis domain block-clast-breccia-gouge assemblage with clasts of Competent Serpentinised Peridotite and Lower Crustal and Cumulate Ultramafic Rocks. Foliated gouge wraps around competent clasts. Hammer for scale. (C) NE boundary of the Artemis domain highlights the chaotic nature of the Artemis domain. The general orientation of the structure is of a low dipping angle.

3.4 Contrasting properties within the Troodos Mantle Sequence

3.4.1 Contrasting Mineralogy

The serpentinisation style within the Olympus domain reflects the partial transformation (~50 to ~70%) of primary olivine and orthopyroxene to serpentine through serpentinisation hydration reactions (Fig. 3.10, Table 3.1). In contrast, the completely serpentinised materials of the Artemis domain reflect multiple and potentially on-going episodes of deformation, alteration, and recrystallisation (Fig. 3.10). Primary and alteration bulk assemblages are estimated from thin section and outcrop observations. Distinguishing between different serpentine polymorphs is challenging (Rooney et al., 2018 and references therein) so consequently we describe them all simply as serpentine, except for fibrous chrysotile and rare occurrences of 'splintery' antigorite.

Table 3.1: Contrasting characteristics, properties and serpentinisation styles exhibited by the proposed Olympus and Artemis domains of the Troodos Mantle Sequence.

	Olympus Domain	***Artemis Domain***
Serpentinisation degree	~50-70%	100%
Serpentinisation style	Hydration of primary igneous mineralogy	Coupled serpentine deformation-alteration-recrystallisation
Fabric	Primary – tectonitised localised serpentinised shears, cm to decimetre wide	Extensive secondary, polyphase shears, weak and soft serpentine breccia with component serpentinised clasts 1 cm to >100 m
Fractures	Minor fracturing	Extensive on all scales from micron to ~100 m
Chrysotile and serpentine veins	None, minor, ~2 mm wide serpentine veins uncommonly occur around domain periphery	Abundant orthogonal, concentric, oblique on all scales from sub-mm to 20 cm

	Olympus Domain	***Artemis Domain***
Shear zones	Laterally continuous up to 100 m, narrow <1 m, discrete, localised shear surfaces orientated 120° apart	Pervasive, dominating entire body from mm to >1 km, anastomosing/surrounding competent, rigid clasts
Competence	Cohesive, hard, blocky	Friable, incohesive
Density	2686 ± 83 kg/m^3	1949 ± 47 kg/m^3
Ground water	Low to very low, few perennial streams, ephemeral streams and seeps, no springs	Moderate to high, numerous ephemeral seeps and springs, several moderate-large perennial streams
Topographic expression	Mt. Olympus high point	Collapsing slopes, valleys
Erosion rate	Low, vegetated slopes, steep, large, rocky outcrops, narrow gorges	High, actively collapsing, vegetation-free steep slopes – angle of repose >30°
Inferred uplift initiation age	~5.5 Ma	<1 Ma?
Oxygen and hydrogen stable isotope values	δ^{18}O +7.1 ± 3 ‰ (1σ) δD -70.3 ± 10.8 ‰ (1σ)	δ^{18}O +11.8 ± 1.2 ‰ (1σ) δD -82.4 ± 8.2 ‰ (1σ)

The rocks of the Olympus domain are predominantly tectonised harzburgites originally composed of olivine, orthopyroxene, chromite and minor interstitial diopside, with subsidiary dunites, and some primary orthopyroxene veins. These rocks are partially to completely altered to olivine-serpentine mesh-textures and some magnetite, with trace dolomite and calcite, and minor ~1 mm-wide serpentine veins. (Fig. 3.10). Serpentine-filled microfractures are abundant at the micron scale (Fig. 3.10).

In contrast, the competent clasts of the Artemis domain are composed of mixed serpentine and chrysotile, including the complete bastitic replacement of primary orthopyroxene. Serpentine, predominantly fibrous chrysotile, occurs as discrete mutually cross-cutting extensional and hybrid crack-seal veins. The breccia matrixes and gouges comprise serpentine variably recrystallised to different grainsizes (Fig. 3.10). Multiple episodes of serpentinisation, deformation, dissolution and recrystallisation are likely

reflected in the breccia matrixes and gouges. In rare occurrences antigorite forms as discrete veins (e.g., Magaritz and Taylor, 1974) and as brecciated clasts (0.1 to 2 mm) surrounded by recrystallised serpentine. Chromite is the only primary mantle phase preserved in the Artemis domain rocks. Globular hydro-andradite occurs throughout the blocks within the Artemis domain, and also forms as discrete veins associated with serpentine veins. Calcite occurs as discrete late stage veins generally cross-cutting serpentine veins.

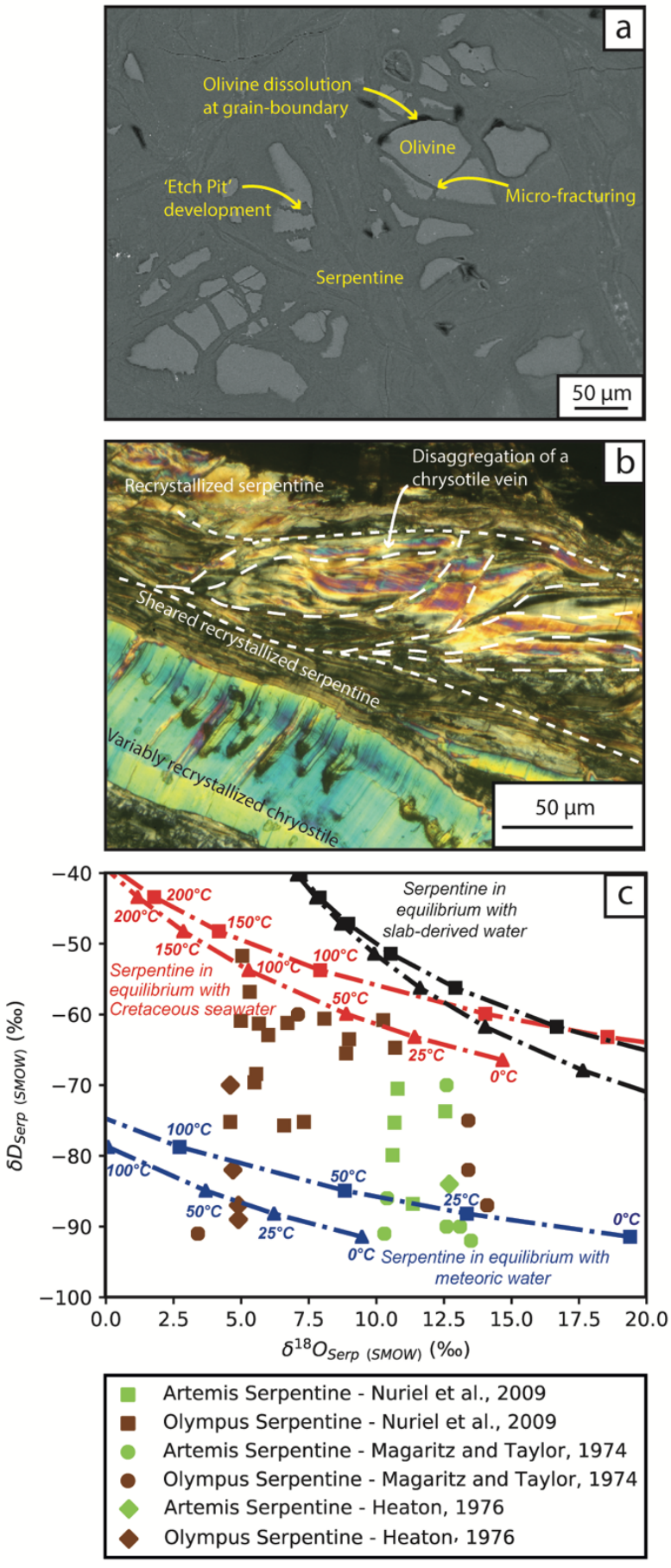
a
Olivine dissolution at grain-boundary
Olivine
'Etch Pit' development
Micro-fracturing
Serpentine
50 µm
b
Recrystallized serpentine
Disaggregation of a chrysotile vein
Sheared recrystallized serpentine
Variably recrystallized chryostile
50 µm
c
Serpentine in equilibrium with slab-derived water
Serpentine in equilibrium with Cretaceous seawater
Serpentine in equilibrium with meteoric water
200°C
150°C
100°C
50°C
25°C
0°C
δDSerp (SMOW) (‰)
δ18OSerp (SMOW) (‰)
−40
−50
−60
−70
−80
−90
−100
0.0
2.5
5.0
7.5
10.0
12.5
15.0
17.5
20.0
Artemis Serpentine - Nuriel et al., 2009
Olympus Serpentine - Nuriel et al., 2009
Artemis Serpentine - Magaritz and Taylor, 1974
Olympus Serpentine - Magaritz and Taylor, 1974
Artemis Serpentine - Heaton, 1976
Olympus Serpentine - Heaton, 1976

Figure 3.10: (A) Scanning electron microscope back-scattered electron (BSE) image of the partly serpentinised Olympus domain with the olivine-serpentine mesh interface highlighted. Common micro-fracturing associated with the dissolution and transformation of primary olivine to secondary serpentine through the serpentinisation style of partial serpentinisation hydration reactions. (B) Cross-polarised light photomicrograph of a typical Artemis domain completely serpentinised competent clast with variable dynamically recrystallised serpentine and associated cataclastic deformation. (C) Oxygen and hydrogen stable isotope plot of published serpentine measurements (Heaton, 1976; Magaritz and Taylor, 1974; Nuriel et al., 2009). Troodos Mantle Sequence values are separated based on sample location either from the Olympus or Artemis domain. Calculated serpentine oxygen and hydrogen stable isotope values in equilibrium with Cyprus meteoric water (δ^{18}O -7 ‰, δD -35 ‰; e.g., Boronina et al., 2005), Cretaceous seawater (δ^{18}O -1 ‰, δD -7 ‰; e.g., Heaton and Sheppard, 1977), and slab-derived metamorphic water (δ^{18}O +7.8 ‰, δD -15 ‰; e.g., Alt and Shanks, 2006) are shown. Triangles represent calculated serpentine values in equilibrium using empirical oxygen isotope fractionation factors from Wenner and Taylor (1971) and hydrogen isotope fractionation factors from Saccocia et al., (2009b). Squares represent calculated serpentine values in equilibrium using semi-empirical oxygen isotope fractionation factors from Zheng (1993) and empirical hydrogen isotope fractionation factors from Saccocia et al. (2009).

3.4.2 Contrasting serpentine oxygen and hydrogen stable isotope values

Published serpentine oxygen and hydrogen stable isotope values (e.g., Magaritz and Taylor, 1974; Heaton, 1976; Nuriel et al., 2009) differ for the Olympus domain and the Artemis domain (Fig. 3.10; Table 3.1). The Artemis domain values exhibit a shift to higher oxygen stable isotope values relative to the Olympus domain (Fig. 3.10; e.g., Magaritz and Taylor, 1974; Heaton, 1976; Nuriel et al., 2009). Calculated serpentine oxygen and hydrogen stable isotope values in equilibrium with meteoric water (δ^{18}O -7 ‰, δD -35 ‰; e.g., Boronina et al., 2005) at temperatures >25°C to <100°C and Cretaceous seawater (δ^{18}O -1 ‰, δD -7 ‰; e.g., Heaton and Sheppard, 1977) at temperatures <150°C fall into the respective outer limits of the Olympus domain values (Fig. 3.10). In contrast, serpentine oxygen and hydrogen stable isotope values of the Artemis domain fall into a narrower range (δ^{18}O +10.3 to +13.5 ‰; δD -70 to -92 ‰) compared to the Olympus domain (δ^{18}O +3.4 to +14.1 ‰; δD -52 to -92 ‰; Fig. 3.10; Magaritz and Taylor, 1974; Heaton, 1976; Nuriel et al., 2009). There is greater range in the Artemis domain hydrogen stable isotope values compared to oxygen stable isotope values (Fig. 3.10). Calculated serpentine oxygen isotope values in equilibrium with meteoric water (δ^{18}O -7 ‰, δD -35 ‰; e.g., Boronina et al., 2005) at temperatures ~25°C to ~50°C fall within the measured range of Artemis domain oxygen isotope values (Fig. 3.10). However, only some of the measured Artemis domain hydrogen stable isotope values match the equivalent equilibrium calculations (Fig. 3.10). The calculated serpentine oxygen and hydrogen stable isotope values in equilibrium with a slab-derived serpentinising fluid (δ^{18}O +7.8 ‰, δD -15 ‰; e.g., Alt and Shanks, 2006) do not match any previously measured oxygen and hydrogen stable isotope values (Fig. 3.10).

3.4.3 Contrasting bulk densities

Bulk dry densities were measured on mini-cores taken from selected representative samples from the Troodos ophiolite Mantle Sequence including samples from each of the Olympus and Artemis domains (Table 3.2). The bulk density of the partly serpentinised peridotites of the Olympus domain is 2686 ± 83 kg/m^3 (1σ, n = 8). In contrast, the serpentinised clasts from the Artemis Domain have bulk densities of 2330 ± 63 kg/m^3 (1σ, n = 5) and the serpentine breccias yield very low densities of 1568 ± 71 kg/m^3 (1σ, n = 6; Table 3.2, Fig. 3.10). Given the approximately 50:50 mix of clasts to breccia across the whole Artemis domain, we estimate a gross bulk density of ~1949 ± 47 kg/m^3 (Table 3.2). Background unserpentinised mantle peridotite has an inherit bulk density of 3300 kg/m^3 (Birch, 1964; Gass and Masson-Smith, 1963).

Table 3.2: New density measurements with estimated primary and secondary modal mineral assemblages. DSDP Leg 37 average density of serpentinised peridotite from Hyndman and Drury (1976). Average density of unserpentinised mantle peridotite from Birch (1961). Calculated errors for differing proportions of Artemis clast and gouge are also shown.

Sample	***Sample Type***	***Density (kg/m^3)***	***Primary Mineralogy Assemblage (%)***	***Secondary Mineralogy Assemblage (%)***
AH2	Olympus Dunite	2760	30-50	50-70
AH1	Olympus Harzburgite	2797	30-50	50-70
AJ2H	Olympus Harzburgite	2565	30-50	50-70
AJ2V	Olympus Harzburgite	2565	30-50	50-70
PP3-20	Olympus Harzburgite	2699	30-50	50-70
PP3-16	Olympus Harzburgite	2706	30-50	50-70
PP2-11	Olympus Dunite	2708	30-50	50-70
PP2-15	Olympus Dunite	2688	30-50	50-70
AR2	Artemis Clast	2292	0	100
AR1	Artemis Clast	2294	0	100
PP1-23	Artemis Clast	2390	0	100
PP1-22	Artemis Clast	2268	0	100
PP1-25	Artemis Clast	2408	0	100
BZ1	Artemis Breccia	1545	0	100

Sample	*Sample Type*	*Density (kg/m^3)*	*Primary Mineralogy Assemblage (%)*	*Secondary Mineralogy Assemblage (%)*
BZ2	Artemis Breccia	1505	0	100
DC1V	Artemis Breccia	1559	0	100
DC2H	Artemis Breccia	1502	0	100
DH1V	Artemis Breccia	1607	0	100
DH2H	Artemis Breccia	1691	0	100
DSDP Leg 37 (n=5)*	Serpentinised peridotite	2699		
Mantle**	Unserpentinised Mantle	3300	100	0

*(Hyndman and Drury, 1976)

**Unserpentinised mantle peridotite (Birch, 1961)

Sample Type	*Average Density (kg/m^3)*	*1σ*	*Competent Clast (%)*	*Serpentine Breccia (%)*
Olympus	2686	86		
Artemis Clast	2330	63 (δa)	100	0
Artemis Breccia	1568	71 (δb)	0	100

Sample Type	*Average Density (kg/m^3)*	*(***) Propagated Error (δz)*	*Competent Clast proportion (x)*	*Serpentine Breccia proportion (y)*
Artemis Breccia	1949	47	0.5	0.5
	1759	56	0.25	0.75
	2139	51	0.75	0.25
	2177	51	0.8	0.2
	1720	58	0.2	0.8
	1873	50	0.4	0.6
	2025	47	0.6	0.4

*** $\delta z = \sqrt{(x \times \delta a)^2 + (y \times \delta b)^2}$

3.5 Mechanistic Uplift Modelling

Explanation of the formation of the unique geometry of the Troodos Massif must address a number of key observations: (i) Uplift must occur within the well-constrained uplift trajectories from circum-Troodos sedimentary sequences (Fig. 2.6; e.g., Robertson, 1977; Follows, 1990; McCallum, 1989; Stow et al., 1995; Poole and Robertson, 1998; Robertson, 1998a, 1998b) and recent thermochronology (Morag et al., 2016). (ii) Invoke a mechanism that explains the differential uplift between the exhumed Troodos Mantle Sequence atop Mount Olympus and the regionally uplifted mantle peridotites that underlie the remaining ocean crustal sequences; (iii) Account for the sub-division of the Troodos Mantle Sequence into two distinct domains and their respective contrasting properties that has induced further uplift and exhumation of the Artemis domain relative to the Olympus domain. Here, we develop a one-dimensional uplift model for the Troodos Mantle Sequence to determine whether it is mechanistically possible to generate the observed ~2000 m relief through a density contrast-driven isostatic response since ~5.5 Ma, whilst parameterising for the sub-division of the Troodos Mantle Sequence.

3.5.1 Model parameters

Using reasonable parameters for the Troodos ophiolite (Table 3.3), elevation is determined in a number of iterative steps by subtracting erosion from the isostatic uplift generated by an advancing one-dimension serpentinisation front within a period of time, from an initial elevation of 0 m (Eq. 3.1, Fig. 7a, Table 3.3).

$$Elevation = Uplift - Erosion \tag{3.1}$$

The serpentinising front advances at an estimated average rate (S_r) for a given time period (η). This generates a depth (S_D) for the serpentinisation front (Eq. 3.2, Fig. 3.11).

$$S_D = S_r \times \eta \tag{3.2}$$

We assume that the advancing serpentinising front occurs within a horizontally confined structure, advancing into background unserpentinised peridotite with a density of 3300 kg/m^3. Serpentinisation reactions reduce density and result in volume expansion. Assuming that the horizontally confined structure expands (Eq. 3.3) in the vertical direction, the total percentage of volume expansion (β) is related to the total average serpentinisation percentage above the

advancing front. The rocks of the Olympus Domain are on average approximately ~50% serpentinised, and this produces a ~20% volume expansion (100% serpentinisation results in ~40% bulk volume expansion).

$$\varphi_D = \left(\frac{S_D}{100}\right) \times \beta \tag{3.3}$$

The total depth of the expanded advanced serpentinising front (φ_D) in a given time period added to the serpentinisation front depth (S_D), yields the total depth (D_D) (Eq. 3.4)

$$D_D = S_D + \varphi_D \tag{3.4}$$

D_D is then input into an isostatic calculation to determine the isostatic change in elevation over an increment of time, to the density difference between background ultramafic unserpentinised mantle (ρ_M) and a horizontally confined, vertical serpentinised body (ρ_D). The uplift due to isostatic response (U_t) of an advancing serpentinisation front is equal to the total uplift (Eq. 3.5) (Fig. 3.11).

$$U_t = \left(\frac{\rho_M - \rho_D}{\rho_M}\right) \times D_D \tag{3.5}$$

We then apply an erosional model (following for example, Cao and Paterson, 2016; Lee et al., 2015; Simoes et al., 2010) to calculate the erosion rate (E_r) for a time period (Eq. 3.6).

$$E_r = \frac{U_t}{\varepsilon_t} \tag{3.6}$$

$$\varepsilon_t = \frac{1}{\tau_e \times \omega} \tag{3.7}$$

$$E = E_r \times \eta \tag{3.8}$$

The erosion rate (E_r) is a function of the isostatic response uplift (U_t) and erosion response time (ε_t). The erosional response time is a function of the bedrock erodibility constant (τ_e) and average annual precipitation (ω) (Eq. 3.7). By multiplying the erosion rate with the time period

(η), the total erosion (E) for that time period can be calculated (Eq. 3.8). Each step is repeated 10000 times over a defined time period of 5.5 Myr.

Table 3.3: Model parameters for the Olympus and Artemis domains used in the mechanistical uplift modelling.

Symbol	***Definition***	***Olympus Domain Parameters***	***Artemis Domain Parameters***	***Unit***
S_D	Serpentinisation front distance			m
S_r	Serpentinisation front rate	(200, 1000, 2000, 3000)	(600, 3000, 6000, 9000)	m/Myr
η	Time period			Myr
	Time steps	10000	2000	
φ_D	Stretching distance			m
β	Stretching percentage	20% = 50% Serpentinisation	40% = 100% Serpentinisation	
D_D	Domain thickness/depth			m
U_t	Total uplift from isostatic response			m
ρ_M	Density of residual material	3300 (background lithospheric mantle)	2700 (Olympus)	kg/m^3
ρ_D	Domain density	2700 (Olympus)	2000 (Artemis)	kg/m^3
E_r	Erosion rate			m/Myr
ε_t	Erosion response time			Myr
τ_e	Bedrock erodibility coefficient	$1.5x10^{-6}$	$6.4x10^{-6}$	m
ω	Precipitation	910	910	mm/yr
E	Erosion			m

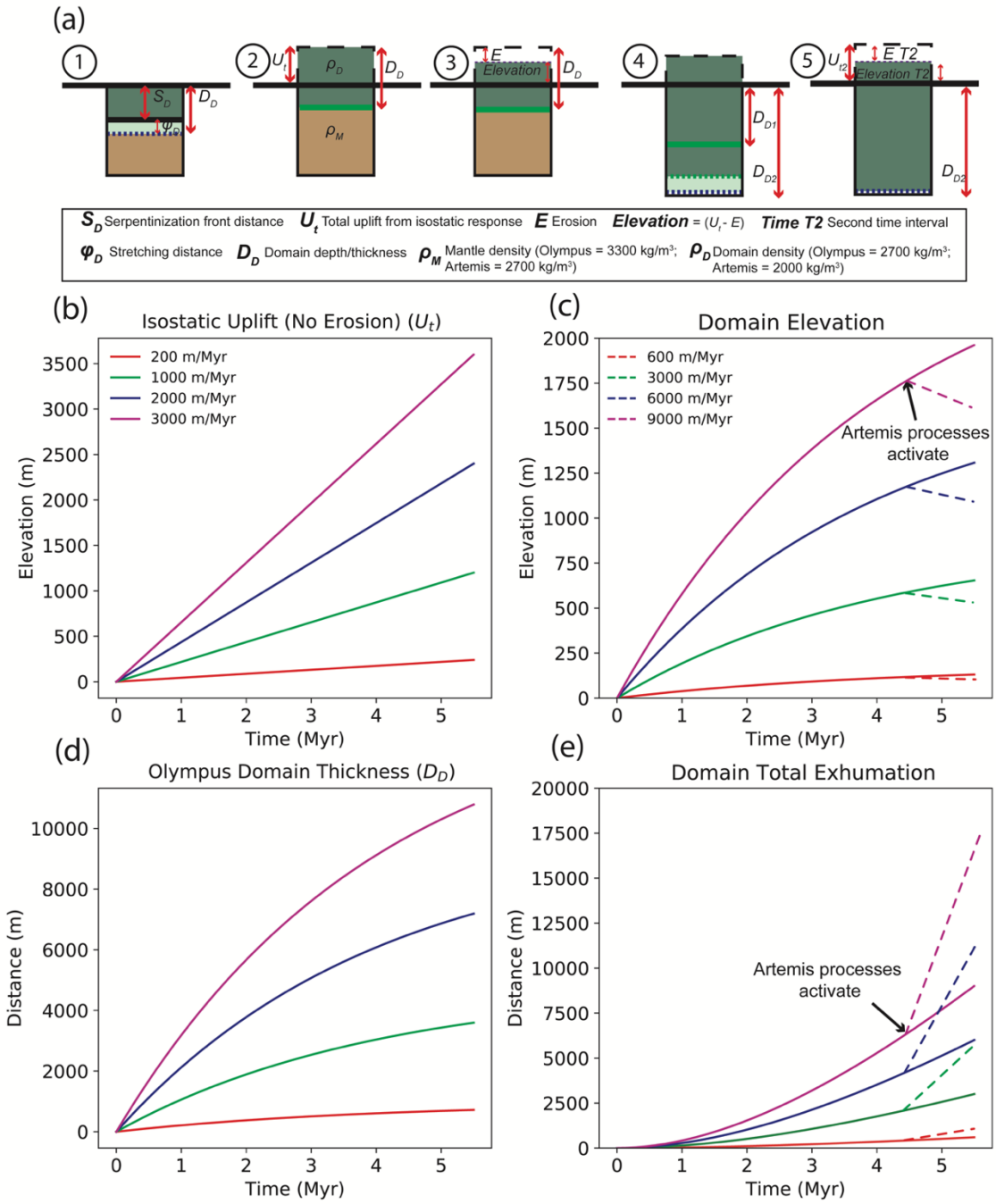

Figure 3.11: (A) Uplift model set up. One-dimensional horizontally confined model where elevation is determined by subtracting erosion from the isostatic uplift in response to an advancing average serpentinisation transformation front. Model is repeated over a number of iterative steps from an initial elevation of 0 m for a total run time of 5.5 Myr. Differing parameters are utilised for each domain (see Table 3.3). (B) Olympus domain isostatic uplift output shown with no erosion applied. Output highlights the theoretical maximum surface uplift that can be generated through an advancing average serpentinisation transformation front. (C) Olympus domain elevation model output shown, where differential erosional parameters are applied to the uplift model, generating an elevation value through subtracting erosion from surface uplift. Artemis domain total elevation output is also shown in dashed. Inflection point at 4.4 Myr highlights the change in parameterisation from Olympus to Artemis (Table 3.3). (D) Olympus domain evolving thickness output shown highlights the interplay between erosion and the advancing serpentinisation front in producing the thickness of the domain. (E) Olympus domain exhumation total is shown along with the Artemis domain exhumation total (in dashed). Inflection point at 4.4 Myr represents the activation of Artemis parameters (see Table 3.3).

A range of one-dimensional average advancing serpentinisation front *(S_r)* rates are input into the Olympus mechanistical uplift model (Table 3.3) to determine the contribution of an advancing serpentinisation front to uplift and unroofing of the Troodos Massif mantle peridotites. The range of Olympus domain one-dimensional serpentinisation front advancement rates *(S_r*; 200 to 3000 m/Myr) used in our model is broadly equivalent to serpentinisation rates proposed with other serpentinisation studies in seafloor settings (e.g., Lowell and Rona, 2002) and experimentally determined one-dimensional serpentinisation hydration reaction 'diffusion' rates that range between ~200 m/Myr and ~4000 m/Myr (e.g., Lamadrid et al., 2017; Macdonald and Fyfe, 1985; Martin and Fyfe, 1970; McCollom et al., 2016). However, the rate of our advancing one-dimensional serpentinisation front *(S_r)* is not strictly equivalent to an experimentally determined serpentinisation diffusion rate because our simple uplift model does not explicitly consider fluid channelling or the spacing of cracks and channels.

In contrast, the Artemis domain does not express a simple progressive hydration/serpentinisation style but coupled near-surficial to surficial deformation-alteration-recrystallisation serpentinisation processes. Surficial to near-surficial serpentinisation rates are interpreted to be geologically rapid (e.g., Craw et al., 1987). Modelling of the interplay between chrysotile dissolution-recrystallisation rates (e.g., Thom et al., 2013) and grain size in differing surficial (22°C), fluid-saturated pH conditions indicates that pH 8 a ~1 mm chrysotile particle would dissolve and recrystallise in ~20,000 years, whereas under the same conditions a ~1 m-sized particle size would take ~20 Ma (Fig. 3.12). Consequently, due to grainsize reductions, coupled deformation-alteration-recrystallisation mechanisms at surficial conditions within the Artemis domain are likely to occur at faster reaction rates than the hydration serpentinisation style of the Olympus domain. This reflects the contrasting structural characteristics of each domain and is likely to continue to some degree at depth due to greater fracture density within the Artemis domain relative to the Olympus domain. To reflect this within the Artemis uplift model, the Artemis advancing transformation rate *(S_r)* is tripled relative to the Olympus domain.

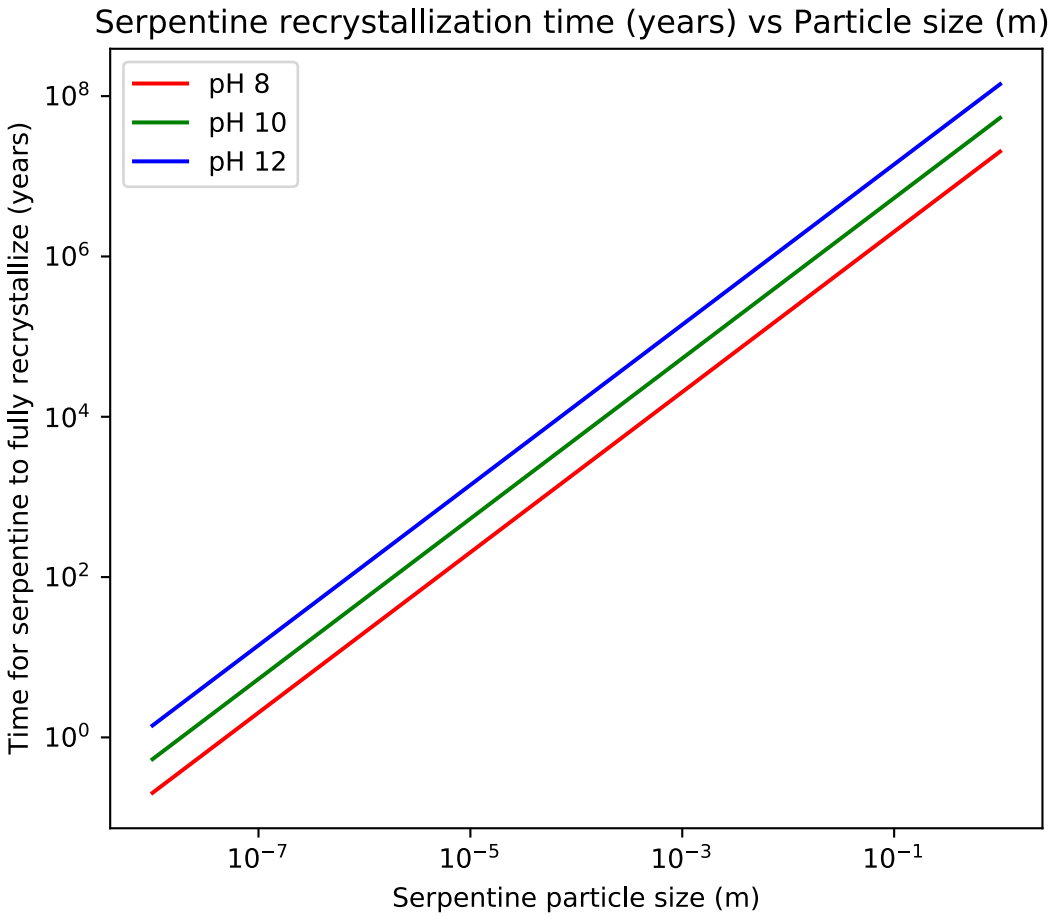

Figure 3.12: Serpentine dissolution time vs particle size under varying pH conditions log-log plot (see main text for details). Serpentine dissolution rate from Thom et al., (2013).

It is assumed that the isostatically uplifted Troodos ocean crust had a similar density and bedrock erodibility constant (τ_e) to partially serpentinised peridotites (2700 kg/m^3). It is assumed that there is no 'lag' time between the advance of the serpentinising front and isostatic uplift. Within the model set-up, we assume a horizontally bound vertical structure, where the advancing serpentinisation front and associated volume expansion occur only in the vertical direction. Although it is easier to conceptualise the model with fluid infiltration from the surface, the model is not reliant on whether the serpentinisation fluid source is from above, below, or a combination of both since the mass-change outcome is the same in our one-dimensional setup. We assume that the advanced serpentinisation front depth (S_D) is an average serpentinisation percentage for the whole vertical structure. The model does not account for gravitational collapse. Nor does it account for thermo-mechanical boundary effects between the serpentinised portion and background unserpentinised mantle during exhumation/uplift. It is assumed that present-day precipitation levels of 910 mm/yr (Prodromos village, 1400 m asl, Cyprus Department of Meteorology) are representative of rainfall throughout the model time

frame. This may be an over-estimation as precipitation generally increases with elevation, and hence may have been lower during the initial stages of uplift. Although during the Plio-Pleistocene periods of greater humidity and precipitation levels than the present-day have been inferred from the relative abundance of sapropels (e.g., Poole and Robertson, 1998 and references therein). We propose a 1.1 Ma date (Mid Pleistocene) for the initiation of the Artemis domain alteration and deformation processes that must start some time between the initial exhumation and protrusion of ultramafic rocks in the Early Pleistocene and the end of the Pleistocene.

3.5.2 Uplift Modelling Results

A serpentinisation transformation front advancing at a rate of 3000 m/Myr will isostatically uplift rock a total of 3600 m in 5.5 Myr, for a density contrast of 600 kg/m^3 (Fig. 3.11). Applying reasonable erosional parameters of 910 mm/yr precipitation and a bedrock erodibility of 1.5x10^{-6} m to the same uplift parameters (S_r =3000 m/Myr, $\Delta\rho$ 600 kg/m^3) yields an elevation of ~1950 m for the Olympus domain after 5.5 Myr (Fig. 3.11). Under the same model conditions, adjustment of the bedrock erodibility parameter from 1.5x10^{-6} m to 1x10^{-6} m and 2x10^{-6} m produces elevation values of ~2350 m and ~1650 m respectively. Calculations of the evolving eroded total thickness (Fig. 3.11) and the total exhumation (Fig. 3.11) of the Olympus domain for different average advancing serpentinisation front rates *(S_r)*, suggests that up to ~9000 m of material has been exhumed from the Olympus domain over 5.5 Myr.

To quantify the dynamic topography resulting from a secondary density contrast between the Artemis (2000 kg/m^3) and Olympus (2700 kg/m^3) domains, the elevation model is re-run using the Artemis model parameters (Table 3.3). After 4.4 Myr of the 5.5 Myr run time, the Artemis domain overprints the Olympus domain, generating a joint contribution to the uplift and differential exhumation of the Artemis domain. The advancing serpentinisation front rate *(S_r)* of the Artemis domain is tripled. The bedrock erodibility constant *(τ_e)* is also increased to 6.4x10^{-6} m to account for the weak, friable, easily erodible material. Calculations using these parameters yield a lower elevation (~1550 m) for the Artemis domain compared to the Olympus domain peak (1952 m) (Fig. 3.11), in line with of the current present elevations. Using the parameters applied, modelling suggests that ~17.5 km of material has been exhumed over 5.5 Myr period (Fig. 3.11, Table 3.3).

3.6 Discussion

3.6.1 Serpentinite Diapirism of the Troodos Mantle Sequence

New measurements of the bulk densities of the Olympus and Artemis domains, and simple modelling indicate that mountains akin to Mount Olympus (~2000 m elevation asl) can form within the required time constraints (~5.5 Myr; see supplementary materials) solely through serpentinisation with the resultant density contrast causing isostatic uplift. Serpentinisation alone is therefore mechanistically capable of producing the progressive uplift and exhumation that has culminated in the solitary, relatively high-altitude peak (1952 m) of Mount Olympus, relative to the low to modest altitude of the sheeted dyke complex (~1000 m). We interpret the Olympus domain as a distinct serpentinite diapir that has resulted in the transportation and protrusion of mantle peridotites to 1952 m asl above the regionally uplifted mantle peridotites that underlie the ophiolitic ocean crust. The minimum differential uplift of the Olympus Diapir compared to the regionally uplifted 'in-situ' Troodos ophiolite mantle peridotites can be estimated by considering the Cyprus Crustal Study Project CY-4 drill hole located near the village of Palaichori (~930 m asl) ~20 km east of Mount Olympus. With a total depth beneath the surface of 2263 m CY-4 penetrated sheeted dykes, gabbro, and lower crustal ultramafic cumulate rocks but did not reach tectonised upper mantle peridotites (Malpas et al., 1989). Assuming that the CY-4 drill hole would have intersected mantle peridotites at a depth of 2500 m beneath the surface (1600 m below sea level) the minimum required relative uplift is ~3600 m.

We interpret the Artemis domain as a second, overprinting and distinct serpentinite diapir that has cannibalised the eastern portion of the Olympus Diapir through coupled deformation-alteration-recrystallisation processes to form a 100% serpentinised region (~1949 ± 47 kg/m^3) with a large proportion of low density breccia (1568 ± 71 kg/m^3). Although the lower density of the Artemis Diapir results in a greater amount of total isostatic uplift, its weak and easily erodible nature results in differential exhumation between both domains and a lower average elevation of the Artemis Diapir (~1550 m) compared to the Olympus Diapir (>1500 m to 1952 m).

Differences between the properties and characteristics of both diapiric boundaries, serpentinisation extents, alteration mineralogy, deformation styles, geomorphology, density, and outcrop patterns indicate that the Artemis domain overprints and builds on pre-existing Olympus Diapir serpentinisation and uplift (Fig. 2.4). This culminates in a distinct coupled serpentine deformation-alteration-recrystallisation serpentinisation style that is in direct contrast to the partial hydration serpentinisation style of the Olympus Diapir.

The initial localisation of greater extents of serpentinisation in the Artemis Diapir must result from structural controls that have been obscured by on-going deformation as the Artemis Diapir expands into the Olympus Diapir. The high altitude of the Troodos Mountains and associated rainfall combined with strongly deformed rocks has enabled the incursion of meteoric fluids into the rocks results in increased serpentinisation of the uplifted peridotites. An inevitable consequence of meteoric water incursion and serpentinisation is the augmentation of a localised deformation-alteration-recrystallisation positive-feedback mechanism that initiated the development of the overprinting Artemis Diapir. These mechanisms induce the formation of the easily erodible rock, and consequently result in further uplift and exhumation relative to the Olympus Diapir. By applying reasonable parameters to the uplift model, the total exhumation of the Artemis Diapir is calculated to range between >3.6 km and ~17.5 km (Fig. 3.11). Testing will require further detailed petrological and thermodynamic investigations.

There are clear geochemical differences between the rocks of the Olympus Diapir and Artemis Diapir. Previous oxygen and hydrogen stable isotope measurements (e.g., Magaritz and Taylor, 1974; Heaton, 1976; Nuriel et al., 2009) yield different measured values for the Olympus and Artemis Diapirs (Fig. 3.10). Calculated oxygen and hydrogen serpentine stable isotope values in equilibrium with meteoric water at varying temperatures (Fig. 3.10) indicate that the Artemis Diapir and portions of the Olympus Diapir serpentinites equilibrated with low-temperature (~25°C to <100°C) meteoric water at or near the surface since the unroofing of mantle peridotites during the Early Pleistocene (Wilson, 1959; Poole and Robertson, 1998a, 1998b), and these reactions and exchanges are probably on-going. Serpentine hydrogen stable isotopes have been proposed to exchange with subsequent fluid episodes, potentially overprinting original values (e.g., Wenner, 1971; Kyser and Kerrich, 1991; Kyser et al., 1999). Since the proportions in the balance between oxygen and hydrogen in the fluid and rock are different, hydrogen is more likely to undergo post-formational isotopic exchange relative to oxygen; serpentine oxygen stable isotope values are likely to be more robust. The high $\delta^{18}O$ values of the Artemis Diapir and portions of the Olympus Diapir ($\delta^{18}O$ +10.3 to +14.1 ‰) suggest formation at low-temperatures, likely with meteoric water (Fig. 3.10). Regardless of whether or not these values have been overprinted, they highlight that discrete portions of the Olympus and Artemis Diapirs have likely interacted and exchanged with differing fluids. Our 1-D models are not sensitive to where fluid ingress and serpentinisation occur and are consistent with a component of the uplift resulting from the focussed upwelling into the overlying mantle wedge of hydrous fluids generated by the dewatering of partially subducted marine sediments and ocean lithosphere beneath the Troodos rocks, as has been proposed to have initially serpentinised the Troodos Mantle Sequence, inducing serpentinite diapirism (Moores and Vine, 1971; Gass, 1977; Robertson, 1977; Robertson, 1998a, 1998b). Although there is strong evidence for two distinct textural and geochemical mantle domains (Batanova and Sobolev, 2000), direct evidence for the initial serpentinising fluid remains elusive. Further geochemical

and isotopic investigations are required to better constrain the sequence of fluid-rock exchanges that have occurred during the progressive serpentinisation of the Troodos Mantle Sequence.

3.6.2 Previous uplift mechanisms attributed to the Troodos Mantle Sequence

Previous studies, either do not or only partially satisfy the key criteria outlined in Section 6 necessary to explain the geometry of the Troodos Massif. Although there is compelling evidence in the Limassol Forest Complex for the Cretaceous seafloor exhumation of mantle rocks (e.g., Murton, 1986; MacLeod; 1988; MacLeod, 1990), geological evidence for similar exposure of the Troodos Massif mantle rocks is less forthcoming. Models that suggest the preservation of Cretaceous seafloor ridge-related detachment faulting (e.g., Nuriel et al., 2009) and Cretaceous ridge-related serpentinite diapirism (e.g., Schuiling et al., 2011) are incompatible with uplift trajectories. These models propose that the exhumation of the Troodos ultramafic rocks occurred on the Cretaceous seafloor. This would require the preservation of original Cretaceous sea-floor relief through its progressive uplift from ocean depths to the current high elevation 1952 m massif, but would also result in an inverted circum-Troodos sedimentary sequence, with the initial sequences rich in ultramafic materials as opposed to the basalts and diabase observed (Follows, 1990; McCallum et al., 1989; Stow et al., 1995; Rouchy et al., 2001).

Miocene to present-day convergence across the Cyprean subduction zone is also invoked as a mechanism for uplifting and exhuming the mantle peridotites that encompass Mount Olympus (Ring and Pantazides, 2019). These authors downplay the role of serpentinisation in forming the Troodos Massif, and favour a west-east elongate doubly plunging anticline with a serpentinite core formed in response to gradual differential shortening. Differential uplift between the Troodos Mantle Sequence and the remaining ocean crustal sequences is proposed to result from the underthrusting of the Eratosthenes seamount (Ring and Pantazides, 2019). This proposed uplift mechanism presents the Troodos Mantle Sequence as a homogenous monolith and does not account for the long-standing sub-division into two separate discrete domains, including evidence that the peridotites from these domains originate from different mantle sources (Batanova and Sobolev, 2000).

3.6.3 A unified model for the uplift of the Troodos Mantle Sequence

Initiation of significant uplift of the Troodos ophiolite is dated as latest Messinian to Early Pliocene (~5.5 Myr). Decoupling between the Olympus Diapir and the regionally uplifted 'in-situ' mantle peridotites of the Troodos ophiolite has resulted in at least >3600 m of differential uplift, transporting mantle peridotites to 1952 m absl (Fig. 3.13). Unroofing and erosion of the first ultramafic clasts is interpreted to have occurred in the Early Pleistocene, suggesting significant peridotite relief has occurred since then (Fig. 3.13). Once transported to high altitudes, increased rainfall results in the incursion of meteoric water (Fig. 3.13), driving the coupling of deformation-alteration-recrystallisation positive-feedback mechanisms of the intensely deformed Artemis Diapir. The resulting lower density and easily erodible material induces a secondary decoupling that separates the lower density Artemis Diapir from the Olympus Diapir (Fig. 3.13), in consequence differential uplift and exhumation occurs between the Artemis Diapir and the Olympus Diapir.

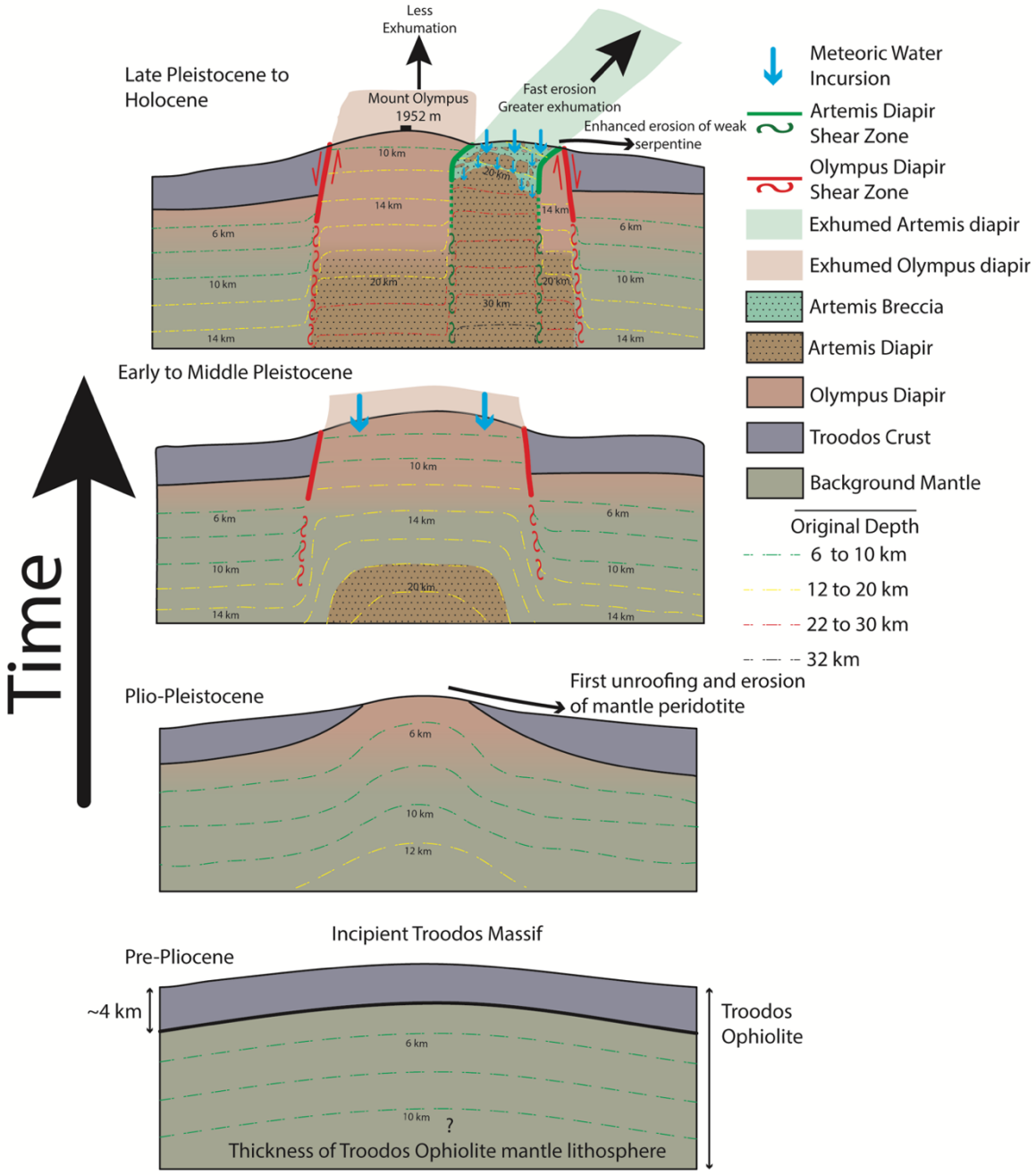

Figure 3.13: A schematic illustration of our uplift model for the Troodos Mantle Sequence Model highlights the temporal evolution within the Troodos Mantle Sequence culminating in differential serpentinite diapirism and exhumation resulting from contrasting serpentinisation styles between both diapiric domains.

3.7 Application of the mechanistic uplift model to other settings

Here we explore whether our simple 1-D mechanistic uplift model is unique to the Troodos Massif or whether it can be applied to a range of other terrestrial and submarine settings including St. Peter and St. Paul Rocks, New Idria Massif, California, Site 637 on the West Iberian Margin, and Macquarie Island (Table 3.4).

Table 3.4. Summary table of parameters utilised in the application of the mechanistic uplift model to other settings.

Area	***St. Peter and St. Paul Rocks***	***Macquarie Island***	***ODP Leg 103 Site 637/'5100 m Hill'***	***New Idria Serpentinite***
Elevation High (m)	22 m asl	410 m asl	~-4948 m	1605 m asl
Surrounding Elevation (m)	~-4000 m	-	~-5300 m	~544 m asl
Parameters				
Time Period (Myr)	10	0.65	-	12
Diapir Density (kg/m3)	2800	2700	2400	2000
Mantle' Density (kg/m3)	3300	3300	2900	2700
Volume Expansion (%)	15	20	-	40
Bedrock Erodibility Constant (m)	-	0.0000015	-	0.0000064
Precipitation (m/yr)	-	0.98	-	0.64
Independent Constraints				
Uplift Rate	1.5 mm/yr (Campos et al., 2010)	0.8 mm/yr (avg.; Adamson et al., 1996)	-	1.7 to 4 mm/yr (Coleman, 1996)

Area	***St. Peter and St. Paul Rocks***	***Macquarie Island***	***ODP Leg 103 Site 637/'5100 m Hill'***	***New Idria Serpentinite***
Erosion Rate	-	0.1 mm/yr (coastal erosion; Smith and Bayliss-Smith, 1998)	-	4 mm/yr (Woodward and Clyde, 1989)
Results				
Isostatic Uplift (Ut; No Erosion) (m)	~3500 m (2000 m/Myr)	~425 m (3000 m/Myr)	~350 m	~20000 m (3000 m/Myr)
Diapir Thickness (No Erosion) (m)	~23000 m (2000 m/Myr)	~2335 m (3000 m/Myr)	~2000 m	-
Elevation (m) (Erosion Applied)	-	~390 m (3000 m/Myr)	-	~1000 m (3000 m/Myr)
Additional Thickness (Dd; Erosion Applied)	-	~2150 m (3000 m/Myr)	-	-
Total Exhumation (Erosion Applied)	-	~185 m (3000 m/Myr)	-	~46000 m (3000 m/Myr)
Diapiric Mode	Isostatic Uplift	Isostatic Uplift	Serpentinite Extrusion	Serpentinite Extrusion
Troodos Massif Analogue	Olympus	Olympus	Artemis	Artemis

3.7.1 St. Peter and St. Paul Rocks

The St. Peter and St. Paul Rocks are interpreted as a partially serpentinised serpentinite diapir (e.g., Campos et al., 2005; Campos et al., 2010). Recent interpretation of new bathymetry, seismic, and gravity datasets proposed that the St. Peter and St. Paul Rocks uplifted in response to a ~10 Myr period of transpression at the transform boundary (Maia et al., 2016). They conclude that the present convergence rates at stepovers and transpressive segments are sufficient to uplift the North Ridge Massif some ~3500 m (Maia et al., 2016). However, a gravity anomaly on the southern flank of the massif indicates the presence of a large low-density layer. This is interpreted to be a ~25 km-thick zone of serpentinised mantle, the base of which approximately coincides with the estimated depth of the 500°C isotherm (Maia et al., 2016).

To establish whether isostatic uplift in response to partial serpentinisation reactions can contribute to the overall uplift of the peridotite massif, we apply the mechanistic uplift model (with reasonable parameters; see supplementary materials) to the St. Peter and St. Paul Rocks. Calculations indicate that partial serpentinisation (~40%) of a body in response to a serpentinisation front advancing at an average rate of 2000 m/Myr, will isostatically uplift rock a total of ~3500 m in the required time frame (10 Myr; Maia et al., 2016), generating a body of moderate density (2800 kg/m^3) that is ~23 km in total thickness (Fig. 3.14), in broad agreement with published interpretation of the gravity data (Maia et al., 2016).

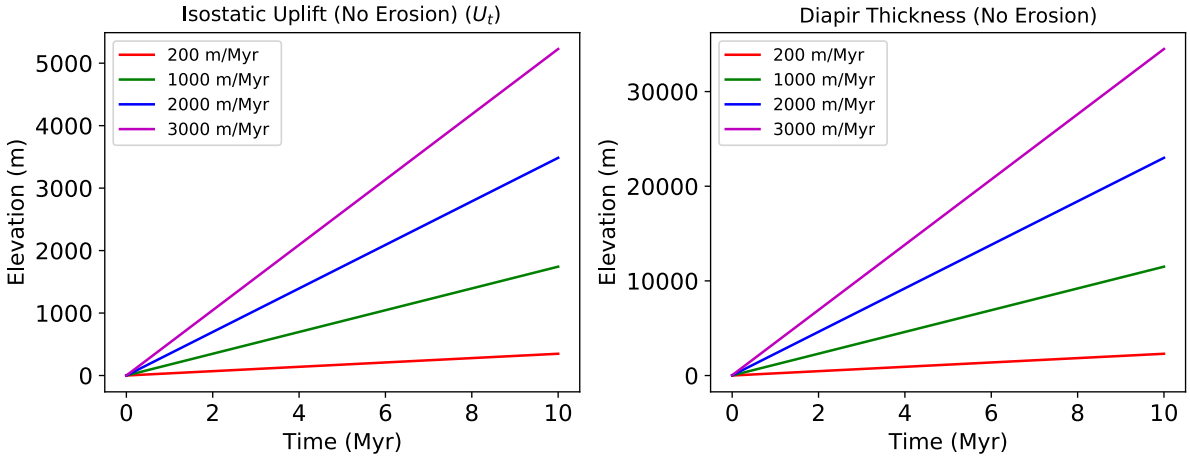

Figure 3.14: Output from the mechanistic uplift model applied to the St. Peter and St. Paul Rocks.

3.7.2 New Idria serpentinite diapir

The moderately elevated (1605 m; prominence 1061 m) New Idria serpentinite diapir is primarily composed of easily erodible, sheared and crushed, incohesive low-density serpentinite breccia (Mumpton and Thompson, 1975; Coleman, 1996). In addition to serpentine, blocks of eclogite are present that are interpreted to have been entrained during diapiric ascent (Tsujimori et al., 2007). Gravity measurements identify a -35 to -55 mGal negative Bouguer gravity anomaly and the New Idria serpentinite is interpreted to be a dome-like body that only extends to ~4 km depth (Byerly, 1966; McPhee et al., 2004). The gravity anomaly coincides with a strong magnetic signature (~210 nT; McPhee et al., 2004). The emergence of the New Idria serpentinite diapir is dated as Mid-Miocene (~12 to ~14 Ma) from the presences of detrital chrysotile serpentine in the Big Blue Formation (Casey and Dickinson, 1976; Coleman, 1996; Vermeesch et al., 2006) and continued serpentinite extrusion occurred throughout the Plio-Pleistocene (Coleman, 1996). Application of the Artemis model parameters (Table 3.3) to the New Idria setting, suggests that an advancing

serpentinisation front of 3000 m/Myr may isostatically produce and maintain an elevation of ~1000 m in response to a ~4000 m-thick low-density body (Fig. 3.15). These results are in agreement with geophysical constraints and suggests that isostatic uplift due to serpentinisation may produce and maintain a serpentinite body of moderate elevation, coincidently generating significant differential uplift and exhumation relative to the surrounding area.

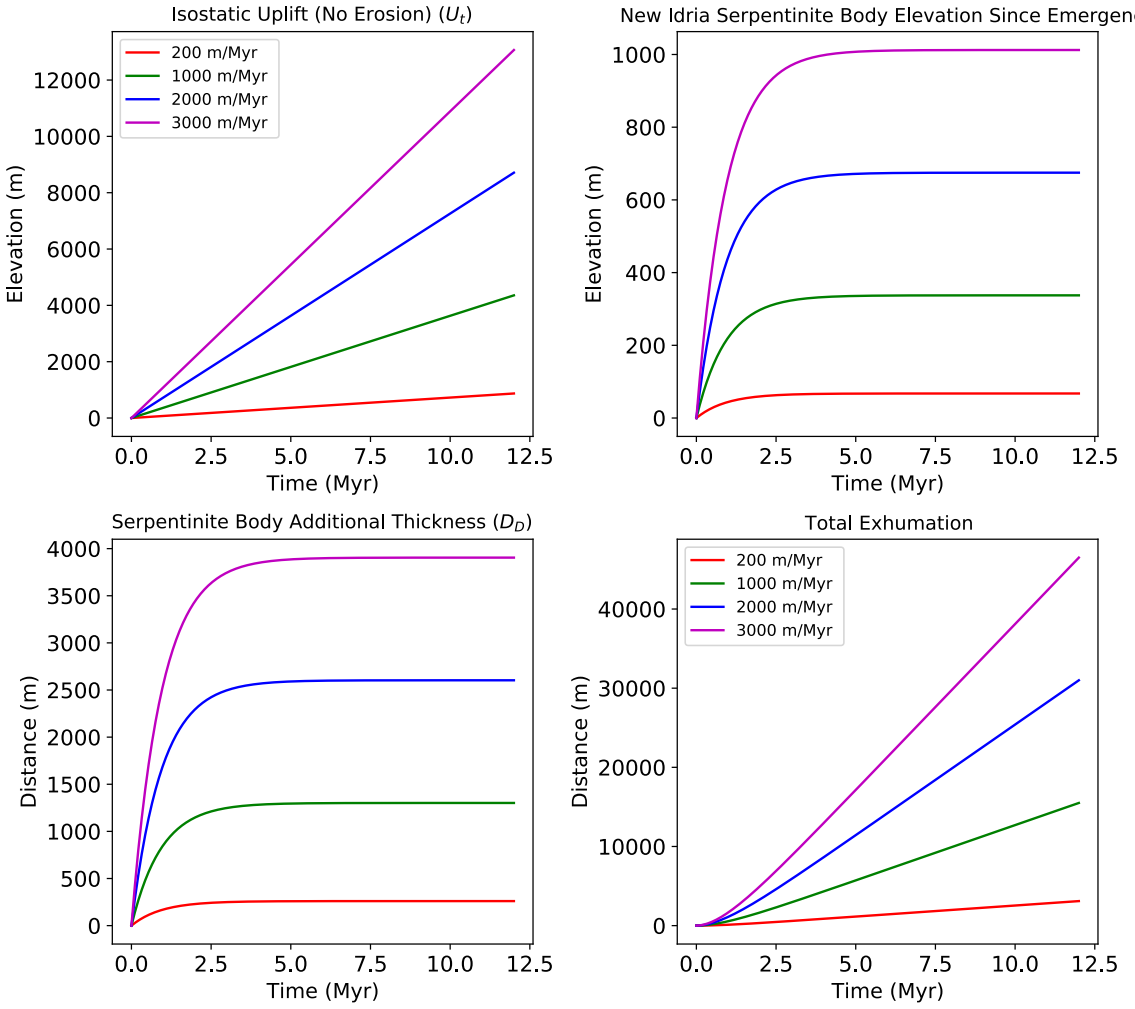

Figure 3.15: Output from the mechanistic uplift model applied to the New Idria Serpentinite Diapir.

3.7.3 ODP Leg 103 Site 637

To the west of the Galicia Bank on the Iberian Margin, ODP Site 637 ('5100 m Hill') is a ~5 km-wide domal serpentinite protrusion, where strongly altered and completely serpentinised plagioclase-bearing sub-continental mantle rocks are uplifted some ~350 m above the surrounding seafloor (Boillot et al., 1988). Late Miocene sediments unconformably overlay, eroded strongly altered and brecciated serpentinised clasts that transition to strongly altered and brecciated serpentinites with increasing depth (Boillot et al., 1988; Evans and Baltuck,

1988). This exhumed peridotite is an elevated basement high, along an inferred ~70 km wide, ~250 km long peridotite ridge, organised into a series of broadly N-S orientated margin parallel segments, some of which extend over tens of kilometres, and generally denote the ocean-continental crust boundary (e.g., Beslier et al., 1993; Whitmarsh et al., 1996; Henning et al., 2004; Minshull et al., 2014). Recent three-dimensional imaging of serpentinised peridotite bodies along the West Iberian Margin shows that the volume of serpentinised peridotite is related to the amount of displacement along each fault, the implication being that serpentinisation occurs when these large brittle normal faults are active (Bayrakci et al., 2016). In response to the penetration of seawater into the mantle along normal faults, isostatic uplift as a result of density reduction from serpentinisation reactions is likely to have occurred. Strongly serpentinised (>75%) mantle peridotites are estimated from seismic data to occur on top of the basement with the extent of serpentinisation decreasing to <25% ~2 km below (Minshull et al., 2014). The depth of the unaltered mantle is estimated at ~7.5 km below seafloor (Minshull et al., 2014). Lateral and vertical variations in the extent of serpentinisation likely resulted in differing magnitudes of isostatic uplift. For example, if we assume the completely serpentinised peridotites recovered from Site 637 extend to ~2 km depth and have average bulk densities of 2400 kg/m^3 and these rocks overlay a body of partly serpentinised peridotites of moderate density (2900 kg/m^3) the resulting isostatic uplift due to serpentinisation would be ~350 m. This amount of uplift is equivalent to the relative difference in elevation between the summit of Site 637 and the surrounding seafloor.

3.7.4 Macquarie Island

Macquarie Island is a small (34 km long, 5.5 km wide) subantarctic island that is broadly equidistant from Tasmania, New Zealand, and Antarctica (Selkirk et al., 1990) and is the only sub-aerial exposure of the Macquarie Ridge Complex, a region of shallow bathymetry along the Australian-Pacific plate boundary that runs 1800 km from the southern extent of the Alpine Fault, New Zealand to the Indo-Pacific-Antarctic plate triple junction (Massell et al., 2000). Transpression along the Macquarie Island section of the Macquarie Ridge Complex is invoked to have uplifted and exposed a coherent section of ocean crust and associated upper mantle rocks (Selkirk et al., 1990). These rocks are in faulted contact with subhorizontal pillow lava flows that make up most of the island. The Finch-Langdon Fault that juxtaposes the lava flows and the titled but continuous upper mantle-lower crustal sequence has been interpreted to be an ocean ridge feature (Rivizzigno and Karson, 2004; Wertz et al., 2003). There is no metamorphic sole on Macquarie Island and nor does the geology present evidence for serpentinite diapirism (e.g., Goscombe and Everard, 1998).

Application of the Olympus domain mechanistic uplift model parameters of this study to this Macquarie Island setting suggests that ~400 m of uplift may be generated in response to an average serpentinisation front rate of 3000 m/Myr since the sub-aerial emergence of the island (Fig. 3.16; ~0.65 Ma; Adamson et al., 1996). Despite the extent of serpentinisation and general structure of the rocks beneath Macquarie Island being poorly constrained, these estimations suggest the resulting isostatic response may produce substantial uplift if localised serpentinisation beneath the Macquarie Island section of the Macquarie Ridge Complex has occurred. Although there may be other outcrops of serpentinised ultramafic rocks along the Macquarie Ridge Complex (e.g., Watkins and Gunn, 1971), serpentinisation-induced isostatic uplift of Macquarie Island may be an additional contribution, overprinted onto the overall uplift trajectory of island, coincidentally generating the only sub-aerial portion along this transpressive plate boundary.

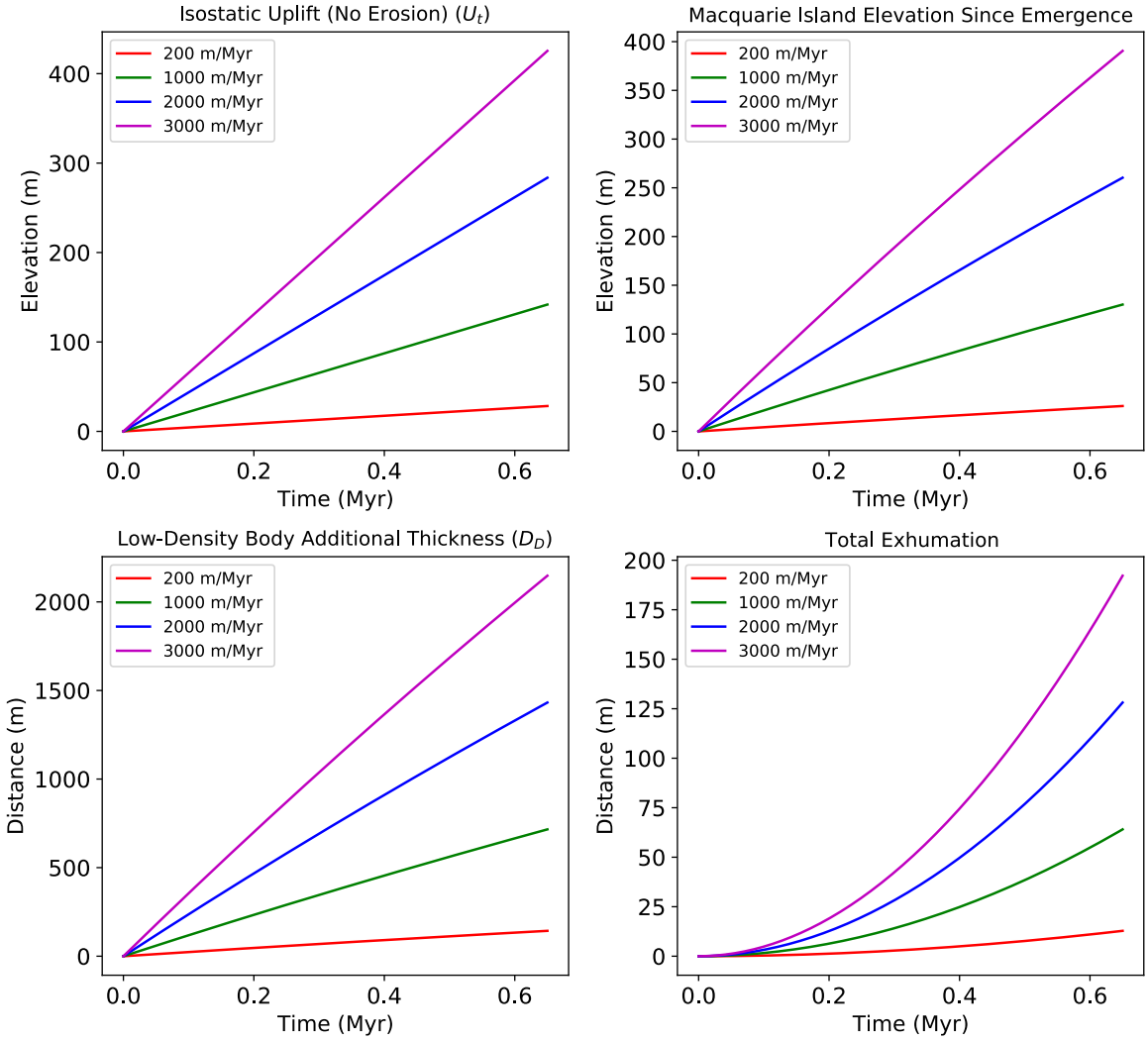

Figure 3.16: Output from the mechanistic uplift model applied to Macquarie Island.

3.7.5 Wider implications of the mechanistic uplift model

Application of our 1-D mechanistic uplift model to other settings suggests that it may be applied universally across the spectrum of serpentinite diapirism occurrence. Calculations from previously reported examples of serpentinite diapirism and Macquarie Island suggest that the required amount of surface uplift to form their respective topographic relief, in the constrained timeframe, may be generated exclusively through serpentinisation reactions. Manifestations of serpentinisation may therefore synchronously induce isostatic uplift. In each of the serpentinised massif settings considered, the overall uplift budget is an interplay between the relative contributions of isostatic uplift and tectonic uplift. For example, for the New Idria Massif the isostatic contribution dominates the overall uplift budget (~4 mm/yr diapiric uplift rate vs regional ~1 mm/yr tectonic uplift rate; Coleman, 1996; Page et al., 1998). In contrast, for the Macquarie Ridge dynamic tectonic uplift is the principal source of uplift with potentially a secondary minor component of isostatic uplift resulting from serpentinisation reactions that has led to the exposure of Macquarie Island.

3.8 Conclusions

1) Contrasting serpentinisation styles are manifest as two distinct serpentinite diapirs within the Troodos ophiolite: (i) a region where the partial hydration of primary minerals results in a strongly serpentinised yet competent and cohesive diapir of moderate density (2686 ± 83 kg/m^3), here termed the Olympus Diapir; and (ii) the completely serpentinised Artemis Diapir that is composed of an intensely deformed, weak and friable block-clast-breccia-gouge assemblage of low density (1949 ± 47 kg/m^3) that results from the positive feedback between coupled deformation-alteration-recrystallisation.

2) Density reduction and coincident volume expansion resulting from serpentinisation reactions induce serpentinite diapirism combined with isostatic uplift transporting and protruding mantle peridotites to high altitude (1952 m). Calculations from isostatic uplift and differential erosion modelling suggest that mountains akin to Mount Olympus (~2000 m asl) may form exclusively through serpentinisation within the required time frame (~5.5 Myr). The CY-4 drill hole geometry indicates that differential uplift of at least >3.6 km has occurred due to the decoupling between the Olympus Diapir and the regional ‘in-situ’ mantle peridotites.

3) The occurrence of mantle peridotites forming the highest elevations of the Troodos Mountains results in strong precipitation, leading to the ingression of meteoric water, as

highlighted by oxygen and hydrogen stable isotope analyses. Activation of coupled mechanisms within the Artemis Diapir form the low density (1568 ± 71 kg/m^3), weak, serpentinite gouge end member; increasing the total exhumation (>3.6 km to ~17.5 km) and localisation of Artemis' deep materials (Batanova and Sobolev, 2000). Despite greater exhumation occurring within the Artemis Diapir, the competent cohesive partially serpentinised peridotites of the Olympus Diapir form the regional summit (Mount Olympus, 1952 m) rather than the weaker deeper materials of the Artemis Diapir.

4) Our 1-D mechanistic uplift model for the Troodos Massif is broadly applicable to a spectrum of other protrusions of serpentinised mantle peridotite. Isostatic uplift is an inevitable manifestation of serpentinisation reactions that result in density-reduction and concomitant volume expansion. For each serpentinised massif, the overall uplift budget will be a combination between the relative contributions of isostatic uplift and dynamic tectonic uplift that jointly contribute to the overall uplift and exposure of serpentinised massifs.

Chapter 4 Serpentine alteration produces high pH >11.5 hyperalkaline waters: Insights from the Troodos Massif, Cyprus

Abstract

Hyperalkaline high pH >11 waters typically emanate from serpentinised massifs and are proposed to reflect the manifestation of ongoing low temperature <100°C serpentinisation hydration reactions between ultramafic rocks and water. However, serpentinised massifs are generally strongly to completely serpentinised and primary mineralogies are minor phases, yet in some completely serpentinised massifs, hyperalkaline high pH >11 waters still occur. As a result, alternative fluid reaction pathways are required to explain how hyperalkaline waters form in strongly to completely serpentinised settings.

In the Troodos Massif, Cyprus hyperalkaline high pH (up to pH 13) Na-K-Cl-OH-SO_4 waters are derived from meteoric water and have extensively interacted with the completely serpentinised mantle rocks. In contrast, lower pH <10 Mg-HCO_3 meteoric-derived surficial waters drain from the Troodos Mantle Sequence with similar waters also emanating from finer-grained mine tailings of the abandoned Amiantos mine. These mine waters yield elevated elemental and molecular concentrations relative to other lower pH <10 surficial waters and some fluid-mobile elements are comparable in concentration to hyperalkaline waters and likely reflect enhanced water rock interaction due to the finer-grained materials. Consequently, enhanced fluid-rock reaction alone is not capable of producing hyperalkaline high pH (up to 13) waters and additional reaction pathways must occur. One such reaction pathway that may occur deeper in the modern hydrological system, where atmospheric influence is limited, is hydroxide generating dissolution of serpentine. This is controlled by the interplay of ongoing serpentine alteration, carbonation and oxidation that manifests as coupling of deformation-alteration-recrystallisation processes. Field observations, geochemical and radiogenic and stable isotope data on bulk rocks, precipitates, and waters discharging from the Troodos Massif, Cyprus indicate multiple overprinting serpentinisation-alteration events have occurred. These respective geochemical and isotopic signals are actively remobilised, redistributed, and progressively modified throughout the Artemis Diapir by the modern meteoric water regime and obscuring fingerprinting of the original event.

4.1 Introduction

Interactions between water and mantle rocks, termed serpentinisation, play critical roles in the Earth system (Kerrick, 2002). Hyperalkaline pH >11 waters associated with serpentinised peridotites, emanate from subaerial and submarine vents and commonly form terraces or chimneys composed of carbonates and brucite (Barnes et al., 1967; Barnes and O'Neil, 1969; Kelley et al., 2001b). It is proposed that these fluids formed through active low-temperature serpentinisation reactions, but their genesis, evolution, and relationship to other water types in the same setting remains enigmatic.

Two contrasting primary water types are reported emanating from continental serpentinised massifs: (1) a meteoric-derived low pH <10, surficial, primarily magnesium-bicarbonate water (often referred to as Type 1 fluids); and (2) a hyperalkaline pH >11, meteoric-derived, primarily calcium-hydroxide water that is sourced from deeper within the hydrological system (e.g., Samail ophiolite, Oman; California, USA; Liguria, Italy; Type 2 fluids' Barnes et al., 1978, 1967; Barnes and O'Neil, 1969; Boschetti et al., 2013; Chavagnac et al., 2013; Giampouras et al., 2019; Kelemen and Matter, 2008; Monnin et al., 2014). These hyperalkaline pH >11 waters are not limited to continental exposures of serpentinised massifs, with such fluids also occurring in the off-axis low-temperature (~100°C) Lost City Hydrothermal Field atop the Atlantis Massif, Mid Atlantic Ridge (Kelley et al., 2001b), in Serpentine Mud Volcanoes in the Mariana Forearc (Mottl et al., 2004), and in Prony Bay, New Caledonia (Monnin et al., 2014).

Previous studies (e.g., Neal and Stanger, 1985) predict that once serpentinisation is complete, hyperalkaline waters will cease to be formed from the completely serpentinised mantle rocks (Barnes et al., 1967; Barnes and O'Neil, 1969). However, most crustal outcrops of mantle peridotites are strongly to completely serpentinised and primary mantle minerals are only minor phases, yet high pH hyperalkaline fluids are present in many systems.

Here we describe a previously unreported hyperalkaline spring emanating high pH (up to 13) water within the completely serpentinised Artemis Diapir (Evans et al., 2021) of the Troodos Mantle Sequence, Cyprus. Through field observations and geochemical and isotopic data, we determine the origin of these hyperalkaline waters as derived from reactions between modern meteoric-water and serpentine rather than active low-temperature serpentinisation hydration reactions of primary mantle minerals. We further characterise the fluid evolution reaction pathways of the differing water types and resultant precipitates that are recycling geochemical and isotopic signatures of previous serpentinisation events within the Troodos Massif, Cyprus.

4.2 Geological Setting

4.2.1 The Troodos Mantle Sequence

Here we focus on the Mantle Sequence that crops out at high altitudes of the Troodos Ophiolite Massif on Cyprus, with serpentinised mantle rocks forming the highest elevations of the island (Mount Olympus, 1952 m asl). These mantle rocks are surrounded by an anticlinal dome comprising concentric annuli of gabbroic and ultramafic cumulate rocks, sheeted dykes, lavas, submarine sediments that crop out at progressively lower altitudes (Fig 4.1).

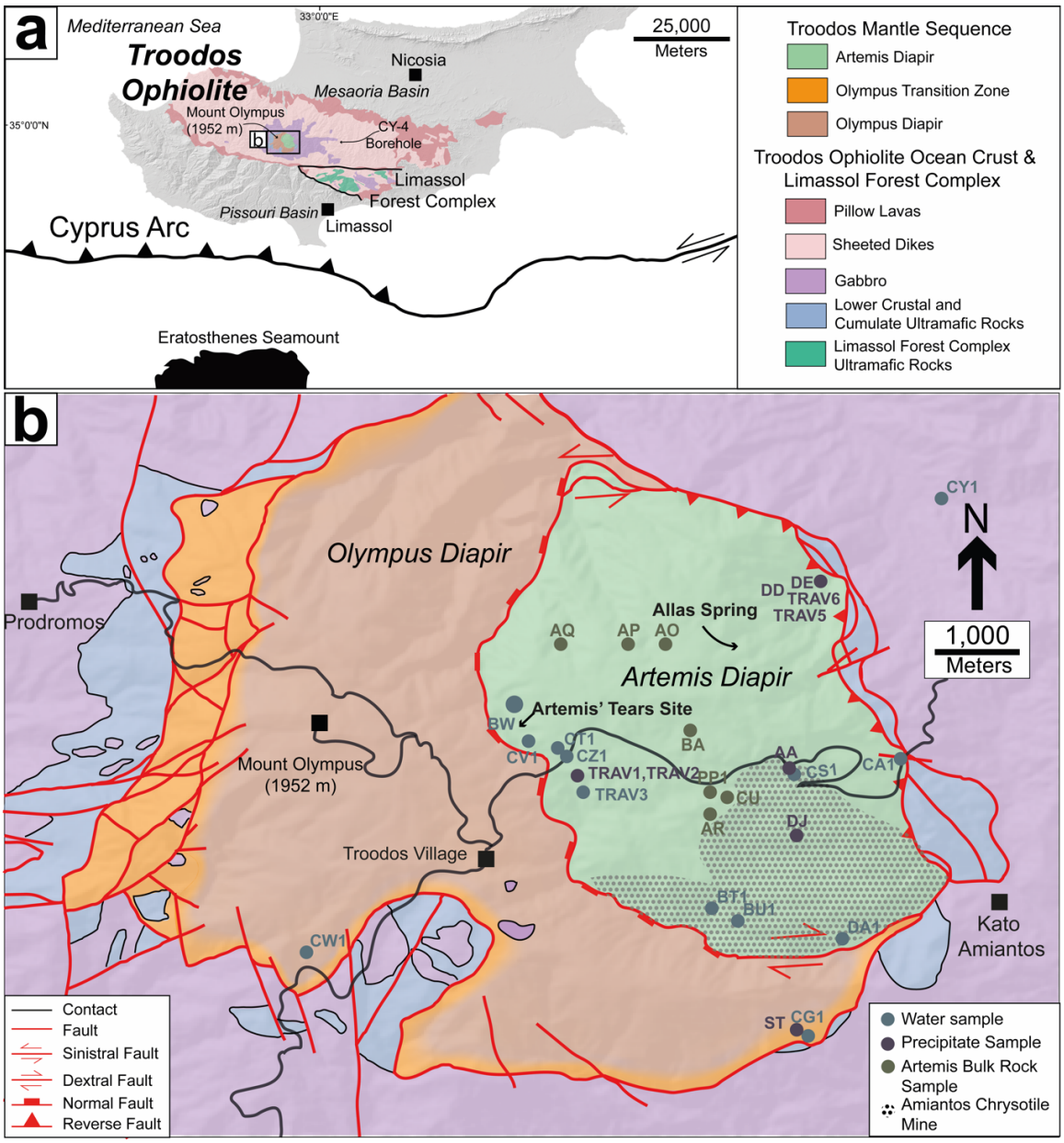

Figure 4.1: (A) Geological map of the Troodos ophiolite with the bullseye geometry of the Mantle Sequence highlighted along with the Limassol Forest Complex terrane, the Cyprus Arc, and northernmost portion of the Eratosthenes Seamount. (B) Geological map of the Troodos Mantle Sequence, adapted and updated from Wilson (1959). Water sample, Precipitate sample, and Artemis Bulk Rock sample locations are shown. Shaded area shows the abandoned Amiantos asbestos mine. Location of the Allas spring is shown (Rizoulis et al., 2016).

The Troodos ophiolite exposes ocean crust and upper mantle rocks that formed ~90-92 Ma at some form of supra-subduction zone spreading ridge in the Neo-Tethyan Ocean (Moores et al., 1984; Moores and Vine, 1971; Mukasa and Ludden, 1987; Pearce et al., 1984). The ~90-km-long and ~30-km-wide ophiolitic sequence yields an elliptical bullseye outcrop pattern, where the stratigraphically deepest rocks, partially serpentinised mantle peridotites, form the highest elevation of the Troodos mountains. The mantle rocks

of the Troodos ophiolite are a self-contained natural laboratory to investigate the modern meteoric mantle-water interactions that produce hyperalkaline waters, since their unique setting removes the potential for additional contributions that could obscure the raw system (e.g., de Obeso and Kelemen, 2018; Giampouras et al., 2019).

The Troodos Mantle Sequence has been sub-divided into two contrasting domains interpreted as nested serpentinite diapirs (Evans et al., 2021; Gass and Masson-Smith, 1963; Moores and Vine, 1971; Wilson, 1959): (i) The Olympus Diapir, an arcuate domain of partially (~50 to ~70%) serpentinised tectonised harzburgites and minor dunites that is juxtaposed by faults against; (ii) the Artemis Diapir, a subcircular domain of completely serpentinised mantle peridotite blocks in a sheared matrix of serpentine breccia composed of comminuted serpentine gouge and clasts. The Artemis Diapir serpentinite breccia endmember is proposed to reflect the ongoing alteration of serpentine through coupling of deformation-alteration-recrystallisation processes that manifest as a distinct serpentinisation style and is in contrast to serpentinisation hydration reactions (Evans et al., 2021).

As detailed in section 2.2., the circum-Troodos sedimentary sequences preserve a progressive uplift and unroofing history with the initiation of significant uplift estimated to occur latest Messinian (~5.5 Ma; Fig 2.6; McCallum, 1989; Poole and Robertson, 1991; Robertson, 1977; Rouchy et al., 2001; Stow et al., 1995). Significant amounts of Troodos-derived diabase and lava clasts occur in latest Messinian / Early Pliocene (~5.5 Ma) strata indicating significant subaerial relief and exposure of the uppermost Troodos crust by this time (McCallum, 1989; Stow et al., 1995; Rouchy et al., 2001). In the southern Pissouri Basin of Cyprus, directly underlying the first occurrence of Troodos-derived igneous clasts is a Messinian evaporite sequence dominated by gypsum and minor selenite (Rouchy et al., 2001; Stow et al., 1995). The Messinian evaporite sequences of Cyprus crop out across the sedimentary sequences of the island (Artiaga et al., 2021; Gass, 1960; Gass and Cockbain, 1961; Manzi et al., 2016; Robertson et al., 1995; Roveri et al., 2014) and preserve a complex stratigraphic record that indicate multistage Messinian evaporite sequences, controlled by localised processes, forming semi-isolated small basins, which are composed of varying proportions of gypsum, halite, and selenite (Artiaga et al., 2021; Follows, 1990; Manzi et al., 2016; Robertson et al., 1995; Rouchy et al., 2001; Stow et al., 1995). Across Mediterranean Messinian evaporite sequences, evidence for localised processes controlling the evaporitic stratigraphy that formed local sub-basins is highlighted by determined $^{87}Sr/^{86}Sr$ ratios of 0.70850 to 0.70905 (Fig. 4.2; Schildgen et al., 2014), which are typically lower than global ~5.5 Myr old seawater (~0.70905; McArthur et al., 2012).

Gypsum and trace amounts of anhydrite occur in recovered drillcores of holes CY-4 and CY2-A from the Cyprus Crustal Study Project (Alt, 1994; Gillis and Robinson, 1990; Herzig and Friedrich, 1987; Jamieson and Lyndon, 1987). These secondary mineral assemblages yield $\delta^{34}S$ values ranging between +21.8 and +22.7 ‰ similar to isotope values of Messinian evaporites (Alt, 1994; Claypool et al., 1980; Jamieson and Lyndon, 1987) and are proposed to form as a result of circulating groundwaters remobilising Messinian sulphate within the Troodos Ocean Crustal rocks (Alt, 1994).

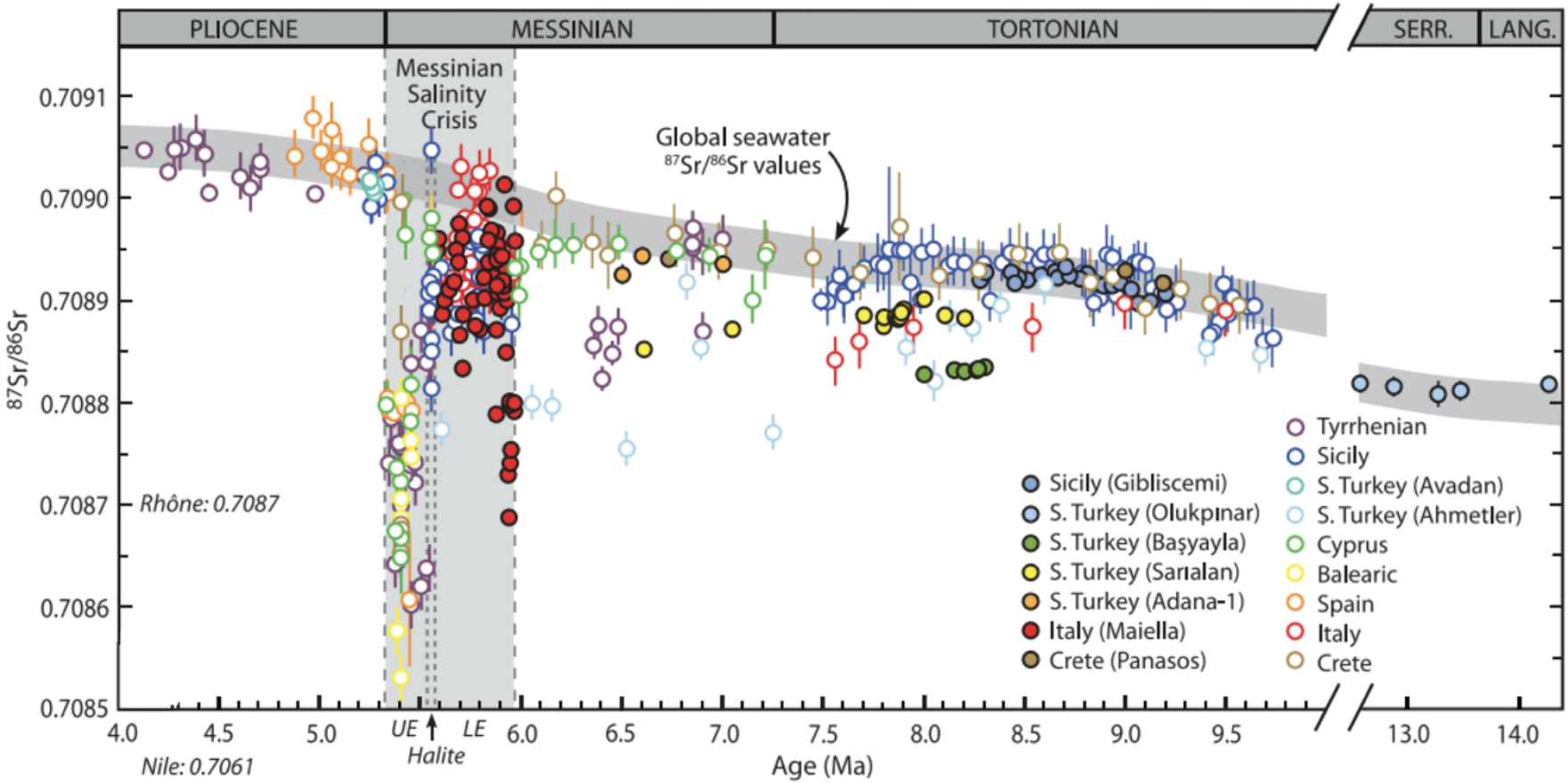

Figure 4.2: Compilation of $^{87}Sr/^{86}Sr$ of published data from sedimentary subbasins of the Mediterranean. Plot is from (Schildgen et al., 2014). Data is sourced from Schildgen et al. (2014; and references therein)

4.2.2 Precipitates from the Troodos Mantle Sequence modern meteoric waters

Incohesive Artemis serpentinite breccias dominate the periphery of the Artemis Diapir, and includes the abandoned Amiantos asbestos mine (~100 Mt; Wilson, 1959). These completely serpentinised breccias are manifestations of progressive coupled deformation-alteration-recrystallisation reactions that have completely serpentinised previously partially serpentinised rocks rather than the hydration of primary igneous mineralogy (Evans et al., 2021). These outcrops comprise friable matrixes of serpentine clay gouge and comminuted serpentine cataclasite (Fig. 4.3) with matrix porosity commonly partly filled by aragonite (Fig. 4.3) and rare serpentine (Fig. 4.3) within the Amiantos mine. Discrete (0.5 to 5 mm-wide) mutually cross-cutting calcite veins occur throughout the Artemis Diapir but are common along the periphery, in competent clasts and more competent serpentinite breccias, and are commonly associated with serpentine (up to ~5 cm-wide) and chrysotile (up to ~3 cm-wide) veins (Fig. 4.3). In some occurrences carbonate veins form a complex hierarchical vein network that generally cross-cut most serpentine veins (Fig. 4.3). In rare occurrences some serpentine veins cross-cut carbonate veins and incohesive serpentinite gouge. A systematic cross-cutting relationship does not occur between the matrix-filling aragonite and discrete carbonate veins. Rare magnesite (ST1-4; Fig. 4.1b) occurs in the SE portion of the Olympus Diapir as a serpentinite-magnesite clast-matrix assemblage composed of serpentinised peridotite clasts hosted in a magnesite matrix (Fig. 4.3). Along the periphery of the Artemis Diapir, rare small (<15 cm wide) fluid seeps, associated with pyroaurite, emanate from the serpentinite breccia, where brucite and minor calcite and halite precipitate, forming a ~0.5 m long surface coating (Fig. 4.3).

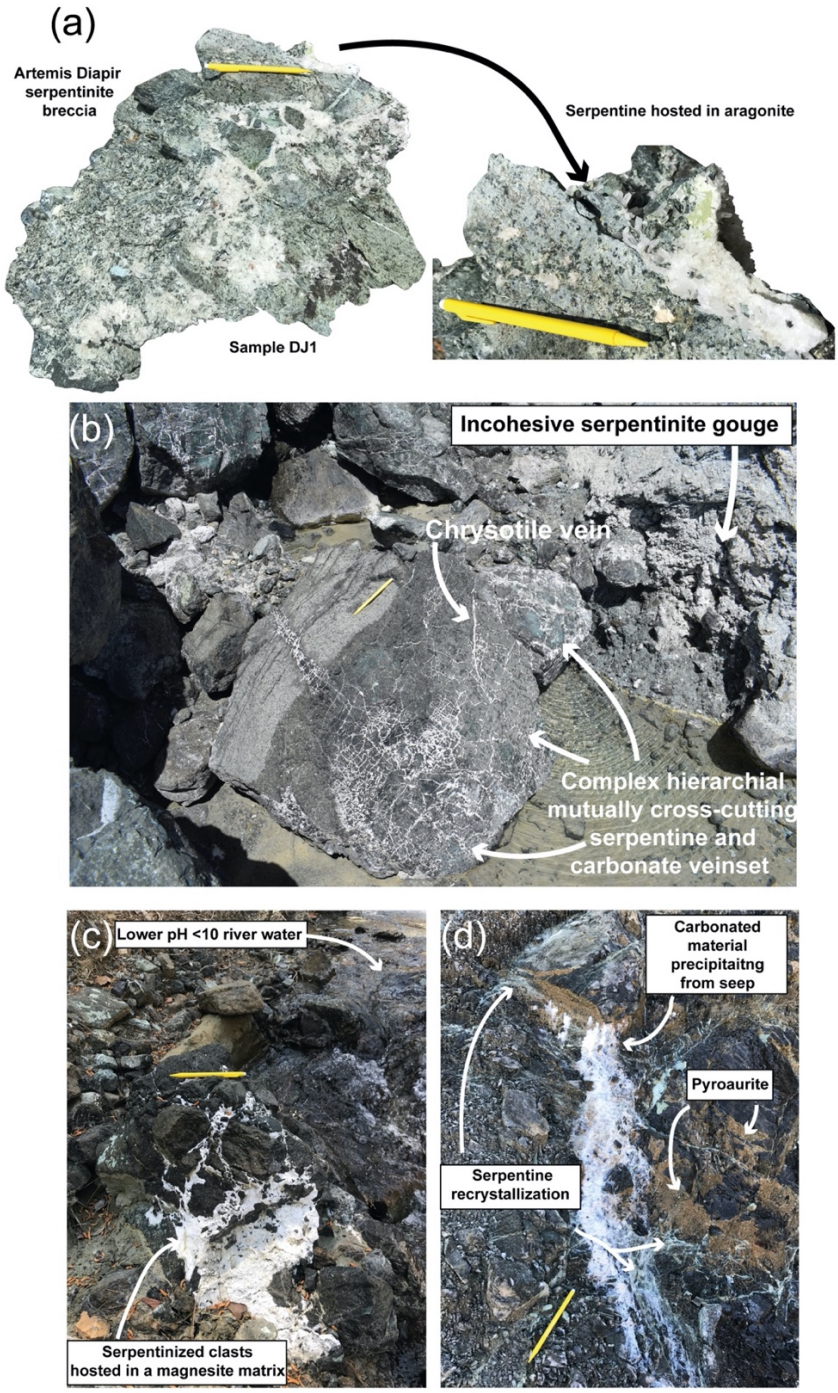

Figure 4.3: (A) Artemis Diapir serpentinite breccia sample DJ1 is shown with aragonite carbonate infilling matrix porosity. Sample shows serpentine vein hosted within the infilling aragonite carbonate. (B) A more competent completely serpentinised clast within the Artemis Diapir yielding a complex hierarchical mutually cross-cutting serpentine and carbonate veinset. Carbonate veins commonly cross-cut most serpentine veins, but in rare occurrences serpentine veins cross-cut carbonate veins. (C) Serpentine-magnesite clast-matrix assemblage. (D) Small hyperalkaline pH >11 seep in the Artemis Diapir associated pyroaurite with precipitation of brucite with minor calcite and halite.

Hyperalkaline springs are hosted by Artemis Diapir serpentinised rocks towards the base of the steep sided valley that delineate the tectonic contact with the Olympus Diapir (Fig. 4.1b). A series of small ~3 m-wide travertine sites occur along the southern extent of this contact (TRAV 1, 2, 3; Fig. 4.1b; Fig. 4.4), where high pH >11 hyperalkaline waters emanate from the serpentinite breccia and partially erode previously precipitated travertine deposits, forming small ~1 m-wide pools (Fig. 4.4). Syntaxial extensional carbonate veins form in the centre of some serpentine veins (Fig. 4.4).

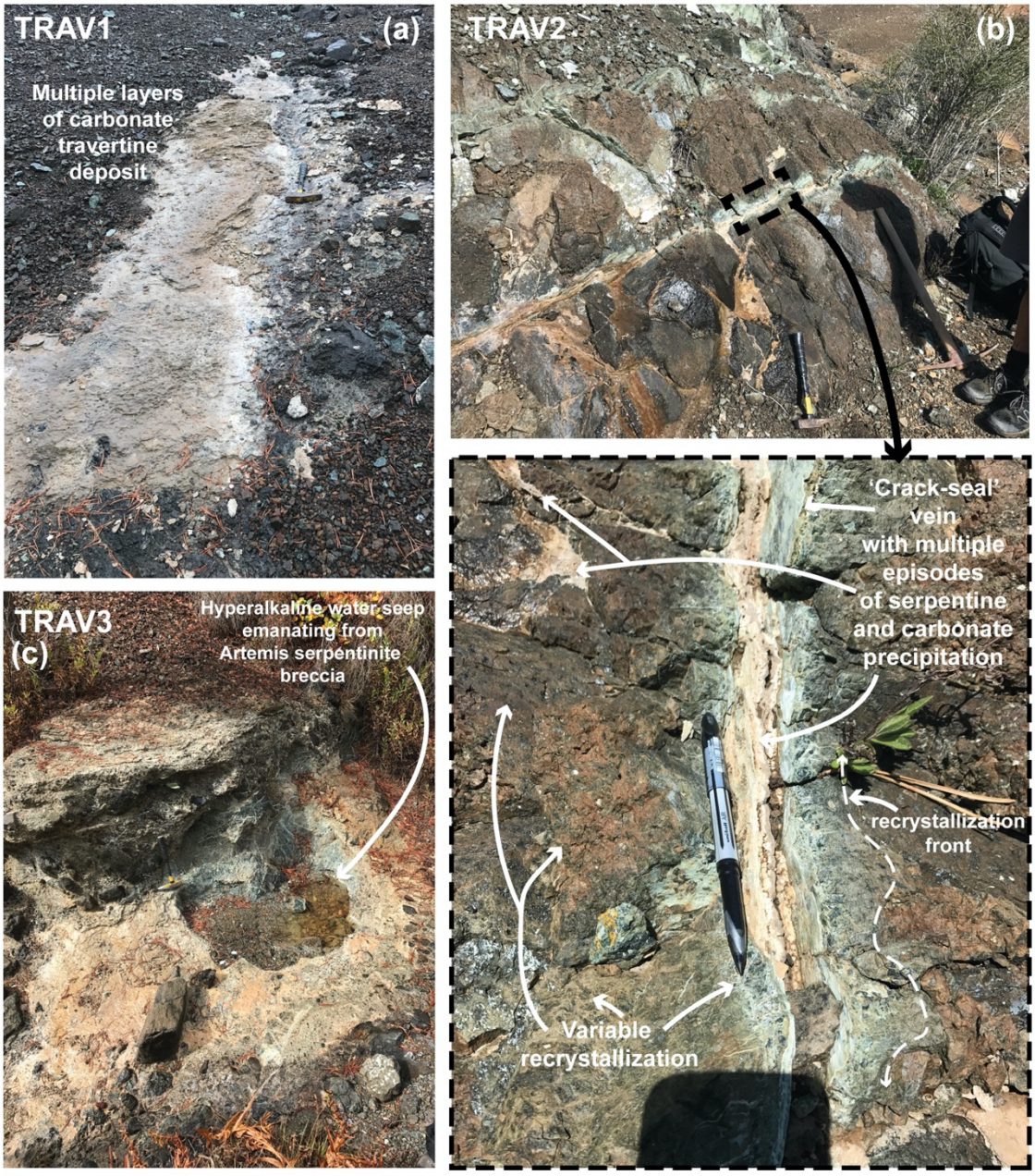

Figure 4.4: (A) TRAV1 travertine deposit highlighting multiple layers of precipitation. Material composed of calcite, aragonite, brucite, halite, and detrital serpentine. Hammer for scale. (B) A portion of the TRAV2 deposit hosted in a crack-seal serpentine-carbonate vein assemblage. Centre of the crack-seal syntaxial vein is composed of calcite displaying multiple episodes of precipitation. Variable recrystallisation of the wall rock is also indicated. (C) TRAV3 travertine deposit highlighting successive travertine precipitation episodes. Hyperalkaline pH 11.5 water seep is shown emanating from the Artemis serpentinite breccia. Hammer for scale.

The best example of a hyperalkaline fluid egress with associated precipitates along this contact is the ~25 m-long Artemis' Tears spring (Fig. 4.5). Here, hyperalkaline waters emanate as discrete springs at low-temperatures (~9-17°C) near the valley floor along the

break in slope (Fig. 4.5) and were observed to emanate for at least a 10-month period (Fig. 4.6). Surrounding these discharge points is a hard, cemented, carbonated material composed of calcite, aragonite, brucite, halite and detrital serpentine (Fig. 4.7; Fig. 4.8). Along the surface drainage path of these hyperalkaline springs soft, tacky, brucite-dominated deposits with minor carbonate, halite, and detrital serpentine have formed where mixing has occurred with pH 8 surface waters (Fig. 4.7; Fig. 4.8). These lower pH <10 waters emanate from a shallow drainage channel forming a creek where waters flow into the river, with fluid mixing between surficial waters with the hyperalkaline waters precipitate softer brucite-dominated material (Fig. 4.5; Fig. 4.6; Fig. 4.7; Fig. 4.8).

Previous studies have also reported hyperalkaline waters emanating from the gabbros of the Troodos ophiolite (e.g., Neal and Shand, 2002) and concluded that such waters were consistent with a dilute residual seawater that has not been sufficiently flushed from the modern aquifer of the ophiolite. Additionally, recent microbiological work reported hyperalkaline (up to pH 11.9) waters emanating from the Allas Spring in the Artemis Diapir (Rizoulis et al., 2016).

Figure 4.5: Artemis' Tears spring site is shown. High pH >11.5 hyperalkaline waters emanate from five discrete seeps (shaded dark blue). Precipitates composed of a harder carbonated material (shaded cream) and a softer brucite-dominated material (shaded grey) are associated with hyperalkaline water discharge. Lower pH 8 waters emanate from a shallow drainage channel forming a creek, waters flow downhill and mix with emanating hyperalkaline waters, precipitating softer brucite-dominated material.

Figure 4.6: Time series of annotated field pictures is shown over a 10-month period (May 2019 – March 2020). (A) & (B) May 2019 field image showing the respective outlines of softer brucite-dominated material and harder carbonated travertine material and sites of hyperalkaline water seeps. (C) July 2019 – softer brucite-dominated and harder carbonated travertine deposits have partially dried up. Hyperalkaline water seep MM2 was actively discharging water and was sampled. Other hyperalkaline seeps had mostly dried up. (D) March 2020 – continuation of hyperalkaline water discharge and precipitation of both harder carbonated travertine deposits and softer-brucite dominated deposits. A new deposit of harder travertine carbonated materials had formed from hyperalkaline water discharge. March 2020 yields marked lower amounts of softer brucite-dominated material relative to May 2019.

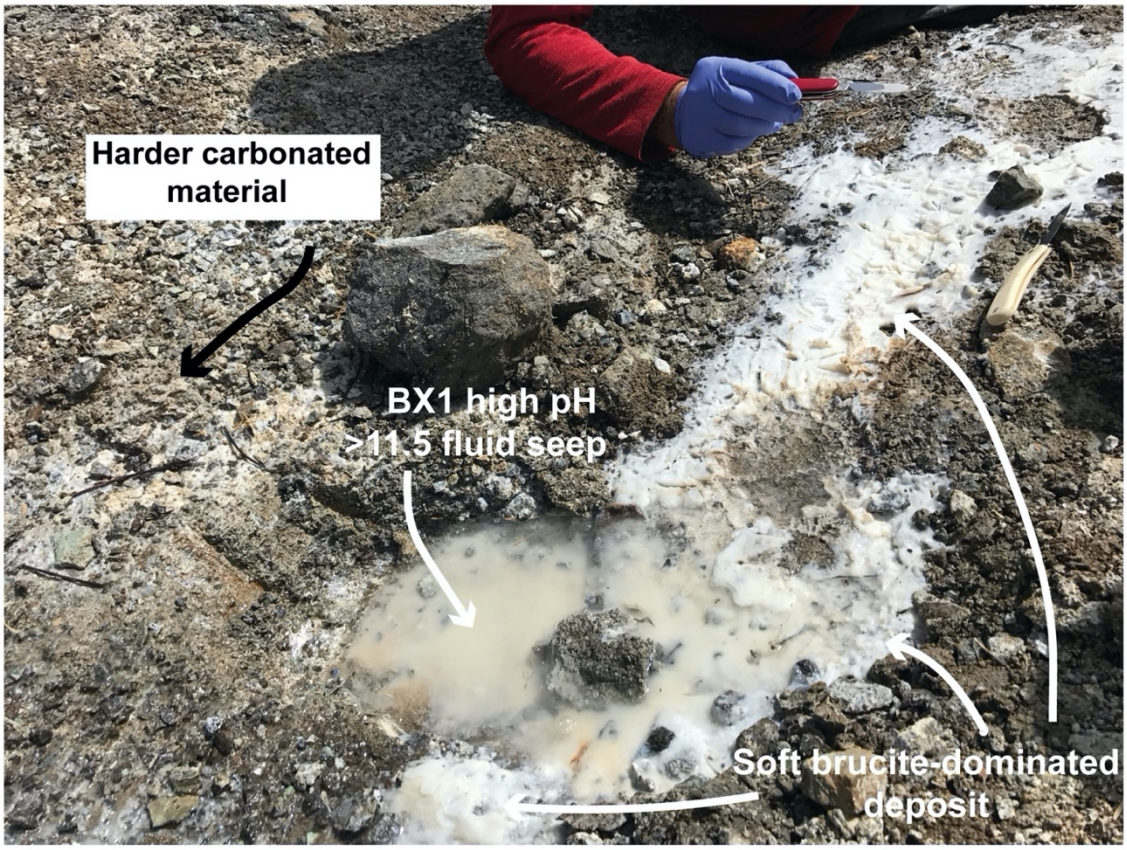

Figure 4.7: Close up field picture showing the pool of high pH >11.5 hyperalkaline water (BX1) associated with soft material primarily composed of brucite with minor calcite, aragonite, halite, and detrital serpentine. Harder material is primarily composed of calcite and aragonite with minor brucite, halite, and detrital serpentine.

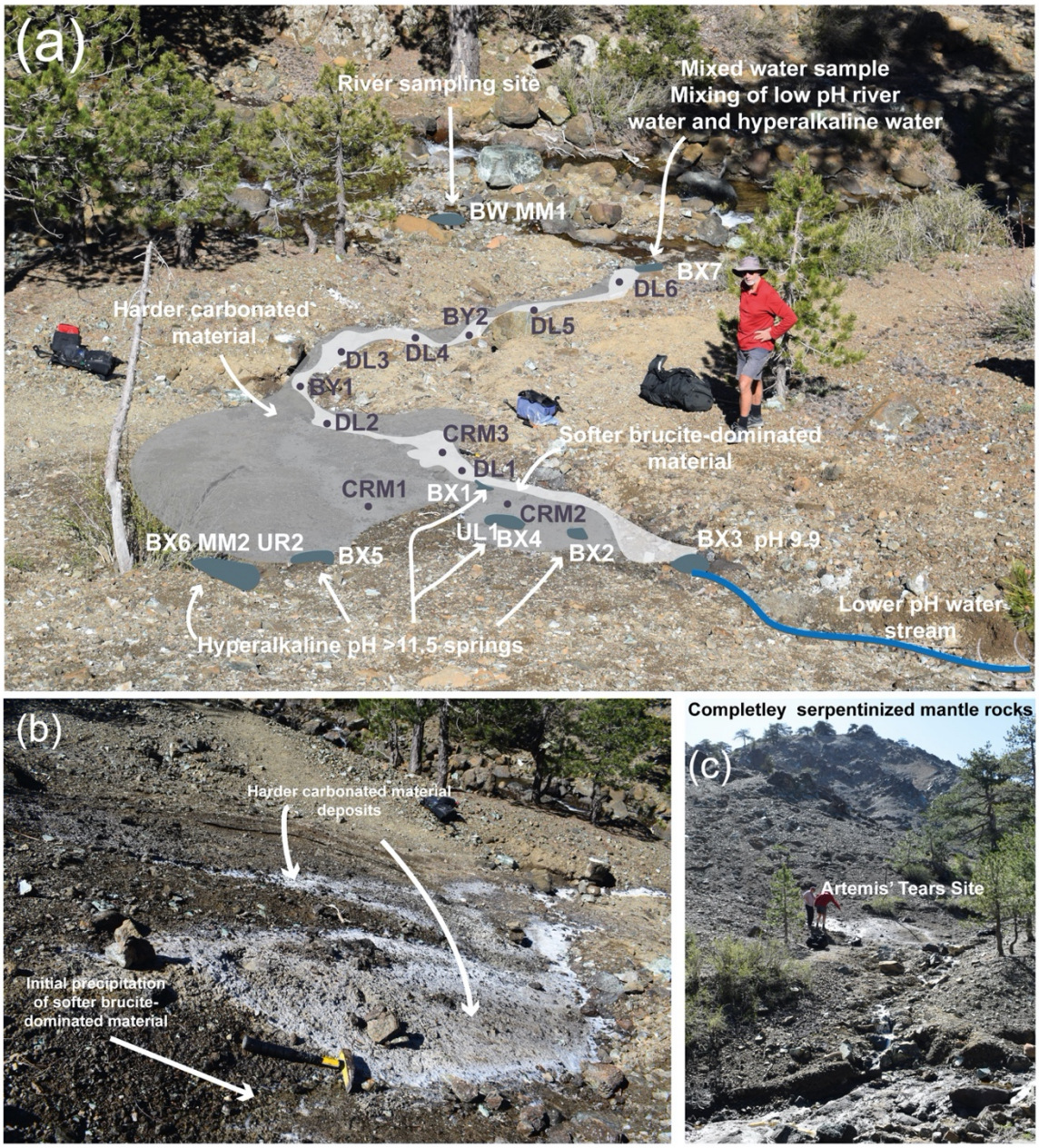

Figure 4.8: (A) Annotated field picture looking downhill into the river, distance from BX3 to BX7 is ~25 m. Dark blue shading denotes seep localities. Purple dots reflect precipitate sampling points. (B) Alternative view of the Artemis' Tears site, highlighting where initial precipitation of softer brucite-dominated material occurs at the point where lower pH 8 surficial stream waters mix with high pH >11.5 waters. (C) Field picture of the Artemis' Tears spring site showing greater context of site location that is located at the floor of a valley, which drains the completely serpentinised mantle rocks (up to 1750 m asl) of the Artemis Diapir.

4.3 Methods

4.3.1 Field sampling

A total of 27 water, 31 precipitates, and 59 bulk rock samples were collected from the Troodos Massif, Cyprus. Water samples were collected and filtered in the field through a pre-contaminated Nalgene vacuum filtration device using Whatman PTFE membrane 0.45 μm filters. Filtered aliquots were sub-divided into different bottles for analyses: (1) 125 mL of water for cation and $^{87}Sr/^{86}Sr$ analyses was collected in 10% HNO_3-cleaned HDPE bottles without headspace and acidified to pH ~2 with 1.25 mL of thermally distilled ultrapure concentrated HNO_3 upon return and once acidified the sample was stored for up to several months prior to analysis; (2) 60 mL of water for anion analyses was collected in Milli-Q water (18.2 MΩ/cm H_2O) rinsed HDPE bottles without a headspace; (3) and (4) 40 mL of water in separate septa borosilicate vials for DIC (Dissolved Inorganic Carbon) analysis and stable oxygen and hydrogen isotopic analyses, both filled without a headspace. Field measurements of pH (± 0.05), temperature (± 0.5 °C), TDS (Total Dissolved Solids; ± 2 % full scale), and EC (Electrical Conductivity; ± 2 % full scale) were measured with a Hanna Instruments HI-98129 probe. The probe was calibrated each morning using Thermo Scientific Orion certified pH 4 and 7 buffer solutions prior to use in the field. Nitrile gloves were worn while sampling. Samples were kept refrigerated and in darkness. GPS locations were taken using a Garmin eTrex 20 (± 3 m position accuracy).

4.3.2 Sample Preparation

Samples were prepared and processed in a Class 100 Clean Laboratory suite of the Geochemistry Research Group, National Oceanography Centre Southampton (NOCS), University of Southampton. Prior to analyses, carbonate veins were rinsed and sonicated in Milli-Q water (18.2 MΩ/cm H_2O) then dried in an oven overnight. Carbonate samples (~100 mg), including veins were dissolved in 10% ultra-pure acetic acid and thermally distilled concentrated HNO_3 was added prior to being dried down. Precipitates and water samples were then appropriately diluted in 3% thermally distilled HNO_3.

Weathering rinds of the Artemis Diapir bulk rocks were removed by a diamond saw and then ground with a high-speed water diamond grinder to remove saw marks. Selected serpentine veins and breccias, including sawn and ground bulk rocks were rinsed and ultra-sonicated multiple times in Milli-Q water (18.2 MΩ/cm H_2O) then dried overnight in an oven at 65°C. Serpentine veins and bulk rock samples were then crushed by an iron fly-press, with samples wrapped in paper between plastic chopping boards to avoid any potential

contamination. Samples were then powdered using a chrome-steel jar mill in a Rocklabs grinder.

Progressive leaching experiments were undertaken on prepared and weighed (0.5 to 3 g) Artemis Diapir rock powders. The initial leaching step was the addition of a 10 % ultra-pure acetic acid solution to rock powders, which was left for 48 hours at room-temperature. Samples were then centrifuged with the leachate removed, dried down, and appropriately diluted in 3 % thermally distilled HNO_3. A 3M HCl solution was added to the already leached powders and left for 48 hours at room-temperature. Samples were then centrifuged, and the 3M HCl leachate removed, dried down, and appropriately diluted in 3 % thermally distilled HNO_3. 200 mg of the respective remaining residues were dissolved using a standard HF-HNO_3 digestion in two separate (100 mg each) pots. In addition, the untreated original bulk rock powders were dissolved following the same manner as bulk residues.

4.3.3 Elemental Analyses

4.3.3.1 Waters and Precipitates

Major and minor cation (Li, B, Na, Mg, Al, K, Ca, Cr, Mn, Fe, Rb, Sr, Cs, Ba, Pb) and silicon concentrations of waters, precipitates, and acetic leachates were measured by inductively coupled plasma-source mass spectrometry (ICP-MS; Thermo X-Series II), in the Geochemistry Research Group of the University of Southampton. Analyses were calibrated using a range of synthetic multi-element standards prepared gravimetrically from single element standard solutions. Anion (Cl, SO_4, and Br) concentrations of water samples were measured by Ion chromatography (Thermo Aquion Ion Chromatography System) at the National Oceanography Centre Southampton (NOCS). Anion measurements were calibrated using a range of synthetic multi-element standards prepared gravimetrically from single element standard solutions. The IAPSO seawater was analysed several times (n=5) and accuracy of the anion analyses was within ± 5 % of expected values. DIC (Dissolved Inorganic Carbon) was measured by the VINDTA 3C (Marianda) using conventional methods (Dickson et al., 2007). The certified reference materials used to determine accuracy are the Batches of CO_2 Seawater Reference Material from Scripps Institute of Oceanography of the University of California, San Diego (Dickson et al., 2007) and a correction factor was applied to the data accordingly. The precision of all measured samples was <3.3 µmol/kg. Total Alkalinity was calculated using pH, DIC, and temperature following the equations of (Zeebe and Wolf-Gladrow, 2001). The total charge balance error of all water samples was <7 % (Table 4.1).

Table 4.1: Sampled Troodos Massif analytical results table; $CBE\ (\%) = 100 \cdot \left(\frac{\Sigma cations - \Sigma anions}{\Sigma cations + \Sigma anions}\right)$

Sample Name	*Diapiric Domain*	*Sample Type*	*Site*	*Precipitates at site*	*Precipitate Type*	*Lat*	*Long*	*Elevation (m)*	*pH*	*TDS (ppm)*	*EC (uS/cm)*	*T (°C)*	*Date*	*Time*	*Cations (meq/kg)*	*Anions (meq/kg)*	*Charge Balance Error (%)*
Snow	Artemis	Snow	-	-	-	-	-	-	-	-	-	-	07/03/2020	14:45	-	-	-
CV1	Olympus	Low pH	Stream flowing into Artemis River	No	-	34.934618	32.883716	1611	8.1	280	562	10.8	17/05/2019	15:30	7	6	6
CT1	Artemis	Low pH	Artemis Creek south of bridge	No	-	34.932823	32.887917	1632	8.2	396	785	19.8	17/05/2019	13:54	10	9	3
CY1	Gabbro	Gabbro	Gabbro Stream	No	-	34.960806	32.929071	933	8.3	317	635	14.4	18/05/2019	15:00	7	6	6
BW1	Artemis	Low pH	Artemis Tears River Site	No	-	34.939042	32.882191	1545	8.3	296	574	12.4	13/05/2019	10:43	7	6	7
CW1W	Olympus	Low pH	Dunite Corner River	Yes	white dusting on surface of rocks	34.911710	32.860505	1490	8.4	278	556	10.4	18/05/2019	10:00	7	6	4
BT1	Artemis	Low pH - Amiantos	Asbestos Lake	No	-	34.916326	32.904042	1348	8.5	358	740	15.6	12/05/2019	13:49	9	8	7

Sample Name	Diapiric Domain	Sample Type	Site	Precipitates at site	Precipitate Type	Lat	Long	Elevation (m)	pH	TDS (ppm)	EC (uS/cm)	T (°C)	Date	Time	Cations (meq/kg)	Anions (meq/kg)	Charge Balance Error (%)
		Mine Water															
BU1	Artemis	Low pH - Amiantos Mine Water	Asbestos Tailing Seep	No	-	34.915250	32.906372	1368	8.7	840	1682	15.2	12/05/2019	14:35	19	18	4
MM1	Artemis	Low pH	Artemis Tears River Site	No	-	34.939050	32.882214	1545	8.7	nd	539	19.1	17/07/2019	14:15	8	7	3
TRAV3R	Artemis	Low pH	River adjacent to TRAV3	No	-	34.929369	32.889958	1565	8.8	285	570	17.2	12/05/2019	09:14	7	7	0
CS1	Artemis	Low pH - Amiantos Mine Water	Amiantos Mine River	Yes	calcite	34.930913	32.913197	1399	8.8	437	876	16.3	17/05/2019	13:20	10	10	4
CA1	Artemis	Low pH	Nicosia-Troodos Road Spring	No	-	34.932623	32.924511	1307	9.0	268	548	13.4	13/05/2019	16:46	7	7	1
DA1	Artemis	Low pH - Amiantos Mine Water	Asbestos Tailing River	Yes	white dusting on surface of rocks	34.913257	32.918373	1181	9.0	626	1252	13.5	19/05/2019	09:45	13	13	1

Sample Name	*Diapiric Domain*	*Sample Type*	*Site*	*Precipitates at site*	*Precipitate Type*	*Lat*	*Long*	*Elevation (m)*	*pH*	*TDS (ppm)*	*EC (uS/cm)*	*T (°C)*	*Date*	*Time*	*Cations (meq/kg)*	*Anions (meq/kg)*	*Charge Balance Error (%)*
CG1	Olympus	Low pH	South Eastern Olympus Diapir	Yes	calcite and magnesite	34.902563	32.914635	1170	9.3	504	258	15.0	14/05/ 2019	17:00	7	7	2
BV1	Artemis	Low pH	Artemis Creek	No	-	34.939380	32.882303	1551	9.5	212	424	10.5	13/05/ 2019	10:00	6	6	-5
BX7	Artemis	Mixed water	Artemis Tears	Yes	aragonite, calcite, brucite, halite	34.939050	32.882214	1545	9.6	343	678	14.0	13/05/ 2019	14:30	8	9	-5
CZ1	Artemis	Low pH	Southern Transect	No	-	34.931748	32.888115	1624	9.6	285	574	16.3	18/05/ 2019	11:30	8	9	-7
BX3	Artemis	Mixed water	Artemis Tears	Yes	aragonite, calcite, brucite, halite	34.939050	32.882214	1545	9.9	1938	3982	16.3	13/05/ 2019	12:15	40	40	1
TRAV3	Artemis	High pH	Southern Transect	Yes	aragonite, calcite, brucite, halite	34.929369	32.889958	1565	11.5	>2000	>3999	17.4	12/05/ 2019	11:15	104	93	6
BX1	Artemis	High pH	Artemis Tears	Yes	aragonite, calcite, brucite, halite	34.939050	32.882214	1545	11.5	>2000	>3999	19.6	13/05/ 2019	11:15	130	119	5
BX5	Artemis	High pH	Artemis Tears	Yes	aragonite, calcite, brucite, halite	34.939050	32.882214	1545	11.5	>2000	>3999	22.2	13/05/ 2019	13:15	130	118	5

Sample Name	*Diapiric Domain*	*Sample Type*	*Site*	*Precipitates at site*	*Precipitate Type*	*Lat*	*Long*	*Elevation (m)*	*pH*	*TDS (ppm)*	*EC (uS/cm)*	*T (°C)*	*Date*	*Time*	*Cations (meq/kg)*	*Anions (meq/kg)*	*Charge Balance Error (%)*
BX6	Artemis	High pH	Artemis Tears	Yes	aragonite, calcite, brucite, halite	34.939050	32.882214	1545	12.1	>2000	>3999	11.1	13/05/ 2019	13:45	249	226	5
BX2	Artemis	High pH	Artemis Tears	Yes	aragonite, calcite, brucite, halite	34.939050	32.882214	1545	12.1	>2000	>3999	19.1	13/05/ 2019	11:45	230	224	1
BX4	Artemis	High pH	Artemis Tears	Yes	aragonite, calcite, brucite, halite	34.939050	32.882214	1545	12.2	>2000	>3999	16.3	13/05/ 2019	12:45	273	266	1
MM2	Artemis	High pH	Artemis Tears	Yes	aragonite, calcite, brucite, halite	34.939050	32.882214	1545	12.5	>2000	>3999	14.4	17/07/ 2019	14:45	282	281	0
UL1	Artemis	High pH	Artemis Tears	Yes	aragonite, calcite, brucite, halite	34.939050	32.882214	1545	12.8	>2000	>3999	12.0	07/03/ 2020	14:20	199	-	-
UR2	Artemis	High pH	Artemis Tears	Yes	aragonite, calcite, brucite, halite	34.939050	32.882214	1545	13.0	>2000	>3999	9.0	07/03/ 2020	14:25	228	256	-6

4.3.3.2 Artemis Diapir rocks

Rock and vein trace element concentrations were measured by inductively coupled plasma-source mass spectrometry (ICP-MS; Thermo X-Series II) at the National Oceanography Centre Southampton (NOCS), University of Southampton. Rock and vein major element concentrations were measured by inductively coupled plasma optical emission spectrometry (ICP-OES; Thermo Scientific iCap 6000 series) at the National Oceanography Centre Southampton (NOCS). For the majority of elements precision and accuracy were better than ± 5 %RSD and ± 10 % respectively (Table 4.2).

Table 4.2 (A): Table of precision and accuracy for ICP-MS. Certified values are compiled from GeoReM (Jochum et al., 2005)

	JA-2 (Avg n=4)	***BRR-1 (Avg n=4)***	***BAS206 (Avg n=4)***	***UBN (Avg n=4)***			***JA-2***	***JA-2***	***JA-2***	***UBN***	***UBN***	***UBN***
	%RSD	***%RSD***	***%RSD***	***%RSD***			***Cert. values***	***Average (n=4)***	***Average Accuracy %***	***Cert. values***	***Average (n=4)***	***Average Accuracy %***
Li	0.75	1.96	1.86	0.84	*Li*	*µg/g*	29.1	29.32	0.77	27	25.36	6.07
Sc	1.39	0.93	1.04	0.32	*Sc*	*µg/g*	18.4	18.03	2.01	13	11.29	13.14
Ti	0.73	0.61	0.46	0.73	*Ti*	*µg/g*	4169	4279.67	2.65	560	546.32	2.44
V	0.79	2.68	0.47	0.97	*V*	*µg/g*	122	120.07	1.58	63	60.56	3.88
Cr	1.94	1.31	2.01	1.86	*Cr*	*µg/g*	465	395.23	15.00	2421	2337.21	3.46
Co	0.90	0.84	0.75	1.07	*Co*	*µg/g*	27	27.63	2.35	102	90.20	11.57
Ni	0.71	0.96	0.86	1.07	*Ni*	*µg/g*	134	125.93	6.02	1942	1762.59	9.24
Cu	1.29	1.02	0.85	1.68	*Cu*	*µg/g*	27.9	31.04	11.24	27	23.31	13.67
Zn	1.23	0.90	0.66	0.94	*Zn*	*µg/g*	65	61.28	5.72	84	76.40	9.04
Rb	1.25	2.32	1.72	1.66	*Rb*	*µg/g*	71	72.36	1.92	3.32	2.99	9.87

	JA-2 (Avg n=4)	BRR-1 (Avg n=4)	BAS206 (Avg n=4)	UBN (Avg n=4)			JA-2	JA-2	JA-2	UBN	UBN	UBN
	%RSD	%RSD	%RSD	%RSD			Cert. values	Average (n=4)	Average Accuracy %	Cert. values	Average (n=4)	Average Accuracy %
Sr	1.02	0.68	1.00	1.55	*Sr*	µg/g	250	246.23	1.51	7.7	6.89	10.54
Y	0.91	0.81	0.93	0.86	*Y*	µg/g	18.1	17.27	4.57	2.5	2.48	0.61
Zr	0.77	0.60	0.81	1.40	*Zr*	µg/g	112	115.17	2.83	3.8	3.22	15.16
Nb	0.60	1.30	1.12	7.21	*Nb*	µg/g	9	9.19	2.09	0.06	0.04	36.68
Sn	1.37	1.76	1.44	3.46	*Sn*	µg/g	1.69	1.73	2.37	0.38	0.40	5.10
Cs	1.37	8.17	3.96	1.23	*Cs*	µg/g	4.9	5.09	3.97	11.2	10.75	3.99
Ba	0.68	1.30	0.61	1.39	*Ba*	µg/g	315	336.90	6.95	26.8	22.17	17.28
La	0.49	0.72	0.82	0.88	*La*	µg/g	16.1	16.16	0.37	0.31	0.30	3.50
Ce	0.93	0.86	0.58	1.16	*Ce*	µg/g	33.7	33.16	1.60	0.83	0.73	12.15
Pr	1.13	0.79	1.36	4.12	*Pr*	µg/g	3.7	3.79	2.46	0.12	0.11	7.01
Nd	0.62	0.60	0.69	3.19	*Nd*	µg/g	14.2	14.44	1.71	0.62	0.57	7.56
Sm	1.47	1.24	0.85	4.62	*Sm*	µg/g	3.1	3.11	0.46	0.22	0.21	4.23

	JA-2 (Avg n=4)	BRR-1 (Avg n=4)	BAS206 (Avg n=4)	UBN (Avg n=4)			JA-2	JA-2	JA-2	UBN	UBN	UBN
	%RSD	%RSD	%RSD	%RSD			Cert. values	Average (n=4)	Average Accuracy %	Cert. values	Average (n=4)	Average Accuracy %
Eu	1.37	0.61	1.50	1.63	*Eu*	µg/g	0.91	0.91	0.07	0.08	0.08	0.02
Gd	1.70	0.83	0.97	5.03	*Gd*	µg/g	3	3.05	1.61	0.33	0.32	2.40
Tb	1.82	1.18	1.20	3.44	*Tb*	µg/g	0.48	0.49	2.72	0.06	0.06	1.82
Dy	0.70	0.95	0.87	1.82	*Dy*	µg/g	2.9	2.96	2.07	0.44	0.42	4.36
Ho	1.14	1.32	0.90	3.19	*Ho*	µg/g	0.61	0.61	0.16	0.1	0.09	5.30
Er	0.94	1.10	1.15	1.82	*Er*	µg/g	1.7	1.73	1.92	0.29	0.28	2.73
Tm	1.81	1.48	0.98	2.72	*Tm*	µg/g	0.26	0.26	1.51	0.04	0.04	10.57
Yb	1.06	1.95	1.10	3.38	*Yb*	µg/g	1.68	1.70	1.39	0.3	0.30	1.08
Lu	2.10	1.08	1.37	3.13	*Lu*	µg/g	0.25	0.26	2.28	0.05	0.05	7.51
Hf	0.97	1.16	1.17	4.59	*Hf*	µg/g	2.93	3.00	2.53	0.14	0.12	11.25
Ta	0.72	2.46	1.45	5.78	*Ta*	µg/g	0.7	0.68	3.39	0.02	0.02	17.49
Pb	0.81	2.61	1.79	0.80	*Pb*	µg/g	19.3	20.37	5.53	12.8	12.37	3.38

	JA-2 (Avg n=4)	BRR-1 (Avg n=4)	BAS206 (Avg n=4)	UBN (Avg n=4)			JA-2	JA-2	JA-2	UBN	UBN	UBN
	%RSD	%RSD	%RSD	%RSD			Cert. values	Average (n=4)	Average Accuracy %	Cert. values	Average (n=4)	Average Accuracy %
Th	0.82	2.49	1.10	2.01	*Th*	µg/g	5	4.99	0.27	0.084	0.07	22.44
U	1.09	2.92	1.55	2.98	*U*	µg/g	2.2	2.29	4.30	0.057	0.05	7.92

Table 4.2 (B): Table of precision and accuracy from ICP-OES. Certified values are compiled from GeoReM (Jochum et al., 2005)

	JA-2	BRR-1	BAS-206	UB-N (n=2)		JA-2	JA-2	JA-2	UBN	UBN	UBN
	%RSD	%RSD	%RSD	%RSD		Cert. values	Measured Value	Accuracy (%)	Cert. values	Average (n=2)	Average Accuracy %
Na	0.62	0.35	1.09	5.32	*Na*	23750	23219	2.29	1008	943	6.93
Mg	0.20	0.70	1.10	3.03	*Mg*	44300	43232	2.47	199000	203582	2.25
K	0.92	0.11	0.67	1.62	*K*	16700	15098	10.61		117	
Ca	0.41	0.49	1.15	0.58	*Ca*	45450	44493	2.15	8540	7603	12.33
Fe	0.62	0.71	0.83	0.29	*Fe*	44850	43654	2.74	55633	61823	10.01

4.3.4 $^{87}Sr/^{86}Sr$ determination

For water and precipitates strontium was separated using strontium spec columns (following Harris et al., 2015). Due to the low Sr concentrations of the rock samples, an aliquot of dissolved rock equivalent to ~500 ng of Sr was dried down and redissolved in 2.2M HCl onto a 7 mL cation exchange column filled with BioRad AG50W-X12 cation exchange resin, in order to elute high concentration major elements (e.g., Mg, Fe, Si). After passing through the column, samples were collected and dried down and redissolved in 3M HNO_3 (samples with Ba/Sr >1 were redissolved in 8M HNO_3) and Sr was separated using strontium spec columns (following Harris et al., 2015), with separated samples at the point of digestion combined into a single Sr separated sample. Total combined blanks of the process were <300 pg. Strontium isotopic compositions were analysed using a ThermoFisher Scientific TritonPlus TIMS at the University of Southampton. Standard NBS987 was measured as an external standard. The mean value of NBS987 (n=26) throughout the analytical period was $^{87}Sr/^{86}Sr$ = 0.710243 ± 0.000024 (2σ). Internal precision was monitored by measuring 150 ratios per sample and the error of each measurement is reported as 2 standard errors (2SE).

4.3.5 Stable isotope determination

$\delta^{18}O$ and $\delta^{13}C$ of carbonate samples were analysed using a Thermo Scientific Kiel IV Carbonate device coupled with a MAT253 isotope ratio mass spectrometer at the University of Southampton. Standard external precision based on repeated analysis of in-house standards calibrated to NBS19 was better than ±0.05 ‰ for both systems. $\delta^{18}O$ and δD of waters were analysed at the Scottish Universities Environmental Research Centre (SUERC) in East Kilbride. Analyses were undertaken on a Thermo Finnigan DeltaV coupled with a Thermo Gas Bench II attachment. In-house reference materials of distilled seawater (DSW2), distilled water (DW2/D) and East Kilbride Snow (EKS2) are used for calibration and are calibrated against intentional standards (SMOW, GISP, SLAP). Water samples were bracketed by reference materials at the start, middle, and end of each run and drift was corrected accordingly. $\delta^{18}O$ and δD are reported in per mill notation with respect to VSMOW and $\delta^{13}C$ is reported to VPDB.

4.4 Results

4.4.1 Composition of waters

Waters collected from rivers, seeps, springs, and snow during three separate field campaigns are sub-divided into six distinct groups based on their pH and sampling location (Table 4.1; Table 4.3; Table 4.4): (i) A lower pH <10 surficial water group sampled from rivers and streams draining the Troodos Mantle Sequence; (ii) A lower pH <10 water group sampled from within the abandoned Amiantos Mine, including seeps emanating from tailings; (iii) A Troodos mountains snow sample; (iv) A stream draining from Troodos gabbros; (v) A high pH >11.5 up to 13 hyperalkaline water group emanating from the Artemis Diapir; (vi) A group where fluid mixing is observed between the high pH hyperalkaline waters and lower pH surficial waters during sampling.

The pH of lower pH <10 river and stream waters vary from >8 to <10 (Table 4.3) and the cation budget is dominated by Mg^{2+} (2,645 to 4,457 μmol/kg), which decreases with increasing pH >8 to <10 (Fig. 4.9). Ca^{2+}, Si, and Mg^{2+} concentrations progressively decrease with increasing pH >8 to <10 (Fig. 4.9), Ca^{2+} decreases by an order of magnitude (231 to 35 μmol/kg) and Si decreases by two orders of magnitude (816 to 5 μmol/kg). DIC (Dissolved Inorganic Carbon) concentrations of lower pH <10 river and stream waters vary between 4,134 and 8,075 μmol/kg with the anion budget dominated by HCO_3^- (Table 4.3). Waters sampled from within the abandoned Amiantos mine have similar low pH as lower pH <10 river and stream waters, but yield greater ionic strengths with elevated concentrations of alkali elements, B, Mg^{2+}, DIC, Cl^-, SO_4^{2-} and Br^- relative to lower pH <10 river and stream waters (Table 4.3; Table 4.4).

Table 4.3: Summary table of results.

	Lower pH <10 waters	***Lower pH <10 waters - Amiantos Mine Tailings***	***Hyperalkaline pH >11.5 Waters***	***Mixed samples (BX3, BX7)***	***Troodos Massif Snow***	***Gabbro***	***Lower pH <10 waters (Rizoulis et al., 2016)***	***High pH >11.5 waters (Rizoulis et al., 2016)***	***Lower pH <10 waters (Neal and Shand, 2002)***	***Gabbro emanating High pH waters (Neal and Shand, 2002)***
number of samples	10	4	9	2	1	1	2	3	7	2
pH	>8 to 10	8.5 to 9	>11.5 to 13	10	-	8.3	9.3	11.6	8 to 9.8	11.5
TDS (ppm)	212 to 504	358 to 840	>2000	1938	-	317	-	-		
EC (µS/cm)	258 to 785	740 1682	>3999	3982	-	635	-	-		
T (°C)	10.8 to 19.8	13.5 to 16.3	11.1 to 22.2	16.3	-	14.4	-	-		
Diapir	Olympus and Artemis although predominantly Artemis	Former Amiantos Asbestos Mine	Artemis	-	-	-	Artemis	Artemis		
Sampled Site Type	Springs, river waters, snow	stream, seeps, lake, river	Individual discrete seeps	-	-	-	seep	seep	stream and river	seep

	Lower pH <10 waters	***Lower pH <10 waters - Amiantos Mine Tailings***	***Hyperalkaline pH >11.5 Waters***	***Mixed samples (BX3, BX7)***	***Troodos Massif Snow***	***Gabbro***	***Lower pH <10 waters (Rizoulis et al., 2016)***	***High pH >11.5 waters (Rizoulis et al., 2016)***	***Lower pH <10 waters (Neal and Shand, 2002)***	***Gabbro emanating High pH waters (Neal and Shand, 2002)***
Flow rate	High	variable	Low (Artemis' Tears Site 7.5 L/hr)	-	-	-	Low (Allas Srping)	Low (Allas Srping)	variable	-
	μmol/kg	***μmol/kg***	***μmol/kg***	***μmol/kg***	***μmol/kg***	***μmol/kg***	***μmol/l***	***μmol/l***	***μmol/l***	***μmol/l***
Na	210 to 408	976 to 5,800	100,068 to 272,593	36069	213	1592			143 to 224	16747
Ca	35 to 231	110 to 160	160 to 954	59	20	1586			37 to 127	20
Mg	2,645 4,457	3,856 to 6,577	8 to 2,283	1554	21	1146			2275 to 4608	14
Si	5 to 816	150 to 383	34 to 312	1053	52	815			11 to 694	863
Sr	0.03 to 0.3	0.14 to 0.25	0.2 to 1.1	0.08	0.02	0.9			0.06 to 0.17	0.01
Cs	0.0003 to 0.005	0.02 to 0.67	0.5 to 1.9	0.3	0.002	0.001			-	-
B	9 to 70	40 to 100	657 to 3,134	435	1.3	36			2 to 15	102
Li	0.7 to 3	10 to 25	730 to 2,417	336	1.2	2			-	81

	Lower pH <10 waters	*Lower pH <10 waters - Amiantos Mine Tailings*	*Hyperalkaline pH >11.5 Waters*	*Mixed samples (BX3, BX7)*	*Troodos Massif Snow*	*Gabbro*	*Lower pH <10 waters (Rizoulis et al., 2016)*	*High pH >11.5 waters (Rizoulis et al., 2016)*	*Lower pH <10 waters (Neal and Shand, 2002)*	*Gabbro emanating High pH waters (Neal and Shand, 2002)*
Cl	316 to 400	873 to 6,371	77,643 to 221,749	1,793 to 29,620	246	1102			197 to 254	11847
SO_4	33 to 49	60 to 151	1,655 to 5,179	65 to 805	10	312			22 to 38	2613
Br	12 to 52	9 to 97	<240	29 to 59	10	63			0.3 to 0.4	13
DIC (Dissolved Inorganic Carbon)	4,134 to 8075	6,249 to 10,080	3,774 to 648	4,485 to 4,660	-	4292				
Calculated Total Alkalinity (meq/kg)	5.82 to 8.73	7.01 to 11.30	12.0 to 79.9	6.80 to 8.30	-	4.48				
Mg/Ca (mol/mol)	13.4 to 76	25 to 56	0.001 to 6.5	26	1.1	0.72				
Sr/Ca (ng/g/ug/g)	0.8 to 6.2	2.9 to 3.3	0.6 to 8.3	1.9 to 2.9	2.4	1.2				
Na/Cl (mol/mol)	0.6 to 1	0.9 to 1.1	1.2 to 1.3	1.2	0.865	1.4				

	Lower pH <10 waters	*Lower pH <10 waters - Amiantos Mine Tailings*	*Hyperalkaline pH >11.5 Waters*	*Mixed samples (BX3, BX7)*	*Troodos Massif Snow*	*Gabbro*	*Lower pH <10 waters (Rizoulis et al., 2016)*	*High pH >11.5 waters (Rizoulis et al., 2016)*	*Lower pH <10 waters (Neal and Shand, 2002)*	*Gabbro emanating High pH waters (Neal and Shand, 2002)*
Ca/SO_4 (mol/mol)	1 to 5.8	0.78 to 2.67	0.069 to 0.365	0.073 to 1	1.961	5.076				
$^{87}Sr/^{86}Sr$	0.708365 to 0.708555	0.707854 to 0.708570	0.70563 to 0.70591	0.70627	-	0.7069				
$\delta^{18}O$	-6.5 to -7.6	-7	-3.1 to -5.3	-6.6	-7.2	-	-	-	-6.4 to -8.2	-7.2
δD	-32.8 to -39.1	-35 to -37	-29.3 to -33.1	-34.1	-36.4	-	-	-	-41 to -42.2	-38.7 to -40

Table 4.4: Table of Troodos Massif waters analytical results.

Sample Name	Diapiric Domain	Sample Type	Li (µmol/kg)	B (µmol/kg)	Na (µmol/kg)	Mg (µmol/kg)	Al (µmol/kg)	Si (µmol/kg)	K (µmol/kg)	Ca (µmol/kg)	Cr (µmol/kg)	Mn (µmol/kg)	Fe (µmol/kg)	Rb (µmol/kg)	Sr (µmol/kg)	Cs (µmol/kg)	Ba (µmol/kg)	Pb (µmol/kg)
Snow	Artemis	Snow	1.18	1.34	213	20.6	nd	51.8	39.2	19.5	0.09	nd	nd	0.0072	0.021	0.0015	0.0119	0.004686
CV1	Olympus	Low pH	0.80	18.3	210	3294	0.12	816	6.29	142	0.19	0.005	0.07	0.0016	0.216	0.0007	0.0113	0.000054
CT1	Artemis	Low pH	0.79	14.7	286	4457	0.10	370	5.61	189	0.92	0.009	0.05	0.0028	0.296	bd	0.0288	0.000054
CY1	Gabbro	Gabbro	2.05	36.1	1592	1146	2.82	815	12.4	1586	0.01	0.045	0.71	0.0022	0.875	0.0004	0.0061	0.000005
BW1	Artemis	Low pH	0.67	13.1	227	3434	0.13	696	7.58	140	0.26	0.006	0.19	0.0022	0.211	0.0007	0.0146	0.000054
CW1W	Olympus	Low pH	1.40	29.4	234	3085	0.17	527	8.90	231	0.06	0.002	bd	0.0023	0.257	0.0004	0.0173	bd
BT1	Artemis	Low pH - Amiantos Mine Water	9.52	40.3	976	3926	0.65	383	29.2	160	0.65	0.097	2.03	0.0249	0.245	0.0207	0.0751	0.000126
BU1	Artemis	Low pH - Amiantos Mine Water	17.0	99.8	5800	6577	0.83	168	252	118	0.83	0.130	4.50	0.4186	0.158	0.6751	0.3684	0.000054
MM1	Artemis	Low pH	3.06	69.6	312	3463	0.70	632	21.1	174	0.26	0.020	0.08	0.0050	0.234	0.0015	0.0173	0.000054
TRAV3R	Artemis	Low pH	3.84	58.6	408	3233	0.13	120	15.4	125	0.30	0.005	0.02	0.0097	0.180	0.0026	0.0140	bd
CS1	Artemis	Low pH - Amiantos Mine Water	25.4	50.7	2225	3949	0.02	254	65	127	0.80	0.010	0.17	0.0853	0.189	0.1423	0.2304	bd
CA1	Artemis	Low pH	0.55	9.00	240	3416	0.35	69.5	9.67	73.0	0.55	0.001	bd	0.0059	0.087	0.0245	0.0175	0.000030

Sample Name	Diapiric Domain	Sample Type	Li (µmol/kg)	B (µmol/kg)	Na (µmol/kg)	Mg (µmol/kg)	Al (µmol/kg)	Si (µmol/kg)	K (µmol/kg)	Ca (µmol/kg)	Cr (µmol/kg)	Mn (µmol/kg)	Fe (µmol/kg)	Rb (µmol/kg)	Sr (µmol/kg)	Cs (µmol/kg)	Ba (µmol/kg)	Pb (µmol/kg)
DA1	Artemis	Low pH - Amiantos Mine Water	12.6	41.3	5391	3856	0.27	150	163	110	0.56	0.006	0.14	0.1930	0.143	0.2273	0.1254	bd
CG1	Olympus	Low pH	0.96	22.1	257	3344	1.16	41.9	12.4	75.4	0.05	0.004	0.01	0.0027	0.027	bd	0.0005	bd
BV1	Artemis	Low pH	2.20	36.2	290	2645	0.75	20.8	11.3	34.8	0.14	0.057	1.53	0.0055	0.028	0.0050	0.0167	0.000078
BX7	Artemis	Mixed water	19.0	43.8	2195	2750	0.88	78.5	58.3	63.3	0.21	0.101	3.32	0.0440	0.056	0.0239	0.0078	0.000199
CZ1	Artemis	Low pH	1.67	30.4	292	3788	0.38	5.30	11.0	66.9	0.14	0.008	0.05	0.0046	0.190	0.0034	0.0051	0.000054
BX3	Artemis	Mixed water	336	435	36069	1554	0.67	19.0	1053	59.1	0.20	0.047	2.15	0.7561	0.078	0.2856	0.0241	0.000005
TRAV3	Artemis	High pH	730	657	100068	44.6	3.97	52.0	3306	299	0.35	0.024	1.01	2.1901	1.143	0.4866	0.1824	0.000054
BX1	Artemis	High pH	1163	1399	124104	1035	5.13	71.1	3712	160	0.46	0.190	10.28	2.6006	0.214	0.9605	0.0763	0.001312
BX5	Artemis	High pH	1139	1417	121272	1830	12.8	312	3702	837	2.17	0.970	56.10	2.6416	0.221	0.9895	0.0868	0.011407
BX6	Artemis	High pH	2204	2629	238888	328	6.65	115	7190	918	0.74	0.437	22.46	4.8064	0.546	1.6849	0.1844	0.006127
BX2	Artemis	High pH	2059	2518	220110	739	5.48	86.8	6517	786	0.52	0.271	14.69	4.4273	0.451	1.5935	0.1557	0.001114
BX4	Artemis	High pH	2321	2810	260966	1329	6.48	125	7822	954	0.64	0.367	21.32	5.1390	0.528	1.8094	0.1747	0.000269
MM2	Artemis	High pH	2417	2892	272593	8.21	1.98	33.6	8051	851	0.01	0.019	0.30	5.2970	0.577	1.8786	0.1779	0.000125
UL1	Artemis	High pH	1785	3134	186706	2283	14.8	205	6119	728	1.73	1.322	49.27	3.7610	0.508	1.3167	0.1357	0.043270
UR2	Artemis	High pH	2031	3034	218554	448	7.46	52.8	7353	714	0.21	0.154	5.78	4.4517	0.548	1.5406	0.1567	0.005037

Table 4.4 continued:

Sample Name	Diapiric Domain	Sample Type	Cl (µmol/kg)	Br (µmol/kg)	SO_4 (µmol/kg)	Na/Cl (molar)	Ca/SO4 (molar)	Mg/Ca (molar)	Sr/Ca (µmol/mmol)	B/Li (molar)	$^{87}Sr/^{86}Sr$	2SE ($1x10^6$)	$\delta^{18}O$	δD	Alkalinity (meq/kg)	DIC (µmol/kg)
Snow	Artemis	Snow	246	9.46	9.94	0.9	2.0	1.1	1.1	1.1	nd	-	-7.2	-36	nd	nd
CV1	Olympus	Low pH	334	18.2	35.9	0.6	4.0	23	1.5	23	0.708503	14	-7.6	-39	5.82	5679
CT1	Artemis	Low pH	401	12.3	49.2	0.7	3.8	24	1.6	19	nd	-	-7.1	-36	8.42	8075
CY1	Gabbro	Gabbro	1102	62.8	312	1.4	5.1	0.7	0.6	18	0.706936	10	nd	nd	4.48	4292
BW1	Artemis	Low pH	341	13.3	37.1	0.7	3.8	25	1.5	20	0.708509	13	-7.5	-34	5.94	5710
CW1W	Olympus	Low pH	316	bd	39.5	0.7	5.8	13	1.1	21	0.708555	13	-6.8	-34	5.94	5659
BT1	Artemis	Low pH - Amiantos Mine Water	873	8.60	60.0	1.1	2.7	25	1.5	4.2	0.708191	19	-7.0	-35	7.01	6500
BU1	Artemis	Low pH - Amiantos Mine Water	6371	97.5	151	0.9	0.8	56	1.3	5.9	0.708570	187	-7.0	-37	11.3	10080

Sample Name	Diapiric Domain	Sample Type	Cl (µmol/kg)	Br (µmol/kg)	SO_4 (µmol/kg)	Na/Cl (molar)	Ca/SO4 (molar)	Mg/Ca (molar)	Sr/Ca (µmol/mmol)	B/Li (molar)	$^{87}Sr/^{86}Sr$	2SE ($1x10^6$)	$\delta^{18}O$	δD	Alkalinity (meq/kg)	DIC (µmol/kg)
MM1	Artemis	Low pH	347	15.2	36.2	0.9	4.8	20	1.3	23	nd	-	-7.4	-39	6.79	5957
TRAV3R	Artemis	Low pH	397	13.7	35.3	1.0	3.5	26	1.4	15	0.708365	14	nd	nd	6.62	5713
CS1	Artemis	Low pH - Amiantos Mine Water	2061	25.8	93.2	1.1	1.4	31	1.5	2.0	0.708121	14	-7.1	-36	7.35	6389
CA1	Artemis	Low pH	343	12.0	42.1	0.7	1.7	47	1.2	17	0.708477	20	-7.2	-37	6.61	5485
DA1	Artemis	Low pH - Amiantos Mine Water	5505	29.8	111	1.0	1.0	35	1.3	3.3	0.707854	12	-7.0	-36	7.49	6249
CG1	Olympus	Low pH	329	15.7	45.4	0.8	1.7	44	0.4	23	nd	-	-6.6	-33	6.39	4711
BV1	Artemis	Low pH	323	12.4	33.4	0.9	1.0	76	0.8	16	nd	-	-7.4	-38	5.90	4134
BX7	Artemis	Mixed water	1793	29.4	64.8	1.2	1.0	43	0.9	2.3	0.708078	223	nd	nd	6.80	4485
CZ1	Artemis	Low pH	336	51.6	40.8	0.9	1.6	57	2.8	18	0.708555	17	-7.2	-36	8.73	5665

Sample Name	Diapiric Domain	Sample Type	Cl (µmol/kg)	Br (µmol/kg)	SO_4 (µmol/kg)	Na/Cl (molar)	Ca/SO4 (molar)	Mg/Ca (molar)	Sr/Ca (µmol/mmol)	B/Li (molar)	$^{87}Sr/^{86}Sr$	2SE ($1x10^6$)	$\delta^{18}O$	δD	Alkalinity (meq/kg)	DIC (µmol/kg)
BX3	Artemis	Mixed water	29620	58.5	805	1.2	0.1	26	1.3	1.3	0.706266	39	-6.5	-34	8.30	4660
TRAV3	Artemis	High pH	77643	bd	1655	1.3	0.2	0.1	3.8	0.9	0.705627	13	-5.4	-32	12.0	3774
BX1	Artemis	High pH	100432	bd	2336	1.2	0.1	6.5	1.3	1.2	0.705892	13	nd	nd	13.7	3678
BX5	Artemis	High pH	96263	239	2295	1.3	0.4	2.2	0.3	1.2	0.705913	13	-5.1	-33	16.4	3654
BX6	Artemis	High pH	192168	bd	4033	1.2	0.2	0.4	0.6	1.2	0.705688	12	nd	nd	25.3	691
BX2	Artemis	High pH	183493	bd	4096	1.2	0.2	0.9	0.6	1.2	0.705711	13	-3.7	-29	31.9	2221
BX4	Artemis	High pH	201900	bd	4486	1.3	0.2	1.4	0.6	1.2	0.705691	13	nd	nd	55.4	648
MM2	Artemis	High pH	221749	bd	5179	1.2	0.2	0.0	0.7	1.2	0.705851	12	-3.0	-30	49.1	848
UL1	Artemis	High pH	138319	bd	3211	1.3	0.2	3.1	0.7	1.8	0.705818	10	-4.7	-31	nd	nd
UR2	Artemis	High pH	168986	bd	3518	1.3	0.2	0.6	0.8	1.5	0.705691	11	-4.2	-33	79.9	863

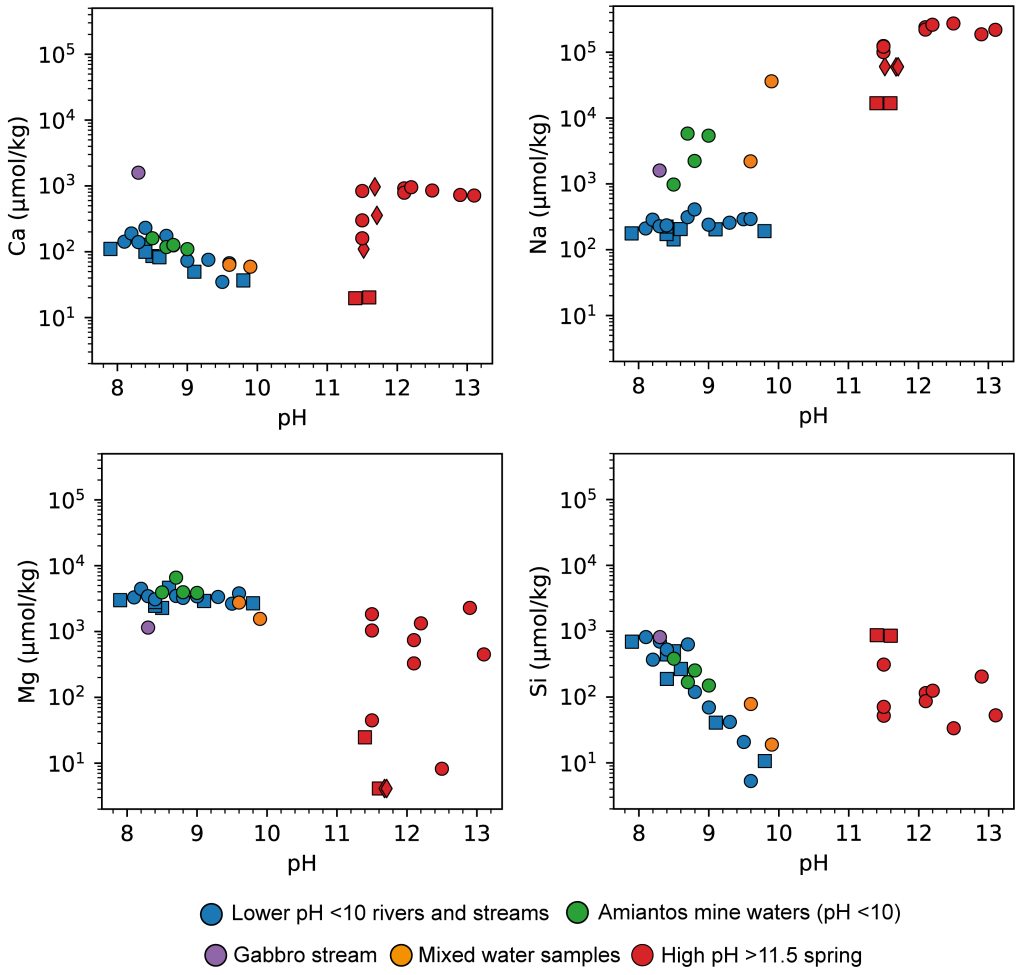

Figure 4.9: Plots of Ca, Na, Mg, and Si (log scale) vs pH. Scales are equal in all subplots. Circles reflect data from this study. Squares reflect data from (Neal and Shand, 2002) and diamonds reflect data from (Rizoulis et al., 2016).

High pH >11.5 to 13 hyperalkaline waters emanating from the Artemis Diapir are primarily characterised as Na-K-Cl-OH-SO_4 waters and have contrasting elemental concentrations relative to lower pH <10 water groups (Table 4.3; Table 4.4). Ca^{2+} concentrations are higher (160 up to 954 µmol/kg) in the high pH >11.5 waters relative to the lower pH <10 waters (35 to 231 µmol/kg). Na^+ is the dominant cation with concentrations ranging between 100,068 up to 272,593 µmol/kg (Fig. 4.9) and Cl^- is the dominant anion and in terms of charge balance OH^- is second to Cl^-. Cl^- concentrations range between 77,643 up to 221,749 µmol/kg, significantly higher than the lower pH <10 water types, which range between 976 up to 5,800 µmol/kg and 873 to 6,371µmol/kg respectively. SO_4^{2-} concentrations vary by up to two orders of magnitude between lower pH <10 water groups (33 to 151 µmol/kg) and the high pH >11.5 waters (1,655 and 5,179 µmol/kg) (Fig. 4.10;

Table 4.3; Table 4.4). High pH >11.5 hyperalkaline waters yield lower DIC concentrations (3,774 to 648 μmol/kg) and higher calculated total alkalinity (12 to 79.9 meq/kg) relative to lower pH <10 water types (4,134 to 10,080 μmol/kg and 5.82 to 11.30 meq/kg respectively). Mg^{2+} concentrations in the high pH >11.5 hyperalkaline waters vary by three orders of magnitude (8 to 2,283 μmol/kg), with Si exhibiting a smaller range of an order of magnitude (34 to 312 μmol/kg; Fig. 4.9).

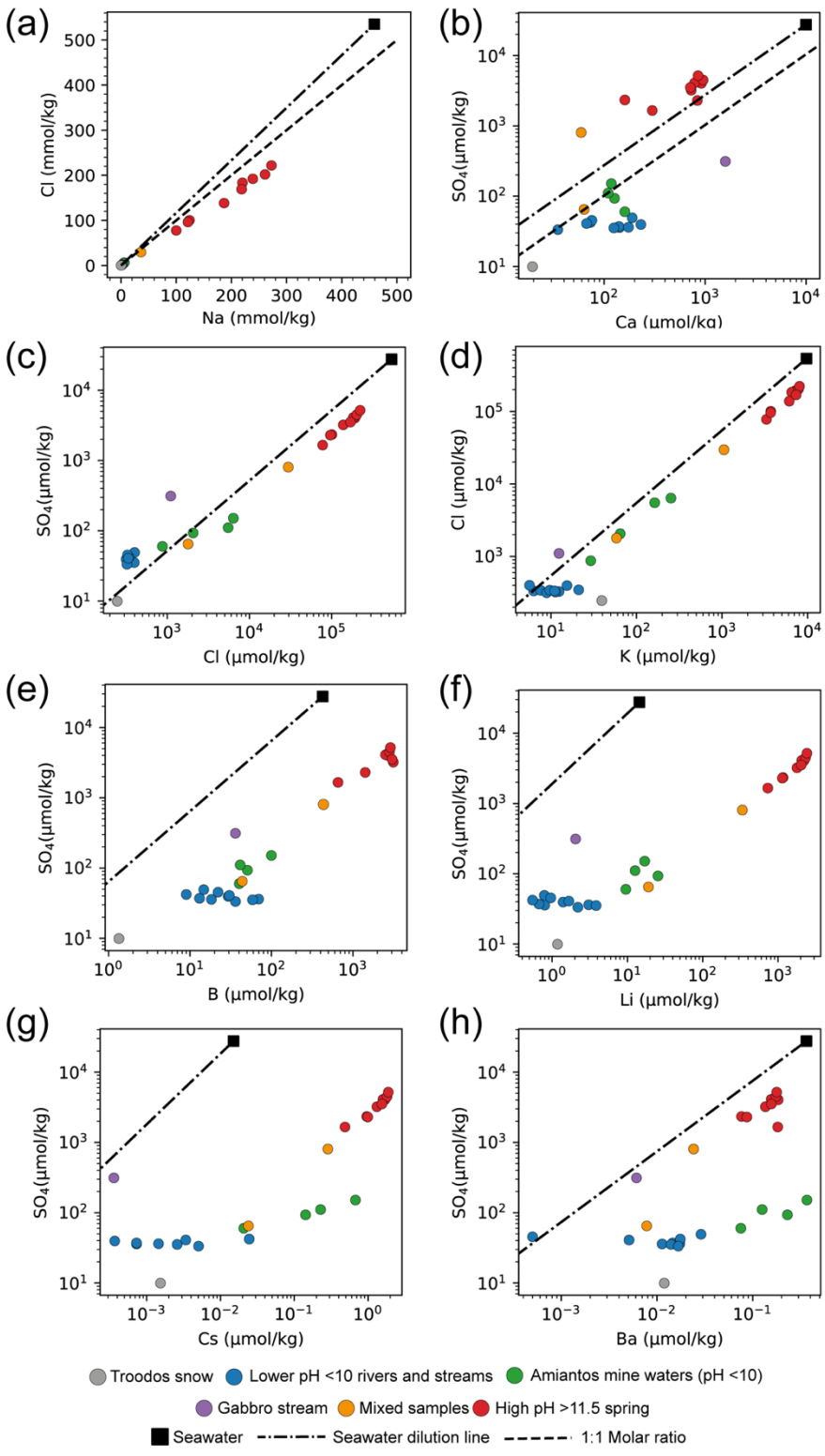

Figure 4.10: (A) Cl vs Na plot of Troodos Mantle Sequence waters, dashed line reflects a 1:1 molar ratio, which in this case denotes a halite dissolution line. Dashed and dotted line reflets the seawater dilution line. Lower pH <10 waters yield low Na and Cl concentrations. (B) SO_4 vs Ca plot. Dashed 1:1 molar line in this case reflects the gypsum dilution line. (C) SO_4 vs Cl plot. (D) Cl vs K plot. (E) SO4 vs B. (F) SO_4 vs Li. (G) SO_4 vs Cs. (H) SO_4 vs Ba.

Water samples for which there was clear field evidence of mixing from different sources are classified separately as mixed water samples (Table 4.3) and their compositions fall between lower pH <10 water types and high pH >11.5 waters. A sample of snow was sampled from the Olympus Diapir yields very low elemental concentrations relative to other water types (Table 4.3).

The alkali metals and B follow a similar trend to Na^+ concentrations with an increase in concentration with increasing pH denoted by a marked significant increase between lower pH <10 and high pH >11.5 water (Fig. 4.10) and concentrations in the alkali metals generally co-vary. Concentrations of B in hyperalkaline pH >11.5 waters vary from 657 to 3,134 μmol/kg, Li varies from 730 to 2,417 μmol/kg, and Cs varies from 0.5 to 1.9 μmol/kg (Fig. 4.10; Table 4.3). These concentrations are significantly higher than the lower pH <10 water groups with B varying between 9 to 100 μmol/kg, Li between 0.7 and 25 μmol/kg, and Cs 0.0003 to 0.67 μmol/kg (Fig. 4.10; Table 4.3). In contrast, Ba concentrations in the high pH >11.5 waters (0.08 to 0.18 μmol/kg) and the lower pH Amiantos waters (0.08 to 0.37 μmol/kg) are similar (Fig. 4.10; Table 4.3; Table 4.4). The fluid evolution trajectory of the Amiantos mine waters is different to the hyperalkaline dilution line, which is apparent in elemental anion against cation plots (Fig. 4.10). SO_4^{2-} plotted against Li^+ shows the Amiantos mine water samples trajectory plotting below the hyperalkaline dilution line (Fig 4.10), whereas other fluid mobile tracers such as Cs^+ (Fig. 4.10) and Ba^{2+} (Fig. 4.10) plot above the hyperalkaline dilution line. However, some fluid mobile tracers such as K^+ (Fig. 4.10) and B (Fig. 4.10) plot on the corresponding hyperalkaline dilution line.

The Mg/Ca (mol/mol) also highlights a marked difference between lower pH <10 waters and high pH >11.5 waters, with a progressive increase in Mg/Ca (mol/mol) from pH >8 to <10 and yielding low Mg/Ca (mol/mol) ratios (Fig. 4.11; Table 4.3; Table 4.5; Table 4.6). Mg/Ca (mol/mol) values generally do not match seawater values (5.2; Table 4.5). The Sr/Ca (μmol/mmol) also shows a marked difference between the lower pH <10 waters and high pH >11.5 waters (Fig. 4.11) and do not match modern day seawater values of 8.5 and Cretaceous ~90 Ma seawater values of ~2 (Coggon et al., 2010). The lowest pH waters yield Sr/Ca (μmol/mmol) of 1.5 and as pH increases Sr/Ca (μmol/mmol) generally decreases to ~0.8. However, variability occurs at pH >9.2 to <10 with measured Sr/Ca (μmol/mmol) ranging between 0.4 and 2.8. The highest pH 13 samples yield Sr/Ca (μmol/mmol) of 0.8 and decrease to ~0.5 with decreasing pH and at pH ~11.5 significant variability also occurs in Sr/Ca (μmol/mmol) values, which vary between 0.3 and 3.8 (Fig. 4.11). The Na/Cl (mol/mol) of the lower pH <10 water groups vary between 0.6 and 1.1 and high pH >11.5 waters vary between 1.2 and 1.3, higher than values expected from halite

dissolution (~1). In contrast, the Troodos snow sample yields seawater-like Na/Cl (mol/mol) values of 0.87 (Fig. 4.12; Table 4.3; Table 4.5). Sampled hyperalkaline waters pH >11.5 waters of the Artemis Diapir yield similar Na/Cl (mol/mol) ratios as the Samail ophiolite, Oman (Fig. 4.12; Evans and Matter, unpublished data; Leong et al., 2021). The Ca/SO_4 (mol/mol) ratios of the Artemis Diapir hyperalkaline pH >11.5 waters are similar to seawater ratios ~0.36 (Fig. 4.12; Table 4.5) and significantly lower than values expected from gypsum/anhydrite dissolution (~1). In contrast, the Ca/SO_4 (mol/mol) ratios of sampled hyperalkaline waters of the Samail ophiolite show significant variability (~1 to ~10^3) (Fig. 4.12 ; Table 4.5; Leong et al., 2021). High pH >11.5 waters sampled in the Artemis Diapir yield higher Rb/K (μmol/mmol) values and lower Rb/Cs (μmol/nmol) relative to seawater (Table 4.5). In addition, ratios of Artemis Diapir hyperalkaline waters yield higher B/Cl (μmol/mmol) and generally lower Cl/Br (mol/mol) relative to seawater and fourteenfold evaporated seawater (Table 4.5; McCaffrey et al., 1987; Vengosh et al., 1998).

Table 4.5: Elemental ratios summary table (molar).

	Mg/Ca (mol/mol)	**Sr/Ca (μmol/mmol)**	**Na/Cl (mol/mol)**	**Ca/SO_4 (mol/mol)**	**Rb/K (μmol/mmol)**	**Rb/Cs (μmol/nmol)**	**B/Cl (μmol/mmol)**	**Cl/Br (mol/mol)**
Seawater	5.2	8.5	0.86	0.36	0.13	0.65	0.81	659
Fourteenfold Evaporated Seawater (McCaffrey et al., 1987; Vengosh et al., 1998)	186	-	0.78	0.014	-	-	1.01	511
Halite	-	-	1	-	-	-	-	Cl/Br > seawater = halite dissolution
Gypsum	-	(0.65 to 2.1; ODP Leg 107; Müller et al., 1990)	-	1	-	-	-	-

Lower pH <10 waters values	0.72 to 76.10	0.36 to 2.83	0.63 to 1.45	0.07 to 5.84	0.17 to 1.66	0.0002 to 0.006	7.5 to 200	6.5 to 185
High pH >11.5 waters values	0.01 to 6.50; 0.2 to 1.2 (Neal and Shand, 2002); 0.004 to 0.011 (Rizoulis et al., 2016)	0.26 to 0.77; 0.56 to 0.57 (Neal and Shand, 2002)	1.2 to 1.35; 1.41 (Neal and Shand, 2002); 0.95 to 1.06 (Rizoulis et al., 2016)	0.07 to 0.36**;** 0.004 to 0.017 (Neal and Shand, 2002) 0.08 to 0.72 (Rizoulis et al., 2016)	0.61 to 0.71	0.0027 to 0.0029	8.46 to 22.7; 8.52 to 8.65 (Neal and Shand, 2002)	402 to >506; 902 (Neal and Shad, 2002)
Troodos Massif Snow	0.72	1.1	0.87	2	0.2	0.01	5.5	26

Table 4.6: Elemental summary table.

	Mg/Ca (μg/g/μg/g)	Sr/Ca (ng/g/μg/g)	Na/Cl (μg/g/μg/g)	Ca/SO_4 (μg/g/μg/g)
Seawater	3.2	19.5	0.55	0.15
Messinian Evaporites	-	1.43 to 4.58	-	-
Lower pH <10 waters values	0.44 to 46.15	0.78 to 6.20	0.40 to 0.94	0.03 to 2.44
High pH >11.5 waters values	0.01 to 3.92	0.58 to 8.35	0.78 to 0.88	0.03 to 0.15

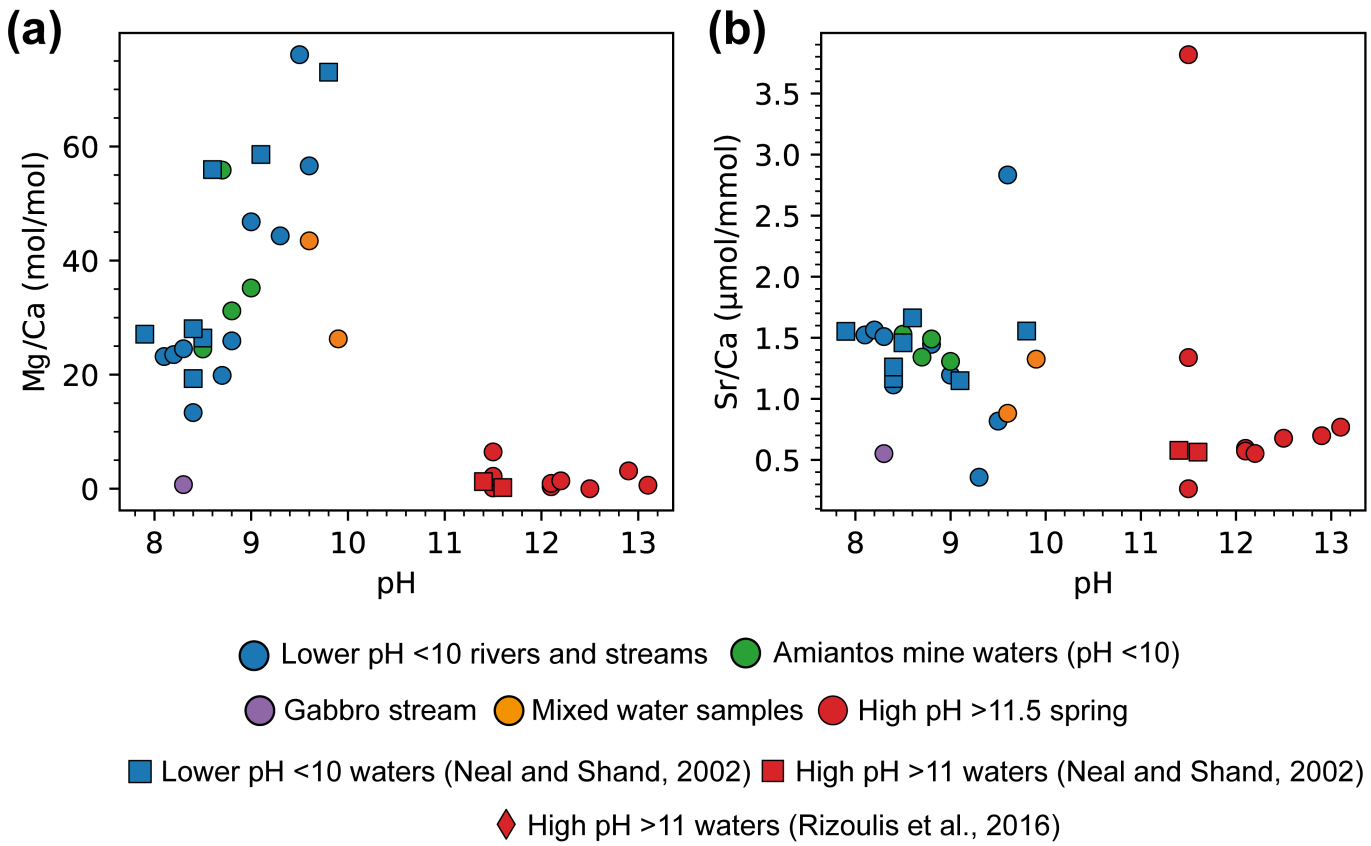

Figure 4.11: A) Plot of Mg/Ca (mol/mol) and pH. (B) Plot of Sr/Ca (µmol/mmol) and pH. Clear distinction between lower pH <10 waters and high pH >11.5 waters is shown. Mg/Ca (mol/mol) of modern seawater is ~5.2 (e.g., Coggon et al., 2010) and Sr/Ca (µmol/mmol) is ~8.5 (e.g., Coggon et al., 2010). Cretaceous ~90 Ma seawater Mg/Ca (mol/mol) is ~1.5 and Sr/Ca (µmol/mmol) is ~2 (Coggon et al., 2010).

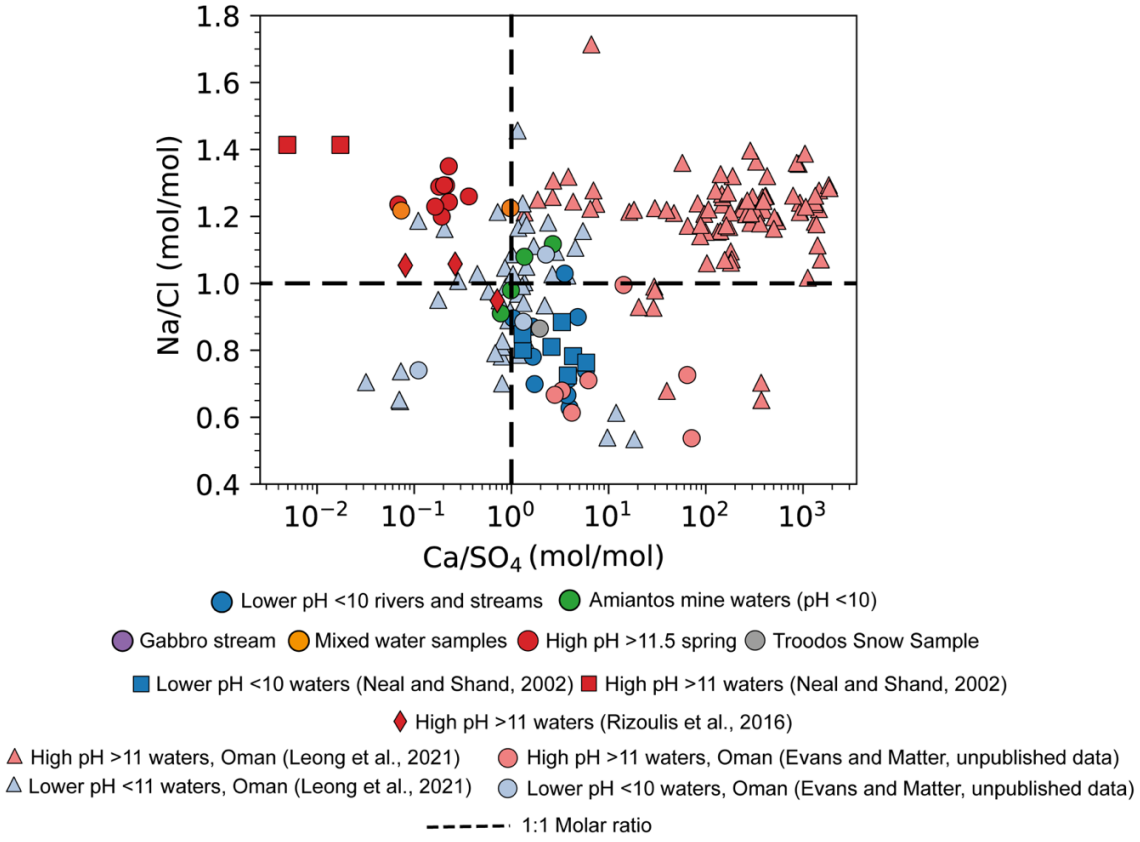

Figure 4.12: Plot of Na/Cl (mol/mol) and Ca/SO_4 (mol/mol). Ca/SO_4 is log scale. 1:1 Molar ratio line refers to the respective halite and gypsum dissolution line.

The chemistries of the Artemis hyperalkaline pH >11.5 waters differ from the predominantly calcium-hydroxide hyperalkaline waters previously reported in other settings (Fig. 4.13; Leong et al., 2021). Na^+ concentrations of Artemis Diapir hyperalkaline waters are generally an order of magnitude >10^5 μmol/kg higher than hyperalkaline waters sampled from the Samail ophiolite ~10^4 μmol/kg (Fig. 4.13). Mg^{2+} in hyperalkaline waters between both ophiolites is also highly variable with ~10^3 to ~10^1 μmol/kg in the Artemis Diapir and ~0.1 to ~10^2 μmol/kg in the Samail ophiolite. Lower pH <10 waters in the Troodos Mantle Sequence yield lower Na^+ (~10^2 μmol/kg) relative to the Samail ophiolite (~10^3 to <10^4 μmol/kg; Fig. 4.13) and similar Mg^{2+} concentrations (~10^3 μmol/kg; Fig. 4.13). Si concentrations in Samail ophiolite hyperalkaline waters are significantly lower (>0.1 to ~10^2 μmol/kg) than the Artemis Diapir (~10^2 to ~10^3 μmol/kg) and lower pH <10 waters yield similar Si concentrations (~10^3 μmol/kg) across both ophiolites (Fig. 4.13). Cl^- concentrations of Artemis Diapir hyperalkaline waters are over an order of magnitude higher (~10^5 μmol/kg) relative to the Samail ophiolite (~10^4 μmol/kg) and Troodos Mantle Sequence lower pH <10 river waters are an order of magnitude lower (~10^2 μmol/kg) relative to the Samail ophiolite (~10^3

μmol/kg; Fig. 4.13). Respective Ca^{2+} concentrations of hyperalkaline waters (~10^3 μmol/kg) and lower pH <10 waters (~10^2 μmol/kg) from both ophiolites are similar (Fig. 4.13).

$^{87}Sr/^{86}Sr$ isotopic compositions of the Troodos Mantle Sequence waters fall into three groups (Fig. 4.14): (1) The low pH >8 to <10 surficial waters yield an average $^{87}Sr/^{86}Sr$ of 0.708343 ± 488 (2σ; 1x10-^{6}); (2) the hyperalkaline pH >11.5 waters yield an average $^{87}Sr/^{86}Sr$ of 0.705765 ± 209 (2σ; 1x10^6); (3) a mixed fluid sample (sample BX3) that clearly involved mixing between sources yields an intermediate value of 0.706266. Sample CY1 from a stream emanating in gabbroic rocks with no input from the Troodos Mantle Sequence falls outside of both groups with a $^{87}Sr/^{86}Sr$ value of 0.706936. The Sr/Ca (ng/g/μg/g) of the corresponding low pH waters generally falls between >2 and <4 with hyperalkaline Sr/Ca (ng/g/μg/g) ratios typically ~1.5 (Fig. 4.15) and do not match either a seawater (19.5) or a dissolved Messinian evaporite origin (average = 2.8 ± 0.9, 1σ; n=17; Müller et al., 1990); instead fall within the Sr/Ca range of the Artemis Diapir rocks (Fig. 4.15). Oxygen and hydrogen stable isotope compositions of waters sampled from the Troodos Mantle Sequence fall along the Cyprus meteoric water line (Boronina et al., 2005) except for hyperalkaline pH >11.5 waters. These deviate from the Cyprus meteoric water line with higher oxygen and hydrogen stable isotope compositions (Fig. 4.16).

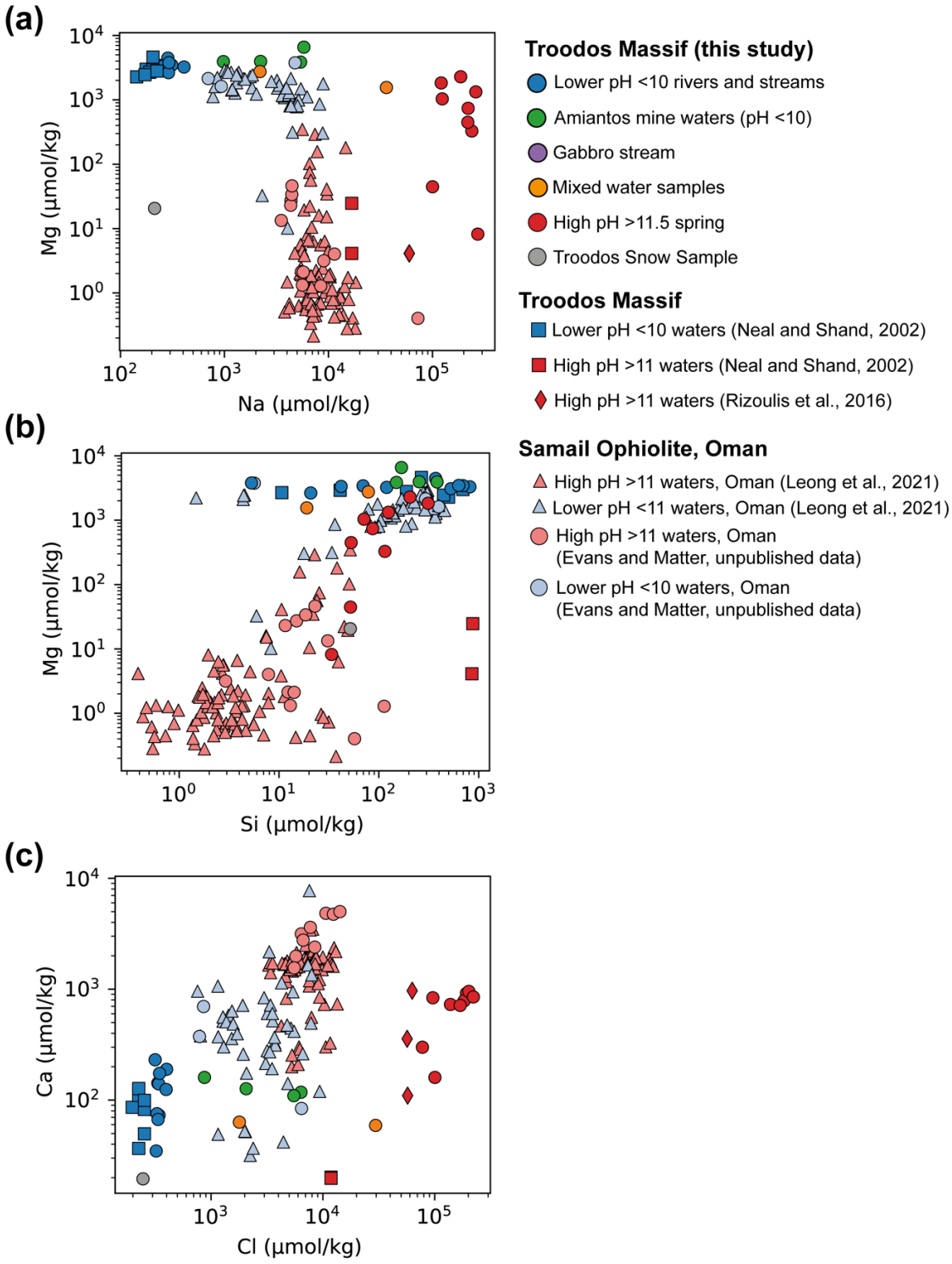

Figure 4.13: (A) Plot of Mg and Na concentrations in Troodos Massif waters from this study and others. Waters from the Samail ophiolite, Oman are also shown. (B) Plot of Mg and Si concentrations in Troodos Massif waters from this study and others. Waters from the Samail ophiolite, Oman are also shown. (C) Plot of Ca and Cl concentrations in Troodos Massif waters from this study and others. Waters from the Samail ophiolite, Oman are also shown.

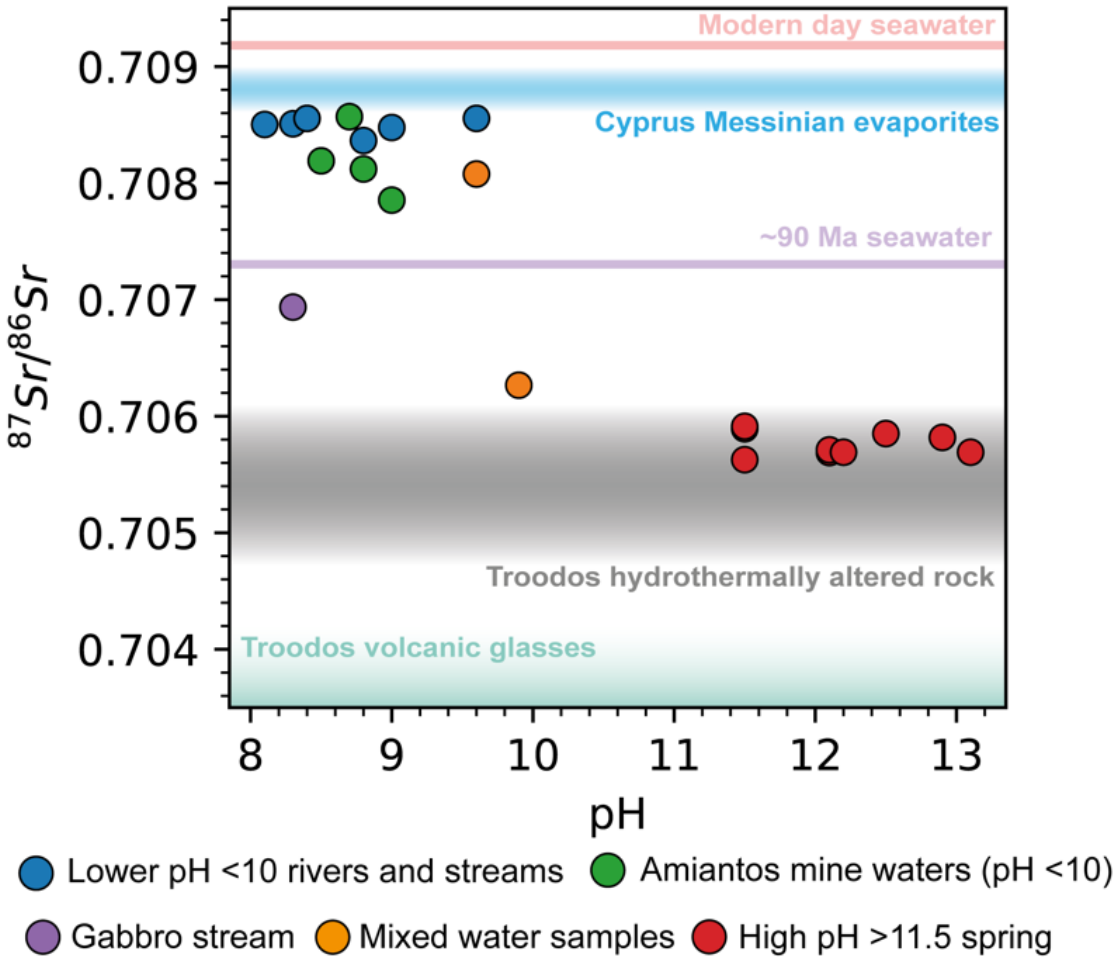

Figure 4.14: Plot of sampled waters and their respective groups $^{87}Sr/^{86}Sr$ vs pH. Boundaries of Troodos volcanic glasses (Rautenschlein et al., 1985), Troodos hydrothermally altered rock (Bickle and Teagle, 1992), Cretaceous ~90 Ma and modern day seawater (McArthur et al., 2012), and Cyprus Messinian evaporites (Flecker and Ellam, 2006; McCulloch and Deckker, 1989; Müller and Mueller, 1991) are shown.

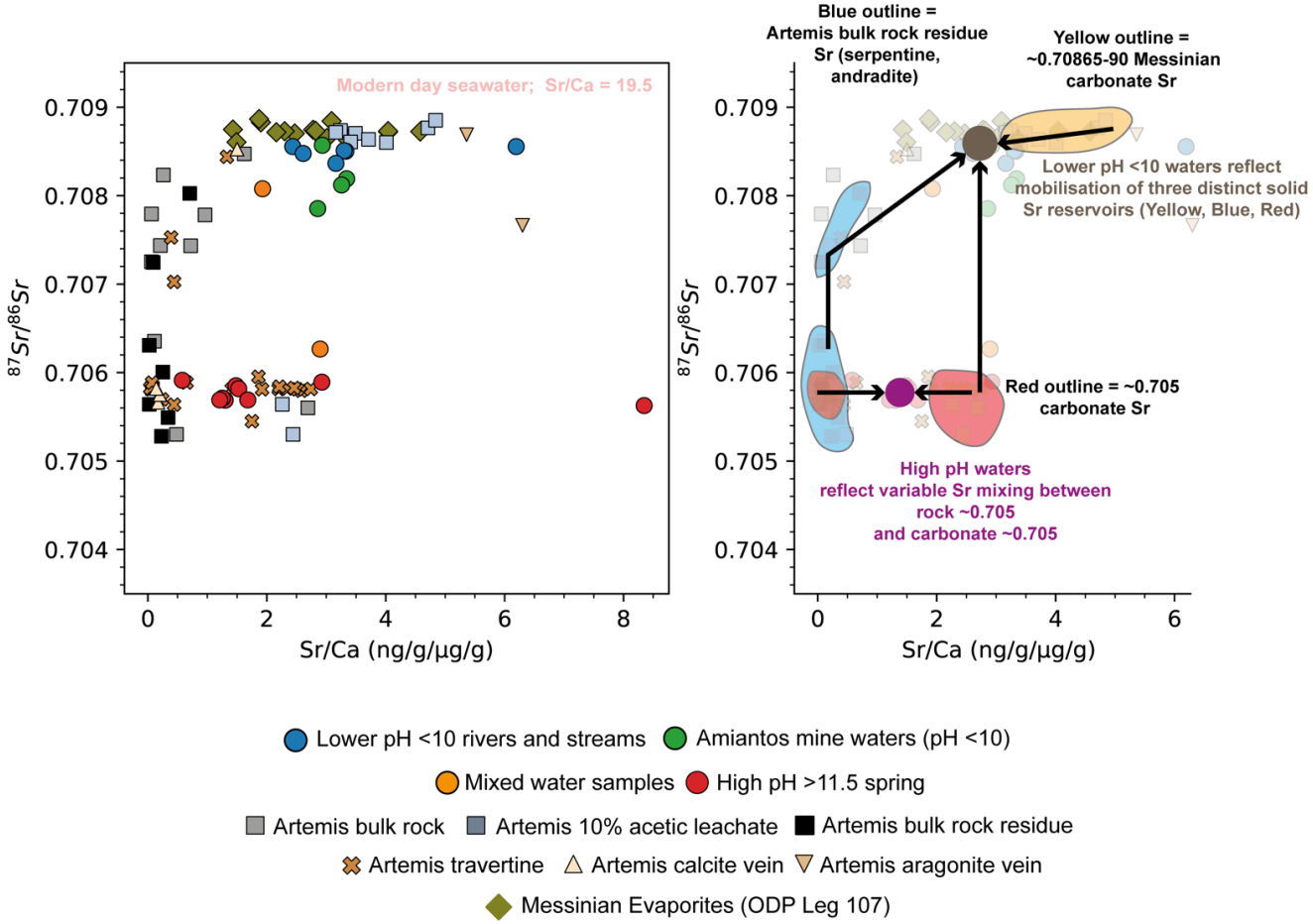

Figure 4.15: Plot of $^{87}Sr/^{86}Sr$ and Sr/Ca (ng/g/µg/g) of Troodos Mantle Sequence waters, Artemis bulk rock, Artemis 10% acetic leachate, Artemis bulk rock residue, Artemis travertine, Artemis calcite vein, Artemis aragonite vein. Messinian evaporite compositions are from ODP Leg 107 (Müller et al., 1990). High pH >11.5 waters reflect variable mixing of contrasting Sr reservoirs located in trace carbonates and rock. Lower pH <10 waters likely reflect relative mixing of three distinct solid Sr reservoirs. See text for details.

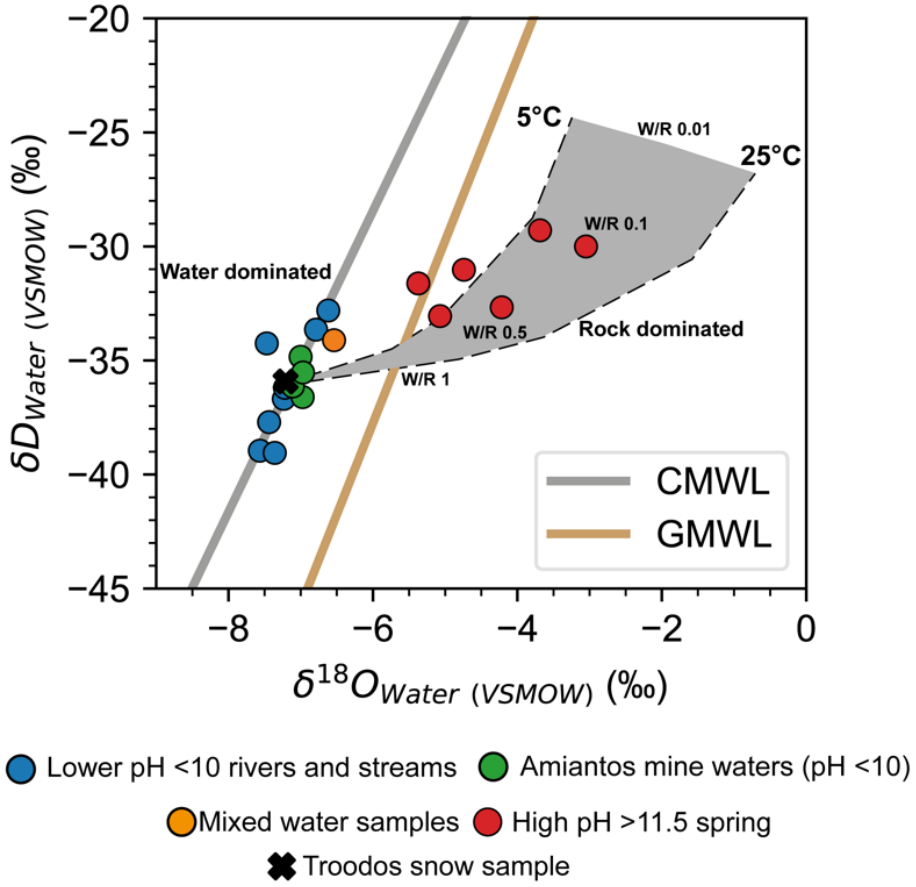

Figure 4.16: Plot of $\delta^{18}O_{Water}$ and δD_{Water} values of sampled Troodos Mantle Sequence waters. Global meteoric water line (GMWL) is plotted (Craig, 1961). The local Cyprus meteoric water line is also plotted (Boronina et al., 2005). Shaded area reflects a closed system water-rock equilibrium model (Taylor, 1977) with differing proportions of W/R shown.

4.4.2 Precipitates and Artemis Diapir rocks

Calcite veins, aragonite veins, and travertine composed of carbonate, brucite, and halite; calcite; aragonite; and magnesite stable and radiogenic isotopic compositions and elemental concentrations are reported in Table 4.7. Strontium isotopic compositions range between 0.70545 and 0.70869 and fall into three discrete groups that generally correspond to measured Artemis Diapir water types (Fig. 4.17; Fig. 4.18; Table 4.7). Measured $\delta^{18}O$ values of precipitates range between +18.8 to +34.7 ‰ (Table 4.7; Fig. 4.18). Calculated $\delta^{18}O$ values of calcite, aragonite, magnesite (in equilibrium with lower pH <10 water ($\delta^{18}O$ = -7.6 ‰) and high pH >11.5 hyperalkaline water ($\delta^{18}O$ = -3.5 ‰) at temperatures between 0 and 25°C match all measured carbonate $\delta^{18}O$ values (Fig. 4.18; fractionation factors of Zheng (1999)). Measured $\delta^{13}C$ values of precipitates generally range between -14.7 to +2.5 ‰ (Fig. 4.19; Table 4.7). Some travertine deposits with hibschite yield very high $\delta^{13}C$ values of +11.6 and +19.6 ‰. The majority of samples fall between atmospheric and mantle reservoirs (Fig. 4.19).

Table 4.7: Table of Troodos Mantle Sequence precipitates analytical results.

Sample Name	*Diapiric Domain*	*Sample Type*	$\delta^{13}C$ *(VPDB)*	$\delta^{18}O$ *(VSMOW)*	$^{87}Sr/^{86}Sr$	*2SE (1x10^6)*	*Sr (µg/g)*	*Ca (µg/g)*	*Sr/Ca (ng/g/µg/g)*
DJ1	Artemis	Aragonite vein	-6.84	25.97	0.707665	11	2600	412720	6.3
TRAV6	Artemis	Aragonite vein	-4.65	25.72	0.708690	11	2424	451840	5.4
CG1	Artemis	Calcite vein	-0.81	26.31	0.708526	12	524	349760	1.5
AA5	Artemis	Calcite vein	-3.52	33.88	0.705751	13	83.4	412480	0.2
AA2	Artemis	Calcite vein	-6.82	34.48	0.705821	11	48.2	344640	0.1
AA1	Artemis	Calcite vein	-8.01	32.68	0.705662	11	70.1	415520	0.2
AA5	Artemis	Calcite vein	-3.52	33.88	0.705741	12	83.4	412480	0.2
ST1	Olympus	Magnesite	2.43	29.87	nd	-	0.64	594	1.1
ST2	Olympus	Magnesite	0.01	30.18	nd	-	0.24	223	1.1
ST3	Olympus	Magnesite	0.82	29.79	nd	-	0.24	281	0.9
ST4	Olympus	Magnesite	0.95	29.58	nd	-	0.4	434	0.9

Sample Name	Diapiric Domain	Sample Type	$\delta^{13}C$ (VPDB)	$\delta^{18}O$ (VSMOW)	$^{87}Sr/^{86}Sr$	2SE ($1x10^{6}$)	Sr (µg/g)	Ca (µg/g)	Sr/Ca (ng/g/µg/g)
ST5	Olympus	Travertine	-5.78	26.47	0.708440	13	562	423360	1.3
DE2A	Artemis	Hibschite	19.55	33.47	0.705886	12	29.0	407600	0.1
DD1	Artemis	Travertine	-14.56	24.55	0.707025	12	30.7	70024	0.4
DL3	Artemis	Travertine	-6.94	26.38	0.705815	15	29.8	10896	2.7
DL5	Artemis	Travertine	-12.10	25.34	0.705811	13	35.3	14056	2.5
DL9	Artemis	Travertine	-7.55	26.47	0.705827	14	34.6	14024	2.5
DE2BY	Artemis	Hibschite	11.62	27.91	0.705813	11	20.4	409680	0.0
CRM2	Artemis	Travertine	-7.84	27.69	0.705841	14	17.0	7713	2.2
DL4	Artemis	Travertine	-10.09	30.84	0.705795	21	21.9	8512	2.6
CRM3	Artemis	Travertine	-7.90	26.60	0.705811	12	19.4	10096	1.9
DE2BX	Artemis	Hibschite	17.97	34.69	0.705825	12	16.3	399840	0.0
BY1	Artemis	Travertine	-9.18	31.38	0.705819	12	20.2	8664	2.3
TRAV5	Artemis	Travertine	-14.10	22.29	0.707528	13	61.7	156880	0.4
BY2	Artemis	Travertine	-8.12	27.61	0.705815	13	8.56	3898	2.2

Sample Name	Diapiric Domain	Sample Type	$\delta^{13}C$ (VPDB)	$\delta^{18}O$ (VSMOW)	$^{87}Sr/^{86}Sr$	2SE ($1x10^{6}$)	Sr (µg/g)	Ca (µg/g)	Sr/Ca (ng/g/µg/g)
CRM1	Artemis	Travertine	-8.86	28.55	0.705953	14	10.3	5541	1.9
DL2	Artemis	Travertine	-8.85	31.27	0.705813	13	14.2	10008	1.4
DL1	Artemis	Travertine	-7.88	27.57	0.705888	12	6.08	9384	0.6
TRAV1	Artemis	Travertine	-14.74	18.83	0.705450	11	732	417280	1.8
TRAV2	Artemis	Travertine	-3.48	21.05	0.705638	13	164	374480	0.4
CRM6	Artemis	Travertine	-14.23	20.27	0.705697	12	30.1	127360	0.2

Table 4.7 continued:

Sample Name	Diapiric Domain	Sample Type	Li (µg/g)	B (µg/g)	Na (µg/g)	Mg (µg/g)	Al (µg/g)	Si (µg/g)	K (µg/g)	Cr (µg/g)	Mn (µg/g)	Fe (µg/g)	Rb (µg/g)	Cs (µg/g)	Ba (µg/g)	Pb (µg/g)
DJ1	Artemis	Aragonite vein	bd	227	169	66.2	31.2	942	618	0.40	0.56	19.0	bd	bd	472	bd
TRAV6	Artemis	Aragonite vein	bd	186	65.4	3215	161	1037	582	0.32	0.8	13.5	bd	0.4	287	bd
CG1	Artemis	Calcite vein	58.5	2598	572	14704	67.0	1133	677	0.80	9.12	17.6	0.08	bd	14.2	bd
AA5	Artemis	Calcite vein	104	4340	1194	157	31.3	891	702	0.64	149	29.5	0.08	bd	35.0	bd

Sample Name	Diapiric Domain	Sample Type	Li (µg/g)	B (µg/g)	Na (µg/g)	Mg (µg/g)	Al (µg/g)	Si (µg/g)	K (µg/g)	Cr (µg/g)	Mn (µg/g)	Fe (µg/g)	Rb (µg/g)	Cs (µg/g)	Ba (µg/g)	Pb (µg/g)
AA2	Artemis	Calcite vein	9.36	984	118	387	32.6	1048	612	0.80	32.3	21.8	bd	bd	3.60	0.08
AA1	Artemis	Calcite vein	36.9	1859	354	479	28.7	1004	692	0.48	36.5	16.3	0.08	bd	4.00	bd
AA5	Artemis	Calcite vein	104	4340	1194	157	31.3	891	702	0.64	149	29.5	0.08	bd	35.0	bd
ST1	Olympus	Magnesite	bd	263	40.7	289360	27.2	1022	620	1.36	31.8	599	bd	bd	bd	bd
ST2	Olympus	Magnesite	bd	169	35.7	210000	37.5	1610	616	18.6	235	7410	bd	bd	bd	bd
ST3	Olympus	Magnesite	1.20	471	131	239280	45.9	1532	598	20.4	189	6590	bd	bd	bd	bd
ST4	Olympus	Magnesite	bd	162	50.0	269920	39.8	1075	648	4.72	35.0	589	bd	bd	bd	0.08
ST5	Olympus	Travertine	bd	213	103	2209	25.8	1111	630	0.32	2.88	13.0	bd	bd	0.48	bd
DE2A	Artemis	Hibschite	8.88	851	136	143	51.0	1065	628	0.32	4.72	25.7	bd	bd	bd	0.08
DD1	Artemis	Travertine	10.2	503	517	175680	125	1258	628	46.8	178	3088	0.16	0.4	4.80	0.48
DL3	Artemis	Travertine	212	780	24048	321040	26.5	1232	2433	1.60	0.80	15.7	2.88	1.84	16.6	0.48
DL5	Artemis	Travertine	95.8	644	39432	304000	26.7	1126	2814	0.56	0.72	15.0	3.28	2.16	19.1	0.32
DL9	Artemis	Travertine	33.8	722	9712	329280	30.6	1154	1098	0.88	1.36	17.1	0.88	0.56	18.9	0.48
DE2BY	Artemis	Hibschite	4.00	593	125	1427	38.2	1170	634	0.24	17.4	43.5	bd	0.08	bd	bd
CRM2	Artemis	Travertine	25.0	664	5511	113840	29.4	1074	927	0.96	1.68	25.2	0.40	0.24	9.28	0.24
DL4	Artemis	Travertine	107	973	30256	310240	10.3	1183	2217	1.12	0.64	13.3	2.48	1.76	12.5	0.40

Sample Name	*Diapiric Domain*	*Sample Type*	*Li (µg/g)*	*B (µg/g)*	*Na (µg/g)*	*Mg (µg/g)*	*Al (µg/g)*	*Si (µg/g)*	*K (µg/g)*	*Cr (µg/g)*	*Mn (µg/g)*	*Fe (µg/g)*	*Rb (µg/g)*	*Cs (µg/g)*	*Ba (µg/g)*	*Pb (µg/g)*
CRM3	Artemis	Travertine	15.4	494	4388	101200	29.0	1077	826	2.08	1.36	27.3	0.32	0.24	11.0	0.16
DE2BX	Artemis	Hibschite	bd	336	60.2	986	87.7	1106	606	0.40	14.5	34.2	bd	bd	bd	bd
BY1	Artemis	Travertine	16.1	391	5271	148640	26.8	1046	944	0.80	0.80	17.5	0.40	0.24	11.0	0.16
TRAV5	Artemis	Travertine	30.2	1280	882	134720	63.0	1210	671	46.1	117	1503	0.16	0.24	24.1	0.24
BY2	Artemis	Travertine	311	12032	6700	105440	2.7	910	1110	1.44	1.04	20.5	0.48	0.32	4.08	0.16
CRM1	Artemis	Travertine	10.0	384	3258	70824	43.1	1070	736	14.5	16.0	165	0.32	0.16	5.92	0.32
DL2	Artemis	Travertine	34.6	389	12968	112320	28.1	859	1270	1.60	1.28	28.2	1.04	0.64	7.84	0.24
DL1	Artemis	Travertine	91.4	2052	21088	264800	39.7	2101	1816	1.36	4.00	37.0	1.92	0.8	47.3	0.56
TRAV1	Artemis	Travertine	9.68	190	1140	15560	94.2	1120	612	10.8	20.3	245	0.16	0.24	219	0.32
TRAV2	Artemis	Travertine	1.36	306	760	7559	276	1131	690	8.24	93.6	177	0.24	0.24	49.6	0.32
CRM6	Artemis	Travertine	42.4	826	1331	45976	104	1019	664	50.7	181	1274	0.16	0.16	14.6	0.24

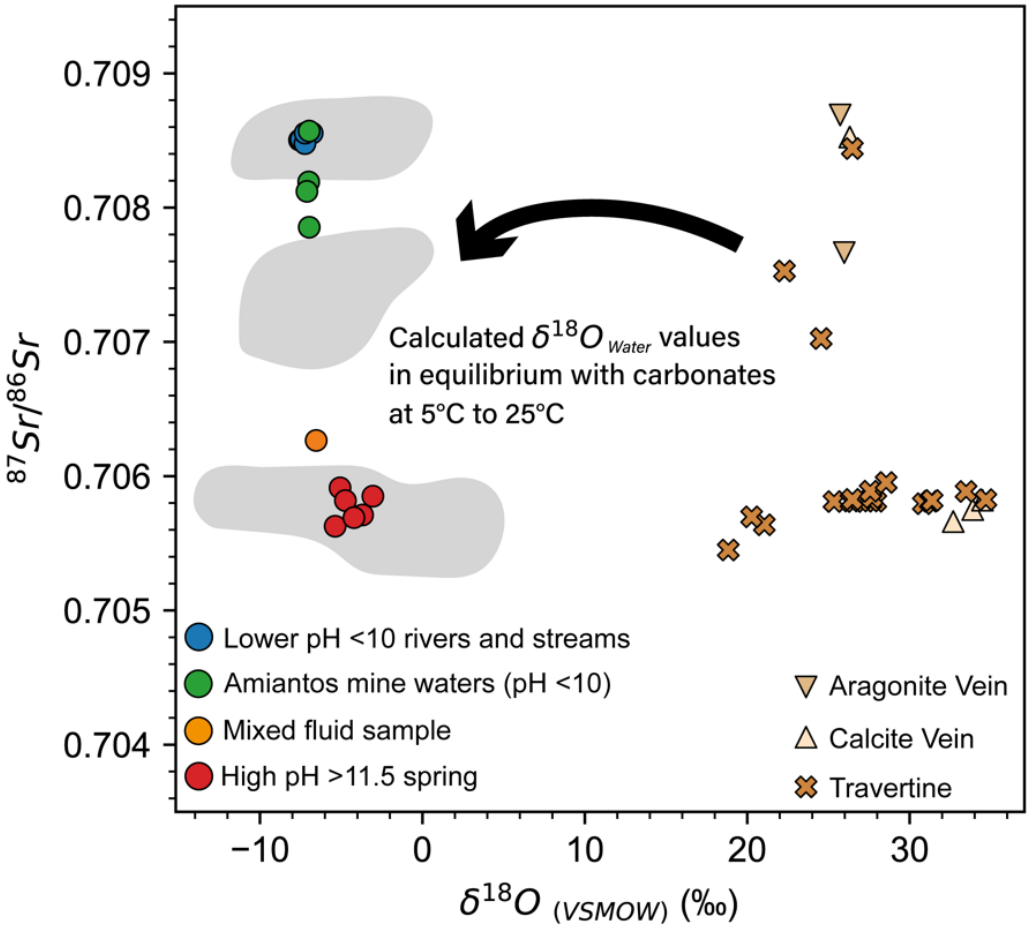

Figure 4.17: Plot of $^{87}Sr/^{86}Sr$ and $\delta^{18}O$ of sampled waters and precipitates. Calculated $\delta^{18}O_{Water}$ values in equilibrium with carbonates (calcite and aragonite) at temperatures of 5°C to 25°C are shaded in grey. Calcite and aragonite fractionation factors of Zheng (1999) were used.

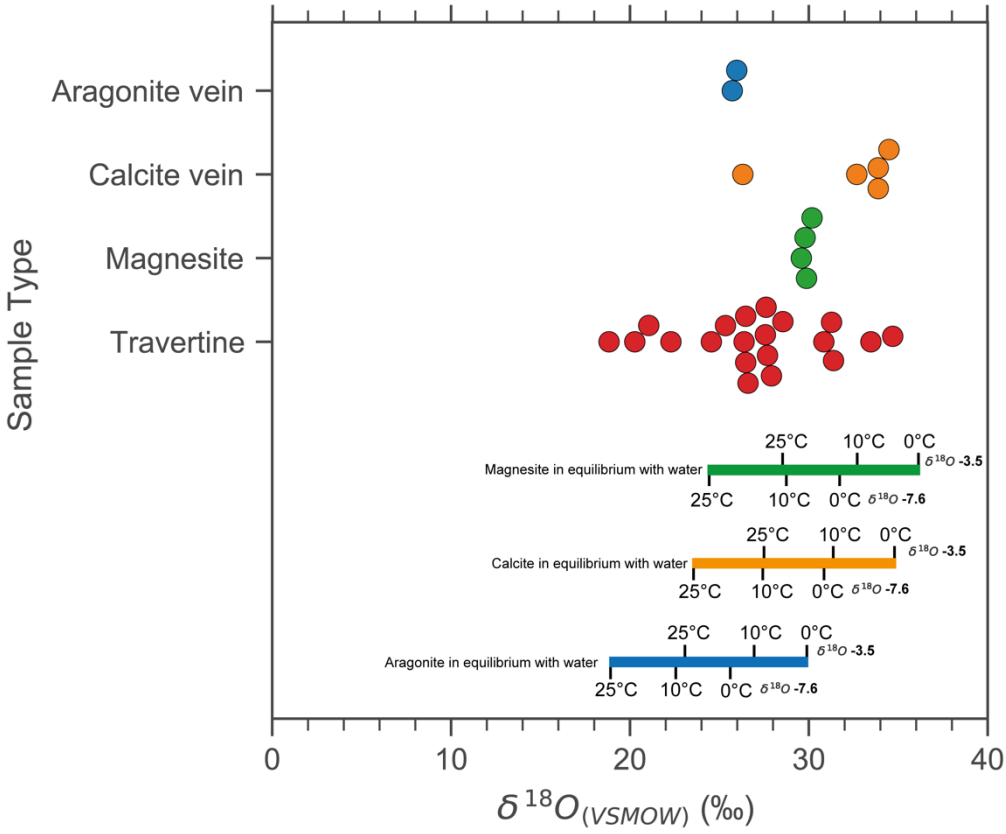

Figure 4.18: Oxygen stable isotope values of precipitates sampled within the Troodos Mantle Sequence. Precipitates are grouped into Travertine, Magnesite, Calcite veins and Aragonite veins. Calculated ranges of oxygen stable isotope values in equilibrium with lower pH <10 water ($\delta^{18}O$ -7.6 ‰) and high pH >11.5 hyperalkaline water ($\delta^{18}O$ -3.5 ‰) at temperatures between 0 and 25°C are shown. Respective magnesite, calcite, and aragonite fractionation factors of Zheng (1999) were used.

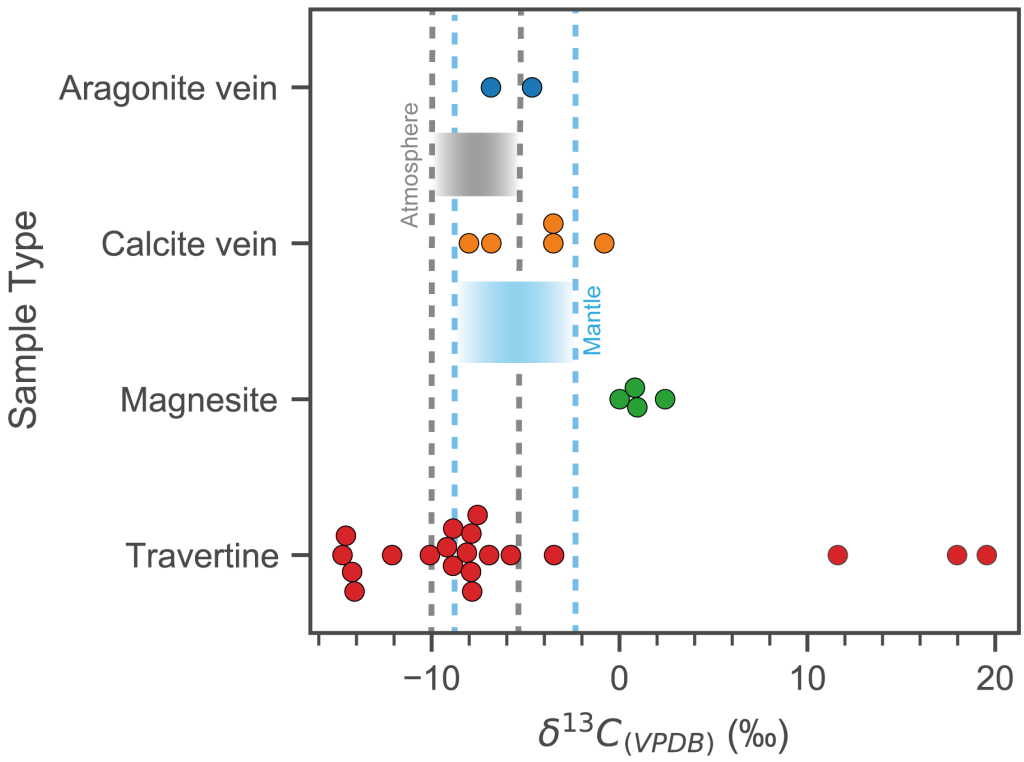

Figure 4.19: $\delta^{13}C_{(VPDB)}$ Caltech plot of precipitates sampled within the Troodos Mantle Sequence. Boundaries of Atmospheric $\delta^{13}C_{(VPDB)}$ composition (Keeling, 1958) and Mantle $\delta^{13}C_{(VPDB)}$ composition (Rollinson, 2014) are shown.

Strontium isotope compositions of the Artemis Diapir bulk rocks range (Fig. 4.20; Table 4.8) between 0.705301 and 0.708531. In contrast, the initial 10 % Acetic leachate, from a series of progressive leaching experiments (Table 4.9), falls into two discrete groups: (1) A small sample set that yield low Sr isotope signature between 0.705302 and 0.705642 and (2) the majority of the samples that ranges between 0.708601and 0.708767 (Fig. 4.20). The next 3M HCl leaching step yields isotopic compositions similar to bulk rock (Fig. 4.20; Table 4.10). The final rock residue falls into two discrete groups: (1) most samples yield relatively low, more primitive Sr isotope ratios between 0.705280 and 0.706308 whereas (2) a small group has $^{87}Sr/^{86}Sr$ ratios between 0.707245 and 0.708026 (Fig. 4.20; Table 4.11). Sr concentrations in the Artemis Diapir bulk rocks vary by an order of magnitude (553 to 5,982 ng/g), with the samples with the lowest Sr isotope compositions generally having the highest fluid-mobile (e.g., B, Li, Cs, Rb, K, Cu, Ba, Sr) trace element concentrations (Table 4.8). Each leaching step typically represents ~33 % of the overall Sr budget as measured in the bulk rock (Fig. 4.20). Late-stage serpentinite phases such as serpentine and chrysotile veins or incohesive fault rocks have lower fluid mobile trace element concentrations (e.g., Li, other elements) relative to overall bulk rock concentrations (e.g., Fig. 4.21).

Variations in trace element concentrations and strontium isotopic compositions occurs over outcrop (Fig. 4.22) and hand-specimen scales (Fig. 4.23). Outcrop site AR demonstrates these variations (Fig. 4.22) with the periphery of the outcrop (sample AR1) bulk rock yielding a mixed $^{87}Sr/^{86}Sr$ composition through a radiogenic Sr (0.7086) contribution from the easily-mobile leachate and a more primitive Sr (0.7062) contribution from the bulk residue. In contrast, the texturally different central portions of the outcrop (sample AR2) bulk rock yields a low Sr composition of 0.7056, with the easily-mobile and bulk residue portions yielding similar Sr isotopic compositions. Sample CU highlights variations on a decimetre scale with the bulk rock $^{87}Sr/^{86}Sr$ reflecting the relative contributions of more primitive Sr as displayed in the residue portion and radiogenic Sr in the easily mobile leachate (Fig. 4.23). The serpentine vein of CU5 and chrysotile vein of CU3 yield relatively radiogenic Sr isotopic compositions with lower bulk rock Sr concentrations (Fig. 4.23).

Table 4.8: Table of Artemis Diapir whole rock analytical results.

Sample	Diapiric Domain	Group	$^{87}Sr/^{86}Sr$ (Bulk)	2SE ($1x10^6$)	ICP-OES Mg (wt.%)	ICP-OES Fe (wt.%)	Mg#	ICP-OES Ca (wt.%)	ICP-OES Na (µg/g)	ICP-OES K (µg/g)	ICP-MS Li (µg/g)	ICP-MS Sc (µg/g)	ICP-MS Ti (µg/g)	ICP-MS V (µg/g)	ICP-MS Cr (µg/g)	ICP-MS Co (µg/g)	ICP-MS Ni (µg/g)	ICP-MS Cu (µg/g)	ICP-MS Zn (µg/g)
AN2	Artemis	Artemis Bulk Rock	nd	-	21.88	5.46	80.0	0.18	303	29.1	4.07	7.16	18.4	23.4	1,374	87.7	1,951	6.6	35.0
AO2	Artemis	Artemis Bulk Rock	0.705301	16	21.63	5.56	79.5	1.25	188	11.7	5.01	9.61	114	47.6	2,076	83.6	1,772	19.9	34.9
AP2	Artemis	Artemis Bulk Rock	0.708472	18	20.35	4.53	81.8	0.10	19.2	20.8	1.68	7.24	90.4	29.0	2,412	105	2,277	23.9	26.0
AQ2	Artemis	Artemis Bulk Rock	0.708233	13	19.21	5.29	78.4	1.00	179	10.2	3.49	10.1	149	51.9	2,346	88.7	1,865	12.9	35.1
AR1	Artemis	Artemis Bulk Rock	0.707782	11	20.61	4.50	82.1	0.18	52.1	10.4	4.20	8.75	78.2	35.3	2,372	91.1	2,054	8.8	35.8
AR2	Artemis	Artemis Bulk Rock	0.705602	14	20.18	5.29	79.2	0.12	84.8	0.28	2.18	8.73	89.1	41.1	3,222	92.7	1,929	9.5	57.5
BA1C	Artemis	Artemis Bulk Rock	0.706355	13	19.50	5.09	79.3	1.26	22.6	6.38	2.70	8.26	64.1	32.3	2,246	107	1,939	16.8	19.6
CU1	Artemis	Artemis Bulk Rock	0.707434	12	19.76	4.89	80.2	0.30	bd	7.60	2.27	9.18	87.2	44.3	2,843	107	2,038	16.1	61.1
PP1	Artemis	Artemis Bulk Rock	0.707793	13	19.18	5.17	78.8	2.06	105	7.01	4.85	28.6	492	180	3,578	48.3	1,174	29.4	16.2
AA4-2	Artemis	Artemis Bulk Rock Halo	0.706794	33	19.11	6.25	75.4	2.04	30.1	7.50	2.56	7.97	117	43.6	1,844	113	1,817	12.3	24.8

Sample	Diapiric Domain	Group	$^{87}Sr/^{86}Sr$ (Bulk)	2SE ($1x10^6$)	ICP-OES Mg (wt.%)	ICP-OES Fe (wt.%)	Mg#	ICP-OES Ca (wt.%)	ICP-OES Na (µg/g)	ICP-OES K (µg/g)	ICP-MS Li (µg/g)	ICP-MS Sc (µg/g)	ICP-MS Ti (µg/g)	ICP-MS V (µg/g)	ICP-MS Cr (µg/g)	ICP-MS Co (µg/g)	ICP-MS Ni (µg/g)	ICP-MS Cu (µg/g)	ICP-MS Zn (µg/g)
AA4-4	Artemis	Artemis Bulk Rock Halo	nd	-	18.12	6.91	72.4	3.20	3.28	7.28	2.95	10.5	168	59.4	2,216	91.2	2,035	14.9	20.5
AO3C	Artemis	Artemis Bulk Rock Halo	0.708531	11	20.04	5.70	77.9	0.82	193	22.1	3.93	10.2	127	52.0	2,294	92.6	1,958	10.5	33.4
BA1B	Artemis	Artemis Bulk Rock Halo	0.706930	17	18.82	5.43	77.6	1.46	31.5	6.10	2.88	8.91	66.2	35.4	4,060	91.9	2,039	17.4	58.6
CU2	Artemis	Artemis Bulk Rock Halo	0.707436	11	19.54	4.84	80.1	0.94	53.1	3.83	2.14	9.50	85.6	46.8	2,632	103	2,010	14.5	47.7
CU4	Artemis	Artemis Bulk Rock Halo	0.707253	13	18.54	5.43	77.4	2.46	130	6.28	2.01	9.79	81.3	43.3	2,457	82.6	1,952	10.9	31.3
AX1	Artemis	Chrysotile vein	nd	-	nd	nd	nd	nd	nd	nd	2.38	1.98	7.27	5.15	111	38.3	408	2.05	11.7
AZ1	Artemis	Chrysotile vein	nd	-	20.68	2.71	88.4	0.05	67.1	93.4	1.49	0.81	22.4	5.48	23.3	31.8	417	1.49	8.39
CR1	Artemis	Chrysotile vein	0.706909	13	22.07	3.65	85.8	0.04	17.8	6.90	2.66	0.93	33.5	15.5	213	40.9	188	0.87	13.4
CR1	Artemis	Chrysotile vein	nd	-	22.07	3.65	85.8	0.04	17.8	6.90	2.66	0.93	33.5	15.5	213	40.9	188	0.87	13.4
CU3	Artemis	Chrysotile vein	0.707677	14	19.66	3.65	84.3	0.07	13.3	8.25	3.45	0.14	1.88	12.7	115	45.4	307	5.05	11.9
DI1	Artemis	Chrysotile vein	0.707376	26	21.79	3.67	85.6	0.02	109	20.1	12.9	1.76	16.1	10.1	207	39.0	316	0.67	14.4

Sample	Diapiric Domain	Group	$^{87}Sr/^{86}Sr$ (Bulk)	2SE ($1x10^6$)	ICP-OES Mg (wt.%)	ICP-OES Fe (wt.%)	Mg#	ICP-OES Ca (wt.%)	ICP-OES Na (µg/g)	ICP-OES K (µg/g)	ICP-MS Li (µg/g)	ICP-MS Sc (µg/g)	ICP-MS Ti (µg/g)	ICP-MS V (µg/g)	ICP-MS Cr (µg/g)	ICP-MS Co (µg/g)	ICP-MS Ni (µg/g)	ICP-MS Cu (µg/g)	ICP-MS Zn (µg/g)
DI1A	Artemis	Chrysotile vein	nd	-	nd	nd	nd	nd	nd	nd	3.98	0.89	8.44	10.1	47.2	28.8	86	0.36	13.8
DI2	Artemis	Chrysotile vein	0.707116	13	18.34	3.13	85.4	0.07	2,331	127	14.7	1.29	16.3	14.1	215	27.2	158	0.43	21.1
DI3	Artemis	Chrysotile vein	nd	-	20.56	5.14	80.0	0.10	20.7	30.0	1.34	5.00	39.0	17.0	1,512	87.2	1,693	2.49	24.6
DI5	Artemis	Chrysotile vein	nd	-	20.63	3.31	86.2	0.04	152	10.1	4.62	0.67	53.6	15.0	33.4	75.5	70.9	0.29	10.5
BM1	Artemis	Cohesive Artemis Fault Rock	0.707818	12	20.40	4.79	81.0	0.76	bd	7.39	1.55	10.7	47.2	32.4	1,485	124	1,524	5.11	21.8
BN1	Artemis	Cohesive Artemis Fault Rock	0.706344	12	9.41	4.91	65.7	7.70	3,237	888	129	40.9	529	190	527	38.1	85.0	72.5	24.8
BO1	Artemis	Cohesive Artemis Fault Rock	0.705681	12	17.54	5.47	76.2	7.17	436	20.4	10.8	4.28	63.1	36.4	1,747	34.6	660	7.47	5.21
BO2	Artemis	Cohesive Artemis Fault Rock	nd	-	20.77	2.66	88.6	0.03	142	42.2	0.36	5.85	59.6	26.5	873	111	1,751	2.34	32.3
BO3	Artemis	Cohesive Artemis Fault Rock	0.705657	12	18.00	2.51	87.8	8.49	2,176	119	29.8	1.45	8.21	8.35	644	37.8	753	4.54	6.89

Sample	Diapiric Domain	Group	$^{87}Sr/^{86}Sr$ (Bulk)	2SE ($1x10^6$)	ICP-OES Mg (wt.%)	ICP-OES Fe (wt.%)	Mg#	ICP-OES Ca (wt.%)	ICP-OES Na (µg/g)	ICP-OES K (µg/g)	ICP-MS Li (µg/g)	ICP-MS Sc (µg/g)	ICP-MS Ti (µg/g)	ICP-MS V (µg/g)	ICP-MS Cr (µg/g)	ICP-MS Co (µg/g)	ICP-MS Ni (µg/g)	ICP-MS Cu (µg/g)	ICP-MS Zn (µg/g)
DB1	Artemis	Cohesive Artemis Fault Rock	nd	-	17.09	5.11	77.0	0.22	126	20.2	16.0	12.3	114	48.5	2,924	72.1	737	4.40	30.4
DB2	Artemis	Cohesive Artemis Fault Rock	nd	-	19.12	6.23	75.4	0.19	167	20.5	35.0	5.65	50.2	20.4	1,497	104	1,078	2.68	23.8
DE1B	Artemis	Cohesive Artemis Fault Rock	nd	-	17.93	3.85	82.3	1.24	104	6.06	6.17	2.23	5.95	3.10	194	30.2	872	0.34	30.5
DE2BZ	Artemis	Cohesive Artemis Fault Rock	0.705820	29	15.74	3.73	80.8	8.41	101	7.72	13.9	1.76	6.21	4.20	231	53.8	1,017	0.40	14.1
AB3	Artemis	Incohesive Artemis Breccia	nd	-	20.40	4.17	83.0	0.09	65.8	14.6	2.15	7.02	48.0	24.9	2,320	76.3	1,918	4.77	29.9
AB4	Artemis	Incohesive Artemis Breccia	nd	-	20.53	3.54	85.3	0.65	148	80.5	2.21	2.44	52.8	15.1	690	46.9	625	5.19	15.7
AI1	Artemis	Incohesive Artemis Breccia	nd	-	nd	nd	nd	nd	nd	nd	0.27	5.56	33.1	20.9	1,364	96.4	2,015	5.99	28.2
AK1	Artemis	Incohesive Artemis Breccia	nd	-	21.05	4.53	82.3	0.27	133	2.27	0.87	5.76	21.8	24.0	1,081	72.5	2,281	8.69	16.1

Sample	Diapiric Domain	Group	$^{87}Sr/^{86}Sr$ (Bulk)	2SE ($1x10^{6}$)	ICP-OES Mg (wt.%)	ICP-OES Fe (wt.%)	Mg#	ICP-OES Ca (wt.%)	ICP-OES Na (µg/g)	ICP-OES K (µg/g)	ICP-MS Li (µg/g)	ICP-MS Sc (µg/g)	ICP-MS Ti (µg/g)	ICP-MS V (µg/g)	ICP-MS Cr (µg/g)	ICP-MS Co (µg/g)	ICP-MS Ni (µg/g)	ICP-MS Cu (µg/g)	ICP-MS Zn (µg/g)
AN1	Artemis	Incohesive Artemis Breccia	nd	-	18.02	6.58	73.2	3.08	98.9	4.20	2.08	4.51	20.6	31.5	1,154	66.5	1,507	4.72	12.2
AN3	Artemis	Incohesive Artemis Breccia	nd	-	21.05	4.99	80.8	0.60	bd	12.2	3.55	7.45	23.3	24.0	1,747	115	2,084	5.49	22.2
AS2	Artemis	Incohesive Artemis Breccia	nd	-	22.52	5.30	81.0	0.39	bd	8.01	1.23	8.47	27.4	25.5	1,203	83.1	2,117	4.68	16.5
AS3	Artemis	Incohesive Artemis Breccia	0.706077	20	20.46	4.52	81.9	0.51	bd	4.27	1.76	19.8	159	36.2	2,810	96.0	1,148	3.70	51.4
AU1	Artemis	Incohesive Artemis Breccia	nd	-	19.43	4.02	82.8	0.08	76.2	17.8	1.13	9.29	31.0	36.2	1,419	79.8	1,686	10.0	17.4
BZ1	Artemis	Incohesive Artemis Breccia	0.705884	20	20.55	4.75	81.2	0.04	42.5	1.38	0.22	7.22	18.9	20.1	1,066	97.1	1,977	6.59	19.8
BZ2	Artemis	Incohesive Artemis Breccia	nd	-	12.81	2.83	81.9	0.13	22.7	2.19	0.82	5.50	25.5	18.7	1,109	77.7	1,495	5.99	21.1
DC2H	Artemis	Incohesive Artemis Breccia	nd	-	17.29	7.23	70.5	4.37	100	3.51	1.94	8.36	49.1	35.6	2,588	73.0	1,756	4.57	15.2

Sample	Diapiric Domain	Group	$^{87}Sr/^{86}Sr$ (Bulk)	2SE ($1x10^6$)	ICP-OES Mg (wt.%)	ICP-OES Fe (wt.%)	Mg#	ICP-OES Ca (wt.%)	ICP-OES Na (µg/g)	ICP-OES K (µg/g)	ICP-MS Li (µg/g)	ICP-MS Sc (µg/g)	ICP-MS Ti (µg/g)	ICP-MS V (µg/g)	ICP-MS Cr (µg/g)	ICP-MS Co (µg/g)	ICP-MS Ni (µg/g)	ICP-MS Cu (µg/g)	ICP-MS Zn (µg/g)
DH1V	Artemis	Incohesive Artemis Breccia	nd	-	14.82	8.03	64.8	6.74	104	6.96	1.65	2.55	41.0	17.7	704	31.1	537	2.39	8.57
AA3	Artemis	Serpentine vein	0.707716	81	49.28	9.24	84.2	0.68	bd	12.3	1.66	0.22	19.3	24.6	9.8	18.5	12.8	0.93	9.82
AA4-1	Artemis	Serpentine vein	nd	-	20.58	3.85	84.2	0.30	77.9	7.35	2.00	1.29	17.7	26.3	301	32.8	182	4.07	12.6
AA4X	Artemis	Serpentine vein	nd	-	21.06	2.85	88.1	0.03	124	8.53	1.14	0.28	8.42	7.73	77.1	17.5	37.1	1.91	11.3
AA4Y	Artemis	Serpentine vein	nd	-	20.81	4.15	83.4	0.06	35.6	29.2	0.90	1.04	28.3	22.7	28.4	23.8	23.1	0.77	13.7
AN4	Artemis	Serpentine vein	0.708417	14	21.87	3.85	85.0	0.15	157	18.9	1.30	2.40	4.71	10.8	25.8	10.3	39.7	2.06	12.3
AN5	Artemis	Serpentine vein	nd	-	20.25	5.47	78.7	1.59	37.0	21.2	1.75	1.17	38.0	18.6	50.4	17.4	38.9	1.69	14.1
AP1	Artemis	Serpentine vein	nd	-	19.99	3.49	85.1	0.04	93.1	14.5	1.01	1.01	9.81	3.65	44.5	30.3	431	2.21	10.5
AW2	Artemis	Serpentine vein	0.707991	22	21.31	4.32	83.2	0.01	bd	8.08	1.16	1.71	6.39	9.96	199	20.8	235	0.76	9.41
AW3	Artemis	Serpentine vein	nd	-	20.21	4.52	81.7	0.02	13.9	3.78	1.35	3.82	12.3	15.7	1,303	58.1	1,419	2.67	19.4

Sample	Diapiric Domain	Group	$^{87}Sr/^{86}Sr$ (Bulk)	2SE ($1x10^6$)	ICP-OES Mg (wt.%)	ICP-OES Fe (wt.%)	Mg#	ICP-OES Ca (wt.%)	ICP-OES Na (µg/g)	ICP-OES K (µg/g)	ICP-MS Li (µg/g)	ICP-MS Sc (µg/g)	ICP-MS Ti (µg/g)	ICP-MS V (µg/g)	ICP-MS Cr (µg/g)	ICP-MS Co (µg/g)	ICP-MS Ni (µg/g)	ICP-MS Cu (µg/g)	ICP-MS Zn (µg/g)
AY2	Artemis	Serpentine vein	nd	-	21.11	3.45	86.0	0.05	148	12.2	0.39	1.36	5.61	9.56	233	20.9	65.1	1.05	11.2
BA1A	Artemis	Serpentine vein	0.707177	12	20.03	5.09	79.7	1.49	61.5	4.98	1.95	2.97	103	42.9	187	25.8	162	2.21	8.82
CU5	Artemis	Serpentine vein	0.708375	14	21.33	3.55	85.7	0.02	48.9	11.6	1.14	0.04	1.36	9.88	71.9	29.5	151	1.32	13.9

Table 4.8 continued:

Sample	Diapiric Domain	Group	ICP-MS Rb (ng/g)	ICP-MS Sr (ng/g)	ICP-MS Y (ng/g)	ICP-MS Zr (ng/g)	ICP-MS Nb (ng/g)	ICP-MS Sn (ng/g)	ICP-MS Cs (ng/g)	ICP-MS Ba (ng/g)	ICP-MS La (ng/g)	ICP-MS Ce (ng/g)	ICP-MS Pr (ng/g)	ICP-MS Nd (ng/g)	ICP-MS Sm (ng/g)	ICP-MS Eu (ng/g)
AN2	Artemis	Artemis Bulk Rock	72	535	39	37	2	21	332	739	6.47	15.6	1.88	6.70	2.06	bd
AO2	Artemis	Artemis Bulk Rock	520	5,982	720	170	3	20	3,566	39,250	0.93	0.64	0.50	5.62	12.7	6.15
AP2	Artemis	Artemis Bulk Rock	64	1,681	298	129	16	8	8	4,790	137	181	28.2	109	24.1	4.02
AQ2	Artemis	Artemis Bulk Rock	32	2,584	734	88	4	20	56	7,744	8.02	12.0	4.01	12.0	16.0	8.02
AR1	Artemis	Artemis Bulk Rock	21	1,688	411	37	2	22	11	4,239	bd	1.23	0.50	1.79	4.94	bd

			ICP-MS	ICP-MS	ICP-MS	ICP-MS	ICP-MS	ICP-MS	ICP-MS	ICP-MS	ICP-MS	ICP-MS	ICP-MS	ICP-MS	ICP-MS	ICP-MS
Sample	**Diapiric Domain**	**Group**	**Rb (ng/g)**	**Sr (ng/g)**	**Y (ng/g)**	**Zr (ng/g)**	**Nb (ng/g)**	**Sn (ng/g)**	**Cs (ng/g)**	**Ba (ng/g)**	**La (ng/g)**	**Ce (ng/g)**	**Pr (ng/g)**	**Nd (ng/g)**	**Sm (ng/g)**	**Eu (ng/g)**
AR2	Artemis	Artemis Bulk Rock	9	3,331	383	21	bd	9	13	11,781	bd	bd	bd	bd	4.25	bd
BA1C	Artemis	Artemis Bulk Rock	16	1,392	661	94	12	12	4	3,232	15.7	27.5	3.93	19.7	7.86	3.93
CU1	Artemis	Artemis Bulk Rock	27	2,171	368	76	4	67	4	8,313	4.49	13.5	bd	8.97	4.49	bd
PP1	Artemis	Artemis Bulk Rock	20	1,178	2,988	67	bd	12	16	2,810	bd	bd	bd	43.5	87.0	51.4
AA4-2	Artemis	Artemis Bulk Rock Halo	21	997	490	284	4	239	8	5,565	12.4	28.8	4.12	20.6	8.24	8.24
AA4-4	Artemis	Artemis Bulk Rock Halo	22	955	852	587	9	49	9	5,150	40.3	130	13.4	67.2	26.9	13.4
AO3C	Artemis	Artemis Bulk Rock Halo	121	4,325	732	199	22	52	30	16,645	64.9	130	13.0	60.6	21.6	8.66
BA1B	Artemis	Artemis Bulk Rock Halo	25	1,778	679	93	4	42	4	4,909	12.7	17.0	4.24	17.0	12.7	4.24
CU2	Artemis	Artemis Bulk Rock Halo	11	1,957	422	33	4	22	bd	6,673	bd	3.70	bd	bd	3.70	bd
CU4	Artemis	Artemis Bulk Rock Halo	4	1,383	433	54	4	120	bd	2,507	8.92	8.92	bd	4.46	4.46	bd
AX1	Artemis	Chrysotile vein	24	1,738	36	101	8	221	8	978	36.2	68.4	8.05	32.2	4.02	bd
AZ1	Artemis	Chrysotile vein	404	2,167	289	647	96	31	96	7,136	273	558	69.3	269	53.9	11.5
CR1	Artemis	Chrysotile vein	29	470	139	249	7	32	71	819	14.3	32.1	3.56	24.9	10.7	3.56
CR1	Artemis	Chrysotile vein	29	470	139	249	7	32	71	819	14.3	32.1	3.56	24.9	10.7	3.56

			ICP-MS	ICP-MS	ICP-MS	ICP-MS	ICP-MS	ICP-MS	ICP-MS	ICP-MS	ICP-MS	ICP-MS	ICP-MS	ICP-MS	ICP-MS	ICP-MS
Sample	**Diapiric Domain**	**Group**	**Rb (ng/g)**	**Sr (ng/g)**	**Y (ng/g)**	**Zr (ng/g)**	**Nb (ng/g)**	**Sn (ng/g)**	**Cs (ng/g)**	**Ba (ng/g)**	**La (ng/g)**	**Ce (ng/g)**	**Pr (ng/g)**	**Nd (ng/g)**	**Sm (ng/g)**	**Eu (ng/g)**
CU3	Artemis	Chrysotile vein	bd	589	16	32	bd	48	bd	584	bd	bd	bd	bd	bd	bd
DI1	Artemis	Chrysotile vein	660	277	51	55	bd	36	2,761	565	3.65	10.9	bd	3.65	bd	bd
DI1A	Artemis	Chrysotile vein	110	195	51	72	bd	93	589	284	bd	4.2	bd	4.24	bd	bd
DI2	Artemis	Chrysotile vein	439	415	61	82	bd	48	1,342	2,701	3.41	6.81	bd	3.41	3.41	bd
DI3	Artemis	Chrysotile vein	76	415	80	197	22	36	40	1,967	43.7	98.3	10.9	40.1	10.9	3.64
DI5	Artemis	Chrysotile vein	30	506	159	57	bd	14	179	831	3.38	10.1	bd	6.75	6.75	3.38
BM1	Artemis	Cohesive Artemis Fault Rock	8	2,056	99	33	bd	12	4	1,229	bd	4.14	bd	bd	bd	bd
BN1	Artemis	Cohesive Artemis Fault Rock	1,019	55,764	2,901	866	93	24	11,926	29,159	68.5	161	28.2	197.4	133	101
BO1	Artemis	Cohesive Artemis Fault Rock	40	6,088	88	60	bd	36	40	3,046	3.99	3.99	bd	bd	bd	bd
BO2	Artemis	Cohesive Artemis Fault Rock	81	1,085	1,150	565	49	65	4	719	89.4	179	24.4	130	48.7	8.12
BO3	Artemis	Cohesive Artemis Fault Rock	206	28,775	27	101	12	23	171	12,746	23.3	42.7	3.89	15.5	3.89	bd

			ICP-MS	ICP-MS	ICP-MS	ICP-MS	ICP-MS	ICP-MS	ICP-MS	ICP-MS	ICP-MS	ICP-MS	ICP-MS	ICP-MS	ICP-MS	ICP-MS
Sample	**Diapiric Domain**	**Group**	**Rb (ng/g)**	**Sr (ng/g)**	**Y (ng/g)**	**Zr (ng/g)**	**Nb (ng/g)**	**Sn (ng/g)**	**Cs (ng/g)**	**Ba (ng/g)**	**La (ng/g)**	**Ce (ng/g)**	**Pr (ng/g)**	**Nd (ng/g)**	**Sm (ng/g)**	**Eu (ng/g)**
DB1	Artemis	Cohesive Artemis Fault Rock	62	780	550	199	12	47	1,319	3,125	7.80	23.4	3.90	31.2	23.4	11.70
DB2	Artemis	Cohesive Artemis Fault Rock	62	937	251	197	15	12	698	5,960	15.4	34.7	3.85	27.0	11.6	7.71
DE1B	Artemis	Cohesive Artemis Fault Rock	11	1,408	22	50	4	57	40	657	3.59	7.18	bd	3.59	bd	bd
DE2BZ	Artemis	Cohesive Artemis Fault Rock	33	4,954	25	45	bd	8	345	362	bd	bd	bd	bd	bd	bd
AB3	Artemis	Incohesive Artemis Breccia	51	2,658	203	82	8	8	144	2,557	27.3	42.9	7.79	27.3	7.79	bd
AB4	Artemis	Incohesive Artemis Breccia	267	9,606	183	396	46	25	313	2,844	104	188	25.0	95.9	16.7	4.17
AI1	Artemis	Incohesive Artemis Breccia	17	280	112	121	4	52	9	2,756	4.31	8.63	bd	4.31	bd	bd
AK1	Artemis	Incohesive Artemis Breccia	14	174	69	14	9	41	bd	184	18.4	55.1	4.59	23.0	4.59	bd
AN1	Artemis	Incohesive Artemis Breccia	8	172	68	76	bd	68	20	156	bd	bd	bd	bd	bd	bd

			ICP-MS	ICP-MS	ICP-MS	ICP-MS	ICP-MS	ICP-MS	ICP-MS	ICP-MS	ICP-MS	ICP-MS	ICP-MS	ICP-MS	ICP-MS	ICP-MS
Sample	**Diapiric Domain**	**Group**	**Rb (ng/g)**	**Sr (ng/g)**	**Y (ng/g)**	**Zr (ng/g)**	**Nb (ng/g)**	**Sn (ng/g)**	**Cs (ng/g)**	**Ba (ng/g)**	**La (ng/g)**	**Ce (ng/g)**	**Pr (ng/g)**	**Nd (ng/g)**	**Sm (ng/g)**	**Eu (ng/g)**
AN3	Artemis	Incohesive Artemis Breccia	33	595	62	25	bd	17	99	685	bd	bd	bd	bd	bd	bd
AS2	Artemis	Incohesive Artemis Breccia	4	258	67	21	4	17	67	463	bd	bd	bd	bd	bd	bd
AS3	Artemis	Incohesive Artemis Breccia	16	417	199	43	bd	4	86	4,210	bd	bd	bd	bd	bd	bd
AU1	Artemis	Incohesive Artemis Breccia	8	455	89	109	bd	4	12	8,154	bd	bd	bd	bd	bd	bd
BZ1	Artemis	Incohesive Artemis Breccia	4	742	44	99	bd	60	4	12,866	bd	bd	bd	bd	bd	bd
BZ2	Artemis	Incohesive Artemis Breccia	8	450	57	49	4	41	4	10,108	8.18	12.3	bd	4.09	bd	bd
DC2H	Artemis	Incohesive Artemis Breccia	4	98	132	45	bd	34	11	64	bd	bd	bd	bd	bd	bd
DH1V	Artemis	Incohesive Artemis Breccia	4	158	161	81	bd	15	11	209	bd	bd	bd	3.67	3.67	7.33
AA3	Artemis	Serpentine vein	13	420	115	331	13	30	4	1,243	17.0	21.2	4.24	21.2	4.24	4.24
AA4-1	Artemis	Serpentine vein	8	458	113	44	bd	64	12	2,978	24.1	48.2	8.04	36.2	12.1	4.02

Sample	Diapiric Domain	Group	ICP-MS Rb (ng/g)	ICP-MS Sr (ng/g)	ICP-MS Y (ng/g)	ICP-MS Zr (ng/g)	ICP-MS Nb (ng/g)	ICP-MS Sn (ng/g)	ICP-MS Cs (ng/g)	ICP-MS Ba (ng/g)	ICP-MS La (ng/g)	ICP-MS Ce (ng/g)	ICP-MS Pr (ng/g)	ICP-MS Nd (ng/g)	ICP-MS Sm (ng/g)	ICP-MS Eu (ng/g)
AA4X	Artemis	Serpentine vein	19	465	202	111	8	2,515	4	453	57.2	137	26.7	114	34.3	7.62
AA4Y	Artemis	Serpentine vein	124	578	149	322	45	211	25	1,383	86.7	194	24.8	86.7	20.6	4.13
AN4	Artemis	Serpentine vein	53	1,640	38	113	11	238	94	1,602	34.0	71.8	7.56	30.2	7.56	bd
AN5	Artemis	Serpentine vein	20	346	130	106	8	63	12	453	19.7	51.2	7.87	31.5	7.87	3.93
AP1	Artemis	Serpentine vein	32	673	24	105	bd	20	8	467	28.4	8.1	4.06	12.2	4.06	bd
AW2	Artemis	Serpentine vein	29	351	25	83	12	347	4	194	12.4	24.8	4.13	8.26	bd	bd
AW3	Artemis	Serpentine vein	13	561	56	26	4	51	4	514	4.28	8.57	bd	4.28	bd	bd
AY2	Artemis	Serpentine vein	38	492	83	108	8	188	4	375	45.8	100	12.5	66.7	16.7	4.17
BA1A	Artemis	Serpentine vein	9	712	452	58	4	116	bd	1,232	22.4	53.7	4.48	22.4	8.96	4.48
CU5	Artemis	Serpentine vein	21	993	160	42	4	21	13	770	109	46.3	33.6	126	25.2	4.21

Table 4.8 continued:

Sample	Diapiric Domain	Group	ICP-MS Gd (ng/g)	ICP-MS Tb (ng/g)	ICP-MS Dy (ng/g)	ICP-MS Ho (ng/g)	ICP-MS Er (ng/g)	ICP-MS Tm (ng/g)	ICP-MS Yb (ng/g)	ICP-MS Lu (ng/g)	ICP-MS Hf (ng/g)	ICP-MS Ta (ng/g)	ICP-MS Pb (ng/g)	ICP-MS Th (ng/g)	ICP-MS U (ng/g)	Sr/Ca
AN2	Artemis	Artemis Bulk Rock	4.23	0.77	7.66	2.64	11.0	2.40	25.1	4.82	1.56	9.87	45.2	0.30	0.20	0.30
AO2	Artemis	Artemis Bulk Rock	51.0	12.6	108	29.8	98.6	16.6	127	19.8	9.26	7.97	107	0.53	0.37	0.48
AP2	Artemis	Artemis Bulk Rock	32.2	8.04	44.2	12.1	36.2	4.02	40.2	8.04	4.02	4.02	96.5	12.1	12.1	1.62
AQ2	Artemis	Artemis Bulk Rock	48.1	12.0	104	28.1	96.3	16.0	124	20.1	8.02	4.01	bd	4.01	bd	0.26
AR1	Artemis	Artemis Bulk Rock	23.8	6.53	58.1	17.4	61.8	11.4	85.9	15.8	3.18	31.6	6.49	0.32	0.49	0.96
AR2	Artemis	Artemis Bulk Rock	12.8	4.25	46.8	12.8	55.3	12.8	85.1	17.0	bd	bd	bd	bd	bd	2.69
BA1C	Artemis	Artemis Bulk Rock	43.3	11.8	98.3	27.5	86.5	15.7	98.3	15.7	3.93	3.93	bd	3.93	bd	0.11
CU1	Artemis	Artemis Bulk Rock	13.5	4.49	44.9	13.5	49.3	8.97	76.3	13.5	4.49	4.49	8.97	4.49	bd	0.72
PP1	Artemis	Artemis Bulk Rock	292	71.1	526	119	348	51.4	336	51.4	23.7	19.8	bd	bd	bd	0.06
AA4-2	Artemis	Artemis Bulk Rock Halo	24.7	8.24	61.8	16.5	61.8	12.4	82.4	12.4	12.4	20.6	57.7	4.12	4.12	0.05
AA4-4	Artemis	Artemis Bulk Rock Halo	58.3	13.4	117	26.9	103	17.9	139	22.4	26.9	4.48	628	8.97	8.97	0.03
AO3C	Artemis	Artemis Bulk Rock Halo	47.6	13.0	104	26.0	90.9	17.3	113	21.6	13.0	4.33	99.6	13.0	64.9	0.53
BA1B	Artemis	Artemis Bulk Rock Halo	46.7	12.7	97.6	25.5	89.1	12.7	102	17.0	4.24	bd	17.0	4.24	4.24	0.12

Sample	Diapiric Domain	Group	ICP-MS Gd (ng/g)	ICP-MS Tb (ng/g)	ICP-MS Dy (ng/g)	ICP-MS Ho (ng/g)	ICP-MS Er (ng/g)	ICP-MS Tm (ng/g)	ICP-MS Yb (ng/g)	ICP-MS Lu (ng/g)	ICP-MS Hf (ng/g)	ICP-MS Ta (ng/g)	ICP-MS Pb (ng/g)	ICP-MS Th (ng/g)	ICP-MS U (ng/g)	Sr/ Ca
CU2	Artemis	Artemis Bulk Rock Halo	14.8	3.70	55.5	14.8	59.2	11.1	85.1	14.8	3.70	7.40	9.00	bd	bd	0.21
CU4	Artemis	Artemis Bulk Rock Halo	17.8	4.46	58.0	17.8	62.4	13.4	84.8	13.4	4.46	4.46	bd	4.46	bd	0.06
AX1	Artemis	Chrysotile vein	4.02	bd	4.02	bd	4.02	bd	4.02	bd	4.02	12.1	96.6	4.02	bd	-
AZ1	Artemis	Chrysotile vein	50.0	7.70	46.2	7.70	23.1	3.85	23.1	3.85	15.4	15.4	512	53.9	42.3	4.26
CR1	Artemis	Chrysotile vein	17.8	3.56	21.4	3.56	14.3	3.56	14.3	3.56	10.7	17.8	67.7	3.56	3.56	1.11
CR1	Artemis	Chrysotile vein	17.8	3.56	21.4	3.56	14.3	3.56	14.3	3.56	10.7	17.8	67.7	3.56	3.56	1.11
CU3	Artemis	Chrysotile vein	bd	bd	bd	bd	bd	bd	5.31	bd	bd	5.31	10.6	bd	bd	0.85
DI1	Artemis	Chrysotile vein	3.65	bd	7.30	bd	7.30	bd	10.9	3.65	3.65	7.30	14.6	bd	bd	1.47
DI1A	Artemis	Chrysotile vein	bd	bd	4.24	bd	4.24	bd	8.47	bd	4.24	4.24	bd	bd	bd	-
DI2	Artemis	Chrysotile vein	3.41	bd	6.81	3.41	6.81	bd	10.2	3.41	3.41	6.81	17.03	bd	bd	0.59
DI3	Artemis	Chrysotile vein	10.9	3.64	10.9	3.64	10.9	3.64	18.2	3.64	7.29	7.29	127.5	10.9	3.64	0.43
DI5	Artemis	Chrysotile vein	20.3	3.38	23.6	6.75	16.9	3.38	16.9	3.38	3.38	6.75	10.1	3.38	bd	1.17
BM1	Artemis	Cohesive Artemis Fault Rock	4.14	bd	12.4	4.14	16.5	4.14	29.0	4.14	bd	4.14	4.14	bd	bd	0.27

Sample	Diapiric Domain	Group	ICP-MS Gd (ng/g)	ICP-MS Tb (ng/g)	ICP-MS Dy (ng/g)	ICP-MS Ho (ng/g)	ICP-MS Er (ng/g)	ICP-MS Tm (ng/g)	ICP-MS Yb (ng/g)	ICP-MS Lu (ng/g)	ICP-MS Hf (ng/g)	ICP-MS Ta (ng/g)	ICP-MS Pb (ng/g)	ICP-MS Th (ng/g)	ICP-MS U (ng/g)	Sr/ Ca
BN1	Artemis	Cohesive Artemis Fault Rock	278	60.4	467	113	347	56.4	395	60.4	52.4	12.1	101	12.1	8.06	0.72
BO1	Artemis	Cohesive Artemis Fault Rock	3.99	bd	12.0	3.99	12.0	3.99	27.9	3.99	3.99	16.0	24.0	bd	bd	0.08
BO2	Artemis	Cohesive Artemis Fault Rock	89.4	16.2	138	36.6	110	16.2	102	16.2	20.3	12.2	191	12.2	12.2	3.42
BO3	Artemis	Cohesive Artemis Fault Rock	3.89	bd	3.89	bd	3.89	bd	3.89	bd	3.89	bd	101	7.77	3.89	0.34
DB1	Artemis	Cohesive Artemis Fault Rock	50.7	11.7	89.7	23.4	70.2	11.7	78.0	11.7	11.7	7.80	11.7	3.90	bd	0.35
DB2	Artemis	Cohesive Artemis Fault Rock	27.0	3.85	34.7	7.71	30.8	3.85	38.5	7.71	7.71	23.1	19.3	3.85	3.85	0.50
DE1B	Artemis	Cohesive Artemis Fault Rock	3.59	bd	3.59	bd	3.59	bd	7.18	bd	3.59	14.4	14.4	bd	bd	0.11
DE2BZ	Artemis	Cohesive Artemis Fault Rock	bd	bd	4.11	bd	4.11	bd	8.22	bd	bd	8.22	bd	bd	bd	0.06
AB3	Artemis	Incohesive Artemis Breccia	11.7	3.90	27.3	7.79	27.3	3.90	39.0	7.79	3.90	35.1	42.9	3.90	bd	3.01

Sample	Diapiric Domain	Group	ICP-MS Gd (ng/g)	ICP-MS Tb (ng/g)	ICP-MS Dy (ng/g)	ICP-MS Ho (ng/g)	ICP-MS Er (ng/g)	ICP-MS Tm (ng/g)	ICP-MS Yb (ng/g)	ICP-MS Lu (ng/g)	ICP-MS Hf (ng/g)	ICP-MS Ta (ng/g)	ICP-MS Pb (ng/g)	ICP-MS Th (ng/g)	ICP-MS U (ng/g)	Sr/Ca
AB4	Artemis	Incohesive Artemis Breccia	20.8	4.17	29.2	8.34	20.8	4.17	25.0	4.17	12.5	8.34	638	20.8	8.34	1.48
AI1	Artemis	Incohesive Artemis Breccia	4.31	bd	17.3	4.31	17.3	4.31	30.2	4.31	4.31	8.63	21.6	bd	bd	-
AK1	Artemis	Incohesive Artemis Breccia	4.59	bd	9.18	4.59	9.18	4.59	18.4	4.59	bd	4.59	4.59	bd	bd	0.06
AN1	Artemis	Incohesive Artemis Breccia	bd	bd	8.00	4.00	8.00	4.00	24.0	4.00	4.00	8.00	8.00	bd	bd	0.01
AN3	Artemis	Incohesive Artemis Breccia	bd	bd	8.26	4.13	8.26	4.13	20.6	4.13	bd	4.13	bd	bd	bd	0.10
AS2	Artemis	Incohesive Artemis Breccia	bd	bd	8.34	4.17	8.34	4.17	20.8	4.17	bd	4.17	bd	bd	bd	0.07
AS3	Artemis	Incohesive Artemis Breccia	3.89	3.89	27.3	7.79	35.1	7.79	58.4	7.79	bd	3.89	3.89	bd	bd	0.08
AU1	Artemis	Incohesive Artemis Breccia	bd	bd	7.78	3.89	15.6	3.89	38.9	7.78	3.89	7.78	bd	bd	bd	0.55
BZ1	Artemis	Incohesive Artemis Breccia	bd	bd	3.97	bd	7.94	bd	15.9	3.97	3.97	7.94	bd	bd	bd	1.66

Sample	Diapiric Domain	Group	ICP-MS Gd (ng/g)	ICP-MS Tb (ng/g)	ICP-MS Dy (ng/g)	ICP-MS Ho (ng/g)	ICP-MS Er (ng/g)	ICP-MS Tm (ng/g)	ICP-MS Yb (ng/g)	ICP-MS Lu (ng/g)	ICP-MS Hf (ng/g)	ICP-MS Ta (ng/g)	ICP-MS Pb (ng/g)	ICP-MS Th (ng/g)	ICP-MS U (ng/g)	Sr/Ca
BZ2	Artemis	Incohesive Artemis Breccia	4.09	bd	8.18	bd	8.18	bd	16.4	4.09	bd	4.09	32.7	bd	bd	0.35
DC2H	Artemis	Incohesive Artemis Breccia	3.77	bd	11.3	3.77	22.6	3.77	41.5	7.54	3.77	7.54	3.77	bd	bd	0.00
DH1V	Artemis	Incohesive Artemis Breccia	11.0	3.67	25.7	7.33	22.0	3.67	25.7	3.67	7.33	11.0	bd	bd	bd	0.00
AA3	Artemis	Serpentine vein	8.49	bd	8.49	4.24	8.49	4.24	21.2	4.24	8.49	4.24	38.2	4.24	8.49	0.06
AA4-1	Artemis	Serpentine vein	12.1	4.02	16.1	4.02	12.1	bd	16.1	4.02	bd	60.3	358	4.02	bd	0.15
AA4X	Artemis	Serpentine vein	34.3	7.62	34.3	7.62	19.1	3.81	19.1	3.81	3.81	7.62	1,082	19.1	7.62	1.62
AA4Y	Artemis	Serpentine vein	20.6	4.13	24.8	4.13	16.5	4.13	20.6	4.13	8.26	12.4	314	24.8	8.26	0.95
AN4	Artemis	Serpentine vein	7.56	bd	7.56	bd	3.78	bd	3.78	bd	3.78	3.78	351	7.56	3.78	1.08
AN5	Artemis	Serpentine vein	7.87	bd	15.7	3.93	15.7	3.93	31.5	7.87	3.93	3.93	897	11.8	11.8	0.02
AP1	Artemis	Serpentine vein	bd	bd	4.06	bd	bd	bd	4.06	bd	4.06	8.11	28.4	bd	bd	1.85
AW2	Artemis	Serpentine vein	bd	bd	4.13	bd	4.13	bd	4.13	bd	4.13	24.8	8.26	4.13	bd	3.63
AW3	Artemis	Serpentine vein	4.28	bd	8.57	4.28	8.57	bd	12.9	4.28	bd	bd	bd	bd	bd	2.90

Sample	Diapiric Domain	Group	ICP-MS Gd (ng/g)	ICP-MS Tb (ng/g)	ICP-MS Dy (ng/g)	ICP-MS Ho (ng/g)	ICP-MS Er (ng/g)	ICP-MS Tm (ng/g)	ICP-MS Yb (ng/g)	ICP-MS Lu (ng/g)	ICP-MS Hf (ng/g)	ICP-MS Ta (ng/g)	ICP-MS Pb (ng/g)	ICP-MS Th (ng/g)	ICP-MS U (ng/g)	Sr/ Ca
AY2	Artemis	Serpentine vein	16.7	4.17	16.7	4.17	8.33	bd	8.33	bd	4.17	12.5	575	8.33	4.17	1.00
BA1A	Artemis	Serpentine vein	22.4	4.48	53.7	13.4	49.3	8.96	85.1	13.4	4.48	4.48	13.4	4.48	bd	0.05
CU5	Artemis	Serpentine vein	29.4	4.21	21.0	4.21	12.6	bd	8.41	bd	bd	bd	bd	4.21	8.41	4.01

Table 4.9: 10 % Acetic Leachates

Sample	Diapiric Domain	Group	Leaching Step	$^{87}Sr/^{86}Sr$	2SE (1x 10^6)	Na (µg/g)	Mg (µg/g)	Al (µg/g)	Si (µg/g)	K (µg/g)	Ca (µg/g)	Cr (µg/g)	Mn (µg/g)	Fe (µg/g)	Li (ng/g)	B (ng/g)	Rb (ng/g)	Sr (ng/g)	Cs (ng/g)	Ba (ng/g)	Pb (ng/g)	Mg/Ca	Sr/Ca (ng/g /ug/g)
AR2L	Artemis	Artemis Bulk Rock	10% Acetic Acid Leachate	0.705642	13	2.40	12638	2.93	168	0.25	457	395	49.3	189	37.1	6344	0.20	1036	0.13	2025	0.03	27.6	2.3
AQ2L	Artemis	Artemis Bulk Rock	10% Acetic Acid Leachate	0.708767	12	6.68	8122	1.76	134	1.93	193	37.3	63.0	292	83.0	1842	2.64	910	0.19	1205	0.04	42.1	4.7
AP2L	Artemis	Artemis Bulk Rock	10% Acetic Acid Leachate	0.708705	12	6.40	5682	1.44	143	2.63	194	52.1	54.5	164	29.9	762	4.63	679	0.04	932	1.07	29.2	3.5
AO2L	Artemis	Artemis Bulk Rock	10% Acetic Acid Leachate	0.705302	13	7.71	16332	2.22	224	4.04	496	32.5	141	2549	280	15961	124	1210	227	2209	2.15	33.0	2.4
PP1L	Artemis	Artemis Bulk Rock	10% Acetic Acid Leachate	0.708737	12	8.71	4893	5.23	141	2.11	117	49.0	55.9	98.6	49.7	856	2.51	379	0.12	439	0.04	41.8	3.2
CU1L	Artemis	Artemis Bulk Rock	10% Acetic Acid Leachate	0.708607	11	5.17	5645	7.69	252	1.93	231	41.9	20.5	117	19.2	1727	1.63	789	bd	915	0.85	24.4	3.4
AR1L	Artemis	Artemis Bulk Rock	10% Acetic Acid Leachate	0.708601	13	9.86	11100	2.22	195	2.57	144	65.4	100	173	84.9	2121	2.01	577	0.12	849	0.18	77.2	4.0

Sample	Diapiric Domain	Group	Leaching Step	$^{87}Sr/^{86}Sr$	2SE (1x 10^6)	Na (µg/g)	Mg (µg/g)	Al (µg/g)	Si (µg/g)	K (µg/g)	Ca (µg/g)	Cr (µg/g)	Mn (µg/g)	Fe (µg/g)	Li (ng/g)	B (ng/g)	Rb (ng/g)	Sr (ng/g)	Cs (ng/g)	Ba (ng/g)	Pb (ng/g)	Mg/Ca	Sr/Ca (ng/g /ug/g)
AO3CL	Artemis	Artemis Bulk Rock Halo	10% Acetic Acid Leachate	0.708852	13	22.2	5780	131	989	4.38	523	22.6	69.7	674	501	29441	10.3	2531	0.9	3049	6.58	11.1	4.8
CU2L	Artemis	Artemis Bulk Rock Halo	10% Acetic Acid Leachate	0.708636	13	6.19	5690	8.23	286	1.95	206	32.1	19.5	78.2	25.2	2546	1.64	764	0.08	920	277	27.6	3.7
BA1BL	Artemis	Artemis Bulk Rock Halo	10% Acetic Acid Leachate	nd	-	4.98	5305	76	1081	0.33	146	33.9	31.0	267	56.8	5671	1.91	498	0.38	794	1.52	36.2	3.4
CU4L	Artemis	Artemis Bulk Rock Halo	10% Acetic Acid Leachate	0.708716	14	3.74	5154	18.5	394	0.92	171	31.0	39.3	126	22.7	1982	1.05	539	bd	405	0.75	30.2	3.2
CU5L	Artemis	Serpentine vein	10% Acetic Acid Leachate	0.708621	13	4.70	3024	70.1	578	3.94	250	6.47	7.39	424	21.4	1434	2.76	608	bd	356	0.69	12.1	2.4
BA1AL	Artemis	Serpentine vein	10% Acetic Acid Leachate	0.708852	13	2.40	1266	33.5	203	0.71	78.1	3.12	22.2	81.2	15.3	654	1.45	213	0.19	169	4.06	16.2	2.7
DE2BZL	Artemis	Cohesive Artemis Fault Rock	10% Acetic Acid Leachate	0.705848	13	80.5	4423	35.3	661	7.61	91345	0.62	51.6	154	2250	33254	21.8	3541	103	149	1.67	0.05	0.0
BO1L	Artemis	Cohesive Artemis Fault Rock	10% Acetic Acid Leachate	0.705663	11	995	98167	7.72	376	52.9	19334	22.3	24.2	136	8464	101460	95.8	3671	84.4	1684	15.0	5.08	0.2

Sample	*Diapiric Domain*	*Group*	*Leaching Step*	*$^{87}Sr/^{86}Sr$*	*2SE (1x 10^6)*	*Na (µg/g)*	*Mg (µg/g)*	*Al (µg/g)*	*Si (µg/g)*	*K (µg/g)*	*Ca (µg/g)*	*Cr (µg/g)*	*Mn (µg/g)*	*Fe (µg/g)*	*Li (ng/g)*	*B (ng/g)*	*Rb (ng/g)*	*Sr (ng/g)*	*Cs (ng/g)*	*Ba (ng/g)*	*Pb (ng/g)*	*Mg/Ca*	*Sr/Ca (ng/g /ug/ g)*
BN1L	Artemis	Cohesive Artemis Fault Rock	10% Acetic Acid Leachate	0.707031	12	376	2984	2573	2005	46.3	14628	1.74	17.0	51.3	1408	5084	61.5	13170	357	5783	2.54	0.20	0.9
BO3L	Artemis	Cohesive Artemis Fault Rock	10% Acetic Acid Leachate	0.705640	13	3519	54934	13.2	650	141	73937	28.8	36.2	300	29818	101985	252	29621	220	11596	41.2	0.74	0.4
BM1L	Artemis	Cohesive Artemis Fault Rock	10% Acetic Acid Leachate	0.707985	13	11.4	12478	152	725	1.90	617	100	208	2930	256	9315	3.05	794	1.39	467	2.77	20.2	1.3

Table 4.10: 3M HCl Table.

Sample	AO2	AP2	AQ2	AR1	AR2	CU1	PP1	AO3C	BA1B	CU2	CU4	BM1	BN1	BO1	BO3	DE2BZ	BA1A	CU5
Location	Artemis	Artemis	Artemis	Artemis	Artemis	Artemis	Artemis	Artemis	Artemis	Artemis	Artemis	Artemis	Artemis	Artemis	Artemis	Artemis	Artemis	Artemis
Group	Artemis Bulk Rock	Artemis Bulk Rock	Artemis Bulk Rock	Artemis Bulk Rock	Artemis Bulk Rock	Artemis Bulk Rock	Artemis Bulk Rock	Artemis Bulk Rock Halo	Artemis Bulk Rock Halo	Artemis Bulk Rock Halo	Artemis Bulk Rock Halo	Cohesive Artemis Fault Rock	Cohesive Artemis Fault Rock	Cohesive Artemis Fault Rock	Cohesive Artemis Fault Rock	Cohesive Artemis Fault Rock	Serpentine vein	Serpentine vein
Leaching Step	3M HCl Leachate	3M HCl Leachate	3M HCl Leachate	3M HCl Leachate	3M HCl Leachate	3M HCl Leachate	3M HCl Leachate	3M HCl Leachate	3M HCl Leachate	3M HCl Leachate	3M HCl Leachate	3M HCl Leachate	3M HCl Leachate	3M HCl Leachate	3M HCl Leachate	3M HCl Leachate	3M HCl Leachate	3M HCl Leachate
$^{87}Sr/^{86}Sr$	0.705299	0.708555	0.708507	0.707922	0.705650	0.707268	0.708310	0.707988	0.706053	0.707302	0.706744	0.706534	0.706311	0.705660	0.705661	0.705713	0.706963	0.707353
2SE ($1x10^6$)	12	13	11	13	13	13	12	14	11	14	12	12	12	11	12	14	13	34
Mg (µg/g)	71418	39969	44325	76667	43941	102813	41680	197367	164526	89724	131365	151787	44738	206987	146170	94129	65985	156420
Ca (µg/g)	883	102	228	122	306	163	561	372	298	160	360	4050	9258	32514	7066	4702	636	bd
Sc (µg/g)	1.81	0.45	1.46	1.04	0.44	1.62	0.99	7.99	1.42	1.00	1.43	6.52	4.58	1.57	0.75	1.45	0.33	0.26
Ti (µg/g)	0.25	0.02	0.16	0.19	0.09	0.99	0.16	38.3	3.41	0.55	1.69	14.1	12.6	1.78	3.75	0.92	0.92	0.34
V (µg/g)	5.20	1.05	0.94	3.16	0.73	10.5	7.64	39.1	14.0	6.95	10.1	18.8	21.2	6.15	7.09	3.04	4.93	7.14
Cr (µg/g)	249	353	233	348	457	778	411	1313	1002	546	740	414	68.9	635	517	22.6	41.9	50.5
Mn (µg/g)	292	183	210	289	226	462	212	763	473	428	419	338	101	246	212	307	172	217
Fe (µg/g)	11716	3136	5552	9381	2093	15572	4996	49587	29327	12041	19511	28927	8589	20751	17837	19064	12216	22993

Sample	AO2	AP2	AQ2	AR1	AR2	CU1	PP1	AO3C	BA1B	CU2	CU4	BM1	BN1	BO1	BO3	DE2BZ	BA1A	CU5
Co (µg/g)	52.8	50.1	39.8	52.0	35.8	94.3	23.8	81.2	80.9	90.0	81.4	45.5	7.48	35.6	21.9	49.2	9.87	18.1
Ni (µg/g)	1116	670	590	929	643	1238	527	1845	1624	1119	1555	467	22.8	725	443	702	78.2	115
Cu (µg/g)	8.85	6.32	4.08	4.69	0.74	10.1	13.6	12.9	17.9	9.25	10.6	2.20	61.8	8.85	4.55	0.44	1.61	1.05
Zn (µg/g)	12.4	6.26	5.46	8.29	9.77	21.9	5.50	bd	0.06	18.8	23.4	4.32	13.2	bd	bd	7.17	0.70	bd
Li (ng/g)	1152	241	620	1002	250	854	766	3310	1598	577	919	489	111151	9199	6043	9528	617	621
Rb (ng/g)	242	13.7	8.27	9.11	5.75	11.4	11.5	37.4	7.54	6.34	10.1	1.60	492	20.8	35.2	13.1	bd	bd
Sr (ng/g)	2987	502	878	495	992	757	310	1466	613	638	474	283	19208	7242	3261	1004	141	119
Y (ng/g)	111	89.2	89.9	129	158	131	94.8	294	7.54	41.0	5.07	57.5	170	8.68	7.82	18.9	13.9	78.0
Zr (ng/g)	2.42	0.78	0.55	0.87	0.27	1.20	0.27	18.7	7.54	0.49	4.22	1.60	17.5	1.74	25.4	1.64	0.53	4.87
Nb (ng/g)	bd	0.26	bd	bd	0.27	0.60	0.27	bd	bd	0.49	0.84	bd	bd	bd	13.7	1.64	bd	bd
Cs (ng/g)	1752	0.26	8.55	3.47	1.09	1.20	3.20	18.7	2.51	0.49	0.84	1.60	7504	27.8	45.0	224	1.07	4.87
Ba (ng/g)	12776	1329	2095	1391	2944	3323	952	11206	1716	2542	1007	195	19855	2906	1236	153	283	110
La (ng/g)	0.81	63.3	2.21	bd	bd	1.80	bd	18.7	bd	bd	bd	bd	13.5	3.47	3.91	bd	1.60	53.6
Ce (ng/g)	1.21	84.3	3.31	0.43	bd	4.19	0.27	32.7	bd	bd	bd	bd	24.3	5.21	11.7	1.64	0.53	19.5
Pr (ng/g)	bd	12.4	0.55	bd	bd	0.60	0.27	4.67	bd	bd	bd	bd	4.04	bd	1.96	bd	0.53	17.1

Sample	AO2	AP2	AQ2	AR1	AR2	CU1	PP1	AO3C	BA1B	CU2	CU4	BM1	BN1	BO1	BO3	DE2BZ	BA1A	CU5
Nd (ng/g)	0.81	49.0	2.76	0.43	0.27	1.20	5.87	23.3	bd	bd	bd	bd	17.5	1.74	5.87	1.64	1.07	63.3
Sm (ng/g)	0.81	8.56	1.38	1.30	0.82	1.20	5.07	4.67	bd	0.49	bd	bd	6.74	bd	1.96	0.82	0.53	14.6
Eu (ng/g)	0.40	2.07	0.55	bd	0.55	0.60	2.67	bd	bd	bd	bd	bd	12.13	bd	bd	bd	bd	2.44
Gd (ng/g)	4.03	11.4	3.86	7.38	4.92	6.59	11.7	14.0	bd	2.44	bd	1.60	13.5	bd	1.96	1.64	1.07	12.2
Tb (ng/g)	1.21	1.82	1.10	1.74	1.64	1.80	1.87	4.67	bd	0.49	bd	bd	2.70	bd	bd	bd	bd	2.44
Dy (ng/g)	12.5	11.9	10.2	16.9	17.0	14.4	13.1	32.7	bd	3.90	0.84	6.39	22.9	bd	1.96	2.46	1.60	12.2
Ho (ng/g)	4.03	2.85	3.03	4.77	5.20	4.19	2.94	9.34	bd	0.98	bd	1.60	5.39	bd	bd	0.82	0.53	2.44
Er (ng/g)	15.7	8.30	12.1	16.5	19.7	15.0	8.81	42.0	bd	3.90	0.84	7.98	21.6	1.74	bd	2.46	1.60	7.31
Tm (ng/g)	3.22	1.30	2.48	3.04	3.83	3.00	1.34	9.34	bd	0.98	bd	1.60	4.04	bd	bd	0.82	bd	bd
Yb (ng/g)	28.2	9.60	22.6	24.7	32.3	24.0	10.4	70.0	2.51	7.81	0.84	14.4	28.3	1.74	1.96	4.92	2.13	4.87
Lu (ng/g)	5.24	1.56	4.13	5.21	6.02	5.39	2.14	14.0	bd	1.95	bd	3.19	5.39	bd	bd	0.82	0.53	bd
Pb (ng/g)	36.3	50.3	3.03	4.77	1.92	9.59	0.53	65.4	bd	bd	2.53	3.19	64.7	29.5	25.4	1.64	17.1	bd
Th (ng/g)	bd	1.04	0.28	bd	bd	0.60	bd	4.67	bd	bd	bd	bd	2.70	1.74	1.96	bd	bd	bd
U (ng/g)	bd	3.37	0.28	bd	bd	bd	bd	28.0	bd	bd	bd	bd	bd	bd	bd	bd	0.53	2.44

Table 4.11: Bulk Rock Residue.

Sample	*AR2*	*AP2*	*AO2*	*AR1*	*CU1*	*AQ2*	*PP1*	*BA1B*	*CU2*	*CU4*	*CU5*	*BA1A*
Diapiric Domain	Artemis	Artemis	Artemis	Artemis	Artemis	Artemis	Artemis	Artemis	Artemis	Artemis	Artemis	Artemis
Sample Type	Artemis Bulk Rock	Artemis Bulk Rock	Artemis Bulk Rock	Artemis Bulk Rock	Artemis Bulk Rock	Artemis Bulk Rock	Artemis Bulk Rock	Artemis Bulk Rock Halo	Artemis Bulk Rock Halo	Artemis Bulk Rock Halo	Serpentine vein	Serpentine vein
Leaching Step	Residue HF + HNO_3 Digest	Residue HF + HNO_3 Digest	Residue HF + HNO_3 Digest	Residue HF + HNO_3 Digest	Residue HF + HNO_3 Digest	Residue HF + HNO_3 Digest	Residue HF + HNO_3 Digest	Residue HF + HNO_3 Digest	Residue HF + HNO_3 Digest	Residue HF + HNO_3 Digest	Residue HF + HNO_3 Digest	Residue HF + HNO_3 Digest
$^{87}Sr/^{86}Sr$	0.705492	0.708026	0.705280	0.706223	0.706006	0.707245	0.706308	0.705889	0.705821	0.705642	0.708347	0.705656
2SE ($1x10^6$)	26	16	25	35	14	15	15	65	25	20	952	76
Li (µg/g)	2.07	1.37	4.24	3.61	1.36	2.98	4.32	1.50	1.42	0.87	0.06	1.04
Sc (µg/g)	8.98	7.18	9.51	9.31	10.2	8.39	29.7	3.97	10.7	11.4	0.004	10.5
Ti (µg/g)	86.0	83.6	135	93.6	86.6	122	460	121	94.1	90.0	0.62	62.8
V (µg/g)	39.6	26.6	48.0	36.0	34.6	42.6	161	46.2	43.9	39.1	5.27	20.7
Cr (µg/g)	3295	2300	2570	2838	2116	2438	3658	158	2645	2868	5.73	2630
Co (µg/g)	66.5	56.3	44.2	42.6	27.4	50.4	25.8	20.3	28.2	21.3	14.8	10.5
Ni (µg/g)	1284	1596	763	1073	829	1196	641	52.9	996	699	7.96	515
Cu (µg/g)	7.75	16.6	6.81	4.04	5.56	8.27	14.4	0.35	5.72	2.30	bd	0.65

Sample	AR2	AP2	AO2	AR1	CU1	AQ2	PP1	BA1B	CU2	CU4	CU5	BA1A
Zn (µg/g)	58.7	22.5	30.7	32.0	34.5	33.0	13.2	10.0	34.3	28.4	7.81	21.1
Rb (ng/g)	5.97	52.5	229	9.67	9.36	16.7	11.2	bd	bd	bd	2.06	bd
Sr (ng/g)	1308	522	2558	507	665	852	465	348	689	536	158	407
Y (ng/g)	203	185	749	288	298	657	3182	634	488	532	2.06	872
Zr (ng/g)	21.9	130	31.0	32.9	46.8	63.3	57.6	70.8	23.5	18.5	30.8	56.1
Nb (ng/g)	1.99	16.3	1.94	1.93	3.74	5.58	1.86	5.67	1.81	1.85	2.06	bd
Sn (ng/g)	7.96	32.6	23.2	17.4	28.1	16.7	24.2	42.5	30.8	13.0	20.6	12.0
Cs (ng/g)	10	5.43	1913	7.74	1.87	42.8	11.2	bd	1.81	bd	6.17	2.00
Ba (ng/g)	5741	2078	26375	2196	3412	4055	1237	790	3014	2033	67.9	1307
La (ng/g)	bd	54.3	bd	bd	1.87	5.58	bd	2.83	bd	bd	2.06	bd
Ce (ng/g)	bd	70.6	bd	bd	1.87	7.44	bd	2.83	bd	bd	bd	bd
Pr (ng/g)	bd	10.9	bd	bd	bd	1.86	1.86	bd	bd	bd	bd	bd
Nd (ng/g)	bd	43.5	5.81	bd	bd	7.44	40.9	2.83	bd	bd	2.06	4.01
Sm (ng/g)	1.99	9.06	15.5	1.93	1.87	13.0	96.7	8.50	3.62	3.71	bd	14.0
Eu (ng/g)	bd	1.81	7.75	bd	bd	5.58	52.1	5.67	1.81	1.85	bd	6.01
Gd (ng/g)	9.95	18.1	52.3	9.67	7.49	42.8	312	31.2	16.3	20.4	bd	52.1
Tb (ng/g)	1.99	3.62	13.6	3.87	3.74	11.2	74.4	8.50	5.43	7.42	bd	14.0

Sample	AR2	AP2	AO2	AR1	CU1	AQ2	PP1	BA1B	CU2	CU4	CU5	BA1A
Dy (ng/g)	27.9	30.8	112	40.6	41.2	98.6	558	76.5	63.3	68.6	bd	126
Ho (ng/g)	7.96	7.25	29.0	11.6	13.1	26.1	126	19.8	18.1	20.4	bd	34.1
Er (ng/g)	31.9	23.5	96.8	44.5	46.8	83.7	370	76.5	70.6	76.0	bd	118
Tm (ng/g)	5.97	3.62	15.5	7.74	9.36	14.9	55.8	14.2	12.7	13.0	bd	20.0
Yb (ng/g)	47.8	23.5	107	56.1	67.4	100	364	122	105	111	bd	136
Lu (ng/g)	7.96	3.62	17.4	9.67	9.36	16.7	55.8	19.8	18.1	20.4	bd	22.1
Hf (ng/g)	1.99	3.62	9.68	3.87	3.74	7.44	26.0	8.50	1.81	3.71	bd	6.01
Ta (ng/g)	5.97	5.43	3.87	3.87	3.74	7.44	7.44	17.0	5.43	3.71	6.17	10.0
Pb (ng/g)	13.9	56.2	21.3	13.5	16.9	13.0	11.2	19.8	14.5	29.7	20.6	14.0
Th (ng/g)	bd	9.06	bd	bd	bd	1.86	bd	bd	bd	bd	bd	bd
U (ng/g)	bd	5.43	bd	bd	bd	bd	bd	bd	bd	bd	bd	bd

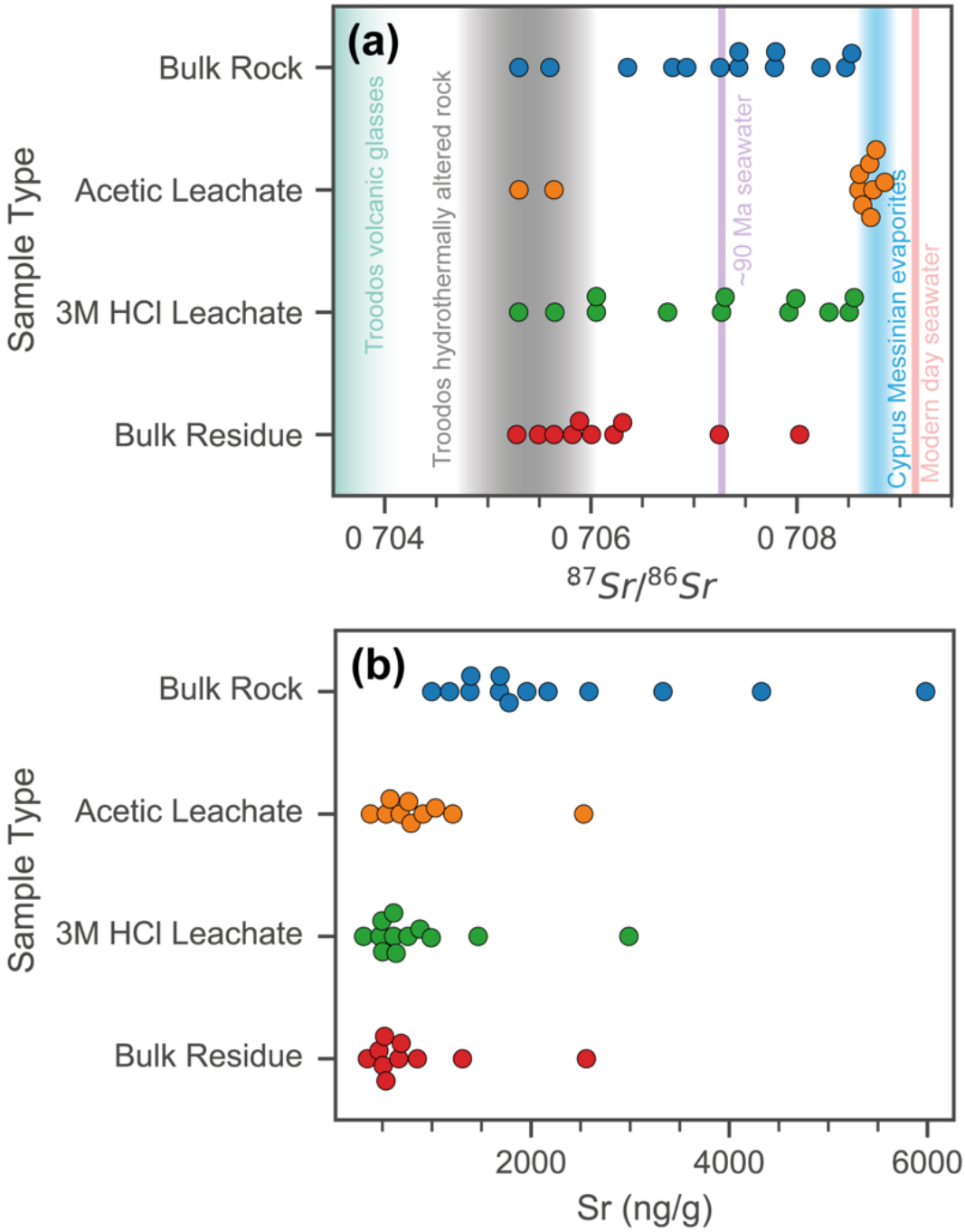

Figure 4.20: (A) $^{87}Sr/^{86}Sr$ Caltech plot of progressive leaching results of completely serpentinised whole rocks sampled within the Artemis Diapir. Boundaries of Troodos volcanic glasses (Rautenschlein et al., 1985), Troodos hydrothermally altered rock (Bickle and Teagle, 1992), Cretaceous ~90 Ma and modern day seawater (McArthur et al., 2012), and Cyprus Messinian evaporites (Flecker and Ellam, 2006; McCulloch and Deckker, 1989; Müller and Mueller, 1991) are shown. (B) Sr (ng/g) concentration Caltech plot of progressive leaching results of whole rocks.

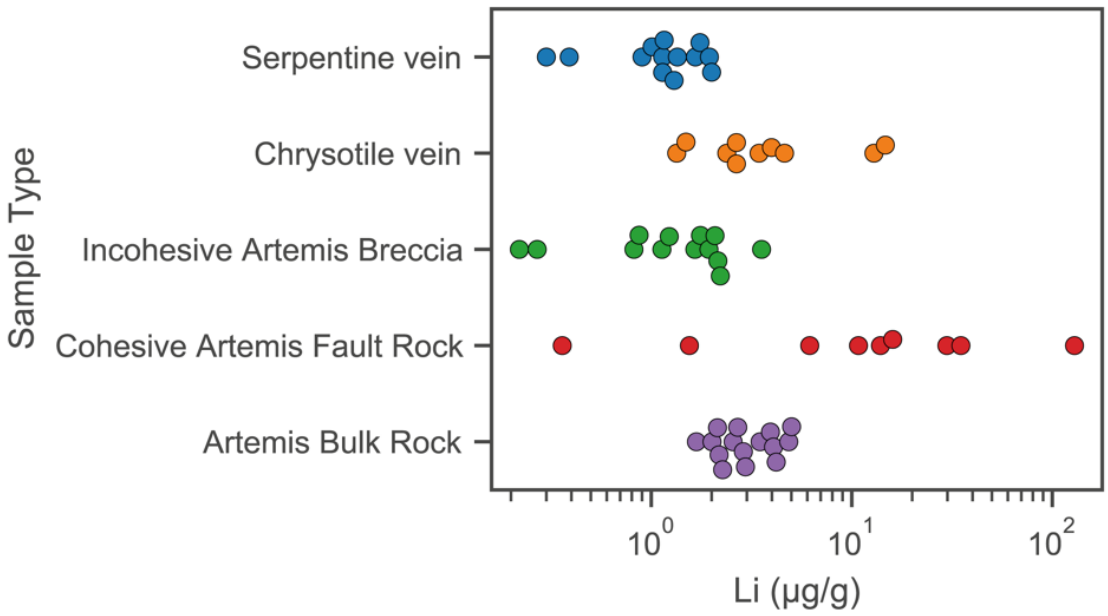

Figure 4.21: Caltech plot of Li (µg/g) concentration (log scale) in different rock types within the completely serpentinised Artemis Diapir.

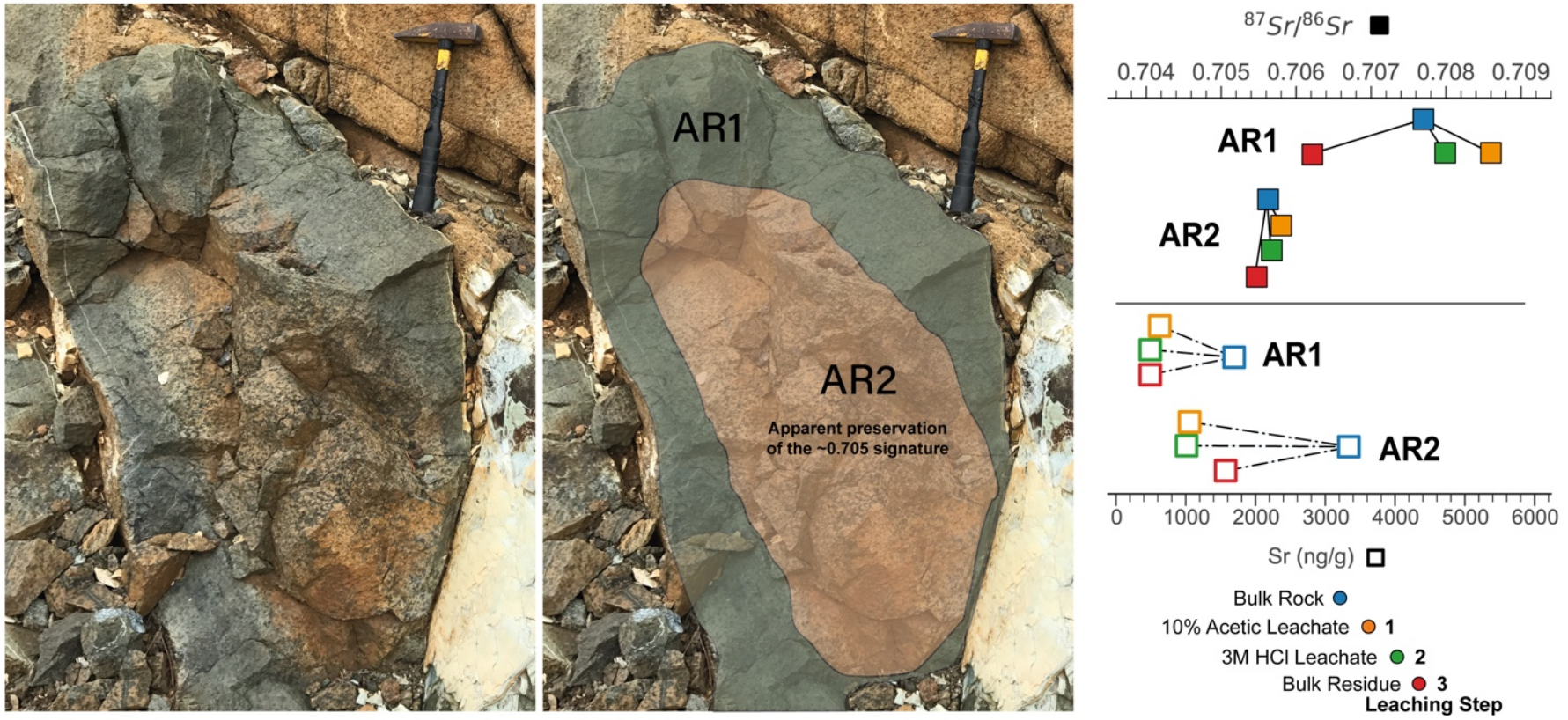

Figure 4.22: Completely serpentinised mantle rock block within the Artemis Diapir. Sample AR1 surrounds the margin of the block and yields more radiogenic $^{87}Sr/^{86}Sr$ ratios and lower Sr (ng/g) concentrations relative to the centre of the block (sample AR2). Filled squares reflect $^{87}Sr/^{86}Sr$ ratios. Empty squares reflect Sr (ng/g) concentration. Each colour reflects a progressive leaching step. Each leaching step balances against the bulk rock value.

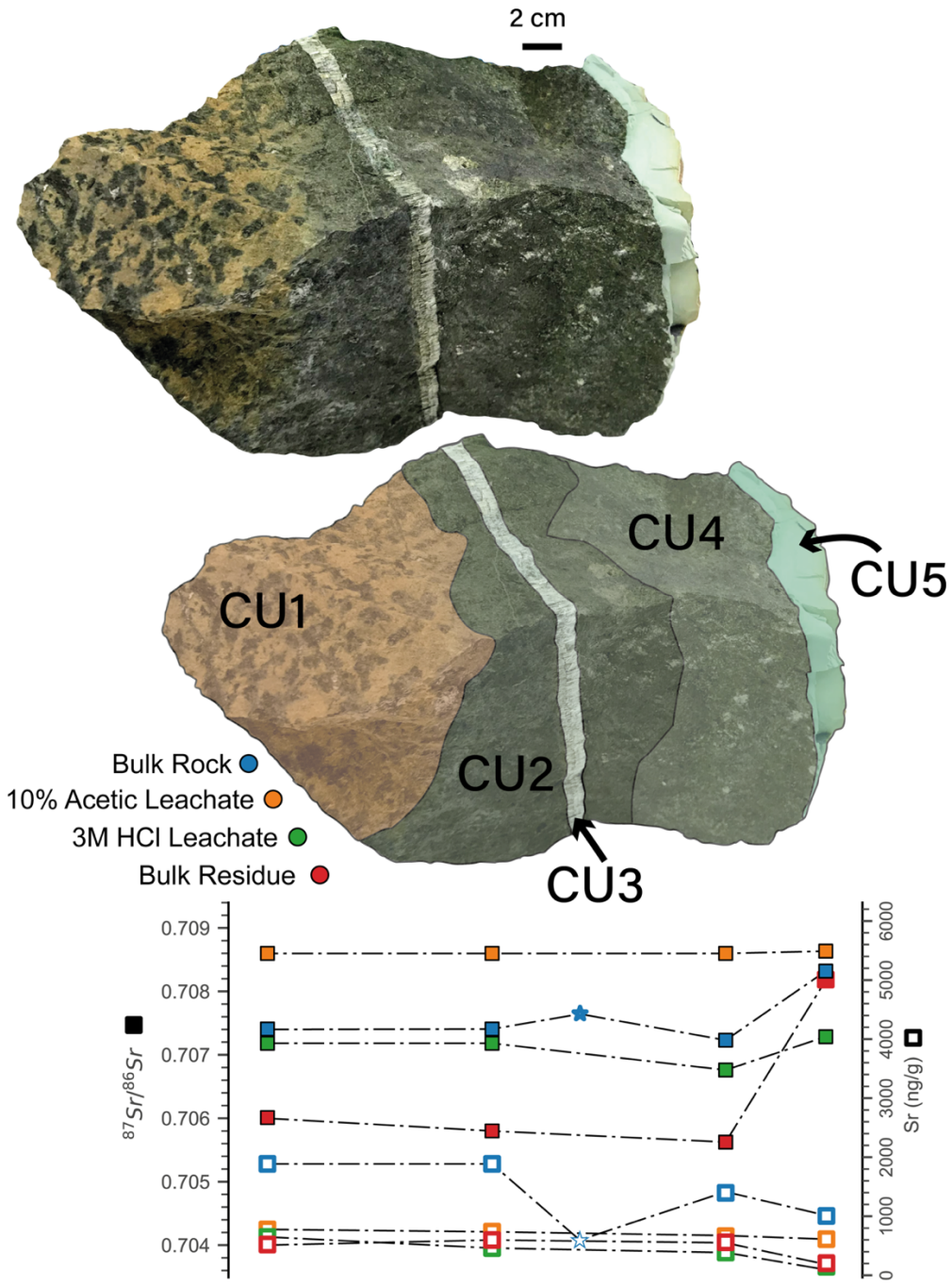

Figure 4.23: Sample CU unannotated and annotated image pairs. Progressive leaching analytical results ($^{87}Sr/^{86}Sr$ and Sr (ng/g) concentration) are shown. Star reflects chrysotile vein CY3. Respective colours reflect each leaching step. Filled squares/star reflect $^{87}Sr/^{86}Sr$ ratios and empty squares/star reflect Sr (ng/g). CU1, CU2, CU4 yield differing serpentine textures at the outcrop scale, but similar $^{87}Sr/^{86}Sr$ values and Sr (ng/g) concentrations. Progressive leaching results show contrasting $^{87}Sr/^{86}Sr$ reservoirs (~0.705-6 and ~0.7087) are preserved, culminating in a mixed whole rock $^{87}Sr/^{86}Sr$ signal (~0.7073). The serpentine vein CU5 sample yields more radiogenic $^{87}Sr/^{86}Sr$ values, but lower Sr (ng/g) concentrations.

4.4.3 Summary

The completely serpentinised rocks of the Artemis Diapir yield whole rock Sr isotope compositions that reflect variable proportions of two distinct Sr reservoirs, a more primitive 0.7053-62 signal and a radiogenic 0.70865-0.7089 signal (Fig. 4.20). Sampled waters within the Artemis Diapir show contrasting chemistries. In rivers and streams lower pH <10 Mg-HCO_3 waters occur, waters sampled within the abandoned Amiantos mine are also lower pH <10 Mg-HCO_3 waters, but generally yield radiogenic Sr (~0.7083) Sr isotope compositions and higher fluid-mobile trace element and molecular concentrations (Fig. 4.10; Fig. 4.14). In contrast to these surficial waters, high pH >11.5 hyperalkaline Na-K-Cl-OH-SO_4 waters with more primitive (0.7058) Sr isotope compositions emanate from the Artemis Diapir (Table 4.3). At sites of discharge, these high pH >11.5 waters form travertine material composed of aragonite, calcite, brucite, halite, and detrital serpentine. Fluid mixing between discharging hyperalkaline waters and surficial low pH <10, precipitates soft brucite-dominated material with low ~0.7058 $^{87}Sr/^{86}Sr$ ratios (Fig. 4.5). Some calcite and aragonite veins yield more radiogenic (~0.7087) Sr isotope compositions, similar to lower pH <10 waters. Calculated stable oxygen isotope values for carbonates in equilibrium with meteoric water match measured stable oxygen isotope values of all sampled precipitates within the Artemis Diapir (Fig. 4.18).

4.5 Discussion

4.5.1 Origin of the Troodos Mantle Sequence waters

The lower pH <10 water types sampled in the Troodos Mantle Sequence yield stable oxygen and hydrogen values that fall along the Cyprus meteoric water line (Fig. 4.16; Boronina et al., 2005) and are derived from meteoric water, consistent with previous studies (Neal and Shand, 2002). In contrast, Artemis Diapir high pH >11.5 hyperalkaline waters, do not plot along the Cyprus Meteoric water line (Fig. 4.16). Previous studies propose that hyperalkaline waters emanating from the Troodos Massif reflect a diluted residual seawater, which has not been sufficiently flushed from the ocean crustal and mantle rocks of the Troodos ophiolite (Neal and Shand, 2002). This assertion is based on similarities between a seawater dilution curve and the consistent relationship of Cl and Br in sampled waters. However, the Cl/Br (mol/mol) of the hyperalkaline water (902; Neal and Shand, 2002) is higher than seawater (659), which suggests a component of halite dissolution (e.g.,

Cartwright et al., 2006). In addition, as stated in 4.2, portions of the Troodos ophiolite ocean crustal rocks have been proposed to interact with groundwaters that remobilised Messinian sulphate from the overlying evaporite sedimentary sequences (e.g., Alt, 1994). Consequently, the origin of high pH >11.5 waters hyperalkaline waters of the Artemis Diapir may be sourced from either: (1) meteoric-derived water that has interacted with the Artemis Diapir completely serpentinised rocks; (2) a diluted and residual, evaporated seawater that has not been sufficiently flushed from the Troodos Mantle Sequence; and (3) a meteoric-derived water that interacted with overlying evaporites, yielding a dissolved evaporite geochemical and isotopic fingerprint, which has not been sufficiently flushed from the Troodos Mantle Sequence.

Elemental and molecular ratios such as Na/Cl and Ca/SO_4 are a useful tool for fingerprinting the origin of fluids, specifically whether sampled waters are derived from a seawater or a dissolved evaporite source. If the hyperalkaline waters of the Artemis Diapir are sourced from a residual partially evaporated seawater or a meteoric-derived dissolved evaporite water, the ratios of sampled waters would yield consistent and strong distinctive geochemical signals (Table 4.3; Table 4.5; Table 4.6). For example, high pH hyperalkaline waters yield Na/Cl (mol/mol) ratios of ~1.2 and are higher than seawater (~0.86) and halite dissolution (~1); Ca/SO_4 (mol/mol) ratios of 0.36 are similar to seawater, but lower than gypsum/anhydrite dissolution (~1); Cl/Br (mol/mol) ratios are variable ranging between 402 and 902 (Table 4.5; Table 4.6). The contrasting ratios displayed by the Artemis hyperalkaline waters (Fig. 4.11; Fig. 4.12; Table 4.5; Table 4.6) do not suggest a distinct fluid source of uniform origin such as a residual dilute seawater or dissolved evaporite water. Alternatively, these ratios are best explained by a modern meteoric water that has likely extensively interacted with the rocks of the Artemis Diapir. Consequently, the resultant geochemical and isotopic fingerprints of the modern waters reflect cumulative water-rock interaction events that have previously occurred within the Artemis Diapir.

This interpretation is supported by modelling oxygen and hydrogen stable isotope compositions. Determined oxygen and hydrogen stable isotope compositions are modelled along differing water-rock reaction paths for fluids in equilibrium with the Artemis Diapir through different water-rock ratios and temperatures ranging from 5 to 25 °C using Eq. (4.1) and serpentine-water oxygen and hydrogen fractionation factors (Saccocia et al., 2009a; Wenner and Taylor, 1971). The model represents a closed system (e.g., Field and Fifarek, 1985; Taylor, 1974,1977) where after equilibrating with serpentine of the Artemis domain (δ_r^i), the final composition of water (δ_w^f) depends on the water-rock ratio (W/R = mass ratio of O and H in water to rock), temperature of water-rock interaction, and the initial water isotopic composition (δ_w^i).

$$\delta_w^f = \frac{\delta_r^i - \Delta_{r-w} + [\left(\frac{W}{r}\right)(\delta_w^i)]}{1 + (\frac{W}{r})}$$

(4.1)

Modelled reaction paths highlight that measured hyperalkaline pH >11.5 oxygen and hydrogen stable isotope compositions may be reproduced by low-temperature (>5°C to <25°C) water-rock interaction between a meteoric-derived water and the completely serpentinised Artemis Diapir under a predominantly rock dominated regime (W/R >0.1 to <1; Fig. 4.16). Additionally, this interpretation is also supported by the $^{87}Sr/^{86}Sr$ isotopic compositions of the Artemis hyperalkaline pH >11.5 waters and associated travertine precipitates. These match the most primitive $^{87}Sr/^{86}Sr$ rock residue compositions (~0.7053-0.7062) are significantly lower than the more radiogenic Sr isotope signatures of the Messinian evaporates or Messinian Mediterranean seawater (Fig. 4.14).

In addition to geochemical evidence, simple mass balance calculations highlight that precipitation levels of the Mount Olympus region are sufficient to completely serpentinise the Artemis Diapir to a depth of 4000 m in the estimated time period since the estimated emergence of the Artemis Diapir (Evans et al., 2021), under the assumption that the proportion of infiltration is 0.001 (Table 4.12). The potential for the infiltration of significant amounts of meteoric water in combination with the progressive uplift and exhumation of the Troodos Mantle Sequence would have likely resulted in the flushing of such a residual water from the uplifted mantle rocks.

Table 4.12: Mass balance calculation of meteoric water infiltration.

Artemis Serpentinisation Extent	100
Proportion of water in Artemis	0.13
Artemis Parameters	3000 x 5000 x 4000 (m)
Artemis Bulk Density	2000 kg/m^3
Mass of rock Artemis	1.2x10^{14} kg
Mass of water in Artemis	1.56x10^{13} kg
Rainfall	1 m/yr
Water density	1000 kg/m^3
Rainfall (kg/yr over area) Artemis	1.5x10^{10} kg/m^2/yr
Proportion of infiltration	0.001
Time	1.1 Myr
Water infiltrated in 1.1 Myr	1.65x10^{13} kg
Water budget fulfilled (%)	106 %

4.5.2 Origin of salinity and high fluid-mobile elemental concentrations in hyperalkaline waters

Concentrations of Cl, SO_4, B, and alkali metals (Li, Na, K, Rb, Cs) in the sampled Artemis Diapir hyperalkaline waters are generally higher relative to typical hyperalkaline waters emanating from continental massifs (e.g., Fig. 4.12; Barnes et al., 1978, 1967; Barnes and O'Neil, 1969; Chavagnac et al., 2013; Giampouras et al., 2019; Leong et al., 2021; Monnin et al., 2014). As we interpret the Artemis hyperalkaline waters as meteoric-derived waters, the origin of these elevated concentrations is limited to two potential origins: (1) Marine aerosols/ atmospheric deposition entering the system via precipitation as rain and/or snow; (2) Water soluble inclusions and/or the serpentine in the rock itself.

Marine aerosols are unlikely to be the source of the high abundance of salinity and fluid mobile elements in Artemis hyperalkaline waters as Na/Cl (mol/mol) in the Troodos snow sample show seawater-like values (Table 4.3; Table 4.5) and contrasting ratios to hyperalkaline waters (Table 4.3). In addition, since even >99 % evaporation would not result

in the elemental and molecular concentrations measured in the hyperalkaline fluids, they must originate from the rocks of the Artemis Diapir.

Water-soluble inclusions within serpentinised mantle rocks are a reservoir for fluid-mobile trace elements (e.g., Deschamps et al., 2013; Peters et al., 2017) that attach to the serpentine structure. Some fluid-mobile tracers within serpentinites are water-soluble inclusions with high concentrations of Na^+ (up to 900 μg/g), Cl^- (up to 5100 μg/g), SO_4^{-2} (up to 900 μg/g in rock), and Mg^{2+} (up to 1600 μg/g) (e.g., Alt and Shanks, 1998; Huang et al., 2018; Sharp and Barnes, 2004). Experimental studies have shown that re-equilibration of serpentine with distilled water at low temperatures (~25 °C) results in ~40% loss of Cl^- from the serpentine into the aqueous solution (Huang et al., 2018). This suggests that the high concentrations of Na^+, Cl^-, and SO_4^{-2} in the Artemis hyperalkaline waters may be derived from weakly bound saline and sulphate inclusions within serpentine. The high Na/Cl (mol/mol) ratio of ~1.2 in the hyperalkaline waters may result from the preferential sequestration of Cl^- into surficial to near surface weathering-related minerals such as pyroaurite (Turvey et al., 2018) or recrystallised serpentine (Sharp and Barnes, 2004), which occurs within the Artemis serpentinite breccia. This could explain the increase in Na/Cl (molar) from ~1, resulting from the dissolution of saline inclusions in serpentine, to the measured Na/Cl (molar) ratios of ~1.2 within the hyperalkaline fluids (Fig. 4.10).

The high concentrations of boron and lithium in the Artemis hyperalkaline waters are likely sourced from the serpentine itself. Boron is a fluid-mobile element (e.g., Foster et al., 2010) and is abundant in serpentine; up to 200 μg/g (Pabst et al., 2011). It has long been considered that additional B uptake in serpentinites occurs at low temperatures (e.g., Bonatti et al., 1984; Spivack and Edmond, 1987) but new evidence suggests that B uptake results from formation of other low-temperature secondary minerals palygorskite and carbonates rather than serpentine (Boschi et al., 2008). Recent work proposes that release of B is driven by serpentine recrystallisation (e.g., Kodolányi and Pettke, 2011; Pabst et al., 2011) and dissolution of serpentine can release B (e.g., Su and Suarez, 2004). This indicates that ongoing serpentine alteration through coupled deformation-alteration-recrystallisation processes within the Artemis Diapir is likely releasing B into the Artemis hyperalkaline waters, generating the high concentrations up to 3,134 μmol/kg (Table 4.3).

Lithium is also considered to be a sink in serpentine (e.g., Decitre et al., 2002), with variable concentrations measured in serpentinites across various geodynamic settings (e.g., Deschamps et al., 2013; Peters et al., 2017). The more primitive, lower $^{87}Sr/^{86}Sr$ bulk rock samples, generally yield higher Li concentrations than Artemis Diapir recrystallised incohesive breccias, and serpentine veins (Fig. 4.21). This suggests that Li is being mobilised and lost from the bulk rocks through the alteration of serpentine related to the

coupled deformation-alteration-recrystallisation serpentinisation style. Some late stage mutually cross-cutting chrysotile veins also have high concentrations of Li (up to 15 μg/g; Fig. 4.21) and also have the mixed $^{87}Sr/^{86}Sr$ bulk rock signature (Fig. 4.23; CU3) suggesting they may have precipitated directly from the mixing of the two Artemis Diapir primary water types.

As serpentine is a source of water-soluble inclusions that yield high concentrations of Na, Cl, and SO_4; elevated concentrations in the meteoric-derived Artemis hyperalkaline waters are sourced from the Artemis rocks. The alteration of serpentine, mediated through the coupled deformation-alteration-recrystallisation serpentinisation style, results in meteoric-derived hyperalkaline waters with high concentrations of fluid-mobile elements and late, serpentinite phases generally yielding lower trace element concentrations.

4.5.3 Contrasting Sr reservoirs in sampled waters of the Troodos Mantle Sequence

Completely serpentinised rocks of the Artemis Diapir have whole rock Sr isotope compositions that reflect variable proportions of two distinct Sr signals, a more primitive 0.7053-62 source and a radiogenic 0.70865-0.7089 source. These contrasting $^{87}Sr/^{86}Sr$ ratios highlight that a series of progressive serpentinisation events have occurred within the Artemis Diapir, resulting in the mixing of strontium reservoirs that yield a mixed $^{87}Sr/^{86}Sr$ value in the bulk rocks (Fig. 4.15; Fig. 4.24). Although the aim of this chapter is not to constrain the progressive sequence of serpentinisation events, we briefly outline the respective Sr sources and their potential origins, which contribute to the geochemical makeup of waters emanating from the Troodos Mantle Sequence.

Results from progressive leaching experiments suggest that an initial pervasive serpentinisation event overprinted primitive mantle $^{87}Sr/^{86}Sr$ values (assumed as ~0.7037; Rautenschlein et al., 1985) with a ~0.705 signal. This ~0.705 signal is similar to the estimated Cretaceous Troodos hydrothermal fluid endmember composition of 0.7054 ± 7 (Bickle and Teagle, 1992) and could be sourced from hydrothermal fluids penetrating into deeper levels of the Troodos ophiolite and beyond the crust-mantle transition zone, into the Troodos lithospheric mantle. Alternatively, a long-standing assertion is that the exhumation of Troodos Mantle Sequence rocks is related to the collision of the Eratosthenes Seamount with the Cyprus Arc Subduction, focussing dewatering marine sediments and dehydrating altered ocean crust beneath the Mount Olympus elevation high (Gass, 1977; Gass and Masson-Smith, 1963; Robertson, 1977; Robertson, 1998a).

The contrasting radiogenic $^{87}Sr/^{86}Sr$ values of 0.7086-0.7089 preserved in the Artemis Diapir easily-mobile leachates, 3M HCl leachates, and some bulk rock residues (Fig. 4.20) have similar values to Cyprus Messinian evaporite sequences (Fig. 4.2), Cyprus submarine sediments (Makarona et al., 2012), and Burdigalian seawater (McArthur et al., 2012). As stated in 4.2, Cyprus Messinian sedimentary sequences show evidence of localised processes, which are interpreted to reflect evaporite deposition in isolated marginal sub-basins (Artiaga et al., 2021; Follows, 1990; Manzi et al., 2016; Robertson et al., 1995; Rouchy et al., 2001; Stow et al., 1995). In addition, oxygen and hydrogen stable isotope values of Messinian gypsum hydration water show that the Messinian evaporite brine waters were composed with a strong component of meteoric water (Evans et al., 2015). This suggests that Messinian evaporite sequences likely formed in shallow isolated sub-basins, which resulted in the decoupling of $^{87}Sr/^{86}Sr$ values from Messinian age global seawater values of ~0.70905 to lower values of 0.7865 to 0.7089. We interpret the radiogenic $^{87}Sr/^{86}Sr$ ratios of 0.7086-0.7089 preserved throughout the Artemis Diapir originate from the previously overlying Messinian evaporite sequences, where subsequent subaerial fluids interacted and mobilised this Messinian signal into the Troodos Mantle Sequence inducing further serpentinisation. Such a scenario is proposed to occur in other portions of the Troodos ophiolite, where groundwaters with Messinian sulphate isotope signals have contaminated ocean crustal rocks (Alt, 1994).

Previous studies have shown that weathering of trace carbonate is enough to dominate the Ca and Sr loads of discharging rivers (e.g., Andrews and Jacobson, 2017; Jacobson et al., 2015). The waters and precipitates of the Troodos Mantle Sequence reflect varying proportions of contrasting Sr reservoirs. Lower pH <10 surficial and Amiantos mine waters of the Troodos Mantle Sequence are dominated by $^{87}Sr/^{86}Sr$ values that range between 0.70785 and 0.70857 and are lower than the $^{87}Sr/^{86}Sr$ values of Messinian evaporites (Fig. 4.15; 0.7086-89; Müller et al., 1990). The Sr isotope composition of lower pH <10 waters are dominated by the dissolution of carbonate phases that have a Messinian evaporite signal, with a minor component of more primitive ~0.705 carbonate phases (Fig. 4.15) and typically have similar Sr/Ca (ng/g/μg/g) ratios of ~2.5 (Fig. 4.15).

In contrast to lower pH <10 waters, hyperalkaline waters are dominated by the ~0.705 signal, which is present in both rocks and precipitates. The Sr/Ca (ng/g/μg/g) ratios of ~0.705 bulk rock residues and carbonates (<0.5) differ to some ~0.705 whole-rocks, acetic leachates, and carbonates (>2) and most sampled hyperalkaline waters have Sr/Ca (ng/g/μg/g) values of 1 to 1.5. This suggests most sampled hyperalkaline waters are mobilisation differing solid components that yield contrasting Sr/Ca (ng/g/μg/g).

Consequently, the remobilisation and redistribution of pre-existing serpentine, carbonates, and hydroxides from previous serpentinisation and serpentine alteration episodes is actively occurring within the Artemis Diapir, which results in the progressive modification and overprinting of recorded geochemical and isotopic fingerprints (Fig. 4.24).

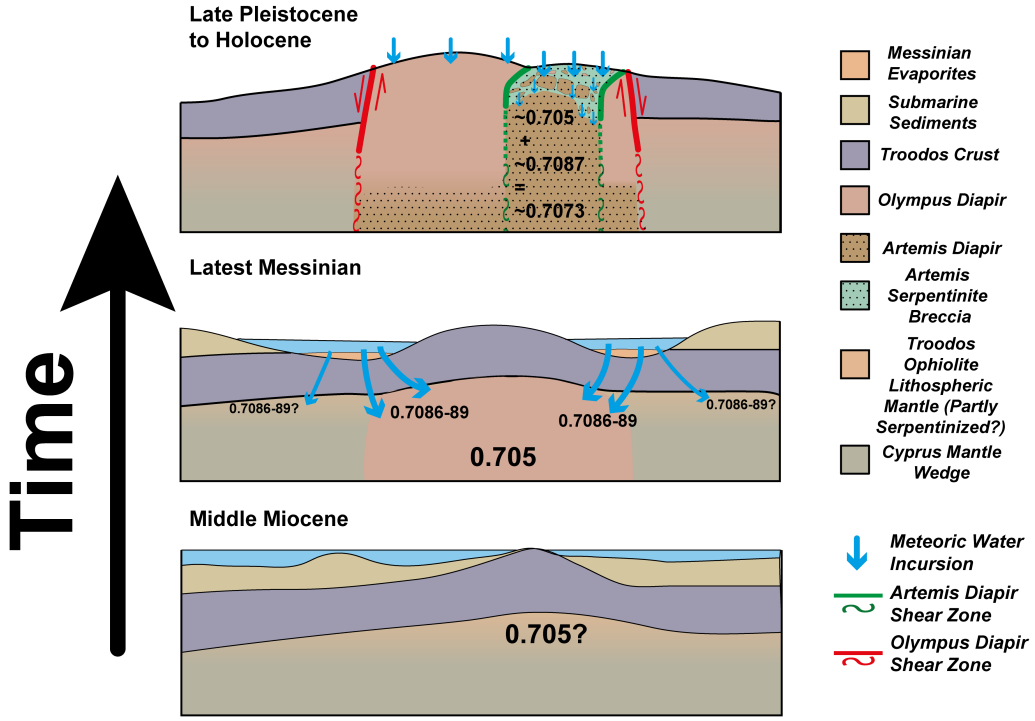

Figure 4.24. A schematic illustration of the Troodos Mantle Sequence highlighting the temporal evolution of contrasting Sr reservoirs reflected in the whole rock samples. A pre-Messinian pervasive serpentinisation event modifies the radiogenic Sr isotope composition of the Troodos Mantle Sequence from assumed mantle values of ~0.7037 (Rautenschlein et al., 1985) to 0.705-6. Subsequent serpentinisation by waters with a Messinian evaporite $^{87}Sr/^{86}Sr$ signal of ~0.7086-89 contaminates the underlying mantle rocks. Once mantle rocks are exhumed, the infiltration of meteoric water is inevitable. This results in the remobilisation and redistribution of geochemical and isotopic signals from previous serpentinisation events, culminating in mixing of these distinct reservoirs as reflected in the whole rocks of the Artemis Diapir.

4.5.4 Evolution of the Troodos Mantle Sequence waters

The sampled hyperalkaline waters and the low pH surficial waters, including the mine tailing waters, are modern, meteoric-derived waters that have experienced at least some degree of fluid-rock interaction. It is proposed that the hyperalkaline pH >11 fluid forms due to progressive evolution along a deeper fluid reaction path compared to the surficial pH <10 waters, and that the contrasting chemistries between both water types are a reflection of

both the residence time and the distance travelled within the system (e.g., Kelemen et al., 2011; Neal and Stanger, 1985). However, recent work has shown that low pH and hyperalkaline waters evolve along contrasting fluid pathways and that mixing between both end members is prevalent, likely obscuring the underlying contrasting fluid evolution pathways (Leong et al., 2021).

The Troodos Mantle Sequence provides a natural laboratory to investigate the fluid evolution pathways that generate hyperalkaline waters. Since it forms the highest elevations of Cyprus its setting precludes any external additional rock-derived contribution into the hydrological system. Meteoric water enters the completely serpentinised Artemis Diapir at an elevation of ~1,750 m above sea level and hyperalkaline water (up to pH 13) emanates onto the Artemis Diapir valley floor at an elevation of 1,545 m above sea level. In contrast low pH waters flow within surficial sediment deposits and with run off form streams and creeks, before eventually washing into rivers at similar elevations to the hyperalkaline spring sites. As a result, each water type reflects generally similar transport distances prior to sampling, in contrast to other serpentinised massifs (e.g., Samail Ophiolite; Neal and Stanger, 1985).

The Artemis Diapir is completely serpentinised with all primary mantle minerals replaced by serpentine or other phases. Consequently, serpentinisation hydration reactions cannot be invoked to form the hyperalkaline waters. The underlying fluid evolution pathways between water types may still be investigated and aided by the physical constraints that govern the Troodos Mantle Sequence. Here, we outline the respective fluid evolution pathways of (1) low pH surficial waters, (2) low pH mine tailing waters, and (3) high pH hyperalkaline waters with the aim of elucidating whether hyperalkaline waters form as a function of residence time along the same fluid evolution pathway, or contrasting fluid evolution pathways (Fig. 4.25).

4.5.4.1 Evolution of the low pH surficial waters

High levels of precipitation within the Troodos Mantle Sequence (910 mm/yr; Prodromos village, 1,400 m asl, Cyprus Department of Meteorology) results in perennial rivers and streams that discharge into the lower elevations of Cyprus (Fig. 4.25). Atmospheric deposition (e.g., precipitation as rain and snow, marine aerosols, dust) yields Troodos Mantle Sequence snow with generally low elemental and molecular concentrations (Table 4.3) and seawater-like Na/Cl ratios (0.87; Table 4.5) Major and minor cation and silicon solute concentrations (e.g., Mg, Si, Ca, B) of low pH waters generally cannot be explained through atmospheric deposition alone. As the magnesium-bicarbonate low pH surficial waters evolve and pH increases from >8 to <10, alkali metal concentrations increase by at

least an order of magnitude (Fig. 4.9). This suggests that an additional reservoir of alkali metal elements is being released into the low pH waters, most likely through mineral dissolution reactions. Such dissolution of minerals (e.g., brucite, carbonate, serpentine) is induced by slightly acidic rainwater (pH ~5.6) and atmospheric CO_2 (Leong and Shock, 2020) through the following dissolution reactions (e.g., Eq. 4.2 and 4.3 (Neal and Stanger, 1985); 4.4):

$$Mg(OH)_2 + 2CO_2 \rightleftharpoons Mg^{2+} + 2HCO_3^- \quad (4.2)$$

$$CaCO_3 + CO_2 + H_2O \rightleftharpoons Ca^{2+} + 2HCO_3^- \quad (4.3)$$

$$Mg_3Si_2O_5(OH)_4 + H_2O + 6CO_2 \rightleftharpoons 3Mg^{2+} + 2SiO_{2\,(aq)} + 6HCO_3^- \quad (4.4)$$

pH initially increases from ~5.6 to >8 with the highest concentrations of Mg^{2+}, Si, Ca^{2+}, Sr^{2+} occurring in the lowest pH surficial waters (Fig. 4.9). In these waters, the Mg/Si (mol/mol) ratio is ~4 (Table 4.4), significantly higher than the Mg/Si (mol/mol) ratio expected if dissolution reactions were dominated by serpentine (~1.3). This suggests brucite dissolution may be the dominant source of Mg^{2+} solute concentration in the lower pH <10 Mg-HCO_3 surficial waters. As pH progressively increases, concentrations of Mg^{2+}, Si, Ca^{2+}, Sr^{2+} progressively decrease (Fig. 4.9), suggesting these cations and silicon are progressively removed from the fluid by partitioning into secondary minerals such as serpentine, carbonates, andradite, and surficial weathering minerals such as pyroaurite. Evidence of this is presented by carbonates with stable oxygen isotope compositions that suggest formation at low temperatures (>5°C to <25°C) in equilibrium with meteoric waters (Fig. 4.17; Fig. 4.18) and radiogenic strontium isotope compositions that match the $^{87}Sr/^{86}Sr$ Troodos Mantle Sequence waters (Fig. 4.17). In addition, direct evidence of modern low-temperature serpentine precipitation is provided by sample DJ1, serpentine hosted in an aragonite filled void (Fig. 4.3). A $^{87}Sr/^{86}Sr$ of 0.707665 for the aragonite indicates that fluid mixing between low pH surficial water ($^{87}Sr/^{86}Sr$ 0.7083) and hyperalkaline water ($^{87}Sr/^{86}Sr$ 0.7058) occurred.

4.5.4.2 Increased fluid-rock interaction within mine tailings

The lower pH <10 waters sampled within the Amiantos asbestos mine generally yield higher elemental and molecular concentrations (Fig. 4.10; Table 4.3) relative to the lower pH <10 surficial waters (Fig. 4.10; Table 4.3). Sampling of waters where mixing between both primary water types is observed in the field (samples BX3 and BX7) provides insight into whether these mine tailing waters are the result of efficient mixing of primary water types within the finer-grained mine tailings or the result of greater fluid-rock interaction due to greater reactive surface area.

In the case of some elemental and molecular plots (e.g., Fig. 4.10), lower pH <10 Amiantos mine waters do not consistently plot on the hyperalkaline dilution line. This indicates that the lower pH <10 Amiantos mine waters occur due to enhanced fluid-rock interaction with the finer-grained mine tailings that have a larger reactive surface area, which would result in faster serpentine dissolution rates (Fig. 3.12; Evans et al., 2021; Thom et al., 2013). As a result, Amiantos mine waters yield higher trace element concentrations relative to lower pH waters and some fluid-mobile elements (e.g., Ba, Cs) have concentrations comparable to high pH >11.5 hyperalkaline waters. In agreement with this interpretation, the $^{87}Sr/^{86}Sr$ ratios of Amiantos mine waters (0.7078 to 0.7086) reflect a greater contribution of more primitive rock-derived Sr relative to lower pH <10 surficial waters (0.7084 to 0.7086) (Fig. 4.25).

However, some fluid mixing may occur in Amiantos mine tailings between high pH >11.5 waters, with high Li concentrations (up to 17 μg/g) and lower $^{87}Sr/^{86}Sr$ ratios (0.7058), and lower pH <10 surficial waters with low Li concentrations (<0.01 to 0.18 μg/g) and higher $^{87}Sr/^{86}Sr$ ratios (0.7084 to 0.7086). This is highlighted by some chrysotile veins with high Li concentrations (3.5 to 15 μg/g) but lower $^{87}Sr/^{86}Sr$ ratios (~0.7077) and the serpentine-aragonite carbonate sample DJ1 (Fig. 4.3), where the low-temperature meteoric water equilibrated sample is infilling porosity generated by serpentine alteration processes.

4.5.4.3 Evolution of the high pH hyperalkaline waters

Alternative fluid-rock reactions that do not involve serpentinisation of primary mantle minerals are required to explain how meteoric-derived hyperalkaline waters form in a completely serpentinised setting. Evidence of extensive water-rock interaction is sourced from rock-derived stable and radiogenic isotopic signatures (Fig. 4.16). This indicates that the ongoing alteration of serpentine, through interaction between meteoric water and completely serpentinised mantle rocks, is a dominant reaction occurring across water types in the Artemis Diapir. The progressive increase in alkali metal and boron concentrations

combined with evidence of greater water-rock interaction as pH increases, initially suggests that these waters evolved from low pH to high pH along the same evolution pathway involving serpentine alteration. A key difference between both primary waters is that DIC poor, hyperalkaline waters evolved in a rock-dominated system, where atmospheric influence is limited, and low pH, high DIC surficial waters evolve in a water-dominated system under atmospheric conditions (Fig. 4.16). Although these low-temperature interactions are invariably complex and a full suite of fluid reaction pathways is unknown, we propose that this distinction is the result of contrasting fluid evolution pathways relating to the alteration of serpentine mediated through coupling of deformation-alteration-recrystallisation processes.

Dissolution reactions drive the increase of pH to ~8 (e.g., Eq. 4.2). This reaction occurs under atmospheric influence and is mediated by relatively high concentrations of DIC. Whereas, in a higher pH environment, hydrogen ions have already been consumed in prior reactions, resulting in serpentine dissolution reactions to occur through the consumption of water:

$$Mg_3Si_2O_5(OH)_4 + H_2O \rightleftharpoons 3Mg^{2+} + 2SiO_{2\,(aq)} + 6OH^- \quad (4.5)$$

It is likely this reaction only occurs under a rock-dominated regime, with limited atmospheric influence as highlighted by low DIC concentrations in hyperalkaline waters. This water-mediated dissolution reaction releases magnesium, silicon, and additional hydroxides, along with fluid-mobile trace elements into the water.

Additional reactions must take place to produce the chemistries of the sampled hyperalkaline waters as the proportions of Mg, Si, and OH^- are not equal to Eq. 4.5. Mg and Si are likely removed from the waters and are sequestered into silicates such as serpentine and andradite; hydroxides and oxy-hydroxides sequestered into brucite and pyroaurite; and carbonates are sequestered into magnesite, and as trace components in calcite and aragonite. In addition, further hydroxide generating reaction pathways are likely responsible for generating high pH 13 values of the Artemis' tears spring waters. Such pathways include the oxidation of ferrous iron that produces ferric iron, hydroxide, and hydrogen gas, this reaction can be expressed as such by Eq. 4.6 (Chavagnac et al., 2013).

$$Fe^{II} + 2H_2O \rightleftarrows Fe^{III} + H_2 + 2OH^- \quad (4.6)$$

Iron oxidation produces not only additional hydroxide that increases the pH of the fluid to its highest values but also hydrogen gas that is typically attributed as a key characteristic of

serpentinising systems (e.g., Lang et al., 2021; McCollom and Bach, 2009; Sleep et al., 2004).

As a consequence of these complex serpentine alteration reactions, high pH >11.5 meteoric-derived hyperalkaline waters, with high concentrations of fluid-mobile elements, emanate on the Artemis Diapir valley floor (Fig. 4.25). Although such waters likely reflect a longer residence time and progressive water-rock interaction, they have likely evolved along contrasting fluid pathways relative to lower pH <10 water types (Fig. 4.25). Lower pH waters likely reflect reactions dominated by brucite and carbonate dissolution, with a minor component of serpentine dissolution under the influence of atmospheric CO_2. In contrast, high pH >11.5 hyperalkaline waters may reflect a reaction pathway dominated by hydroxide generating serpentine dissolution without atmospheric input (e.g., Milliken et al., 1996) and additional reactions that need to be constrained in subsequent investigations.

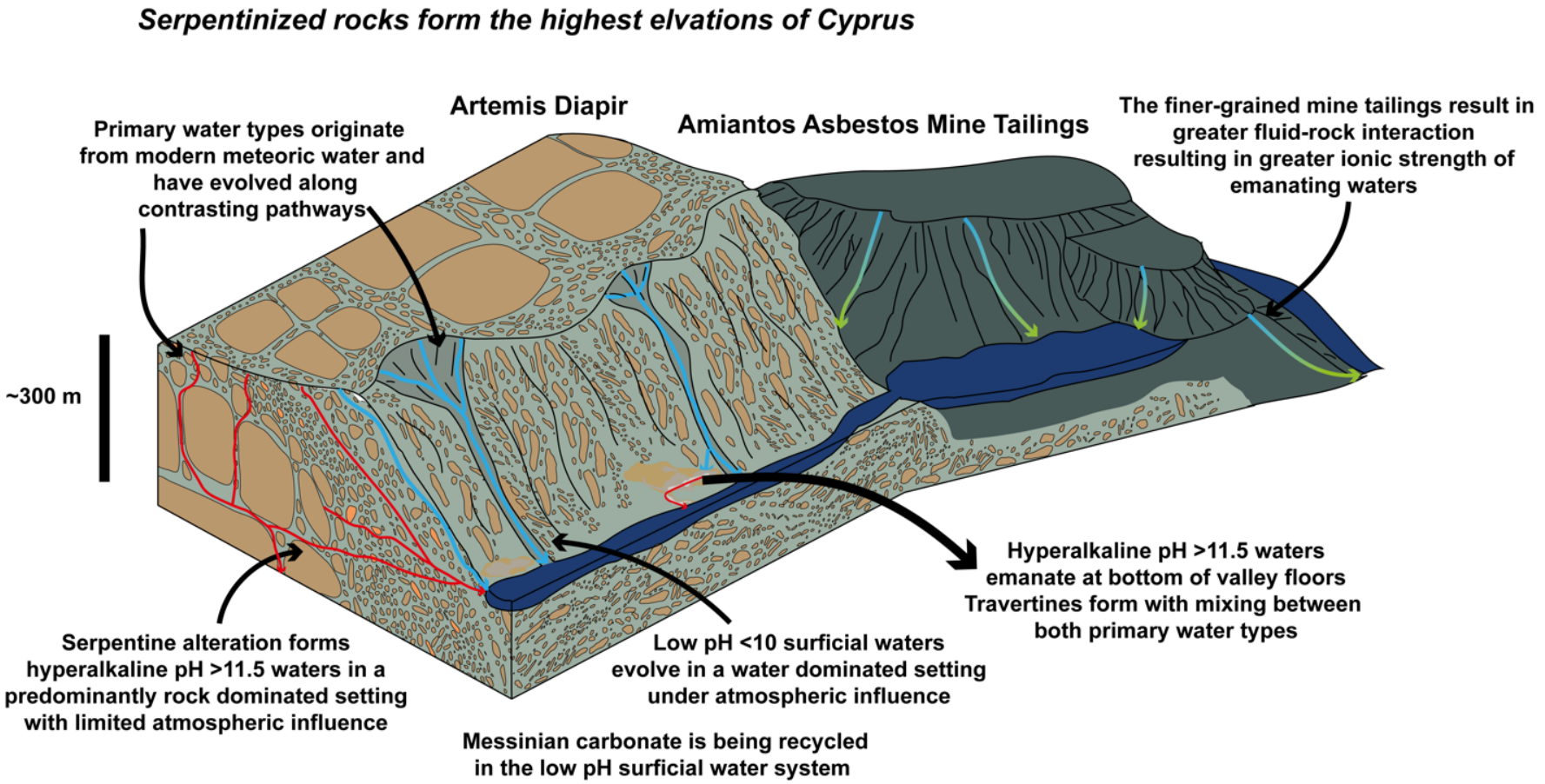

Figure 4.25: Schematic diagram of the Artemis Diapir, Cyprus, highlighting how contrasting fluid evolution pathways result in hyperalkaline pH >11.5 waters (red), lower pH <10 surficial waters (blue), and lower pH <10 Amiantos mine waters (green) emanating from the Artemis Diapi

4.6 Conclusions

1) Hyperalkaline, up to pH 13, Na-K-Cl-OH-SO_4 waters emanate from the completely serpentinised mantle rocks of the Artemis Diapir. Evidence from stable and radiogenic isotope compositions and contrasting elemental ratios in combination with the physical constraints provided by the Troodos Mantle Sequence demonstrates that the Artemis hyperalkaline pH >11.5 waters are modern waters derived from meteoric water and form through extensive interaction with the completely serpentinised rocks of the Artemis Diapir.

2) Lower pH <10 Mg-HCO_3 surficial waters are meteoric-derived waters where remobilisation and redistribution of pre-existing serpentine, carbonates, and hydroxides is actively occurring within the Artemis Diapir. Progressive dissolution and interaction with these phases evolve surface water compositions to pH >8. As pH increases, major cation (Mg, Ca) and silicon solute concentrations decrease, likely sequestering into new recycled secondary phases.

3) Lower pH <10 Mg-HCO_3 waters sampled from within the Amiantos Mine generally yield elevated fluid-mobile concentrations and lower $^{87}Sr/^{86}Sr$ ratios relative to lower pH <10 surficial waters. These Amiantos mine waters have likely interacted with the finer-grained mine tailings, enhancing serpentine dissolution reactions, increasing some fluid-mobile elemental and molecular concentrations to similar values as hyperalkaline waters. Yet, the pH of the Amiantos mine waters is <10, indicating additional hydroxide generating reactions must occur to form hyperalkaline high pH >11.5 waters. Consequently, the Artemis Diapir hyperalkaline waters and lower pH <10 waters likely evolved along contrasting fluid reaction pathways.

4) Waters emanating from the Troodos Mantle Sequence reflect remobilised geochemical and isotopic signals from previous serpentinisation events. These waters result in the redistribution and progressive modification of distinct geochemical and isotopic fingerprints preserved in the Artemis Diapir rocks.

Chapter 5 Unravelling a progressive serpentinisation-alteration history: Geochemical and isotopic fingerprinting within the Troodos Mantle Sequence, Cyprus

Abstract

Serpentinised mantle rocks typically reflect a progressive sequence of multiple serpentinisation events. However, establishing the conditions of distinct serpentinisation episodes remains challenging, especially as mantle rocks typically reveal complex geological histories such as the Troodos Mantle Sequence, Cyprus. Elemental concentrations, radiogenic strontium and stable isotope ($\delta^{11}B$, $\delta^{18}O$, δD) compositions of whole rocks, leachates, veins, fault rocks, and residues are exploited to unravel the progressive sequence of overprinting serpentinisation events that have culminated in variably altered mantle rocks forming the highest elevations of Cyprus. Determined $^{87}Sr/^{86}Sr$ whole rock values of ~0.705-6 and $\delta^{11}B$ values of +7 to +18 ‰, in combination with some previously published $\delta^{18}O$ and δD values of +3.4 to +8 ‰ and -52 to -65 ‰, are consistent with a slab-derived fluid sourced from the downgoing dehydrating and dewatering Cyprus slab. These waters were harvested from the slab at estimated temperatures of >100 to <150 °C and focussed beneath the differentially uplifted Troodos Mantle Sequence, resulting in the pervasive serpentinisation at temperatures of >150 to <300 °C, inducing serpentinisation-isostatic uplift, consistent with Troodos ophiolite uplift trajectories. Mass balance calculations suggest that enough water is located in the dehydrating slab window to serpentinise the Troodos Mantle Sequence, in the required time frame, to a reaction extent of ~66 %. An inevitable consequence of serpentinisation-induced uplift is the incursion of evolving meteoric waters that had initially interacted with overlying submarine sediments and Messinian evaporites. These meteoric waters resulted in further serpentinisation of the Troodos Mantle Sequence, where continued meteoric water incursion produces a low density serpentinite gouge endmember through ongoing serpentine alteration manifest as coupled deformation-alteration-recrystallisation processes. The Troodos Mantle Sequence reflects a progressive series of overprinting serpentinisation and alteration events with up to 66 % of serpentinisation occurring by slab-derived fluids and the up to remaining 33 % by meteoric-derived waters.

5.1 Introduction

The interaction of water and mantle rocks, termed serpentinisation, is a critical process within the earth system (Kerrick, 2002). Serpentinisation aids plate tectonic movements (e.g., Guillot et al., 2015), forms mountains by inducing isostatic uplift (e.g., Evans et al., 2021), acts as a geological sponge for water, carbon, and fluid-mobile elements (e.g., Deschamps et al., 2013; Hacker, 2008; Kelemen and Manning, 2015; Kodolányi and Pettke, 2011), and may be instrumental in the origin of life on Earth and other planetary bodies (e.g., Ehlmann and Mustard, 2010; Schrenk et al., 2013; Sleep et al., 2004).

Due to the importance of serpentinisation, a long standing motivation for investigation is to elucidate where, when, and to what extent serpentinisation reactions occur (e.g., Alt et al., 2013; Barnes and O'Neil, 1969; Coleman, 1971; Früh-Green et al., 1990; Kelemen et al., 2011; Merrill, 1899; Wenner and Taylor, 1973). Serpentinisation is inferred to occur, in varying magnitudes, over a range of geodynamic settings such as slow spreading mid ocean ridges (e.g., Francis, 1981; Mével, 2003), bend faults (Ranero et al., 2003; Ranero and Sallarès, 2004), subduction zones (Fryer et al., 1985; Hyndman and Peacock, 2003), rifted margins (e.g., Bayrakci et al., 2016; Boillot et al., 1980), strike-slip plate boundaries (e.g., Moore and Rymer, 2007), and serpentinised massifs within ophiolite sequences (e.g., Barnes and O'Neil, 1969; Magaritz and Taylor, 1974; Wenner and Taylor, 1973, 1971). However, direct in-situ observation and sampling of many of these settings remains unaccomplished (e.g., Teagle and Ildefonse, 2011). As a result, attention has been focussed on samples that are relatively easily accessible on both land and the oceans, which may not be representative of where serpentinisation reactions occurred.

Evidence from cross-cutting relationships and stable oxygen and hydrogen isotopic compositions of recovered surface to near-surface serpentinite samples suggest serpentinisation occurred as a progressive series of reactions, potentially through multiple and distinct water-rock interaction episodes (e.g., Alt and Shanks, 2006; Burkhard and O'Neil, 1988; Früh-Green et al., 1990; Kyser et al., 1999; O'Hanley, 1991; O'Hanley and Offler, 1992; Peacock, 1987; Wenner and Taylor, 1974, 1973, 1971). However, establishing the conditions of distinct serpentinisation episodes remains challenging as serpentinised mantle rocks typically reveal complex geological histories and isotopic records are commonly overprinted by subsequent fluid rock interaction events (Kyser and Kerrich, 1991; O'Hanley, 1991; O'Hanley et al., 1992; O'Hanley and Offler, 1992). Consequently, measured stable isotope compositions from serpentinised massifs with complex geological histories may reflect serpentinisation events across discrete tectonic settings, at distinct points in time, with fluids of differing origin, which may still be actively serpentinising in their present locations (e.g., Barnes and O'Neil, 1969).

Here, we aim to unravel the serpentinisation-alteration history of a serpentinised massif by leveraging novel ($\delta^{11}B$) and traditional ($^{87}Sr/^{86}Sr$, $\delta^{18}O$, δD) isotopic analyses and trace element geochemistry of serpentinised mantle rocks from the Troodos Mantle Sequence, Cyprus. We establish the progressive serpentinisation history of the serpentinised mantle rocks forming the highest elevations of the Troodos Massif and estimate the relative partitioning of each distinct serpentinisation event into the overall serpentinisation fluid budget.

5.2 Geological Setting

Here, we focus on the Troodos Mantle Sequence within the Troodos Massif, Cyprus, one of the world's best preserved and least deformed ophiolite sequences (Gass, 1968). The geological history of the Troodos ophiolite is generally well-constrained, from its formation ~90 to ~92 Ma at some form of supra-subduction zone spreading ridge in the Neo-Tethyan Ocean (Moores et al., 1984; Moores and Vine, 1971; Mukasa and Ludden, 1987; Pearce et al., 1984), to its progressive uplift and exhumation from the latest Messinian to today that has resulted in a serpentinised massif forming the highest elevations of Cyprus (Evans et al., 2021; Morag et al., 2016; Poole and Robertson, 1998, 1991; Robertson, 1977). The Troodos Mantle Sequence is sub-divided into two nested serpentinite diapirs: (1) the Olympus Diapir, an arcuate region of partially to strongly serpentinised mantle peridotites, mostly comprising tectonised harzburgites with minor dunites and chromities; and (2) a completely serpentinised diapir of peridotite blocks hosted in a sheared serpentinite breccia, termed the Artemis Diapir (Fig. 5.1) (Evans et al., 2021; Wilson, 1959). Cr-numbers (Cr/Cr + Al) of chrome spinels from the Olympus and Artemis Diapirs indicate that the completely serpentinised rocks of the Artemis Diapir originate from a region of relatively fertile mantle lherzolite (Cr# ~0.22-0.28) that contrast with the refractory shallow mantle harzburgites and dunites of the Olympus Diapir (Cr# ~0.51-0.70) (Batanova and Sobolev, 2000).

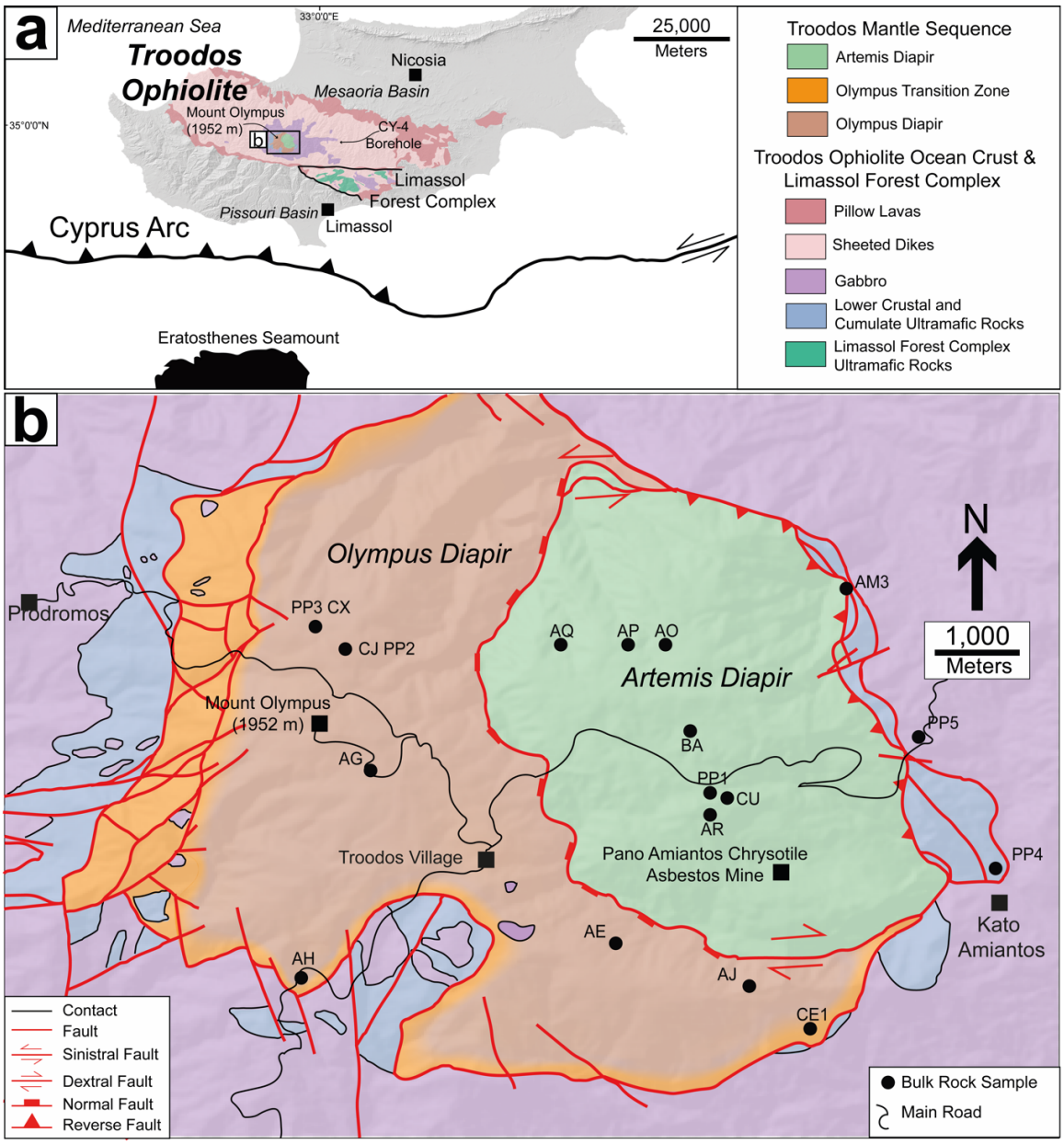

Figure 5.1: (A) Geological map of the Troodos ophiolite with the bullseye geometry of the Mantle Sequence highlighted along with the Limassol Forest Complex terrane, the Cyprus Arc, and northernmost portion of the Eratosthenes Seamount. (B) Geological map of the Troodos Mantle Sequence, adapted and updated from Wilson (1959). Bulk Rock sample locations are shown.

The mantle rocks of the Troodos Mantle Sequence may have undergone a progressive sequence of serpentinisation events with waters of differing fluid origins (Fig. 5.2; Heaton, 1976; Magaritz and Taylor, 1974; Nuriel et al., 2009; Sheppard, 1980). Some studies have proposed that Cretaceous seawater serpentinised the Troodos Mantle Sequence (Fig. 5.2; Nuriel et al., 2009; Schuiling, 2011) at temperatures 100 to 180°C along a hypothetical detachment fault structure that was active on the Cretaceous seafloor and would have generated significant submarine uplift and exposure of the mantle peridotites

(Nuriel et al., 2009). In contrast, other studies have proposed that the Troodos Mantle Sequence was serpentinised with 'metamorphic waters' at temperatures between 200°C and 300°C sourced from the downgoing subducting Cyprus slab (Fig. 3.10; Heaton, 1976; Sheppard, 1980). In addition, high $\delta^{18}O$ values (+10.3 to +14.1 ‰) and low δD values (-68 to -93 ‰) from Artemis Diapir samples and some from the Olympus Diapir are interpreted to reflect exchange with meteoric waters at low temperatures of <50 °C (Fig. 5.2; Heaton, 1976; Magaritz and Taylor, 1974; Nuriel et al., 2009; Sheppard, 1980). As some of the Troodos Mantle Sequence samples yield very high $\delta^{18}O$ values (+10.3 to +14.1 ‰), it has been proposed that these have been modified by Messinian evaporites, evolving the serpentinising fluids to isotopically heavier values (Fig. 5.2; Magaritz and Taylor, 1974; Sheppard, 1980).

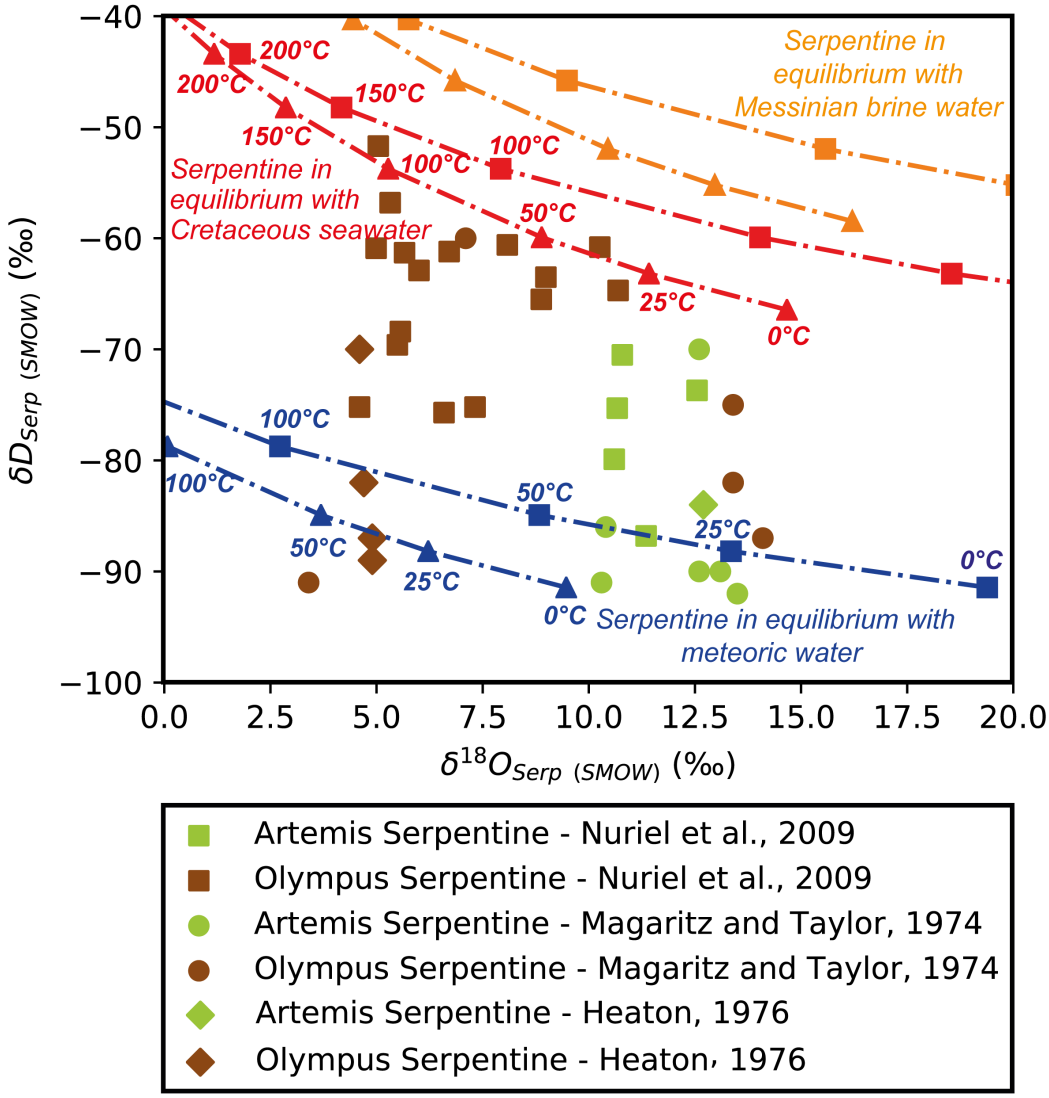

Figure 5.2: Oxygen and hydrogen stable isotope plot of published serpentine measurements (Heaton, 1976; Magaritz and Taylor, 1974; Nuriel et al., 2009). Troodos Mantle Sequence values are separated based on sample location either from the Artemis or Olympus Diapirs. Calculated serpentine oxygen and hydrogen stable isotope values in equilibrium with Cyprus meteoric water ($\delta^{18}O$ -7 ‰; δD -35 ‰; e.g., Boronina et al., 2005), Cretaceous seawater ($\delta^{18}O$ -1 ‰; δD -7 ‰; e.g., Heaton and Sheppard, 1977), and Messinian brine water ($\delta^{18}O$ +0.6 ‰; δD +1.1 ‰; e.g., Evans et al., 2015) are shown. Triangles represent calculated serpentine values in equilibrium using empirical oxygen isotope fractionation factors from Wenner and Taylor (1971) and hydrogen isotope fractionation factors from Saccocia et al. (2009b). Squares represent calculated serpentine values in equilibrium using semi-empirical oxygen isotope fractionation factors from Zheng (1993) and empirical hydrogen isotope fractionation factors from Saccocia et al. (2009).

5.3 Methods

5.3.1 Field sampling and sample preparation

A total of 100 bulk rock and vein samples were collected from the Troodos Massif, Cyprus. Samples were prepared at the National Oceanography Centre Southampton (NOCS), University of Southampton. Samples were sawn to remove surficial weathering horizons and grinded to remove contamination from the saw blade. Samples were then washed and ultra-sonicated in Milli-Q (18.2 MΩ H_2O) water and left to dry overnight in an oven at 65 °C. After drying, samples were crushed using a manual iron fly-press, with samples wrapped in paper between plastic chopping boards to avoid trace metal contamination. Samples were then powdered using a chrome-steel jar mill in a Rocklabs grinder.

Progressive leaching experiments were undertaken on weighed (0.5 to 3 g) aliquots of Troodos Mantle Sequence rock powders. The initial leaching step was the addition of a 10 % ultra-pure acetic acid solution to rock powders, which was left for 48 hours at room-temperature and shaken periodically. Samples were then centrifuged with the leachate removed, dried down, and appropriately diluted in 3 % thermally distilled HNO_3. A 3M HCl solution was added to the leached powders and left for 48 hours at room-temperature. Samples were then centrifuged, and the 3M HCl leachate removed, dried down, and appropriately diluted in 3 % thermally distilled HNO_3. 200 mg of the remaining residues were dissolved using a standard HF-HNO_3 digestion in two separate (100 mg each) pots. In addition, the untreated original bulk rock powders were dissolved following the same manner as bulk residues.

5.3.2 Major and Trace Elements

Rock and vein trace element concentrations were measured by inductively coupled plasma-source mass spectrometry (ICP-MS; Thermo X-Series II) at the National Oceanography Centre Southampton (NOCS), University of Southampton. For the majority of elements precision and accuracy were better than ± 5 %RSD and ± 10 % respectively (Table 4.2).

Rock and vein major element concentrations were also measured by inductively coupled plasma optical emission spectrometry (ICP-OES; Thermo Scientific iCap 6000 series) at the National Oceanography Centre Southampton (NOCS). For the majority of elements precision and accuracy were better than ± 5 %RSD and ± 10 % respectively (Table 4.2).

5.3.3 $^{87}Sr/^{86}Sr$ determination

Due to the low Sr concentrations of the rock samples, an aliquot of dissolved rock equivalent to ~500 ng of Sr (100 to 450 mg of rock) was dried down and redissolved in 2.2M HCl onto a 7 mL cation exchange column filled with BioRad AG50W-X12 cation exchange resin to elute high concentration major elements (e.g., Mg, Fe, Si). After passing through the column, samples were collected and dried down and redissolved in 3M HNO_3 (samples with Ba/Sr >1 were redissolved in 8M HNO_3) and Sr was separated using strontium spec columns (following Harris et al., 2015), with samples subdivided before digestion combined into a single Sr separated sample. Total combined blanks of the process were <350 pg. Strontium isotopic compositions were analysed using a ThermoFisher Scientific TritonPlus TIMS at the University of Southampton. Standard NBS987 was measured as an external standard. The mean value of NBS987 (n=26) throughout the analytical period was $^{87}Sr/^{86}Sr$ = 0.710243 ± 0.000024 (2σ). Internal precision was monitored by measuring 150 ratios per sample and the error of each measurement is reported as 2 standard errors (±2SE).

5.3.4 *In situ* $\delta^{11}B$ determination

Boron isotope analysis through laser ablation was performed at the University of Southampton using a Neptune Plus MC-ICP mass spectrometer equipped with nine Faraday cup detectors and a central ion counter, which has a Retarding Potential Quadrupole lens. A 193 nm Excimer laser ablation system (New Wave Research) with a TwoVol2 ablation cell (Elemental Scientific Lasers, Bozeman, MT, USA) is coupled to the Neptune Plus MC-ICP-MS.

Prior to analysis, powdered standards UB-N and BCR-2 were pressed into pellets using a manual hydraulic press under a pressure equivalent to a mass of 10 T over a period of 30 minutes. An additional standard BCR2-G was mounted in epoxy resin and polished. Polished thick sections (~300 μm) were prepared from sawn and grinded samples at the University of Southampton Rock Preparatory Laboratories. Tuning protocols for the LA-MC-ICP-MS method were designed to achieve a balance between maximum sensitivity and precision. Typical operating parameters for the laser ablation system were a beam area of 50 x 150 μm, laser power at 50 %, repetition rate of 50 Hz, raster ablation mode tracking of 10 μm/s, and a laser power density of ~6.7 J/cm^2. Prior to the acquisition of data, samples and standards were pre-ablated at reduced power (20 %; laser fluence ~2.5 J/cm^2), a lower repetition rate (10 Hz), and a faster raster ablation mode (200 μm/s) to remove any contaminants from the surface of the prepared polished thick section. Acquisition of reference materials and samples typically integrate ~100 cycles, manifesting as ~1 mm in length on the surface of the thick sections sample. Samples were run with a forward and

backward ablation, resulting in a total ~2 mm ablated distance. Gas flow rates during analyses were typically: 750 ml/minute for He, 17 ml/minute for N, and 1.035 ml/minute for Ar. An on-peak gas blank was analysed before and after ablation, both 40 seconds duration, with 24 seconds allowed for sample wash-out prior to the latter. Dynamic blank corrections were applied cycle by cycle assuming a linear relationship between the preceding and succeeding blank measurements. Instrumental mass bias was corrected by sample-standard bracketing with glass reference material BCR-2G and using the reference value $^{11}B/^{10}B$ of 4.035, $\delta^{11}B$ -3.83 ‰ (Kimura et al., 2016). Typically, two analyses of BCR-2G would bracket an analysis of reference serpentinite UB-N pellet with <20 minutes ablation time between analyses of BCR-2G. Data was evaluated offline with cycles falling outside of 3σ of the mean removed. Integration time of the instrument was set to ~2 seconds per cycle.

The mean internal precision (2 SE) of the pressed powder pellet reference materials UB-N and BCR-2 were ± 0.58 ‰ and ± 1.33 ‰ respectively. The mean $\delta^{11}B$ values of UB-N and BCR-2 were +13.45 ± 2 ‰ (2σ, n=20) and -5.50 ± 2.20 ‰ (2σ, n=12), resulting in mean inaccuracies ($\Delta\delta^{11}B$, defined as $\delta^{11}B_{Reported} - \delta^{11}B_{Laser}$; e.g., Standish et al., 2019) of 0.35 ‰ for UB-N and -0.40 ‰ for BCR-2 (Table 5.1).

Table 5.1: *$\delta^{11}B$ Precision and accuracy table for LA-MC-ICP-MS and LA-ICP-MS*

	$\delta^{11}B$ (‰) Reference Value	*$\delta^{11}B$ (‰) This study*	*$\Delta\delta^{11}B$*	*B (μg/g) Reference Value*	*B (μg/g) This study*	*ΔB*
UB-N (pellet)	**+13.1 ‰** (Gangjian et al., 2013)	**+13.5 ± 2 ‰** (2σ, n=20)	**+0.4 ‰**	**140 µg/g** (Govindaraju, 1995)	**136.4 ± 8.4 µg/g** (2σ, n=80)	**3.6 µg/g**
BCR-2 (pellet)	**-5.9 ‰** (Gangjian et al., 2013)	**-5.5 ± 2.2 ‰** (2σ, n=12)	**-0.4 ‰**	**4.3 ± 3.9 µg/g** (2σ; n=7; compiled (Jochum et al., 2005)	-	-
BCR-2G (glass)	**-3.8 ‰** (Kimura et al., 2016)	-	-	**8 ± 8.1 µg/g** (2σ; n=34; compiled Jochum et al., 2005)	**2.7 ± 1.2 µg/g** (2σ, n=80)	**5.3 µg/g**

5.3.5 *In situ* B concentration determination and elemental mapping

In situ boron concentrations were determined using the laser ablation system coupled to a Thermo Element 2 ICP-MS. Typical operating parameters for the laser ablation system were a beam area of 50 x 150 μm, repetition rate of 30 Hz, raster ablation mode tracking of 10 μm/s, and a laser power density of ~6.7 J/cm^2. Prior to the acquisition of data, samples and standards were pre-ablated at reduced power (20 %), lower repetition rate (10 Hz), and a faster raster ablation mode (200 μm/s) to remove any contaminants from the surface of the prepared polished thick section. The integration time was 2 seconds per cycle. Gas flow rates during analyses were typically: 800 ml/minute for He, 4 ml/minute for N, and 0.6 ml/minute for Ar. Data was evaluated offline and was both manually dynamic blank corrected, and drift corrected. The mean internal precision (2 SE) of the reference materials UB-N and BCR-2G for boron concentration determination were ± 4.39 μg/g and ± 0.35 μg/g respectively. The mean determined B concentrations of UB-N and BCR-2G were 136.40 ± 8.43 μg/g (2σ, n=80) and 2.65 ± 1.21 μg/g (2σ, n=80) respectively, resulting in mean inaccuracies (ΔB, defined as $B_{Reported}$ - B_{Laser}) of 3.59 μg/g for UB-N and 5.31 μg/g for BCR-2G (Table 5.1). However, there is a large range in reported concentrations for BCR-2G, ranging from 3.29 to 22 μg/g (Jochum et al., 2005), resulting in respective inaccuracies of 0.64 μg/g and 19.35 μg/g for BCR-2G.

During elemental mapping, the laser ablation system was coupled to an Agilent 8900 Triple Quadrupole ICP-MS. Typical operating parameters for the laser ablation system were a beam area of 10 x 10 μm, repetition rate of 50 Hz, raster ablation mode tracking of 20 μm/s, and a laser power density of ~10 J/cm^2. Prior to the acquisition of data, samples and standards were pre-ablated at reduced power (20 %), lower repetition rate (20 Hz), and a faster raster ablation mode (200 μm/s) to remove any contaminants from the surface of the polished thick section. The Agilent ICP-MS acquisition time was ~0.375 seconds per cycle. Gas flow rates during analyses were typically: 800 ml/minute for He, 4 ml/minute for N, and 0.6 ml/minute for Ar. The area mapped was 3336 x 3000 μm, requiring ~18 hours of instrument acquisition time.

5.4 Analytical Results

Radiogenic strontium and stable *in situ* boron isotopic compositions, and trace element concentrations of whole-rocks, serpentine veins, cohesive fault rocks, and incohesive serpentinite breccias are reported in Table 5.2. Trace element concentrations and radiogenic strontium isotopic compositions from each step of a progressive leaching experiment are reported in Table 5.3; Table 5.4; Table 5.5. Whole rock and progressive leaching analytical results are summarised in Table 5.6.

Table 5.2: Analytical results of whole-rocks, serpentine veins, cohesive fault rocks, and incohesive serpentinite breccias.

Sample	Location	Sample Type	$^{87}Sr/^{86}Sr$	2SE (1x10^6)	$\delta^{11}B$	±2SE	B (µg/g)	±2SE	Mg (wt.%)	Fe (wt.%)	Mg#	Ca (wt.%)	Na (µg/g)	K (µg/g)	Li (µg/g)	Sc (µg/g)
AE1	Olympus	Olympus Bulk Rock	-	-	-	-	-	-	22.4	5.42	80.5	0.27	155	9.73	1.03	5.54
AG1	Olympus	Olympus Bulk Rock	0.705562	14	-	-	-	-	22.1	5.37	80.4	0.58	146	5.90	2.86	7.51
AG2	Olympus	Olympus Bulk Rock	0.705575	20	-	-	58.18	2.25	21.7	5.33	80.3	0.59	155	11.8	3.24	7.74
AH1	Olympus	Olympus Bulk Rock	0.705354	13	8.58	0.86	36.23	0.69	22.5	5.53	80.3	0.48	138	38.9	1.64	8.23
AH2	Olympus	Olympus Bulk Rock	0.706070	37	12.79	2.03	11.24	2.12	23.8	5.31	81.8	0.16	252	1.72	1.48	4.01
AJ2	Olympus	Olympus Bulk Rock	0.709096	49	-	-	-	-	18.4	4.37	80.8	0.20	32.5	20.9	0.94	4.63
CX1	Olympus	Olympus Bulk Rock	0.707261	34	-	-	6.83	0.48	22.5	5.92	79.2	0.08	82.8	9.65	1.50	3.53
PP2	Olympus	Olympus Bulk Rock	0.706380	21	-	-	26.29	0.52	20.6	5.32	79.5	0.54	87.6	8.41	1.74	11.6
CJ1	Olympus	Olympus Bulk Rock	0.706495	12	-	-	10.23	0.49	23.1	5.76	80.0	0.09	119	1.56	0.60	3.25
AJ1	Olympus Margin	Antigorite vein	-	-	6.91	0.14	9.80	0.18	22.2	1.76	92.7	0.01	81.6	7.30	0.30	0.24
CO1B	Olympus Margin	Olympus Margin	0.708630	11	-	-	2.50	0.55	18.4	4.73	79.6	2.45	bd	60.7	1.49	3.03

Sample	Location	Sample Type	$^{87}Sr/^{86}Sr$	2SE (1x10^6)	$\delta^{11}B$	±2SE	B (µg/g)	±2SE	Mg (wt.%)	Fe (wt.%)	Mg#	Ca (wt.%)	Na (µg/g)	K (µg/g)	Li (µg/g)	Sc (µg/g)
CW1	Olympus Margin	Olympus Margin	0.709151	17	-	-	10.06	2.11	22.2	2.26	90.7	0.03	66.0	32.6	1.77	7.36
CO2	Olympus Margin	Olympus Margin	-	-	-	-	2.91	0.59	nd	nd	nd	nd	nd	nd	0.86	1.51
CO2R	Olympus Margin	Olympus Margin	0.708845	14	-	-	-	-	20.8	3.90	84.2	0.23	bd	45.8	0.78	1.51
CP1	Olympus Margin	Olympus Margin	0.708590	13	-	-	-	-	20.7	4.50	82.2	0.07	51.9	53.2	1.61	3.45
CB4	Olympus Margin	Olympus Margin	-	-	-	-	-	-	18.3	7.30	71.5	1.94	199	18.5	0.54	14.7
CO1	Olympus Margin	Olympus Margin	-	-	-	-	-	-	20.4	7.59	72.9	0.07	16.1	6.75	0.17	4.76
CO3	Olympus Margin	Olympus Margin	-	-	-	-	-	-	16.5	5.67	74.4	3.49	180	40.5	1.14	27.7
CB2Y	Olympus Margin	Olympus Margin	0.705838	13	-	-	-	-	5.44	3.77	59.1	19.58	73.3	17.2	3.10	1.48
CQ2	Olympus Margin	Olympus Margin	-	-	-	-	-	-	20.1	3.11	86.6	1.46	97.7	40.8	0.39	2.79
CB1Y	Olympus Margin	Olympus Margin	-	-	-	-	-	-	18.3	7.24	71.7	1.55	140	13.1	0.49	12.9
CJ2	Olympus Margin	Olympus Margin	-	-	-	-	-	-	20.2	2.58	88.7	0.80	66.8	38.7	0.32	3.37
CB3	Olympus Margin	Olympus Margin	-	-	-	-	-	-	19.4	3.50	84.7	1.95	267	42.4	0.90	3.86
CK4	Olympus Margin	Olympus Margin	-	-	-	-	-	-	18.3	5.14	78.1	0.03	133	36.7	0.93	28.7

Sample	Location	Sample Type	$^{87}Sr/^{86}Sr$	2SE (1x10^6)	$\delta^{11}B$	±2SE	B (µg/g)	±2SE	Mg (wt.%)	Fe (wt.%)	Mg#	Ca (wt.%)	Na (µg/g)	K (µg/g)	Li (µg/g)	Sc (µg/g)
CI1	Olympus Margin	Olympus Margin	-	-	-	-	-	-	18.7	5.91	76.0	0.03	9.23	59.8	0.51	4.99
BB1	Limassol Forest Complex	Limassol Forest Complex	0.706650	12	45.20	1.92	12.74	4.93	19.1	7.60	71.5	1.79	1,060	81.0	0.73	11.8
BB2	Limassol Forest Complex	Limassol Forest Complex	0.708682	25	-	-	-	-	19.3	6.97	73.5	0.11	154	28.1	0.18	8.26
BB3	Limassol Forest Complex	Limassol Forest Complex	0.708679	13	-	-	-	-	19.8	7.94	71.4	0.09	99.1	34.1	0.31	8.09
BC1	Limassol Forest Complex	Limassol Forest Complex	-	-	-	-	-	-	21.3	5.35	79.9	0.02	159	3.27	0.02	5.97
BC2	Limassol Forest Complex	Limassol Forest Complex	-	-	-	-	-	-	9.53	11.06	46.3	4.02	52.0	16.4	2.42	41.8
BC3	Limassol Forest Complex	Limassol Forest Complex	-	-	-	-	-	-	13.5	3.56	79.2	6.76	194	17.3	0.90	10.6
BC4	Limassol Forest Complex	Limassol Forest Complex	-	-	-	-	-	-	8.58	9.21	48.2	5.88	117	29.2	3.09	50.1
BD1	Limassol Forest Complex	Limassol Forest Complex	0.708587	13	-	-	-	-	21.1	5.81	78.4	0.03	183	10.1	0.78	8.36
BD2	Limassol Forest Complex	Limassol Forest Complex	0.708661	32	-	-	-	-	21.7	5.01	81.2	0.02	45.2	5.41	0.15	6.60
BD3	Limassol Forest Complex	Limassol Forest Complex	0.708549	21	-	-	-	-	19.2	5.69	77.1	0.31	54.3	26.1	1.06	13.2
AM3	Gabbros & Cumulate Ultramafic Rocks	Gabbros	0.705771	16	-	-	-	-	10.1	4.10	71.2	8.86	746	63.2	284	32.0

Sample	Location	Sample Type	$^{87}Sr/^{86}Sr$	2SE (1x10^6)	$\delta^{11}B$	±2SE	B (µg/g)	±2SE	Mg (wt.%)	Fe (wt.%)	Mg#	Ca (wt.%)	Na (µg/g)	K (µg/g)	Li (µg/g)	Sc (µg/g)
PP4	Gabbros & Cumulate Ultramafic Rocks	Gabbros	0.703739	12	-	-	-	-	15.7	8.08	66.0	4.54	1,485	51.6	1.18	24.1
AS5	Gabbros & Cumulate Ultramafic Rocks	Gabbros	0.704737	27	-	-	-	-	4.52	2.82	61.6	11.29	6,021	756	7.28	20.1
DF1	Gabbros & Cumulate Ultramafic Rocks	Gabbros	-	-	-	-	-	-	17.4	6.89	71.6	6.38	273	22.2	1.43	20.6
PP5	Gabbros & Cumulate Ultramafic Rocks	Gabbros	0.704744	11	-	-	-	-	7.49	3.78	66.5	10.26	3,440	227.1	1.77	39.9
CE1	Gabbros & Cumulate Ultramafic Rocks	Gabbros	0.705790	12	-	-	-	-	nd	nd	nd	nd	nd	nd	8.41	38.6
AA3	Artemis	Serpentine vein	0.707716	81	7.08	0.94	3.05	0.09	49.3	9.24	84.2	0.68	bd	12.3	1.66	0.22
BA1A	Artemis	Serpentine vein	0.707177	12	18.41	0.98	3.78	0.17	20.0	5.09	79.7	1.49	61.5	4.98	1.95	2.97
CU5	Artemis	Serpentine vein	0.708375	14	-	-	3.49	0.36	21.3	3.55	85.7	0.02	48.9	11.6	1.14	0.04
AN4	Artemis	Serpentine vein	0.708417	14	-	-	-	-	21.9	3.85	85.0	0.15	157	18.9	1.30	2.40
AA4X	Artemis	Serpentine vein	-	-	-	-	-	-	21.1	2.85	88.1	0.03	124	8.53	1.14	0.28
AN5	Artemis	Serpentine vein	-	-	-	-	-	-	20.3	5.47	78.7	1.59	37.0	21.2	1.75	1.17
AW2	Artemis	Serpentine vein	0.707991	22	-	-	-	-	21.3	4.32	83.2	0.01	bd	8.08	1.16	1.71
AW3	Artemis	Serpentine vein	-	-	-	-	-	-	20.2	4.52	81.7	0.02	13.9	3.78	1.35	3.82
AY2	Artemis	Serpentine vein	-	-	-	-	-	-	21.1	3.45	86.0	0.05	148	12.2	0.39	1.36
AA4Y	Artemis	Serpentine vein	-	-	-	-	-	-	20.8	4.15	83.4	0.06	35.6	29.2	0.90	1.04

Sample	Location	Sample Type	$^{87}Sr/^{86}Sr$	2SE (1x10^6)	$\delta^{11}B$	±2SE	B (µg/g)	±2SE	Mg (wt.%)	Fe (wt.%)	Mg#	Ca (wt.%)	Na (µg/g)	K (µg/g)	Li (µg/g)	Sc (µg/g)
AA4-1	Artemis	Serpentine vein	-	-	-	-	-	-	20.6	3.85	84.2	0.30	77.9	7.35	2.00	1.29
AP1	Artemis	Serpentine vein	-	-	-	-	-	-	20.0	3.49	85.1	0.04	93.1	14.5	1.01	1.01
CR1	Artemis	Chrysotile vein	0.706909	13	-	-	-	-	22.1	3.65	85.8	0.04	17.8	6.90	2.66	0.93
DI1A	Artemis	Chrysotile vein	-	-	-	-	-	-	nd	nd	nd	nd	nd	nd	3.98	0.89
AX1	Artemis	Chrysotile vein	-	-	-	-	-	-	nd	nd	nd	nd	nd	nd	2.38	1.98
CU3	Artemis	Chrysotile vein	0.707677	14	-	-	13.87	0.86	19.7	3.65	84.3	0.07	13.3	8.25	3.45	0.14
AZ1	Artemis	Chrysotile vein	-	-	-	-			20.7	2.71	88.4	0.05	67.1	93.4	1.49	0.81
DI1	Artemis	Chrysotile vein	0.707376	26	-	-	-	-	21.8	3.67	85.6	0.02	109	20.1	12.9	1.76
DI3	Artemis	Chrysotile vein	-	-	-	-	-	-	20.6	5.14	80.0	0.10	20.7	30.0	1.34	5.00
CR1	Artemis	Chrysotile vein	-	-	-	-	-	-	22.1	3.65	85.8	0.04	17.8	6.90	2.66	0.93
DI5	Artemis	Chrysotile vein	-	-	-	-	-	-	20.6	3.31	86.2	0.04	152	10.1	4.62	0.67
DI2	Artemis	Chrysotile vein	0.707116	13	-	-	-	-	18.3	3.13	85.4	0.07	2,331	127	14.7	1.29
DH1V	Artemis	Incohesive Artemis Breccia	-	-	-	-	-	-	14.8	8.03	64.8	6.74	104	6.96	1.65	2.55
BZ2	Artemis	Incohesive Artemis Breccia	-	-	-	-	-	-	12.8	2.83	81.9	0.13	22.7	2.19	0.82	5.50
BZ1	Artemis	Incohesive Artemis Breccia	0.705884	20	-	-	-	-	20.5	4.75	81.2	0.04	42.5	1.38	0.22	7.22

Sample	Location	Sample Type	$^{87}Sr/^{86}Sr$	2SE (1x10^6)	$\delta^{11}B$	±2SE	B (µg/g)	±2SE	Mg (wt.%)	Fe (wt.%)	Mg#	Ca (wt.%)	Na (µg/g)	K (µg/g)	Li (µg/g)	Sc (µg/g)
DC2H	Artemis	Incohesive Artemis Breccia	-	-	-	-	-	-	17.3	7.23	70.5	4.37	100	3.51	1.94	8.36
AK1	Artemis	Incohesive Artemis Breccia	-	-	-	-	-	-	21.1	4.53	82.3	0.27	133	2.27	0.87	5.76
AB4	Artemis	Incohesive Artemis Breccia	-	-	-	-	-	-	20.5	3.54	85.3	0.65	148	80.5	2.21	2.44
AB3	Artemis	Incohesive Artemis Breccia	-	-	-	-	-	-	20.4	4.17	83.0	0.09	65.8	14.6	2.15	7.02
AN1	Artemis	Incohesive Artemis Breccia	-	-	-	-	-	-	18.0	6.58	73.2	3.08	98.9	4.20	2.08	4.51
AI1	Artemis	Incohesive Artemis Breccia	-	-	-	-	-	-	nd	nd	nd	nd	nd	nd	0.27	5.56
AS3	Artemis	Incohesive Artemis Breccia	0.706077	20	-	-	24.69	4.14	20.5	4.52	81.9	0.51	bd	4.27	1.76	19.8
AU1	Artemis	Incohesive Artemis Breccia	-	-	-	-	-	-	19.4	4.02	82.8	0.08	76.2	17.8	1.13	9.29
AN3	Artemis	Incohesive Artemis Breccia	-	-	-	-	-	-	21.0	4.99	80.8	0.60	bd	12.2	3.55	7.45
AS2	Artemis	Incohesive Artemis Breccia	-	-	-	-	-	-	22.5	5.30	81.0	0.39	bd	8.01	1.23	8.47
BM1	Artemis	Cohesive Artemis Fault Rock	0.707818	12	-	-	41.31	7.72	20.4	4.79	81.0	0.76	bd	7.39	1.55	10.7
BN1	Artemis	Cohesive Artemis Fault Rock	0.706344	12	-	-	6.03	1.73	9.41	4.91	65.7	7.70	3,237	888	129	40.9

Sample	Location	Sample Type	$^{87}Sr/^{86}Sr$	2SE (1x10^6)	$\delta^{11}B$	±2SE	B (µg/g)	±2SE	Mg (wt.%)	Fe (wt.%)	Mg#	Ca (wt.%)	Na (µg/g)	K (µg/g)	Li (µg/g)	Sc (µg/g)
DB2	Artemis	Cohesive Artemis Fault Rock	-	-	-	-	-	-	19.1	6.23	75.4	0.19	167	20.5	35.0	5.65
DE1B	Artemis	Cohesive Artemis Fault Rock	-	-	-	-	-	-	17.9	3.85	82.3	1.24	104	6.06	6.17	2.23
DE2BZ	Artemis	Cohesive Artemis Fault Rock	0.705820	29	-	-	-	-	15.7	3.73	80.8	8.41	101	7.72	13.9	1.76
DB1	Artemis	Cohesive Artemis Fault Rock	-	-	-	-	-	-	17.1	5.11	77.0	0.22	126	20.2	16.0	12.3
BO3	Artemis	Cohesive Artemis Fault Rock	0.705657	12	-	-	92.20	57.09	18.0	2.51	87.8	8.49	2,176	119	29.8	1.45
BO1	Artemis	Cohesive Artemis Fault Rock	0.705681	12	-	-	144.34	24.84	17.5	5.47	76.2	7.17	436	20.4	10.8	4.28
BO2	Artemis	Cohesive Artemis Fault Rock	-	-	-	-	-	-	20.8	2.66	88.6	0.03	142	42.2	0.36	5.85
AA4-2	Artemis	Artemis Bulk Rock Halo	0.706794	33	7.49	0.79	27.60	0.67	19.1	6.25	75.4	2.04	30.1	7.50	2.56	7.97
AA4-4	Artemis	Artemis Bulk Rock Halo	-	-	-	-	-	-	18.1	6.91	72.4	3.20	3.28	7.28	2.95	10.5
AO3C	Artemis	Artemis Bulk Rock Halo	0.708531	11	-	-	35.26	1.42	20.0	5.70	77.9	0.82	193	22.1	3.93	10.2
BA1B	Artemis	Artemis Bulk Rock Halo	0.706930	17	15.52	0.65	28.88	2.00	18.8	5.43	77.6	1.46	31.5	6.10	2.88	8.91
CU4	Artemis	Artemis Bulk Rock Halo	0.707253	13	-	-	25.89	2.32	18.5	5.43	77.4	2.46	130	6.28	2.01	9.79

Sample	Location	Sample Type	$^{87}Sr/^{86}Sr$	2SE (1x10^6)	$\delta^{11}B$	±2SE	B (µg/g)	±2SE	Mg (wt.%)	Fe (wt.%)	Mg#	Ca (wt.%)	Na (µg/g)	K (µg/g)	Li (µg/g)	Sc (µg/g)
CU2	Artemis	Artemis Bulk Rock Halo	0.707436	11	-	-	43.11	2.82	19.5	4.84	80.1	0.94	53.1	3.83	2.14	9.50
BA1C	Artemis	Artemis Bulk Rock	0.706355	13	11.22	0.56	23.70	0.56	19.5	5.09	79.3	1.26	22.6	6.38	2.70	8.26
AN2	Artemis	Artemis Bulk Rock	-	-	-	-	-	-	21.9	5.46	80.0	0.18	303	29.1	4.07	7.16
AO2	Artemis	Artemis Bulk Rock	0.705301	16	-	-	75.77	10.36	21.6	5.56	79.5	1.25	188	11.7	5.01	9.61
AR1	Artemis	Artemis Bulk Rock	0.707782	11	-	-	30.48	1.71	20.6	4.50	82.1	0.18	52.1	10.4	4.20	8.75
CU1	Artemis	Artemis Bulk Rock	0.707434	12	-	-	38.37	4.45	19.8	4.89	80.2	0.30	bd	7.60	2.27	9.18
AR2	Artemis	Artemis Bulk Rock	0.705602	14	-	-	79.54	6.35	20.2	5.29	79.2	0.12	84.8	0.28	2.18	8.73
AP2	Artemis	Artemis Bulk Rock	0.708472	18	-	-	-	-	20.3	4.53	81.8	0.10	19.2	20.8	1.68	7.24
AQ2	Artemis	Artemis Bulk Rock	0.708233	13	-	-	-	-	19.2	5.29	78.4	1.00	179	10.2	3.49	10.1
PP1	Artemis	Artemis Bulk Rock	0.707793	13	-	-	16.68	0.65	19.2	5.17	78.8	2.06	105	7.01	4.85	28.6

Table 5.2: continued

Sample	Location	Sample Type	Ti (µg/g)	V (µg/g)	Cr (µg/g)	Co (µg/g)	Ni (µg/g)	Cu (µg/g)	Zn (µg/g)	Rb (ng/g)	Sr (ng/g)	Y (ng/g)	Zr (ng/g)	Nb (ng/g)
AE1	Olympus	Olympus Bulk Rock	15.2	14.5	655	93.7	2,000	2.17	29.6	236	133	21	47	4
AG1	Olympus	Olympus Bulk Rock	14.3	25.9	1,240	87.0	1,882	4.91	28.9	154	2,674	19	99	1
AG2	Olympus	Olympus Bulk Rock	14.9	25.3	1,233	87.6	1,863	9.21	29.6	171	2,687	18	13	1
AH1	Olympus	Olympus Bulk Rock	12.9	24.6	1,007	91.8	1,978	8.90	30.4	107	1,158	10	68	5

Sample	Location	Sample Type	Ti (µg/g)	V (µg/g)	Cr (µg/g)	Co (µg/g)	Ni (µg/g)	Cu (µg/g)	Zn (µg/g)	Rb (ng/g)	Sr (ng/g)	Y (ng/g)	Zr (ng/g)	Nb (ng/g)
AH2	Olympus	Olympus Bulk Rock	5.24	6.36	334	110	2,530	4.59	25.0	82	694	bd	34	5
AJ2	Olympus	Olympus Bulk Rock	12.3	10.2	415	83.6	1,910	2.77	23.6	189	155	1	22	2
CX1	Olympus	Olympus Bulk Rock	8.42	6.91	1,105	109	1,901	0.78	31.8	79	201	24	43	bd
PP2	Olympus	Olympus Bulk Rock	47.3	47.4	2,249	86.8	1,739	10.9	30.8	182	1,044	61	36	bd
CJ1	Olympus	Olympus Bulk Rock	9.34	5.92	933	103	2,265	0.46	26.5	28	619	28	60	bd
AJ1	Olympus Margin	Antigorite vein	1.97	4.95	1.09	76.3	556	0.99	21.8	12	276	20	64	bd
CO1B	Olympus Margin	Olympus Margin	37.8	25.4	774	56.8	512	1.20	30.2	185	5,072	285	97	8
CW1	Olympus Margin	Olympus Margin	69.0	19.8	224	144	3,508	20.9	46.4	407	2,956	455	911	120
CO2	Olympus Margin	Olympus Margin	40.1	22.9	19.5	61.8	143	3.05	32.8	111	2,701	259	107	8
CO2R	Olympus Margin	Olympus Margin	44.1	23.9	35.2	63.2	157	3.12	33.4	146	3,262	333	191	16
CP1	Olympus Margin	Olympus Margin	26.2	9.15	355	82.0	1,161	1.75	31.6	102	2,334	267	111	13
CB4	Olympus Margin	Olympus Margin	342	73.7	1,443	102	1,230	2.79	22.6	8	1,095	2,976	2,379	192
CO1	Olympus Margin	Olympus Margin	25.0	13.3	1,632	129	2,135	1.28	37.5	16	1,948	87	59	4
CO3	Olympus Margin	Olympus Margin	232	90.4	4,269	66.9	808	4.14	31.5	138	3,779	798	190	20
CB2Y	Olympus Margin	Olympus Margin	567	41.0	4.28	21.9	51.8	0.54	36.9	48	4,309	3,451	17,785	423
CQ2	Olympus Margin	Olympus Margin	13.4	6.82	1,075	88.8	2,034	1.04	31.7	105	15,333	60	121	12
CB1Y	Olympus Margin	Olympus Margin	236	59.8	2,467	92.8	1,069	1.80	22.1	48	1,212	1,570	918	64
CJ2	Olympus Margin	Olympus Margin	13.2	5.26	564	93.4	2,229	1.11	22.7	101	6,596	63	127	15
CB3	Olympus Margin	Olympus Margin	144	44.6	219	40.9	511	1.31	32.1	181	1,078	1,912	2,578	118

Sample	Location	Sample Type	Ti (µg/g)	V (µg/g)	Cr (µg/g)	Co (µg/g)	Ni (µg/g)	Cu (µg/g)	Zn (µg/g)	Rb (ng/g)	Sr (ng/g)	Y (ng/g)	Zr (ng/g)	Nb (ng/g)
CK4	Olympus Margin	Olympus Margin	988	175	684	47.1	276	9.56	61.8	182	1,038	2,299	2,398	447
CI1	Olympus Margin	Olympus Margin	43.1	15.8	1,506	105	1,828	11.2	29.6	305	1,471	265	778	80
BB1	Limassol Forest Complex	Limassol Forest Complex	266	38.6	928	84.5	790	12.8	43.5	95	3,309	1,417	2,146	119
BB2	Limassol Forest Complex	Limassol Forest Complex	81.3	31.4	1,398	97.3	1,388	4.60	31.7	55	3,656	476	382	71
BB3	Limassol Forest Complex	Limassol Forest Complex	74.0	31.5	1,015	103	1,457	1.10	33.1	58	3,776	454	319	71
BC1	Limassol Forest Complex	Limassol Forest Complex	16.3	18.3	1,386	80.0	2,499	5.25	13.5	12	771	70	26	3
BC2	Limassol Forest Complex	Limassol Forest Complex	3,433	355	292	103	260	1.46	20.8	24	7,330	15,008	13,901	5,181
BC3	Limassol Forest Complex	Limassol Forest Complex	408	66.9	1,310	42.4	957	0.86	5.13	21	1,798	3,638	2,104	663
BC4	Limassol Forest Complex	Limassol Forest Complex	3,405	361	228	81.3	272	1.57	17.9	23	18,034	18,561	15,053	4,400
BD1	Limassol Forest Complex	Limassol Forest Complex	25.0	27.5	1,203	104	2,378	0.91	22.0	13	909	57	72	4
BD2	Limassol Forest Complex	Limassol Forest Complex	42.8	25.4	1,612	70.7	1,922	1.03	23.9	7	555	473	160	20
BD3	Limassol Forest Complex	Limassol Forest Complex	95.9	63.4	2,566	103	1,955	2.77	38.9	33	1,390	401	171	63
AM3	Gabbros & Cumulate Ultramafic Rocks	Gabbros	465	118	343	31.8	144	8.53	15.8	629	16,900	2,829	1,414	122
PP4	Gabbros & Cumulate Ultramafic Rocks	Gabbros	388	78.6	702	110	755	85.6	49.9	75	32,276	1,602	747	14
AS5	Gabbros & Cumulate Ultramafic Rocks	Gabbros	373	75.1	232	16.5	51.3	12.9	12.7	857	37,510	2,051	1,282	94
DF1	Gabbros & Cumulate Ultramafic Rocks	Gabbros	171	65.9	2,219	91.8	535	6.37	33.4	46	1,299	885	224	19

Sample	Location	Sample Type	Ti (µg/g)	V (µg/g)	Cr (µg/g)	Co (µg/g)	Ni (µg/g)	Cu (µg/g)	Zn (µg/g)	Rb (ng/g)	Sr (ng/g)	Y (ng/g)	Zr (ng/g)	Nb (ng/g)
PP5	Gabbros & Cumulate Ultramafic Rocks	Gabbros	499	147	440	35.2	128	12.3	20.9	332	36,464	2,303	643	29
CE1	Gabbros & Cumulate Ultramafic Rocks	Gabbros	545	126	1210	38.5	220	145	24.9	51.5	7531	3405	1322	75.2
AA3	Artemis	Serpentine vein	19.3	24.6	9.8	18.5	12.8	0.93	9.82	13	420	115	331	13
BA1A	Artemis	Serpentine vein	103	42.9	187	25.8	162	2.21	8.82	9	712	452	58	4
CU5	Artemis	Serpentine vein	1.36	9.88	71.9	29.5	151	1.32	13.9	21	993	160	42	4
AN4	Artemis	Serpentine vein	4.71	10.8	25.8	10.3	39.7	2.06	12.3	53	1,640	38	113	11
AA4X	Artemis	Serpentine vein	8.42	7.73	77.1	17.5	37.1	1.91	11.3	19	465	202	111	8
AN5	Artemis	Serpentine vein	38.0	18.6	50.4	17.4	38.9	1.69	14.1	20	346	130	106	8
AW2	Artemis	Serpentine vein	6.39	9.96	199	20.8	235	0.76	9.41	29	351	25	83	12
AW3	Artemis	Serpentine vein	12.3	15.7	1,303	58.1	1,419	2.67	19.4	13	561	56	26	4
AY2	Artemis	Serpentine vein	5.61	9.56	233	20.9	65.1	1.05	11.2	38	492	83	108	8
AA4Y	Artemis	Serpentine vein	28.3	22.7	28.4	23.8	23.1	0.77	13.7	124	578	149	322	45
AA4-1	Artemis	Serpentine vein	17.7	26.3	301	32.8	182	4.07	12.6	8	458	113	44	bd
AP1	Artemis	Serpentine vein	9.81	3.65	44.5	30.3	431	2.21	10.5	32	673	24	105	bd
CR1	Artemis	Chrysotile vein	33.5	15.5	213	40.9	188	0.87	13.4	29	470	139	249	7
DI1A	Artemis	Chrysotile vein	8.44	10.1	47.2	28.8	86	0.36	13.8	110	195	51	72	bd
AX1	Artemis	Chrysotile vein	7.27	5.15	111	38.3	408	2.05	11.7	24	1,738	36	101	8
CU3	Artemis	Chrysotile vein	1.88	12.7	115	45.4	307	5.05	11.9	bd	589	16	32	bd

Sample	Location	Sample Type	Ti (µg/g)	V (µg/g)	Cr (µg/g)	Co (µg/g)	Ni (µg/g)	Cu (µg/g)	Zn (µg/g)	Rb (ng/g)	Sr (ng/g)	Y (ng/g)	Zr (ng/g)	Nb (ng/g)
AZ1	Artemis	Chrysotile vein	22.4	5.48	23.3	31.8	417	1.49	8.39	404	2,167	289	647	96
DI1	Artemis	Chrysotile vein	16.1	10.1	207	39.0	316	0.67	14.4	660	277	51	55	bd
DI3	Artemis	Chrysotile vein	39.0	17.0	1,512	87.2	1,693	2.49	24.6	76	415	80	197	22
CR1	Artemis	Chrysotile vein	33.5	15.5	213	40.9	188	0.87	13.4	29	470	139	249	7
DI5	Artemis	Chrysotile vein	53.6	15.0	33.4	75.5	70.9	0.29	10.5	30	506	159	57	bd
DI2	Artemis	Chrysotile vein	16.3	14.1	215	27.2	158	0.43	21.1	439	415	61	82	bd
DH1V	Artemis	Incohesive Artemis Breccia	41.0	17.7	704	31.1	537	2.39	8.57	4	158	161	81	bd
BZ2	Artemis	Incohesive Artemis Breccia	25.5	18.7	1,109	77.7	1,495	5.99	21.1	8	450	57	49	4
BZ1	Artemis	Incohesive Artemis Breccia	18.9	20.1	1,066	97.1	1,977	6.59	19.8	4	742	44	99	bd
DC2H	Artemis	Incohesive Artemis Breccia	49.1	35.6	2,588	73.0	1,756	4.57	15.2	4	98	132	45	bd
AK1	Artemis	Incohesive Artemis Breccia	21.8	24.0	1,081	72.5	2,281	8.69	16.1	14	174	69	14	9
AB4	Artemis	Incohesive Artemis Breccia	52.8	15.1	690	46.9	625	5.19	15.7	267	9,606	183	396	46
AB3	Artemis	Incohesive Artemis Breccia	48.0	24.9	2,320	76.3	1,918	4.77	29.9	51	2,658	203	82	8
AN1	Artemis	Incohesive Artemis Breccia	20.6	31.5	1,154	66.5	1,507	4.72	12.2	8	172	68	76	bd
AI1	Artemis	Incohesive Artemis Breccia	33.1	20.9	1,364	96.4	2,015	5.99	28.2	17	280	112	121	4
AS3	Artemis	Incohesive Artemis Breccia	159	36.2	2,810	96.0	1,148	3.70	51.4	16	417	199	43	bd
AU1	Artemis	Incohesive Artemis Breccia	31.0	36.2	1,419	79.8	1,686	10.0	17.4	8	455	89	109	bd
AN3	Artemis	Incohesive Artemis Breccia	23.3	24.0	1,747	115	2,084	5.49	22.2	33	595	62	25	bd
AS2	Artemis	Incohesive Artemis Breccia	27.4	25.5	1,203	83.1	2,117	4.68	16.5	4	258	67	21	4

Sample	Location	Sample Type	Ti (µg/g)	V (µg/g)	Cr (µg/g)	Co (µg/g)	Ni (µg/g)	Cu (µg/g)	Zn (µg/g)	Rb (ng/g)	Sr (ng/g)	Y (ng/g)	Zr (ng/g)	Nb (ng/g)
BM1	Artemis	Cohesive Artemis Fault Rock	47.2	32.4	1,485	124	1,524	5.11	21.8	8	2,056	99	33	bd
BN1	Artemis	Cohesive Artemis Fault Rock	529	190	527	38.1	85.0	72.5	24.8	1,019	55,764	2,901	866	93
DB2	Artemis	Cohesive Artemis Fault Rock	50.2	20.4	1,497	104	1,078	2.68	23.8	62	937	251	197	15
DE1B	Artemis	Cohesive Artemis Fault Rock	5.95	3.10	194	30.2	872	0.34	30.5	11	1,408	22	50	4
DE2BZ	Artemis	Cohesive Artemis Fault Rock	6.21	4.20	231	53.8	1,017	0.40	14.1	33	4,954	25	45	bd
DB1	Artemis	Cohesive Artemis Fault Rock	114	48.5	2,924	72.1	737	4.40	30.4	62	780	550	199	12
BO3	Artemis	Cohesive Artemis Fault Rock	8.21	8.35	644	37.8	753	4.54	6.89	206	28,775	27	101	12
BO1	Artemis	Cohesive Artemis Fault Rock	63.1	36.4	1,747	34.6	660	7.47	5.21	40	6,088	88	60	bd
BO2	Artemis	Cohesive Artemis Fault Rock	59.6	26.5	873	111	1,751	2.34	32.3	81	1,085	1,150	565	49
AA4-2	Artemis	Artemis Bulk Rock Halo	117	43.6	1,844	113	1,817	12.3	24.8	21	997	490	284	4
AA4-4	Artemis	Artemis Bulk Rock Halo	168	59.4	2,216	91.2	2,035	14.9	20.5	22	955	852	587	9
AO3C	Artemis	Artemis Bulk Rock Halo	127	52.0	2,294	92.6	1,958	10.5	33.4	121	4,325	732	199	22
BA1B	Artemis	Artemis Bulk Rock Halo	66.2	35.4	4,060	91.9	2,039	17.4	58.6	25	1,778	679	93	4
CU4	Artemis	Artemis Bulk Rock Halo	81.3	43.3	2,457	82.6	1,952	10.9	31.3	4	1,383	433	54	4
CU2	Artemis	Artemis Bulk Rock Halo	85.6	46.8	2,632	103	2,010	14.5	47.7	11	1,957	422	33	4
BA1C	Artemis	Artemis Bulk Rock	64.1	32.3	2,246	107	1,939	16.8	19.6	16	1,392	661	94	12
AN2	Artemis	Artemis Bulk Rock	18.4	23.4	1,374	87.7	1,951	6.6	35.0	72	535	39	37	2
AO2	Artemis	Artemis Bulk Rock	114	47.6	2,076	83.6	1,772	19.9	34.9	520	5,982	720	170	3
AR1	Artemis	Artemis Bulk Rock	78.2	35.3	2,372	91.1	2,054	8.8	35.8	21	1,688	411	37	2

Sample	Location	Sample Type	Ti (µg/g)	V (µg/g)	Cr (µg/g)	Co (µg/g)	Ni (µg/g)	Cu (µg/g)	Zn (µg/g)	Rb (ng/g)	Sr (ng/g)	Y (ng/g)	Zr (ng/g)	Nb (ng/g)
CU1	Artemis	Artemis Bulk Rock	87.2	44.3	2,843	107	2,038	16.1	61.1	27	2,171	368	76	4
AR2	Artemis	Artemis Bulk Rock	89.1	41.1	3,222	92.7	1,929	9.5	57.5	9	3,331	383	21	bd
AP2	Artemis	Artemis Bulk Rock	90.4	29.0	2,412	105	2,277	23.9	26.0	64	1,681	298	129	16
AQ2	Artemis	Artemis Bulk Rock	149	51.9	2,346	88.7	1,865	12.9	35.1	32	2,584	734	88	4
PP1	Artemis	Artemis Bulk Rock	492	180	3,578	48.3	1,174	29.4	16.2	20	1,178	2,988	67	bd

Table 5.2: continued

Sample	Location	Sample Type	Sn (ng/g)	Cs (ng/g)	Ba (ng/g)	La (ng/g)	Ce (ng/g)	Pr (ng/g)	Nd (ng/g)	Sm (ng/g)	Eu (ng/g)	Gd (ng/g)	Tb (ng/g)	Dy (ng/g)
AE1	Olympus	Olympus Bulk Rock	38	113	bd	bd	5.07	0.09	bd	0.49	bd	1.21	0.49	5.87
AG1	Olympus	Olympus Bulk Rock	46	893	828	bd	bd	0.06	bd	bd	bd	0.50	0.39	4.47
AG2	Olympus	Olympus Bulk Rock	18	1,028	922	0.08	bd	bd	bd	0.43	bd	bd	0.18	3.94
AH1	Olympus	Olympus Bulk Rock	35	286	87	1.85	4.31	0.59	3.72	1.96	bd	1.51	0.75	3.88
AH2	Olympus	Olympus Bulk Rock	34	277	10	0.17	0.85	0.04	0.70	bd	bd	1.07	0.19	1.61
AJ2	Olympus	Olympus Bulk Rock	18	85	bd	bd	bd	0.09	bd	0.12	bd	1.59	0.44	3.36
CX1	Olympus	Olympus Bulk Rock	106	103	16	bd	bd	bd	bd	bd	bd	bd	bd	3.94
PP2	Olympus	Olympus Bulk Rock	16	578	117	bd	bd	bd	bd	bd	bd	bd	bd	4.04
CJ1	Olympus	Olympus Bulk Rock	60	44	bd	bd	bd	bd	bd	bd	bd	bd	bd	3.99
AJ1	Olympus Margin	Antigorite vein	60	4	320	12.0	16.0	4.00	12.0	4.00	bd	4.00	bd	4.00

Sample	Location	Sample Type	Sn (ng/g)	Cs (ng/g)	Ba (ng/g)	La (ng/g)	Ce (ng/g)	Pr (ng/g)	Nd (ng/g)	Sm (ng/g)	Eu (ng/g)	Gd (ng/g)	Tb (ng/g)	Dy (ng/g)
CO1B	Olympus Margin	Olympus Margin	17	21	21,592	92.4	75.6	12.6	50.4	12.6	8.40	16.8	4.20	29.4
CW1	Olympus Margin	Olympus Margin	64	32	4,634	360	647	79.9	304	63.9	16.0	55.9	7.99	63.9
CO2	Olympus Margin	Olympus Margin	66	12	8,949	140	152	28.7	111	20.5	4.10	24.6	4.10	32.8
CO2R	Olympus Margin	Olympus Margin	28	20	13,006	240	285	44.7	179	32.5	8.13	40.7	4.07	40.7
CP1	Olympus Margin	Olympus Margin	18	165	1,657	35.6	75.7	8.91	53.5	22.3	4.45	35.6	8.91	49.0
CB4	Olympus Margin	Olympus Margin	47	bd	75	137	444	82.4	503	220	43.2	353	70.7	491
CO1	Olympus Margin	Olympus Margin	12	bd	4,530	11.9	7.92	3.96	11.9	3.96	bd	7.92	bd	11.9
CO3	Olympus Margin	Olympus Margin	24	20	9,636	20.3	40.5	4.05	28.4	16.2	16.2	48.6	12.2	109
CB2Y	Olympus Margin	Olympus Margin	44	4	707	224	563	95.9	559	252	471	431	87.9	563
CQ2	Olympus Margin	Olympus Margin	121	60	1,025	28.1	52.3	8.04	32.2	8.04	bd	8.04	bd	8.04
CB1Y	Olympus Margin	Olympus Margin	44	4	433	63.6	183	31.8	207	91.4	31.8	167	35.8	258
CJ2	Olympus Margin	Olympus Margin	60	48	1,214	33.5	59.6	7.45	26.1	7.45	3.72	7.45	bd	7.45
CB3	Olympus Margin	Olympus Margin	43	16	2,042	126	303	43.3	216	94.4	19.7	193	39.4	279
CK4	Olympus Margin	Olympus Margin	1,075	12	2,920	227	533	66.2	318	141	16.5	277	53.8	405
CI1	Olympus Margin	Olympus Margin	84	84	3,351	156	261	40.1	160	36.1	12.0	36.1	8.02	44.1
BB1	Limassol Forest Complex	Limassol Forest Complex	58	3	329	101	259	42.1	246	102	40.8	171	33.1	232
BB2	Limassol Forest Complex	Limassol Forest Complex	52	2	2,216	54.2	91.7	10.7	49.1	17.2	5.94	40.9	9.65	70.5
BB3	Limassol Forest Complex	Limassol Forest Complex	30	1	1,090	72.0	166	22.6	98.9	28.3	8.03	46.1	9.57	74.9
BC1	Limassol Forest Complex	Limassol Forest Complex	30	2	bd	35.3	56.8	6.89	24.2	8.14	6.57	8.64	1.89	11.9

Sample	Location	Sample Type	Sn (ng/g)	Cs (ng/g)	Ba (ng/g)	La (ng/g)	Ce (ng/g)	Pr (ng/g)	Nd (ng/g)	Sm (ng/g)	Eu (ng/g)	Gd (ng/g)	Tb (ng/g)	Dy (ng/g)
BC2	Limassol Forest Complex	Limassol Forest Complex	56	4	352	2,317	3,583	391	1,750	791	423	1,494	324	2,413
BC3	Limassol Forest Complex	Limassol Forest Complex	81	4	578	204	463	63.8	349	183	38.3	374	80.8	574
BC4	Limassol Forest Complex	Limassol Forest Complex	72	8	670	1,637	2,928	369	1,844	900	282	1,750	391	2,891
BD1	Limassol Forest Complex	Limassol Forest Complex	21	1	732	10.7	8.19	2.21	8.41	3.02	0.54	4.69	1.38	10.1
BD2	Limassol Forest Complex	Limassol Forest Complex	14	bd	78	27.2	54.5	10.22	51.1	30.7	6.81	57.9	10.2	71.5
BD3	Limassol Forest Complex	Limassol Forest Complex	54	4	88	70.9	104	8.35	29.2	12.5	12.52	25.0	4.17	54.2
AM3	Gabbros & Cumulate Ultramafic Rocks	Gabbros	119	4,389	2,745	80.0	167	27.7	187	127	86.6	277	61.2	457
PP4	Gabbros & Cumulate Ultramafic Rocks	Gabbros	46	4	1,541	35.8	111	21.5	154	89.4	53.6	168	35.8	257
AS5	Gabbros & Cumulate Ultramafic Rocks	Gabbros	30	8	2,250	75.3	189	33.5	200	115	72.1	217	48.4	349
DF1	Gabbros & Cumulate Ultramafic Rocks	Gabbros	4	50	2,625	19.3	30.9	7.73	46.4	38.7	15.5	77.3	19.3	143
PP5	Gabbros & Cumulate Ultramafic Rocks	Gabbros	36	58	953	28.9	86.6	21.7	155	116	68.6	242	54.2	386
CE1	Gabbros & Cumulate Ultramafic Rocks	Gabbros	75.2	23.8	408	59.4	178	39.6	269	186	111	372	79.2	586
AA3	Artemis	Serpentine vein	30	4	1,243	17.0	21.2	4.24	21.2	4.24	4.24	8.49	bd	8.49
BA1A	Artemis	Serpentine vein	116	bd	1,232	22.4	53.7	4.48	22.4	8.96	4.48	22.4	4.48	53.7
CU5	Artemis	Serpentine vein	21	13	770	109	46.3	33.6	126	25.2	4.21	29.4	4.21	21.0

Sample	Location	Sample Type	Sn (ng/g)	Cs (ng/g)	Ba (ng/g)	La (ng/g)	Ce (ng/g)	Pr (ng/g)	Nd (ng/g)	Sm (ng/g)	Eu (ng/g)	Gd (ng/g)	Tb (ng/g)	Dy (ng/g)
AN4	Artemis	Serpentine vein	238	94	1,602	34.0	71.8	7.56	30.2	7.56	bd	7.56	bd	7.56
AA4X	Artemis	Serpentine vein	2,515	4	453	57.2	137	26.7	114	34.3	7.62	34.3	7.62	34.3
AN5	Artemis	Serpentine vein	63	12	453	19.7	51.2	7.87	31.5	7.87	3.93	7.87	bd	15.7
AW2	Artemis	Serpentine vein	347	4	194	12.4	24.8	4.13	8.26	bd	bd	bd	bd	4.13
AW3	Artemis	Serpentine vein	51	4	514	4.28	8.57	bd	4.28	bd	bd	4.28	bd	8.57
AY2	Artemis	Serpentine vein	188	4	375	45.8	100	12.5	66.7	16.7	4.17	16.7	4.17	16.7
AA4Y	Artemis	Serpentine vein	211	25	1,383	86.7	194	24.8	86.7	20.6	4.13	20.6	4.13	24.8
AA4-1	Artemis	Serpentine vein	64	12	2,978	24.1	48.2	8.04	36.2	12.1	4.02	12.1	4.02	16.1
AP1	Artemis	Serpentine vein	20	8	467	28.4	8.1	4.06	12.2	4.06	bd	bd	bd	4.06
CR1	Artemis	Chrysotile vein	32	71	819	14.3	32.1	3.56	24.9	10.7	3.56	17.8	3.56	21.4
DI1A	Artemis	Chrysotile vein	93	589	284	bd	4.2	bd	4.24	bd	bd	bd	bd	4.24
AX1	Artemis	Chrysotile vein	221	8	978	36.2	68.4	8.05	32.2	4.02	bd	4.02	bd	4.02
CU3	Artemis	Chrysotile vein	48	bd	584	bd	bd	bd	bd	bd	bd	bd	bd	bd
AZ1	Artemis	Chrysotile vein	31	96	7,136	273	558	69.3	269	53.9	11.5	50.0	7.70	46.2
DI1	Artemis	Chrysotile vein	36	2,761	565	3.65	10.9	bd	3.65	bd	bd	3.65	bd	7.30
DI3	Artemis	Chrysotile vein	36	40	1,967	43.7	98.3	10.9	40.1	10.9	3.64	10.9	3.64	10.9
CR1	Artemis	Chrysotile vein	32	71	819	14.3	32.1	3.56	24.9	10.7	3.56	17.8	3.56	21.4
DI5	Artemis	Chrysotile vein	14	179	831	3.38	10.1	bd	6.75	6.75	3.38	20.3	3.38	23.6
DI2	Artemis	Chrysotile vein	48	1,342	2,701	3.41	6.81	bd	3.41	3.41	bd	3.41	bd	6.81

Sample	Location	Sample Type	Sn (ng/g)	Cs (ng/g)	Ba (ng/g)	La (ng/g)	Ce (ng/g)	Pr (ng/g)	Nd (ng/g)	Sm (ng/g)	Eu (ng/g)	Gd (ng/g)	Tb (ng/g)	Dy (ng/g)
DH1V	Artemis	Incohesive Artemis Breccia	15	11	209	bd	bd	bd	3.67	3.67	7.33	11.0	3.67	25.7
BZ2	Artemis	Incohesive Artemis Breccia	41	4	10,108	8.18	12.3	bd	4.09	bd	bd	4.09	bd	8.18
BZ1	Artemis	Incohesive Artemis Breccia	60	4	12,866	bd	bd	bd	bd	bd	bd	bd	bd	3.97
DC2H	Artemis	Incohesive Artemis Breccia	34	11	64	bd	bd	bd	bd	bd	bd	3.77	bd	11.3
AK1	Artemis	Incohesive Artemis Breccia	41	bd	184	18.4	55.1	4.59	23.0	4.59	bd	4.59	bd	9.18
AB4	Artemis	Incohesive Artemis Breccia	25	313	2,844	104	188	25.0	95.9	16.7	4.17	20.8	4.17	29.2
AB3	Artemis	Incohesive Artemis Breccia	8	144	2,557	27.3	42.9	7.79	27.3	7.79	bd	11.7	3.90	27.3
AN1	Artemis	Incohesive Artemis Breccia	68	20	156	bd	bd	bd	bd	bd	bd	bd	bd	8.00
AI1	Artemis	Incohesive Artemis Breccia	52	9	2,756	4.31	8.63	bd	4.31	bd	bd	4.31	bd	17.3
AS3	Artemis	Incohesive Artemis Breccia	4	86	4,210	bd	bd	bd	bd	bd	bd	3.89	3.89	27.3
AU1	Artemis	Incohesive Artemis Breccia	4	12	8,154	bd	bd	bd	bd	bd	bd	bd	bd	7.78
AN3	Artemis	Incohesive Artemis Breccia	17	99	685	bd	bd	bd	bd	bd	bd	bd	bd	8.26
AS2	Artemis	Incohesive Artemis Breccia	17	67	463	bd	bd	bd	bd	bd	bd	bd	bd	8.34
BM1	Artemis	Cohesive Artemis Fault Rock	12	4	1,229	bd	4.14	bd	bd	bd	bd	4.14	bd	12.4
BN1	Artemis	Cohesive Artemis Fault Rock	24	11,926	29,159	68.5	161	28.2	197.4	133	101	278	60.4	467
DB2	Artemis	Cohesive Artemis Fault Rock	12	698	5,960	15.4	34.7	3.85	27.0	11.6	7.71	27.0	3.85	34.7
DE1B	Artemis	Cohesive Artemis Fault Rock	57	40	657	3.59	7.18	bd	3.59	bd	bd	3.59	bd	3.59
DE2BZ	Artemis	Cohesive Artemis Fault Rock	8	345	362	bd	bd	bd	bd	bd	bd	bd	bd	4.11
DB1	Artemis	Cohesive Artemis Fault Rock	47	1,319	3,125	7.80	23.4	3.90	31.2	23.4	11.70	50.7	11.7	89.7

Sample	Location	Sample Type	Sn (ng/g)	Cs (ng/g)	Ba (ng/g)	La (ng/g)	Ce (ng/g)	Pr (ng/g)	Nd (ng/g)	Sm (ng/g)	Eu (ng/g)	Gd (ng/g)	Tb (ng/g)	Dy (ng/g)
BO3	Artemis	Cohesive Artemis Fault Rock	23	171	12,746	23.3	42.7	3.89	15.5	3.89	bd	3.89	bd	3.89
BO1	Artemis	Cohesive Artemis Fault Rock	36	40	3,046	3.99	3.99	bd	bd	bd	bd	3.99	bd	12.0
BO2	Artemis	Cohesive Artemis Fault Rock	65	4	719	89.4	179	24.4	130	48.7	8.12	89.4	16.2	138
AA4-2	Artemis	Artemis Bulk Rock Halo	239	8	5,565	12.4	28.8	4.12	20.6	8.24	8.24	24.7	8.24	61.8
AA4-4	Artemis	Artemis Bulk Rock Halo	49	9	5,150	40.3	130	13.4	67.2	26.9	13.4	58.3	13.4	117
AO3C	Artemis	Artemis Bulk Rock Halo	52	30	16,645	64.9	130	13.0	60.6	21.6	8.66	47.6	13.0	104
BA1B	Artemis	Artemis Bulk Rock Halo	42	4	4,909	12.7	17.0	4.24	17.0	12.7	4.24	46.7	12.7	97.6
CU4	Artemis	Artemis Bulk Rock Halo	120	bd	2,507	8.92	8.92	bd	4.46	4.46	bd	17.8	4.46	58.0
CU2	Artemis	Artemis Bulk Rock Halo	22	bd	6,673	bd	3.70	bd	bd	3.70	bd	14.8	3.70	55.5
BA1C	Artemis	Artemis Bulk Rock	12	4	3,232	15.7	27.5	3.93	19.7	7.86	3.93	43.3	11.8	98.3
AN2	Artemis	Artemis Bulk Rock	21	332	739	6.47	15.6	1.88	6.70	2.06	bd	4.23	0.77	7.66
AO2	Artemis	Artemis Bulk Rock	20	3,566	39,250	0.93	0.64	0.50	5.62	12.7	6.15	51.0	12.6	108
AR1	Artemis	Artemis Bulk Rock	22	11	4,239	bd	1.23	0.50	1.79	4.94	bd	23.8	6.53	58.1
CU1	Artemis	Artemis Bulk Rock	67	4	8,313	4.49	13.5	bd	8.97	4.49	bd	13.5	4.49	44.9
AR2	Artemis	Artemis Bulk Rock	9	13	11,781	bd	bd	bd	bd	4.25	bd	12.8	4.25	46.8
AP2	Artemis	Artemis Bulk Rock	8	8	4,790	137	181	28.2	109	24.1	4.02	32.2	8.04	44.2
AQ2	Artemis	Artemis Bulk Rock	20	56	7,744	8.02	12.0	4.01	12.0	16.0	8.02	48.1	12.0	104
PP1	Artemis	Artemis Bulk Rock	12	16	2,810	bd	bd	bd	43.5	87.0	51.4	292	71.1	526

Table 5.2: continued

Sample	Location	Sample Type	Ho (ng/g)	Er (ng/g)	Tm (ng/g)	Yb (ng/g)	Lu (ng/g)	Hf (ng/g)	Ta (ng/g)	Pb (ng/g)	Th (ng/g)	U (ng/g)
AE1	Olympus	Olympus Bulk Rock	1.78	7.58	2.01	15.4	3.28	0.94	11.8	6.69	0.30	0.43
AG1	Olympus	Olympus Bulk Rock	1.81	8.83	2.13	20.8	3.77	2.08	33.1	77.2	0.49	0.46
AG2	Olympus	Olympus Bulk Rock	1.43	9.10	2.30	23.1	5.62	0.41	7.29	5.34	0.33	0.06
AH1	Olympus	Olympus Bulk Rock	1.41	6.95	1.65	18.4	3.65	1.63	4.12	7.22	0.51	0.69
AH2	Olympus	Olympus Bulk Rock	0.78	3.83	0.99	7.89	1.93	1.54	9.58	32.8	0.32	1.37
AJ2	Olympus	Olympus Bulk Rock	1.28	5.46	1.16	10.8	2.23	0.89	8.80	4.86	0.02	0.14
CX1	Olympus	Olympus Bulk Rock	bd	3.94	bd	7.89	3.94	bd	3.94	bd	bd	bd
PP2	Olympus	Olympus Bulk Rock	4.04	12.1	4.04	36.4	8.09	bd	4.04	16.2	bd	bd
CJ1	Olympus	Olympus Bulk Rock	bd	3.99	bd	7.98	3.99	bd	51.9	bd	bd	bd
AJ1	Olympus Margin	Antigorite vein	bd	4.00	bd	4.00	bd	bd	4.00	4.00	4.00	bd
CO1B	Olympus Margin	Olympus Margin	8.40	25.2	4.20	33.6	4.20	4.20	4.20	46.2	4.20	4.20
CW1	Olympus Margin	Olympus Margin	16.0	47.9	7.99	63.9	16.0	24.0	16.0	368	63.9	24.0
CO2	Olympus Margin	Olympus Margin	8.21	24.6	4.10	28.7	4.10	4.10	4.10	1,108	4.10	4.10
CO2R	Olympus Margin	Olympus Margin	8.13	32.5	4.07	36.6	4.07	8.13	4.07	1,728	12.2	8.13
CP1	Olympus Margin	Olympus Margin	8.91	26.7	4.45	26.7	4.45	4.45	13.4	80.2	4.45	4.45
CB4	Olympus Margin	Olympus Margin	118	353	58.9	404	66.7	114	15.7	39.3	27.5	3.93
CO1	Olympus Margin	Olympus Margin	3.96	11.9	3.96	23.8	3.96	3.96	3.96	bd	bd	bd

Sample	Location	Sample Type	Ho (ng/g)	Er (ng/g)	Tm (ng/g)	Yb (ng/g)	Lu (ng/g)	Hf (ng/g)	Ta (ng/g)	Pb (ng/g)	Th (ng/g)	U (ng/g)
CO3	Olympus Margin	Olympus Margin	28.4	109	20.3	150	28.4	8.10	60.8	20.3	8.10	4.05
CB2Y	Olympus Margin	Olympus Margin	128	367	55.9	383	63.9	779	59.9	347.5	51.9	20.0
CQ2	Olympus Margin	Olympus Margin	4.02	8.04	bd	12.1	4.02	4.02	4.02	217.1	8.04	4.02
CB1Y	Olympus Margin	Olympus Margin	59.6	183	31.8	207	35.8	35.8	19.9	131.1	15.9	3.97
CJ2	Olympus Margin	Olympus Margin	3.72	7.45	bd	14.9	3.72	3.72	11.2	163.9	7.45	3.72
CB3	Olympus Margin	Olympus Margin	66.9	212	35.4	240	43.3	138	23.6	1,031	47.2	27.5
CK4	Olympus Margin	Olympus Margin	99.2	294	49.6	335	57.9	116	49.6	5,450	78.6	41.4
CI1	Olympus Margin	Olympus Margin	8.02	32.1	4.01	36.1	8.02	24.1	16.0	176	48.1	20.0
BB1	Limassol Forest Complex	Limassol Forest Complex	54.3	166	27.4	196	29.9	79.3	12.9	39.5	17.9	7.26
BB2	Limassol Forest Complex	Limassol Forest Complex	17.6	57.5	10.2	73.0	12.4	16.0	11.8	16.9	8.01	3.43
BB3	Limassol Forest Complex	Limassol Forest Complex	16.8	59.8	10.1	70.8	12.2	12.0	29.9	17.4	9.54	4.60
BC1	Limassol Forest Complex	Limassol Forest Complex	3.08	12.8	2.62	22.6	4.4	1.17	12.8	18.6	0.29	0.67
BC2	Limassol Forest Complex	Limassol Forest Complex	575.2	1,782	284	1,881	280	667	435	7.99	435	192
BC3	Limassol Forest Complex	Limassol Forest Complex	140	434	72.3	519	80.8	85.0	63.8	bd	59.50	34.00
BC4	Limassol Forest Complex	Limassol Forest Complex	693	2,187	346	2,349	354	708	399	41.4	339	177
BD1	Limassol Forest Complex	Limassol Forest Complex	2.95	11.5	2.45	24.8	4.63	1.71	11.54	67.2	0.67	0.60
BD2	Limassol Forest Complex	Limassol Forest Complex	17.0	47.7	10.2	64.7	10.2	3.41	17.0	6.81	bd	3.41
BD3	Limassol Forest Complex	Limassol Forest Complex	16.7	54.2	8.35	79.3	12.5	8.35	8.35	41.7	4.17	8.35
AM3	Gabbros & Cumulate Ultramafic Rocks	Gabbros	110	339	54.2	376	57.5	72.8	52.5	62.0	11.3	10.0

Sample	Location	Sample Type	Ho (ng/g)	Er (ng/g)	Tm (ng/g)	Yb (ng/g)	Lu (ng/g)	Hf (ng/g)	Ta (ng/g)	Pb (ng/g)	Th (ng/g)	U (ng/g)
PP4	Gabbros & Cumulate Ultramafic Rocks	Gabbros	60.8	186	28.6	204	32.2	32.2	67.9	64.4	3.58	bd
AS5	Gabbros & Cumulate Ultramafic Rocks	Gabbros	79.1	245	38.3	263	38.1	59.3	18.3	100	11.0	6.89
DF1	Gabbros & Cumulate Ultramafic Rocks	Gabbros	34.8	108	15.5	120	19.3	11.6	3.9	23.2	3.87	3.87
PP5	Gabbros & Cumulate Ultramafic Rocks	Gabbros	93.9	278	43.3	289	43.3	43.3	7.2	57.8	3.61	3.61
CE1	Gabbros & Cumulate Ultramafic Rocks	Gabbros	135	412	63	408	63	75	24	174	8	8
AA3	Artemis	Serpentine vein	4.24	8.49	4.24	21.2	4.24	8.49	4.24	38.2	4.24	8.49
BA1A	Artemis	Serpentine vein	13.4	49.3	8.96	85.1	13.4	4.48	4.48	13.4	4.48	bd
CU5	Artemis	Serpentine vein	4.21	12.6	bd	8.41	bd	bd	bd	bd	4.21	8.41
AN4	Artemis	Serpentine vein	bd	3.78	bd	3.78	bd	3.78	3.78	351	7.56	3.78
AA4X	Artemis	Serpentine vein	7.62	19.1	3.81	19.1	3.81	3.81	7.62	1,082	19.1	7.62
AN5	Artemis	Serpentine vein	3.93	15.7	3.93	31.5	7.87	3.93	3.93	897	11.8	11.8
AW2	Artemis	Serpentine vein	bd	4.13	bd	4.13	bd	4.13	24.8	8.26	4.13	bd
AW3	Artemis	Serpentine vein	4.28	8.57	bd	12.9	4.28	bd	bd	bd	bd	bd
AY2	Artemis	Serpentine vein	4.17	8.33	bd	8.33	bd	4.17	12.5	575	8.33	4.17
AA4Y	Artemis	Serpentine vein	4.13	16.5	4.13	20.6	4.13	8.26	12.4	314	24.8	8.26
AA4-1	Artemis	Serpentine vein	4.02	12.1	bd	16.1	4.02	bd	60.3	358	4.02	bd
AP1	Artemis	Serpentine vein	bd	bd	bd	4.06	bd	4.06	8.11	28.4	bd	bd
CR1	Artemis	Chrysotile vein	3.56	14.3	3.56	14.3	3.56	10.7	17.8	67.7	3.56	3.56
DI1A	Artemis	Chrysotile vein	bd	4.24	bd	8.47	bd	4.24	4.24	bd	bd	bd

Sample	Location	Sample Type	Ho (ng/g)	Er (ng/g)	Tm (ng/g)	Yb (ng/g)	Lu (ng/g)	Hf (ng/g)	Ta (ng/g)	Pb (ng/g)	Th (ng/g)	U (ng/g)
AX1	Artemis	Chrysotile vein	bd	4.02	bd	4.02	bd	4.02	12.1	96.6	4.02	bd
CU3	Artemis	Chrysotile vein	bd	bd	bd	5.31	bd	bd	5.31	10.6	bd	bd
AZ1	Artemis	Chrysotile vein	7.70	23.1	3.85	23.1	3.85	15.4	15.4	512	53.9	42.3
DI1	Artemis	Chrysotile vein	bd	7.30	bd	10.9	3.65	3.65	7.30	14.6	bd	bd
DI3	Artemis	Chrysotile vein	3.64	10.9	3.64	18.2	3.64	7.29	7.29	127.5	10.9	3.64
CR1	Artemis	Chrysotile vein	3.56	14.3	3.56	14.3	3.56	10.7	17.8	67.7	3.56	3.56
DI5	Artemis	Chrysotile vein	6.75	16.9	3.38	16.9	3.38	3.38	6.75	10.1	3.38	bd
DI2	Artemis	Chrysotile vein	3.41	6.81	bd	10.2	3.41	3.41	6.81	17.03	bd	bd
DH1V	Artemis	Incohesive Artemis Breccia	7.33	22.0	3.67	25.7	3.67	7.33	11.0	bd	bd	bd
BZ2	Artemis	Incohesive Artemis Breccia	bd	8.18	bd	16.4	4.09	bd	4.09	32.7	bd	bd
BZ1	Artemis	Incohesive Artemis Breccia	bd	7.94	bd	15.9	3.97	3.97	7.94	bd	bd	bd
DC2H	Artemis	Incohesive Artemis Breccia	3.77	22.6	3.77	41.5	7.54	3.77	7.54	3.77	bd	bd
AK1	Artemis	Incohesive Artemis Breccia	4.59	9.18	4.59	18.4	4.59	bd	4.59	4.59	bd	bd
AB4	Artemis	Incohesive Artemis Breccia	8.34	20.8	4.17	25.0	4.17	12.5	8.34	638	20.8	8.34
AB3	Artemis	Incohesive Artemis Breccia	7.79	27.3	3.90	39.0	7.79	3.90	35.1	42.9	3.90	bd
AN1	Artemis	Incohesive Artemis Breccia	4.00	8.00	4.00	24.0	4.00	4.00	8.00	8.00	bd	bd
AI1	Artemis	Incohesive Artemis Breccia	4.31	17.3	4.31	30.2	4.31	4.31	8.63	21.6	bd	bd
AS3	Artemis	Incohesive Artemis Breccia	7.79	35.1	7.79	58.4	7.79	bd	3.89	3.89	bd	bd
AU1	Artemis	Incohesive Artemis Breccia	3.89	15.6	3.89	38.9	7.78	3.89	7.78	bd	bd	bd

Sample	Location	Sample Type	Ho (ng/g)	Er (ng/g)	Tm (ng/g)	Yb (ng/g)	Lu (ng/g)	Hf (ng/g)	Ta (ng/g)	Pb (ng/g)	Th (ng/g)	U (ng/g)
AN3	Artemis	Incohesive Artemis Breccia	4.13	8.26	4.13	20.6	4.13	bd	4.13	bd	bd	bd
AS2	Artemis	Incohesive Artemis Breccia	4.17	8.34	4.17	20.8	4.17	bd	4.17	bd	bd	bd
BM1	Artemis	Cohesive Artemis Fault Rock	4.14	16.5	4.14	29.0	4.14	bd	4.14	4.14	bd	bd
BN1	Artemis	Cohesive Artemis Fault Rock	113	347	56.4	395	60.4	52.4	12.1	101	12.1	8.06
DB2	Artemis	Cohesive Artemis Fault Rock	7.71	30.8	3.85	38.5	7.71	7.71	23.1	19.3	3.85	3.85
DE1B	Artemis	Cohesive Artemis Fault Rock	bd	3.59	bd	7.18	bd	3.59	14.4	14.4	bd	bd
DE2BZ	Artemis	Cohesive Artemis Fault Rock	bd	4.11	bd	8.22	bd	bd	8.22	bd	bd	bd
DB1	Artemis	Cohesive Artemis Fault Rock	23.4	70.2	11.7	78.0	11.7	11.7	7.80	11.7	3.90	bd
BO3	Artemis	Cohesive Artemis Fault Rock	bd	3.89	bd	3.89	bd	3.89	bd	101	7.77	3.89
BO1	Artemis	Cohesive Artemis Fault Rock	3.99	12.0	3.99	27.9	3.99	3.99	16.0	24.0	bd	bd
BO2	Artemis	Cohesive Artemis Fault Rock	36.6	110	16.2	102	16.2	20.3	12.2	191	12.2	12.2
AA4-2	Artemis	Artemis Bulk Rock Halo	16.5	61.8	12.4	82.4	12.4	12.4	20.6	57.7	4.12	4.12
AA4-4	Artemis	Artemis Bulk Rock Halo	26.9	103	17.9	139	22.4	26.9	4.48	628	8.97	8.97
AO3C	Artemis	Artemis Bulk Rock Halo	26.0	90.9	17.3	113	21.6	13.0	4.33	99.6	13.0	64.9
BA1B	Artemis	Artemis Bulk Rock Halo	25.5	89.1	12.7	102	17.0	4.24	bd	17.0	4.24	4.24
CU4	Artemis	Artemis Bulk Rock Halo	17.8	62.4	13.4	84.8	13.4	4.46	4.46	bd	4.46	bd
CU2	Artemis	Artemis Bulk Rock Halo	14.8	59.2	11.1	85.1	14.8	3.70	7.40	9.00	bd	bd
BA1C	Artemis	Artemis Bulk Rock	27.5	86.5	15.7	98.3	15.7	3.93	3.93	bd	3.93	bd
AN2	Artemis	Artemis Bulk Rock	2.64	11.0	2.40	25.1	4.82	1.56	9.87	45.2	0.30	0.20

Sample	Location	Sample Type	Ho (ng/g)	Er (ng/g)	Tm (ng/g)	Yb (ng/g)	Lu (ng/g)	Hf (ng/g)	Ta (ng/g)	Pb (ng/g)	Th (ng/g)	U (ng/g)
AO2	Artemis	Artemis Bulk Rock	29.8	98.6	16.6	127	19.8	9.26	7.97	107	0.53	0.37
AR1	Artemis	Artemis Bulk Rock	17.4	61.8	11.4	85.9	15.8	3.18	31.6	6.49	0.32	0.49
CU1	Artemis	Artemis Bulk Rock	13.5	49.3	8.97	76.3	13.5	4.49	4.49	8.97	4.49	bd
AR2	Artemis	Artemis Bulk Rock	12.8	55.3	12.8	85.1	17.0	bd	bd	bd	bd	bd
AP2	Artemis	Artemis Bulk Rock	12.1	36.2	4.02	40.2	8.04	4.02	4.02	96.5	12.1	12.1
AQ2	Artemis	Artemis Bulk Rock	28.1	96.3	16.0	124	20.1	8.02	4.01	bd	4.01	bd
PP1	Artemis	Artemis Bulk Rock	119	348	51.4	336	51.4	23.7	19.8	bd	bd	bd

Table 5.3: Progressive leaching experiments analytical results – 10% Acetic Acid Leachate.

Sample	*Location*	*Sample Type*	$^{87}Sr/^{86}Sr$	*2SE (1x10^6)*	*Na (µg/g)*	*Mg (µg/g)*	*Al (µg/g)*	*Si (µg/g)*	*K (µg/g)*	*Ca (µg/g)*	*Cr (µg/g)*	*Mn (µg/g)*	*Fe (µg/g)*	*Li (ng/g)*
AR2L	Artemis	Artemis Bulk Rock	0.705642	13	2.40	12638	2.93	168	0.25	457	395	49.3	189	37.1
AQ2L	Artemis	Artemis Bulk Rock	0.708767	12	6.68	8122	1.76	134	1.93	193	37.3	63.0	292	83.0
AP2L	Artemis	Artemis Bulk Rock	0.708705	12	6.40	5682	1.44	143	2.63	194	52.1	54.5	164	29.9
AO2L	Artemis	Artemis Bulk Rock	0.705302	13	7.71	16332	2.22	224	4.04	496	32.5	141	2549	280
PP1L	Artemis	Artemis Bulk Rock	0.708737	12	8.71	4893	5.23	141	2.11	117	49.0	55.9	98.6	49.7
CU1L	Artemis	Artemis Bulk Rock	0.708607	11	5.17	5645	7.69	252	1.93	231	41.9	20.5	117	19.2
AR1L	Artemis	Artemis Bulk Rock	0.708601	13	9.86	11100	2.22	195	2.57	144	65.4	100	173	84.9
AO3CL	Artemis	Artemis Bulk Rock Halo	0.708852	13	22.2	5780	131	989	4.38	523	22.6	69.7	674	501
CU2L	Artemis	Artemis Bulk Rock Halo	0.708636	13	6.19	5690	8.23	286	1.95	206	32.1	19.5	78.2	25.2
BA1BL	Artemis	Artemis Bulk Rock Halo	-	-	4.98	5305	76	1081	0.33	146	33.9	31.0	267	56.8
CU4L	Artemis	Artemis Bulk Rock Halo	0.708716	14	3.74	5154	18.5	394	0.92	171	31.0	39.3	126	22.7
CU5L	Artemis	Serpentine vein	0.708621	13	4.70	3024	70.1	578	3.94	250	6.47	7.39	424	21.4
BA1AL	Artemis	Serpentine vein	0.708852	13	2.40	1266	33.5	203	0.71	78.1	3.12	22.2	81.2	15.3
DE2BZL	Artemis	Cohesive Artemis Fault Rock	0.705848	13	80.5	4423	35.3	661	7.61	91345	0.62	51.6	154	2250

Sample	Location	Sample Type	$^{87}Sr/^{86}Sr$	2SE (1x10^6)	Na (µg/g)	Mg (µg/g)	Al (µg/g)	Si (µg/g)	K (µg/g)	Ca (µg/g)	Cr (µg/g)	Mn (µg/g)	Fe (µg/g)	Li (ng/g)
BO1L	Artemis	Cohesive Artemis Fault Rock	0.705663	11	995	98167	7.72	376	52.9	19334	22.3	24.2	136	8464
BN1L	Artemis	Cohesive Artemis Fault Rock	0.707031	12	376	2984	2573	2005	46.3	14628	1.74	17.0	51.3	1408
BO3L	Artemis	Cohesive Artemis Fault Rock	0.705640	13	3519	54934	13.2	650	141	73937	28.8	36.2	300	29818
BM1L	Artemis	Cohesive Artemis Fault Rock	0.707985	13	11.4	12478	152	725	1.90	617	100	208	2930	256
BB1L	Limassol Forest Complex	Limassol Forest Complex	0.708528	13	18.3	5539	19.1	595	19.5	263	10.4	91.8	913	16.3
BB2L	Limassol Forest Complex	Limassol Forest Complex	0.708781	13	14.1	8385	0.80	141	7.63	402	21.2	69.1	161	8.26
BB3L	Limassol Forest Complex	Limassol Forest Complex	0.708731	12	19.2	6026	0.87	141	7.39	462	11.7	59.4	176	6.65
BD1L	Limassol Forest Complex	Limassol Forest Complex	0.708734	12	19.2	8618	0.19	198	4.29	126	35.9	66.5	58.5	28.4
BD2L	Limassol Forest Complex	Limassol Forest Complex	0.708784	12	13.2	5204	0.60	139	2.27	91.9	7.23	39.3	89.7	4.27
BD3L	Limassol Forest Complex	Limassol Forest Complex	-	-	11.9	5412	0.96	71.4	2.47	108	25.0	65.9	410	20.4
AH1L	Olympus	Olympus Bulk Rock	0.705497	12	5.32	19151	0.36	249	2.44	494	11.7	176	2872	590

Sample	Location	Sample Type	$^{87}Sr/^{86}Sr$	2SE (1x10^6)	Na (µg/g)	Mg (µg/g)	Al (µg/g)	Si (µg/g)	K (µg/g)	Ca (µg/g)	Cr (µg/g)	Mn (µg/g)	Fe (µg/g)	Li (ng/g)
PP2L	Olympus	Olympus Bulk Rock	0.706535	15	3.64	10236	0.07	71.9	1.42	829	6.98	87.4	54.8	262
AH2L	Olympus	Olympus Bulk Rock	0.706040	13	5.55	22454	0.01	58.5	1.12	562	0.01	35.3	0.48	290
AG1L	Olympus	Olympus Bulk Rock	0.705605	12	9.02	21191	0.51	228	3.83	840	30.3	204	4251	794
AG2L	Olympus	Olympus Bulk Rock	0.705558	13	9.21	20572	0.14	204	3.90	835	30.8	192	2845	760
CJ1L	Olympus	Olympus Bulk Rock	0.706790	14	1.57	20567	0.01	52.5	0.18	275	0.01	144	96.9	96.3
CO2L	Olympus Margin	Olympus Margin	-	-	6.89	2743	86	987	13.8	595	1.26	214	518	129.6
CB2YL	Olympus Margin	Olympus Margin	-	-	1.62	1339	551	939	1.77	606	4.27	18.2	479	78.1
CP1L	Olympus Margin	Olympus Margin	0.708678	14	12.4	2304	48.8	407	9.58	399	3.41	104	139	26.0
CO1BL	Olympus Margin	Olympus Margin	0.708819	12	3.73	878	11.9	147	4.79	211	1.63	23.7	71.5	6.19
CW1L	Olympus Margin	Olympus Margin	-	-	1.11	611	7.58	140	0.70	27.3	0.62	8.83	48.4	1.51

Table 5.3: continued

Sample	Location	Sample Type	B (ng/g)	Rb (ng/g)	Sr (ng/g)	Cs (ng/g)	Ba (ng/g)	Pb (ng/g)	Mg/Ca	Sr/Ca (ng/g/µg/g)	Rb/K
AR2L	Artemis	Artemis Bulk Rock	6344	0.20	1036	0.13	2025	0.03	27.6	2.3	0.78
AQ2L	Artemis	Artemis Bulk Rock	1842	2.64	910	0.19	1205	0.04	42.1	4.7	1.37
AP2L	Artemis	Artemis Bulk Rock	762	4.63	679	0.04	932	1.07	29.2	3.5	1.76

Sample	Location	Sample Type	B (ng/g)	Rb (ng/g)	Sr (ng/g)	Cs (ng/g)	Ba (ng/g)	Pb (ng/g)	Mg/Ca	Sr/Ca (ng/g/µg/g)	Rb/K
AO2L	Artemis	Artemis Bulk Rock	15961	124	1210	227	2209	2.15	33.0	2.4	30.62
PP1L	Artemis	Artemis Bulk Rock	856	2.51	379	0.12	439	0.04	41.8	3.2	1.19
CU1L	Artemis	Artemis Bulk Rock	1727	1.63	789	bd	915	0.85	24.4	3.4	0.84
AR1L	Artemis	Artemis Bulk Rock	2121	2.01	577	0.12	849	0.18	77.2	4.0	0.78
AO3CL	Artemis	Artemis Bulk Rock Halo	29441	10.3	2531	0.9	3049	6.58	11.1	4.8	2.36
CU2L	Artemis	Artemis Bulk Rock Halo	2546	1.64	764	0.08	920	277	27.6	3.7	0.84
BA1BL	Artemis	Artemis Bulk Rock Halo	5671	1.91	498	0.38	794	1.52	36.2	3.4	5.84
CU4L	Artemis	Artemis Bulk Rock Halo	1982	1.05	539	bd	405	0.75	30.2	3.2	1.14
CU5L	Artemis	Serpentine vein	1434	2.76	608	bd	356	0.69	12.1	2.4	0.70
BA1AL	Artemis	Serpentine vein	654	1.45	213	0.19	169	4.06	16.2	2.7	2.05
DE2BZL	Artemis	Cohesive Artemis Fault Rock	33254	21.8	3541	103	149	1.67	0.0	0.0	2.87
BO1L	Artemis	Cohesive Artemis Fault Rock	101460	95.8	3671	84.4	1684	15.0	5.1	0.2	1.81
BN1L	Artemis	Cohesive Artemis Fault Rock	5084	61.5	13170	357	5783	2.54	0.2	0.9	1.33
BO3L	Artemis	Cohesive Artemis Fault Rock	101985	252	29621	220	11596	41.2	0.7	0.4	1.79
BM1L	Artemis	Cohesive Artemis Fault Rock	9315	3.05	794	1.39	467	2.77	20.2	1.3	1.61
BB1L	Limassol Forest Complex	Limassol Forest Complex	1285	10.4	887	bd	38.2	0.80	21.1	3.4	0.53
BB2L	Limassol Forest Complex	Limassol Forest Complex	759	4.99	1826	bd	417	0.13	20.9	4.5	0.65

Sample	Location	Sample Type	B (ng/g)	Rb (ng/g)	Sr (ng/g)	Cs (ng/g)	Ba (ng/g)	Pb (ng/g)	Mg/Ca	Sr/Ca (ng/g/µg/g)	Rb/K
BB3L	Limassol Forest Complex	Limassol Forest Complex	359	2.92	1832	bd	157	0.17	13.0	4.0	0.40
BD1L	Limassol Forest Complex	Limassol Forest Complex	2138	1.89	405	bd	228	0.95	68.6	3.2	0.44
BD2L	Limassol Forest Complex	Limassol Forest Complex	656	1.21	282	bd	4.10	0.27	56.6	3.1	0.53
BD3L	Limassol Forest Complex	Limassol Forest Complex	523	0.68	398	bd	3.48	0.28	50.2	3.7	0.28
AH1L	Olympus	Olympus Bulk Rock	2604	37.6	494	26.6	45.4	0.39	38.8	1.0	15.39
PP2L	Olympus	Olympus Bulk Rock	1698	35.0	343	25.5	35.9	0.08	12.4	0.4	24.64
AH2L	Olympus	Olympus Bulk Rock	392	12.5	124	10.7	1.24	0.03	39.9	0.2	11.12
AG1L	Olympus	Olympus Bulk Rock	8631	45.5	991	97.8	347	1.08	25.2	1.2	11.88
AG2L	Olympus	Olympus Bulk Rock	7897	51.3	1041	102	349	0.50	24.6	1.2	13.15
CJ1L	Olympus	Olympus Bulk Rock	174	2.97	164	0.78	0.45	0.04	74.9	0.6	16.69
CO2L	Olympus Margin	Olympus Margin	24026	23.1	2291	bd	5791	187	4.6	3.9	1.68
CB2YL	Olympus Margin	Olympus Margin	4525	3.62	78.1	0.30	151	10.6	2.2	0.1	2.04
CP1L	Olympus Margin	Olympus Margin	1693	5.17	1209	0.15	456	3.80	5.8	3.0	0.54
CO1BL	Olympus Margin	Olympus Margin	289	3.85	1087	bd	1531	0.69	4.2	5.1	0.80
CW1L	Olympus Margin	Olympus Margin	420	1.51	102	bd	144	10.8	22.4	3.7	2.15

Table 5.4: Progressive leaching experiments analytical results – 3M HCl Leachate.

Sample	Location	Group	$^{87}Sr/^{86}Sr$	2SE (1x10^6)	Mg (µg/g)	Ca (µg/g)	Sc (µg/g)	Ti (µg/g)	V (µg/g)	Cr (µg/g)	Mn (µg/g)	Fe (µg/g)	Co (µg/g)	Ni (µg/g)	Cu (µg/g)
AO2	Artemis	Artemis Bulk Rock	0.705299	12	71418	883	1.81	0.25	5.20	249	292	11716	52.8	1116	8.85
AP2	Artemis	Artemis Bulk Rock	0.708555	13	39969	102	0.45	0.02	1.05	353	183	3136	50.1	670	6.32
AQ2	Artemis	Artemis Bulk Rock	0.708507	11	44325	228	1.46	0.16	0.94	233	210	5552	39.8	590	4.08
AR1	Artemis	Artemis Bulk Rock	0.707922	13	76667	122	1.04	0.19	3.16	348	289	9381	52.0	929	4.69
AR2	Artemis	Artemis Bulk Rock	0.705650	13	43941	306	0.44	0.09	0.73	457	226	2093	35.8	643	0.74
CU1	Artemis	Artemis Bulk Rock	0.707268	13	102813	163	1.62	0.99	10.5	778	462	15572	94.3	1238	10.1
PP1	Artemis	Artemis Bulk Rock	0.708310	12	41680	561	0.99	0.16	7.64	411	212	4996	23.8	527	13.6
AO3C	Artemis	Artemis Bulk Rock Halo	0.707988	14	197367	372	7.99	38.3	39.1	1313	763	49587	81.2	1845	12.9
BA1B	Artemis	Artemis Bulk Rock Halo	0.706053	11	164526	298	1.42	3.41	14.0	1002	473	29327	80.9	1624	17.9
CU2	Artemis	Artemis Bulk Rock Halo	0.707302	14	89724	160	1.00	0.55	6.95	546	428	12041	90.0	1119	9.25
CU4	Artemis	Artemis Bulk Rock Halo	0.706744	12	131365	360	1.43	1.69	10.1	740	419	19511	81.4	1555	10.6
BM1	Artemis	Cohesive Artemis Fault Rock	0.706534	12	151787	4050	6.52	14.1	18.8	414	338	28927	45.5	467	2.20
BN1	Artemis	Cohesive Artemis Fault Rock	0.706311	12	44738	9258	4.58	12.6	21.2	68.9	101	8589	7.48	22.8	61.8
BO1	Artemis	Cohesive Artemis Fault Rock	0.705660	11	206987	32514	1.57	1.78	6.15	635	246	20751	35.6	725	8.85
BO3	Artemis	Cohesive Artemis Fault Rock	0.705661	12	146170	7066	0.75	3.75	7.09	517	212	17837	21.9	443	4.55
DE2BZ	Artemis	Cohesive Artemis Fault Rock	0.705713	14	94129	4702	1.45	0.92	3.04	22.6	307	19064	49.2	702	0.44

Sample	Location	Group	$^{87}Sr/^{86}Sr$	2SE (1x10^6)	Mg (µg/g)	Ca (µg/g)	Sc (µg/g)	Ti (µg/g)	V (µg/g)	Cr (µg/g)	Mn (µg/g)	Fe (µg/g)	Co (µg/g)	Ni (µg/g)	Cu (µg/g)
BB1	Limassol Forest Complex	Limassol Forest Complex	0.708256	13	49030	245	1.97	8.60	3.67	70.6	256	15787	27.7	254	6.23
BB2	Limassol Forest Complex	Limassol Forest Complex	0.708723	21	70213	292	4.24	3.79	7.16	136	294	10681	67.4	661	1.51
BB3	Limassol Forest Complex	Limassol Forest Complex	0.708693	11	65480	276	3.12	2.90	7.79	108	302	10137	67.2	619	0.39
BD1	Limassol Forest Complex	Limassol Forest Complex	0.708655	12	64754	59.7	3.88	1.53	7.38	312	225	7133	64.2	782	0.43
BD2	Limassol Forest Complex	Limassol Forest Complex	0.708746	12	47295	50.4	2.01	0.65	2.11	36.8	158	4700	39.5	644	0.27
BD3	Limassol Forest Complex	Limassol Forest Complex	0.708687	11	40759	121	3.07	0.18	7.07	164	237	7795	34.0	571	1.29
AG1	Olympus	Olympus Bulk Rock	0.705531	11	64484	573	1.69	0.02	3.02	132	244	12796	49.3	704	3.48
AG2	Olympus	Olympus Bulk Rock	0.705506	11	61440	532	1.71	0.04	1.45	133	245	11917	52.3	698	4.94
AH1	Olympus	Olympus Bulk Rock	0.705341	12	46272	242	1.15	0.09	0.84	80.2	205	9572	45.5	517	3.41
AH2	Olympus	Olympus Bulk Rock	0.706028	13	40139	390	0.18	0.02	0.22	6.21	264	5045	43.6	527	0.05
CJ1	Olympus	Olympus Bulk Rock	0.706392	24	45473	271	0.70	0.07	0.21	9.7	301	10517	42.7	748	0.14
PP2	Olympus	Olympus Bulk Rock	0.706334	14	43027	571	1.03	0.05	0.76	168	218	6149	49.5	521	4.15
CB2Y	Olympus Margin	Olympus Margin	0.706222	28	3499	2871	0.16	5.08	2.83	0.43	34.3	1286	0.81	2.25	0.03
CO1B	Olympus Margin	Olympus Margin	0.708785	11	55361	637	0.70	2.18	7.50	116	432	10223	16.7	164	0.49
CO2	Olympus Margin	Olympus Margin	0.708747	14	187011	39.1	1.77	22.9	29.1	27.0	877	31865	49.5	113	3.03

Sample	Location	Group	$^{87}Sr/^{86}Sr$	2SE (1x10^6)	Mg (µg/g)	Ca (µg/g)	Sc (µg/g)	Ti (µg/g)	V (µg/g)	Cr (µg/g)	Mn (µg/g)	Fe (µg/g)	Co (µg/g)	Ni (µg/g)	Cu (µg/g)
CP1	Olympus Margin	Olympus Margin	0.708336	13	83134	181	1.79	4.24	4.30	56.5	571	17034	60.5	646	2.48
CW1	Olympus Margin	Olympus Margin	-	-	21214	bd	0.42	1.43	5.36	5.97	20.4	1780	5.12	157	0.79
BA1A	Artemis	Serpentine vein	0.706963	13	65985	636	0.33	0.92	4.93	41.9	172	12216	9.87	78.2	1.61
CU5	Artemis	Serpentine vein	0.707353	34	156420	bd	0.26	0.34	7.14	50.5	217	22993	18.1	115	1.05

Table 5.4: continued

Sample	Location	Group	Zn (µg/g)	Li (ng/g)	Rb (ng/g)	Sr (ng/g)	Y (ng/g)	Zr (ng/g)	Nb (ng/g)	Cs (ng/g)	Ba (ng/g)	La (ng/g)	Ce (ng/g)	Pr (ng/g)	Nd (ng/g)
AO2	Artemis	Artemis Bulk Rock	12.4	1152	242	2987	111	2.42	bd	1752	12776	0.81	1.21	bd	0.81
AP2	Artemis	Artemis Bulk Rock	6.26	241	13.7	502	89.2	0.78	0.26	0.26	1329	63.3	84.3	12.4	49.0
AQ2	Artemis	Artemis Bulk Rock	5.46	620	8.27	878	89.9	0.55	bd	8.55	2095	2.21	3.31	0.55	2.76
AR1	Artemis	Artemis Bulk Rock	8.29	1002	9.11	495	129	0.87	bd	3.47	1391	bd	0.43	bd	0.43
AR2	Artemis	Artemis Bulk Rock	9.77	250	5.75	992	158	0.27	0.27	1.09	2944	bd	bd	bd	0.27
CU1	Artemis	Artemis Bulk Rock	21.9	854	11.4	757	131	1.20	0.60	1.20	3323	1.80	4.19	0.60	1.20
PP1	Artemis	Artemis Bulk Rock	5.50	766	11.5	310	94.8	0.27	0.27	3.20	952	bd	0.27	0.27	5.87
AO3C	Artemis	Artemis Bulk Rock Halo	bd	3310	37.4	1466	294	18.7	bd	18.7	11206	18.7	32.7	4.67	23.3
BA1B	Artemis	Artemis Bulk Rock Halo	0.06	1598	7.54	613	7.54	7.54	bd	2.51	1716	bd	bd	bd	bd
CU2	Artemis	Artemis Bulk Rock Halo	18.8	577	6.34	638	41.0	0.49	0.49	0.49	2542	bd	bd	bd	bd
CU4	Artemis	Artemis Bulk Rock Halo	23.4	919	10.1	474	5.07	4.22	0.84	0.84	1007	bd	bd	bd	bd

Sample	Location	Group	Zn (µg/g)	Li (ng/g)	Rb (ng/g)	Sr (ng/g)	Y (ng/g)	Zr (ng/g)	Nb (ng/g)	Cs (ng/g)	Ba (ng/g)	La (ng/g)	Ce (ng/g)	Pr (ng/g)	Nd (ng/g)
BM1	Artemis	Cohesive Artemis Fault Rock	4.32	489	1.60	283	57.5	1.60	bd	1.60	195	bd	bd	bd	bd
BN1	Artemis	Cohesive Artemis Fault Rock	13.2	111151	492	19208	170	17.5	bd	7504	19855	13.5	24.3	4.04	17.5
BO1	Artemis	Cohesive Artemis Fault Rock	bd	9199	20.8	7242	8.68	1.74	bd	27.8	2906	3.47	5.21	bd	1.74
BO3	Artemis	Cohesive Artemis Fault Rock	bd	6043	35.2	3261	7.82	25.4	13.7	45.0	1236	3.91	11.7	1.96	5.87
DE2BZ	Artemis	Cohesive Artemis Fault Rock	7.17	9528	13.1	1004	18.9	1.64	1.64	224	153	bd	1.64	bd	1.64
BB1	Limassol Forest Complex	Limassol Forest Complex	15.3	209	35.7	629	138	9.01	0.39	0.78	41.5	13.3	30.2	4.31	21.2
BB2	Limassol Forest Complex	Limassol Forest Complex	13.1	108	32.1	1539	208	6.75	1.59	0.79	951	18.7	32.1	3.97	18.7
BB3	Limassol Forest Complex	Limassol Forest Complex	11.1	135	31.9	1495	214	3.07	1.54	0.38	721	37.3	84.2	11.9	49.6
BD1	Limassol Forest Complex	Limassol Forest Complex	8.33	328	4.72	222	41.7	1.18	0.39	0.79	402	5.12	2.36	1.18	5.12
BD2	Limassol Forest Complex	Limassol Forest Complex	6.71	103	3.22	213	225	2.69	0.27	bd	78.2	13.2	26.6	4.03	25.5
BD3	Limassol Forest Complex	Limassol Forest Complex	8.52	224	12.4	589	143	0.55	0.28	0.55	30.1	28.7	42.0	3.32	10.2
AG1	Olympus	Olympus Bulk Rock	11.4	1018	76.0	1214	9.25	0.40	bd	541	441	0.80	1.21	0.40	0.80
AG2	Olympus	Olympus Bulk Rock	12.2	966	85.9	1167	10.3	0.73	bd	594	432	bd	bd	bd	bd
AH1	Olympus	Olympus Bulk Rock	10.9	446	48.9	361	5.91	0.27	bd	155	37.1	0.54	1.34	0.27	0.81
AH2	Olympus	Olympus Bulk Rock	5.80	530	31.2	157	6.41	0.27	bd	107	12.0	0.27	0.80	bd	0.53
CJ1	Olympus	Olympus Bulk Rock	9.27	147	12.9	255	11.8	0.54	bd	20.9	8.32	0.27	0.27	bd	0.27
PP2	Olympus	Olympus Bulk Rock	12.1	497	98.6	374	10.9	2.40	0.27	247	59	0.53	0.80	bd	0.27
CB2Y	Olympus Margin	Olympus Margin	bd	196	bd	61.4	33.2	96.3	bd	bd	bd	4.98	9.96	1.66	9.96
CO1B	Olympus Margin	Olympus Margin	7.90	398	35.3	643	75.2	1.39	0.93	3.25	6019	20.0	17.6	2.32	9.75

Sample	Location	Group	Zn (µg/g)	Li (ng/g)	Rb (ng/g)	Sr (ng/g)	Y (ng/g)	Zr (ng/g)	Nb (ng/g)	Cs (ng/g)	Ba (ng/g)	La (ng/g)	Ce (ng/g)	Pr (ng/g)	Nd (ng/g)
CO2	Olympus Margin	Olympus Margin	bd	2879	71.0	584	197	23.7	7.89	15.8	5403	118	126	23.7	78.9
CP1	Olympus Margin	Olympus Margin	19.1	955	42.1	965	187	3.51	bd	58.5	1231	18.7	43.3	5.85	29.2
CW1	Olympus Margin	Olympus Margin	bd	294	bd	1.8	10.7	3.56	bd	bd	bd	5.34	8.91	1.78	3.56
BA1A	Artemis	Serpentine vein	0.70	617	bd	141	13.9	0.53	bd	1.07	283	1.60	0.53	0.53	1.07
CU5	Artemis	Serpentine vein	bd	621	bd	119	78.0	4.87	bd	4.87	110	53.6	19.5	17.1	63.3

Table 5.4: continued

Sample	Location	Group	Sm (ng/g)	Eu (ng/g)	Gd (ng/g)	Tb (ng/g)	Dy (ng/g)	Ho (ng/g)	Er (ng/g)	Tm (ng/g)	Yb (ng/g)	Lu (ng/g)	Pb (ng/g)	Th (ng/g)	U (ng/g)
AO2	Artemis	Artemis Bulk Rock	0.81	0.40	4.03	1.21	12.5	4.03	15.7	3.22	28.2	5.24	36.3	bd	bd
AP2	Artemis	Artemis Bulk Rock	8.56	2.07	11.4	1.82	11.9	2.85	8.30	1.30	9.60	1.56	50.3	1.04	3.37
AQ2	Artemis	Artemis Bulk Rock	1.38	0.55	3.86	1.10	10.2	3.03	12.1	2.48	22.6	4.13	3.03	0.28	0.28
AR1	Artemis	Artemis Bulk Rock	1.30	bd	7.38	1.74	16.9	4.77	16.5	3.04	24.7	5.21	4.77	bd	bd
AR2	Artemis	Artemis Bulk Rock	0.82	0.55	4.92	1.64	17.0	5.20	19.7	3.83	32.3	6.02	1.92	bd	bd
CU1	Artemis	Artemis Bulk Rock	1.20	0.60	6.59	1.80	14.4	4.19	15.0	3.00	24.0	5.39	9.59	0.60	bd
PP1	Artemis	Artemis Bulk Rock	5.07	2.67	11.7	1.87	13.1	2.94	8.81	1.34	10.4	2.14	0.53	bd	bd
AO3C	Artemis	Artemis Bulk Rock Halo	4.67	bd	14.0	4.67	32.7	9.34	42.0	9.34	70.0	14.0	65.4	4.67	28.0
BA1B	Artemis	Artemis Bulk Rock Halo	bd	bd	bd	bd	bd	bd	bd	bd	2.51	bd	bd	bd	bd
CU2	Artemis	Artemis Bulk Rock Halo	0.49	bd	2.44	0.49	3.90	0.98	3.90	0.98	7.81	1.95	bd	bd	bd

Sample	Location	Group	Sm (ng/g)	Eu (ng/g)	Gd (ng/g)	Tb (ng/g)	Dy (ng/g)	Ho (ng/g)	Er (ng/g)	Tm (ng/g)	Yb (ng/g)	Lu (ng/g)	Pb (ng/g)	Th (ng/g)	U (ng/g)
CU4	Artemis	Artemis Bulk Rock Halo	bd	bd	bd	bd	0.84	bd	0.84	bd	0.84	bd	2.53	bd	bd
BM1	Artemis	Cohesive Artemis Fault Rock	bd	bd	1.60	bd	6.39	1.60	7.98	1.60	14.4	3.19	3.19	bd	bd
BN1	Artemis	Cohesive Artemis Fault Rock	6.74	12.13	13.5	2.70	22.9	5.39	21.6	4.04	28.3	5.39	64.7	2.70	bd
BO1	Artemis	Cohesive Artemis Fault Rock	bd	bd	bd	bd	bd	bd	1.74	bd	1.74	bd	29.5	1.74	bd
BO3	Artemis	Cohesive Artemis Fault Rock	1.96	bd	1.96	bd	1.96	bd	bd	bd	1.96	bd	25.4	1.96	bd
DE2BZ	Artemis	Cohesive Artemis Fault Rock	0.82	bd	1.64	bd	2.46	0.82	2.46	0.82	4.92	0.82	1.64	bd	bd
BB1	Limassol Forest Complex	Limassol Forest Complex	7.84	4.70	12.9	2.35	19.2	4.70	16.1	3.14	23.9	4.31	18.0	2.35	0.78
BB2	Limassol Forest Complex	Limassol Forest Complex	8.34	3.57	17.1	3.97	30.6	7.54	25.4	4.37	33.3	5.56	3.18	2.78	1.19
BB3	Limassol Forest Complex	Limassol Forest Complex	14.2	5.00	21.9	4.23	32.3	7.69	24.6	4.23	30.4	5.38	12.3	4.61	1.92
BD1	Limassol Forest Complex	Limassol Forest Complex	1.18	0.79	1.97	0.39	4.33	1.18	5.51	1.18	10.6	2.36	43.3	bd	0.39
BD2	Limassol Forest Complex	Limassol Forest Complex	14.2	2.95	26.6	5.10	32.2	7.52	22.8	3.76	27.7	4.57	7.25	0.27	1.34
BD3	Limassol Forest Complex	Limassol Forest Complex	3.59	5.53	8.57	2.21	18.2	4.97	18.2	3.59	28.7	5.25	27.4	1.11	2.21
AG1	Olympus	Olympus Bulk Rock	bd	bd	bd	bd	0.80	0.40	2.01	0.40	5.63	1.21	1.21	bd	bd
AG2	Olympus	Olympus Bulk Rock	bd	bd	bd	bd	0.73	0.37	1.84	0.73	6.24	1.47	3.30	bd	bd
AH1	Olympus	Olympus Bulk Rock	0.27	bd	0.27	bd	0.54	0.27	1.07	0.27	2.69	0.81	2.69	bd	bd
AH2	Olympus	Olympus Bulk Rock	bd	bd	bd	bd	0.53	0.27	1.07	0.27	2.67	0.53	1.60	bd	bd

Sample	Location	Group	Sm (ng/g)	Eu (ng/g)	Gd (ng/g)	Tb (ng/g)	Dy (ng/g)	Ho (ng/g)	Er (ng/g)	Tm (ng/g)	Yb (ng/g)	Lu (ng/g)	Pb (ng/g)	Th (ng/g)	U (ng/g)
CJ1	Olympus	Olympus Bulk Rock	bd	bd	0.54	bd	1.34	0.27	1.88	0.27	3.49	0.81	0.54	bd	bd
PP2	Olympus	Olympus Bulk Rock	bd	bd	bd	bd	0.53	0.27	2.13	0.53	6.66	1.33	4.26	bd	bd
CB2Y	Olympus Margin	Olympus Margin	1.66	19.92	4.98	bd	4.98	1.66	3.32	bd	3.32	bd	64.7	1.66	bd
CO1B	Olympus Margin	Olympus Margin	2.32	1.39	4.64	0.93	6.03	1.86	6.03	0.93	7.42	1.39	29.7	0.93	0.93
CO2	Olympus Margin	Olympus Margin	15.8	7.89	15.8	bd	23.7	7.89	15.8	bd	23.7	7.89	1388	7.89	bd
CP1	Olympus Margin	Olympus Margin	12.9	3.51	23.4	4.68	32.8	7.02	19.9	2.34	17.5	3.51	84.2	3.51	1.17
CW1	Olympus Margin	Olympus Margin	bd	bd	bd	bd	1.78	bd	1.78	bd	1.78	bd	33.8	1.78	bd
BA1A	Artemis	Serpentine vein	0.53	bd	1.07	bd	1.60	0.53	1.60	bd	2.13	0.53	17.1	bd	0.53
CU5	Artemis	Serpentine vein	14.6	2.44	12.2	2.44	12.2	2.44	7.31	bd	4.87	bd	bd	bd	2.44

Table 5.5: Progressive leaching experiments analytical results – Bulk Residue.

Sample	*Location*	*Sample Type*	*$^{87}Sr/^{86}Sr$*	*2SE (1x10^6)*	*Li (µg/g)*	*Sc (µg/g)*	*Ti (µg/g)*	*V (µg/g)*	*Cr (µg/g)*	*Co (µg/g)*	*Ni (µg/g)*	*Cu (µg/g)*	*Zn (µg/g)*	*Rb (ng/g)*	*Sr (ng/g)*
AR2	Artemis	Artemis Bulk Rock	0.705492	26	2.07	8.98	86.0	39.6	3295	66.5	1284	7.75	58.7	5.97	1308
AP2	Artemis	Artemis Bulk Rock	0.708026	16	1.37	7.18	83.6	26.6	2300	56.3	1596	16.6	22.5	52.5	522
AO2	Artemis	Artemis Bulk Rock	0.705280	25	4.24	9.51	135	48.0	2570	44.2	763	6.81	30.7	229	2558
AR1	Artemis	Artemis Bulk Rock	0.706223	35	3.61	9.31	93.6	36.0	2838	42.6	1073	4.04	32.0	9.67	507
CU1	Artemis	Artemis Bulk Rock	0.706006	14	1.36	10.2	86.6	34.6	2116	27.4	829	5.56	34.5	9.36	665
AQ2	Artemis	Artemis Bulk Rock	0.707245	15	2.98	8.39	122	42.6	2438	50.4	1196	8.27	33.0	16.7	852
PP1	Artemis	Artemis Bulk Rock	0.706308	15	4.32	29.7	460	161	3658	25.8	641	14.4	13.2	11.2	465
BA1B	Artemis	Artemis Bulk Rock Halo	0.705889	65	1.50	3.97	121	46.2	158	20.3	52.9	0.35	10.0	bd	348
CU2	Artemis	Artemis Bulk Rock Halo	0.705821	25	1.42	10.7	94.1	43.9	2645	28.2	996	5.72	34.3	bd	689
CU4	Artemis	Artemis Bulk Rock Halo	0.705642	20	0.87	11.4	90.0	39.1	2868	21.3	699	2.30	28.4	bd	536
CU5	Artemis	Serpentine vein	0.708347	952	0.06	0.004	0.62	5.27	5.73	14.8	7.96	bd	7.81	2.06	158
BA1A	Artemis	Serpentine vein	0.705656	76	1.04	10.5	62.8	20.7	2630	10.5	515	0.65	21.1	bd	407
BB1	Limassol Forest Complex	Limassol Forest Complex	0.704915	14	0.64	12.2	325	44.8	1541	68.0	623	5.92	34.3	62.8	1815
BD1	Limassol Forest Complex	Limassol Forest Complex	0.707868	14	0.48	4.84	22.9	24.1	1912	45.6	1482	0.13	18.1	1.88	151
BD3	Limassol Forest Complex	Limassol Forest Complex	-	-	0.84	9.92	77.8	49.5	2821	67.7	1287	0.89	33.7	20.5	403
PP2	Olympus	Olympus Bulk Rock	0.706185	13	0.94	10.6	40.9	39.4	2140	43.4	1218	6.61	20.7	61.6	278

Sample	Location	Sample Type	$^{87}Sr/^{86}Sr$	2SE (1x10^6)	Li (µg/g)	Sc (µg/g)	Ti (µg/g)	V (µg/g)	Cr (µg/g)	Co (µg/g)	Ni (µg/g)	Cu (µg/g)	Zn (µg/g)	Rb (ng/g)	Sr (ng/g)
AH1	Olympus	Olympus Bulk Rock	0.705320	24	0.75	9.36	16.1	32.3	1925	62.8	1625	3.72	25.9	32.0	363
CJ1	Olympus	Olympus Bulk Rock	0.706184	12	0.35	3.10	10.1	9.62	1666	82.1	1855	0.09	24.8	7.28	238
AG2	Olympus	Olympus Bulk Rock	0.705552	12	1.38	7.63	18.4	32.9	2430	41.3	1293	2.61	29.6	51.0	647
AG1	Olympus	Olympus Bulk Rock	0.705560	14	1.48	6.72	18.2	30.2	2451	37.9	1200	2.44	22.5	48.3	757
AH2	Olympus	Olympus Bulk Rock	0.706068	14	0.40	2.91	4.41	5.04	580	48.2	1313	0.14	14.7	19.1	291

Table 5.5: continued

Sample	Location	Sample Type	Y (ng/g)	Zr (ng/g)	Nb (ng/g)	Sn (ng/g)	Cs (ng/g)	Ba (ng/g)	La (ng/g)	Ce (ng/g)	Pr (ng/g)	Nd (ng/g)	Sm (ng/g)	Eu (ng/g)	Gd (ng/g)
AR2	Artemis	Artemis Bulk Rock	203	21.9	1.99	7.96	10	5741	bd	bd	bd	bd	1.99	bd	9.95
AP2	Artemis	Artemis Bulk Rock	185	130	16.3	32.6	5.43	2078	54.3	70.6	10.9	43.5	9.06	1.81	18.1
AO2	Artemis	Artemis Bulk Rock	749	31.0	1.94	23.2	1913	26375	bd	bd	bd	5.81	15.5	7.75	52.3
AR1	Artemis	Artemis Bulk Rock	288	32.9	1.93	17.4	7.74	2196	bd	bd	bd	bd	1.93	bd	9.67
CU1	Artemis	Artemis Bulk Rock	298	46.8	3.74	28.1	1.87	3412	1.87	1.87	bd	bd	1.87	bd	7.49
AQ2	Artemis	Artemis Bulk Rock	657	63.3	5.58	16.7	42.8	4055	5.58	7.44	1.86	7.44	13.0	5.58	42.8
PP1	Artemis	Artemis Bulk Rock	3182	57.6	1.86	24.2	11.2	1237	bd	bd	1.86	40.9	96.7	52.1	312
BA1B	Artemis	Artemis Bulk Rock Halo	634	70.8	5.67	42.5	bd	790	2.83	2.83	bd	2.83	8.50	5.67	31.2
CU2	Artemis	Artemis Bulk Rock Halo	488	23.5	1.81	30.8	1.81	3014	bd	bd	bd	bd	3.62	1.81	16.3
CU4	Artemis	Artemis Bulk Rock Halo	532	18.5	1.85	13.0	bd	2033	bd	bd	bd	bd	3.71	1.85	20.4

Sample	Location	Sample Type	Y (ng/g)	Zr (ng/g)	Nb (ng/g)	Sn (ng/g)	Cs (ng/g)	Ba (ng/g)	La (ng/g)	Ce (ng/g)	Pr (ng/g)	Nd (ng/g)	Sm (ng/g)	Eu (ng/g)	Gd (ng/g)
CU5	Artemis	Serpentine vein	2.06	30.8	2.06	20.6	6.17	67.9	2.06	bd	bd	2.06	bd	bd	bd
BA1A	Artemis	Serpentine vein	872	56.1	bd	12.0	2.00	1307	bd	bd	bd	4.01	14.0	6.01	52.1
BB1	Limassol Forest Complex	Limassol Forest Complex	1441	2482	135	44.4	1.85	362	86.9	235	40.7	238	96.1	42.5	164
BD1	Limassol Forest Complex	Limassol Forest Complex	30.1	48.9	1.88	16.9	bd	86.6	1.88	bd	bd	1.88	bd	bd	1.88
BD3	Limassol Forest Complex	Limassol Forest Complex	225	190	55.9	22.4	1.86	65.2	37.3	52.2	5.59	18.6	7.45	7.45	16.8
PP2	Olympus	Olympus Bulk Rock	52.8	22.9	1.76	14.1	264	37.0	bd	1.76	bd	bd	bd	bd	bd
AH1	Olympus	Olympus Bulk Rock	41.4	37.6	3.76	30.1	130	39.5	1.88	3.76	bd	3.76	1.88	bd	1.88
CJ1	Olympus	Olympus Bulk Rock	21.8	25.5	3.64	14.6	20	9.10	bd	bd	bd	bd	bd	bd	1.82
AG2	Olympus	Olympus Bulk Rock	49.0	51.0	2.04	36.7	349	237	2.04	2.04	bd	bd	bd	bd	bd
AG1	Olympus	Olympus Bulk Rock	37.6	32.2	1.79	28.6	386	225	bd	bd	bd	bd	bd	bd	bd
AH2	Olympus	Olympus Bulk Rock	11.1	11.1	3.18	22.3	105	71.5	bd	1.59	bd	bd	bd	bd	bd

Table 5.5: continued

Sample	Location	Sample Type	Tb (ng/g)	Dy (ng/g)	Ho (ng/g)	Er (ng/g)	Tm (ng/g)	Yb (ng/g)	Lu (ng/g)	Hf (ng/g)	Ta (ng/g)	Pb (ng/g)	Th (ng/g)	U (ng/g)
AR2	Artemis	Artemis Bulk Rock	1.99	27.9	7.96	31.9	5.97	47.8	7.96	1.99	5.97	13.9	bd	bd
AP2	Artemis	Artemis Bulk Rock	3.62	30.8	7.25	23.5	3.62	23.5	3.62	3.62	5.43	56.2	9.06	5.43

Sample	Location	Sample Type	Tb (ng/g)	Dy (ng/g)	Ho (ng/g)	Er (ng/g)	Tm (ng/g)	Yb (ng/g)	Lu (ng/g)	Hf (ng/g)	Ta (ng/g)	Pb (ng/g)	Th (ng/g)	U (ng/g)
AO2	Artemis	Artemis Bulk Rock	13.6	112	29.0	96.8	15.5	107	17.4	9.68	3.87	21.3	bd	bd
AR1	Artemis	Artemis Bulk Rock	3.87	40.6	11.6	44.5	7.74	56.1	9.67	3.87	3.87	13.5	bd	bd
CU1	Artemis	Artemis Bulk Rock	3.74	41.2	13.1	46.8	9.36	67.4	9.36	3.74	3.74	16.9	bd	bd
AQ2	Artemis	Artemis Bulk Rock	11.2	98.6	26.1	83.7	14.9	100	16.7	7.44	7.44	13.0	1.86	bd
PP1	Artemis	Artemis Bulk Rock	74.4	558	126	370	55.8	364	55.8	26.0	7.44	11.2	bd	bd
BA1B	Artemis	Artemis Bulk Rock Halo	8.50	76.5	19.8	76.5	14.2	122	19.8	8.50	17.0	19.8	bd	bd
CU2	Artemis	Artemis Bulk Rock Halo	5.43	63.3	18.1	70.6	12.7	105	18.1	1.81	5.43	14.5	bd	bd
CU4	Artemis	Artemis Bulk Rock Halo	7.42	68.6	20.4	76.0	13.0	111	20.4	3.71	3.71	29.7	bd	bd
CU5	Artemis	Serpentine vein	bd	bd	bd	bd	bd	bd	bd	bd	6.17	20.6	bd	bd
BA1A	Artemis	Serpentine vein	14.0	126	34.1	118	20.0	136	22.1	6.01	10.0	14.0	bd	bd
BB1	Limassol Forest Complex	Limassol Forest Complex	33.3	233	53.6	163	25.9	174	27.7	88.7	22.2	29.6	14.8	5.54
BD1	Limassol Forest Complex	Limassol Forest Complex	bd	3.76	1.88	3.76	1.88	9.41	1.88	1.88	5.65	47.0	bd	bd
BD3	Limassol Forest Complex	Limassol Forest Complex	3.73	33.5	9.32	31.7	5.59	46.6	7.45	9.32	5.59	31.7	3.73	5.59
PP2	Olympus	Olympus Bulk Rock	bd	3.52	1.76	10.6	3.52	29.9	7.04	bd	3.52	12.3	bd	bd
AH1	Olympus	Olympus Bulk Rock	bd	3.76	1.88	7.52	1.88	18.8	3.76	1.88	5.64	11.3	bd	bd
CJ1	Olympus	Olympus Bulk Rock	bd	1.82	1.82	3.64	bd	7.28	1.82	bd	1.82	10.9	bd	bd
AG2	Olympus	Olympus Bulk Rock	bd	4.08	2.04	8.16	2.04	18.4	4.08	bd	6.12	26.5	bd	bd
AG1	Olympus	Olympus Bulk Rock	bd	3.58	1.79	7.16	1.79	16.1	3.58	1.79	3.58	17.9	bd	bd
AH2	Olympus	Olympus Bulk Rock	bd	1.59	bd	1.59	bd	4.77	1.59	bd	3.18	14.3	bd	bd

Table 5.6: Summary Table.

	Olympus Whole Rock	***Artemis Whole Rock***	***LFC Whole Rock***	***Olympus 10 % Acetic Leachate***	***Artemis 10 % Acetic Leachate***	***LFC 10 % Acetic Leachate***	***Olympus 3M HCl***	***Artemis 3M HCl***	***LFC 3M HCl***	***Olympus Residue***	***Artemis Residue***	***LFC Residue***
Number of samples	8	13	6	6	10	6	6	11	6	6	10	2
$^{87}Sr/^{86}Sr$	0.705354 to 0.709096	0.705301 to 0.708531	0.70665 to 0.708682	0.705497 to 0.706790	0.705301 to 0.708852	0.708528 to 0.708784	0.705341 to 0.706392	0.705299 to 0.708555	0.708256 to 0.708746	0.70532 to 0.706185	0.705280 to 0.708026	0.704915 to 0.707868
Sr (ng/g) (ICP-MS)	155 to 2,687	997 to 5,982	555 to 3,776	124 to 1,041	379 to 2,531	282 to 1,832	157 to 1,214	310 2,987	213 to 1,539	238 to 757	348 to 2,558	151 to 1,815
Li (ng/g) (ICP-MS)	599 to 3,241	1,677 to 5,010	146 to 1,060	96 to 794	19 to 501	4.3 to 28.4	147 to 1,018	241 to 3,310	103 to 328	351 to 1,476	866 to 4,322	480 to 638
Cu (ng/g) (ICP-MS)	455 to 10,938	8.8 to 29,375	1,025 to 12,770	230 to 4390 (mb)	449 to 8,040 (mb)	494 to 618 (mb)	54 to 4,940	744 to 17,862	267 to 6,228	86 to 6,610	354 to 16,646	132 to 5,924
Rb (ng/g) (ICP-MS)	28 to 189	4 to 520	7 to 95	3 to 51	1 to 124	0.7 to 10.4	13 to 107	6 to 242	3 to 36	7 to 62	2 to 229	2 to 63
Cs (ng/g) (ICP-MS)	44 to 1,028	4 to 3,566	1 to 4	1 to 102	1 to 227	bd	21 to 594	1 to 1,752	0.1 to 1	20 to 386	2 to 1,913	0.1 to 2

	Olympus Whole Rock	***Artemis Whole Rock***	***LFC Whole Rock***	***Olympus 10 % Acetic Leachate***	***Artemis 10 % Acetic Leachate***	***LFC 10 % Acetic Leachate***	***Olympus 3M HCl***	***Artemis 3M HCl***	***LFC 3M HCl***	***Olympus Residue***	***Artemis Residue***	***LFC Residue***
Ba (ng/g) (ICP-MS)	0.1 to 922	2,507 to 39,250	78 to 2,216	1 349	405 to 3,049	3.5 to 420	8 to 441	952 to 12,776	30 to 951	9 to 237	790 to 26,375	87 to 362
K (μg/g)	1.6 to 38.9	0.3 to 22.1	5.4 to 81	0.2 to 3.9	0.3 to 4.4	2.3 to 19.4	0.7 to 3.2	0.2 to 7.3	1.4 to 22	-	-	-
B (μg/g) (LA-ICP-MS; Whole Rock) (ICP-MS; 10% Acetic Leachate)	6.8 to 58.2 (n=6)	16.7 to 79.6 (n=11)	12.7 (n=1)	0.2 to 8.6	0.8 to 29.4	0.4 to 2.1	-	-	-	-	-	-
Rb/K (ng/g/μg/g)	2.8 to 47.7	0.6 to 44.6	0.8 to 2	10.7 to 24.7	0.8 to 30.7	0.3 to 0.7	0.1 to 0.6	2.5 to 68	1.5 to 2.8	-	-	-
Rb/Cs	0.2 to 2.2	1 to 8	8.0 to 42	0.5 to 3.8	0.55 to 10	bd	34 to 132	0.1 to 11	5 to 36	0.1 to 0.4	0.1 to 10.6	34

5.4.1 Radiogenic strontium isotopic compositions

$^{87}Sr/^{86}Sr$ whole-rock values in samples from the Olympus Diapir fall into a wide range between 0.7053 and 0.7091 (Fig. 5.3; Fig. 5.4), samples from the Artemis Diapir also fall into a wide range between 0.7053 and 0.7085 (Fig. 5.3; Fig. 5.4; Table 5.6). In contrast, whole rock $^{87}Sr/^{86}Sr$ values from the Limassol Forest Complex display a narrow range between 0.70855 and 0.70868 except for a single sample with $^{87}Sr/^{86}Sr$ 0.7066 (Fig. 5.3; Fig. 5.4). Progressive leaching experiments yield differences in $^{87}Sr/^{86}Sr$ values between each respective leaching step and sample area (Table 5.6). The initial 10 % Acetic acid leachate of the Olympus Diapir matches the corresponding whole-rock $^{87}Sr/^{86}Sr$ value (Fig. 5.3; Fig. 5.4; Table 5.6). In contrast, 10 % Acetic acid leachates of the Artemis Diapir fall into two discrete groups: (1) Two samples yield low strontium isotopic compositions between 0.7053 and 0.7056 and (2) the majority of the samples that range between 0.7086 and 0.7088 (Fig. 5.3; Fig. 5.4). 10 % Acetic acid leachates from the Limassol Forest Complex fall into a narrow range that ranges between 0.7085 to 0.7088 (Fig. 5.3; Fig. 5.4). In the Artemis Diapir and Limassol Forest Complex, the 3M HCl leachates have $^{87}Sr/^{86}Sr$ values that match whole-rock values (Fig. 5.3; Fig. 5.4). The final rock residue $^{87}Sr/^{86}Sr$ values of the Olympus Diapir are similar to whole-rock values. In contrast, final rock $^{87}Sr/^{86}Sr$ residues of the Artemis Diapir shift closer to primitive values, falling into two discrete groups: (1) most samples yield relatively low Sr isotope ratios between 0.705280 and 0.706308 whereas (2) a small group has $^{87}Sr/^{86}Sr$ between 0.707245 and 0.708026 (Fig. 5.3; Fig. 5.4).

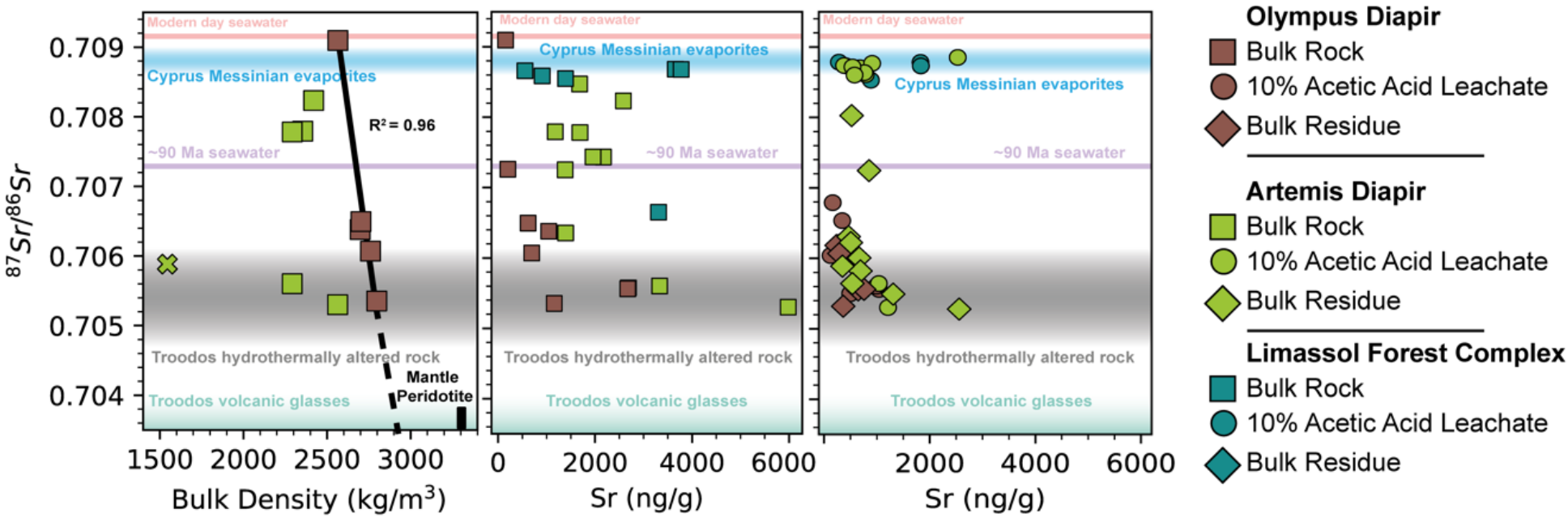

Figure 5.3: (Left) Plot of Bulk Rock $^{87}Sr/^{86}Sr$ and Bulk Density (kg/m^3) of samples from the Troodos Mantle Sequence. A least squares regression through samples from the Olympus Diapir has a R^2 value of 0.96. (Middle) Plot of $^{87}Sr/^{86}Sr$ vs Sr (ng/g) concentration of Bulk Rock samples located within the Olympus Diapir, Artemis Diapir, and Limassol Forest Complex. (Right) Plot of $^{87}Sr/^{86}Sr$ vs Sr (ng/g) concentration of 10% Acetic Acid Leachates and Bulk Residue samples located within the Olympus Diapir, Artemis Diapir, and Limassol Forest Complex. Boundaries of Troodos volcanic glasses (Rautenschlein et al., 1985), Troodos hydrothermally altered rock (Bickle and Teagle, 1992), Cretaceous ~90 Ma and modern day seawater (McArthur et al., 2012), and Cyprus Messinian evaporites (Flecker and Ellam, 2006; McCulloch and Deckker, 1989; Müller and Mueller, 1991) are shown.

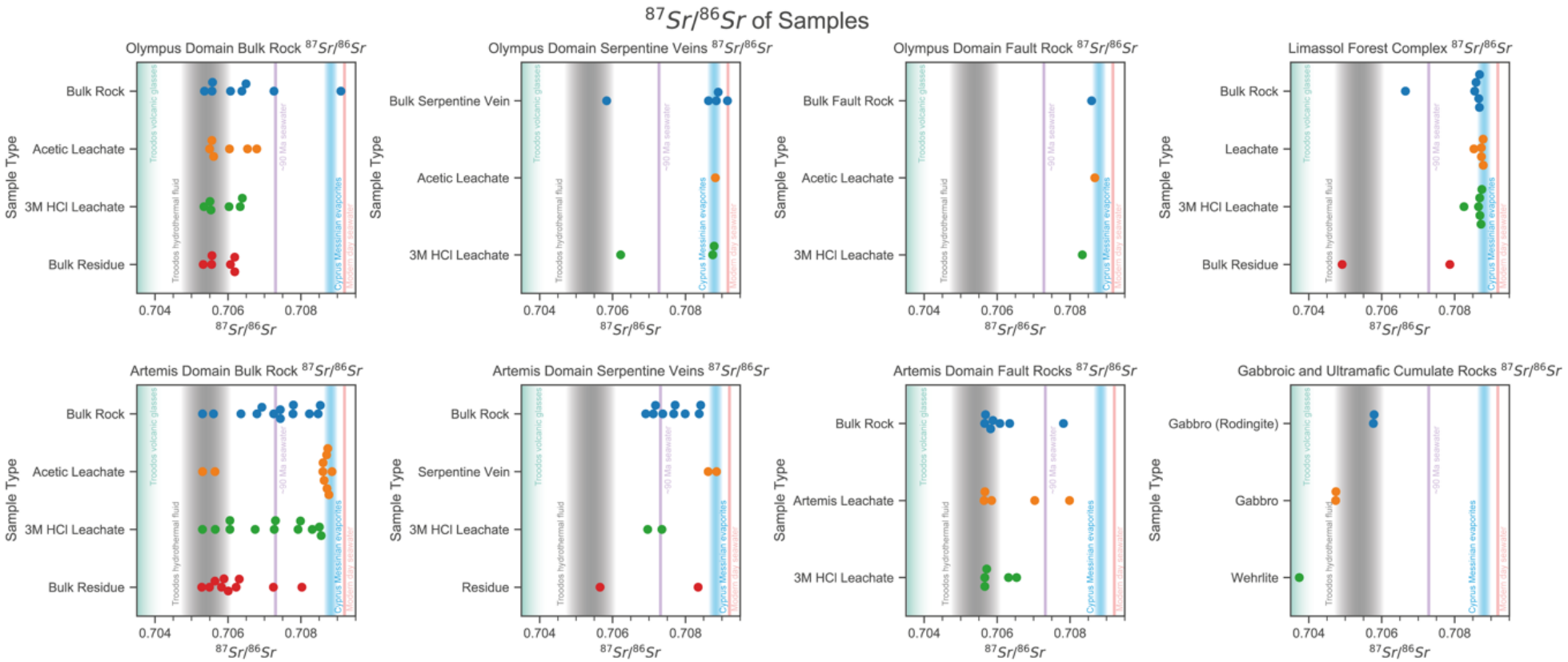

Figure 5.4: A series of Caltech plots of determined $^{87}Sr/^{86}Sr$ ratios from progressive leaching step results of respective sample types within the Troodos Massif and Limassol Forest Complex. Boundaries of Troodos volcanic glasses (Rautenschlein et al., 1985), Troodos hydrothermally altered rock (Bickle and Teagle, 1992), Cretaceous ~90 Ma and modern day seawater (McArthur et al., 2012), and Cyprus Messinian evaporites (Flecker and Ellam, 2006; McCulloch and Deckker, 1989; Müller and Mueller, 1991) are shown.

A strong linear correlation (R^2 = 0.96) occurs between the whole-rock radiogenic strontium isotopic composition and bulk density of the Olympus Diapir, with the highest bulk density (2797 kg/m^3) yielding the lowest $^{87}Sr/^{86}Sr$ (0.7053) value and the lowest bulk density (2,565 kg/m^3) sample yields the highest $^{87}Sr/^{86}Sr$ (0.7091) value (Fig. 5.3; Fig. 5.4). In contrast, there is no correlation between radiogenic strontium isotopic compositions and bulk density in samples from the Artemis Diapir. Artemis Diapir whole-rock samples fall into two separate groups of similar bulk densities (2200 to 2550 kg/m^3) but different $^{87}Sr/^{86}Sr$ ratios ~0.7055 and ~0.7080 respectively. Sr concentrations in the Olympus Diapir whole-rocks ranges between 155 ng/g to 2687 ng/g, whole-rocks in the Artemis Diapir vary by an order of magnitude (553 to 5982 ng/g), and whole-rock samples in the Limassol Forest Complex ranges between 555 and 3776 ng/g (Fig. 5.5; Table 5.6). Samples with lower Sr isotopic compositions yield higher concentrations of fluid-mobile trace elements (e.g., Li, B, Sr, Rb, Cs, Ba) in serpentinised samples within the Troodos Mantle Sequence (Fig. 5.6; Fig. 5.7). Primitive mantle normalised trace element concentrations show that fluid-mobile trace elements (e.g., Li, Sr, Rb, Cs, Ba, U) in Olympus and Artemis are enriched relative to typically fluid immobile elements such as Nd and Pr (Fig. 5.7). Each Progressive leaching step typically represents ~30 to 40% of the overall Sr budget as measured in the whole rock (Table 5.6).

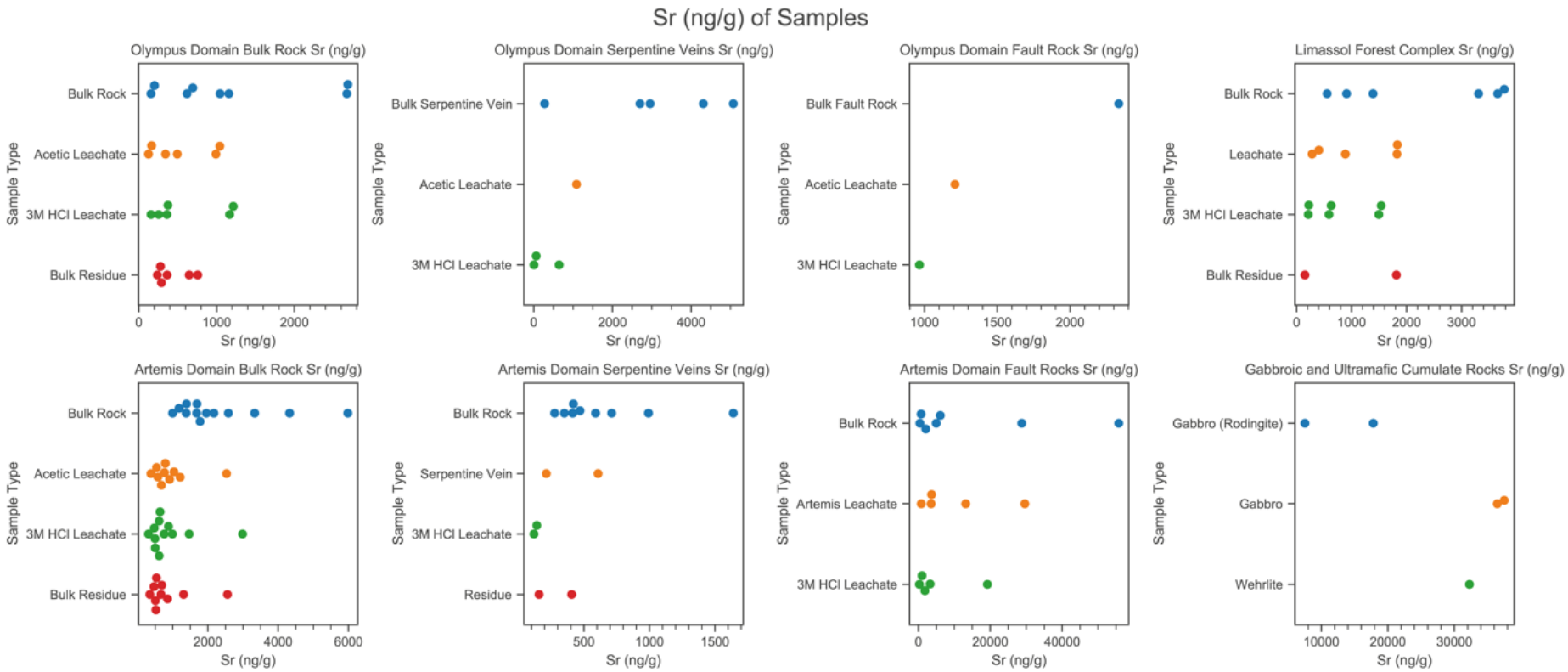

Figure 5.5: A series of Caltech plots of Sr (ng/g) concentrations from progressive leaching step results of respective sample types within the Troodos Massif and Limassol Forest Complex.

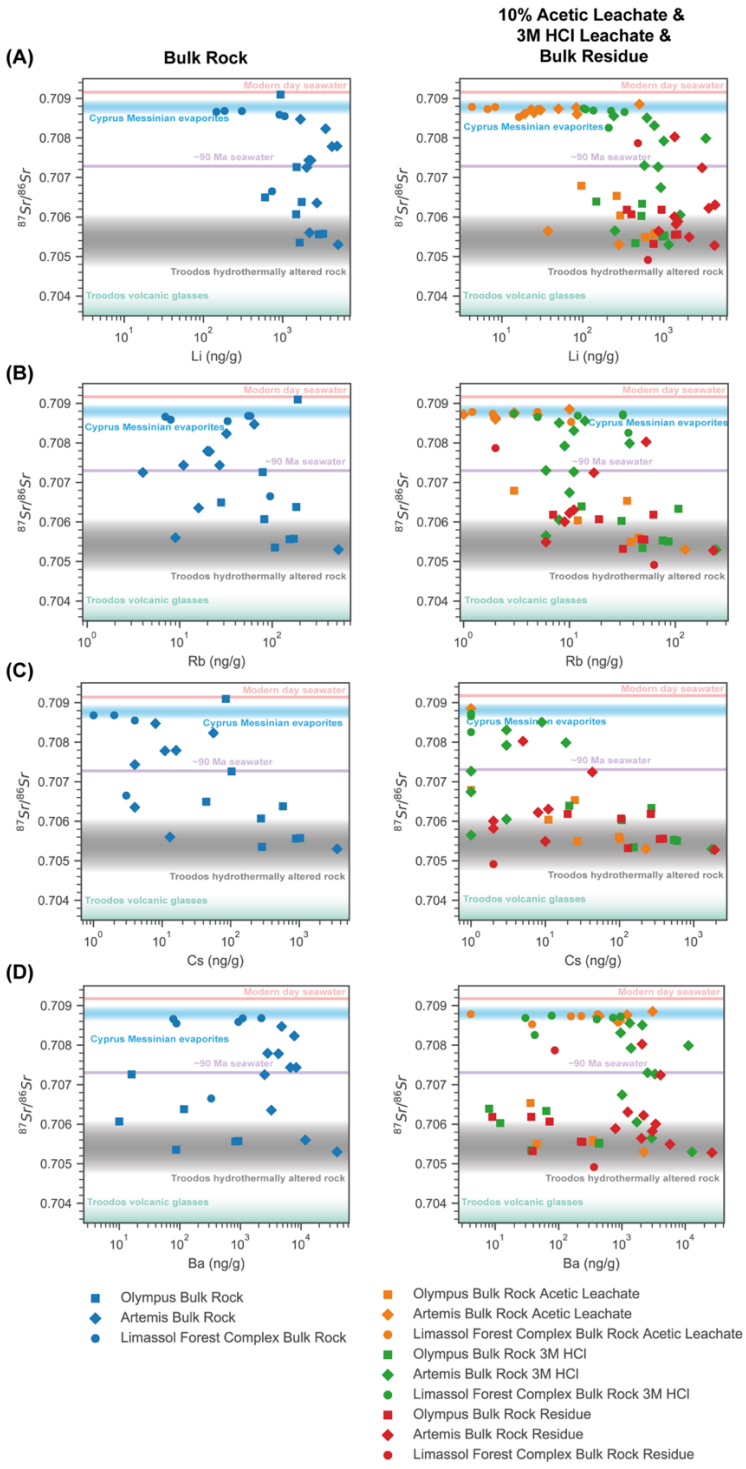

Figure 5.6: (A) Plot of $^{87}Sr/^{86}Sr$ and Li (ng/g) of Bulk Rocks with a parallel plot of progressive leaching steps 10% Acetic Leachate, 3M HCl Leachate, and Bulk Residue. (B) Plot of $^{87}Sr/^{86}Sr$ and Li (ng/g) of Bulk Rocks with a parallel plot of progressive leaching steps 10% Acetic Leachate, 3M HCl Leachate, and Bulk Residue. (C) Plot of $^{87}Sr/^{86}Sr$ and Li (ng/g) of Bulk Rocks with a parallel plot of progressive leaching steps 10% Acetic Leachate, 3M HCl Leachate, and Bulk Residue. (D) Plot of $^{87}Sr/^{86}Sr$ and Li (ng/g) of Bulk Rocks with a parallel plot of progressive leaching steps 10 % Acetic Leachate, 3M HCl Leachate, and Bulk Residue. Boundaries of Troodos volcanic glasses (Rautenschlein et al., 1985), Troodos hydrothermally altered rock (Bickle and Teagle, 1992), Cretaceous ~90 Ma and modern day seawater (McArthur et al., 2012), and Cyprus Messinian evaporites (Flecker and Ellam, 2006; McCulloch and Deckker, 1989; Müller and Mueller, 1991) are shown.

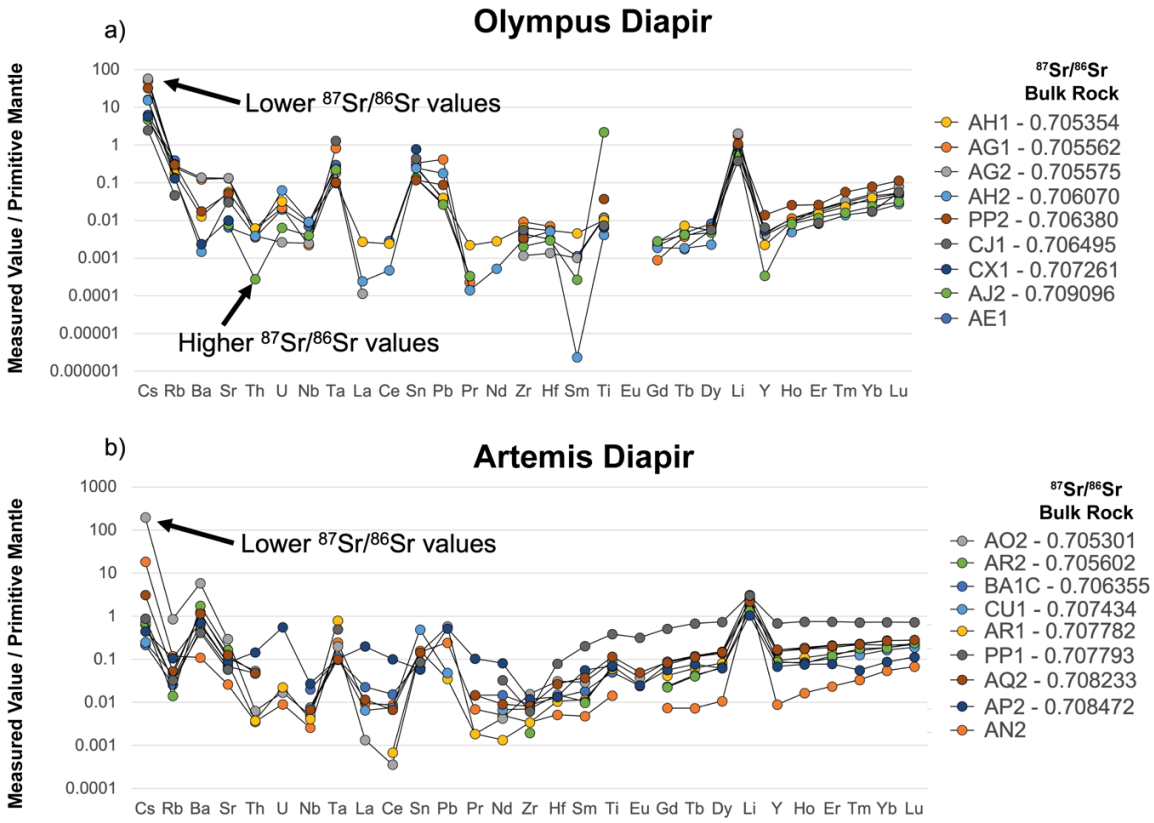

Figure 5.7: Primitive mantle normalised trace element plots using primitive mantle values from Palme and O'Neill (2014). (A) Refers to whole rock samples from the Olympus Diapir and (B) whole rock samples from the Artemis Diapir.

5.4.2 Trace element ratios

Trace element ratios Rb/K, Rb/Cs, and K/Cs plotted vs. $^{87}Sr/^{86}Sr$ ratios (Fig. 5.8) from samples from the Olympus and Artemis Diapirs highlight a progressive evolution of whole rock samples from low $^{87}Sr/^{86}Sr$ values (~0.705) with relatively lower Rb/Cs (~0.1 to ~1), lower K/Cs (~3 to ~50), and higher Rb/K (~10 to 45); to radiogenic $^{87}Sr/^{86}Sr$ values ~0.708 to 0.709 with relatively higher Rb/Cs (~1 to ~30), higher K/Cs (~>10^2 to ~<10^5), and lower Rb/K (~0.2 to ~2; Fig. 5.8).

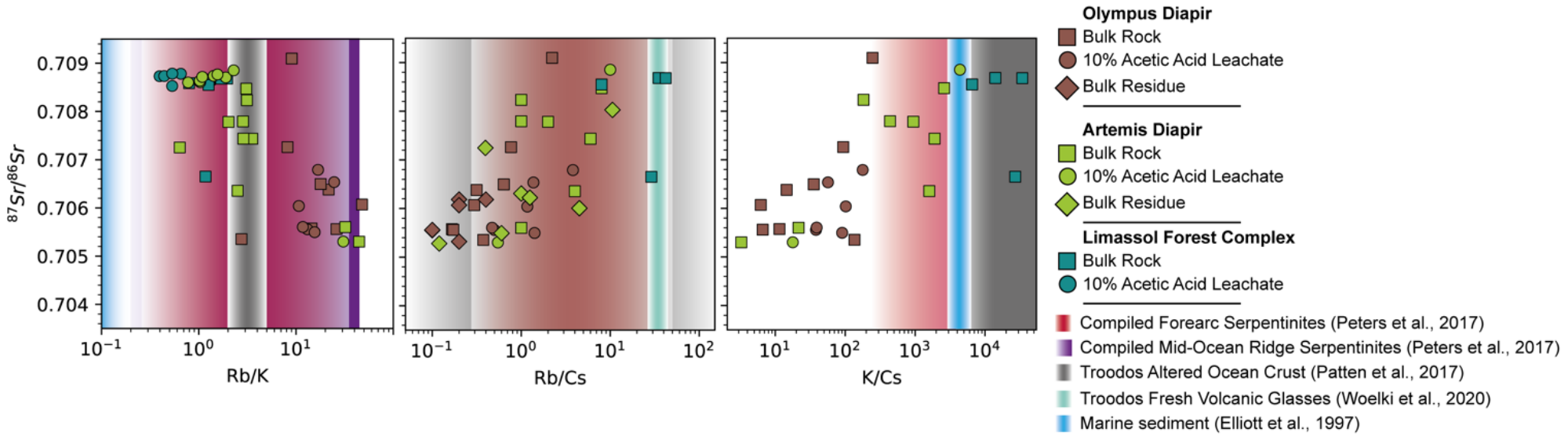

Figure 5.8: Plots of $^{87}Sr/^{86}Sr$ and Rb/K (ng/g/µg/g), Rb/Cs and K/Cs. Previously published serpentine ratio values are also shown as shaded areas. Shaded areas reflect the reported range, which typically spans several orders of magnitude (e.g., Peters et al. (2017) and references therein). In addition, Troodos volcanic glasses, Marine sediment, and Troodos Altered Ocean Crust values are also shown (Elliott et al., 1997; Patten et al., 2017; Woelki et al., 2020).

5.4.3 Boron isotopic composition and concentration

In situ boron isotopic compositions of mesh-textured serpentine and serpentine veins yield similar values for both the Olympus and Artemis Diapirs. In the Olympus Diapir, all determined in situ boron isotopic compositions range between 6.89 and 16.24 ‰, with an average of 10.6 ± 3.2 ‰ (1σ, n = 11; Fig. 5.9; Fig. 5.10; Table 5.7). In comparison, in the Artemis Diapir, all determined in situ boron isotopic compositions vary between 6.72 and 18.41 ‰, with an average of 12.5 ± 2.9 ‰ (1σ, n = 37; Fig. 5.9; Fig. 5.10; Table 5.7). In contrast, samples from the Limassol Forest Complex yield *in situ* boron isotopic compositions ranging between 32.7 and 47.7 ‰ with an average of 42.7 ± 5.9 ‰ (1σ, n = 5; Fig. 5.9; Fig. 5.10; Table 5.7). Despite the narrow range of serpentine boron isotopic compositions for the Olympus and Artemis Diapirs, in situ boron concentrations range between 3.1 to 48.7 μg/g with higher values measured in the Artemis Diapir (22.7 ± 14.2 μg/g, 1σ, n = 37) relative to the Olympus Diapir (15.9 ± 9.1 μg/g, 1σ, n = 37; Fig. 5.9; Fig. 5.10; Fig. 5.11). In the Limassol Forest Complex, the *in situ* boron concentrations are lower than the Artemis and Olympus Diapirs (12.7 ± 5.5 μg/g, 1σ, n = 5; Fig. 5.9; Fig. 5.10; Fig. 5.11). The serpentines measured display a wide range of boron concentrations but there are distinct differences between the different serpentine types (Fig. 5.9; Fig. 5.10; Fig. 5.11). Mesh textured serpentine in both the Olympus and Artemis Diapirs yields higher average values μg/g of 20.2 ± 9.2 and 29.5 ± 11.4 μg/g (1σ) respectively relative to serpentine veins average B concentrations of 9.1 ± 1.9 μg/g (1σ) in the Olympus Diapir and 8.9 ± 6.2 μg/g (1σ) in the Artemis Diapir. Chrysotile serpentine veins in the Artemis Diapir yield similar high B concentrations (34.6 ± 5.6 μg/g) to mesh textured serpentine and contrast with the low concentrations of non-fibrous serpentine veins. Boron concentrations of samples from the Limassol Forest Complex are on average lower (12.8 ± 5.5 μg/g) than the Olympus and Artemis Diapir, with no difference in the boron concentrations between respective serpentine types (Fig. 5.9; Fig. 5.10; Fig. 5.11).

Comparison of whole-rock and 10% Acetic acid leachates B concentrations and $^{87}Sr/^{86}Sr$ ratios highlights higher B concentrations in samples with lower $^{87}Sr/^{86}Sr$ ratios (Fig. 5.9) and a general progression to more radiogenic Sr isotopic compositions with decreasing B concentration. The majority of 10% Acetic acid leachates from the Artemis and Limassol Forest Complex fall into a distinct radiogenic Sr isotopic composition (~0.7087) group (Fig. 5.9).

In situ Boron elemental count mapping of a completely serpentinised sample from the Artemis Diapir highlights serpentine phases with distinct B concentrations (Fig. 5.12). In general, 3 distinct serpentine phases occur within the mapped region: (1) A high B serpentine phase that pseudomorphs the original olivine grain morphology; (2) A moderate B serpentine phase surrounding the high B serpentine phase; and (3) a low B serpentine phase located within discrete but irregular serpentine veins and some areas of the mesh-textured background serpentine.

Table 5.7: $\delta^{11}B$ (LA-MC-ICP-MS) and B (LA-ICP-MS) concentration analytical result table

Sample Name	***Sample Type***	***Sample Area***	***$^{11}B/^{10}B$***	***±2SE***	***δ11B***	***±2SE***	***B (µg/g)***	***±2SE***
AA4-1	Mesh texture	Artemis	4.0776	0.0028	6.72	0.70	11.30	0.34
AA4-3	Mesh texture	Artemis	4.0807	0.0032	7.49	0.79	27.60	0.67
AA4-5	Serpentine Vein	Artemis	4.0835	0.0058	8.18	1.41	4.65	0.67
AA4-7	Serpentine Vein	Artemis	4.0790	0.0038	7.08	0.94	3.05	0.09
AA4-9	Serpentine Vein	Artemis	4.0833	0.0039	8.15	0.95	3.82	0.23
AA4-11	Serpentine Vein	Artemis	4.0886	0.0036	9.46	0.89	3.97	0.07
AH1-3 2	Mesh texture	Olympus	4.0851	0.0035	8.58	0.86	36.23	0.69
AH1-3 4	Mesh texture	Olympus	4.0845	0.0043	8.43	1.04	29.00	1.37
AH1-3 5	Mesh texture	Olympus	4.0853	0.0053	8.63	1.29	20.41	0.63
AR3-1 conc line	Mesh texture	Artemis	4.1068	0.0008	13.97	0.19	35.27	0.58
AR3-1 Andradite	Andradite Vein	Artemis	4.1000	0.0007	12.27	0.18	33.96	0.35

Sample Name	*Sample Type*	*Sample Area*	*$^{11}B/^{10}B$*	*±2SE*	*δ11B*	*±2SE*	*B (µg/g)*	*±2SE*
AR3-1 chrysotile	Chrysotile Vein	Artemis	4.1170	0.0009	16.50	0.22	34.86	0.52
AR3-1 recrystallised	Mesh texture	Artemis	4.1034	0.0016	13.11	0.40	41.75	1.48
AR3-1 lower chrysotile	Chrysotile Vein	Artemis	4.1114	0.0015	15.09	0.37	28.07	1.70
AR3-1 Ribbon	Mesh texture	Artemis	4.1040	0.0040	13.27	0.99	46.24	1.81
AR3-1 Serpentine in centre	Serpentine Vein	Artemis	4.1067	0.0054	13.95	1.32	48.65	0.47
AH2-1 1	Mesh texture	Olympus	4.0936	0.0063	10.69	1.53	11.87	0.49
AH2-1 6	Black fine grained serpentine vein	Olympus	4.1074	0.0058	14.11	1.40	6.28	0.98
AH2-1 black vein	Black fine grained serpentine vein	Olympus	4.0879	0.0019	9.28	0.47	10.58	0.44
AH2-1 2	Mesh texture	Olympus	4.1049	0.0022	13.51	0.53	12.52	0.70
AH2-1 3	Mesh texture	Olympus	4.1160	0.0021	16.24	0.52	13.08	0.60
AH2-1 4	Mesh texture	Olympus	4.1024	0.0015	12.88	0.38	13.08	1.61

Sample Name	*Sample Type*	*Sample Area*	*$^{11}B/^{10}B$*	*±2SE*	*δ11B*	*±2SE*	*B (µg/g)*	*±2SE*
BB1-1	Mesh texture	Limassol Forest Complex	4.2347	0.0070	45.65	1.65	8.98	3.74
BB1-2	Mesh texture	Limassol Forest Complex	4.2428	0.0037	47.67	0.87	15.55	4.73
BB1-3	Mesh texture	Limassol Forest Complex	4.2291	0.0034	44.28	0.81	4.94	2.10
BB1-4	Mesh texture	Limassol Forest Complex	4.2248	0.0043	43.21	1.01	17.51	3.67
BB1-5 oblique	Serpentine Vein	Limassol Forest Complex	4.1822	0.0023	32.66	0.54	16.72	3.82
BA1-X1	Mesh texture	Artemis	4.0957	0.0023	11.22	0.56	23.70	0.56
BA1-X2	Mesh texture	Artemis	4.0943	0.0019	10.87	0.47	22.41	0.75
BA1 X3	Mesh texture	Artemis	4.1131	0.0027	15.52	0.65	28.88	2.00
BA1 X4	Serpentine Vein	Artemis	4.1160	0.0027	16.24	0.67	13.22	1.59
BA1 X5	Serpentine Vein	Artemis	4.1204	0.0031	17.33	0.76	3.83	0.20
BA1 X6	Serpentine Vein	Artemis	4.1248	0.0040	18.41	0.98	3.78	0.17

Sample Name	*Sample Type*	*Sample Area*	*$^{11}B/^{10}B$*	*±2SE*	*δ11B*	*±2SE*	*B (µg/g)*	*±2SE*
BA1 Y1	Mesh texture	Artemis	4.1033	0.0046	13.09	1.12	20.66	1.92
BA1 Y2	Serpentine Vein	Artemis	4.1095	0.0042	14.64	1.01	6.61	0.50
BA1 Y3	Serpentine Vein	Artemis	4.1147	0.0028	15.93	0.68	13.57	0.65
BA1 Y4	Black serpentine vein	Artemis	4.1150	0.0030	16.01	0.73	46.98	1.92
BA1 Y5	Mesh texture	Artemis	4.1139	0.0031	15.72	0.75	25.44	0.66
BA1 Z1	Serpentine Vein	Artemis	4.0981	0.0025	11.80	0.61	10.60	0.91
BA1 Z2	Serpentine Vein	Artemis	4.0987	0.0027	11.95	0.67	8.21	0.44
BA1 Z3	Serpentine Vein	Artemis	4.1024	0.0030	12.87	0.72	22.27	0.94
AX1 X1 mesh	Mesh texture	Artemis	4.0993	0.0010	12.10	0.25	18.36	0.34
AX1 X2 mesh	Mesh texture	Artemis	4.0974	0.0009	11.63	0.22	30.18	0.57
AX1 X3 recryz	Mesh texture	Artemis	4.0961	0.0013	11.32	0.32	33.33	0.40
AX1 X4 bastite	Mesh texture	Artemis	4.0900	0.0020	9.80	0.49	33.92	0.63
AX1 X5 vein edge	Mesh texture	Artemis	4.0970	0.0011	11.54	0.26	7.20	0.40
AX1 X6 polyg vein	Serpentine Vein	Artemis	4.0917	0.0009	10.22	0.22	17.80	0.59

Sample Name	*Sample Type*	*Sample Area*	$^{11}B/^{10}B$	*±2SE*	*δ11B*	*±2SE*	*B (µg/g)*	*±2SE*
AX1 X7 recryz veined	Mesh texture	Artemis	4.0966	0.0012	11.44	0.30	9.02	0.22
AX1 X8 recryz	Mesh texture	Artemis	4.0970	0.0013	11.54	0.31	34.71	0.84
AX1 X9 mesh	Mesh texture	Artemis	4.1017	0.0013	12.69	0.31	38.97	0.49
AX1 X10 chrysotile	Chrysotile Vein	Artemis	4.1082	0.0010	14.30	0.25	41.68	0.76
AJ1 Ant Back 1	Antigorite Vein	Olympus	4.0783	0.0006	6.91	0.14	9.80	0.18
AJ1 Ant Back 2	Antigorite Vein	Olympus	4.0782	0.0006	6.89	0.15	9.67	0.13

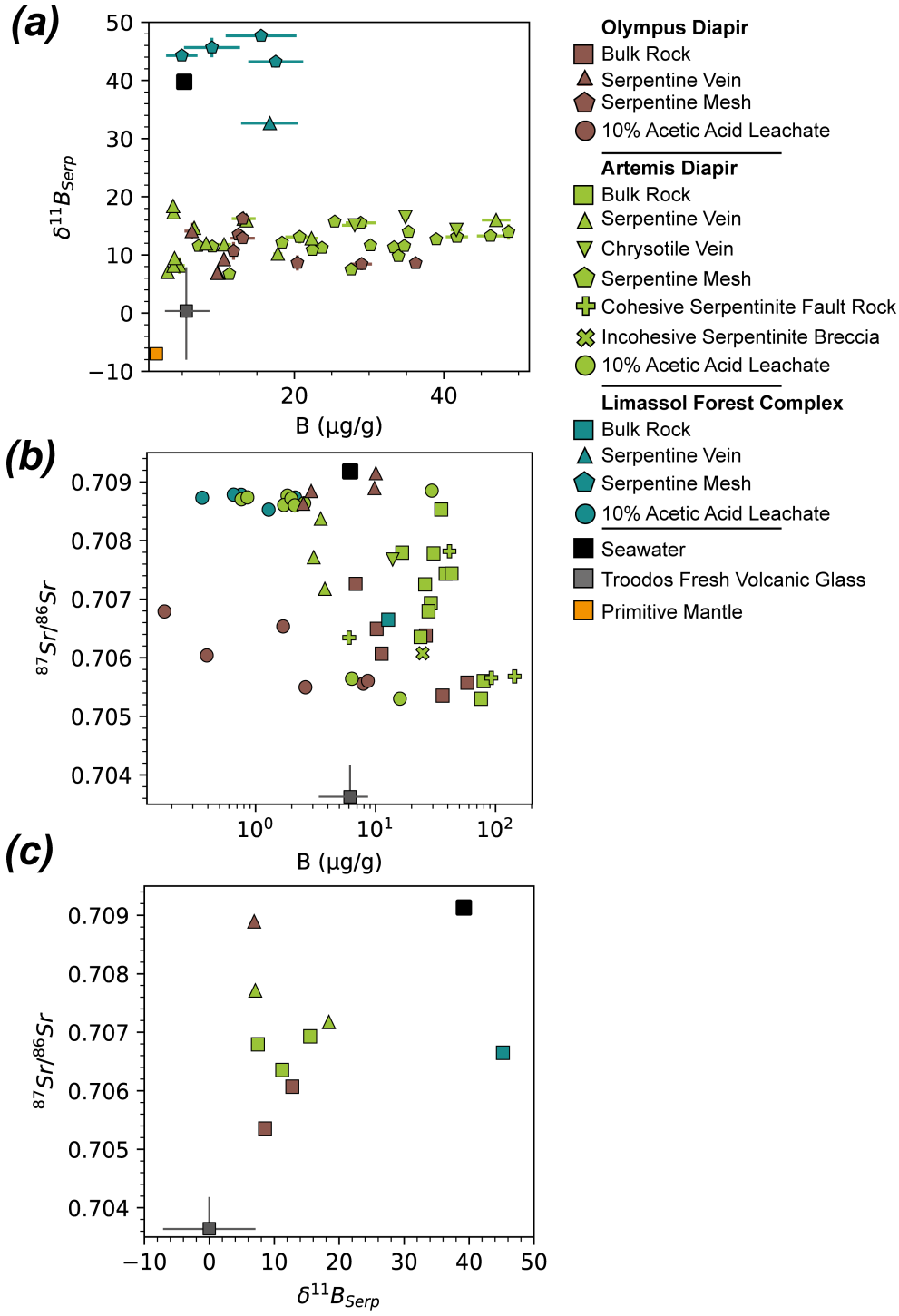

Figure 5.9: (A) Plot of δ^{11}B and B (µg/g) of *in situ* LA-MC-ICP-MS and LA-ICP-MS data. Error bars are ±2SE of the mean of 100 integration cycles. Most symbols are larger than the ±2SE of the analysis. (B) Plot of $^{87}Sr/^{86}Sr$ and B (µg/g) is shown. 10% Acetic Leachates were measured by ICP-MS and rock samples were prepared as pressed powder pellets and measured by LA-ICP-MS. (C) Plot of $^{87}Sr/^{86}Sr$ and δ^{11}B. Troodos Fresh Volcanic Glass values (Fonseca et al., 2017) are shown and error bars are equivalent to ±2σ of the mean of reported values. Seawater values (Foster et al., 2010; Spivack et al., 1987) and primitive mantle values (Chaussidon and Jambon, 1994) are also shown.

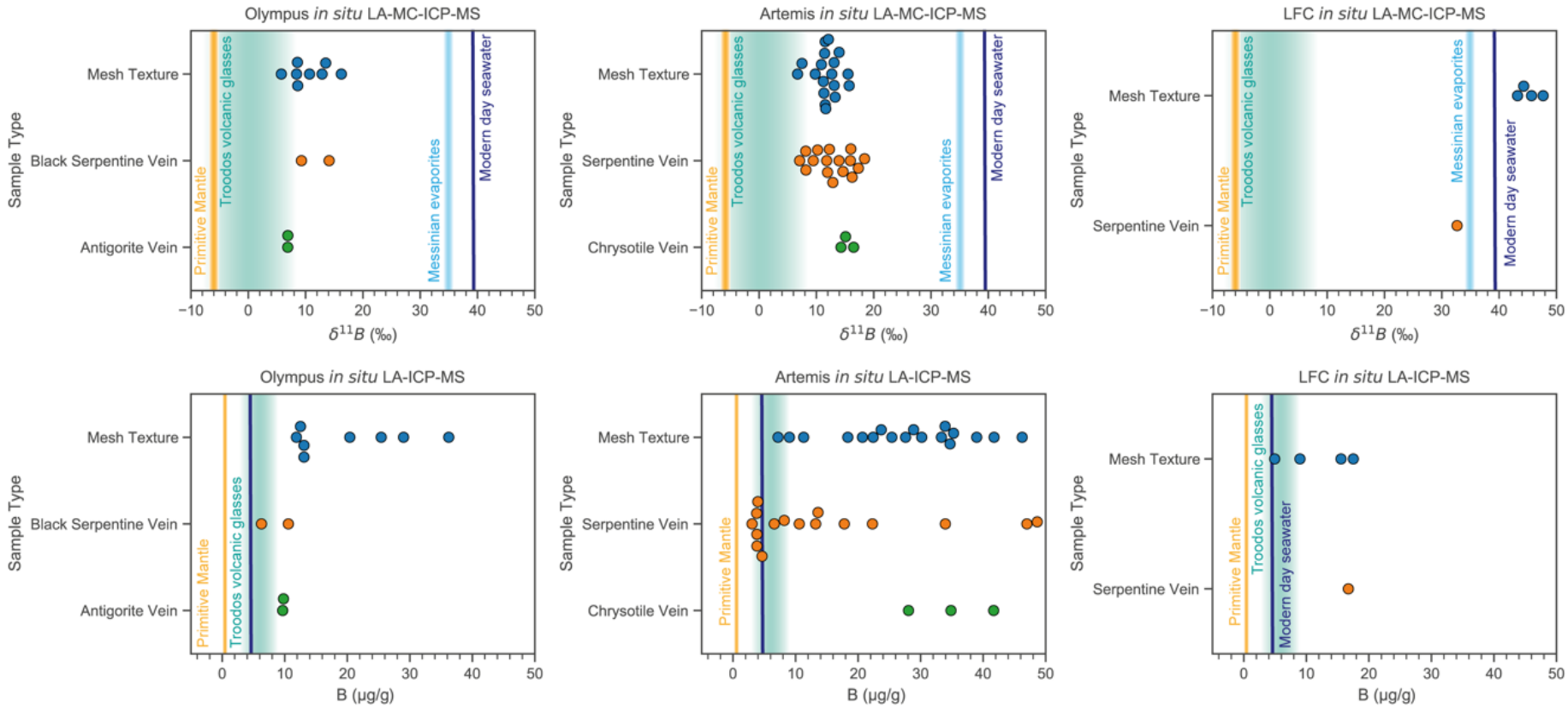

Figure 5.10: A series of Caltech plots showing $\delta^{11}B$ and B (µg/g) concentration data from LA-MC-ICP-MS on samples from the Olympus Diapir, Artemis Diapir, and Limassol Forest Complex. Boundaries of $\delta^{11}B$ of Troodos volcanic glasses (Fonseca et al., 2017), Messinian evaporites (Paris et al., 2010), modern day seawater (Foster et al., 2010), and primitive mantle (Chaussidon and Jambon, 1994) are shown. Boundaries of B (µg/g) of Troodos volcanic glasses (Fonseca et al., 2017), modern day seawater (Spivack et al., 1987), and primitive mantle (Chaussidon and Jambon, 1994) are also shown. Shading is equivalent to 2σ of the reported value.

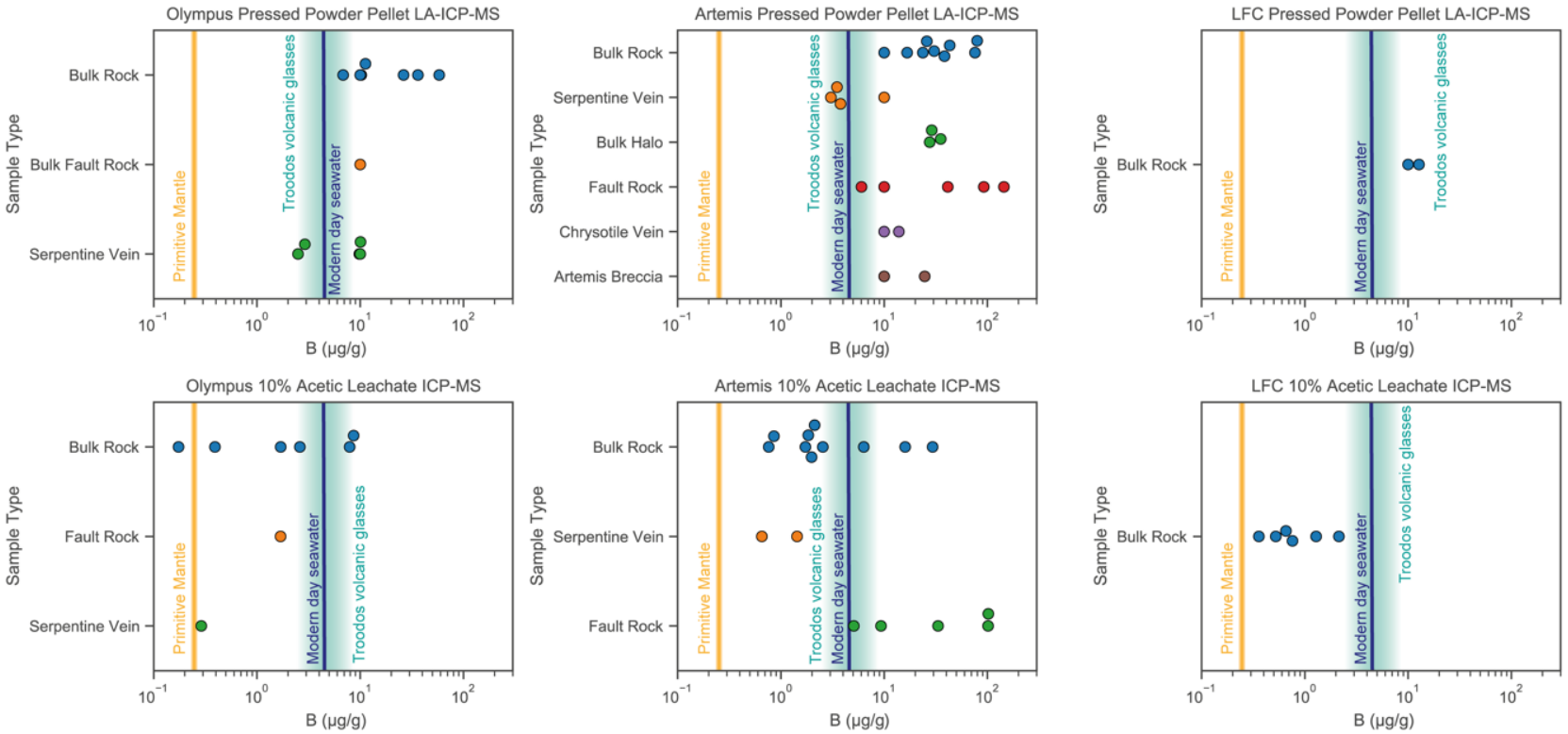

Figure 5.11: A series of Caltech plots showing B (µg/g) concentration data from LA-MC-ICP-MS on pressed powder pellets and 10% Acetic leachate ICP-MS data from the Olympus Diapir, Artemis Diapir, and Limassol Forest Complex. Boundaries of B (µg/g) of Troodos volcanic glasses (Fonseca et al., 2017), modern day seawater (Spivack et al., 1987), and primitive mantle (Chaussidon and Jambon, 1994) are also shown. Shading is equivalent to 2σ of the reported value.

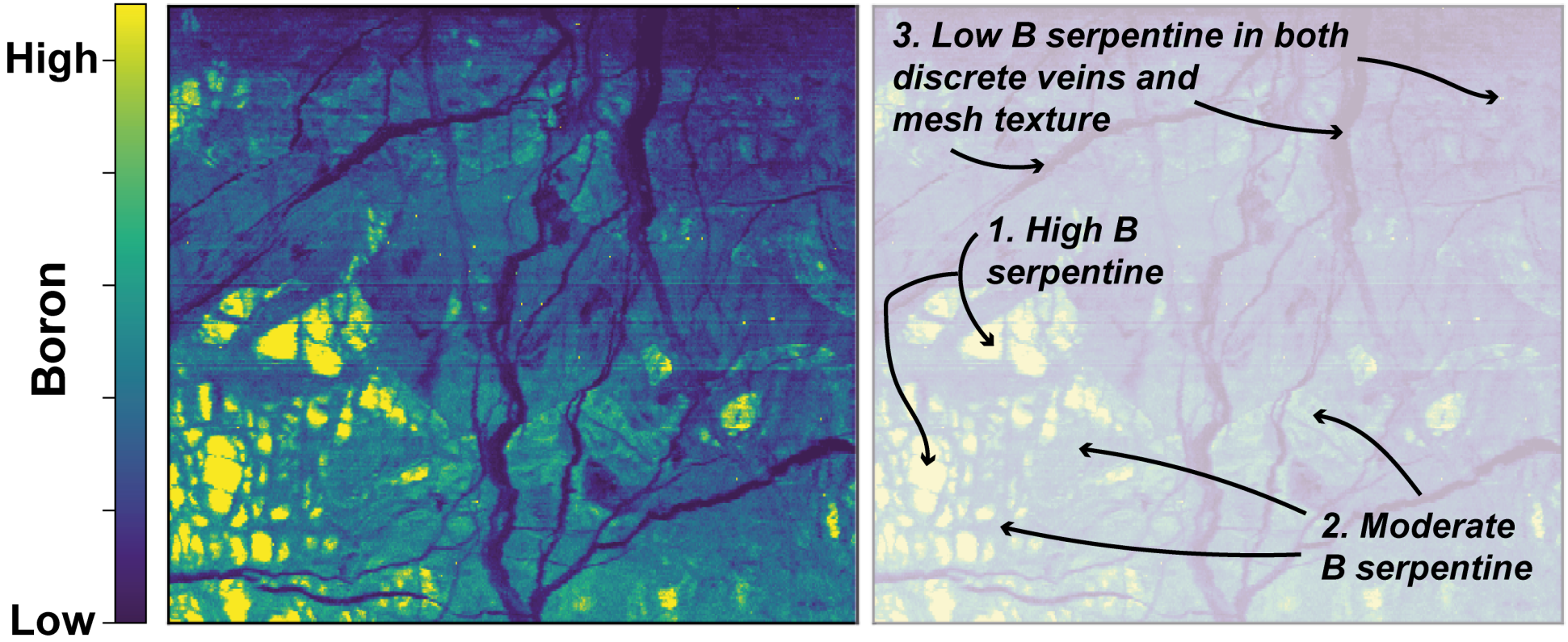

Figure 5.12: *In situ* Boron element map of a completely serpentinised sample from within the Artemis Diapir. Boron data is plotted as counts per second and the relative differences are colour mapped accordingly. Three distinct B phases are reflected within the map.

5.5 Comparison with previous serpentine geochemical and isotopic data

5.5.1 Isotope values

Results from whole rock and progressive leaching experiments of trace element and strontium isotopic compositions and in situ boron isotopic compositions and concentrations indicates that discrete portions of the variably serpentinised Troodos Mantle Sequence have interacted with fluids of differing composition. Whole rock $^{87}Sr/^{86}Sr$ ratios from the Olympus and Artemis Diapirs display a wide range in values from ~0.705 to ~0.709. Samples with higher bulk densities, which are less serpentinised, generally yield more primitive $^{87}Sr/^{86}Sr$ ratios (~0.705, Fig. 5.3). Progressive leaching steps highlight that whole rock $^{87}Sr/^{86}Sr$ values reflect mixing between two distinct Sr reservoirs: a ~0.705 end member and a more radiogenic ~0.7087 end member. The relative proportions of each end member and their respective Sr concentration culminates in a final whole-rock $^{87}Sr/^{86}Sr$ value. Whole rock samples with lower $^{87}Sr/^{86}Sr$ ~0.705, generally display higher concentrations in fluid-mobile elements (Na, Li, B, Li, B, Sr, Rb, Cs, Ba, Cu). In contrast to the wide range in $^{87}Sr/^{86}Sr$ ratios within the Olympus and Artemis Diapirs, boron isotopic compositions display a narrow range +7 to +18.4 ‰ (Fig. 5.9). Although there is no discernible difference in $\delta^{11}B$ between serpentine veins, chrysotile veins, and mesh-textured serpentine, each respective serpentine type yields differing B concentrations with the highest B concentrations corresponding to more primitive $^{87}Sr/^{86}Sr$ ~0.705 whole rock samples (Fig. 5.9). There are few published measurements of radiogenic strontium isotopic compositions for serpentinised mantle rock and the whole-rock $^{87}Sr/^{86}Sr$ values reported may be contaminated by trace amounts of carbonate (Boschi et al., 2008; McCaig et al., 2010).

Boron isotopic compositions of samples from the Olympus and Artemis Diapirs are similar to published serpentinite boron isotopic compositions (Fig. 5.13), including samples from the Mid-Atlantic Ridge and Mariana Forearc mud volcanoes. Although the compiled published serpentinite analyses are from contrasting geological settings and have interacted with fluids of differing origins (Benton, 1997; Benton et al., 2001; Boschi et al., 2008; Harvey et al., 2014; Martin et al., 2016; Spivack and Edmond, 1987), most samples fall into a narrow range between of $\delta^{11}B$ of +6 and +18 ‰, although some Mariana Forearc serpentinite samples have values up to +24 ‰ (Fig. 5.13). In contrast, serpentinite samples from the Limassol Forest Complex, Cyprus yield the highest measured values from compiled previously reported boron isotopic compositions (Fig. 5.13) of up to +47.5 ‰, which is higher than seawater +39.61 ‰ (Foster et al., 2010). Previously measured

serpentinites from the Mid-Atlantic Ridge ODP Leg 209 (Vils et al., 2009) yield heavy $\delta^{11}B$ isotopic compositions +32 to +40 ‰ and are heavier compared to other exhumed serpentinised massifs along the Mid-Atlantic Ridge such as the Atlantis Massif (Fig. 5.13; Boschi et al., 2008). These high boron isotopic compositions in recovered samples from ODP Leg 209 are interpreted as a result of progressive exchange between serpentinised mantle rocks and seawater resulting in evolved boron isotopic compositions of the serpentinising fluid with values higher than seawater (Vils et al., 2009).

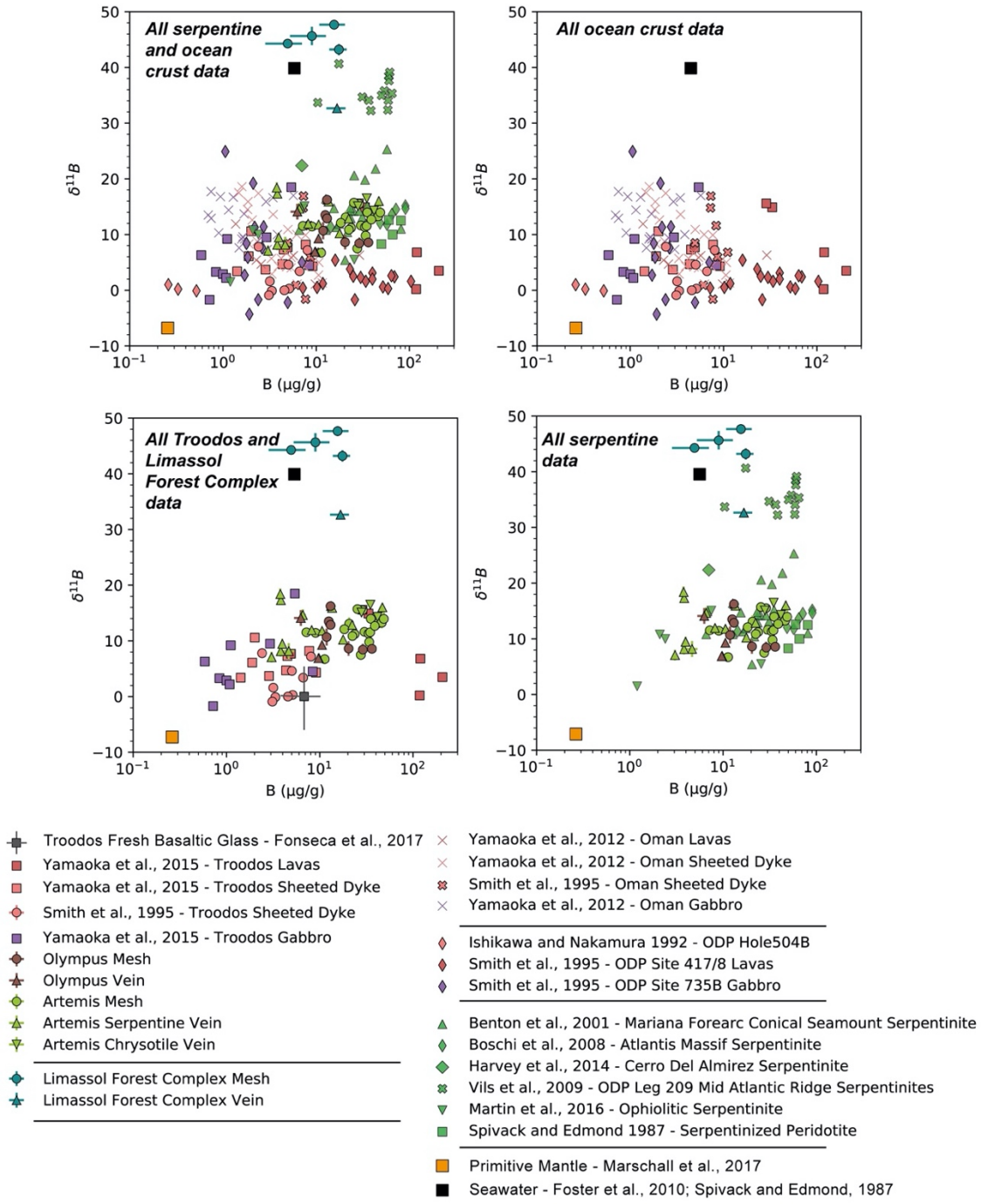

Figure 5.13: Plots of δ^{11}B and B (µg/g) of published serpentine and ocean crust values. Errors bars are equivalent to ±2SE of the mean and most error bars are smaller than markers. Plots are divided into groupings of showing all serpentine and ocean crust values, all ocean crust data, all Troodos and Limassol Forest Complex data, and all serpentine data (Benton et al., 2001; Boschi et al., 2008; Fonseca et al., 2017; Foster et al., 2010; Harvey et al., 2014; Ishikawa and Nakamura, 1992; Marschall et al., 2017; Martin et al., 2016; Smith et al., 1995; Spivack and Edmond, 1987; Vils et al., 2009; Yamaoka et al., 2012, 2015a).

5.5.2 Trace element ratios

Altered and unalerted ‘fresh’ Mid-Ocean Ridge Basalts yield contrasting trace element ratios (Rb/K, Rb/Cs, and K/Cs; Table 5.8; Hart, 1969). Varying proportions of exchange between seawater and fresh and altered basalts yields hydrothermal fluids with distinct elemental ratios (James et al., 1995; Palmer and Edmond, 1989). A previous time-series study of Rb/K, Rb/Cs, and K/Cs interpreted change in the fluid composition of sampled hydrothermal fluid as a result of an evolving fluid front shifting relatively towards less altered basalts (Palmer and Edmond, 1989). Continued hydrothermal alteration of ocean crust induces a shift in Rb/K, Rb/Cs, and K/Cs away from mantle/MORB values towards hydrothermal values (e.g., Alt and Teagle, 2003; Hart, 1969; Patten et al., 2017).

In addition, there are compositional differences between hydrothermal fluids from mid-ocean ridges and back-arc spreading centres (Table 5.8). These fluid composition variations between respective ocean crust types reflect the contrasting characteristics between typical mid-ocean ridges and oceanic crust formed at some form of supra-subduction zones (Alt et al., 1998; Alt and Teagle, 2000; Fonseca et al., 2017; Miyashiro, 1973; Moores et al., 1984; Pearce et al., 1984; Rautenschlein et al., 1985; Woelki et al., 2020). These differing characteristics of ocean crust forming at some kind of supra-subduction zone, such as the Troodos ophiolite, manifest in shifted geochemical and isotopic compositions of fresh unaltered volcanic glasses relative to typical MORB values (Table 5.8; Fonseca et al., 2017; Miyashiro, 1973; Rautenschlein et al., 1985; Woelki et al., 2020). Consequently, determined trace element ratios of the altered Troodos ocean crust yield contrasting values to typical altered mid-ocean ridges (Table 5.8; Alt and Teagle, 2003; Patten et al., 2017).

The contrasting geochemical characteristics between mid-ocean ridge basalts and ocean crust formed at supra-subduction zones are important when geochemically fingerprinting fluid origins of serpentinites. The wide variation in trace element ratios Rb/Cs, Rb/K, K/Cs, which span several orders of magnitude and overlaps between abyssal seafloor serpentinites and forearc serpentinites (Fig. 5.8; Table 5.8; Peters et al., 2017), compelling and distinct geochemical differences have been reported for these respective settings (Kodolányi et al., 2012; Kodolányi and Pettke, 2011; Peters et al., 2017).

However, sampled serpentinites at abyssal seafloor and forearc settings reflect a heterogenous sample spectrum, which have likely undergone progressive interactions between differing fluid sources. For example, in seafloor settings, serpentinites typically sampled near the seafloor likely reflect exchange with both high temperature hydrothermal fluids and low temperature seawater (Bonatti et al., 1984; Boschi et al., 2008; Früh-Green et al., 1996) and in forearc settings, diverse slab-derived fluids reflect variable proportions

of dehydrating altered ocean crust and sediments (Albers et al., 2020; Kahl et al., 2015; Menzies et al., 2022).

Serpentinised mantle rock trace element ratios of Rb/K, Rb/Cs, K/Cs in samples from the Olympus Diapir, Artemis Diapir, and Limassol Forest Complex variably overlap with several contrasting sources (Fig. 5.8; Table 5.8). Consequently, using trace element ratios to establish a fluid origin of a distinct serpentinisation event within the Troodos Mantle Sequence may not be appropriate. Due to the complexity, underlying uncertainties, and potential obscurity related to applying a compiled global abyssal serpentinite and forearc serpentinite dataset to lithospheric mantle formed at some kind of supra-subduction zone.

Table 5.8: Trace element ratio summary table.

Rb/Cs Seawater	100	***Rb/K (ppb/ppm) Seawater***	0.53	***K/Cs Seawater***	190,000
Rb/Cs Mid-Ocean Ridge Hydrothermal Fluid	60 ± 17 (James et al., 1995; Palmer and Edmond, 1989)	***Rb/K (ppb/ppm) Hydrothermal Fluid***	2 ± 1 (James et al., 1995; Palmer and Edmond, 1989)	***K/Cs Hydrothermal Fluid***	39,009 ± 4,447 (Palmer and Edmond, 1989; James et al., 1995)
Rb/Cs Back-arc Hydrothermal fluid	24 ± 7 (Campbell and Edmond, 1989; Ishibashi et al., 2015)	***Rb/K (ppb/ppm) Back-arc Hydrothermal fluid***	2 ± 0.05 (Campbell and Edmond, 1989; Ishibashi et al., 2015)	***K/Cs Back-arc Hydrothermal fluid***	11,027 ± 3,209 (Campbell and Edmond, 1989; Ishibashi et al., 2015)
Rb/Cs Marine sediment, Mariana Forearc	22 (Bulk sediment; Elliott et al., 1997)	***Rb/K (ppb/ppm) Marine sediment, Mariana Forearc***	0.0031 ($3.1x10^{-3}$) (Bulk sediment; Elliott et al., 1997)	***K/Cs Marine sediment, Mariana Forearc***	7142 ($7.1x10^{3}$) (Bulk sediment; Elliott et al., 1997)
Rb/Cs GLOSS II sediment compilation	17 (Plank, 2014)	***Rb/K (ppb/ppm) GLOSS II sediment compilation***	0.045 (Plank, 2014)	***K/Cs GLOSS II sediment compilation***	3755 ($3.8x10^{3}$) (Plank, 2014)
Rb/Cs Altered Ocean Crust, Mariana Forearc	>10 (Albers et al., 2020) 88 ± 38 (ODP Site 801 (Alt and Teagle, 2003)	***Rb/K (ppb/ppm) Altered Ocean Crust, Mariana Forearc***	2 ± 1 (ODP Site 801 (Alt and Teagle, 2003)	***K/Cs Altered Ocean Crust, Mariana Forearc***	50,646 ± 38,942 (ODP Site 801 (Alt and Teagle, 2003)

Rb/Cs Troodos, Altered Ocean Crust	Average = 54 ± 51 (σ) Max = 262 Min = 0.06 Median = 53 (Patten et al., 2017)	***Rb/K (ppb/ppm) Troodos Ocean Crust***	Average = 1.44 ± 0.90 (1σ) Max = 5.24 Min = 0.26 Median = 1.24 (Patten et al., 2017)	***K/Cs Troodos, Altered Ocean Crust***	Average = 77,192 ± 92,981 (1σ) Max = 454,418 Min = 3,365 Median = 59,192 (Patten et al., 2017)
Rb/Cs 'Fresh' Ocean Ridge Basalt	75 (Hart, 1969)	***Rb/K (ppb/ppm) 'Fresh' Ocean Ridge Basalt***	1.14 (Hart, 1969)	***K/Cs 'Fresh' Ocean Ridge Basalt***	64,583 (Hart, 1969)
Rb/Cs Altered Ocean Ridge Basalt	15 (Hart, 1969)	***Rb/K (ppb/ppm) Altered Ocean Ridge Basalt***	3.93 (Hart, 1969)	***K/Cs Altered Ocean Ridge Basalt***	3,846 (Hart, 1969)
Rb/Cs MORB Global Compilation	85 (Gale et al., 2013)	***Rb/K (ppb/ppm) MORB Global Compilation***	2.17 (Gale et al., 2013)	***K/Cs MORB Global Compilation***	39,050 (Gale et al., 2013)
Rb/Cs Serpentine and Brucite Mariana Forearc	<5 to ~10 (Albers et al., 2020)				
Rb/Cs Depleted Mantle	67 (Salters and Stracke, 2004)	***Rb/K (ppb/ppm) Depleted Mantle***	1.47 (Salters and Stracke, 2004)	***K/Cs Depleted Mantle***	45,454 (Salters and Stracke, 2004)
Rb/Cs Primitive Mantle	34 (Palme and O'Neill, 2014)	***Rb/K (ppb/ppm) Primitive Mantle***	2.32 (Palme and O'Neill, 2014)	***K/Cs Primitive Mantle***	14,444 (Palme and O'Neill, 2014)

Rb/Cs Compiled 'Mid Ocean Ridge Serpentinite' values	Average = 34 ± 22 (1σ) Max = 182 Min = 2 Median = 31	***Rb/K (ppb/ppm) Compiled 'Mid Ocean Ridge Serpentinite' values***	Average = 1.66 ± 2.84 (1σ) Max = 33 Min = 0.02 Median = 1.24 (Compiled Peters et al., 2017)	***K/Cs Compiled 'Mid Ocean Ridge Serpentinite' values***	Average = 50,321 ± 61685 (1σ) Max = 406,685 Min = 746 Median = 29,741 (Compiled (Peters et al., 2017)
Rb/Cs Compiled 'Forearc Serpentinite' values	Average = 4.6 ± 5.3 (1σ) Max = 40 Min = 0.2 Median = 3.2 (Compiled (Peters et al., 2017)	***Rb/K (ppb/ppm) Compiled 'Forearc Serpentinite' values***	Average = 3.79 ± 4.80 (1σ) Max = 24 Min = 0.17 Median = 2.38 (Compiled (Peters et al., 2017)	***K/Cs Compiled 'Forearc Serpentinite' values***	Average = 6,506 ± 15,880 (1σ) Max = 118,939 Min = 155 Median = 1,368 (Compiled (Peters et al., 2017)
Rb/Cs 'Fresh' Troodos Volcanic Glasses	23.27 ± 8.01 (Woelki et al., 2020)	***Rb/K (ppb/ppm) Fresh Troodos Volcanic Glasses***	3.13 ± 0.70 (Woelki et al., 2020)	***K/Cs Fresh Troodos Volcanic Glasses***	7,960 ± 3,479 (Woelki et al., 2020)

5.6 Cretaceous seafloor serpentinisation

Serpentinising fluids may yield distinct isotopic compositions reflective of their origin (Wenner and Taylor, 1974, 1973, 1971). Here, by estimating the isotopic composition of the serpentinising fluid in equilibrium with the measured isotopic compositions of the Troodos Mantle Sequence serpentinised mantle rocks, we evaluate whether Cretaceous hydrothermal fluids pervasively serpentinised both the refractory Olympus Diapir, composed of harzburgites and dunites, and the fertile Artemis Diapir primarily composed of lherzolite (Batanova and Sobolev, 2000).

5.6.1 $^{87}Sr/^{86}Sr$ Constraints

Previous studies have determined the strontium isotopic composition of hydrothermally altered ocean crustal rocks of the Troodos ophiolite (e.g., Bickle and Teagle, 1992; Chapman and Spooner, 1977; Gillis and Robinson, 1990; Spooner et al., 1977; Staudigel and Gillis, 1990).

A $^{87}Sr/^{86}Sr$ profile through the Troodos lavas, sheeted dykes, and upper gabbros interpreted the altered ocean crustal rocks to be in equilibrium with Cretaceous hydrothermal fluid through ~1 km vertical distance of Sheeted Dykes (Bickle and Teagle, 1992) and estimated the $^{87}Sr/^{86}Sr$ ratio of the Cretaceous hydrothermal fluid end-member as 0.7054 ± 7 (Bickle and Teagle, 1992) (Fig. 5.14; Table 5.9).

Table 5.9: Isotope Summary Table.

$\delta^{18}O$ – Modern Seawater	+0 ‰	**δD – Modern Seawater**	+0 ‰	**$\delta^{11}B$ – Modern Seawater**	+39.61 ‰ (Foster et al., 2010)	**$^{87}Sr/^{86}Sr$ – Modern Seawater**	0.70918 (McArthur et al., 2012)
$\delta^{18}O$ – Cretaceous Seawater	-1 ‰ (Heaton and Sheppard, 1977)	**δD – Cretaceous Seawater**	-7 ‰ (Heaton and Sheppard, 1977)	-	-	**$^{87}Sr/^{86}Sr$ – Cretaceous Seawater**	~0.7073 (McArthur et al., 2012)
$\delta^{18}O$ – Hydrothermal Fluid	+0 to +2.4 (Bickle and Teagle, 1992)	**δD – Hydrothermal Fluid**	+0 to +2.5 ‰ (Bowers, 1989; James et al., 2014)	**$\delta^{11}B$ – Hydrothermal Fluid**	+24.3 to +36.8 ‰ (James et al., 1995; Palmer, 1991; Spivack et al., 1987; You et al., 1994)	**$^{87}Sr/^{86}Sr$ – Hydrothermal Fluid**	e.g., 0.70319 (TAG; Elderfield et al., 1993).
				$\delta^{11}B$ – Back-arc Hydrothermal Fluid	+13.5 to +29.7 ‰ (Yamaoka et al., 2015a)	**$^{87}Sr/^{86}Sr$ – Back-arc Hydrothermal Fluid**	0.7036 to 0.7046 (Gamo, 1995) ~0.705 (endmember; Roberts et al., 2003)
$\delta^{18}O$ – Estimated Troodos Hydrothermal Fluid	+2.7 ± 0.7 ‰ (1σ; n=4; Turchyn et al., 2013)	**δD – Estimated Troodos Hydrothermal Fluid**	-7 ‰ (Heaton and Sheppard, 1977)	**$\delta^{11}B$ – Estimated Troodos Hydrothermal Fluid**	+22 ‰ (This Study)	**$^{87}Sr/^{86}Sr$ – Estimated Troodos Hydrothermal Fluid**	0.7054 ± 7 (Bickle and Teagle, 1992)
$\delta^{18}O$ – Serpentine, Mariana Forearc	+6 to +11.2 ‰ (Benton 1997) +6.5 to +8.5 ‰ (Alt and Shanks, 2006)	**δD – Serpentine, Mariana Forearc**	-55 to -82 ‰ (Benton 1997) -29.5 to -45.5 ‰ (Antigorite serpentine; Alt and Shanks, 2006) -52 to -84 ‰ (Chrysotile; Alt and Shanks, 2006)	**$\delta^{11}B$ – Serpentine, Mariana Forearc**	+5.4 to +25.3 ‰; Average = +14.46 ± 4.48 ‰ (1σ) (Benton et al., 2001)	**$^{87}Sr/^{86}Sr$ – Serpentine, Mariana Forearc**	>20 mbsf 0.7047 to 0.7055 (Savov et al., 2007)

$\delta^{18}O$ – Pore waters, Mariana Forearc	-1.4 to +4.4 ‰ (Benton, 1997)	**δD – Pore waters, Mariana Forearc**	-4.8 to +14.2 ‰ (Benton, 1997)	**$\delta^{11}B$ – Pore waters, Mariana Forearc**	+10 to +15 ‰ (Menzies, unpublished IODP Expedition 366 Data)	**$^{87}Sr/^{86}Sr$ – Pore waters, Mariana Forearc**	0.70525 to 0.70912 (Haggerty and Chaudhuri, n.d.) >2 mbsf 0.70514 to 0.70870 (Bickford et al., 2008)
$\delta^{18}O$ – Subducted sediments, Mariana Forearc	+12.2 to +35.9 ‰ (Alt and Shanks, 2006)	**δD – Volcaniclastic Turbidites, Western Pacific, ODP Site 800**	-50 ‰ (Alt and Shanks, 2006)	**$\delta^{11}B$ – Marine sediments**	Desorbable B = +14 to +16 (Spivack et al., 1987)	**$^{87}Sr/^{86}Sr$ – Western Pacific, ODP Site 801 – clay, chert, volcaniclastic turbidites, radiolarite**	0.7045 to 0.7106 Bulk sediment = 0.7062 (Elliott et al., 1997)
$\delta^{18}O$ - Calculated fluid in equilibrium with Mariana forearc serpentine	+6.5 to +9 ‰ (Alt and Shanks, 2006)	**δD – Calculated fluid in equilibrium with Mariana forearc serpentine**	-4 to -26 ‰ (Alt and Shanks, 2006)	**$\delta^{11}B$ – Estimated fluid in equilibrium with Mariana forearc serpentine**	+13 ‰ (Benton et al., 2001)	-	-
$\delta^{18}O$ – Proposed fluid source (Mariana Forearc)	Sediment dehydration reactions (<200°C slab; 300 to 375 °C mantle wedge/serpentinisation temperature)	**δD – Proposed fluid source (Mariana Forearc)**	Sediment dehydration reactions (<200°C slab; 300 to 375 °C mantle wedge/serpentinisation temperature)	**$\delta^{11}B$ – Proposed fluid source (Mariana Forearc)**	Mixing of slab-derived marine sediment and shallow low-temperature seawater (Benton et al., 2001)	**$^{87}Sr/^{86}Sr$ – Proposed fluid source (Mariana Forearc)**	Slab dehydration mixed with seawater and/or marine sediments (Albers et al., 2019)

$\delta^{18}O_{(VSMOW)}$ – Messinian Evaporite, Cyprus	+19 ‰ (Pierre, 1982) +11 to +14 ‰ (Artiaga et al., 2021)	-	-	**$\delta^{11}B$ – Messinian Evaporite**	+34.2 to +36.1 ‰ (Paris et al., 2010)	**$^{87}Sr/^{86}Sr$ – Messinian Evaporite**	0.70865 to 0.7090 (Flecker and Ellam, 2006; McCulloch and Deckker, 1989; Müller and Mueller, 1991)
						$^{87}Sr/^{86}Sr$ – Lefkara Formation, Cyprus	0.70859 to 0.70907 (Makarona et al., 2012)
						$^{87}Sr/^{86}Sr$ – All Hole 1256D	0.70343 ± 0.00037 (Harris et al., 2015)
						$^{87}Sr/^{86}Sr$ – Troodos hydrothermally altered rocks	0.7054 ± 7 (Bickle and Teagle, 1992)
						$^{87}Sr/^{86}Sr$ – GLOSS II	0.701236 (Planck, 2014)

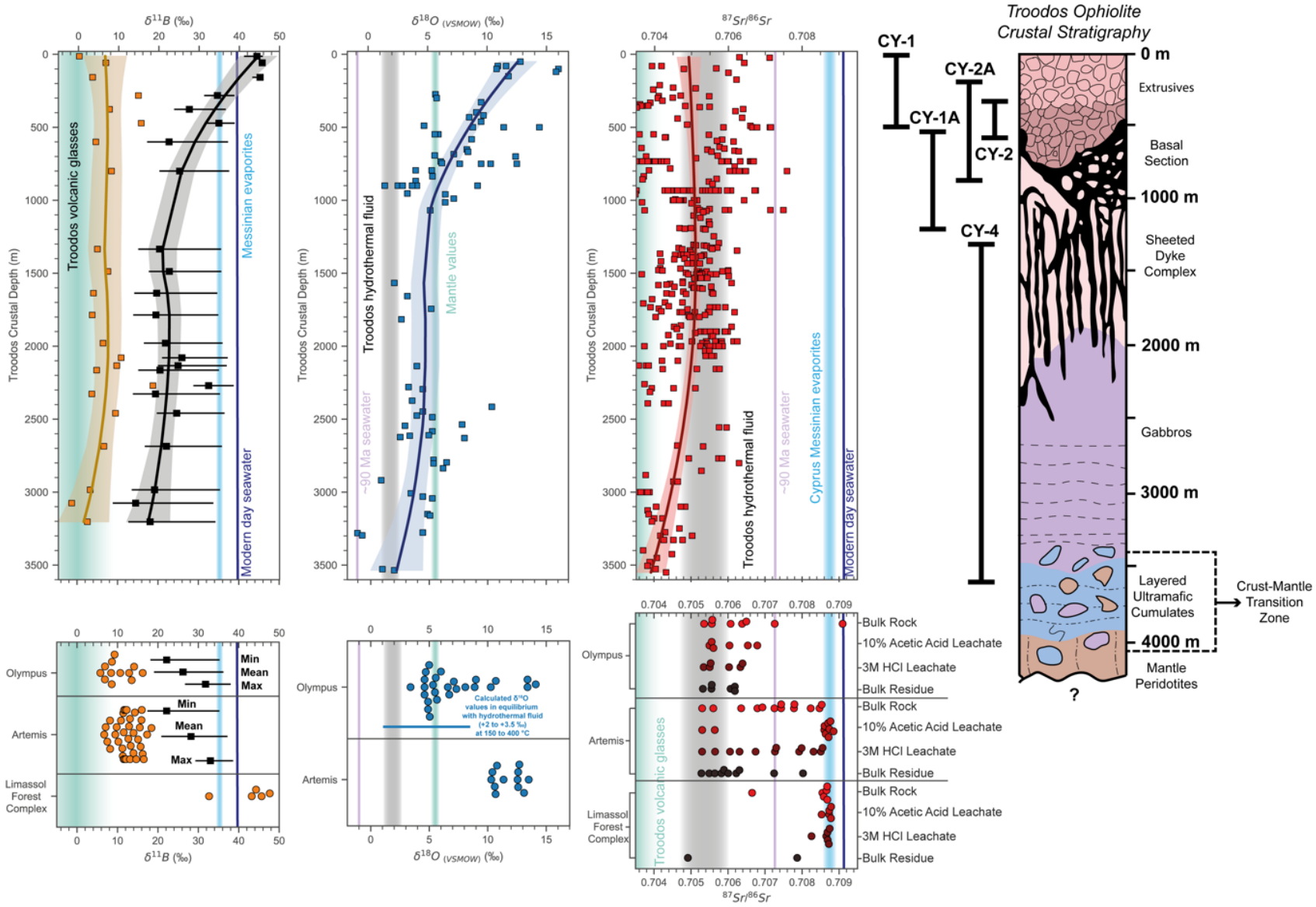
δ11B (‰)
δ18O (VSMOW) (‰)
87Sr/86Sr
Troodos Crustal Depth (m)
Troodos volcanic glasses
Messinian evaporites
Modern day seawater
Troodos hydrothermal fluid
Mantle values
~90 Ma seawater
Cyprus Messinian evaporites
Olympus
Artemis
Limassol Forest Complex
Min
Mean
Max
Calculated δ18O values in equilibrium with hydrothermal fluid (+2 to +3.5 ‰) at 150 to 400 °C
Bulk Rock
10% Acetic Acid Leachate
3M HCl Leachate
Bulk Residue
Troodos volcanic glasses
Troodos Ophiolite Crustal Stratigraphy
CY-1
CY-1A
CY-2A
CY-2
CY-4
0 m
Extrusives
Basal Section
1000 m
Sheeted Dyke Complex
2000 m
Gabbros
3000 m
Layered Ultramafic Cumulates
4000 m
Mantle Peridotites
?
Crust-Mantle Transition Zone

Figure 5.14: Troodos ophiolite isotope-depth plot of ocean crustal rocks and Troodos Mantle Sequence. Troodos ophiolite crustal stratigraphy is adapted from Malpas et al. (1989). Depths of samples have been scaled accordingly to the stacked crustal stratigraphy of Malpas et al. (1989). Troodos ocean crust $\delta^{11}B$ data (Yamaoka et al., 2015b), $\delta^{18}O$ (Gillis and Robinson, 1990; Heaton and Sheppard, 1977; Rautenschlein et al., 1985; Rommel et al., 1987; Schiffman and Smith, 1988; Spooner et al., 1977, 1974; Vibetti, 1993, 1987), $^{87}Sr/^{86}Sr$ (Bickle and Teagle, 1992; Chapman and Spooner, 1977; Gillis and Robinson, 1990; Kawahata and Scott, 1990; Rautenschlein et al., 1985; Rommel et al., 1987; Spooner et al., 1977) are plotted with depth. In the $\delta^{11}B$-depth plot, black squares reflect $\delta^{11}B_{Fluid}$ values calculated in equilibrium from measured rock $\delta^{11}B$ values using the boron equilibrium model coupled with a Bayesian inversion engine (Appendix A) using reasonable priors (Table 5.12), error bars are equivalent to $\pm 2\sigma$ error. The $\delta^{11}B_{Fluid}$ values in equilibrium with Troodos Mantle Sequence serpentinites is also shown with respective minimum, mean, and maximum measured serpentine values inverted to yield estimated $\delta^{11}B_{Fluid}$ values, error bars are equivalent to $\pm 2\sigma$ error. The range of calculated $\delta^{18}O_{Serp}$ values in equilibrium with Troodos hydrothermal fluid ($\delta^{18}O_{HydrothermalFluid}$ +2 to +3.5 ‰; Turchyn et al., 2013) is shown. Previously published serpentine $\delta^{18}O$ published isotope values are shown (Heaton, 1976; Magaritz and Taylor, 1974; Nuriel et al., 2009). A LOWESS (Locally weighted scatterplot smoothing; Cleveland, 1979) is a non-parametric fitting technique and was applied to measured rock isotope values (yellow, red, blue) and calculated fluid isotope values (black), with shading equivalent to $\pm 2\sigma$ error. Boundaries of respective $\delta^{11}B$ signatures of Troodos volcanic glasses (Fonseca et al., 2017), Messinian evaporites (Paris et al., 2010), and modern day seawater (Foster et al., 2010) are shown. Boundaries of respective $\delta^{18}O$ signatures of mantle values (Mattey et al., 1994), Cretaceous seawater (Heaton and Sheppard, 1977), Troodos hydrothermal fluid (Turchyn et al., 2013) are shown. Boundaries of respective $^{87}Sr/^{86}Sr$ signatures of Troodos volcanic glasses (Rautenschlein et al., 1985), Troodos hydrothermal fluid (Bickle and Teagle, 1992), Cretaceous seawater (McArthur et al., 2012); Cyprus Messinian evaporites (Flecker and Ellam, 2006; McCulloch and Deckker, 1989; Müller and Mueller, 1991) are shown.

The $^{87}Sr/^{86}Sr$ signature of fresh Troodos volcanic glasses vary between 0.7033 and 0.7042 (Rautenschlein et al., 1985) and are elevated relative to Mid-Ocean Ridge Basalt (Table 5.9; MORB; 0.70287 ± 0.00004; e.g., Harris et al., 2015) due to the supra-subduction setting of the Troodos ophiolite (Fonseca et al., 2017; Moores et al., 1984; Pearce et al., 1984; Rautenschlein et al., 1985; Woelki et al., 2020). The $^{87}Sr/^{86}Sr$ signature of Cretaceous seawater is ~0.7073 (Table 5.9; Burke et al., 1982; McArthur et al., 2012). Consequently, the $^{87}Sr/^{86}Sr$ of the Troodos Cretaceous hydrothermal fluid reflects the relative proportions of isotopic exchange between these respective $^{87}Sr/^{86}Sr$ signatures (Bickle and Teagle, 1992).

Lower Troodos Ocean crust $^{87}Sr/^{86}Sr$ determinations (Teagle unpublished data; King et al., 2003) of gabbroic and cumulate ultramafic rocks suggests that the Troodos hydrothermal fluid $^{87}Sr/^{86}Sr$ signal continues into deeper levels of the Troodos ophiolite (Fig. 5.14). Rare hydrothermally altered rocks and associated secondary vein assemblages yield Troodos hydrothermal fluid values (Fig. 5.14) with some lower ocean crust whole-rock samples yielding lower than hydrothermal fluid $^{87}Sr/^{86}Sr$ ratios, closer towards primitive values (Fig. 5.14). The decrease in $^{87}Sr/^{86}Sr$ ratios with depth through the lower Troodos ophiolite indicates significant channelling and the transport of an evolved Cretaceous seawater $^{87}Sr/^{86}Sr$ signal into the deepest portions of the Troodos ophiolite ocean crustal rocks (Fig. 5.14). In addition, rodingitised gabbros from the Olympus Transition Zone (Table 5.2; Fig. 5.4) yield $^{87}Sr/^{86}Sr$ values of 0.7058, consistent with the penetration of hydrothermal fluids into the Troodos crust-mantle transition zone at or near the active Troodos spreading ridge.

Bulk residue $^{87}Sr/^{86}Sr$ ratios and Sr concentrations in the Artemis Diapir are similar to whole-rock and bulk residue $^{87}Sr/^{86}Sr$ ratios and Sr concentrations in the Olympus Diapir (Fig 5.3; Fig. 5.6; Fig. 5.7) indicating similar serpentinisation histories, at least initially, with the overprinting of assumed unaltered Troodos mantle $^{87}Sr/^{86}Sr$ signatures of 0.7037 (Rautenschlein et al., 1985) to a pervasive 0.705 signal. If this is the case, Cretaceous hydrothermal ~0.705 fluids would need to penetrate not only the shallower refractory mantle source that is the Olympus Diapir, but also into the deeper, fertile mantle source of the Artemis Diapir (Batanova and Sobolev, 2000). This scenario is difficult to reconcile without the aid of a large fault zone that would likely induce significant vertical displacement, which contradicts the inferred uplift trajectories of the Troodos ophiolite (Fig. 2.6; Batanova and Sobolev, 2000, Evans et al., 2021).

5.6.2 Oxygen and Hydrogen Isotopic Constraints

Although due to temperature sensitive mineral-fluid fractionations the stable oxygen isotopic composition through the Troodos ophiolite ocean crustal rocks differs to the $^{87}Sr/^{86}Sr$ profile, both respective profiles yield similar patterns with increasing crustal depth (Fig. 5.14). Troodos upper lavas yield high $\delta^{18}O$ values >10 ‰ that are reflective of large mineral-fluid fractionation factors resulting from low-temperature seafloor alteration and are significantly heavier than mantle stable oxygen isotopic composition of +5.5 ± 0.4 ‰ (Table 5.9; Mattey et al., 1994). The stable oxygen isotopic compositions of the lower Troodos lavas and upper sheeted dykes yield a large variation between +1 and +14.5 ‰, where with increasing depth, measured $\delta^{18}O$ values are lower (Fig. 5.14). This depth relationship indicates variable seawater-rock exchange, where temperatures of isotopic exchange increase with depth, likely leading to a decrease in fluid-mineral fractionation. At the upper sheeted dykes (~1,000 mbsf; Fig. 5.14), the LOWESS smoothed average measured stable oxygen isotopic composition yields mantle-like values of +5 ‰ (Fig. 5.14) and continues with increasing depth through the sheeted dyke sequence into the upper gabbros similarly to the $^{87}Sr/^{86}Sr$ profile. In the lower portions of the Troodos Ocean crust (>2500 m; Fig. 5.14) $\delta^{18}O$ values decrease from mantle-like values of +5 to +2 ‰, indicating equilibrium with seawater at higher temperatures of fluid-rock exchange within deeper levels of the Troodos ocean crust. This is in contrast to $^{87}Sr/^{86}Sr$ values that show evidence of fluid channelling due to more primitive $^{87}Sr/^{86}Sr$ in deeper levels of the ophiolite (Fig. 5.14) and is likely a consequence of the respective tracer transport distance between strontium and oxygen, with oxygen transported ~x17 further relative to Sr (e.g., Bickle and Teagle, 1992). Previous studies have estimated the Troodos stable oxygen isotopic composition of the Cretaceous hydrothermal fluid from epidosites within the Sheeted Dyke Complex, yielding estimated hydrothermal fluid $\delta^{18}O_{Fluid}$ values of +2.7 ± 0.7 ‰ (1σ, n=4; Table 5.9; Turchyn et al., 2013). Calculated serpentine isotope values in equilibrium with such hydrothermal fluid $\delta^{18}O$ values, yield similar stable oxygen isotopic compositions to those measured on Troodos Mantle Sequence serpentine samples (Fig. 5.14).

Hydrogen is significantly more abundant in water relative to rock, as a result, it is a sensitive geochemical tracer of fluid origins. This is highlighted in measured hydrogen stable isotopic compositions of sampled hydrothermal vent fluids, which reflect seawater to near-seawater values of +0 to +2.5 ‰, due to minimal isotopic exchange with rock (e.g., Bowers, 1989; James et al., 2014). Estimation of stable hydrogen isotope values in equilibrium with the Cretaceous Troodos hydrothermal fluid end-member (~-7 ‰; Heaton and Sheppard, 1977) indicate that the hydrogen stable isotopic composition of Cretaceous seawater or modern seawater are too isotopically heavy to be consistent with an

interpretation of serpentinisation by hydrothermal fluids or seawater in mantle peridotites of the Olympus and Artemis Diapirs (Nuriel et al., 2009).

5.6.3 Boron Isotope Constraints

5.6.3.1 Boron Isotopes Systematics

Here we outline boron isotope systematics to understand boron isotopic compositions of fluids and ocean crustal rocks, with the eventual aim of evaluating whether the penetration of hydrothermal fluids into the Troodos Mantle Sequence is the source of the initial serpentinisation event within the serpentinised mantle rocks.

The boron isotopic composition of sampled end-member hydrothermal fluid from high temperature vent sites is interpreted to reflect simple mixing between two components of constant isotopic composition, composed of seawater and a hydrothermal boron component (Spivack and Edmond, 1987). Extrapolation of this linear mixing relationship ($\delta^{11}B_{Fluid}$ vs. $B_{Seawater}/B_{HydrothermalFluid}$) intercepts the hydrothermal boron end-member at fresh basalt-like values ($\delta^{11}B$ -5.6 ± 4.8 ‰; Spivack and Edmond, 1987). Consequently, high temperature (>150°C) hydrothermal alteration is previously proposed to occur without observable fractionation (James et al., 1995; Spivack and Edmond, 1987). However, extrapolation of recently published hydrothermal vent fluid data (Fig. 5.15) indicates that this previously proposed extrapolation may not be valid. We propose boron isotopic fractionation likely occurs between basalt and seawater at temperatures greater than 150°C, resulting in heavier rock stable boron isotopic compositions of hydrothermally exchanged boron than previously suggested (Fig. 5.15). For example, extrapolation of this amended mixing relationship between seawater and hydrothermal fluid indicates that the hydrothermal B end-member intercepts at $\delta^{11}B_{Fluid}$ of ~+8 ‰ (Fig. 5.15). A fluid in equilibrium with a MORB-source mantle $\delta^{11}B$ value of -7 ± 1 ‰ (Chaussidon and Jambon, 1994) at a temperature of 150°C is calculated (using the boron equilibrium model outlined in Appendix A) to yield a $\delta^{11}B_{Fluid}$ value of +8 ‰ (Fig. 5.15). This indicates that the sampled boron isotopic compositions of hydrothermal vent fluids may reflect simple mixing between B derived from seawater and isotopically fractionated B derived from fresh and altered ocean basalts.

At mid-ocean ridges hydrothermal fluids at sediment-starved sites yield B concentrations ranging from 3.8 to 6.1 μg/g and $\delta^{11}B_{Fluid}$ values of +24.3 to +36.8 ‰ (Fig. 5.15; Table 5.9; James et al., 1995; Palmer, 1991; Spivack and Edmond, 1987; You et al., 1994). In contrast, end-member hydrothermal fluids sampled at sediment-starved Back-arc vent sites yield higher B concentrations ranging between 5.7 and 16.4 μg/g and lower

$\delta^{11}B_{Fluid}$ values of +13.5 and +29.7 ‰ (Fig. 5.15; Yamaoka et al., 2015a). All previously reported hydrothermal fluids from high-temperature vent sites are isotopically lighter than seawater (Fig. 5.15). Differences in the boron isotopic compositions of hydrothermal vent fluids between mid-ocean ridges and back-arc settings may be related to the contrasting characteristics between oceanic crust formed at some form of supra-subduction zones and typical ocean crust formed at a mid-ocean ridge. Fresh unaltered volcanic glasses within the Troodos ophiolite yield B concentrations an order of magnitude higher (5.43 ± 1.5 μg/g, 1σ, n = 21; Fonseca et al., 2017) than fresh unaltered mid-ocean ridge basalt (0.39 ± 0.03 and 0.46 ± 0.03 μg/g, 1σ, n = 4; Spivack and Edmond, 1987). Consequently, the isotopically lighter hydrothermal $\delta^{11}B_{Fluid}$ values and higher B concentrations (Fig. 5.15) sampled in back-arc hydrothermal systems (Yamaoka et al., 2015a) may occur as a consequence of higher B concentrations in unaltered ocean crust in these back-arc and arc settings.

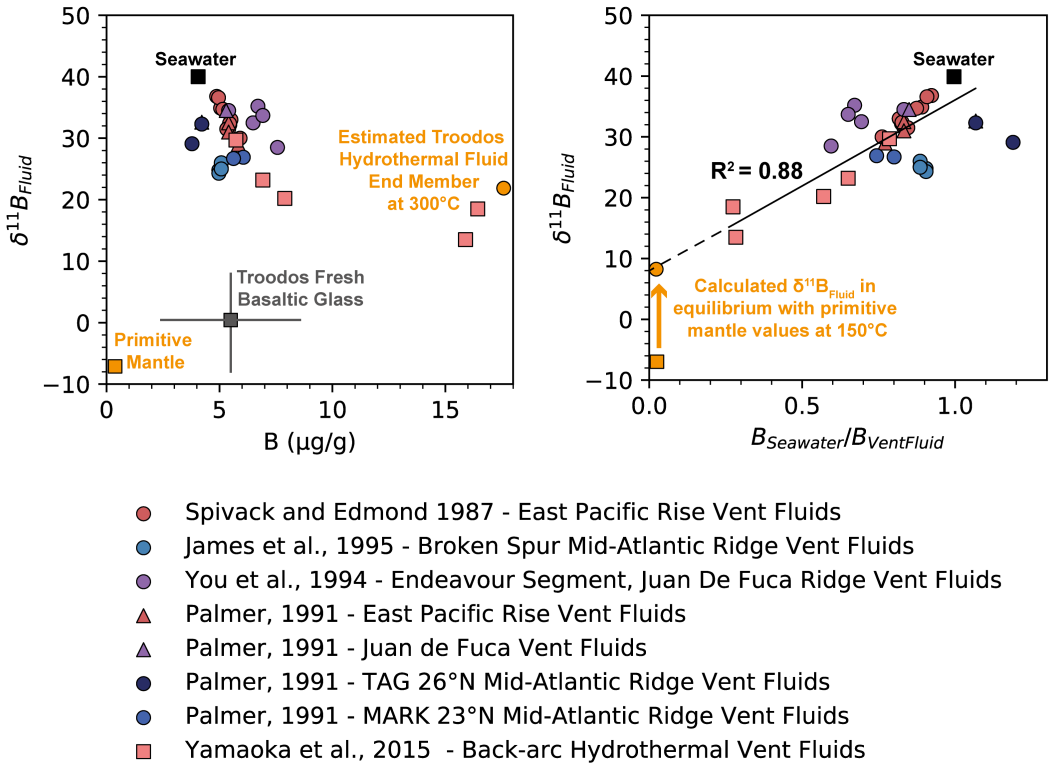

Figure 5.15: Plot of $\delta^{11}B$ and B (μg/g) and $B_{Seawater}/B_{VentFluid}$ with previously published hydrothermal vent fluid data. A least squares regression through the Back-arc hydrothermal vent fluids and the East Pacific Rise fluids yields an R^2 value of 0.88. The Cretaceous Troodos hydrothermal fluid $\delta^{11}B$ endmember is also shown and is estimated through the boron equilibrium model (see Appendix A). Seawater values are from Foster et al. (2010; Spivack et al., 1987). Primitive Mantle values are from Chaussidon and Jambon (1994). Troodos Basaltic Glass values are from Fonseca et al. (2017) and error bars reflect 2σ of the mean value.

5.6.3.2 Serpentinisation of the Troodos Mantle Sequence by a seawater-derived hydrothermal fluid

In order to evaluate whether boron isotope systematics are consistent with a model in which Cretaceous Troodos hydrothermal fluids initially serpentinised the Troodos Mantle Sequence, first we constrain the evolution of fluid $\delta^{11}B$ from seawater to hydrothermal fluid values (Fig. 5.14) during seafloor hydrothermal alteration. This is achieved by robustly estimating the boron isotopic composition of the fluid in equilibrium with previously measured Troodos ocean crust $\delta^{11}B$ rock values (Yamaoka et al., 2015b). The model does not include a tracer transport element and only calculates the boron isotope value of a rock in equilibrium with fluid and additional required parameters (see Appendix A). Here, we utilise a Bayesian Inversion approach to robustly constrain the uncertainty of parameters that make up the boron isotope equilibrium model (see Appendix A). The result of this Bayesian Inversion approach highlights that as seawater penetrates into the lower lavas and upper sheeted dykes, the estimated fluid $\delta^{11}B$ value evolves from heavy seawater values ($\delta^{11}B_{Seawater}$ +39.61 ‰; Foster et al., 2010) towards modified isotopically lighter values ($\delta^{11}B_{Fluid}$, ~+22 ‰; Fig. 5.14). The average LOWESS smoothed estimated median hydrothermal fluid $\delta^{11}B$ value of +22 ‰ continues into deeper levels of the Troodos ophiolite (Fig. 5.14) and in the lower gabbro sections, where corresponding $^{87}Sr/^{86}Sr$ and $\delta^{18}O$ values indicate significant fluid channelling, the estimated $\delta^{11}B_{Fluid}$ decreases to isotopically lighter $\delta^{11}B_{Fluid}$ values of +18 ‰. These calculated downhole boron isotope values in equilibrium with hydrothermal fluid (Fig. 5.14) are consistent with sampled hydrothermal fluids at high-temperature venting sites (Fig. 5.14) at both mid-ocean ridges (James et al., 1995; Palmer, 1991; Spivack and Edmond, 1987; You et al., 1994) and back-arc hydrothermal systems (Yamaoka et al., 2015a).

We estimate the B concentration of the Troodos Cretaceous hydrothermal fluid by following a isotopic fluid evolution Raleigh-type distillation model (Eq. 5.1; James et al., 1995; Spivack and Edmond, 1987), using a fractionation factor (α = 4.0529/4.1067; Eq. 5.2; $\Delta^{11}B_{Mineral-Fluid}$ = -13.3 ‰) α of 0.987, estimated from the boron equilibrium model calculations of hydrothermally altered Troodos ocean crustal rocks (Fig. 5.14). Calculations suggest a hydrothermal fluid endmember with a boron isotopic composition of +22 ‰ requires a B concentration of 17.5 μg/g, assuming Cretaceous seawater had a similar B concentration and isotopic composition as today ($\delta^{11}B_{Seawater}$ = +39.61; Foster et al., 2010). This estimation is consistent with modern hydrothermal fluids sampled in sediment-starved basalt-hosted back-arc hydrothermal vent sites (Fig. 5.15; Yamaoka et al., 2015a).

$$\delta^{11}B_{Fluid} = (\delta^{11}B_{Seawater} + 1000)\left[\frac{[B_{Fluid}]}{[B_{Seawater}]}\right]^{(\alpha-1)} - 1000$$

(5.1)

$$\alpha = \frac{^{11}B/^{10}B_{Altered\ Rock}}{^{11}B\,^{10}B_{Fluid}}$$

(5.2)

In contrast to high temperature hydrothermal isotopic exchange, boron isotopic systematics during low-temperature seawater-basalt exchange results in B being removed from circulating seawater and taken up in low-temperature phyllosilicate and carbonate mineral assemblages. Using the empirical fractionation factor between altered basalt and seawater (α = 0.968; James et al., 1995; Spivack and Edmond, 1987), the boron isotopic composition of the modified fluid becomes isotopically heavier than seawater (>39.61 ‰; James et al., 1995; Spivack and Edmond, 1987) as isotopically lighter B is preferentially taken up in secondary alteration minerals in the rocks. This relationship is expressed in the highest portions of the Troodos ocean crust stratigraphy, where the boron equilibrium model, estimates modified $\delta^{11}B_{Fluid}$ values in equilibrium with phyllosilicate minerals at low-temperatures <25°C as isotopically heavier than seawater (up to $\delta^{11}B_{Fluid}$ values of +47 ‰; Fig. 5.14). Similar boron isotope characteristics have been proposed in serpentinising systems at the Mid-Atlantic Ridge (Vils et al., 2009) where isotopically heavy serpentinites (+32 to +40 ‰; Vils et al., 2009; Fig. 5.13) are interpreted to have formed from progressively evolving isotopically heavy fluids which have higher $\delta^{11}B$ values than seawater ($\delta^{11}B_{Seawater}$ = +39.61; Foster et al., 2010). This is a result of B being removed from the serpentinising fluid and being taken up in serpentine, as evidenced by high B concentrations in serpentine (up to 200 μg/g; Pabst et al., 2011). In the case of the Troodos Mantle Sequence, it is likely that serpentinisation would drive the boron isotopic composition of the serpentinising fluid to progressively isotopically heavier values. Consequently, in a scenario where hydrothermal fluids pervasively serpentinised the Troodos Mantle Sequence, boron isotope systematics indicate that serpentinising fluids should progressively evolve to isotopically heavier fluid compositions as B-rich serpentine is formed.

The Troodos Mantle Sequence estimated serpentinising fluid $\delta^{11}B_{Fluid}$ values in equilibrium with serpentinised mantle rock are consistent with the estimated $\delta^{11}B_{Fluid}$ values in equilibrium with lower ocean crustal rocks (Fig. 5.14).The ~10 ‰ range between minimum and maximum measured rock $\delta^{11}B$ values in the Olympus and Artemis Diapirs reflects a similar range in estimated median $\delta^{11}B_{Fluid}$ values calculated in equilibrium with minimum

and maximum measured $\delta^{11}B_{Rock}$ values using the Bayesian Inversion boron equilibrium model (Fig. 5.14).

Under the assumption that during serpentinisation, the boron isotopic composition of the initial serpentinising fluid evolved from +22 to +32 ‰ (Fig. 5.14), the loss of boron from the Cretaceous hydrothermal fluid can be estimated. Calculations using equation 5.1 suggest that if the fractionation factor is α = 0.987 and the initial serpentinising fluid had a starting B concentration of 17.5 μg/g (Fig. 5.15), then approximately half the boron (8.75 μg/g) would need to be removed and partitioned into the high B serpentine to induce a shift of ~10 ‰ in the $\delta^{11}B_{SerpFluid}$ values.

Full quantification of the respective proportions of fluid to rock during alteration of the Troodos Ophiolite and associated Mantle Sequence are outside the primary aims of this study. However, simple calculations suggests that if ~50% of B is lost from the serpentinising hydrothermal fluid and the newly formed serpentine has high B concentrations (up to 90 μg/g in the relatively more primitive $^{87}Sr/^{86}Sr$ 0.705 samples; Fig. 5.9), the proportion of fluid to rock required to serpentinise the Troodos Mantle Sequence is high (~10) and would be a fluid dominated regime (e.g., Taylor, 1977). In contrast, the boron isotope systematics of the Troodos ocean crust suggests a component of fluid channelling (Fig. 5.14).

5.6.4 Summary

Serpentine $^{87}Sr/^{86}Sr$ ratios, stable oxygen and boron isotope values are consistent with the penetration of seawater-derived hydrothermal fluids to deep levels in the Troodos ocean crust and into at least the Troodos crust-mantle transition zone. The 0.705 $^{87}Sr/^{86}Sr$ signal recorded in the Olympus Transition Zone rodingites (Fig. 5.4) is likely sourced from Cretaceous hydrothermal fluids that induced rodingitisation and localised serpentinisation of the Troodos lithospheric mantle. This signal is consistent with Sr isotope compositions of whole rock and alteration vein samples in the lower crustal portions of the CY-4 borehole that yield $^{87}Sr/^{86}Sr$ ratios of 0.7037-0.7054, elevated from assumed Troodos mantle compositions of ~0.7037 (King et al., 2003; Teagle unpublished data; Rautenschlein et al., 1985).

Progressive leaching experiment results of $^{87}Sr/^{86}Sr$ and trace element concentrations highlight parallel serpentinisation histories within the Olympus and Artemis Diapirs (Fig. 5.3), suggesting that hydrothermal fluids would be required to penetrate beyond the crust-mantle transition zone and refractory dunites and harzburgites of the

Olympus Diapir, into the potentially deeper fertile mantle lherzolite source of the Artemis Diapir (Batanova and Sobolev, 2000; Evans et al., 2021). Although the thickness of the Olympus Diapir is unknown, the penetration of significant volumes of hydrothermal fluid into fertile mantle would result in significant serpentinisation-induced isostatic uplift (Evans et al., 2021). This is in contrast to circum-Troodos sedimentary sequences that record the progressive uplift and exhumation of mantle rocks from the Messinian to recent, which indicate that the mantle peridotites of the Olympus and Artemis Diapir were not exhumed or near to the surface of the Cretaceous seafloor (Fig. 2.6). Furthermore, pervasive serpentinisation of the Olympus and Artemis Diapirs requires significant amounts of water. Boron mass balance constraints indicate fluid to rock ratio would be high (~10), resulting in a water dominated regime. In addition, measured serpentine hydrogen isotope compositions from both the Olympus and Artemis Diapirs are not in equilibrium with either modern or Cretaceous seawater or reasonable hydrothermal fluids, and suggest exchange with an isotopically lighter fluid (Fig. 5.2). Although Troodos rodingites within the Olympus Transition indicate some serpentinisation of the Troodos lithospheric mantle occurred at or near the active Troodos spreading ridge, pervasive serpentinisation of both the Olympus and Artemis by Troodos Cretaceous hydrothermal fluids is unlikely and additional explanations are required.

5.7 Miocene Slab-derived Serpentinisation of the Troodos Mantle Sequence

The Eastern Mediterranean region yields a complex geological history with several supra-subduction zones occurring throughout the Mesozoic (e.g., Robertson, 1998c) and in one such supra-subduction zone the Troodos ophiolite formed ~92 to 90 Ma (Moores et al., 1984; Mukasa and Ludden, 1987; Pearce et al., 1984). Recent studies of the Troodos ophiolite lavas have proposed an origin from a highly depleted mantle source, where more than one melt event had preceded above a subduction zone prior to the formation of the Troodos ophiolite (Woelki et al., 2020, 2019). This highlights that the mantle peridotites of the Troodos Mantle Sequence are long associated with subduction.

The Cyprus Arc subduction zone in its present form is a broadly west-east striking, north dipping system, located some ~20 km south of Cyprus and is proposed to have initiated from the earliest Miocene (Robertson, 1998a, 1998b), subducting either old (Triassic/Permian/Carboniferous age) and cold oceanic crust (Granot, 2016; Müller et al., 2008) or stretched and thinned continental crust (Symeou et al., 2018). Presently, the subduction zone is proposed to have stalled due to collision with the ~80-km-wide and ~120-

km-long Eratosthenes Seamount, which is inferred to have occurred during the Pliocene (Ergün et al., 2005; Kempler and Ben-Avraham, 1987; Robertson, 1998a, 1998b, 1998c).

It has long been suggested that the serpentinisation of the Troodos Mantle Sequence and subduction along the Cyprus Arc are related (Gass, 1977; Gass and Masson-Smith, 1963; Moores and Vine, 1971; Robertson, 1977). A causal relationship has previously been proposed between the progressive uplift and unroofing of mantle peridotites, as recorded by the circum-Troodos sedimentary sequences, and the collision, subsidence, and under-thrusting of the Eratosthenes Seamount with the Cyprus subduction zone (Robertson, 1998a, 1998b). Dehydration of the downgoing subducting Cyprus slab may have focussed fluids beneath the Mount Olympus region, inducing serpentinisation and significant uplift of the ophiolite (Robertson, 1998a, 1998b). Geophysical data from Cyprus is broadly in agreement with such a model as the variably serpentinised outcrops of the Troodos Mantle Sequence spatially coincide with a large negative Bouguer gravity anomaly (80 to 120 mGal; Gass and Masson-Smith, 1963; Shelton, 1993) superimposed onto the regional trend of what. Previous studies have modelled this negative gravity anomaly as a vertical cylindrical body of lower density serpentinised peridotite (2,670 kg/m^3) extending to ~11 km in depth, hosted within a higher density background of unserpentinised mantle (3,300 kg/m^3; Gass and Masson-Smith, 1963; Shelton, 1993). Additionally, recent P-wave velocity models of the structure beneath Cyprus suggest velocities beneath the Troodos ophiolite range between 5 to 6.5 km/s down to a depth of ~10 km (Feld et al., 2017), potentially reflecting serpentinisation to depths where the downgoing Cyprus slab intersects beneath the Mount Olympus region.

The geometry of the Cyprus subduction zone is generally poorly constrained, the depth at which the Cyprus slab intersects beneath the Mount Olympus region is estimated to be between 12 and 36 km, with a slab dip angle ranging between 11 to 33° (Feld et al., 2017; Hayes et al., 2018; Mackenzie et al., 2006). Assuming the low Cyprus geothermal gradient of 10 to 15 °C per km (Florides et al., 2011; Morgan, 1973) extends to such depths, the estimated serpentinisation temperatures within the Cyprus mantle wedge would range between ~150 to 450 °C (Table 5.10). Additionally, recent seismic imaging of the Cyprus Arc has indicated that Miocene sediments have been accreted to the Cyprus margin with only the older Upper Cretaceous and Paleogene marine carbonates inferred to be subducting under Cyprus (Reiche et al., 2016). As a result, the subducting sediment package of the downgoing Cyprus slab is likely dominated by marine carbonates and the bulk composition of the subducting slab may be generally sediment poor.

Here, we estimate the isotopic composition ($^{87}Sr/^{86}Sr$, $\delta^{11}B$, $\delta^{18}O$, δD) of the serpentinising fluids during serpentinisation of the Troodos Mantle Sequence and evaluate

whether the resulting fluid isotopic compositions may have originated from dehydration of sediments and altered ocean crust from a downgoing slab along the Cyprus Arc (Fig. 5.16).

Table 5.10: Cyprus subduction zone characteristics.

Cyprus subduction zone characteristics	***Slab Setting***
Cyprus geothermal gradient	10 to 15 °C (Florides et al., 2011; Morgan, 1973)
Mount Olympus Depth to Slab	~12 km (Hayes et al., 2018; Kounoudis et al., 2020) ~20 km (Feld et al., 2017); ~36 km (Mackenzie et al., 2006)
Slab dip angle (°)	13° (Feld et al., 2017); 33° (Mackenzie et al. 2006)
Estimated temperature at slab-mantle wedge interface below Mount Olympus	150°C; 250°C; 450°C
Nature of subducting material	Pre-Miocene sediments and ocean crust (Reiche et al., 2016) Triassic/Permian Oceanic Crust (Müller et al., 2008) Carboniferous ocean crust (Granot, 2016)

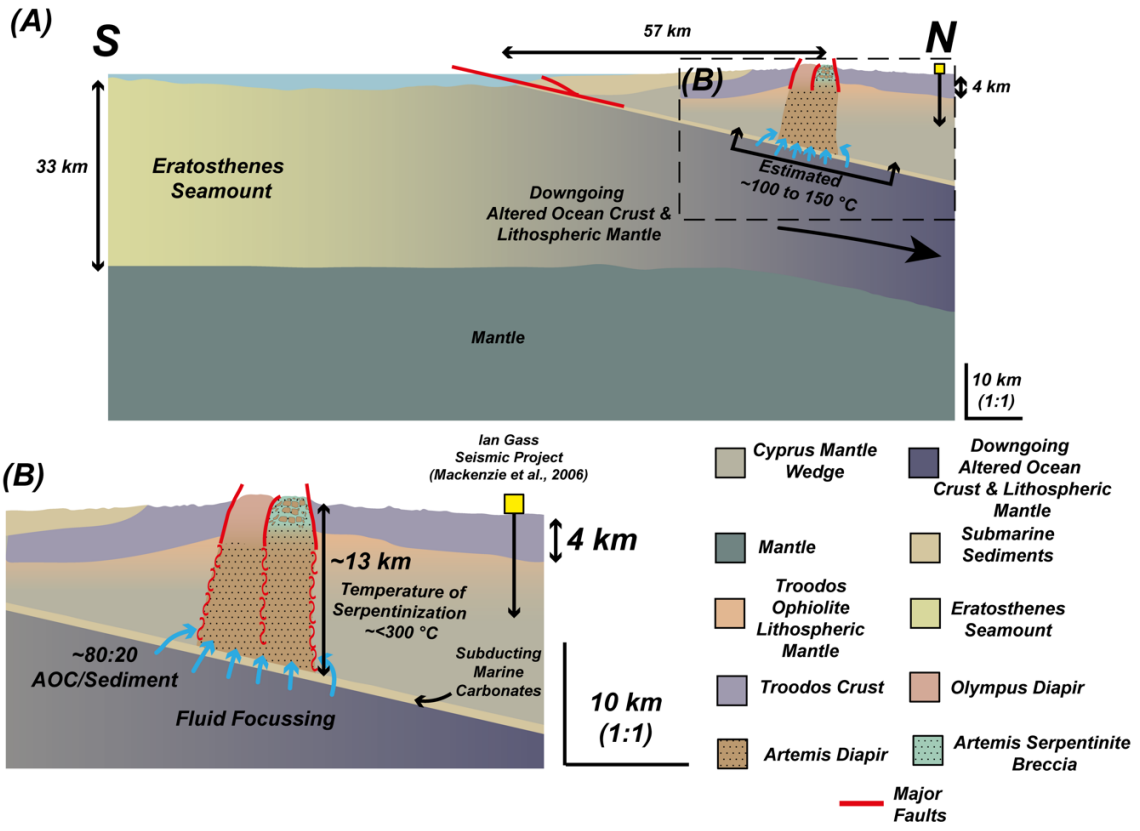

Figure 5.16: (A) Cross-section of the present-day scenario of the current geometry of the Cyprus Arc subduction zone. (B) Cross-section of the Troodos Mantle Sequence and estimated location of the slab beneath the Mount Olympus region. Scale is 1:1.

5.7.1 $\delta^{18}O$ and δD

Previously measured oxygen and hydrogen isotopes show distinct differences between the Olympus and Artemis Diapirs (Fig. 5.17; Heaton, 1976; Magaritz and Taylor, 1974; Nuriel et al., 2009). Calculated serpentine oxygen and hydrogen isotope values in equilibrium with serpentinising fluids of $\delta^{18}O$ = ~+2.5 to +5 ‰ and δD -16 to -28 ‰ match previously measured serpentine stable oxygen and hydrogen isotopic compositions (Fig. 5.17). Such fluids may be sourced from the dehydration of altered ocean crust and subducting marine carbonates.

Considering the geometry of the Cyprus subduction zone and as the Cyprus slab is likely at relatively shallow depths under Cyprus (Table 5.10; Fig. 5.16), we assume a reasonable temperature of ~100 to 150°C within the downgoing slab, where it occurs, below the Troodos ophiolite. In a downgoing slab, these temperatures are inferred to correspond with the dehydration of smectite to illite in marine sediments (e.g., Stern, 2002; Vannuchi et al., 2008) and smectite to chlorite in the altered ocean crust (e.g., Hyndman, 1997; Kamura et al., 2017).

The oxygen isotopic composition of fluids in equilibrium with smectite in Troodos-like altered ocean crust ($\delta^{18}O$ = +12.7 ± 2.5 ‰; 1σ; n=7; Heaton and Sheppard, 1977) at ~125°C would be +0.6 ‰ (Table 5.11). Pore waters in equilibrium with Late Cretaceous marine carbonate sediment (e.g., +33.6 ‰; Schönfeld et al., 1991) at similar temperatures would yield values of +19 ‰ (Table 5.11). Mixing (80:20) of these respective end members would produce a fluid with a $\delta^{18}O$ of ~+4 ‰, consistent with the inferred serpentinising fluid oxygen isotopic composition (Table 5.11; Fig. 5.17).

In addition, hydrogen-bound minerals in a subducting sedimentary sequence dominated by marine carbonates, such as what may be subducting in the Cyprus arc (Reiche et al., 2016), are likely generally limited relative to typical subducting sediments (Elliott et al., 1997; Plank, 2014). As a result, dehydrating of marine carbonates would likely result in limited hydrogen isotopic exchange and dehydrating δD_{Fluid} values would likely be close to seawater values. Further, if the dehydrating smectite had stable hydrogen isotopic compositions similar to the altered lavas of the Troodos ophiolite (δD = -53 ± 11 ‰; 1σ; n=11; Heaton and Sheppard, 1977) rather than ODP Site 801, Western Pacific (δD = -90 to -120; Alt, 2003), the hydrogen isotopic composition of a fluid in equilibrium with smectite in dehydrating altered ocean crust at 125°C is -28 ‰. This falls into the estimated range of hydrogen stable isotopic fluid compositions of the serpentinising fluids (Table 5.11; Fig. 5.17). It is also consistent with a model of fluid freshening by mixing (~80:20) between the dehydrating smectite from upper ocean crust and marine carbonate sediments (Table 5.11).

These calculations suggest that the estimated oxygen and hydrogen isotopic compositions of the Troodos Mantle Sequence serpentinising fluids, at serpentinisation temperatures of >100°C to <300°C, are consistent with a slab-derived fluid source, at low temperatures 100 to 150°C within the downgoing slab. The serpentinising fluids would be dominated by dehydrating altered ocean crust source with a minor component of dehydrating marine carbonates.

Table 5.11: Estimated Cyprus slab-derived fluid isotope compositions. Smectite oxygen-water fractionation factor (Savin and Lee, 1988); Smectite hydrogen-water fractionation factor (Yeh, 1980). Phyllosilicate boron fractionation factor (Boschi et al., 2008; Liu and Tossell, 2005). Oxygen calcite-water fractionation factor (Zheng, 1999).

80:20 (Dehydrating Ocean Curst/ Marine Carbonates)	*Estimated Dehydrating Altered Ocean Crust composition*	*Estimated dehydrating marine carbonate composition*	*Estimated slab-derived fluid composition*	*Dehydrating altered ocean crust fluid end member (125°C) Smectite-Chlorite Transition*	*Dehydrating marine carbonate sediment fluid end member (125°C)*	*Proportion sourced from altered ocean crust*	*Proportion sourced from marine carbonates*
87Sr/86Sr	0.7028 to 0.7070	0.7082-0.7089 (Upper Cretaceous/ Palaeogene Marine Carbonates, Lefkara Formation, Cyprus; Makarona et al., 2012)	0.7055	0.7047	0.7085	79 %	21 %
δ18O (‰)	+12.7	+33.6 (Schönfeld et al., 1991)	+4	+0.6	+19	81%	19 %
δD (‰)	-53	N/A	-23	-28.8	+0 (pore water)	80 %	20 %
δ11B (‰)	+1	+8 to +26 (Marine Carbonates; Vengosh et al., 1991)	+22	+18	+39.6	81 %	19 %

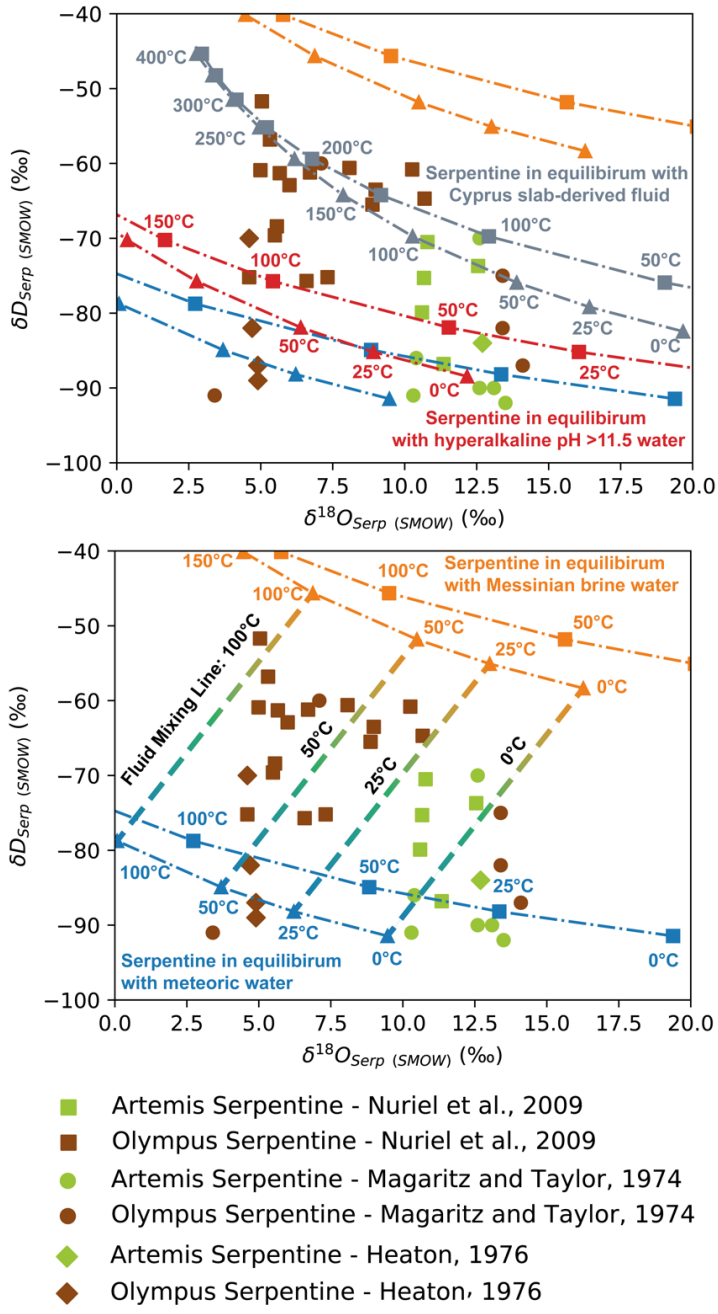

Figure 5.17: Oxygen and hydrogen stable isotope plot of published serpentine measurements (Heaton, 1976; Magaritz and Taylor, 1974; Nuriel et al., 2009). Troodos Mantle Sequence values are separated based on sample location either from the Artemis or Olympus Diapirs. Calculated serpentine oxygen and hydrogen stable isotope values in equilibrium with Cyprus meteoric water ($\delta^{18}O$ -7 ‰; δD -35 ‰; e.g., Boronina et al., 2005); hyperalkaline high pH >11.5 waters ($\delta^{18}O$ -3.5 ‰; δD -28 ‰; Chapter 4); Cyprus slab-derived fluid ($\delta^{18}O$ +4 ‰; δD -23 ‰; this study), and Messinian brine water ($\delta^{18}O$ +0.6 ‰; δD +1.1 ‰; e.g., Evans et al., 2015)) are shown. Triangles represent calculated serpentine values in equilibrium using empirical oxygen isotope fractionation factors from (Wenner and Taylor, 1971) and hydrogen isotope fractionation factors from Saccocia et al. (2009b). Squares represent calculated serpentine values in equilibrium using semi-empirical oxygen isotope fractionation factors from Zheng (1993) and empirical hydrogen isotope fractionation factors from Saccocia et al. (2009). Fluid mixing trajectories at constant temperatures between Cyprus meteoric water and Messinian brine water is shown.

5.7.2 $^{87}Sr/^{86}Sr$ Constraints

The $^{87}Sr/^{86}Sr$ ratios of ~0.705 measured in the whole rock samples of the Olympus Diapir and bulk residues of the Artemis Diapir are within the range of previously measured $^{87}Sr/^{86}Sr$ values of altered upper ocean crust (Bach et al., 2003; Harris et al., 2015; Teagle et al., 1998a, 1998b) and the Troodos ophiolite (e.g., Bickle and Teagle, 1992; Chapman and Spooner, 1977; Gillis and Robinson, 1990; Spooner et al., 1977; Staudigel and Gillis, 1990) (Table 5.9). Similar $^{87}Sr/^{86}Sr$ values measured in the Olympus and Artemis Diapirs are reported from serpentinised harzburgite clasts within the Mariana Forearc Mud Volcanoes, which yield $^{87}Sr/^{86}Sr$ values ranging between 0.704 and 0.706 (Bickford et al., 2008; Savov et al., 2007, 2005). Consequently, the pervasive 0.705 $^{87}Sr/^{86}Sr$ signal recorded in both the Artemis and Olympus Diapirs may reflect a fluid source primarily composed of dehydrating altered ocean crust, which is potentially mixed with dehydration of marine carbonate sediments. $^{87}Sr/^{86}Sr$ ratios of the marine carbonate Lefkara Formation in Cyprus vary between 0.70859 to 0.70907 (Makarona et al., 2012). In addition, progressive leaching experiments of smectite-group minerals in Hole 1256D, a complete section of recovered fast spread crust down to the dyke-gabbro transition, yield mean initial leachate $^{87}Sr/^{86}Sr$ ratios of 0.704365 ± 0.001003 (1σ; n=8; Harris et al., 2015). This indicates that during proposed dehydration of smectite to chlorite at 100-150°C, the most easily mobile portions of the smectite-group minerals may be a source of radiogenic Sr relative to typical fresh MORB values (e.g., 0.70287 ± 0.00004; 1σ; n=6; Harris et al., 2015) and mobilised from the downgoing slab during dehydration reactions.

Consequently, we estimate the $^{87}Sr/^{86}Sr$ of the serpentinising fluid originating from a mixture dominated (80:20) by dehydrating altered ocean crust of 0.7047 and a minor component of dehydrating marine carbonates of 0.7085 (Table 5.11).

5.7.3 $\delta^{11}B$ constraints

The boron isotopic composition of the serpentinising fluids can be robustly estimated by applying the boron equilibrium model (Appendix A) with reasonable prior likelihoods (Table 5.12; Table 5.13) to measured rock values. Calculations suggest that lower $\delta^{11}B_{Serp}$ values of +7 ± 1 ‰ occur in equilibrium with a $\delta^{11}B_{Fluid}$ value of $+23.3^{+6.9}_{-3.4}$ ‰ (1σ-equivalent) at a temperature of 230^{+116}_{-143} °C (1σ-equivalent; Fig. 5.18a). Measured higher $\delta^{11}B_{Serp}$ values within the Troodos Mantle Sequence of +18.4 ± 1 ‰ are calculated to be in equilibrium with a $\delta^{11}B_{Fluid}$ value of $+33.2^{+3.7}_{-2.6}$ ‰ (1σ-equivalent) at a temperature of 236^{+114}_{-122} °C (1σ-

equivalent) (Fig. 5.18d). The measured range of $\delta^{11}B_{Serp}$ values and the robustly estimated $\delta^{11}B_{Fluid}$ values, using mantle wedge serpentinisation prior likelihoods (Table 5.12) and are consistent with an interpretation of pervasive serpentinisation removing B from the fluid, into serpentine, consequently evolving the $\delta^{11}B_{Fluid}$ to heavier values. Robustly estimated fluid $\delta^{11}B$ values in equilibrium with the mean $\delta^{11}B_{Serp}$ value of the Troodos Mantle Sequence ($\delta^{11}B_{Serp}$ = 12.5 ± 3.2 ‰,1σ-equivalent) yields a $\delta^{11}B_{Fluid}$ value of $+28.4^{+5.7}_{-4.7}$ ‰ (1σ-equivalent) at a temperature of 231^{+115}_{-139} °C (1σ-equivalent) (Fig. 5.18b).

The estimated equilibrium boron isotopic fluid compositions are consistent with serpentinising temperatures estimations from stable oxygen isotope values (Fig. 5.17). Such boron isotopic compositions of serpentinising fluids may be derived from the dehydration of marine carbonates and dehydration of altered upper ocean crust in a subducting slab. Under the assumption that the altered upper ocean crust in the downgoing Cyprus slab had a boron isotope value of +2.5 ± 2.5 ‰, consistent with previously measured values of altered ocean crust (Spivack and Edmond, 1987; Yamaoka et al., 2015b, 2012). Calculations indicate fluids in equilibrium with such a composition of altered ocean crust would yield $\delta^{11}B_{Fluid}$ values of $+20.8^{+11.0}_{-3.3}$ ‰ (1σ-equivalent) at a temperature of 125^{+15}_{-15} °C (1σ-equivalent) (Fig. 5.18c), consistent with the estimated $\delta^{11}B_{Fluid}$ values of the serpentinising fluids. The dehydrating smectite is likely a significant source of B, since altered upper ocean crust typically yield high B concentrations. For example, the Troodos lavas, which range between 3.8 to 206.8 μg/g B (Table 5.14; Yamaoka et al., 2015b) and have abundant saponite (Mg-rich smectite; Gillis and Robinson, 1990).

To our knowledge, varied temperature dependent boron isotope fractionation factors between carbonates and water, similar to reported phyllosilicate fractionation factors (Boschi et al., 2008), do not exist in the literature. However, at low temperatures and pressures (23°C, 0.1 MPa) $\Delta^{11}B_{carbonate\text{-}fluid}$ fractionation factors are reported as -16.5 ‰ (Hemming et al., 1995) and marine carbonates have been reported to yield $\delta^{11}B$ values ranging between +8.9 to +26.2 ‰ (Vengosh et al., 1991). Consequently, if dehydration of marine carbonates in the Cyprus slab is in equilibrium with a fluid, the resulting fluid boron isotopic composition would be consistent with a model of serpentinising fluids originating from primarily a dehydrating altered ocean crust source with a minor component of marine carbonates (Table 5.11).

Table 5.12: Boron equilibrium model coupled with a Bayesian inversion engine prior likelihoods table ('hydrothermal' conditions >50°C to <500°C).

Hydrothermal equations from Arcis et al. (2017)	***Pressure (MPa)***	***Salinity (g/kg)***	***Temperature (°C)***	$\delta^{11}B_{Fluid}$ ***(‰)***	***pH***	***Fluid Density (kg/m^3)***
Cretaceous Hydrothermal Fluid (Fig. 5.14)						
Prior Probability Distribution	Gaussian	Gaussian	Uniform	Uniform	Uniform	Gaussian
Range (± 1σ)	X ± 10 (x = to 4000 m water depth and Troodos ophiolite crustal depth. Assuming densities of 1,000 kg/m^3 and 3,000 kg/m^3)	35 ± 10	200 to 500	10 to 39.61	0 to 12	x ± 150 Calculated from equation of state (e.g., Safarov et al., 2009
Cyprus slab-derived fluid (Fig. 5.18)						
Prior Probability Distribution	Gaussian	Gaussian	Uniform	Uniform	Uniform	Gaussian
Range (± 1 σ)	Equivalent to 13 km depth	35 ± 30	150 to 400	10 to 39.61	8 to 12	x ± 150 Calculated from equation of state (e.g., Safarov et al., 2009
Meteoric water with a Messinian evaporite component (Fig. 5.20)						
Prior Probability Distribution	Gaussian	Gaussian	Uniform	Uniform	Uniform	Gaussian
Range (± 1 σ)	Equivalent to 3 km depth	55 ± 30	0 to 100	10 to 46	6 to 12	x ± 150

Hydrothermal equations from Arcis et al. (2017)	***Pressure (MPa)***	***Salinity (g/kg)***	***Temperature (°C)***	$\delta^{11}B_{Fluid}$ ***(‰)***	***pH***	***Fluid Density (kg/m^3)***
						Calculated from equation of state (e.g., Safarov et al., 2009
Smectite dehydration in downgoing Cyprus slab (Fig. 5.18)						
Prior Probability Distribution	Gaussian	Gaussian	Gaussian	Uniform	Uniform	Gaussian
Range (± 1σ)	Equivalent to 13 km depth	35 ± 30	125 ± 25	5 to 39.61	0 to 12	x ± 150 Calculated from equation of state (e.g., Safarov et al., 2009

Table 5.13: Boron equilibrium model coupled with a Bayesian inversion engine prior likelihoods table ('seawater' conditions >0°C to <50°C).

Low temperature pKB using equations from Dickson et al. (1990)	*Rock Depth (m)*	*Water Depth (m)*	*Salinity (g/kg)*	*Temperature (°C)*	$\delta^{11}B_{Fluid}$ *(‰)*	*pH*
Low temperature seawater-basalt exchange (Fig. 5.14)						
Prior Probability Distribution	Gaussian	Gaussian	Gaussian	Uniform	Uniform	Uniform
Range (± 1σ)	100 ± 10	3000 ± 100	35 ± 5	1 to 10 °C	39.61 to 48	8 to 8.2
Meteoric water (Fig. 5.20)	Gaussian	Gaussian	Gaussian	Uniform	Uniform	Uniform
Range (± 1σ)	300 ± 100	0	18 ± 20	0.1 to 50°C	10 to 39.61	8 to 12

Table 5.14: Troodos ophiolite lavas geochemical and isotopic characteristics.

	$^{87}Sr/^{86}Sr$	$\delta^{18}O$ (‰)	δD (‰)	$\delta^{11}B$ (‰)	B (μg/g)	H_2O (wt.%)
Troodos Lavas	0.7051 ± 0.0011 (1σ, n=85) 0.7032 to. 0.7076	+12.7 ± 2.5 (1σ, n=7; Heaton and Sheppard, 1977)	-53 ± 11.3 (1σ, n=18; Heaton and Sheppard, 1977)	+8.1 ± 6.1 (1σ, n=6; Yamaoka et al., 2015)	3.8 to 206.8 63.2 ± 58 ug/g (1σ, n=13; Yamaoka et al., 2015)	5 to 7 % (Gillis and Robinson, 1990)

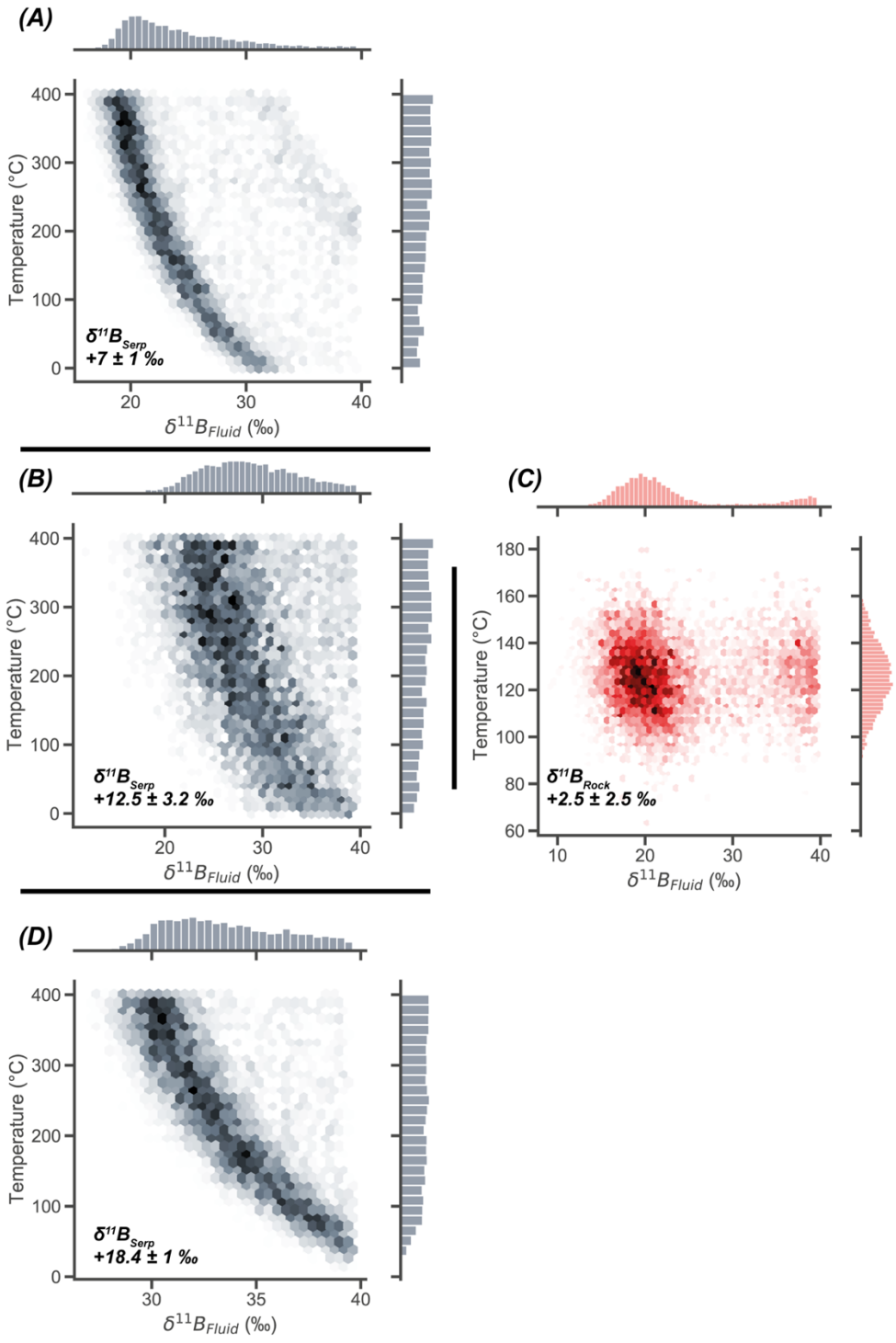

Figure 5.18: Temperature-$\delta^{11}B_{Fluid}$ density hexbin plot with marginal posterior probability distributions from the Bayesian inversion boron equilibrium model (Appendix A). (A) Plot reflects an inversion output of a $\delta^{11}B_{Serp}$ value of +7 ± 1 ‰ (lowest $\delta^{11}B_{Serp}$ value; Table 5.7) with Cyprus slab-derived fluid priors (Table 5.12). (B) Plot reflects an inversion output of a $\delta^{11}B_{Serp}$ value of +12.5 ± 3.2 ‰ (average value of Troodos Mantle Sequence $\delta^{11}B_{Serp}$ data; 1σ; n = 48; Table 5.7) with Cyprus slab-derived fluid priors (Table 5.12). (C) Plot reflects an inversion output of a $\delta^{11}B_{Rock}$ value of +2.5 ± 2.5 ‰ (estimated composition of slab-derived smectite; Yamaoka et al., 2015b) with Cyprus slab-derived fluid priors (Table 5.12). (D) Plot reflects an inversion output of a $\delta^{11}B_{Serp}$ value of +18.4 ± 1 ‰ (highest $\delta^{11}B_{Serp}$ value; Table 5.7) with Cyprus slab-derived fluid priors (Table 5.12). Note: Estimated $\delta^{11}B_{Fluid}$ compositions of (B) and (C) are similar.

5.7.4 Mass Balance Calculation

Here, we evaluate whether enough water is released from the downgoing Cyprus slab to pervasively serpentinise the Troodos Mantle Sequence during an initial serpentinisation event that resulted in whole rock $^{87}Sr/^{86}Sr$ ratios of 0.7053 and the reduction of bulk density from 3,300 kg/m^3 to ~2,800 kg/m^3, equivalent to a 66 % serpentinisation reaction extent (Fig. 5.3). Recent serpentinisation-induced isostatic uplift modelling highlighted that serpentinisation alone can generate significant uplift (Evans et al., 2021). Consequently, interpreted Troodos Massif uplift trajectories (McCallum, 1989; Morag et al., 2016; Poole and Robertson, 1998, 1991; Robertson, 1977; Stow et al., 1995) and the occurrence of serpentinisation in the Troodos Massif are likely related. Assuming these constraints, the time period between the initiation of significant uplift at ~5.5 Ma and the inferred stalling of subduction in the Pliocene (~3 Ma) is ~2.5 Ma (Morag et al., 2016; Robertson, 1998a, Robertson, 1998b).

There is significant uncertainty in the nature of the Cyprus subduction zone with estimates of depth to the Cyprus slab beneath the Mount Olympus region varying between 12 to 36 km (Table 5.10; Hayes et al., 2018; Mackenzie et al., 2006). For the purposes of the following calculations, we assume the depth to the Cyprus slab beneath Mount Olympus as 13 km, in agreement with previous estimations from modelling of gravity data (Gass and Masson-Smith, 1963; Shelton, 1993).

A completely serpentinised rock has a H_2O content of ~13.5 wt.% and consequently a partially 66% serpentinised mantle rock will have ~8.9 wt.% water. Assuming the Troodos Mantle Sequence is a truncated cone with a top diameter of 8 km, a length of 13 km, a bottom diameter of 15 km and a density of 2800 kg/m^3, we estimate the total volume of water (ρ_{Water} = 1000 kg/m^3) within this body is ~347 km^3 (Table 5.15).

Consequently, a similar volume of water is required to be released from the downgoing Cyprus slab to balance against the volume of water incorporated during initial partial serpentinisation of the Olympus and Artemis Diapirs. Based on the geochemical and isotopic evidence presented in this study (see previous section), we infer that the fluid origin of this initial serpentinisation event is a fluid primarily composed of a dehydrating altered ocean crust source, with a minor component of pore water dehydration in marine carbonates, at temperatures 100 to 150°C within the slab. In a subducting slab, these temperatures are inferred to reflect the dehydration and transformation of smectite to illite in marine sediments and smectite to chlorite in the altered ocean crust (Hyndman et al., 1997; Kameda et al., 2017; Saffer et al., 2008; Stern, 2002), such transformation results in ~33 % water loss from the rock by mass (Saponite, 18.8 wt.% H_2O; Chlorite, 12.1 wt.% H_2O).

As the sediment package of the downgoing Cyprus slab is likely primarily composed of marine carbonates (Reiche et al., 2016) with minimal clay abundance, we assume that the conversion of smectite to chlorite in the downgoing slab is the primary dehydration reaction. Altered lavas in the Troodos ophiolite yields water contents ranging between ~5 to 7 wt.% (Gillis and Robinson, 1990). In comparison, the water content of altered ocean crust at the intermediate spreading rate Hole 504B ranges between ~0.5 to 7% wt.% (Alt et al., 1996). Other studies have estimated the water content of a 2.5 km thick basalt layer as ~2 wt. % (Peacock, 1990) and the water content of the upper ocean crust to range between ~2 and 3 wt.% (Staudigel, 2014; Staudigel et al., 1995).

As the majority of the water content of altered ocean crust is inferred to be located in smectite (Alt and Shanks, 2006; Alt and Teagle, 2003) and under the assumption that the downgoing Cyprus slab is of ocean crust of Triassic or Permian (Müller et al., 2008) or even Carboniferous (Granot, 2016) age, and is therefore old, with a potentially greater likelihood for off-axis low temperature exchange to form smectite-group minerals in the upper ocean crust. For the following calculations (Table 5.15), we assume the water content of the altered ocean crust of the downgoing Cyprus slab to be either 1, 3, and 6 wt.% respectively. We calculate that a 33% loss of water during transformation from smectite to chlorite would produce a total ~0.33, ~1, and ~2 wt.% loss of water from the downgoing altered ocean crust. At the depth of inferred slab temperatures (~100 to 150°C), where the downgoing slab is proposed to intersect below the Mount Olympus region, sediment dehydration of marine carbonates has progressively occurred. Fluid mixing calculations (Table 5.11) indicate a minor sedimentary (80:20) component in the serpentinising fluids beneath the Troodos Massif. Consequently, we assume an equivalent 0.4, 1.25, and 2.5 wt.% (80:20) total water loss from the downgoing Cyprus slab during smectite-chlorite dehydration. Consequently, this indicates that per volume unit, there is not enough water coming from the dehydrating slab (~0.4 to 2.5 wt. % vs ~8.9 wt.%) to account for the required extent of serpentinisation.

However, as previously outlined, the Eratosthenes Seamount may have influenced the dynamics of the Cyprus subduction zone, potentially focussing and channelling fluids from a downgoing slab into the Mount Olympus region. We test this long-standing hypothesis by estimating the total volume of water released during dehydration of sediments and smectite in the downgoing altered ocean crust.

For the purposes of the following calculation, we vary the volume of water being harvested from the downgoing slab by modifying width (40, 80, and 100 km) and length (60 and 150 km) parameters but keep the thickness of the dehydrating portion (2 km) constant (Table 5.15; Fig. 5.19). Although the distance from the Cyprus trench to Mount Olympus is 57 km, we assume the length of dehydrating slab within the 100 to 150°C window to be ~25

km, similar to the width of the ophiolite. The respective length parameters (60 and 150 km) used in the calculation are composed of the ~25 km window and an additional length of subducted slab assumed to reflect increased subduction time. The 60 km length parameter is composed of the ~25 km window and an additional 35 km of slab (28° Slab dip angle; 8 mm/yr convergence rate; Feld et al., 2017; Wdowinski et al., 2006), assumed to have been subducted between stalling of the subduction zone at ~3 Ma and the initiation of fluid focussing at ~7 Ma (Morag et al., 2016; Robertson, 1998a, 1998b). Between the initial fluid focusing and the deposition and circum-Troodos igneous clasts that indicate the initiation of significant uplift at ~5.5 Ma (Fig. 2.6), we assume a time lag of ~1.5 Myr, consistent with Troodos Massif (U-Th)/He dating (Morag et al., 2016). The 150 km length parameter is composed of the ~25 km window and an additional 125 km of slab that reflects ~15.5 Myr of fluid focussing since the Early Miocene initiation of the current Cyprus subduction zone geometry. A fluid focussing factor is calculated by dividing the area of the harvested slab by the area of the Troodos Mantle Sequence bottom circle (Table 5.15; Fig. 5.19).

The total estimated volume of water released from a dehydrating slab of 40 km x 60 km x 2 km and a released water content of 2.5 wt.% is estimated as 336 km^3 and requires a fluid focussing factor of 6 (Table 5.15); whereas a dehydrating slab of 80 x 60 x 2 km and a released water content of 1.25 wt.% is estimated as 336 km^3 and requires a fluid focussing factor of 11 (Table 5.15); and a dehydrating slab of 100 x 150 x 2 km with a released water content of 0.4 wt.% is estimated as 336 km^3, requiring a fluid focussing factor of 14 (Table 5.15). These estimated water volumes are similar to the water volume of the Troodos Mantle Sequence, which is estimated as 347 km^3. The chosen parameters in the calculation are likely reasonable given the area of the Eratosthenes Seamount (up to 100 km wide, 120 km length) and that a feature of this size would likely influence the subduction zone dynamics (Robertson, 1998a, 1998b), channelling fluids over a wide area into a narrower discrete zone ~13 km beneath Mount Olympus (Fig. 5.16).

Table 5.15: Mass Balance Calculation.

		Olympus and Artemis Diapirs		***Dehydrating slab 6 wt. % H_2O***	***Dehydrating slab 3 wt. % H_2O***	***Dehydrating slab 1 wt. % H_2O***	***Comments***
	Serpentinisation Extent	66% (3,300 to 2,800 kg/m^3 bulk density reduction)					(80/20 ratio; 80 % dehydration of saponite, 20 % from dehydration of marine carbonate sediments; ~100 to 150°C).
	Water content	~9 %		~2.5 %	~1.25 %	~0.4 %	80 % dehydration of saponite sourced from a 33 % loss of H_2O during saponite-chlorite transition at ~100 to 150 °C.
	Bulk Density	2800 kg/m^3		2,800 kg/m^3	2,800 kg/m^3	2,800 kg/m^3	Convergence between Cyprus and African plate ~8 mm/yr (Wdowinski et al., 2006).
Total Volume	*Truncated Cone* $V = \frac{1}{3}\pi h(r^2 + rR + R^2)$ *h = 13 km* *r = top radius = 4 km* *R = bottom radius = 7.5 km*	1.40x10^{12} m^3	Cuboid $V = wlh$ w = 40 to 100 km width; l = 60 to 150 km length; h = 2 km height	4.80x10^{12} m^3 (40 x 60 x 2 km)	9.60x10^{12} m^3 (80 x 60 x 2 km)	3.00x10^{13} m^3 (100 x 150 x 2 km)	Initiation of significant uplift = 5.5 Ma Stalling of subduction zone due to collision with the Eratosthenes Seamount = 3 Ma

					Estimated length of dehydration slab portion within the 100 to 150 °C window = 25 km length
Total Mass	3.90x10^{15} kg	1.34x10^{16} kg	2.69x10^{16} kg	8.40x10^{16} kg	60 km length parameter is based on a 25 km window and an assumed additional 35 km since ~7 Ma.
Water Mass	3.47x10^{14} kg	3.36x10^{14} kg	3.36x10^{14} kg	3.36x10^{14} kg	Assumed 1.5 Myr lag between initiation of fluid focussing (7 Ma) and significant uplift (5.5 Ma).
Water Volume (Water density 1,000 kg/m^3)	3.47x10^{11} m^3	3.36x10^{11} m^3	3.36x10^{11} m^3	3.36x10^{11} m^3	
	347 km^3	**336 km^3**	**336 km^3**	**336 km^3**	
Fluid Focussing Factor (66 % Serpentinisation extent)		**x6**	**x11**	**x14**	150 km length parameter is based on a 25 km window and 15.5 Myr of fluid-focussed subduction
Fluid Focussing Factor (33 % Serpentinisation extent)		**x3**	**x5.5**	**x7**	Eratosthenes (~100 km width x ~120 km length)

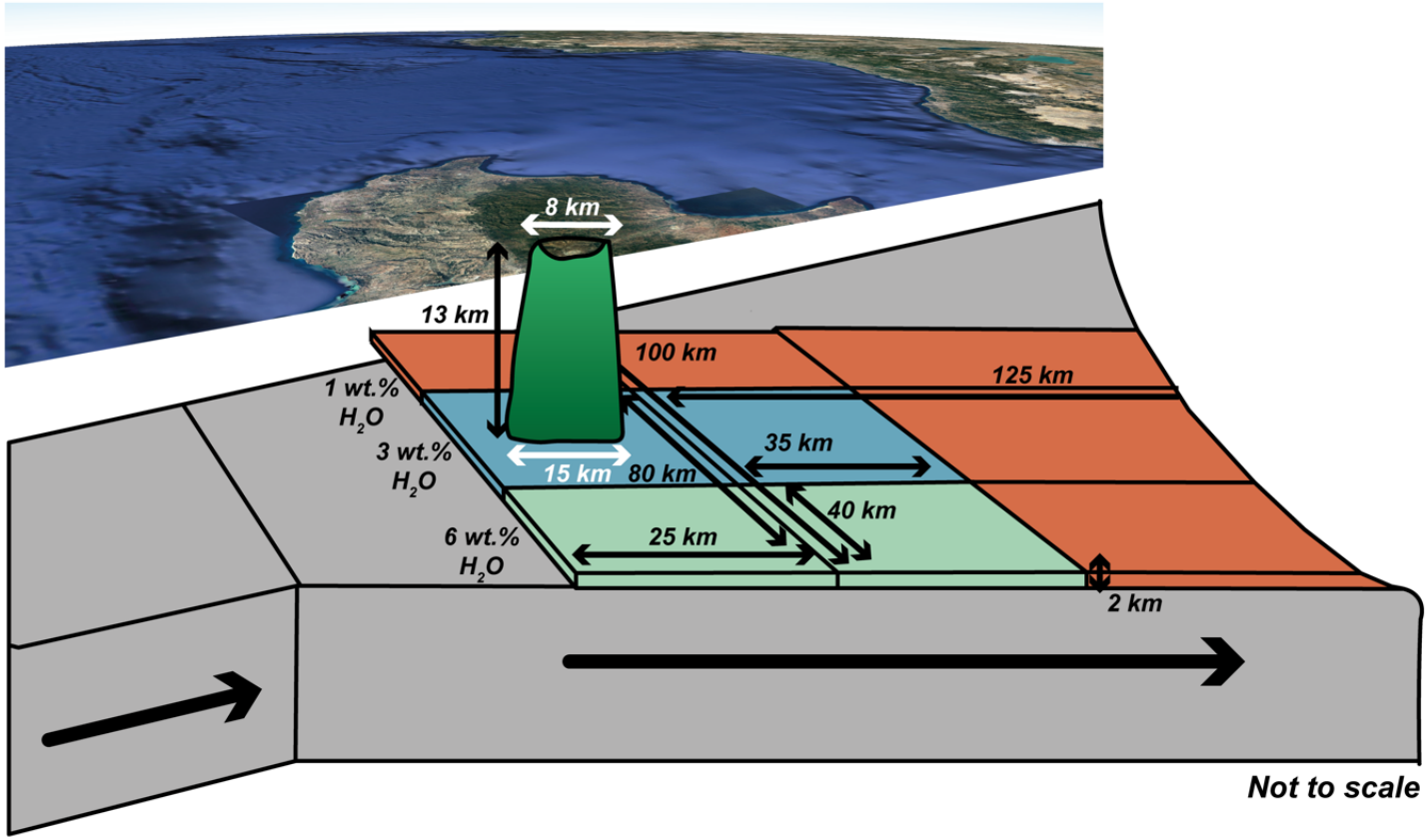

Figure 5.19: Illustration of the set up for the mass balance calculation. The assumed proportions of the Troodos Mantle Sequence and the respective volume of dehydrating downgoing Cyprus slab required to harvest H_2O and focus into the Mount Olympus region are shown. Orange denotes 1 wt.% H_2O and a volume of 100 x 150 x 2 km. Blue denotes 3 wt.% H_2O and a volume of 80 x 60 x 2 km. Green denotes 6 wt.% H_2O and a volume of 40 x 60 x 2 km. Illustration not to scale. See text for full details.

5.8 Sediment-derived meteoric serpentinisation

Evidence of interaction between the underlying Troodos ophiolite oceanic crust and overlying marine sedimentary sequences of Cyprus is recorded by the isotopic composition of secondary mineral assemblages. For example, gypsum and trace amounts of anhydrite occur in recovered drillcores of holes CY-4 and CY-2A from the Cyprus Crustal Study Project (Alt, 1994; Gillis and Robinson, 1990; Herzig and Friedrich, 1987; Jamieson and Lyndon, 1987), and yield $\delta^{34}S$ values ranging between +21.8 and +22.7 ‰ similar to isotope values of Messinian evaporites (Alt, 1994; Claypool et al., 1980; Jamieson and Lyndon, 1987). It is proposed that recovered gypsum and trace anhydrite formed from circulating groundwaters, which had interacted and remobilised sulphate from the overlying Messinian evaporites into secondary mineral assemblages within the Troodos ocean crustal rocks (Alt, 1994). Furthermore, in the CY-1 borehole, similar low temperature mineral assemblages such as gypsum, calcite, palygorskite yield $^{87}Sr/^{86}Sr$ ratios more radiogenic than Cretaceous seawater (~0.7073; McArthur et al., 2012) ranging between 0.70745 and 0.708092 (Staudigel and Gillis, 1990). In addition, other studies have also reported similar $^{87}Sr/^{86}Sr$ values (>0.7073 to 0.7083) of discrete calcite veins hosted in the Troodos lava sequences (Quandt et al., 2019). These calcite veins are interpreted to reflect the ingress of low-temperature seawater into the ophiolite, whilst on the seafloor (Quandt et al., 2019). Some of these calcite veins have stable oxygen isotope values ranging between +26.32 and +28.79 ‰ ($\delta^{18}O_{(SMOW)}$; Quandt et al., 2019) and can be calculated (using the calcite-water fractionation factors; Zheng, 1999) to be in equilibrium, at low-temperatures >5 to <25°C, with modern meteoric water ($\delta^{18}O_{(SMOW)}$ ~-7 ‰; Boronina et al., 2005). In addition, previous studies have reported $^{87}Sr/^{86}Sr$ of springs, rivers, and wells draining from the Troodos lavas ($^{87}Sr/^{86}Sr$ ratios = 0.7060 to 0.70838; Ladegaard-Pedersen et al., 2020) similar to the carbonate veins. This suggests that some of these carbonate veins located in the Troodos lavas are evidence of percolating meteoric-derived groundwaters reflecting variable interaction and mixing extents between meteoric water, overlying sedimentary sequences, and underlying ophiolitic rocks, since initial sub-aerial emergence of the ophiolite during the Miocene (Fig. 2.6; McCallum, 1989; Poole and Robertson, 1998, 1991; Robertson, 1977; Rouchy et al., 2001; Stow et al., 1995).

In the Troodos Mantle Sequence, previous measured stable oxygen and hydrogen isotopic compositions of serpentine from predominantly the Artemis Diapir and discrete portions of the Olympus Diapir have been interpreted to reflect exchange with meteoric-derived waters at low-temperatures (Magaritz and Taylor, 1974). The very high $\delta^{18}O$ values of some serpentinites in the Troodos Mantle Sequence are outside the calculated low-temperature equilibrium window using empirical fractionation factors (Wenner and Taylor,

1971) but not more recent semi-empirical fractionation factors (Zheng, 1993) (Fig. 5.17). Previous studies proposed a role for Messinian evaporites (Magaritz and Taylor, 1974) that may have overlain the Troodos ophiolite rocks before the Troodos Mantle Sequence was exhumed.

Here, we evaluate whether the serpentinised mantle rocks of the Troodos Mantle Sequence isotopically exchanged with serpentinising fluids derived from meteoric waters that may have interacted with marine carbonates and evaporites overlying the ophiolite sequence, resulting in relative mixing between two distinct isotopic compositions.

5.8.1 $^{87}Sr/^{86}Sr$ Constraints

Evidence of a sedimentary component in the serpentinising fluids of the Troodos Mantle Sequence is highlighted in the $^{87}Sr/^{86}Sr$ ratios from progressive leaching experiments. The distinct 0.70865-0.709 endmember (Fig. 5.3) measured in the serpentinised mantle rocks of the Troodos Mantle Sequence reflect a component of isotopic exchange occurred with fluids with a relatively radiogenic signature. The primarily marine carbonates of the Upper Cretaceous/Paleogene Lefkara Formation, Miocene Pakhna Formation, and Pliocene Nicosia Formation overlying the Troodos ophiolite (Robertson, 1977) have $^{87}Sr/^{86}Sr$ ratios ranging between 0.70850 and 0.70907 (Makarona et al., 2012). In addition, Messinian evaporites in Cyprus have $^{87}Sr/^{86}Sr$ ratios ranging between 0.70865 and 0.7090 (Flecker and Ellam, 2006; McCulloch and Deckker, 1989; Müller and Mueller, 1991). Consequently, the radiogenic Sr signal measured in the serpentinised mantle rocks of the Troodos Mantle Sequence may originate from the overlying sedimentary sequences. The samples with lowest bulk densities yield the most radiogenic Sr isotopic compositions (Fig. 5.3), indicating that a serpentinisation event with a radiogenic Sr source of ~0.70865 to 0.7090 overprinted an initial serpentinisation episode involving fluids with a less radiogenic signature ($^{87}Sr/^{87}Sr$ ~0.705, Fig. 5.3).

5.8.2 $\delta^{18}O$ and δD

The $\delta^{18}O$ of some measured serpentinites within the Olympus and Artemis Diapirs are higher than other serpentinised massifs where low temperature serpentinisation is inferred (Magaritz and Taylor, 1974; Wenner and Taylor, 1974, 1973, 1971). As a result, modification of the isotopic composition of the meteoric-derived serpentinising fluids was proposed (Magaritz and Taylor, 1974). Messinian gypsum samples from the Sorbas Basin,

Spain are reported to have precipitated from fluids with $\delta^{18}O$ values of -2.6 to 3.8 ‰ and δD of -16.2 to +18.4 ‰ (Evans et al., 2015). Calculated serpentinites in equilibrium with such waters are isotopically lighter than measured serpentinite δD values (Fig. 5.17). However, all previously measured stable oxygen and hydrogen isotopic compositions of serpentinites within the Troodos Mantle Sequence (Heaton, 1976; Magaritz and Taylor, 1974; Nuriel et al., 2009) fall between serpentine values calculated in equilibrium with meteoric water ($\delta^{18}O$ = -7 ‰; δD = -35; Boronina et al., 2005) and serpentine isotope values calculated in equilibrium with a Messinian brine water (Evans et al., 2015) (Fig. 5.17). The measured serpentine stable oxygen and hydrogen isotope values are consistent if mixing between meteoric-derived water and a water with similar isotopic compositions as the Messinian evaporite brines occurred (Fig. 5.17). Such a scenario could occur if either: (i) The overlying Messinian evaporite brine water penetrated through the overlying ophiolitic rocks and into the already-partly serpentinised mantle peridotites, where subsequent incursion of meteoric water progressively flushed the Messinian evaporite brine water out of the uplifting serpentinite diapirs; or (ii) Soon after formation of the overlying Cyprus Messinian evaporite sequences, significant uplift of the ophiolite occurred, meteoric water may have percolated through and exchanged with overlying evaporites, resulting in the modification of the isotopic composition of the fluid due to relative mixing between two distinct end-member fluid compositions.

Establishing the relative proportions between meteoric water and a Messinian saline brine water are complicated by the apparent significant contribution of a meteoric water signature in the Messinian brine waters of Almeria, Spain (Evans et al., 2015). Further investigations are required to constrain the fluid isotopic composition of the Cyprus Messinian saline brine waters, in order to establish the relative proportions of the respective isotopic endmembers.

5.8.3 $\delta^{11}B$

Previous studies have reported $\delta^{11}B$ values of Messinian halites as +34.66 ± 1.46 ‰ (1σ, n=7; Paris et al., 2010). It is proposed that during halite formation, boron is primarily incorporated into cubic fluid inclusions without apparent fractionation between the fluid and mineral (Liu et al., 2000; Paris et al., 2010). Here, we evaluate whether the measured $\delta^{11}B$ values of the serpentinites in the Troodos Mantle Sequence could have formed in equilibrium at low temperatures (<100°C) with fluids of similar boron isotopic composition to Messinian halite $\delta^{11}B$ values. Application of the Bayesian Inversion boron equilibrium model shows that in such a scenario, the measured serpentine $\delta^{11}B$ values from both the

Olympus and Artemis Diapirs can occur in equilibrium with a $\delta^{11}B_{Fluid}$ value of $+33.6^{+4.9}_{-5.9}$ ‰ (1σ-equivalent) at a temperature of 56^{+40}_{-49} °C (1σ-equivalent) (Fig. 5.20; Table 5.12).

Additionally, Messinian brine waters have previously been proposed to reflect a x12 evaporation of seawater, yielding a boron concentration of ~53 μg/g (Vengosh et al., 1998). Fluid mixing between a Messinian brine waters and meteoric water would produce boron fluid concentrations similar to serpentine boron concentrations of radiogenic Sr whole rocks (~<40 μg/g; Fig. 5.9; Fig. 5.12). Although the partition coefficient between serpentine and fluids is unknown, serpentine boron concentrations are consistent with a model of serpentinisation with either a diluted Messinian brine water or a meteoric water that has, at least, partially exchanged with the overlying sedimentary sequences.

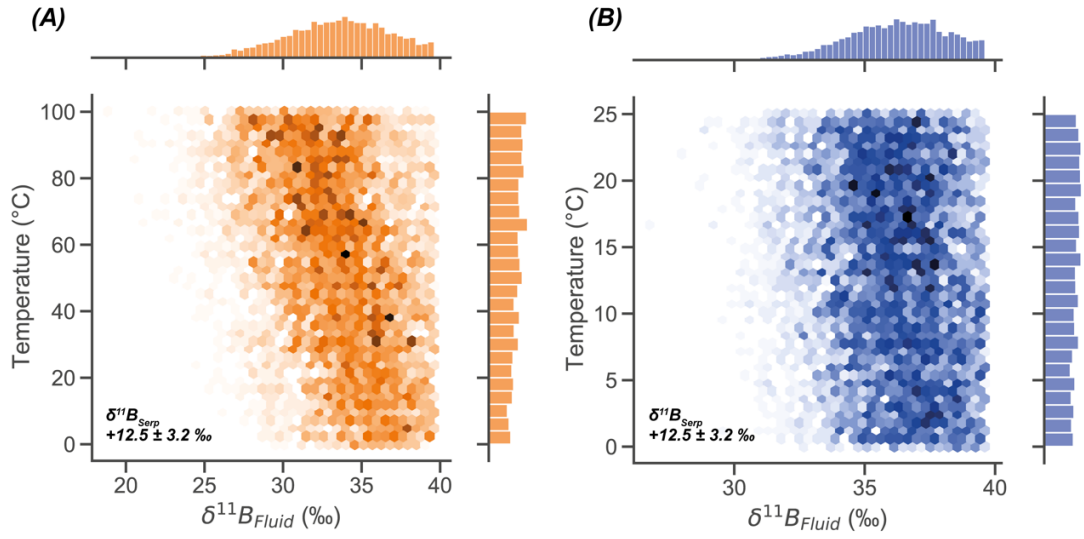

Figure 5.20: Temperature-$\delta^{11}B_{Fluid}$ density hexbin plot with marginal posterior probability distributions from the Bayesian inversion boron equilibrium model (Appendix A). (A) Plot reflects an inversion output of a $\delta^{11}B_{Serp}$ value of +12.5 ± 3.2 ‰ with Messinian meteoric water priors (Table 5.12). (B) Plot reflects an inversion output of a $\delta^{11}B_{Serp}$ value of +12.5 ± 3.2 ‰ with low temperature <50°C priors (Table 5.13).

5.9 Modern serpentinisation-alteration exchange with meteoric water

A detailed evaluation of the Troodos Mantle Sequence modern meteoric fluid-rock regime is presented in earlier chapters (Chapter 3 and 4), so here we only briefly outline the modern meteoric fluid-rock regime to establish whether geochemical and isotopic compositions of the Troodos Mantle Sequence are consistent with fluid-rock reactions in a modern meteoric water setting.

Published serpentine stable oxygen and hydrogen isotopic analyses provide compelling evidence for recent low-temperature exchange between meteoric water and serpentinised mantle rocks of the Olympus and Artemis Diapirs (Heaton, 1976; Magaritz and Taylor, 1974; Nuriel et al., 2009). Discrete portions of the Olympus and Artemis Diapirs yield high $\delta^{18}O$ (+10 to +13.5 ‰) and low δD (-70 to -93 ‰). Calculated oxygen and hydrogen stable isotope values for serpentine in equilibrium with present day Troodos meteoric water ($\delta^{18}O$ -7 ‰, δD -35 ‰; Boronina et al., 2005) and active Troodos high pH hyperalkaline waters ($\delta^{18}O$ -3.5 ‰, δD -26 ‰; Chapter 4) at temperatures from 25°C to <100°C fall within the range of samples from both the Olympus and Artemis Diapirs.

Previous studies have proposed that serpentine hydrogen stable isotopes exchange with subsequent fluid episodes, potentially overprinting original values (Kyser et al., 1999; Kyser and Kerrich, 1991; Wenner, 1971). As the relative proportions of oxygen and hydrogen in water and serpentine are different (W/R ~1.7 for O, ~7.7 for H), hydrogen is more likely to undergo post-formational isotopic exchange with more recent fluids relative to oxygen. Serpentine oxygen stable isotope values are likely to be more robust and better recorders of initial formation conditions. Consequently, the high $\delta^{18}O$ values recorded in the Artemis Diapir and portions of the Olympus Diapir ($\delta^{18}O$ +10.3 to +14.1 ‰) suggest formation serpentine-fluid equilibration at low temperatures most likely with meteoric water (Fig. 5.17).

Application of the global boron meteoric water line (Rose-Koga et al., 2006) (Eq. 5.3) to Cyprus, yields a $\delta^{11}B_{Fluid}$ value of +37.7 ‰ (δD -35 ‰; Boronina et al., 2005).

$$\delta D = 2.6 \cdot \delta^{11}B - 133 \qquad (5.3)$$

Calculations using Bayesian inversion (see Appendix A) of boron isotope values in equilibrium with meteoric waters indicate that the measured range of serpentinised mantle rocks $\delta^{11}B$ are consistent with being in equilibrium with meteoric waters ($\delta^{11}B$ +37.7 ‰) at low temperatures ~25°C (Fig. 5.20; Table 5.13).

5.10 A serpentinisation history of the Troodos Mantle Sequence

Isotopic compositions ($^{87}Sr/^{86}Sr$, $\delta^{11}B$, $\delta^{18}O$, δD) of rocks from the Troodos Mantle Sequence are consistent with a progressive sequence of overprinting serpentinisation events. We propose that Cretaceous hydrothermal fluids penetrated the Troodos crust-mantle transition zone, inducing rodingitisation and localised serpentinisation of the underlying Troodos lithospheric mantle. Evidence of this event is recorded by the strong $^{87}Sr/^{86}Sr$ 0.7058 signal in the Olympus Transition Zone rodingites and in the lower crustal portions of the CY-4 borehole, where whole rocks and secondary veins with $^{87}Sr/^{86}Sr$ ratios of 0.7037-0.7054 are elevated from assumed Troodos mantle compositions of ~0.7037 (King et al., 2003; Teagle unpublished data; Rautenschlein et al., 1985). These values are consistent with the estimated $^{87}Sr/^{86}Sr$ values of Troodos Cretaceous hydrothermal fluid (Bickle and Teagle, 1992).

It has recently been demonstrated that serpentinisation can mechanistically generate significant surface uplift, enough to form the Troodos mountains within a constrained time frame (~5.5 Myr; Evans et al., 2021), highlighting isostatic uplift is an inevitable consequence of serpentinisation reactions. Consequently, pervasive serpentinisation of the Olympus and Artemis Diapirs by Cretaceous hydrothermal fluids would have resulted in significant serpentinisation-induced isostatic uplift of the Cretaceous seafloor. This is incompatible with uplift trajectories of the Troodos Massif (Fig. 2.6). As a result, the extent of this initial serpentinisation event is likely minimal and localised to the upper regions of the Troodos lithospheric mantle. This is also in agreement with boron mass balance calculations that indicate a high W/R of ~10 is required to pervasively serpentinise the Troodos Mantle Sequence. In addition, other pervasive serpentinisation scenarios that are incompatible with uplift trajectories (Fig. 2.6) and serpentinisation-induced isostatic modelling (Evans et al., 2021) such as off-axis seafloor serpentinisation and the ~90° anticlockwise rotation of the Troodos microplate are also dismissed (Clube et al., 1985; Clube and Robertson, 1986).

It is a long-standing assertion that the occurrence of serpentinised mantle rocks at the highest elevations of Cyprus is related to the collision of the Eratosthenes Seamount with the Cyprus Arc subduction zone (Gass, 1977; Gass and Masson-Smith, 1963; Robertson, 1998a, 1998b; Robertson, 1977). This collision has been proposed to alter the dynamics of the Cyprus Arc subduction zone, resulting in the eventual stalling of subduction (~3 Ma) and sustained (~7 to ~3 Ma) focused upwelling of fluids derived from the dehydration of the subducting slab fluids into the overlying mantle wedge beneath the Mount Olympus region (Fig. 5.21ab; Morag et al., 2016; Robertson, 1998a, 1998b).

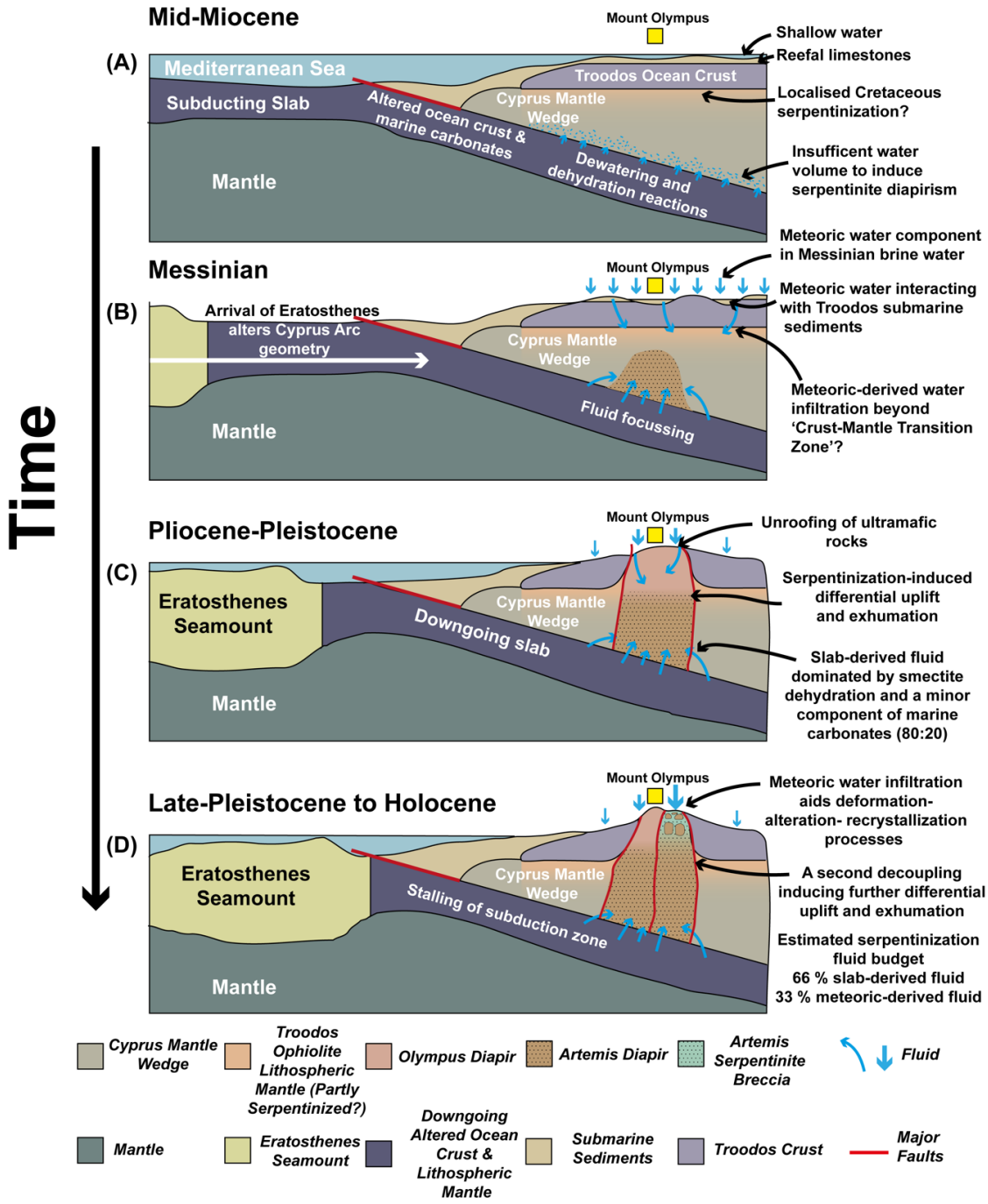

Figure 5.21: Schematic illustration of the Cyprus Arc at differing stages in its evolution from: (A) Mid-Miocene subduction, where dehydration reactions in the downgoing slab are insufficient to induce serpentinite diapirism; (B) the Messinian salinity crisis results in uplifted localised evaporite basins, where meteoric water interacts with overlying Troodos sediments and serpentinises the underlying mantle rocks; the approach of the Eratosthenes seamount induces fluid focussing of the dehydrating Cyprus slab underneath the Mount Olympus region; (C) Pliocene-Pleistocene, Eratosthenes seamount stalls the Cyprus Arc subduction zone, where prolonged fluid focussing has resulted in serpentinisation-induced differential uplift and exhumation forming the Olympus Diapir; (D) Late-Pleistocene to Holocene, meteoric water infiltration results in ongoing serpentine alteration mechanisms that manifest as coupled deformation-alteration-recrystallisation processes that result in the differential exhumation of the completely serpentinised Artemis Diapir.

Serpentinised mantle rocks of the Olympus and Artemis Diapirs yield $^{87}Sr/^{86}Sr$ ratios of 0.705-6 and $\delta^{11}B$ values of +7 to +18 ‰, and portions of the Olympus Diapir have $\delta^{18}O$ values of +3.4 to +8 ‰ and δD values of -52 to -65 ‰ (Fig. 5.2; Fig. 5.3; Fig. 5.9). These measured isotope values are consistent with pervasive serpentinisation of the Troodos Mantle Sequence by a slab-derived fluid, primarily generated by the dehydration of smectite from the downgoing altered ocean crust of the Cyprus slab mixed with a minor component of marine carbonates (80:20; Fig. 5.21b; Table 5.11). These slab-derived dehydration reactions are inferred to occur within the slab at 100-150°C, where the mobilised fluids serpentinise the overlying Cyprus mantle wedge at temperatures >150 to <300°C (Fig. 5.21b). The initial pervasive serpentinisation event is interpreted to have reduced the bulk density of the Troodos Mantle Sequence mantle peridotites from ~3,300 kg/m^3 to ~2,800 kg/m^3 (Fig. 5.3; Evans et al., 2021). This bulk density reduction is equivalent to ~66 % serpentinisation reaction extent and a H_2O content of ~9 wt.% preserved in a serpentinised body equivalent to the volume of a truncated cone with a thickness of 13 km, a top radius of 4 km, and bottom radius of 7.5 km (Table 5.15). Mass balance calculations indicate that to serpentinise the Troodos Mantle Sequence, to a reaction extent of 66%, fluid from a dehydrating downgoing slab, containing 3 wt.% H_2O, would need to be focussed beneath the Mount Olympus region by a factor of 11 (Fig. 5.21bcd; Table 5.15).

A third serpentinisation event is interpreted to occur through reactions with meteoric waters that interacted and partially exchanged with the circum-Troodos submarine sediments that before uplift overlaid the Troodos ophiolite. $^{87}Sr/^{86}Sr$ ratios of 0.7086 to 0.7089 and Sr/Ca (ng/g/µg/g) of 3 to 5 (Fig. 4.15) reflected in the initial progressive leaching step suggest that these meteoric fluids may have interacted with Messinian evaporites within the sedimentary sequence, although this is not required by oxygen and hydrogen stable isotope measurements (Magaritz and Taylor, 1974). This third serpentinisation event is interpreted to have reduced bulk densities further from ~2,800 kg/m^3 to <2,550 kg/m^3 in both the Artemis and Olympus Diapirs and resulted in more radiogenic $^{87}Sr/^{86}Sr$ whole rock values (Fig. 5.3).

As these pervasive serpentinisation events resulted in significant serpentinisation-induced uplift of the Troodos Massif, further incursion of meteoric water into the Troodos Mantle Sequence is inevitable (Fig. 5.21c). Continued alteration of serpentine occurred through progressive coupled deformation-alteration-recrystallisation processes manifested as a weak, incohesive, low density serpentinite breccias and gouge, mostly occurring in the Artemis Diapir (Fig. 5.21d; Evans et al., 2021) and hyperalkaline pH >11.5 waters emanating from the completely serpentinised Artemis Diapir (Evans et al., 2022; Chapter 4). Since the unroofing of ultramafic rocks during the Plio-Pleistocene (Fig. 2.6), our estimated flux of meteoric water into the Troodos Mantle Sequence is sufficient to have

mostly flushed the diluted Messinian brine component from the serpentinised mantle peridotites (Table 4.12, Chapter 4). Consequently, we propose that the ongoing alteration of serpentine within the Troodos Mantle Sequence is related to low temperature exchange with meteoric water and is a distinct fluid-rock interaction event.

The serpentinised mantle rocks of the differentially uplifted Troodos Massif yield evidence of at least four distinct serpentinisation-alteration events with potentially up to 66 % of the initial serpentinisation budget originating from the subducting dehydrating Cyprus slab (Fig. 5.21). Some of this initial serpentinisation budget may be attributed to Cretaceous hydrothermal fluids that induced limited serpentinisation of the Olympus Transition Zone harzburgites and dunites. The remaining third of the serpentinisation fluid budget is proposed to be from meteoric-derived waters, some of which have partially exchanged with the overlying Cyprus submarine sedimentary sequences.

Chapter 6 Serpentinzation-induced mantle rock alteration pathways: Insights from the evolving physical properties of the Troodos Mantle Sequence, Cyprus

Abstract

Altered mantle rocks yield a wide range in measured physical properties values. Some, but not all, of this observed range can be explained by serpentinisation hydration reactions alone, indicating that additional reactions are required to account for the full spectrum in the evolution of physical properties of altering mantle rocks. Field observations and a new physical and hydraulic properties dataset on samples from the Troodos Mantle Sequence, in combination with compiled existing global datasets of variably altered mantle rocks, provide new constraints on the evolution of mantle rock properties. Variable extents of serpentinisation hydration reactions and serpentine alteration manifest as two contrasting, but parallel, mantle rock alteration pathways, which reflect the full spectrum of reported physical properties. In the strongly to completely serpentinised Troodos Mantle Sequence, Cyprus, serpentinisation hydration reactions have reduced mantle rock bulk densities from 3,300 kg/m^3 to 2,565 kg/m^3 with negligible change in porosity. Completely serpentinised serpentinite breccia end members yield lower bulk densities of 1,568 kg/m^3 and display evidence of serpentine alteration through coupled deformation-alteration-recrystallisation processes. Similar low density serpentinite breccia assemblages in other sites of complete serpentinisation have measured porosities of up to ~52 %. The differing relative contributions of contrasting mantle rock alteration pathways to the evolution in bulk density and porosity indicates that quasi-isochemical serpentinisation hydration reactions conserve mass, but serpentine alteration induces differential rates of dissolution-precipitation, resulting in the significant removal of mass. The alteration of serpentine may affect global geochemical cycles as many exposures of serpentinite show evidence of serpentine alteration.

6.1 Introduction

Serpentinisation processes encompass a suite of chemical reactions and physical changes resulting from interactions between water and ultramafic rocks resulting in the hydration of primary minerals such as olivine and pyroxene to secondary serpentine. These serpentinisation reactions change dense (3,300 kg/m^3), mechanically strong, low permeability, anhydrous ultramafic rocks into weak, low density (<2,550 kg/m^3), hydrated (up to 13 wt.% water) serpentinites with affinities for fluid mobile elements such as B, Li, S, Cl, Sr. Although not exclusively involving mantle peridotites, these are the dominant subject of serpentinisation processes, and these reactions can lead to up to 40 % volume expansion (Macdonald and Fyfe, 1985), together with large decreases in ultrasonic P and S wave velocities (e.g., Birch, 1961; Christensen, 1966) and electrical resistivity (e.g., Stesky and Brace, 1973). As a consequent of these physicochemical changes, serpentinisation plays a critical role in plate tectonics (e.g., Guillot et al., 2015; Hirth and Guillot, 2013) with impacts on planetary geochemical budgets (e.g., water, carbon, sulphur, chlorine, lithium, boron; Alt et al., 2013; Barnes and Sharp, 2006; Früh-Green et al., 2004; Hacker, 2008; Kelemen and Manning, 2015), biogeochemical cycles (Früh-Green et al., 2004; Schrenk et al., 2013), and may occur on other planetary bodies (Ehlmann et al., 2009; Ehlmann and Mustard, 2010; Glein et al., 2015; Waite et al., 2017).

Serpentinisation of mantle rocks is inferred to occur in various geological settings such as: slow-spreading ocean crust; at bend faults, prior to entering the subduction channel (Ranero et al., 2003); along crustal-scale strike slip faults (e.g., San Andreas (Moore and Rymer, 2012, 2007)); within the mantle wedge from subducting slab-derived fluids (e.g., Mariana Forearc (Alt and Shanks, 2006; Fryer et al., 1985)); during and after obduction of ocean lithosphere onto continental margins (Magaritz and Taylor, 1976, 1974; Wenner and Taylor, 1974, 1973, 1971). However, direct physical properties measurements on serpentinised mantle peridotites are relatively scarce and when available, highlight a wide range in altered mantle rock physical properties parameters. This wide range in physical properties, such as the up to 50 % reduction in bulk densities in altered mantle rocks in the Mariana Forearc and Troodos Mantle Sequence (Courtier et al., 2004; Morrow et al., 2019; Evans et al., 2021), cannot be explained by serpentinisation hydration reactions alone. Consequently, additional processes are required to explain the total change in the physical properties of altered mantle rocks. An explanation that has been qualitatively inferred, is the continued alteration of serpentine through coupling of deformation-alteration-recrystallisation processes (Evans et al., 2021; O'Hanley, 1991). However, the role of serpentine alteration in the wider alteration of mantle rocks remains poorly constrained (e.g., Geilert et al., 2020; Klein et al., 2017; Snow and Dick, 1995).

Here, we investigate the evolving physical properties of mantle rocks resulting from not only serpentinisation hydration reactions but also the progressive and ongoing alteration and deformation of serpentine. We reconcile our new and previous physical properties determinations on discrete samples from the contrasting serpentinite diapirs of the Mantle Sequence within the Troodos ophiolite, Cyprus (Evans et al., 2021). We combine our results with global mantle rock physical properties data to further show that manifestations of altered mantle rocks display distinct physical properties that reflect discrete points along contrasting evolving mantle rock alteration pathways.

6.2 Geological setting

The Troodos Mantle Sequence provides a unique setting to investigate serpentinisation-induced physicochemical evolution of mantle rocks. The Troodos mountains expose ocean crust and upper mantle rocks, forming the Troodos Massif, one of the best-preserved, least deformed, and most complete ophiolite sequences (Gass, 1968). In the centre of the ~90-km-long and ~30-km-wide ophiolite an elliptical bullseye-patterned welt crops out, with the stratigraphically deepest rocks, mantle peridotites, forming the highest elevation point of Cyprus (Mount Olympus, 1,952 m; Fig. 6.1). In detail, the Troodos Mantle Sequence has long been sub-divided into two distinct domains (Wilson, 1959; Moores and Vine, 1971; Gass and Masson-Smith, 1963) interpreted as contrasting serpentinite diapirs. (Fig. 6.1; Evans et al., 2021). These nested serpentinite diapirs yield contrasting characteristics, resulting from contrasting serpentinisation styles and intensities (Evans et al., 2021).

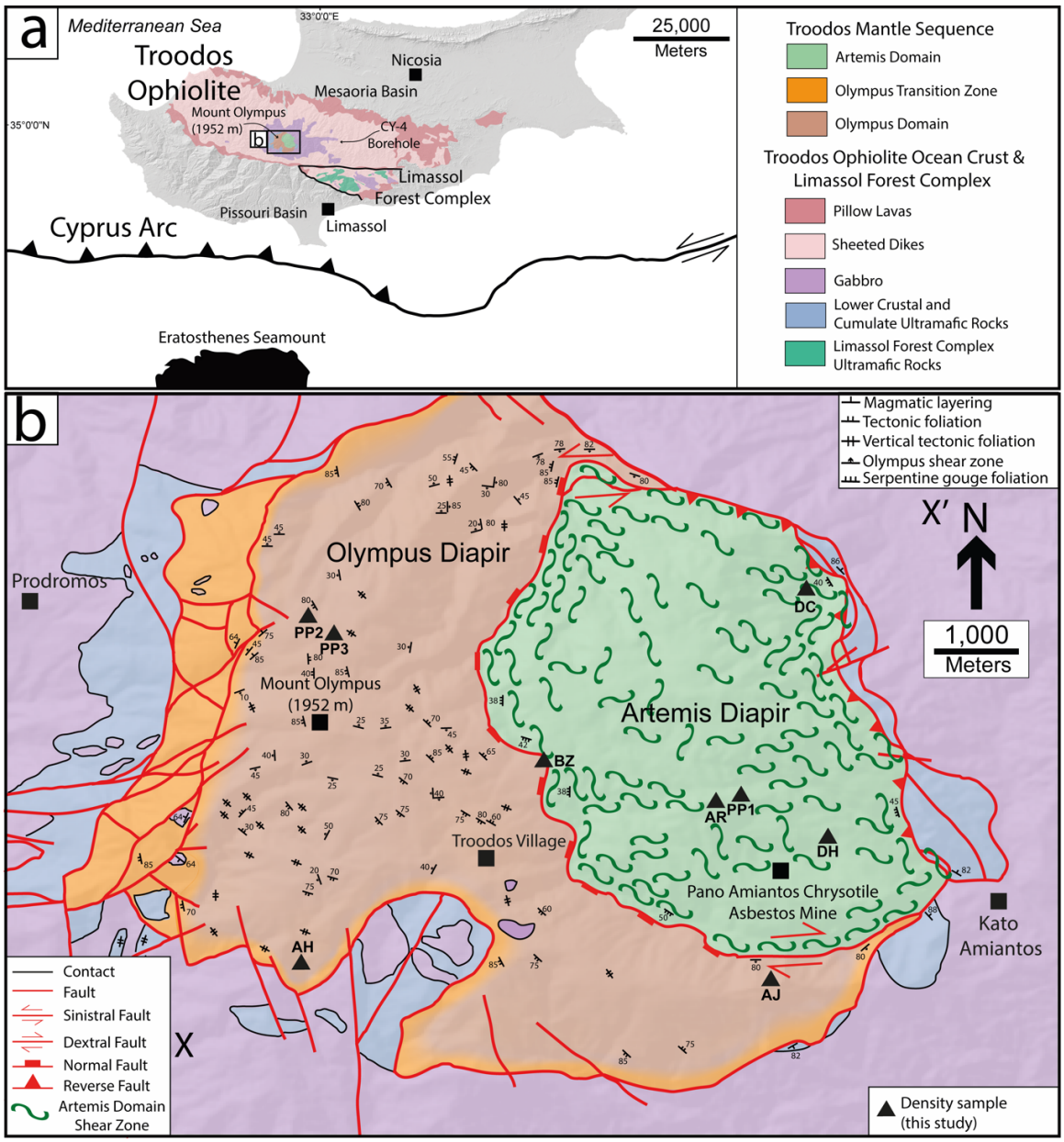

Figure 6.1: (A) Geological map of the Troodos ophiolite with the bullseye geometry of the Mantle Sequence highlighted along with the Limassol Forest Complex terrane, the Cyprus Arc, and northernmost portion of the Eratosthenes Seamount. (B) Geological map of the Troodos Mantle Sequence, adapted and updated from Wilson (1959). X-X' shows line of cross-section (Fig. 2.4). Bulk density sample locations shown.

The Olympus Diapir, is an arcuate region of partially serpentinised tectonised harzburgites with minor dunites (Wilson, 1959; Moores and Vine, 1971) and displays a distinctive, competent, blocky, and cohesive outcrop pattern (Fig. 6.2) that forms rounded, stable hillslopes (Wilson, 1959; Evans et al., 2021; Gass, 1977), interpreted to result from the partial (50 to 70 % replacement of primary phases) serpentinisation of mantle peridotites (Evans et al., 2021). Rocks located from the periphery of the Olympus Diapir are more strongly serpentinised (up to ~90 %; Fig. 6.2). Within the Olympus Diapir, samples with

higher serpentine contents yield lower bulk densities (Table 3.2), but also other indicators of fluid rock interactions such as lower Sr concentrations, higher $^{87}Sr/^{86}Sr$ values, and higher trace amounts of carbonate (Fig. 6.2). Serpentinisation-induced microfractures (e.g., Kelemen and Hirth, 2012) are common throughout the Olympus Diapir samples, with etch-pits forming around the periphery of olivine grains (Evans et al., 2021). In these pits, olivine has dissolved and serpentine precipitated, forming a serpentine-olivine-dominated mesh texture (Fig. 6.2) that encloses large 1 to 4 mm grains of orthopyroxene partially altered to bastite (Fig. 6.2). In the more strongly serpentinised samples, the serpentine-olivine-orthopyroxene dominated texture is commonly cross-cut by discrete (~3 mm wide), irregular, black (in XPL and hand specimen) serpentine veins (Fig. 6.2). These black serpentine veins are irregularly distributed throughout the Olympus Diapir and display a wide range of orientations that are not systematicaly related to a distinct vein network (Fig. 6.2).

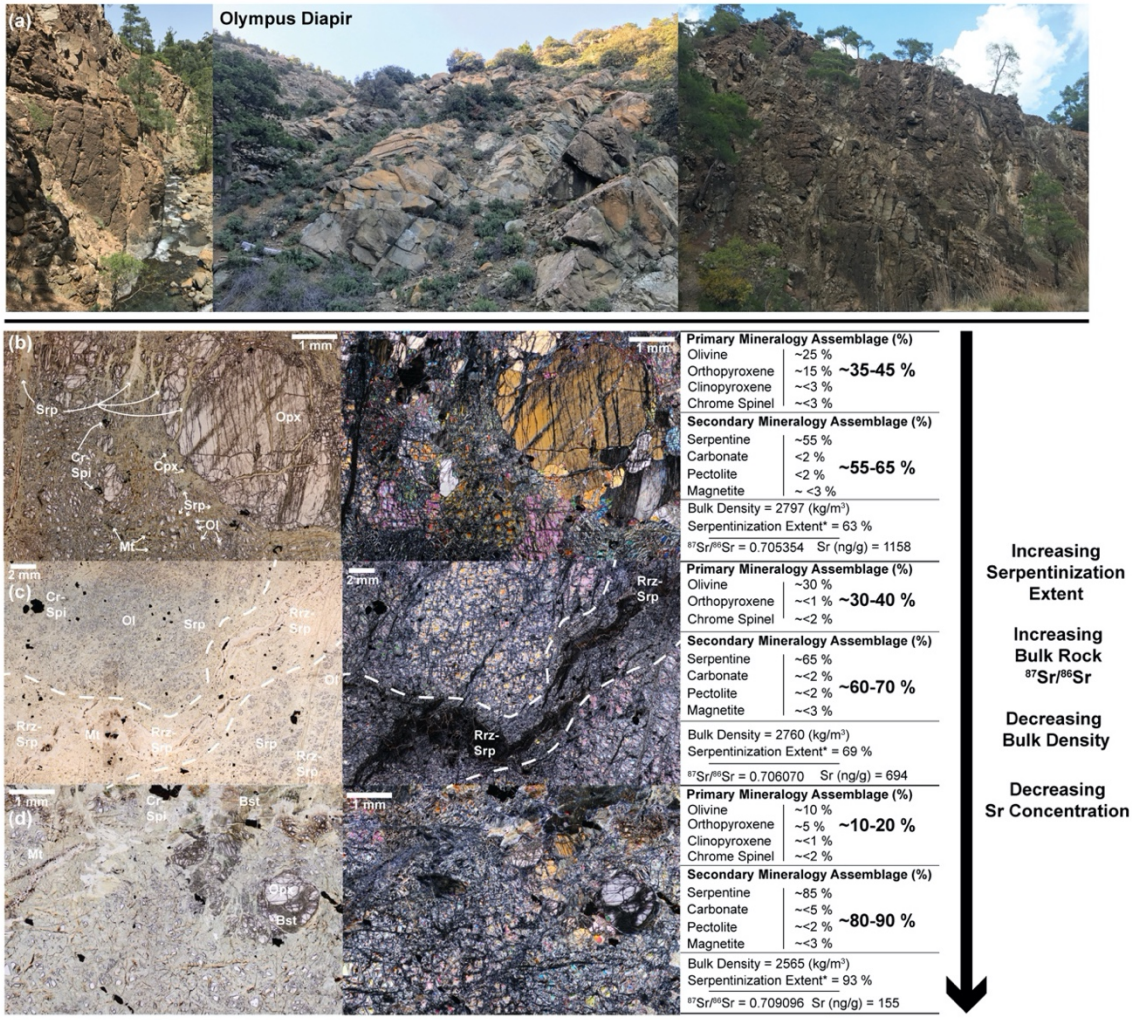

Figure 6.2: (A) Field pictures of the cohesive and competent outcrop pattern of the Olympus Diapir. (B) Photomicrograph in PPL and XPL of Olympus Diapir sample AH1. (C) Photomicrograph in PPL and XPL of Olympus Diapir sample AH2. (D) Photomicrograph in PPL and XPL of Olympus Diapir sample AJ2. (B-D) Show a general decrease in bulk density (kg/m^3), increasing serpentinisation extent, increase in whole-rock $^{87}Sr/^{86}Sr$ and decreasing Sr (ng/g) concentration. PPL and XPL photomicrographs show a general increase in recrystallised serpentine manifested as irregular black serpentine veins. Serpentinisation extent is calculated using the equation of Miller and Christensen (1997).

In contrast, the Artemis Diapir is a sub-circular, ~5 km-wide region of completely serpentinised peridotite blocks and clasts (>100 m to dm; approximately 50:50 clasts to matrix) in a friable, low bulk density, serpentinite breccia matrix of highly comminuted serpentine cataclasite and serpentine clay gouge (Fig. 6.3; Wilson, 1959; Gass and Masson-Smith, 1963; Moores and Vine, 1971; Evans et al., 2021). Coherent completely serpentinised blocks and clasts are heavily fractured (Fig. 6.3) with mutually cross-cutting, orthogonal, concentric, and oblique fibrous asbestiform chrysotile and crack-seal serpentine vein sets occurring within more competent clasts (Evans et al., 2021). The Artemis Diapir competent blocks and clasts are dominated by serpentine (>90 %) with minor andradite

(<5 %) and carbonate (<3 %) (Fig. 6.3). All primary minerals are replaced except for chrome-spinel. In some parts of the Artemis Diapir, serpentinite breccia assemblages surround and anastomose around completely serpentinised competent blocks and clasts (Fig. 6.3; Evans et al., 2021). At the clast-gouge interfaces, the ratios of competent clast to incompetent gouge are heterogenous and highly variable, resulting in a distributed transition from competent to incompetent serpentinite material (Fig 6.3). In some zones, around the periphery of the Artemis Diapir, the proportion of incompetent breccias-gouge to competent blocks-clasts is dominated by the serpentinite breccia-gouge assemblage, resulting in an easily erodible low-density serpentinite breccia end-member (e.g., Evans et al., 2021). The formation of this end member is attributed to progressive coupled deformation-alteration-recrystallisation serpentinisation, where continued interactions of these processes yield regions dominated by the serpentinite breccia-gouge assemblage. This produces weak, unstable, incohesive outcrops and hillslopes (Fig. 6.3) and deeply incised-valleys that are characteristic of the Artemis Diapir (Evans et al., 2021).

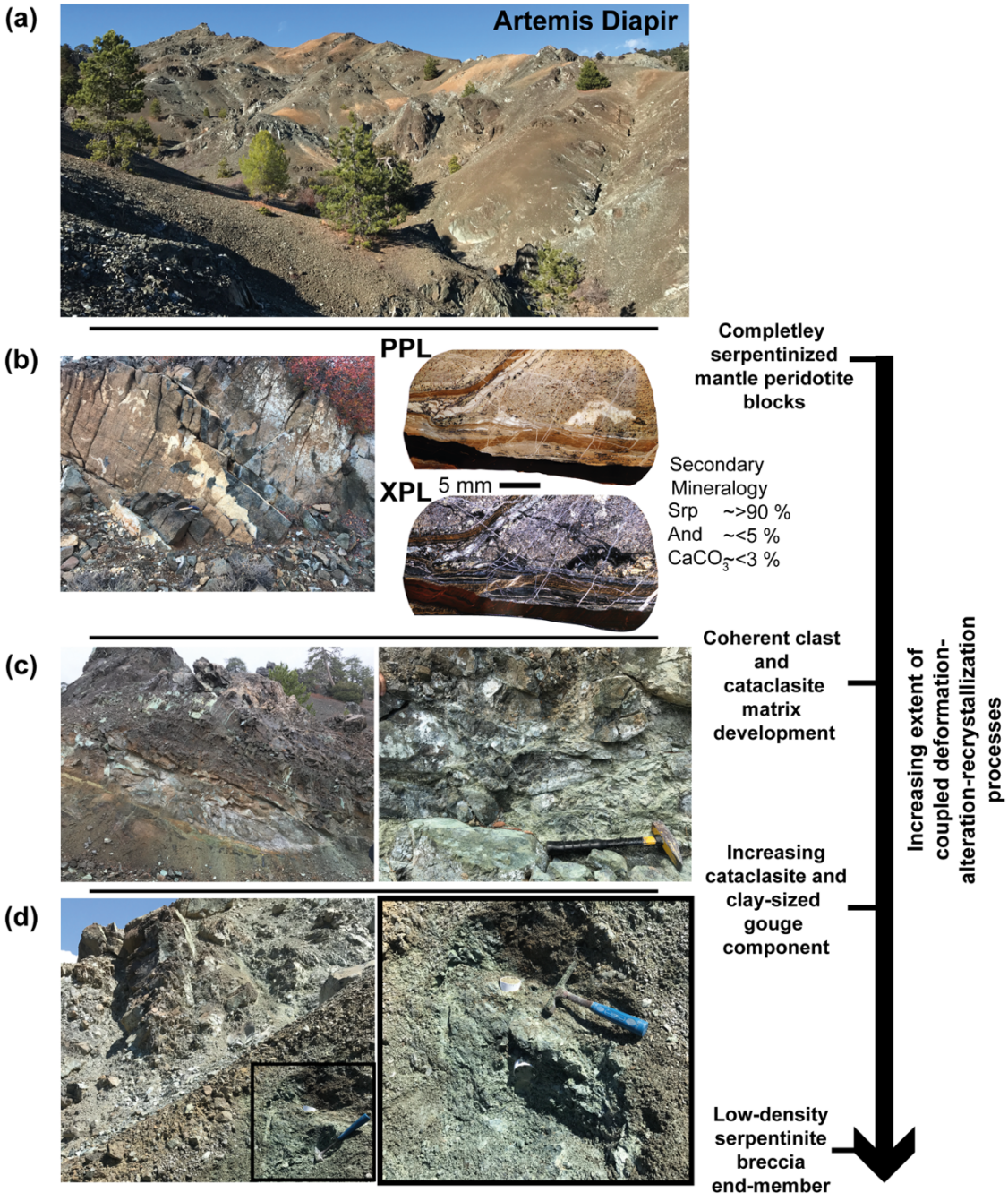

Figure 6.3: (A) Field picture of the Artemis Diapir highlighting the incompetent and incohesive outcrop pattern composed of variable proportions of a completely serpentinised blocks-clasts-breccia-gouge assemblage (Evans et al., 2021). (B) Field picture of a more competent and cohesive completely serpentinised block within the Artemis Diapir with corresponding XPL and PPL photomicrographs. Hammer for scale. (C) Field pictures of coherent completely serpentinised clasts with a progressive cataclasite matrix. Hammer for scale. (D) Field pictures showing the Artemis Diapir periphery serpentinite breccia with a greater extent of cataclasite and an increased component of clay-sized gouge. Hammer for scale. (B-D) Shows a general increase in the extent of serpentine alteration through coupling of deformation-alteration-recrystallisation processes, culminating in the evolution from more competent blocks to a low-density serpentinite breccia endmember (e.g., Evans et al., 2021).

6.3 Methods

6.3.1 Sample Preparation

For this study, we used nine cores extracted from six ~25 kg samples collected from the Troodos Massif. 5 cm diameter cores were drilled from these samples, and the core ends cut and ground flat to provide ~2 cm-length core plugs. The Artemis serpentinite breccias were unable to be cored due to their friable nature, but its bulk density could be determined from the weight of a precisely measured volume of extracted material. The 2-cm core plugs were oven dried at 70 °C and the density obtained by the mass-to-volume ratio. Porosity was measured by He-pycnometer. In order to saturate the samples (following Amalokwu, 2016) the dry core plugs were stored inside a pressure vessel under vacuum for 2 days and then the vessel filled with a degassed 35 g/L NaCl brine solution (electrical resistivity ~0.19 Ω m). Finally, the pore pressure was gradually increased up to 5 MPa and held constant for a period of 16 days.

6.3.2 Experimental setup

For a full description of the experimental setup, we refer to Falcon-Suarez et al. (2016) and (Falcon-Suarez et al., 2017). Here, we briefly outline the methods used to measure ultrasonic P- and S-wave velocities (V_p and V_s) and attenuations (inverse quality factors $1/Q_p$ and $1/Q_s$), electrical resistivity (Ω m), and permeability (m^2). Physical and hydraulic properties were determined using the high-pressure, room-temperature multifluid experimental rig (Fig. 6.4) in the Rock Physics Laboratory at the National Oceanography Centre (NOC RPL), Southampton (e.g., Falcon-Suarez et al., 2016). This rig is assembled around a modified Hoek-type triaxial cell core holder. The cell is designed to host and pressurise 5 cm diameter rock samples up to 65 MPa (both axially, σ_1 and radially σ_3, independently). The setup allows the simultaneous measurement of hydromechanical and geophysical properties on samples up to 2.5 cm in length. The ultrasonic wave velocities were determined using the pulse echo method with an accuracy of ± 0.3 % (95 % confidence), precision of ± 0.1 % (95 % confidence), and an attenuation of ± 5 % (95 % confidence) (Best et al., 2007; McCann and Sothcott, 1992).

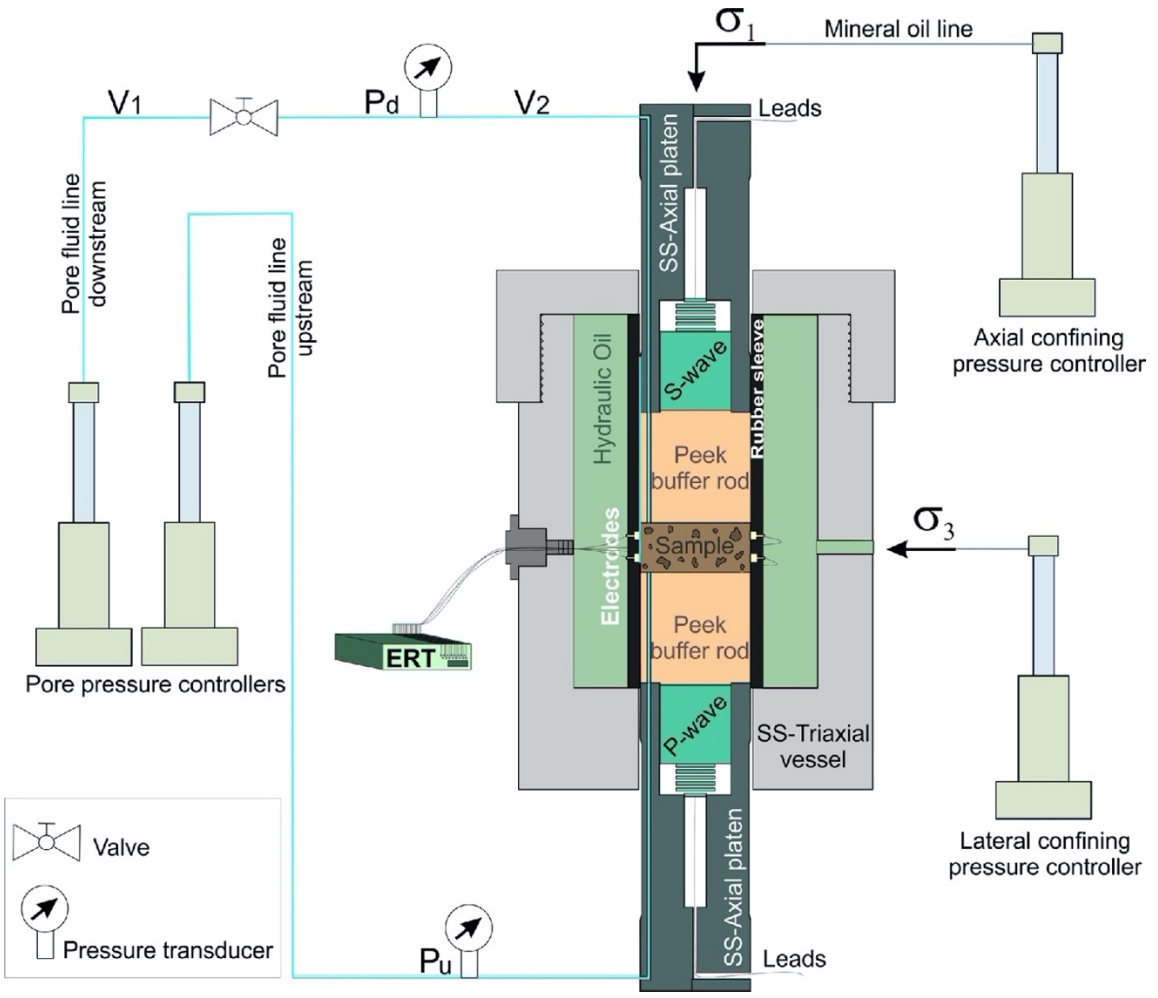

Figure 6.4: Schematic diagram of the experimental rig with ultrasonic pulse-echo (P- & S-wave) and electrical resistivity tomography systems with pore fluid and confining pressure control systems. Figure is from Falcon-Suarez et al. (2017).

Electrical resistivity was determined using 16 electrodes that form an array, which is connected to an electrical resistivity data acquisition system (e.g., Falcon-Suarez et al., 2017). The typical resistivity measurement ranges from <1 % error for samples with homogenous resistivity and up to 5 % error when heterogenous, these errors apply for resistivity at frequencies 1 to 500 Hz and in the range of 1-100 Ω m (Falcon-Suarez et al., 2016; North et al., 2013).

Permeability was determined using the pore pressure transmission method (Falcon-Suarez et al., 2017; Metwally and Sondergeld, 2011) and is based on the pulse decay method (Brace et al., 1968). Experiments were conducted at 19 ± 0.2°C. The lowest permeability to be accurately measured using this PPT method and on the NOCS RPL rig is $5x10^{-23}$ m^2, with an experimental error less than 10 %. The 1σ-error of each permeability measurement was determined (Table 6.1), with a mean error of $4.88x10^{-21}$ ± $2.10x10^{-20}$ m^2 (1σ, n=46). Permeability was not determined in Troodos gabbro samples.

Table 6.1: Table of experimental results on samples from the Troodos Massif. V_p, V_s, Q_p^{-1}, Q_s^{-1}, electrical resistivity, permeability, and the permeability error are shown at differing differential pressures. $P_{Diff} = P_c - P_F$; P_F = 5 MPa.

Sample Number	Sample Type	P_C (MPa)	P_{Diff} (MPa)	V_p (km/s)	Q_p^{-1}	V_s (km/s)	Q_s^{-1}	Resistivity (Ω m)	Permeability (m^2)	Permeability error (1σ)
25-PP1	Artemis	5.5	0.5	4.53	0.08	1.93	0.16	8.10	1.78E-19	4.40E-20
		10	5	4.59	0.05	2.37	0.07	12.43	5.92E-19	1.37E-19
		20	15	4.64	0.04	2.42	0.05	13.48	8.25E-20	3.851E-21
		30	25	4.66	0.04	2.42	0.05	14.16	9.8E-21	1.04E-21
		40	35	4.68	0.04	2.44	0.04	14.96	2.90E-21	1.51E-22
		50	45	4.68	0.04	2.44	0.04	15.54	2.43E-22	2.09E-23
		20	15	4.65	0.04	2.42	0.05	15.12	5.60E-21	1.02E-22
		5.5	0.5	4.53	0.07	2.33	0.13	12.26	1.36E-19	1.97E-20
15-PP2	Olympus Dunite	5.5	0.5	5.70	0.01	3.88	0.19	40.17	bd	bd
		10	5	5.70	0.00	3.11	0.07	519.17	3.49E-20	5.43E-22
		20	15	5.73	0.00	3.09	0.06	1033.96	8.07E-21	9.49E-23
		30	25	5.74	0.00	3.09	0.06	1440.42	1.98E-21	7.78E-23

Sample Number	Sample Type	P_C (MPa)	P_{Diff} (MPa)	V_p (km/s)	Q_p^{-1}	V_s (km/s)	Q_s^{-1}	Resistivity (Ω m)	Permeability (m^2)	Permeability error (1σ)
		40	35	5.74	0.00	3.08	0.06	1676.25	6.42E-22	1.68E-22
		50	45	5.75	0.00	3.10	0.06	1654.58	1.83E-22	1.45E-22
		20	15	5.76	-0.01	3.09	0.07	1099.17	7.74E-23	2.08E-23
		5.5	0.5	5.72	0.00	2.68	0.12	303.23	9.19E-21	3.79E-22
18-PP3	Olympus Harzburgite	5.5	0.5	5.58	0.08	2.88	0.10	82.13	7.52E-22	9.83E-23
		10	5	5.56	0.01	2.87	0.05	497.29	bd	bd
		20	15	5.58	0.01	2.87	0.05	1033.96	5.61E-22	3.68E-23
		30	25	5.59	0.01	2.88	0.06	1068.12	5.00E-23	bd
		40	35	5.59	0.02	2.88	0.06	1892.92	5.00E-23	bd
		50	45	5.59	0.02	2.87	0.06	1952.50	5.00E-23	bd
		20	15	5.58	0.01	2.87	0.05	1265.83	5.00E-23	bd
		5.5	0.5	5.56	0.02	2.57	0.14	247.92	5.00E-23	bd
21-PP5	Gabbro	5.5	0.5	6.74	0.02	3.55	0.21	40.90	5.00E-23	bd
		10	5	6.74	0.01	3.78	0.06	105.00	5.00E-23	bd

Sample Number	Sample Type	P_C (MPa)	P_{Diff} (MPa)	V_p (km/s)	Q_p^{-1}	V_s (km/s)	Q_s^{-1}	Resistivity (Ω m)	Permeability (m^2)	Permeability error (1σ)
		20	15	6.79	0.00	3.82	0.03	150.73	5.00E-23	bd
		30	25	6.82	0.00	3.83	0.03	178.75	5.00E-23	bd
		40	35	6.84	0.00	3.84	0.03	215.94	5.00E-23	bd
		50	45	6.87	0.00	3.86	0.03	247.42	5.00E-23	bd
		20	15	6.82	0.00	3.83	0.03	190.83	5.00E-23	bd
		5.5	0.5	6.72	0.01	3.70	0.17	77.70	5.00E-23	bd
16-PP3	Olympus Harzburgite	5.5	0.5	5.94	0.00	3.50	0.18	56.19	3.56E-21	2.46E-23
		10	5	5.95	0.00	3.13	0.08	266.55	4.41E-20	1.40E-21
		20	15	5.97	0.00	3.12	0.06	447.50	1.73E-20	1.43E-22
		30	25	5.97	0.00	3.11	0.06	445.00	8.65E-21	1.76E-22
		40	35	5.98	0.00	3.12	0.05	530.00	2.92E-21	1.33E-23
		50	45	5.99	0.00	3.12	0.06	590.00	1.11E-21	6.60E-24
		20	15	5.97	0.00	3.11	0.06	343.01	1.20E-21	8.81E-23
		5.5	0.5	5.92	0.00	2.73	0.14	66.39	4.00E-21	1.42E-22

Sample Number	Sample Type	P_C (MPa)	P_{Diff} (MPa)	V_p (km/s)	Q_p^{-1}	V_s (km/s)	Q_s^{-1}	Resistivity (Ω m)	Permeability (m^2)	Permeability error (1σ)
6-PP4	Wehrlite	5.5	0.5	6.79	0.08	3.43	0.19	46.21	bd	bd
		10	5	6.77	0.01	3.63	0.16	206.67	1.13E-21	2.87E-24
		20	15	6.79	0.01	3.67	0.11	353.23	2.04E-21	9.25E-23
		30	25	6.80	0.01	3.65	0.10	362.27	2.71E-21	4.52E-22
		40	35	6.80	0.01	3.64	0.09	314.15	7.41E-22	1.83E-22
		50	45	6.77	0.01	3.62	0.10	412.79	5.00E-23	bd
		20	15	6.80	0.01	3.65	0.10	284.38	1.93E-22	1.20E-23
		5.5	0.5	6.83	0.03	3.46	0.21	112.81	bd	bd
5-PP5	Gabbro	5.5	0.5	6.65	0.00	3.58	0.19	35.52	5.00E-23	bd
		10	5	6.66	0.00	3.71	0.11	119.84	5.00E-23	bd
		20	15	6.68	0.00	3.71	0.04	186.65	5.00E-23	bd
		30	25	6.70	0.00	3.72	0.03	220.94	5.00E-23	bd
		40	35	6.72	0.00	3.73	0.03	250.73	5.00E-23	bd
		50	45	6.74	-0.01	3.74	0.02	274.17	5.00E-23	bd

Sample Number	Sample Type	P_C (MPa)	P_{Diff} (MPa)	V_p (km/s)	Q_p^{-1}	V_s (km/s)	Q_s^{-1}	Resistivity (Ω m)	Permeability (m^2)	Permeability error (1σ)
		20	15	6.71	0.00	3.73	0.04	201.25	5.00E-23	bd
		5.5	0.5	6.65	0.00	3.90	0.16	60.76	5.00E-23	bd
23-PP1	Artemis	5.5	0.5	4.46	0.02	1.87	0.10	9.19	7.66E-21	5.32E-22
		10	5	4.50	0.02	2.30	0.04	11.47	3.75E-20	3.69E-21
		20	15	4.53	0.01	2.32	0.02	12.15	1.05E-20	2.99E-21
		30	25	4.54	0.01	2.32	0.02	12.72	3.67E-21	9.31E-22
		40	35	4.56	0.01	2.32	0.02	13.19	5.54E-21	1.28E-22
		50	45	4.57	0.01	2.32	0.02	13.58	1.62E-21	6.37E-23
		20	15	4.53	0.01	2.32	0.02	12.72	2.10E-21	3.54E-23
		5.5	0.5	4.46	0.02	2.29	0.10	10.56	1.97E-21	2.52E-23
AR3	Artemis	5.5	0.5	4.39	0.03	1.98	0.10	4.94	1.43E-20	1.02E-21
		10	5	4.37	0.02	2.22	0.06	7.93	3.95E-20	4.44E-21
		20	15	4.37	0.02	2.20	0.05	8.52	3.16E-21	2.01E-22
		30	25	4.39	0.03	2.21	0.04	8.69	2.49E-21	1.83E-22

Sample Number	Sample Type	P_C (MPa)	P_{Diff} (MPa)	V_p (km/s)	Q_p^{-1}	V_s (km/s)	Q_s^{-1}	Resistivity (Ω m)	Permeability (m^2)	Permeability error (1σ)
		40	35	4.40	0.02	2.21	0.04	8.89	6.62E-22	3.89E-23
		50	45	4.41	0.02	2.21	0.04	9.03	1.03E-21	9.11E-22
		20	15	4.38	0.02	2.21	0.04	8.70	7.74E-22	7.20E-23
		5.5	0.5	4.38	0.02	2.00	0.09	6.01	7.24E-21	2.03E-22

6.3.3 Experimental Procedure

The 9 samples used in this study were collected from Troodos Mantle Sequence outcrops. Our surface collected samples are not fully representative of the geological bodies at depth due to (i) the generation of stress-release-induced microcracks during the geological uplift, and (ii) rock weathering effects. To understand the evolution of the elastic (V_p, V_s, $1/Q_p$ and $1/Q_s$), electrical (resistivity) and hydraulic (permeability) properties of our rock samples with depth, we configured a loading/unloading stress path covering confining pressures (in a hydrostatic mode, i.e., $P_c = \sigma_1 = \sigma_3$) from 5.5 to 50 MPa, with a constant pore pressure (P_p) of 5 MPa. The stress path included six differential pressure ($P_{diff} = P_c - P_p$) loading-steps at 0.5, 5, 15, 25, 35 and 45 MPa, and two unloading-steps at 20 and 5 MPa.

For each P_{diff} stage, we used a gentle loading/unloading stress rate of ~0.01 MPa/s and waited for one hour for the sample to reach stress-strain equilibrium before each measurement. The ultrasonic and electrical measurements were collected immediately after permeability measurements to yield comparable results between the hydraulic and geophysical properties.

6.4 Results

Bulk densities of competent samples from the Olympus Diapir show a range of bulk densities with a mean measurement of 2686 ± 83 kg/m^3 (1σ, n=8, range 2565 to 2797 kg/m^3; Table 3.1, Fig. 6.5). In contrast, the serpentinised clasts from the Artemis Diapir have mean bulk densities of 2330 ± 63 kg/m^3 (1σ, n=5, range 2268 to 2408 kg/m^3). The Artemis Diapir serpentinite breccias yield very low densities of 1,568 ± 71 kg/m^3 (1σ, n=6, range 1505 to 1691 kg/m^3). Measured porosity (%) of the Olympus Diapir samples ranged from 0.1 to 1.1 %. In contrast, porosities of the Artemis Diapir samples ranged between 7.4 and 8.3 %. Troodos gabbros yield porosities of <0.18 %.

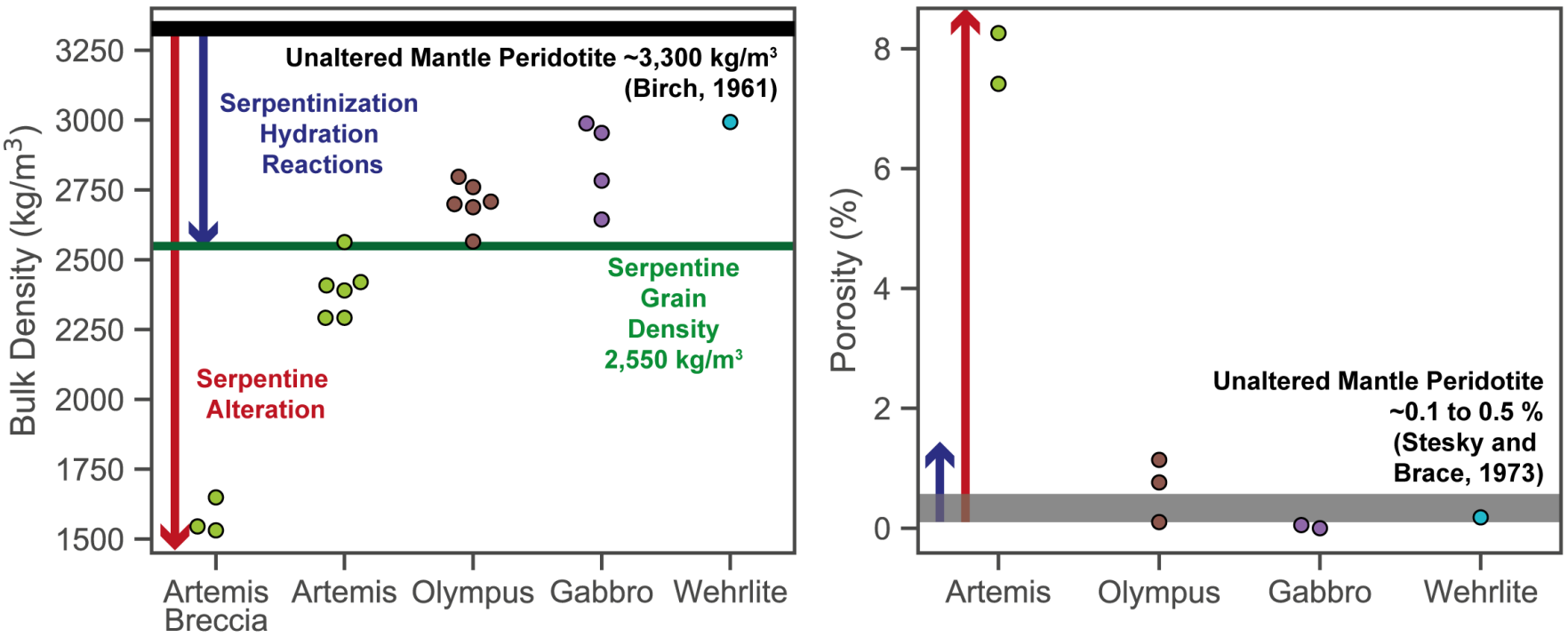

Figure 6.5: Caltech plots showing physical properties Bulk Density (kg/m^3) and Porosity (%). The expected contribution of serpentinisation hydration reactions (blue arrow) and serpentine alteration processes (red arrow) to the overall change in physical properties values is also shown.

Ultrasonic (P and S) wave velocities (V_p and V_s) and their attenuations vary between sample types (Fig. 6.6). P-wave and S-wave velocities decrease with serpentinisation extent (Fig. 6.6). At P_{Diff} ranging from 0.5 to 45 MPa, samples from the partially serpentinised Olympus Diapir yield measured V_p values of 5.76 ± 0.16 km/s (1σ, n=24; Fig. 6.7). In contrast, the completely serpentinised Artemis Diapir samples yields lower measured V_p values of 4.51 ± 0.11 km/s (1σ, n=24; Fig. 6.7) and Troodos Ocean Crustal rocks have measured V_p values of 6.76 ± 0.06 (1σ, n=24; Fig. 6.7). The compiled measured V_s of the Olympus Diapir is 3.03 ± 0.26 km/s (1σ, n=24) and the Artemis Diapir is 2.25 ± 0.16 km/s (1σ, n=24), and the Troodos Ocean crustal rocks is 3.70 ± 0.12 km/s (1σ, n=24) (Fig. 6.6). Although V_p and V_s do not vary greatly with differing applied pressures (Fig. 6.7), V_s varies greatly between P_{Diff} 0.5 and 5 MPa, with the V_s of measured Olympus Diapir samples decreasing by ~0.5 km/s, and V_s of the Artemis Diapir increasing by ~0.5 km/s, as P_{Diff} increased from 0.5 to 5 MPa. In comparison to the altered mantle peridotites, the V_s of Troodos Ocean crustal rocks increases by ~0.25 km/s from P_{Diff} of 0.5 to 5 MPa. In addition, V_p hysteresis effects are negligible, but V_s yields significant hysteresis during unloading from P_{Diff} of 5 to 0.5 MPa (Fig. 6.7) with the effects stronger in samples from the Olympus Diapir.

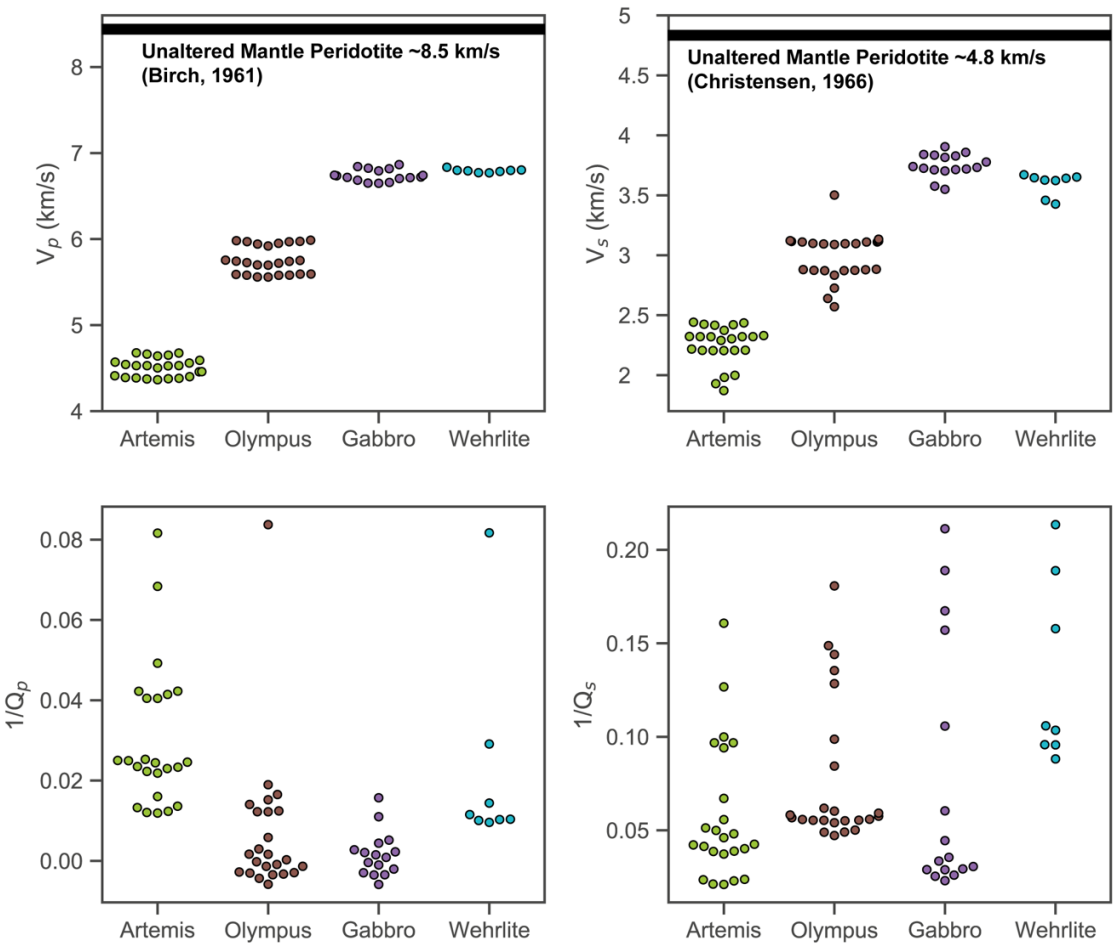

Figure 6.6: Caltech plots showing physical properties V_p (km/s), V_s (km/s) and their attenuations (inverse quality factors, Q_p^{-1} and Q_s^{-1}). The expected values of unaltered mantle peridotites are also shown.

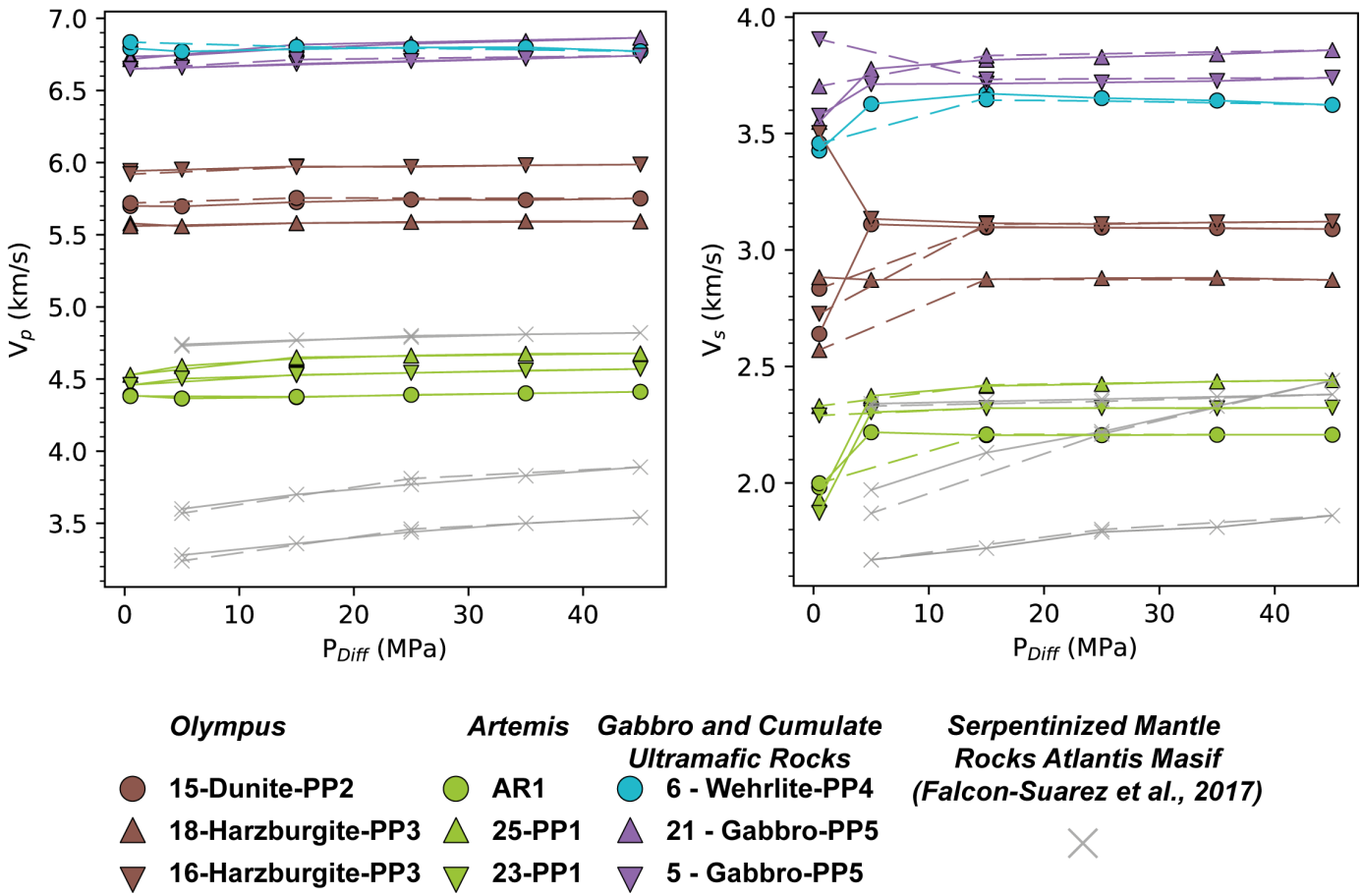

Figure 6.7: Plots of V_p and V_s variation with differential stress (P_{Diff}). Solid lines reflect loading stress and dashed lines reflect unloading stress conditions.

Although electrical resistivity is a stress dependent parameter in all measured samples, the magnitude of change between the Olympus and Artemis differs (Fig. 6.8; Fig. 6.9). Partially serpentinised samples of the Olympus Diapir yield up to an order of magnitude increase in electrical resistivity (e.g., sample PP3-16; 56 to 590 Ω m) with increasing P_{diff}. The highest measured electrical resistivity value of the Olympus Diapir is 1953 Ω m (P_{diff} = 45 MPa; Fig. 6.8). In contrast, clast samples from the Artemis Diapir yield extremely low electrical resistivity values (5 to 16 Ω m; Fig. 6.9) relative to the Olympus Diapir, with values at highest P_{diff} 45 MPa broadly double the initial measurement at P_{diff} 0.5 MPa. Troodos ocean crustal samples yield lower maximum electrical resistivity values relative to the Olympus Diapir (413 and 1953 Ω m respectively) but crustal samples also yield similar, up to an order of magnitude, increases in electrical resistivity (40 to 413 Ω m) with increasing P_{diff} (Fig. 6.8). All samples carry hysteresis during the unloading stress path by varying extents (Fig. Fig. 6.8). Electrical resistivity of samples from the Olympus Diapir, Artemis Diapir, and Troodos ocean crustal rocks generally increases during the unloading stress path (Fig. 6.8). The difference in the measured resistivity values from initial loading and final unloading of the Olympus Diapir is up to 18 % at P_{diff} 15 MPa and up to 67 % at P_{diff} 0.5 MPa. Whereas, in the Artemis Diapir, differences are up to 11 % at P_{diff} 15 MPa and up to 34 % at P_{diff} 0.5 MPa. Troodos ocean crustal rocks yield differences of up to 7 % at P_{diff} 15 MPa and up to 59 % at P_{diff} 0.5 MPa.

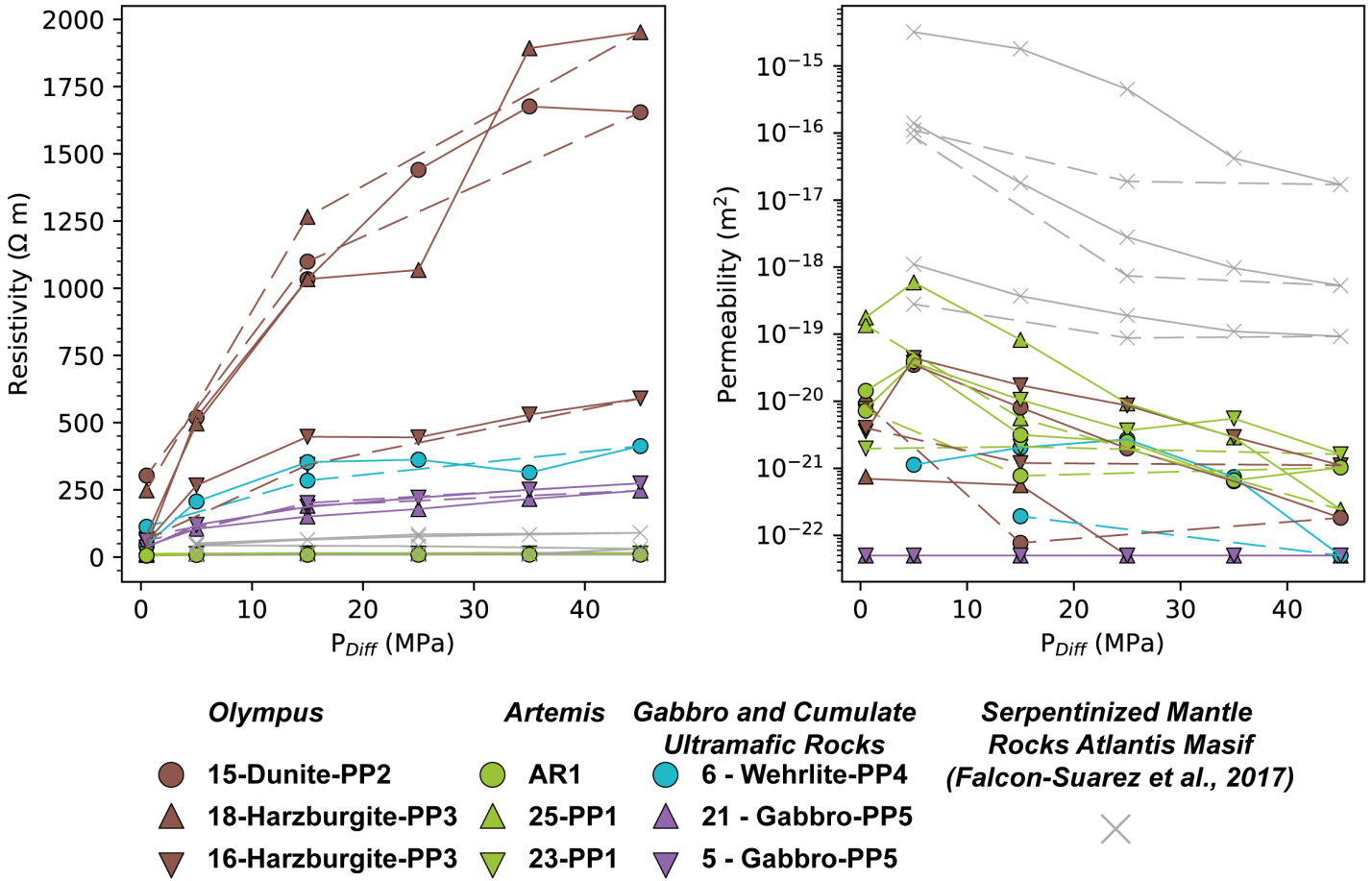

Figure 6.8: Plots of Resistivity and Permeability variation with differential stress (P_{Diff}). Solid lines reflect loading stress and dashed lines reflect unloading stress conditions.

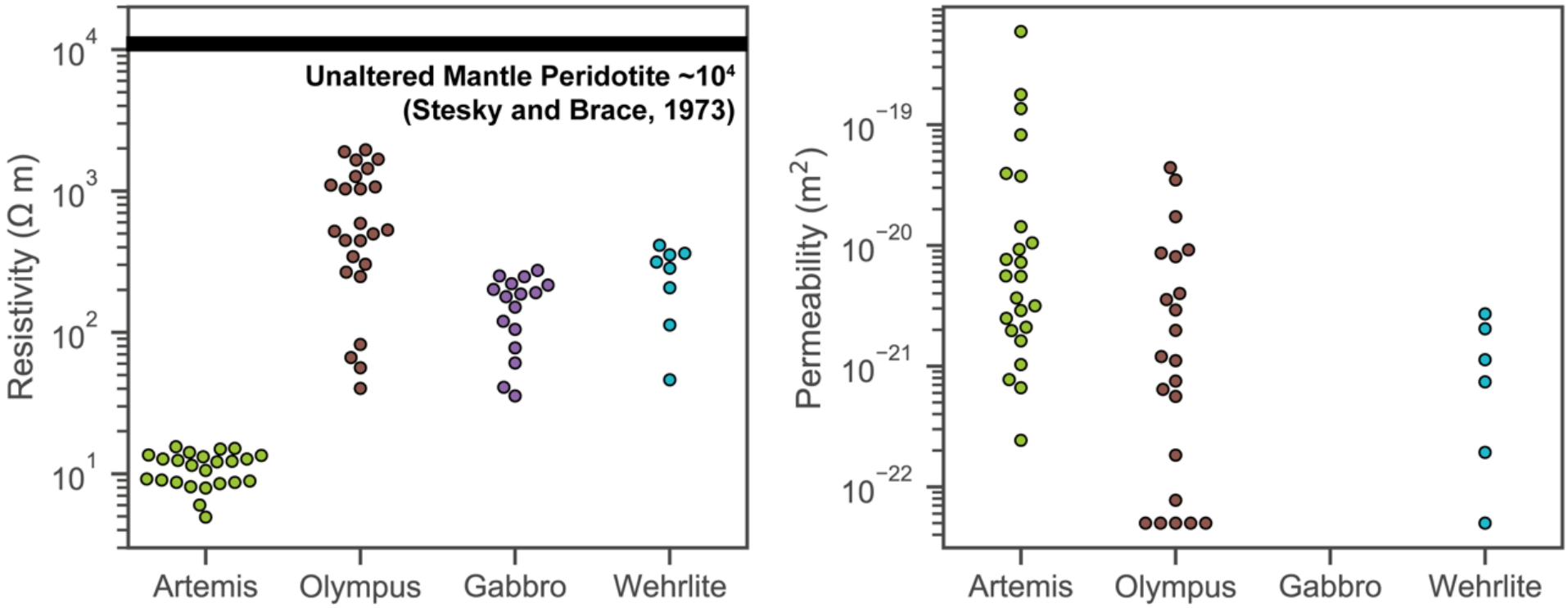

Figure 6.9: Caltech plots of physical properties parameters resistivity (Ω m) and permeability (m^2).

Experimentally derived permeability determinations vary significantly with applied stress (Fig. 6.8; Fig. 6.9). During initial loading from P_{diff} of 0.5 to 5 MPa, permeability values from both the Olympus and Artemis Diapirs increases by up to an order of magnitude (Fig. 6.8), yielding the highest measured permeabilities of $6x10^{-19}$ m^2 for the Artemis Diapir and $4.4x10^{-20}$ m^2 for the Olympus Diapir at P_{diff} 5 MPa. As loading stress is increased progressively, permeability decreases by up to three orders of magnitude in samples from the Artemis Diapir ($2.5x10^{-22}$ m^2 at P_{Diff} 45 MPa; Fig. 6.8) and by up to two orders of magnitude in samples from the Olympus Diapir ($1.8x10^{-22}$ m^2 at P_{Diff} 45 MPa; Fig. 6.8). During stress unloading, permeability increases (Fig. 6.8), but most samples carry hysteresis, resulting in unloading permeability determinations yielding lower values relative to the initial loading permeability determinations (Fig. 6.8).

6.5 Discussion

6.5.1 Comparison with other recovered serpentinised and altered mantle peridotite settings

New measurements of the physical and hydraulic properties of Troodos Massif rocks show stress and compositional dependencies (Fig. 6.10), in agreement with previous data from variably serpentinised rocks (e.g., Bayrakci et al., 2018; Birch, 1960, 1961; Carlson and Miller, 1997; Christensen, 1972; Falcon-Suarez et al., 2017; Miller and Christensen, 1997). Despite the significance of serpentinisation on the Earth system, measured physical and hydraulic properties datasets of serpentinised mantle rocks are relatively scarce. A compilation of some physical properties datasets, across a range of serpentinisation settings, shows parameters bulk density (Fig. 6.11), V_p (Fig. 6.12), V_s (Fig. 6.13), and electrical resistivity (Fig. 6.14) decrease with increasing serpentinisation extent, and porosity (Fig. 6.15) and permeability (Fig. 6.16) increase with increasing serpentinisation extent (Table 6.2). Samples recovered from varying serpentinisation settings such as: the slow spreading Mid-Atlantic Ridge (Bayrakci et al., 2018; Falcon-Suarez et al., 2017; Miller and Christensen, 1997); exhumed fast spreading crust and mantle of Hess Deep (Iturrino et al., 1996); ophiolites such as the Samail ophiolite, Oman (Hatakeyama et al., 2021; Katayama et al., 2020) and the Troodos ophiolite, Cyprus (Evans et al., 2021; Smith et al., 1989); crustal-scale strike-slip faults such as the San Andreas Fault (Morrow et al., 2014; Watt et al., 2014); opposing Iberian and Newfoundland rifted margins (Shipboard Science Party, 2004; Boillot et al., 1987; Goldberg and Zinszner, 1988); and the Mariana forearc

(e.g., Courtier et al., 2004; Morrow et al., 2019) yield a wide range in measured physical properties values (Table 6.2). This wide range in reported values cannot be explained by serpentinisation hydration reactions alone and additional reactions are required to explain the wide range in physical properties values.

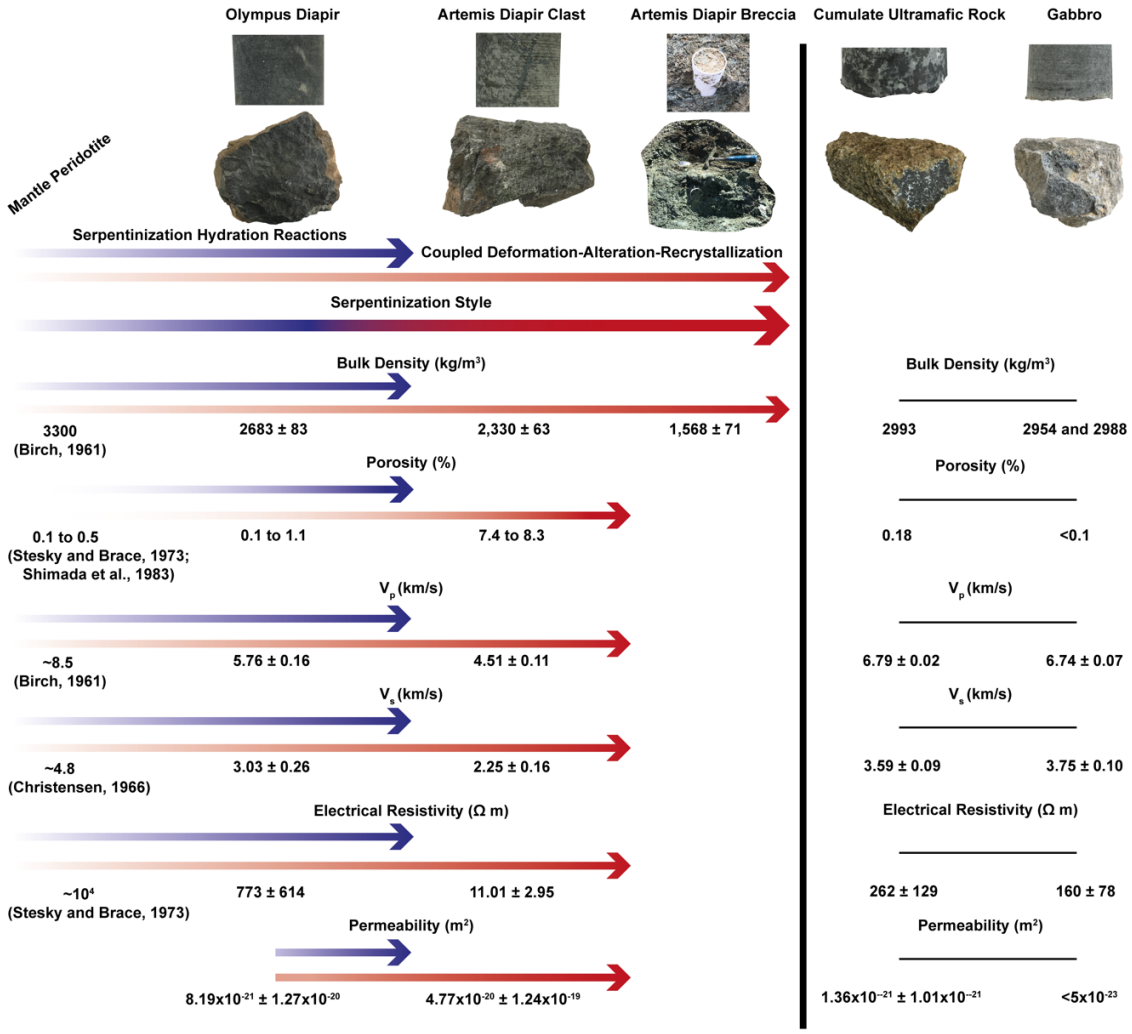

Figure 6.10: Summary figure of physical and hydraulic properties measured in the Troodos Mantle Sequence.

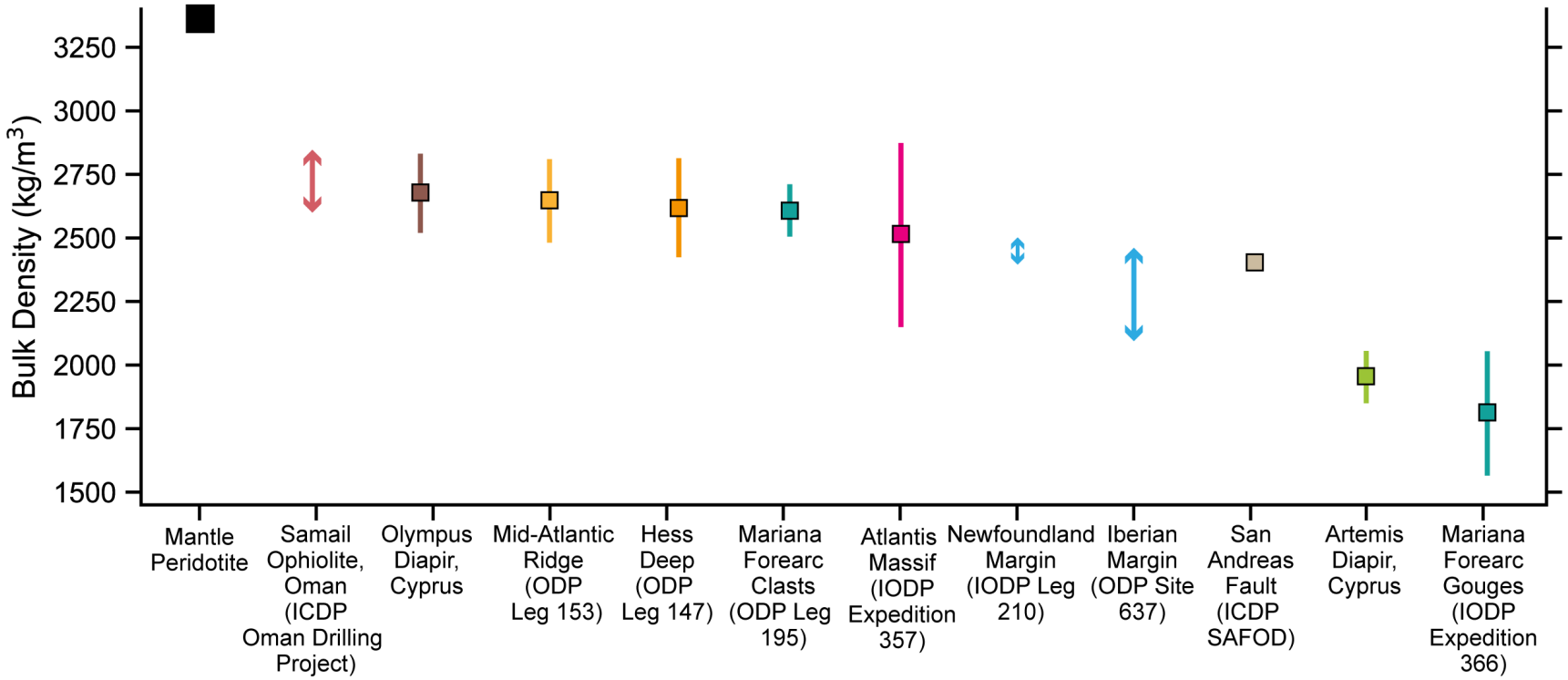

Figure 6.11. Caltech plot of reported Bulk Density (kg/m^3) of serpentinised mantle rocks from a range serpentinisation settings on land and in the oceans. See Table 6.2 for references. Arrows reflect reported range. Squares reflect average values with error bars equivalent to 2σ of the mean.

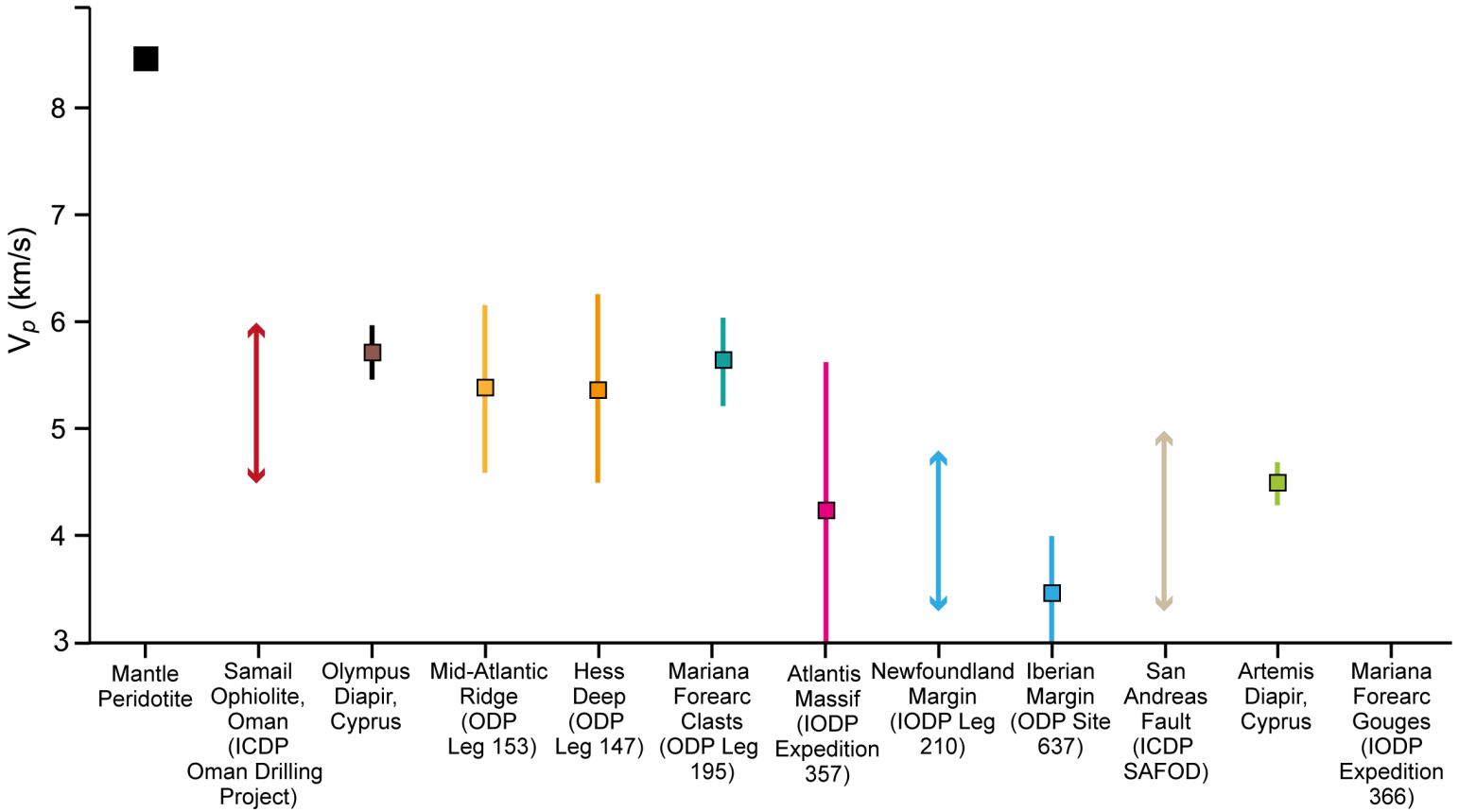

Figure 6.12: Caltech plot of reported V_p (km/s) of serpentinised mantle rocks from a range serpentinisation settings on land and in the oceans. See Table 6.2 for references. Arrows reflect reported range. Squares reflect average values with error bars equivalent to 2σ of the mean.

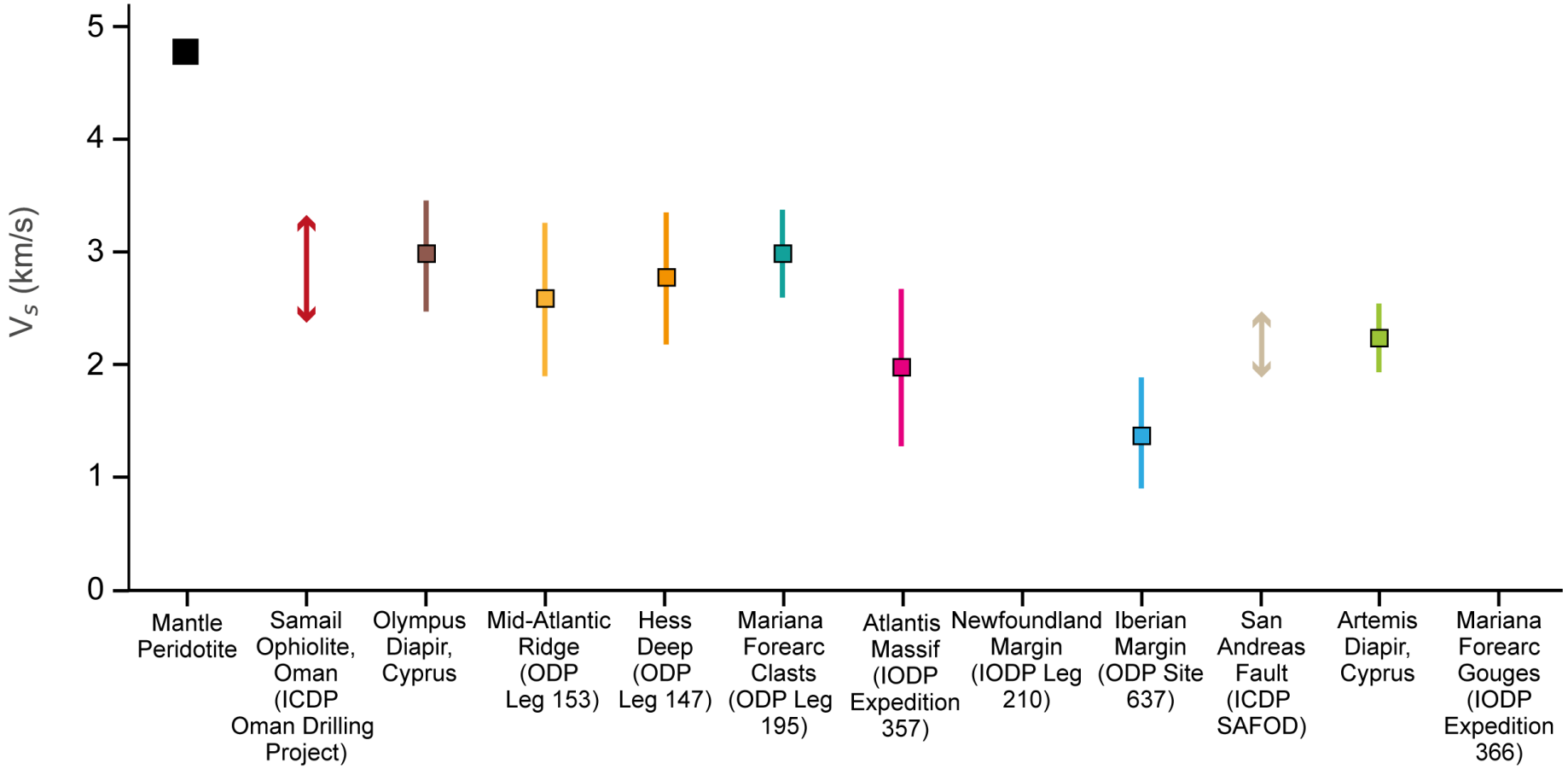

Figure 6.13: Caltech plot of reported V_s (km/s) of serpentinised mantle rocks from a range serpentinisation settings on land and in the oceans. See Table 6.2 for references. Arrows reflect reported range. Squares reflect average values with error bars equivalent to 2σ of the mean.

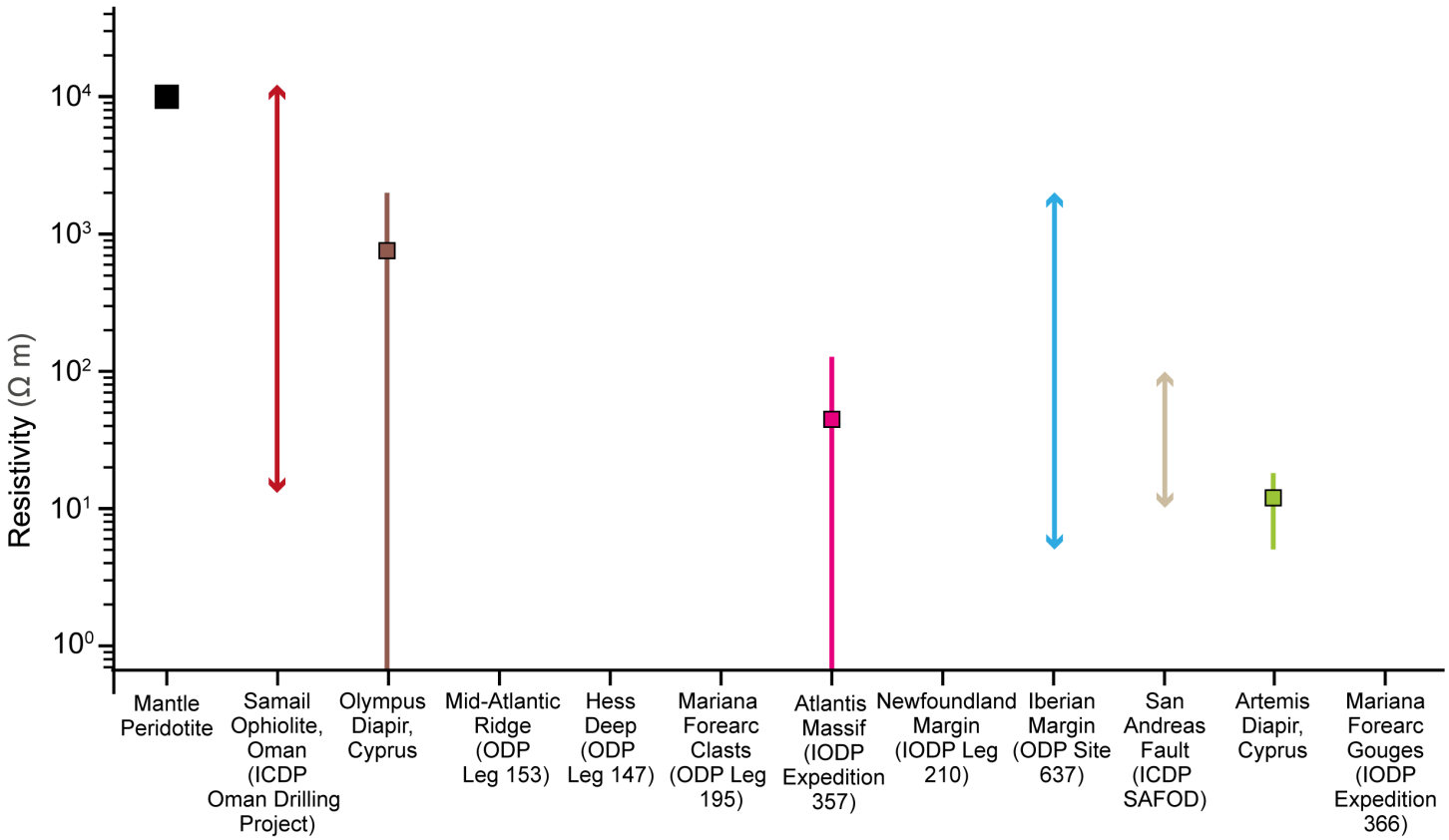

Figure 6.14: Caltech plot of reported electrical resistivity (Ω m) of serpentinised mantle rocks from a range serpentinisation settings on land and in the oceans. See Table 6.2 for references. Arrows reflect reported range. Squares reflect average values with error bars equivalent to 2σ of the mean.

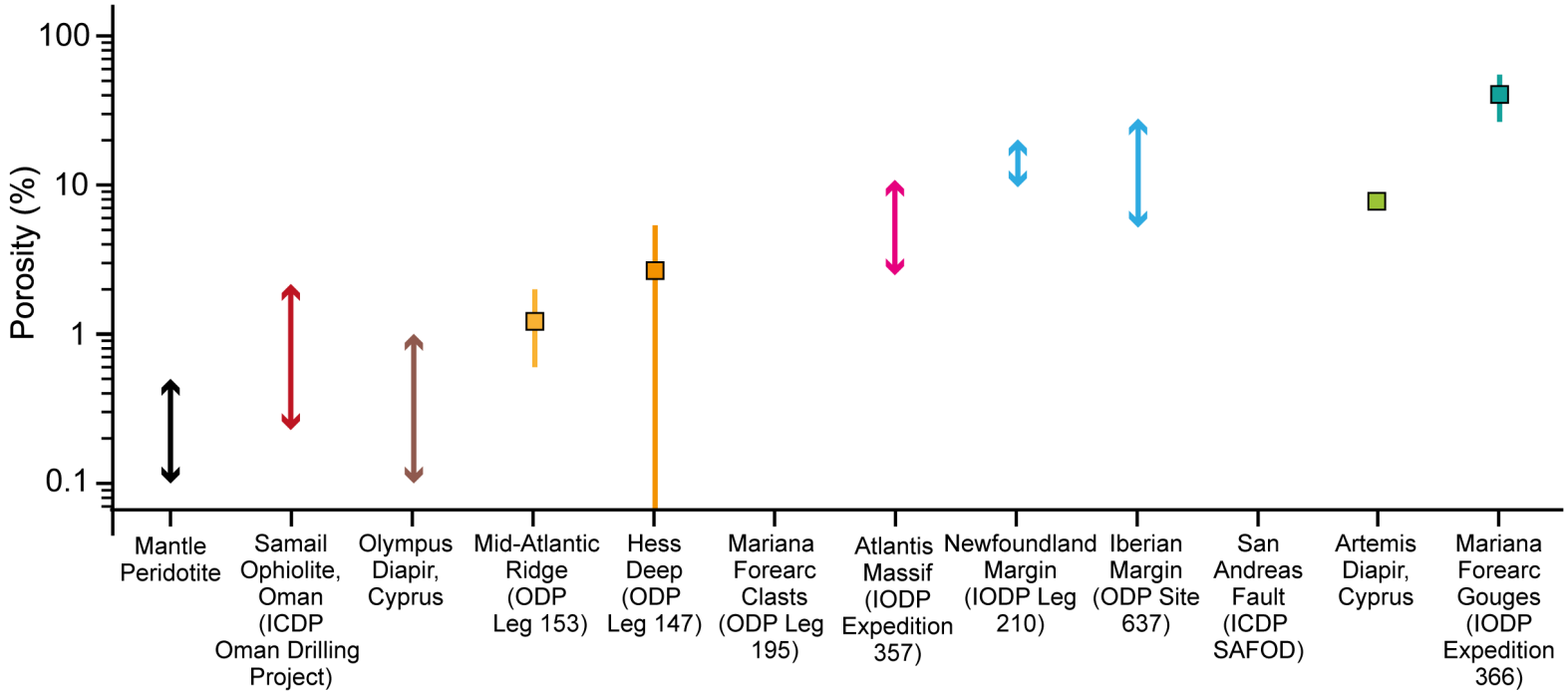

Figure 6.15: Caltech plot of reported Porosity (%) of serpentinised mantle rocks from a range serpentinisation settings on land and in the oceans. See Table 6.2 for references. Arrows reflect reported range. Squares reflect average values with error bars equivalent to 2σ of the mean.

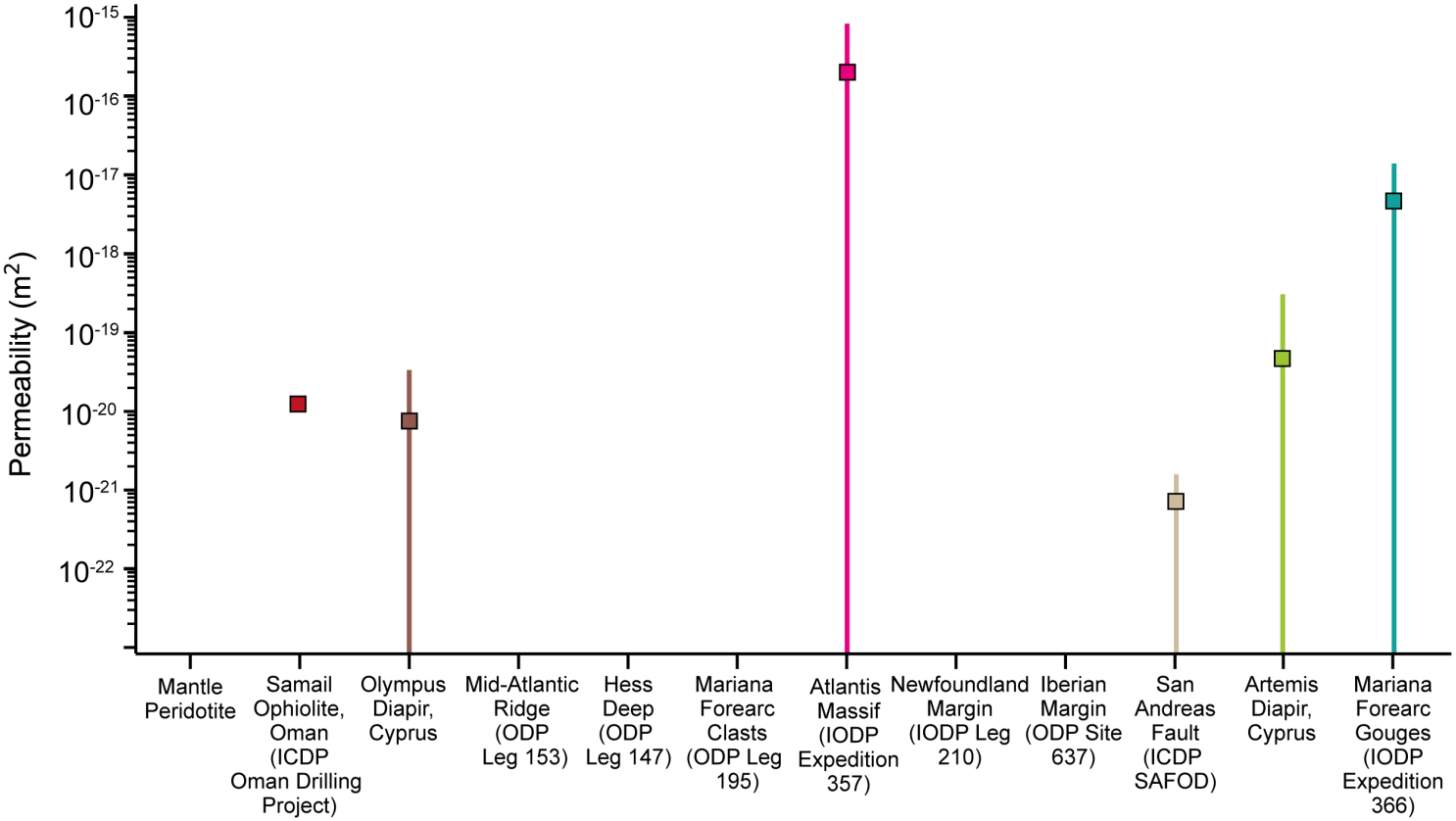

Figure 6.16: Caltech plot of reported Permeability (m^2) of serpentinised mantle rocks from a range serpentinisation settings on land and in the oceans. See Table 6.2 for references. Arrows reflect reported range. Squares reflect average values with error bars equivalent to 2σ of the mean.

Table 6.2: Table compiling reported data of physical and hydraulic properties from a range of serpentinising settings, both on land and in the oceans.

	Unaltered Mantle Peridotite	***Olympus Diapir***	***Artemis Diapir***	***Atlantis Massif (IODP Expedition 357)***	***Mid-Atlantic Ridge (ODP Leg 153)***	***Hess Deep (ODP Leg 147)***	***Samail Ophiolite (ICDP Oman Drilling Project)***	***Iberian Margin (ODP Site 637)***	***Newfoundland Margin (IODP Leg 210)***	***Mariana Forearc (IODP Expedition 366 – Gouges; ODP Leg 195 – Clasts)***	***San Andreas Fault (ICDP SAFOD)***
Exposure	Hard, blocky, Cohesive, Competent	Hard, blocky, cohesive	Weak, incompetent, incohesive	Hard, blocky, generally cohesive	Hard, blocky, cohesive and breccias with weak portions of serpentinite blocks and carbonate/clay matrix	Generally hard, blocky, cohesive	Generally hard, blocky, cohesive with localised portions of weak and incohesive outcrops	Weak, incompetent, incohesive	Weak, incompetent, incohesive	Weak, incompetent, incohesive gouge	Weak, incompetent, incohesive
Serpentinisation Extent	Unaltered	Strongly Serpentinised ~50 to 90%	Completely serpentinised >~99.9%	Strongly to completely serpentinised	Strongly to completely serpentinised	Strongly serpentinised	Strongly serpentinised	Strongly to Completely Serpentinised	Strongly to Completely Serpentinised	Strongly to completely serpentinised	Strongly to completely serpentinised
Dominant Serpentinisation Style	-	Serpentinisation hydration reactions	Coupled deformation-alteration-recrystallisation	Serpentinisation hydration reactions And portions of coupled deformation-alteration-recrystallisation	Serpentinisation hydration reactions	Serpentinisation hydration reactions	Serpentinisation hydration reactions	Coupled deformation-alteration-recrystallisation	Coupled deformation-alteration-recrystallisation	Coupled deformation-alteration-recrystallisation	Coupled deformation-alteration-recrystallisation
Bulk Density	**3,300 kg/m^3** (Birch, 1961)	**2,683 ± 83 kg/m^3** (1σ; Evans et al., 2021)	**1,949 ± 48 kg/m^3** (1σ; Evans et al., 2021; Clast and Matrix)	**2,515 ± 186 kg/m^3** (1σ; Falcon-Suarez et al., 2017)	**2,650 ± 90 kg/m^3** (1σ; Miller and Christensen, 1997)	**2,630 ± 100 kg/m^3** (1σ; Iturrino et al., 1995)	**2,630 to 2,790 kg/m^3** (Hatakeyama et al., 2021)	**2,100 to 2,450 kg/m^3** (Boillot et al., 1987)	**2,400 to 2,500** (Shipboard Science Party, 2004)	**1813 ± 130 kg/m^3** (1σ; Morrow et al., 2019; Gouge) **2611 ± 45 kg/m^3** (1σ; Courtier et al., 2004; Clast)	**~2400 kg/m^3** (Watt et al., 2014)

	Unaltered Mantle Peridotite	***Olympus Diapir***	***Artemis Diapir***	***Atlantis Massif (IODP Expedition 357)***	***Mid-Atlantic Ridge (ODP Leg 153)***	***Hess Deep (ODP Leg 147)***	***Samail Ophiolite (ICDP Oman Drilling Project)***	***Iberian Margin (ODP Site 637)***	***Newfoundland Margin (IODP Leg 210)***	***Mariana Forearc (IODP Expedition 366 – Gouges; ODP Leg 195 – Clasts)***	***San Andreas Fault (ICDP SAFOD)***
Porosity	**0.1 to ~0.5 %** (Stesky and Brace, 1973; Shimada et al., 1983)	**0.1 to 1.1 %**	**7.4 to 8.3 %** (Clast)	**2.6 to 12.8 %** (Falcon-Suarez et al., 2017)	**1.32 ± 0.3 %** (1σ; Miller and Christensen, 1997)	**2.64 ± 1.35 %** (1σ; Iturrino et al., 1995)	**0.25 to 2.13 %** (Hatakeyama et al., 2021)	**5 to 28 %** (Boillot et al., 1987)	**10 to 20 %** (Shipboard science party, 2004)	**40 ± 6 %** (1σ; Morrow et al., 2019; Gouge)	-
Vp	**~8.5 km/s** (Birch, 1961)	**5.76 ± 0.16 km/s** (1σ)	**4.51 ± 0.11 km/s** (1σ; Clast)	**4.23 ± 0.69 km/s** (1σ; Falcon-Suarez et al., 2017)	**5.42 ± 0.39 km/s** (1σ; Miller and Christensen, 1997)	**5.39 ± 0.43 km/s** (1σ; Iturrino et al., 1995)	**4.5 to 6 km/s** (Hatakeyama et al., 2021)	**3.44 ± 0.28** km/s (1σ; Goldberg and Zinszner 1988)	**3.3 to 4.75 km/s** (Shipboard science party, 2004)	**5.65 ± 0.20 km/s** (1σ; Courtier et al., 2004; Clast)	**~3.3 to 5 km/s** (Hickman et al., 2007)
Vs	**~4.8 km/s** (Christensen, 1966)	**3.03 ± 0.26 km/s** (1σ)	**2.25 ± 0.16 km/s** (1σ; Clast)	**2.01 ± 0.36 km/s** (1σ; Falcon-Suarez et al., 2017)	**2.61 ± 0.34 km/s** (1σ; Miller and Christensen, 1997)	**2.80 ± 0.30 km/s** (1σ; Iturrino et al., 1995)	**2.45 to 3.35 km/s** (Hatakeyama et al., 2021)	**1.37 ± 0.23 km/s** (1σ; Goldberg and Zinszner 1988)	**-**	**2.99 ± 0.20 km/s** (1σ; Courtier et al., 2004; Clast)	**~1.9 to 2.5 km/s** (Hickman et al., 2007)
Electrical Resistivity	**~10^4 Ω m** (Stesky and Brace, 1973)	**773 ± 614 Ω m** (1σ)	**11.01 ± 2.95 Ω m** (1σ; Clast)	**42.86 ± 31.06 Ω m** (1σ; Falcon-Suarez et al., 2017)	-	-	**13 to 12,000 Ω m** (Katamaya et al., 2020)	**5 to 2,000 Ω m** (Boillot et al., 1987)	-	-	**~10 to 10^2 Ω m** (Hickman et al., 2007)
Permeability	-	**$8.19x10^{-21}$ ± $1.27x10^{-20}$ m^2** (1σ)	**$4.77x10^{-20}$ ± $1.24x10^{-19}$ m^2** (1σ; Clast)	**$2.08x10^{-16}$ ± $6.87x10^{-16}$ m^2** (1σ; Falcon-Suarez et al., 2017)	-	-	**$1.38x10^{-20}$ m^2** (Median; Katamaya et al., 2020)	-	**-**	**$4.47x10^{-18}$ ± $4.91x10^{-18}$ m^2** (1σ; Morrow et al., 2019; Gouges)	**$7.98x10^{-22}$ ± $4.19x10^{-22}$ m^2** (Gouge; Morrow et al., 2014)

6.5.1.1 Bulk density and porosity

Unaltered mantle rocks yield high bulk densities of 3,300 kg/m^3 and completely serpentinised ultramafic rocks yield bulk densities of <2,550 kg/m^3 (Birch, 1961). Progressive serpentinisation reactions reduce bulk density to lower values (Fig. 6.11). Across several settings strongly serpentinised mantle peridotites, both on land and in the oceans, yield similar bulk densities ranging between 2,500 and 2,900 kg/m^3 (Table 6.2; Fig. 6.11) and low porosities ranging from ~0.1 to ~2.5 % (Fig. 6.15; Table 6.2). Corresponding strongly serpentinised samples from the Olympus Diapir yield similar bulk densities and porosities (Table 3.1; Evans et al., 2021), and show evidence of alteration dominated by serpentinisation hydration reactions with relatively limited carbonate contents (Fig. 6.2).

In contrast, serpentinite breccia samples composed of a clast-matrix assemblage occur in completely serpentinised settings and yield bulk densities that are substantially lower than the grain density of serpentine (2,550 kg/m^3; e.g., Evans, 2004). Some of these samples, such as the Artemis Diapir incompetent serpentinite breccias, yield bulk densities as low as ~1,550 kg/m^3 (Fig. 6.5; Evans et al., 2021). Similar, low density <2,550 kg/m^3, serpentinite breccias occur at the Iberian and Newfoundland margins, within the Mariana Forearc mud volcanoes, and along the San Andreas Fault (Table 6.2, Fig. 6.11). The porosities of these corresponding low density incompetent serpentinite breccias range between ~5 % up to 52 %, significantly higher than competent strongly serpentinised rocks (~0.1 to 2.5 %; Table 6.2; Fig. 6.15). In addition, these serpentinite breccias display evidence of serpentine alteration through coupling of deformation-alteration-recrystallisation processes (Evans et al., 2021; Klein et al., 2017; Milliken et al., 1996).

6.5.1.2 V_p and V_s

The compositional transformation of mantle rock primary minerals such as olivine and orthopyroxene to secondary serpentine through serpentinisation is invoked as a major control on the elastic properties of ultramafic rocks (e.g., Christensen, 2004). A wide range of V_p and V_s values are reported in serpentinised mantle rocks from differing geological settings (Fig. 6.12; Fig. 6.13; Table 6.2). The typical V_p and V_s values of unaltered mantle rocks are 8.5 km/s (Birch, 1961) and 4.8 km/s (Christensen, 1966) respectively. Strongly to completely serpentinised mantle rocks across geological settings yield similar V_p and V_s values as the Olympus Diapir and competent clasts from within the Artemis Diapir (Fig. 6.12; Fig. 6.13; Table 6.2). Despite contrasting geological and serpentinisation histories, the

V_p of samples from the strongly serpentinised Olympus Diapir yield similar values of 5.76 ± 0.11 km/s (1σ, n=24, Table 6.1) as strongly serpentinised mantle rock datasets of Hess Deep (5.39 ± 0.43 km/s; 1σ; Iturrino et al., 1996), Mid-Atlantic Ridge (5.42 ± 0.39 km/s; 1σ; Miller and Christensen, 1997), Samail ophiolite (4.5 to 6 km/s; Hatakeyama et al., 2021), and serpentinised clasts from the Mariana Forearc mud volcanoes (5.65 ± 0.20; 1σ; Courtier et al., 2004).

In contrast, measured samples from completely serpentinised mantle rocks display lower V_p and V_s values relative to strongly serpentinised settings (Fig. 6.12; Fig. 6.13) with the lowest values recorded in samples from the Iberian Margin with V_p of 3.44 ± 0.28 km/s (1σ; Goldberg and Zinszner, 1988) and V_s of 1.37 ± 0.23 km/s (1σ; Goldberg and Zinszner, 1988). The V_p and V_s values of the Iberian Margin serpentinites are significantly lower than other completely serpentinised sites such as the Artemis Diapir (V_p = 4.51 ± 0.11 km/s; V_s = 2.25 ± 0.16 km/s; 1σ, n=24; Table 6.2; Fig. 6.12; Fig. 6.13). This variation in V_p and V_s of completely serpentinised mantle rocks may be related to compositional variations, porosity, and fracture networks.

Greater amounts of carbonate veins occur in samples from the Iberian Margin, yielding higher CaO (wt.%) contents (up to ~40 wt.%; Milliken et al., 1996) relative to the Artemis Diapir (up to 12 wt.% CaO; Table 5.2). Additionally, Iberian Margin samples yield porosities of ~18 % (Goldberg and Zinszner, 1988), in comparison, the Artemis Diapir yields lower porosities ranging between 7.4 and 8.3 % (Table 6.2; Fig. 6.15). Recently, in addition to compositional differences between olivine and serpentine, the presence of fractures has been proposed to exert a strong influence on physical properties due to measured stress-dependent variability of parameters, as confining pressures increase from 10 and 50 MPa (Falcon-Suarez et al., 2017). For example, ultrasonic wave velocities of serpentinised mantle rocks from the Atlantis Massif show the progressive increase of V_p by 7 % and V_s by 20 % between confining pressures of 10 to 50 MPa (Bayrakci et al., 2018; Falcon-Suarez et al., 2017). In contrast, our results yield an increase in V_p of 2 % and V_s of 3 % between confining pressures of 5 to 50 MPa. However, our samples from the Artemis Diapir yield a marked increase of ~19 % in V_s during the initial stages of loading (P_{Conf} 5.5 to 10 MPa), and a contrasting marked decrease in V_s of ~20 % from the Olympus Diapir. These results suggest, despite significant changes in ultrasonic wave velocity during initial loading, samples from the Troodos Mantle Sequence yield less stress-dependent variation compared to the Atlantis Massif. This is further highlighted by contrasting V_p/V_s ratios (Table 6.1), where increasing V_p/V_s with increasing loading stress is inferred due to increased cracking (Falcon-Suarez et al., 2017). Our results indicate little variation in V_p/V_s at P_{Diff} >5 MPa (Table 6.1) compared to samples from the Atlantis Massif (Bayrakci et al., 2018; Falcon-Suarez et al., 2017).

These datasets show contrasting results compiled from strongly serpentinised and completely serpentinised settings. The wide variation in V_p and V_s cannot be explained by serpentinisation reactions alone and additional processes such as compositional variations between serpentine and carbonate, differential porosities, and microfracture patterns may also play a role in evolving physical properties during mantle rock alteration.

6.5.1.3 Resistivity and permeability

The electrical resistivity of unaltered mantle rocks is estimated to be ~10^4 Ω m (Stesky and Brace, 1973). In general, samples with higher serpentine contents yield lower electrical resistivities (Fig. 6.14; Table 6.2). Measured electrical resistivities from the strongly serpentinised Olympus Diapir show significant stress-dependent variation of at least two orders of magnitude (40 to 1892 Ω m). Other studies from sites of strongly serpentinised mantle rocks such as the Samail ophiolite, yield electrical resistivities ranging between four orders of magnitude (13 to 12,000 Ω m; Hatakeyama et al., 2021). Samples from the strongly to completely serpentinised Atlantis Massif are measured to have electrical resistivities of 43 ± 31 Ω m (1σ; Falcon-Suarez et al., 2017). Competent completely serpentinised clasts from the Artemis Diapir yield very low resistivities of 11 ± 3 Ω m (1σ; n=24) with no stress-dependent variation in the determined values. Other completely serpentinised settings such as the Iberian Margin and the San Andreas Fault have similar low measured electrical resistivities of ~10 Ω m (Table 6.2; Fig. 6.14; Boillot et al., 1987; Hickman et al., 2007).

Measured permeabilities of the Troodos Mantle Sequence vary by two to three orders of magnitude (10^{-19} to 10^{-22} m^2; Fig 6.8; Fig. 6.9) with increasing confining pressures (P_{Conf} 5.5 to 50 MPa). Permeabilities of serpentinised samples from the Oman Drilling Project (Kelemen et al., 2020) are inferred from electrical resistivity data using effective medium theory (Katayama et al., 2020). Compiled inferred permeability values in serpentinised harzburgite of OmanDP Hole CM1A, BA1B are 2.44x10^{-20} and 1.57x10^{-21} m^2 respectively and serpentinised dunite of hole CM1A, BA1B, and BA4A are 2.00x10^{-17}, 2.26x10^{-19}, and 3.77x10^{-20} m^2 respectively (Katayama et al., 2020). In contrast to our data, these inferred permeability values are not calculated at different loading stresses, but they broadly agree with the measured permeabilities from the Troodos Mantle Sequence in this study (Fig. 6.9). Samples from the Atlantis Massif (Bayrakci et al., 2018; Falcon-Suarez et al., 2017) were determined at different loading stresses and are up to four orders of magnitude higher (up to 10^{-17} m^2 at P_{Diff} 45 MPa) than our results and other experimentally derived serpentinite permeabilities (e.g., 10^{-19} to 10^{-22} m^2; Katayama et al., 2012; Kawano et al., 2011) at similar confining pressures between 5.5 and 50 MPa. Although our results

indicate some component of stress-dependent variability, it is less than previous data from the Atlantis Massif, which indicates a greater component of stress-dependent variability inferred due to higher fracture density influencing physical properties parameters (Bayrakci et al., 2018; Falcon-Suarez et al., 2017). Serpentinisation hydration reactions result in reaction-induced microcracking, where serpentinisation-induced volume expansion (up to 40 %; Macdonald and Fyfe, 1985) generates a positive feedback mechanism that maintains or increases permeability and reactive surface area (Kelemen and Hirth, 2012). Yet, reaction-induced microcracking is ultimately balanced by fracture filling secondary mineral precipitation (Kelemen et al., 2011; Kelemen and Hirth, 2012). As a result, drilling-induced fracture reactivation (e.g., Miller and Christensen, 1997; Falcon-Suarez et al., 2017; Früh-Green et al., 2017) is proposed as the source of inferred higher fracture density and has influenced the physical properties of the Atlantis Massif samples. In addition, determined permeabilities of incohesive serpentinite breccias reported from serpentinite muds of the Mariana Forearc mud volcanoes and serpentinite gouges of the San Andreas Fault are contrasting. Serpentinite muds yield an average permeability value of $4.5x10^{-18} \pm 4.9x10^{-18}$ m^2 (1σ; Morrow et al., 2019) and serpentinites gouges yield an average permeability value of $8x10^{-22} \pm 4.2x10^{-22}$ m^2 (1σ; Morrow et al., 2014).

6.5.2 Mantle Rock Alteration Pathways

Compiled physical and hydraulic properties datasets of serpentinised mantle rocks from a range of differing geological settings and serpentinisation extents displays a wide range in measured values. The alteration of mantle rocks results in the evolution of physical and hydraulic properties of serpentinised mantle rocks (e.g., Birch, 1961; Christensen, 1966; Falcon-Suarez et al., 2017; Stesky and Brace, 1973). Some of the change in physical and hydraulic properties can be explained by serpentinisation hydration reactions alone, culminating in the compositional transformation of primary mineralogies such as olivine and pyroxene to secondary serpentine. However, additional processes are required to explain the full spectrum of reported physical and hydraulic properties in altered mantle rocks (Table 6.2; Fig. 6.17). A mechanism that has been qualitatively inferred to explain the reported spectrum is the continued alteration of serpentine, as completely serpentinised mantle peridotites display evidence of extensive serpentine deformation, alteration, and recrystallisation (e.g., Fig. 6.3; Bach et al., 2004; Evans et al., 2021; Evans, 2004; Hopkinson et al., 2004; Kahl et al., 2015; Milliken et al., 1996; Milliken and Morgan, 1996; O'Hanley, 1991; Picazo et al., 2013; Rouméjon et al., 2018a). We propose that serpentine alteration processes contribute, in addition to serpentinisation hydration reactions, to the

overall evolving physical and hydraulic properties of altering mantle rocks, producing two contrasting, but parallel, mantle rock alteration pathways.

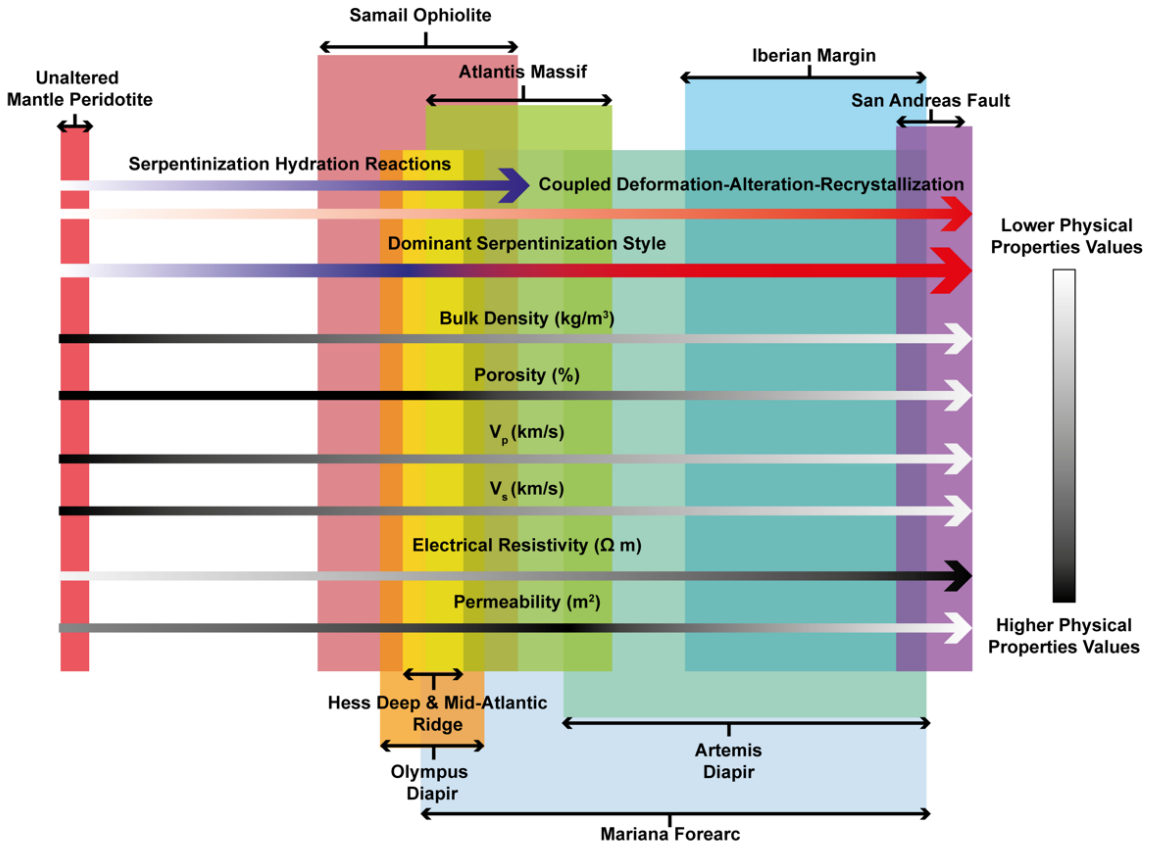

Figure 6.17: Schematic diagram highlighting the relative measured range in physical properties between differing sites of serpentinisation.

A serpentinisation hydration mantle rock alteration pathway is initiated as ultramafic rocks interact with water, and serpentinisation hydration reactions are induced through a complex series of reactions (e.g., Bach et al., 2006; McCollom et al., 2016; McCollom and Bach, 2009). A generalised isochemical serpentinisation reaction is proposed to occur (Eq. 6.1; e.g., Bach et al., 2006):

$$2Mg_2SiO_4 + 3H_2O \longrightarrow Mg_3SiO_2O_5(OH)_4 + Mg(OH)_2 \quad (6.1)$$

As serpentinisation of mantle rocks is induced through interaction with water, physical properties of mantle rocks evolve, typically yielding a strong linear relationship between physical parameters and serpentinisation extent (e.g., bulk density, R^2 = 0.98; Miller and Christensen, 1997). Progressive serpentinisation reactions result in the reduction of bulk density from 3,300 kg/m^3 to ~2,550 kg/m^3 (Fig. 6.11; Birch, 1961) and a negligible change

in porosity (0.1 to <2.5 %; Fig. 6.15). Ultrasonic wave velocities V_p and V_s decrease from 8.5 and 4.8 km/s (Birch, 1961; Christensen, 1966) to ~5 km/s and ~2.5 km/s (Fig. 6.12; Fig. 6.13). Electrical resistivity decreases from ~10^4 Ω m (Stesky and Brace, 1973) to ~10^2 Ω m (at surface conditions; Fig. 6.14). During initial serpentinisation reactions, the serpentinisation hydration mantle rock alteration pathway dominates. Once serpentinisation is complete and primary minerals are exhausted, the serpentinisation hydration mantle rock pathway terminates.

The alteration of serpentine is a second mantle rock alteration pathway, which initiates when serpentine has formed. As progressive serpentinisation reactions occur and the serpentinisation extent of the altering mantle rock increases, the contribution of serpentine alteration to the overall mantle rock alteration budget also increases. The serpentine alteration pathway dominates when primary minerals are exhausted. Continued serpentine alteration processes result in the increasing extent of coupled deformation-alteration-recrystallisation and the progressive development of a serpentinite breccia end member (Fig. 6.3) with distinct physical properties (Fig. 6.10; Table 6.2). These end member serpentinite breccias have low bulk density (~<2100 kg/m^3; Table 6.2); V_p (~3.5 km/s; Table 6.2), V_s (~1.5 km/s; Table 6.2), permeability (~$8x10^{-22}$; Table 6.2), and high porosities (~>5 up to <52 %; Table 6.2). In contrast to the end member serpentinite breccias, completely serpentinised mantle rocks with textural evidence of coupled deformation-alteration-recrystallisation interactions (e.g., Atlantis Massif; Bayrakci et al., 2018; Falcon-Suarez et al., 2017) yield moderate, bulk densities (~2515 kg/m^3; Table 6.1), V_p (~4.2 km/s; Table 6.2), V_s (~2 km/s; Table 6.2), electrical resistivities (~43 Ω m; Table 6.2), and high porosities (>2.6 to <12.8 %; Table 6.2) and permeabilities (~$2x10^{-16}$; Table 6.2).

The contrasting physical properties, between completely serpentinised mantle rocks and serpentinite breccias, reflect variability in the extent and degree of coupled deformation-alteration-recrystallisation interactions and consequently extent of the serpentine alteration pathway (Fig. 6.3). Such interactions likely induce continued progressive evolution of altered mantle rock physical properties through dissolution and subsequent precipitation/recrystallisation of pre-existing serpentine (e.g., Chapter 4; Milliken et al., 1996). Continued interaction of deformation-alteration-recrystallisation processes likely induces serpentine dissolution, consequently increasing porosity (e.g., from ~2 % up to ~50 %; Table 6.2) and decreasing bulk density (e.g., from ~2550 to ~1550 kg/m^3; Table 6.2; Evans et al., 2021). Culminating in the erosion of the weak serpentinite breccia endmember, consequently forming detrital serpentine sedimentary sequences (e.g., Lockwood, 1971).

The increased porosity and corresponding decrease in bulk density of completely serpentinised mantle rocks may be related to the dissolution of serpentine, proposed to occur through the following reaction with seawater (Eq. 6.2; Milliken et al., 1996):

$$Mg_3Si_2O_5(OH)_4 + 5H_2O \longrightarrow 3Mg^{2+} + 2H_4SiO_4 + 6OH^-$$

(6.2)

The dissolution and subsequent precipitation of serpentine from modified meteoric waters at low temperatures (~5 to ~10°C) is proposed to occur (e.g., Craw et al., 1995, 1987). This reaction could occur through the following reactions (Eq. 6.3; Eq. 6.4):

$$Mg_3Si_2O_5(OH)_4 + H_2O + 6CO_2 \rightleftharpoons 3Mg^{2+} + 2SiO_{2\,(aq)} + 6HCO_3^-$$

(6.3)

$$Mg_3Si_2O_5(OH)_4 + H_2O \rightleftharpoons 3Mg^{2+} + 2SiO_{2\,(aq)} + 6OH^-$$

(6.4)

Differential rates of serpentine dissolution and subsequent precipitation of serpentine may explain the general observation of increasing porosities and lower bulk densities (Fig. 6.11; Fig. 6.15). However, some of the porosity generated by progressive serpentine dissolution is likely, at least, partially filled by carbonate precipitation (Eq 6.5; Eq 6.6 (Neal and Stanger, 1985); Eq. 6.7 (Dichicco et al., 2015)):

$$Ca^{2+} + 2HCO_3 \rightleftharpoons CaCO_3 + CO_2 + H_2O$$

(6.5)

$$Ca^{2+} + 2OH^- + CO_2 \rightleftharpoons CaCO_3 + H_2O$$

(6.6)

$$Mg_3Si_2O_5(OH)_4 + 3CO_2 \rightleftharpoons 3MgCO_3 + 2SiO_{2\,(aq)} + 2H_2O$$

(6.7)

Evidence of carbonate precipitation is highlighted by elevated CaO (wt.%) contents of serpentinite breccias relative to mantle from the opposing Iberian and Newfoundland margins (up to 40 % vs ~<2 % CaO; Milliken et al., 1996; Milliken and Morgan, 1996; Robertson, 2007), observed calcite veinlets, up to ~5 mm wide, in serpentinite gouge samples along the San Andreas Fault (Moore and Rymer, 2012), higher trace carbonate contents (up to ~11 % CaO wt.%) in the Artemis Diapir relative to the Olympus Diapir (Table 5.2), and calcium and magnesium carbonate-peridotite breccia assemblages within the Samail Ophiolite, Oman (Kelemen et al., 2011; Kelemen and Matter, 2008). In addition, contrasts between the physical and hydraulic properties of completely serpentinised samples may reflect differing amounts of carbonate precipitation as CaO (wt.%) contents, bulk densities, V_p and V_s of the Artemis Diapir (up to 11 % CaO wt.%; ~1950 kg/m^3; ~4.51

km/s; ~2.25 km/s) differ to the Atlantic Iberian and Newfoundland rifted margins (up to 40 % CaO wt.%; ~2,400 kg/m^3; ~3.44 km/s; ~1.37 km/s).

6.5.3 Implications of contrasting mantle rock alteration pathways

As mantle rocks undergo alteration, expressed by contrasting mantle rock alteration pathways, bulk density is reduced by up to ~47 % (3300 to ~1550 kg/m^3), whilst porosity increases from 0.1 % up to ~52 % (Table 6.2). The respective contribution of each serpentinisation style to the overall physical properties evolution budget differs. As serpentinisation hydration reactions are generally considered an isochemical process (e.g., Coleman and Keith, 1971), serpentinisation induces up to 40 % volume expansion (Macdonald and Fyfe, 1985), whilst the change in porosity is negligible (up to ~1.3 %; Miller and Christensen, 1997). These physical properties changes suggest serpentinisation hydration reactions contribute up to ~23 % of the bulk density reduction budget (3,300 to ~2,550 kg/m^3) and porosity changes are insignificant (~1 %). In contrast, the coupled deformation-alteration-recrystallisation serpentinisation style may initiate serpentine dissolution (e.g., Chapter 4; Craw et al., 1995, 1987; Milliken et al., 1996), generating significant increases in porosity of up to 52 % (Table 6.2) and promoting further reductions in bulk density from ~<2,550 to ~1,550 kg/m^3. If porosity generation of the serpentinite breccia end member is achieved by coupling of deformation-alteration-recrystallisation processes that induce dissolution of pre-existing serpentine, it suggests significant mass removal during serpentinite alteration, but mass conservation during serpentinisation hydration reactions. This removal of mass during serpentinite alteration may have significant implications for serpentinite geochemical budgets (Alt et al., 2013; Früh-Green et al., 2004). Consequently, to define and quantify the role of serpentinite alteration within the Earth system, investigations should focus on serpentine alteration in addition to serpentinisation hydration reactions.

6.6 Conclusions

1) Variably altered mantle rocks of the Troodos Mantle Sequence show a wide variation in physical and hydraulic properties, which have evolved away from initial unaltered values. Distinct differences occur between the partially to strongly serpentinised Olympus Diapir and the completely serpentinised Artemis Diapir. Measured samples from the Olympus Diapir yield bulk densities of 2,683 ± 83 kg/m^3, porosities ranging between 0.1 to 1.1 %, V_p of 5.8 ± 0.2 km/s, V_s of 3 ± 0.3 km/s,

resistivities of 773 ± 614 Ω m, and permeabilities of 8.2×10^{-21} ± 1.3×10^{-20} m^2. In contrast, samples from the Artemis Diapir yield bulk densities of 1,949 ± 48 kg/m^3, porosities ranging between 7.4 to 8.3 %, V_p of 4.5 ± 0.1 km/s, V_s of 2.3 ± 0.2 km/s, resistivities of 11 ± 3 Ω m, and permeabilities of 4.8×10^{-20} ± 1.2×10^{-19} m^2.

2) Compiled physical and hydraulic properties datasets of strongly to completely serpentinised sites from varying geological settings and histories show that the total change in reported physical properties cannot be explained by serpentinisation hydration reactions alone. To explain this discrepancy, serpentine alteration has been proposed to manifest through coupled deformation-alteration-recrystallisation processes, evolving the physical properties of altering mantle rocks to lower bulk density, V_p, V_s, resistivity values, and higher porosity and permeability values.
3) Alteration of mantle rocks occurs through contrasting, but parallel alteration pathways of serpentinisation hydration reactions and serpentine alteration. Variable proportions of serpentinisation hydration and serpentine alteration and carbonation induce significant changes in mantle rock physical properties that results in up to a ~47 % reduction in bulk density from 3,300 kg/m^3 to ~1,550 kg/m^3 and an increase in porosity from 0.1 up to 52 %.
4) The observed changes in porosity of altering mantle rocks suggests that during quasi-isochemical serpentinisation reactions, mass is conserved, but serpentine alteration interactions induce significant mass removal. This may have significant implications on global geochemical budgets since surface mantle rock exposures likely undergo some degree of serpentine alteration.

Chapter 7 Summary and Conclusions

7.1 Summary

Serpentinisation hydration reactions play a critical role in the wider earth system, where significant changes to the physical and chemical characteristics of ultramafic rocks aids plate tectonics, acts as a geological sponge for water, carbon, and other fluid-mobile elements, and may be instrumental in the origin of life. In addition to serpentinisation hydration reactions, subsequent alteration, carbonation, and oxidation of serpentine further modifies the physicochemical characteristics of altered ultramafic rocks. The main aim of this thesis was to unravel the serpentinisation-alteration history of variably altered mantle rocks that have resulted in the occurrence of mantle rocks forming the highest elevations of Cyprus. This was achieved by: (i) Establishing that partial serpentinisation reactions can induce significant isostatic uplift; (ii) Determining the composition of modern meteoric-derived waters emanating from the Troodos Mantle Sequence and establishing that geochemical and isotopic fingerprints reflect cumulative water-rock interaction events that have previously occurred; (iii) Unravelling the sequence of events through geochemical and isotopic fingerprinting using both traditional and novel isotope systems; (iv) Establishing the respective relative contributions of serpentinisation hydration reactions and serpentine alteration to the evolution of physical and hydraulic properties of mantle rocks.

7.2 Conclusions

7.2.1 Serpentinisation-induced uplift

- Contrasting serpentinisation styles manifest as two distinct serpentinite diapirs within the Troodos ophiolite: (i) The Olympus Diapir is an arcuate, competent and cohesive, strongly serpentinised diapir of moderate density (2686 ± 83 kg/m^3); and (ii) the completely serpentinised Artemis Diapir composed of an intensely deformed, weak and friable block-clast-breccia-gouge assemblage of low density (1949 ± 47 kg/m^3) that results from a positive feedback between coupled deformation-alteration-recrystallisation.

- Calculations from isostatic uplift and differential erosion modelling shows that density reduction and coincident volume expansion resulting from serpentinisation reactions can induce serpentinite diapirism combined with isostatic uplift, transporting and protruding mantle peridotites to high altitudes (~2000 m).

Consequently, serpentinisation-induced isostatic uplift can generate significant relief and form mountains akin to Mount Olympus (1,952 m asl) within the required time frame.

- The 1-D mechanistic uplift model developed here is applicable to a spectrum of other serpentinised massifs. Isostatic uplift is an inevitable manifestation of serpentinisation reactions that result in density reduction and concomitant volume expansion. As a result, the uplift budget of respective serpentinised massifs is a combination between the relative contributions of isostatic uplift and dynamic tectonic uplift that jointly contribute to the overall uplift and exposure of serpentinised massifs. Consequently, in some cases, the progressive uplift and unroofing of mantle rocks is likely coupled to when serpentinisation hydration reactions occur.

7.2.2 High pH >11.5 hyperalkaline waters emanating from the completely serpentinised Artemis Diapir and remobilisation of previous geochemical and isotopic signals of previous serpentinisation events

- Hyperalkaline, up to pH 13, Na-K-Cl-OH-SO_4 waters emanate from the completely serpentinised rocks. Stable and radiogenic isotope compositions and contrasting elemental ratios in combination with the physical constraints provided by the Troodos Mantle Sequence demonstrates that the hyperalkaline waters are modern meteoric-derived waters.

- Previous studies have suggested that high pH >11.5 hyperalkaline waters emanating from serpentinised massifs reflect active ongoing low temperature <50°C serpentinisation reactions (Barnes and O'Neil, 1969; Neal and Stanger, 1985) and predict that once serpentinisation has completed, hyperalkaline waters will cease to form from the completely serpentinised rocks. Consequently, the occurrence of meteoric-derived hyperalkaline waters emanating from the completely serpentinised Artemis Diapir shows that additional reaction pathways must be actively occurring in generating high pH waters.

- These additional reaction pathways are likely sourced from varying proportions of brucite, carbonate, and serpentine dissolution, with additional serpentine dissolution hydroxide generating reactions occurring under limited atmospheric influence. In addition, serpentine oxidation reactions are likely occurring, which generate hydroxide and H_2.

- Waters emanating from the Troodos Mantle Sequence reflect remobilised geochemical and isotopic signals from previous serpentinisation events. These waters result in the redistribution and progressive modification of distinct geochemical and isotopic fingerprints preserved in the Artemis Diapir rocks.

7.2.3 Multiple overprinting serpentinisation events

- Isotopic compositions ($^{87}Sr/^{86}Sr$, $\delta^{11}B$, $\delta^{18}O$, δD) of variably serpentinised mantle rocks from the Troodos Mantle Sequence show evidence of multiple overprinting serpentinisation events.

- Sr isotope compositions of the Olympus Transition Zone rodingites are similar to Troodos hydrothermally altered ocean crustal rocks (Bickle and Teagle, 1992), indicating that hydrothermal fluids penetrated the Troodos crust-mantle transition zone and likely induced localised serpentinisation of the underlying Troodos lithospheric mantle. A model of pervasive serpentinisation of the Troodos Mantle Sequence by Cretaceous hydrothermal fluids is inconsistent with Troodos uplift trajectories, serpentinisation-induced isostatic uplift modelling, and boron mass balance.

- A long-standing assertion is that the occurrence of serpentinised mantle rocks at the highest elevations of Cyprus is related to the collision of the Eratosthenes Seamount with the Cyprus Arc, where the collision altered the dynamics of the subduction zone, resulting in the eventual stalling of subduction and a sustained period (~7 to ~3 Ma) of fluid focussing underneath the Mount Olympus. Isotope compositions and uplift trajectories are consistent with a slab-derived fluid formed from dehydrating altered ocean crust and marine carbonates of the Cyprus slab (80:20) at >100 to <150°C. This harvested slab-derived fluid was focussed on the Mount Olympus region and pervasively serpentinised the Troodos Mantle Sequence at temperatures >150 to <300 °C, inducing up to 66 % serpentinisation. Mass balance calculations agree with such a scenario, assuming a fluid focusing factor of ~11.

- A third serpentinisation event is interpreted to occur with meteoric waters that had interacted and partially exchanged with the circum-Troodos submarine sediments that before uplift overlaid the ophiolite. Serpentinisation-induced uplift resulted in the further infiltration of meteoric water. Continued alteration of serpentine occurred

through progressive coupled deformation-alteration-recrystallisation processes manifested as a weak, incohesive, low density serpentinite breccias and gouge.

- Consequently, a progressive sequence of overprinting fluid-rock events is proposed for the Troodos Mantle Sequence, with up to 66 % of the serpentinisation budget derived from slab-derived fluids and up to 33 % by meteoric waters.

7.2.4 Physical properties of altered mantle rocks

- Serpentinisation hydration reactions result in significant changes to physical properties of mantle rocks. Some, but not all, of the observed changes can be explained by serpentinisation hydration reactions alone therefore additional reactions are required to account for the full reported spectrum of evolving mantle rock physical properties.

- Distinct differences in physical properties occur between the Olympus Diapir that is dominated by a serpentinisation style of serpentinisation hydration reactions and the completely serpentinised Artemis Diapir that shows evidence of extensive serpentine alteration through coupled deformation-alteration-recrystallisation processes. To explain this discrepancy, serpentine alteration has been proposed to manifest through coupled deformation-alteration-recrystallisation processes, evolving the physical properties of altering mantle rocks to lower bulk density, V_p, V_s, resistivity values, and higher porosity and permeability values.

- Compiled global mantle rock physical properties datasets show that variable proportions of serpentinisation hydration and serpentine alteration and carbonation induce significant changes in mantle rock physical properties that results in up to a ~47 % reduction in bulk density from 3,300 kg/m^3 to ~1,550 kg/m^3 and an increase in porosity from 0.1 up to 52 %.

- Serpentinisation hydration reactions result in negligible changes in porosity, but serpentine alteration induces increased porosities (up to 52 %). These contrasting characteristics suggest that during quasi-isochemical serpentinisation reactions, mass is conserved, but serpentine alteration interactions induce significant mass removal.

7.3 Further work

- Previous studies utilising novel stable isotope systems such as δ^{7}Li, δ^{34}S, and δ^{37}Cl have identified distinct serpentinisation episodes within serpentinised mantle rocks (Alt et al., 2012; Alt and Shanks, 2006; Barnes et al., 2009; Barnes and Sharp, 2006; Vils et al., 2009). Applying these additional novel isotope systems, in combination with the isotope data of this thesis, may provide further knowledge of the progressive overprinting serpentinisation events reflected in the Troodos Mantle Sequence rocks. In addition, novel barium isotope analyses have been determined and applied in understanding subduction zone systematics including sediment recycling within the mantle wedge (Nielsen et al., 2020, 2018). Consequently, barium isotope analyses of the Troodos Mantle Sequence may help elucidate the source of Ba in the altered mantle rocks of the Troodos ophiolite, which may fingerprint an origin from the Cyprus slab.

- Developing the *in situ* elemental mapping methodology with the eventual aim to produce *in situ* stable isotope maps.

- Apply the isotope equilibrium Bayesian inversion approach developed in this thesis to other isotope systems.

- Apply boron mass balance systematics outlined in this thesis to the Samail ophiolite, in order to elucidate if hydrothermal fluids penetrated the crust-mantle transition zone and pervasively serpentinised the mantle sequence. This could be facilitated through combining recently collected Boron isotope and concentration determinations from the ICDP Oman Drilling Project (Kelemen et al., 2020), previously published data (Yamaoka et al., 2012), and the Boron equilibrium model coupled with the Bayesian inversion engine.

Appendix A Boron equilibrium model

It is proposed that fractionation between the two B isotopes, ^{10}B and ^{11}B, is predominantly controlled by their relative portioning between the trigonal ($B(OH)_3$) and tetrahedral ($B(OH)_4^-$) species (e.g., Kowalski and Wunder, 2018). Fractionation of boron isotopes in seawater is typically expressed by the fractionation factor (Eq. A.1):

$$\alpha_{III-IV} = \frac{\frac{^{11}B}{^{10}B}trigonal}{\frac{^{11}B}{^{10}B}tetrahedral}$$

(A. 1)

α_{III-IV} ranges from ~1.004 at high temperatures to ~1.030 at low-temperatures, indicating an inverse relationship dependent on temperature. These characteristics result in the wide variation of boron isotope compositions observed in nature from -40 ‰ < $\delta^{11}B$ < +60 ‰, with $\delta^{11}B$ expressed through (Eq. A.2):

$$\delta^{11}\mathrm{B} = \left(\frac{\frac{^{11}B}{^{10}B}sample}{\frac{^{11}B}{^{10}B}SRM\ 951} - 1 \right) \cdot 1000$$

(A. 2)

The $\delta^{11}B$ values of phyllosilicate minerals can be calculated in equilibrium with a fluid if the distribution of borate and boric acid, pH, temperature, salinity, and pressure in the fluid are known. We use ab-initio calculated boron fractionation factors determined for phyllosilicate minerals, which provides temperature dependent fractionation factors for respective boron species in seawater and between fluid and minerals (Boschi et al., 2008; Liu and Tossell, 2005). The relative partitioning between boron species can be determined if the boron dissociation constant (pK_B) is known. In seawater, the relative partitioning between boron species stems from the acid-base equilibrium between boric acid and borate (Eq. A.3; Eq. A.4):

$$B(OH)_3 + H_2O \rightleftharpoons H^+ + B(OH)_4{}^-,$$

(A. 3)

$$K_B = \frac{H^+ \cdot B(OH)_4{}^-}{B(OH)_3}$$

(A. 4)

pK_B is a function of temperature, salinity, pH, and pressure, which can be calculated by the following equations (Dickson, 1990; Millero, 1995) (Eq. A.5; Eq. A.6; Eq. A.7):

$$K_B = exp\left[\frac{\left(-8966.9 - 2890.53 \cdot S^{\frac{1}{2}} - 77.942 \cdot S + 1.728 \cdot S^{\frac{3}{2}} - 0.0996 \cdot S^2\right)}{K} + 148.0248 + 137.1942 \cdot S^{\frac{1}{2}} + 1.62142 \cdot S + \left(-24.4344 + 25.085 \cdot S^{\frac{1}{2}} + 0.2474 \cdot S\right) \cdot \ln(K) + 0.053105 \cdot S^{1/2} \cdot K\right]$$

(A. 5)

$$P_{Factor} = \left(\frac{(29.48 - 0.1622 \cdot T + 0.002608 \cdot T^2)}{83.14472 \cdot K}\right) \cdot P + 0.5 \cdot \left(\frac{0.00284}{83.14472 \cdot K}\right) \cdot P^2$$

(A. 6)

$$pK_B = exp(lnK_B + P_{Factor})$$

(A. 7)

Where K is temperature in Kelvin, T is temperature in Celsius, S is salinity in g/kg, P is pressure in bars. As the above approach above is calculated for low temperature (0 to 45 °C) seawater, we use a contrasting approach in calculating the pK_B value of fluids at higher (>50°C) temperatures.

Experimentally derived boron dissociation constants (pK_B) at hydrothermal conditions (25 to 350 °C, 25 MPa) have recently been determined (Arcis et al., 2017). The pK_B of a fluid such as modified seawater at hydrothermal conditions can be calculated through the following (Eq. A.8):

$$pK_B = p_1 + \frac{p_2}{K} + p_3 \cdot log(K) + (p_4 + p_5 \cdot K) \cdot log\rho_{Water}$$

(A. 8)

Where the respective coefficients for parameter p are reported in Table A.1, K is temperature in Kelvin, and ρ_{Water} refers to the density of the solution. The properties of seawater (pressure, density, temperature) can be calculated using an equation of state (e.g., Knudsen, 1901; Millero, 2010), which is based on empirically derived equations from experimental studies. Experiential studies have recently measured the properties of seawater (Safarov et al., 2013, 2012, 2009) at high temperatures (up to 200°C), pressures (up to 140 MPa), and salinities (up to 55 g/kg), where the properties of seawater can be calculated through the following equations (Eq. A.9; Eq. A.10; Eq. A.11; Eq. A.12):

$$P = A^2 + B^8 + C^{12}$$

(A. 9)

$$A = \sum_{i=1}^{5} K^i \sum_{j=0}^{2} a_{ij} S^j$$

(A. 10)

$$B = \sum_{i=0}^{4} K^i \sum_{j=0}^{2} b_{ij} S^j$$

(A. 11)

$$C = \sum_{i=0}^{4} K^i \sum_{j=0}^{2} c_{ij} S^j$$

(A. 12)

Where P is pressure (MPa), and A, B, and C are respectively the density of seawater (g/cm^3), and S is salinity (g/kg). The coefficients of a_{ij}, b_{ij}, and c_{ij} are given in Table A.2. The reported uncertainty of water density using the fitted equations is 0.09 kg/m^3 (Safarov et al., 2013, 2012, 2009).

Once the relative partitioning between boron species is calculated, the boron isotopic composition of the borate and boric acid species in the fluid and the four-coordinated BO_4 structure in serpentine is calculated using the following equations (Boschi et al., 2008) extrapolated by fitting data provided by Liu and Tossell (2005), where K is temperature in Kelvin (Eq. A.13; Eq. A.14; Eq. A.15):

$$1000 \cdot Ln\alpha_{III_{Fluid}-IV_{Fluid}} = 7.2087 \cdot \left(\frac{1000}{K}\right) + 2.3467$$

(A. 13)

$$1000 \cdot Ln\alpha_{III_{Fluid}-IV_{Mineral}} = 13.43 \cdot \left(\frac{1000}{K}\right) + 4.7093$$

(A. 14)

$$1000 \cdot Ln\alpha_{IV_{Fluid}-IV_{Fluid}} = 5.0225 \cdot \left(\frac{1000}{K}\right) + 3.1553$$

(A. 15)

The boron isotopic compositions of the borate and boric acid species in the fluid at different pH and temperatures may be calculated using the following equations (Boschi et al., 2008; Pagani et al., 2005) (Eq. A.16; Eq. A.17; Eq. A.18; Eq. A.19):

$$R_{[B(OH)_4]^-} = R_{Fluid} \cdot \left(\frac{1 + \alpha_{IV-III} 10^{pK_B - pH}}{1 + 10^{pK_B - pH}}\right)$$

(A. 16)

$$R_{[B(OH)_3]} = \frac{R_{[B(OH)_4]^-}}{\alpha_{IV-III}}$$

(A. 17)

$$\alpha_{IV-III} = \frac{1}{\alpha_{III-IV}}$$

(A. 18)

$$R_{Fluid} = \left(\left(\frac{\delta^{11}B_{Fluid}}{1000}\right) + 1\right) \cdot \frac{^{11}B}{^{10}B} SRM951$$

(A. 19)

The $^{11}B/^{10}B$ ratios are converted to $\delta^{11}B$ notation by the following equations, where n is 2 (Eq. A.20; Eq. A.21; Eq. A.22):

$$\delta^{11}B_{Mineral\,(1)} = \left(\frac{\left(1000 + \delta^{11}B_{[B(OH)_3]}\right)}{\alpha_{III_{Fluid}-IV_{Mineral}}}\right) - 1000$$

(A. 20)

$$\delta^{11}B_{Mineral\,(2)} = \left(\frac{\left(1000 + \delta^{11}B_{[B(OH)_4]^-}\right)}{\alpha_{IV_{Fluid}-IV_{Mineral}}}\right) - 1000$$

(A. 21)

$$\delta^{11}B_{Mineral\,(Mean)} = \frac{\sum_{i=1}^{n}\delta^{11}B_i}{n}$$

(A. 22)

The boron equilibrium model described above requires knowledge of multiple physical parameters including temperature, salinity, pressure, water density, and pH that are often poorly constrained in natural systems (e.g., Palmer, 1996). To constrain the uncertainty and the relative sensitivities of the underlying physical parameters that yield a calculated δ^{11}B rock value in equilibrium with a fluid, we combine our boron equilibrium model with a novel Bayesian Inversion approach, which leverages the UltraNest engine (Buchner, 2014, 2017, 2021a). This package implements the Monte Carlo technique Nested Sampling (Skilling, 2004) to explore parameter space, allowing Bayesian Inference on arbitrary user defined likelihoods, constructing posterior probability distributions providing parameter constraints of the data (Buchner, 2021a). The UltraNest engine employs the MLFriends algorithm, where a fixed size of live points (i.e., parameter vectors; n = 1600) are drawn randomly from prior probability distributions and are then clustered into ellipsoids (Buchner, 2021b). The shape of the ellipsoid is determined by the Mahalanobis distance and the ellipsoid size is determined by cross-validation (*i.e.,* bootstrapping; Buchner, 2021a). Inside the ellipsoid, new points are sampled from the prior and the worst fitting point is removed, resulting in the live point sampled volume shrinking by a constant factor (Buchner, 2021b, 2021a). Nested sampling iterates and records the likelihood as the sampled volume decreases, once the remaining volume fails to contribute any probability mass (*i.e.,* when the live points become unimportant), the exploration of the prior distribution is terminated and the volume of the removed points reflect the posterior samples (Buchner, 2021a, 2021b, 2014). This method provides a powerful approach in estimating the parameters of a forward model as it is theoretically justified and free of tuning parameters (Buchner, 2021a, 2014).

Table A.1. Coefficients for Eq. A.8.

	P_1	P_2	P_3	P_4	P_5
Arcis et al., 2017	-29.2076	3359.88	9.17470	10.2855	-0.0160357

Table A.2. Coefficients for Eq. A.10; Eq. A.11; Eq. A.12.

Safarov et al., 2012	***ai***		***bi***		***ci***
a10	1.68E+01	b00	1.78E+03	c00	-1.20E+03
a11	-1.41E-02	b01	-8.45E+00	c01	8.49E+00
a12	2.47E-04	b02	-2.03E-02	c02	0.00E+00
a20	-1.75E-01	b10	-2.40E+01	c10	1.18E+01
a21	3.34E-05	b11	6.16E-02	c11	-5.71E-02
a22	-1.02E-06	b12	0.00E+00	c12	0.00E+00
a30	5.91E-04	b20	1.24E-01	c20	-4.02E-02
a31	0.00E+00	b21	-1.15E-04	c21	9.59E-05
a32	0.00E+00	b22	0.00E+00	c22	1.85E-07
a40	-8.43E-07	b30	-2.31E-04	c30	4.18E-05
a41	0.00E+00	b31	0.00E+00	c31	0.00E+00
a42	4.82E-12	b32	0.00E+00	c32	0.00E+00
a50	4.45E-10	b40	1.42E-07	c40	0.00E+00
a51	-3.47E-14	b41	0.00E+00	c41	0.00E+00
a52	-5.35E-15	b42	5.34E-13	c42	-9.87E-13

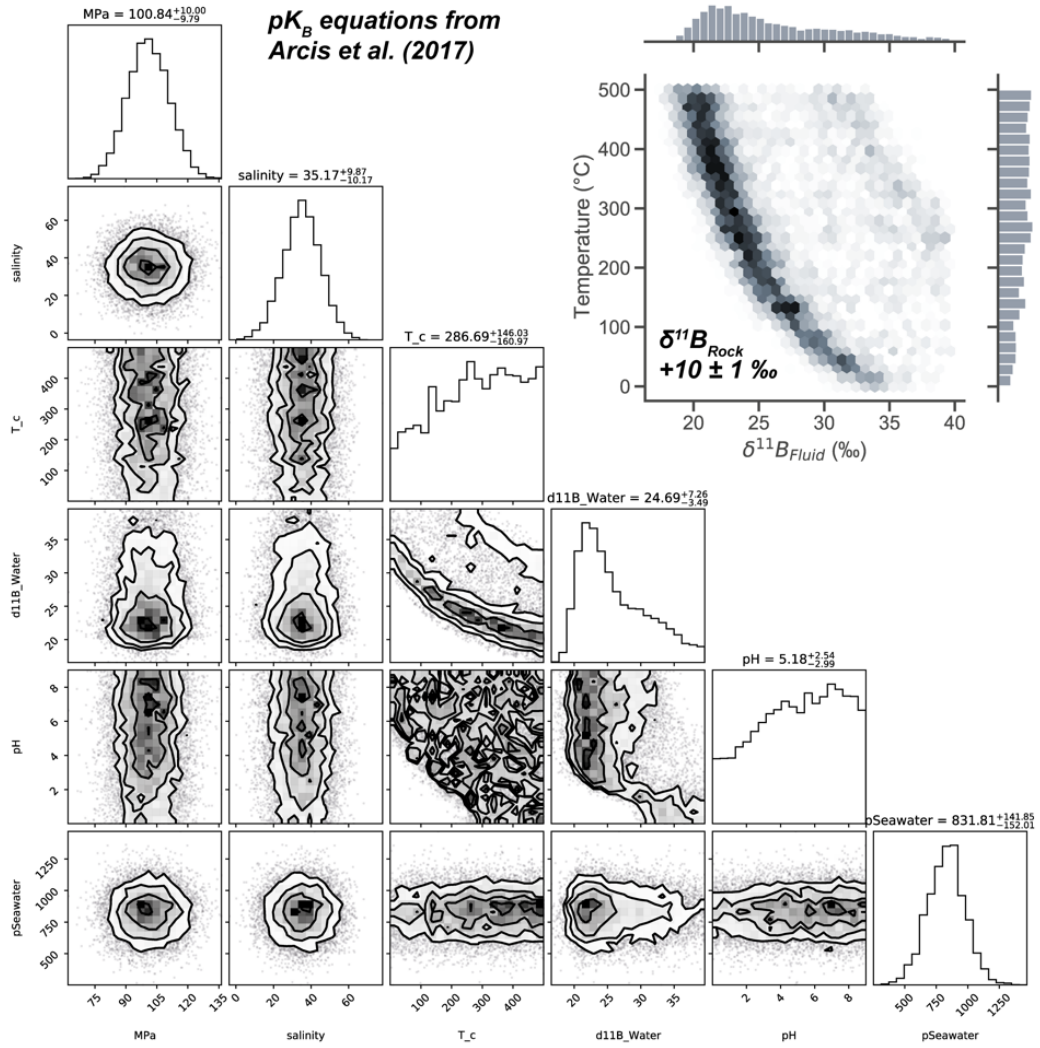

Fig A.1: Posterior probability output of a hydrothermal ocean crust-seawater exchange scenario using priors from Table 5.12.

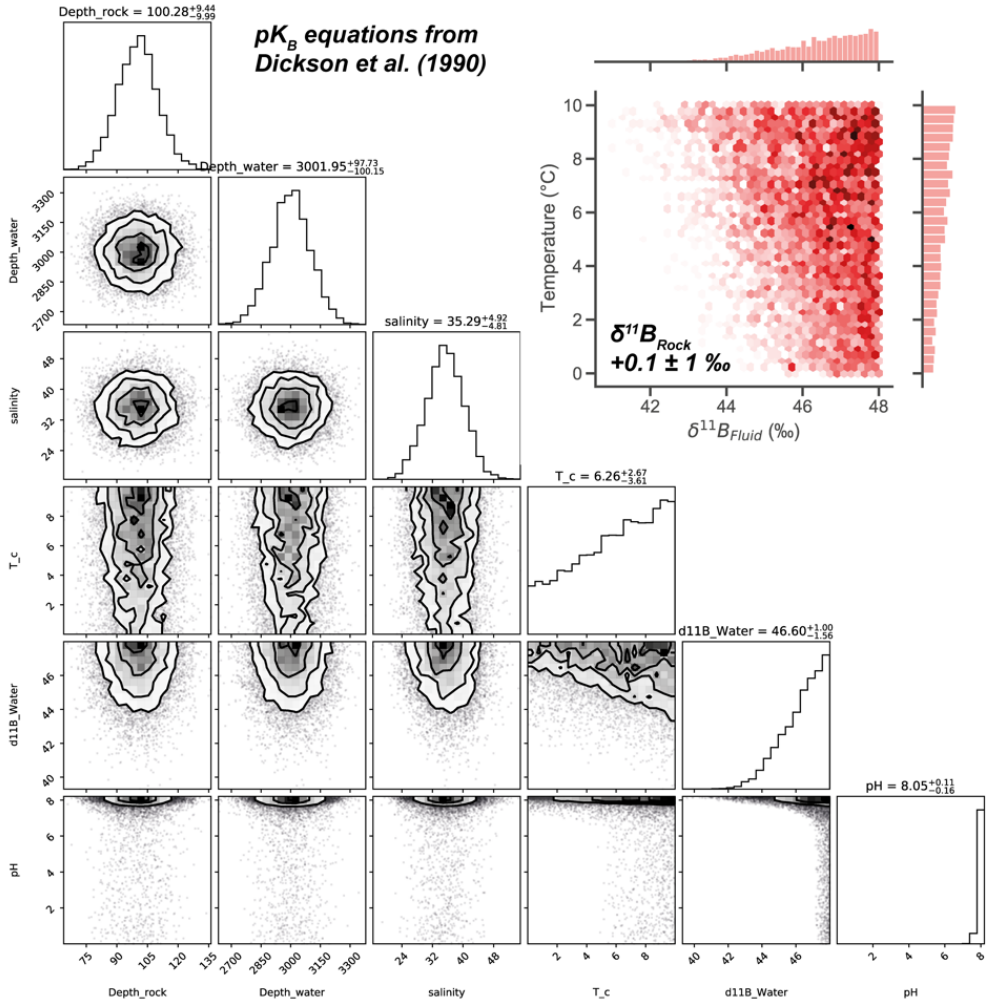

Fig A.2: Posterior probability output for a low temperature basalt-seawater exchange using priors from Table 5.13.

A.1.1 Model output with synthetic data

To validate the approach outlined above, I apply the boron equilibrium model coupled with a Bayesian Inversion engine to a high temperature fluid-rock scenario and a low-temperature basalt-seawater exchange scenario. Application of this novel modelling approach provides constraints on the underlying uncertainties of physical parameters required to calculate a δ^{11}B rock isotope value in equilibrium with a fluid (Fig. A.1). The high temperature (pK_B calculations at temperatures >50 °C; Fig. A.1; Table 5.12; Arcis et al., 2017) model calculations indicate that an ocean crustal rock in equilibrium with hydrothermal fluid at conditions ranging between 200 and 500 °C and pressures of 100 MPa, where the majority of B is located in phyllosilicate minerals with a δ^{11}B value of 10 ± 1 ‰, would require a $\delta^{11}B_{Fluid}$ isotope value of $+24.69^{+7.26}_{-3.49}$ ‰ (1σ). At such conditions, pK_B is calculated using the equations of Arcis et al. (2017), as outlined above, producing pK_B values varying between ~1.8 and ~2.2. In contrast for seawater (pH ~8) pK_B is typically ~8.6 (Dickson, 1990; Rae, 2018). Such low pK_B values of ~1.8 to ~2.2 reflect a fluid dominated by borate, resulting in less fractionation relative to a fluid dominated by boric acid (Fig. A.1). Under these 'hydrothermal conditions' (Arcis et al., 2017), if the pH of the fluid during isotopic exchange is significantly greater than the pK_B, the pH of the fluid is generally insensitive in determining the extent of mineral-fluid fractionation (Fig. A.1). In addition, fluid density, pressure, and salinity also appear to have a minimal effect on $\Delta^{11}B_{Mineral\text{-}Fluid}$ fractionation (Fig. A.1; Table 5.12). By contrast, temperature yields a significant control on $\Delta^{11}B_{Mineral\text{-}Fluid}$ fractionation at the conditions presented (Table 5.12; Fig. A.1) with the model estimating a primarily temperature controlled $\Delta^{11}B_{Mineral\text{-}Fluid}$ value of ~$-14.7^{+7.3}_{-3.5}$ ‰. Previous experimental studies proposed illite/smectite $\Delta^{11}B_{Mineral\text{-}Fluid}$ values of -16 ‰ and -13 ‰ at 300 and 350 °C respectively at 100 MPa and pH = 6 (Williams et al., 2001). This suggests that the boron equilibrium model and Bayesian Inversion engine presented here, yields calculated $\Delta^{11}B_{Mineral\text{-}Fluid}$ factors consistent with experimentally derived boron fractionation factors of similar mineral types at similar conditions. In addition, the estimated $\delta^{11}B_{Fluid}$ value of $+24.7^{+7.3}_{-3.5}$ ‰ (1σ), is consistent with previously measured boron isotopic composition of hydrothermal fluids sampled from high-temperature vent sites (James et al., 1995; Palmer, 1996; Spivack and Edmond, 1987; You et al., 1994).

In contrast to the high temperature model, the low temperature (<50 °C; Table 5.13; Fig. A.2; Dickson, 1990) model indicates that a seafloor basalt altered by seawater with a measured rock δ^{11}B isotope value of 0.1 ± 1 ‰ (e.g., Spivack and Edmond, 1987) in equilibrium with seawater at temperatures ranging between 1 and 10 °C would require a $\delta^{11}B_{Fluid}$ isotope value of $+46.6^{+1}_{-1.6}$ ‰. The boron isotopic composition of seawater is

39.61 ‰ (Foster et al., 2010), indicating that seawater-basalt boron exchange occurred with a modified seawater yielding δ^{11}B values higher than seawater. Such modification is proposed to occur during low temperature seawater-boron exchange as B is removed from seawater and sequestered into low temperature minerals of altered basalts, modifying the boron isotopic composition of seawater to heavier isotopic values (James et al., 1995; Spivack and Edmond, 1987). As the results from the boron equilibrium model coupled with a Bayesian Inversion engine yield reasonable outputs that are consistent with empirical studies, we propose that the modelling approach outlined above is valid.

Appendix B

Check for updates

AGU ADVANCING EARTH AND SPACE SCIENCE

JGR Solid Earth

RESEARCH ARTICLE
10.1029/2020JB021079

Special Section:
Ophiolites and Oceanic Lithosphere, with a focus on the Samail ophiolite in Oman

Uplift and Exposure of Serpentinized Massifs: Modeling Differential Serpentinite Diapirism and Exhumation of the Troodos Mantle Sequence, Cyprus

Aled D. Evans[1], Damon A. H. Teagle[1], Dave Craw[2], Timothy J. Henstock[1], and Ismael Himar Falcon-Suarez[3]

[1]School of Ocean and Earth Science, National Oceanography Centre Southampton, University of Southampton, Southampton, UK, [2]Department of Geology, University of Otago, Dunedin, New Zealand, [3]Marine Geoscience, National Oceanography Centre, Southampton, UK

Abstract Serpentinized mantle peridotites form prominent mountains, including the highest elevations of the Troodos ophiolite in Cyprus (Mount Olympus, 1,952 m), but to date, only qualitative mechanisms have been proposed to explain the uplift of mantle rocks to high altitudes. Serpentinization reactions between mantle rocks and water result in profound changes to the rheology and physical properties of peridotites including significant density reduction (~900 kg/m^3). Field observations, density measurements, and isostatic uplift and erosional modeling provide new constraints on the contribution of serpentinization to the uplift of the Troodos Mantle Sequence. Different serpentinization styles have resulted in two distinct serpentinite domains with contrasting densities. Our modeling shows that the Troodos Mountains can form within the geologically constrained uplift time frame (~5.5 Myr) exclusively through partial serpentinization reactions. We interpret the serpentinite domains as two nested diapirs that formed due to different extents of serpentinization and density reduction. Differential uplift and exhumation have decoupled the two serpentinite diapirs from the originally overlying ocean crustal rocks. Once at high altitudes the incursion of meteoric water reinforced coupled deformation-alteration-recrystallization processes in the shallow subsurface producing a localized low density completely serpentinized diapir. A second decoupling between the contrasting serpentinite diapirs results in localized differential uplift and exhumation, extruding deep materials to the east of Mount Olympus. Application of our modeling to other serpentinite massifs (e.g., St. Peter and St. Paul Rocks, New Idria, California) highlights the contribution of isostasy to the uplift of serpentinized massifs.

Key Points:

- Coupled isostatic uplift-erosion modeling explains the outcrop pattern of the Troodos mountains
- Contrasting extents of serpentinization within the Mantle Sequence induced differential exhumation between two serpentinite domains
- Uplifted serpentinite massifs worldwide, reflect the relative contributions of serpentinization-induced isostasy and tectonics

Supporting Information:

Supporting Information may be found in the online version of this article.

Correspondence to:

A. D. Evans,
A.Evans@southampton.ac.uk

Citation:

Evans, A. D., Teagle, D. A. H., Craw, D., Henstock, T. J., & Falcon-Suarez, I. H. (2021). Uplift and exposure of serpentinized massifs: Modeling differential serpentinite diapirism and exhumation of the Troodos Mantle Sequence, Cyprus. *Journal of Geophysical Research: Solid Earth*, *126*, e2020JB021079. https://doi.org/10.1029/2020JB021079

Received 5 OCT 2020
Accepted 18 MAY 2021

© 2021. The Authors.
This is an open access article under the terms of the Creative Commons Attribution License, which permits use, distribution and reproduction in any medium, provided the original work is properly cited.

1. Introduction

Partially serpentinized mantle rocks form prominent topographic features in numerous locations on Earth, both on land and in the oceans, for example, Ronda Massif, Spain, Dun Mountain, New Zealand, and the Atlantis Massif on the Mid-Atlantic Ridge. Although some of these exposures can be explained by dynamic tectonics, other features require different explanations.

Serpentinization reactions between water and mantle rocks dramatically change high density (3,300 kg/m^3), relatively strong, anhydrous, low permeability, mantle peridotites into low density (2,400 kg/m^3), weak serpentinites, inducing up to 40% volume expansion (Macdonald & Fyfe, 1985; Toft et al., 1990). The reduction in bulk density results in isostatic uplift, that together with serpentinite diapirism, has been proposed to have led to the exposure of serpentinized mantle peridotites at moderate to high altitudes on land in the Troodos Massif, Cyprus (e.g., Gass, 1977; Gass & Masson-Smith, 1963; Moores & Vine, 1971) and the New Idria Massif, California (e.g., Coleman, 1996; Tsujimori et al., 2007), and in the oceans forming the emergent St. Peter and St. Paul Rocks (e.g., Campos et al., 2010).

Here, we investigate the uplift and exposure of the Troodos Massif of Cyprus and combine field observations with new density measurements and isostatic and differential erosion rate calculations to test whether serpentinization can form the Troodos Massif. We document the contrasting manifestations of serpentinization in the exhumed Mantle Sequence and calculate whether the isostatic consequences of the density and rheological differences can develop the distinctive but hitherto poorly explained outcrop pattern of this

Journal of Geophysical Research: Solid Earth 10.1029/2020JB021079

iconic geological terrane. We further apply our mechanistic uplift model to other settings and demonstrate the universality of our approach.

2. Mantle Peridotite Massifs and Serpentinite Diapirism

Although mantle peridotite is the most common rock type on Earth, surface exposures of mantle rocks are relatively rare and predominantly strongly to completely altered by serpentinization reactions (e.g., Kelemen et al., 2011). Major outcrops of mantle peridotites are generally limited to ophiolites and oceanic core complexes. A component of isostasy is an inevitable consequence of serpentinization reactions, but serpentinite diapirism is not ubiquitously invoked in every manifestation of serpentinization. It is unclear whether serpentinite diapirism is overlooked or if subsequent deformation has obliterated geological evidence (e.g., Gass, 1977). Previously reported occurrences of serpentinite diapirism indicate a diverse spectrum of diapiric modes rather than a single mechanism. Here, we briefly outline some previously reported examples of serpentinite diapirism that represent this spectrum of occurrence.

2.1. Examples of Serpentinite Diapirism Associated With Isostatic Uplift

2.1.1. Partially Serpentinized Serpentinite Diapirs

Isolated mantle peridotite massifs have long been associated with variable extents of serpentinization (e.g., Darwin, 1835), and their differential uplift relative to the surrounding seafloor has been proposed to occur due to the lower density of serpentine (e.g., Boillot et al., 1980; Bonatti, 1976; Hess, 1954). Isostatic uplift as a result of density-reduction from partial serpentinization reactions, in combination with transpressional tectonics, has been previously invoked to explain isolated mantle peridotite massifs along oceanic fracture zones (e.g., Bonatti, 1978; Campos et al., 2010; Kil et al., 2010). For example, associated with the St. Paul and St. Peter Fracture Zones (0.6°N and 2.5°N) in the equatorial Atlantic, the St. Peter and St. Paul Rocks archipelago (Campos et al., 2010) is primarily composed of variably serpentinized mylonitized mantle peridotite (e.g., Campos et al., 2005, 2010; Hekinian et al., 2000; Melson et al., 1972). These islands are only the emergent portion of the much larger (~90 × ~20 km^2 at 3,000 m bsl) submerged variably serpentinized North Ridge mantle peridotite massif that rises from abyssal depths (~4,000 mbsl, Campos et al., 2010; Hekinian et al., 2000; Maia et al., 2016). Radiometric dating suggests that the archipelago only became emergent in the past ~6,500 years, with uplift on-going at a minimum uplift rate of >1.5 mm/yr (Campos et al., 2010).

2.1.2. Completely Serpentinized Serpentinite Diapirs

Discreet occurrences of completely serpentinized mantle peridotites have previously been interpreted as distinct serpentinite diapirs. A key characteristic and composition of these surficial serpentinite extrusions is a low-density, mélange-like serpentinite breccia assemblage, where strongly altered and completely serpentinized peridotite clasts are hosted in a finely comminuted serpentinite gouge. These easily erodible materials are commonly associated with elevated topography, and consequently high uplift rates are often inferred to maintain the high relief of these easily erodible serpentinite extrusions. Examples that occur near the San Andreas Fault, California include the ~5 km^2 1,027-m-high Table Mountain (Dickinson, 1966; Moore & Rymer, 2007) and the ~100 km^2 New Idria Massif (1,605 m, Coleman, 1996; Tsujimori et al., 2007). Both features are interpreted as completely serpentinized serpentinite diapirs. A rapid uplift rate of ~4 mm/yr is estimated from the relative displacement of sedimentary indicators (Coleman, 1996). This rapid uplift rate is balanced by an inferred high erosion rate of ~4 mm/yr that indicates ~17 km^3 has been removed from the New Idria serpentinite diapir (Coleman, 1996; Mumpton & Thompson, 1975). The rapid uplift rate (~4 mm/yr) is significantly greater than the estimated regional uplift rate for the Coast Ranges (~1 mm/yr; Page et al., 1998), implying differential uplift and exhumation between the New Idria serpentinite diapir and surrounding area simultaneously producing and maintaining ~1,000 m of elevated relief.

2.2. Examples of Serpentinite Diapirism Not Associated With Isostatic Uplift

The large (~30 km in diameter, ~2 km high) submerged serpentinite mud volcanoes of the Mariana forearc have previously been referred to as examples of serpentinite diapirism (e.g., Fryer et al., 1985, 1992; Ishii et al., 1992). Although these features contain clasts of strongly serpentinized mantle peridotite and

metabasalts, some with sub-blueschist assemblages, these mud volcanoes are predominantly built from multiple effusions of unconsolidated serpentinite muds. These muds are, inferred to be produced by progressive interactions between serpentinized peridotites from the mantle wedge of the upper plate and subducting slab-derived fluids. Over-pressured mud-rich fluids then rise up steeply dipping faults before episodically erupting onto the seafloor (e.g., Fryer, 2012; Mottl et al., 2004). Fluid mass transfer resulting in multiple episodes of mud-eruption have built up these serpentinite seamounts (Fryer, 2012) as opposed to isostatic responses resulting directly from serpentinization reactions. These mud volcanoes therefore differ from other completely serpentinized peridotite diapirs as they are not associated with surface uplift.

3. The Troodos Massif

Here, we investigate the uplift of the Troodos Massif, one of the world's best-preserved, least deformed, and most complete ophiolites (Gass, 1968). The Troodos mountains expose ocean crust and upper mantle rocks that formed ~90–92 Ma at some form of supra-subduction zone spreading ridge in the Neo-Tethyan Ocean (Moores & Vine, 1971; Moores et al., 1984; Mukasa & Ludden, 1987; Pearce et al., 1984). The ~90-km-long and ~30-km-wide ophiolitic sequence crops out as an elliptical bullseye-patterned welt, with the stratigraphically deepest rocks, partially serpentinized mantle peridotites, forming the highest elevation of the Troodos mountains (Mount Olympus, 1,952 m asl). This Mantle Sequence is surrounded by an eroded anticlinal dome comprising concentric annuli of gabbroic and ultramafic cumulate rocks, sheeted dikes, lavas, and submarine sediments that crop out at progressively lower altitudes around the slopes of the massif (Figure 1a).

Unlike other ophiolites, such as the Samail ophiolite of Oman (e.g., Hacker et al., 1996; Searle & Cox, 1999), the Troodos ophiolite was not obducted onto a continental margin soon after its formation and there is no metamorphic sole to the massif. In contrast, significant uplift of the Troodos ophiolite has occurred since 5.5 Ma (e.g., McCallum, 1989; Poole & Robertson, 1991, 1998; Robertson, 1977; Rouchy et al., 2001; Stow et al., 1995) and it is qualitatively inferred that the exposure of the Troodos massif results from the serpentinization of peridotites from the mantle below the ocean crustal rocks of the ophiolite (Gass & Masson-Smith, 1963; Moores & Vine, 1971; Robertson, 1977, 1998).

The initial serpentinization of the Troodos Mantle Sequence is commonly invoked to have occurred due to the collision of the Eratosthenes Seamount continental block with the Cyprean trench to the south of Cyprus that has stalled the northward subduction of the African plate (Ergün et al., 2005; Robertson, 1998). It is proposed that this has resulted in the focused upwelling into the overlying mantle wedge of hydrous fluids generated by the dewatering of partially subducted marine sediments and ocean lithosphere, inducing and focusing serpentinite diapirism onto the Mount Olympus region (Gass, 1977; Moores & Vine, 1971; Robertson, 1977, 1998). The best estimates for the dip of the subducting plate in the Cyprean arc are between ~13° and ~33° (Feld et al., 2017; Mackenzie et al., 2006) with the top of the down-going slab lying between ~13 and ~40 km below Mount Olympus. Oxygen and hydrogen isotopic measurements of the Troodos Mantle Sequence indicate that discrete portions of the Mantle Sequence have interacted with meteoric and "oceanic-like" waters (Magaritz & Taylor, 1974; Nuriel et al., 2009), suggesting the progressive and episodic serpentinization of the Mantle Sequence is likely on-going.

Other mechanisms have also been suggested to explain the geometry of the Troodos Massif including Cretaceous ridge-related serpentine diapirism (Schuiling, 2011) and Cretaceous ridge-related detachment faulting (Nuriel et al., 2009). Recent regional structural analysis downplays the importance of serpentinization and suggests uplift can be generated solely by Miocene to present-day convergence across the Cyprean subduction zone (Ring & Pantazides, 2019).

3.1. The Troodos Massif Mantle Sequence

The highest part of the Troodos Massif (Figure 1a) comprises a ~200 km^2 central region at moderate altitude (>1,200 m) comprising mantle peridotite and surrounding gabbro, characterized by gentle hillslopes and relatively wide, shallow valleys, although the boundary between the gabbros and peridotites is commonly faulted with steep relief in places. In contrast, the surrounding Sheeted Dike Complex is exposed in steep-sided ridges up to ~1,000 m altitude that are deeply incised, with the encompassing Extrusive

Journal of Geophysical Research: Solid Earth 10.1029/2020JB021079

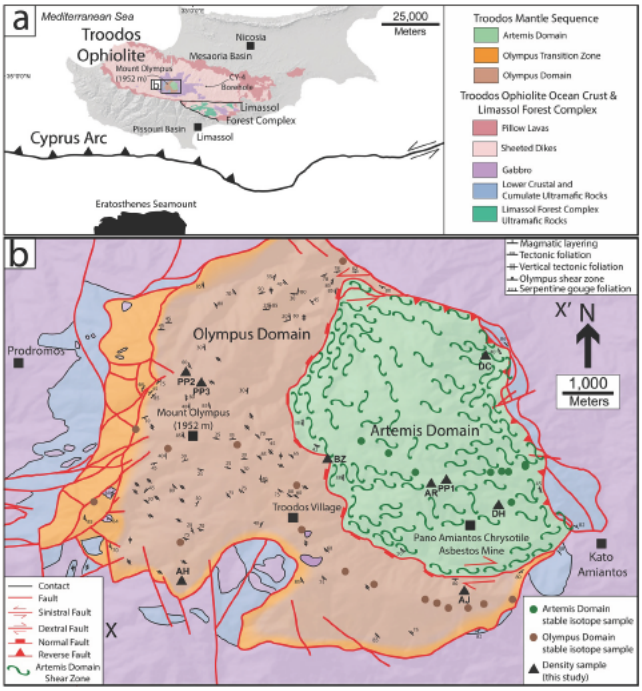

Figure 1. (a) Geological map of the Troodos ophiolite with the bullseye geometry of the Mantle Sequence highlighted along with the Limassol Forest Complex terrane, the Cyprus arc, and northernmost portion of the Eratosthenes Seamount. (b) Geological map of the Troodos Mantle Sequence, adapted and updated from Wilson (1959). *X*–*X*′ shows line of cross-section (see Supporting Information for entire line of cross-section; Figure 2). Density sample locations shown as are sample locations for published oxygen and hydrogen stable isotope analyses by Magaritz and Taylor (1974), Heaton (1976), and Nuriel et al. (2009).

Sequences and circum-Troodos sediments occurring at lower altitudes in gently dipping outcrops best exposed in river canyons.

The Mantle Sequence of the Troodos Massif can be subdivided into two discrete regions (Figure 1b): (a) an arcuate western zone of partially (~50%–~70%) serpentinized tectonized harzburgites with minor dunites, referred to here as the Olympus domain, juxtaposed by faults against (b) an eastern ~5 km diameter, subcircular region of completely serpentinized peridotite blocks in a sheared matrix of serpentine breccia (Figure 2), here named the Artemis domain. The Artemis domain rocks have previously been referred to as the Smash zone (Wilson, 1959) or The Serpentine (Gass & Masson-Smith, 1963), or the remobilized serpentinite plug (Moores & Vine, 1971).

The Cr-number (Cr/Cr + Al) of chrome spinels is a commonly used parameter to identify the tectonic setting of residual mantle peridotites (e.g., Arai, 1994; Dick & Bullen, 1984; Parkinson & Pearce, 1998), contrasting Cr-numbers of Troodos Mantle Sequence chrome spinel (Batanova & Sobolev, 2000) indicate that the completely serpentinized peridotites of the Artemis domain originate from a region of fertile mantle

Journal of Geophysical Research: Solid Earth 10.1029/2020JB021079

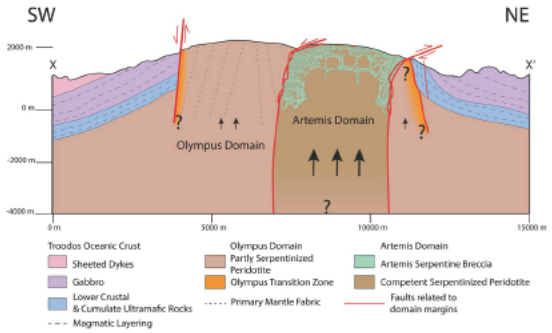

Figure 2. Geological cross-section of the Troodos Mantle Sequence and associated ocean crustal rocks.

lherzolite (Cr# 0.22–0.28) that has been exhumed from depth and juxtaposed against the refractory shallow mantle harzburgites (Cr# 0.51–0.70) of the Olympus domain.

A regional (200 × 100 km^2) oblong positive Bouguer gravity anomaly between +100 and +250 mGal coincides with the Troodos ophiolite (Figure 3a; Gass & Masson-Smith, 1963). This regional positive anomaly generally decreases from west to east across the ophiolite (Figure 3b), with smaller localized anomalies superimposed onto this regional trend (Figure 3a). The variably serpentinized outcrops of the Troodos Mantle Sequence spatially coincide with a large negative gravity anomaly relative to the regional trend (Figure 3a; 80–120 mGal; Gass & Masson-Smith, 1963; Shelton, 1993). This superimposed negative gravity anomaly is broadly centered on the abandoned chrysotile asbestos mine at Pano Amiantos (Figure 1b;

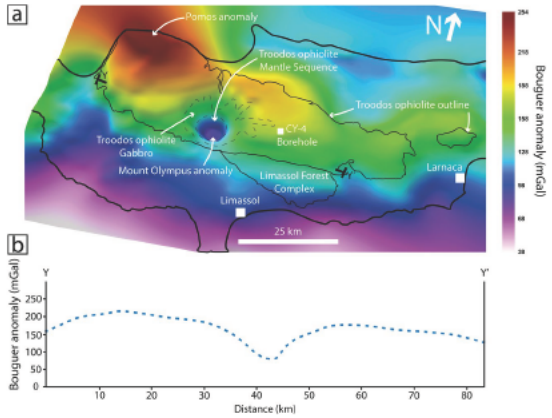

Figure 3. (a) 3D gravity map covering Cyprus, data sourced from Gass and Masson-Smith (1963). (b) Gravity cross-section along line *Y*–*Y*′ again using data of Gass and Masson-Smith (1963), cross-section highlights the asymmetric nature of the Mount Olympus anomaly with the gravity low centered broadly on the former chrysotile asbestos mine of Pano Amiantos.

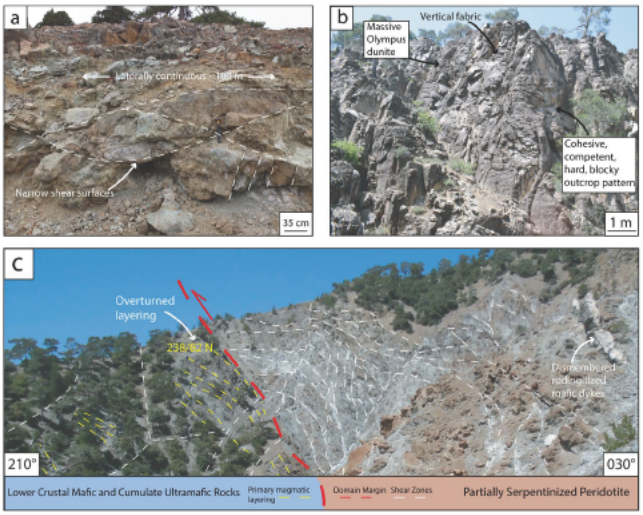

Figure 4. (a) Typical outcrop of partly serpentinized mantle peridotites from the Olympus domain with near horizontal, narrow shear zones orientated 120° apart, that form laterally continuous ~100 m lensoidal geometries. (b) Massive Olympus domain dunite displaying the common hard, blocky, cohesive, partially serpentinized mantle peridotite outcrop pattern. (c) Olympus domain outer boundary highlighting a zone of intensely deformed peridotite and intercalated blocks of overturned layered gabbro.

Gass & Masson-Smith, 1963; Shelton, 1993). In published studies, this negative gravity anomaly is best represented as a vertical, cylindrical body of lower density serpentinized peridotite (2,670 kg/m^3) extending ~11 km deep, within a higher density background of unserpentinized mantle (3,300 kg/m^3; Gass & Masson-Smith, 1963; Shelton, 1993).

3.2. Structure of the Olympus Domain

The rocks of the Olympus domain exhibit a steeply dipping ~NW-SE orientated primary tectonic fabric of elongated orthopyroxene grains, in some places isoclinally folded, that is interpreted as Cretaceous ridge-related high-temperature deformation (Moores & Vine, 1971). Overlaying this primary tectonic foliation are conjugate brittle-plastic shear zones (following Fossen & Cavalcante, 2017; Ramsay, 1980), which in the Olympus domain are thin, localized shear surfaces (~5 cm wide) and laterally continuous for ~100 m (Figure 4a). These shear surfaces intersect and are orientated ~120° to each other (Figure 4a), forming generally undeformed elongated lozenges of partially serpentinized Olympus domain mantle peridotite encompassed by shear surfaces (Figure 4a). Surrounding the summit region of Mount Olympus, conjugate shear zones are orientated at low dip angles and in general progressively steepen away from the summit region to moderate-high dip angles at the margins of the Olympus domain (Figures 1b and 4b). Fracturing at the outcrop scale is minor and manifests as joints and along shear surfaces (Figures 4a and 4b). The Olympus domain displays a distinctive, cohesive, blocky, and competent outcrop pattern (Figure 4b).

There is a complex marginal boundary between the Olympus domain and the encircling plutonic crustal rocks (Figure 4c), which we term here as the Olympus Transition Zone. This zone is of variable width, up to ~1 km at its widest extent, and comprises a generalized transition from predominantly lower ocean crustal cumulate rocks intercalated with localized bodies of dunite and pyroxenite to predominantly mantle rocks

of the Olympus domain, principally harzburgites and dunites with intercalated localized bodies of lower ocean crustal mafic and ultramafic cumulate rocks. Deformation is distributed throughout the Olympus Transition Zone but is mostly localized to an encircling array of steeply dipping interconnected fault-zones that isolate and juxtapose regions of undeformed and massive partially serpentinized bodies with moderately to steeply dipping (60°–>90°) layered gabbros that in places are locally overturned (Figure 4c). This structural style occurs across differing scales from outcrop to hillslope (Figure 1b; see Supporting Information), consequently producing a complex structural unit that anastomoses irregularly around the arcuate periphery of the Olympus domain (Figure 1b). Although on the western slopes of Mount Olympus, some rare, small, fault-isolated regions preserve igneous boundaries between cumulate to mantle rocks, at a larger scale faults always separate the main Olympus domain from the continuous sequences of ultramafic cumulate rocks and gabbros of the lower Troodos ocean crust (Wilson, 1959).

3.3. Structure of the Artemis Domain

To the east of Mount Olympus is the sub-circular Artemis domain that comprises heterogenous assemblages of highly serpentinized blocks and clasts and serpentine gouge, which is juxtaposed by faults against the massive peridotites of the Olympus domain (Figure 5a). The Artemis domain is generally at lower altitude than (>1,200–~1,700 m) the Olympus domain (>1,200–1,952 m) (Figure 5a).

Within the Artemis domain, coherent blocks and clasts (>100 m to dm) are completely serpentinized and occur within a friable matrix of highly comminuted serpentine cataclasite and serpentine clay gouge. In some zones, the serpentine gouges have developed a well-defined secondary foliation fabric (Figure 5b) that anastomoses around the more competent clasts (Figures 5c and 5d). Within the more competent clasts, fibrous asbestiform chrysotile and crack-seal serpentine veining are common on scales from 0.5 mm to ~10 m, forming abundant mutually cross-cutting orthogonal, concentric, and oblique vein sets (Figure 5c). In rare occurrences, serpentine veins cross-cut the Artemis serpentine gouge. Variable proportions and extents of recrystallization occur throughout the Artemis domain (e.g., Figure 5b), with the greatest concentration along localized zones of high strain.

Overall, the Artemis domain comprises an approximately 50:50 mixture of serpentine breccia and gouge to competent serpentinized clasts, although the relative proportions are spatially variable (Figure 5d). The highest proportion of serpentine breccia-gouge to block-clasts is around the subcircular margin of the Artemis domain (~80:20 respectively) with localized regions of 100% recrystallized serpentine gouge (Figure 5b). These areas typically exhibit poorly consolidated steep slopes with active mass wasting and gravity-driven slumping in deeply incised valleys around the periphery of the Artemis domain (Figure 5e).

In contrast, in the central zone of the Artemis domain, the ratio of blocks-clasts to serpentine breccia-gouge is reversed, with large (>100 m) blocks of strongly altered peridotite separated by complex networks of relatively narrow (~10 m) serpentine breccia (Figure 2).

4. Contrasting Properties Within the Troodos Mantle Sequence

4.1. Contrasting Mineralogy

The serpentinization style within the Olympus domain reflects the partial transformation (~50%–~70%) of primary olivine and orthopyroxene to serpentine through serpentinization hydration reactions (Figure 6a, Table 1). In contrast, the completely serpentinized materials of the Artemis domain reflect multiple and potentially on-going episodes of deformation, alteration, and recrystallization (Figure 6b). Primary and alteration bulk assemblages are estimated from thin section and outcrop observations. Distinguishing between different serpentine polymorphs is challenging (Rooney et al., 2018, and references therein) so consequently we describe them all simply as serpentine, except for fibrous chrysotile and rare occurrences of "splintery" antigorite.

The rocks of the Olympus domain are predominantly tectonized harzburgites originally composed of olivine, orthopyroxene, chromite, and minor interstitial diopside, with subsidiary dunites, and some primary orthopyroxene veins. These rocks are partially to completely altered to olivine-serpentine mesh-textures

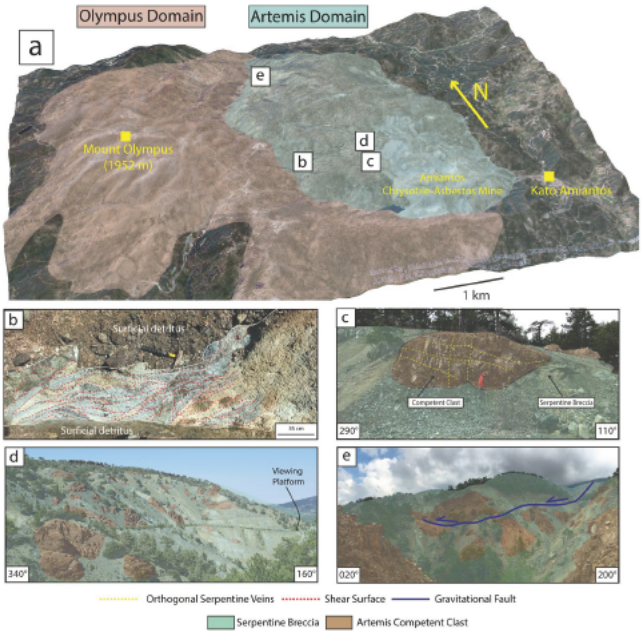

Figure 5. (a) 3D satellite-terrain hybrid image of the Troodos Mantle Sequence, highlighting the extent and differences in terrain and geomorphology between the Olympus and Artemis domains. Locations of inset images (b)–(e) shown. (b) Artemis domain serpentine gouge displaying the complex and intricate structure within recrystallized serpentine breccia-gouge. Hammer for scale. (c) Competent serpentinite block-clast with mutually cross-cutting orthogonally orientated serpentine veins, that is surrounded by highly comminuted serpentine cataclasite and localized serpentine gouge. (d) Artemis domain clast-gouge mountainside structure, highlighting the complex domain-wide network of isolated competent serpentinized block-clasts surrounded by weaker serpentine breccia-gouge. Viewing platform overlooking the former Amiantos asbestos mine for scale. (e) Actively collapsing Artemis domain hillslopes due to high proportions of weak, friable, and serpentine gouge.

and some magnetite, with trace dolomite and calcite, and minor ~1-mm-wide serpentine veins (Figure 6a). Serpentine-filled microfractures are abundant at the micron scale (Figure 6a).

In contrast, the competent clasts of the Artemis domain are composed of mixed serpentine and chrysotile, including the complete bastitic replacement of primary orthopyroxene. Serpentine, predominantly fibrous chrysotile, occurs as discrete mutually cross-cutting extensional and hybrid crack-seal veins. The breccia matrixes and gouges comprise serpentine variably recrystallized to different grain sizes (Figure 6b). Multiple episodes of serpentinization, deformation, dissolution, and recrystallization are likely reflected in the breccia matrixes and gouges. In rare occurrences antigorite forms as discrete veins (e.g., Magaritz & Taylor, 1974) and as brecciated clasts (0.1–2 mm) surrounded by recrystallized serpentine. Chromite is the only primary mantle phase preserved in the Artemis domain rocks. Globular hydro-andradite occurs throughout the blocks within the Artemis domain, and also forms as discrete veins associated with serpentine veins. Calcite occurs as discrete late-stage veins generally cross-cutting serpentine veins.

Journal of Geophysical Research: Solid Earth 10.1029/2020JB021079

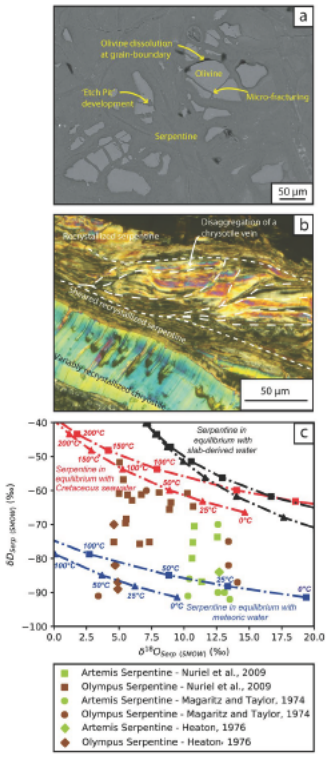

Figure 6. (a) Scanning electron microscope back-scattered electron (BSE) image of the partly serpentinized Olympus domain with the olivine-serpentine mesh interface highlighted. Common micro-fracturing associated with the dissolution and transformation of primary olivine to secondary serpentine through the serpentinization style of partial serpentinization hydration reactions. (b) Cross-polarized light photomicrograph of a typical Artemis domain completely serpentinized competent clast with variable dynamically recrystallized serpentine and associated cataclastic deformation. (c) Oxygen and hydrogen stable isotope plot of published serpentine measurements (Heaton, 1976; Magaritz & Taylor, 1974; Nuriel et al., 2009). Troodos Mantle Sequence values are separated based on sample location either from the Olympus or Artemis domain. Calculated serpentine oxygen and hydrogen stable isotope values in equilibrium with Cyprus meteoric water ($\delta^{18}O$ −7‰, δD −35‰; e.g., Boronina et al., 2005), Cretaceous seawater ($\delta^{18}O$ −1‰, δD −7‰; e.g., Heaton & Sheppard, 1977), and slab-derived metamorphic water ($\delta^{18}O$ +7.8‰, δD −15‰; e.g., Alt & Shanks, 2006) are shown. Triangles represent calculated serpentine values in equilibrium using empirical oxygen isotope fractionation factors from Wenner & Taylor, 1971 and hydrogen isotope fractionation factors from Saccocia et al. (2009). Squares represent calculated serpentine values in equilibrium using semi-empirical oxygen isotope fractionation factors from Zheng (1993) and empirical hydrogen isotope fractionation factors from Saccocia et al. (2009).

Journal of Geophysical Research: Solid Earth 10.1029/2020JB021079

Table 1
Contrasting Characteristics, Properties and Serpentinization Styles Exhibited by the Proposed Olympus and Artemis Domains of the Troodos Mantle Sequence

	Olympus domain	Artemis domain
Serpentinization degree	~50%–70%	100%
Serpentinization style	Hydration of primary igneous mineralogy	Coupled serpentine deformation-alteration-recrystallization
Fabric	Primary—tectonitized localized serpentinized shears, cm to decimeter wide	Extensive secondary, polyphase shears, weak and soft serpentine breccia with component serpentinized clasts 1 cm to >100 m
Fractures	Minor fracturing	Extensive on all scales from micron to ~100 m
Chrysotile and serpentine veins	None, minor, ~2 mm wide serpentine veins uncommonly occur around domain periphery	Abundant orthogonal, concentric, oblique on all scales from sub-mm to 20 cm
Shear zones	Laterally continuous up to 100 m, narrow <1 m, discrete, localized shear surfaces orientated 120° apart	Pervasive, dominating entire body from mm to >1 km, anastomosing/surrounding competent, rigid clasts
Competence	Cohesive, hard, blocky	Friable, incohesive
Density	2,686 ± 83 kg/m^3	1,949 ± 47 kg/m^3
Ground water	Low to very low, few perennial streams, ephemeral streams and seeps, no springs	Moderate to high, numerous ephemeral seeps and springs, several moderate-large perennial streams
Topographic expression	Mt. Olympus high point	Collapsing slopes, valleys
Erosion rate	Low, vegetated slopes, steep, large, rocky outcrops, narrow gorges	High, actively collapsing, vegetation-free steep slopes – angle of repose >30°
Inferred uplift initiation age	~5.5 Ma	<1 Ma?
Oxygen and hydrogen stable isotope values	δ^{18}O +7.1 ± 3‰ (1σ)	δ^{18}O +11.8 ± 1.2‰ (1σ)
	δD −70.3 ± 10.8 ‰ (1σ)	δD −82.4 ± 8.2‰ (1σ)

4.2. Contrasting Serpentine Oxygen and Hydrogen Stable Isotope Values

Published serpentine oxygen and hydrogen stable isotope values (e.g., Heaton, 1976; Magaritz & Taylor, 1974; Nuriel et al., 2009) differ for the Olympus domain and the Artemis domain (Figure 6c; Table 1). The Artemis domain values exhibit a shift to higher oxygen stable isotope values relative to the Olympus domain (Figure 6c; e.g., Heaton, 1976; Magaritz & Taylor, 1974; Nuriel et al., 2009). Calculated serpentine oxygen and hydrogen stable isotope values in equilibrium with meteoric water (δ^{18}O −7‰, δD −35‰; e.g., Boronina et al., 2005) at temperatures >25°C to <100°C and Cretaceous seawater (δ^{18}O −1‰, δD −7‰; e.g., Heaton & Sheppard, 1977) at temperatures <150°C fall into the respective outer limits of the Olympus domain values (Figure 6c). In contrast, serpentine oxygen and hydrogen stable isotope values of the Artemis domain fall into a narrower range (δ^{18}O +10.3‰ to +13.5‰; δD −70‰ to −92‰) compared to the Olympus domain (δ^{18}O +3.4‰ to +14.1‰; δD −52‰ to −92‰; Figure 6c; Heaton, 1976; Magaritz & Taylor, 1974; Nuriel et al., 2009). There is greater range in the Artemis domain hydrogen stable isotope values compared to oxygen stable isotope values (Figure 6c). Calculated serpentine oxygen isotope values in equilibrium with meteoric water (δ^{18}O −7‰, δD −35‰; e.g., Boronina et al., 2005) at temperatures ~25°C–~50°C fall within the measured range of Artemis domain oxygen isotope values (Figure 6c). However, only some of the measured Artemis domain hydrogen stable isotope values match the equivalent equilibrium calculations (Figure 6c). The calculated serpentine oxygen and hydrogen stable isotope values in equilibrium with a slab-derived serpentinizing fluid (δ^{18}O +7.8‰, δD −15‰; e.g., Alt & Shanks, 2006) do not match any previously measured oxygen and hydrogen stable isotope values (Figure 6c).

4.3. Contrasting Bulk Densities

Bulk dry densities were measured on mini-cores taken from selected representative samples from the Troodos ophiolite Mantle Sequence including samples from each of the Olympus and Artemis domains (Table 2). The bulk density of the partly serpentinized peridotites of the Olympus domain is 2,686 ± 83 kg/m^3 (1σ,

Journal of Geophysical Research: Solid Earth 10.1029/2020JB021079

Table 2
New Density Measurements With Estimated Primary and Secondary Modal Mineral Assemblages

Sample	Sample type	Density (kg/m^3)	Primary mineralogy assemblage (%)	Secondary Mineralogy Assemblage (%)
AH2	Olympus Dunite	2,760	30–50	50–70
AH1	Olympus Harzburgite	2,797	30–50	50–70
AJ2H	Olympus Harzburgite	2,565	30–50	50–70
AJ2V	Olympus Harzburgite	2,565	30–50	50–70
PP3-20	Olympus Harzburgite	2,699	30–50	50–70
PP3-16	Olympus Harzburgite	2,706	30–50	50–70
PP2-11	Olympus Dunite	2,708	30–50	50–70
PP2-15	Olympus Dunite	2,688	30–50	50–70
AR2	Artemis Clast	2,292	0	100
AR1	Artemis Clast	2,294	0	100
PP1-23	Artemis Clast	2,390	0	100
PP1-22	Artemis Clast	2,268	0	100
PP1-25	Artemis Clast	2,408	0	100
BZ1	Artemis Breccia	1,545	0	100
BZ2	Artemis Breccia	1,505	0	100
DC1V	Artemis Breccia	1,559	0	100
DC2H	Artemis Breccia	1,502	0	100
DH1V	Artemis Breccia	1,607	0	100
DH2H	Artemis Breccia	1,691	0	100
DSDP Leg 37 ($n = 5$)*	Serpentinized peridotite	2,699		
Mantle**	Unserpentinized Mantle	3,300	100	0

Sample Type	Average Density (kg/m^3)	1σ	Competent Clast (%)	Serpentine Breccia (%)
Olympus	2,686	86		
Artemis Clast	2,330	63 (δa)	100	0
Artemis Breccia	1,568	71 (δb)	0	100

Sample type	Average Density (kg/m^3)	[a] Propagated Error (δz)	Competent Clast proportion (x)	Serpentine Breccia proportion (y)
Artemis Breccia	1,949	47	0.5	0.5
	1,759	56	0.25	0.75
	2,139	51	0.75	0.25
	2,177	51	0.8	0.2
	1,720	58	0.2	0.8
	1,873	50	0.4	0.6
	2,025	47	0.6	0.4

Note. DSDP Leg 37 average density of serpentinized peridotite from Hyndman and Drury (1976). Average density of unserpentinized mantle peridotite from Birch (1961). Calculated errors for differing proportions of Artemis clast and gouge are also shown.

*Hyndman and Drury (1976).

**Unserpentinized mantle peridotite (Birch, 1961).

[a] $\delta z = \sqrt{(x \times \delta a)^2 + (y \times \delta b)^2}$

Journal of Geophysical Research: Solid Earth 10.1029/2020JB021079

$n = 8$). In contrast, the serpentinized clasts from the Artemis Domain have bulk densities of 2,330 ± 63 kg/m^3 (1σ, $n = 5$) and the serpentine breccias yield very low densities of 1,568 ± 71 kg/m^3 (1σ, $n = 6$; Table 2, Figure 4b). Given the approximately 50:50 mix of clasts to breccia across the whole Artemis domain, we estimate a gross bulk density of ~1,949 ± 47 kg/m^3 (Table 2). Background unserpentinized mantle peridotite has an inherit bulk density of 3,300 kg/m^3 (Birch, 1964; Gass & Masson-Smith, 1963).

5. Constraints on the Timing of the Uplift and Exposure of the Troodos Ophiolite

The Troodos ocean crust is relatively thin, only ~4,000 m thick from the top of the extrusive rocks to the uppermost mantle peridotites (Malpas, 1989). However, this still requires that a minimum of ~4,000 m of exhumation must have occurred since the initial subaerial emergence of the Troodos ophiolite. The circum-Troodos sediments in the Mesaoria and Pissouri basins surrounding the Troodos Ophiolite (Figure 1a) preserve stratigraphic records of the unroofing and erosion of progressively deeper levels of the Troodos ophiolite (McCallum, 1989; Poole & Robertson, 1991, 1998; Robertson, 1977; Rouchy et al., 2001; Stow et al., 1995; see supporting information). Significant amounts of Troodos-derived diabase and lava clasts occur in the latest Messinian/Early Pliocene (~5.5 Ma) strata indicating significant subaerial relief and exposure of the uppermost Troodos crust by this time (McCallum, 1989; Rouchy et al., 2001; Stow et al., 1995). Gabbroic clasts are first recorded in the Late Pliocene (McCallum, 1989; Stow et al., 1995). The proportion of gabbroic clasts is significantly greater in the Pleistocene Fanglomerates than the Pliocene successions (McCallum, 1989; Poole & Robertson, 1991, 1998). The first occurrence of ultramafic clasts is recorded within the Lower Pleistocene (<2.58 Ma) sequence (Poole & Robertson, 1991, 1998; Stow et al., 1995; Wilson, 1959). The abundance of ultramafic clasts progressively increases within the Pleistocene Fanglomerate sequences (2.58–0.0117 Ma) (Poole & Robertson, 1991, 1998). The Plio-Pleistocene sedimentary sequences have been interpreted to record pulses of uplift focused on Mount Olympus (e.g., McCallum, 1989; Poole & Robertson, 1991, 1998; Robertson, 1977), with the intensity of the uplift episodes having waned from the Late Pleistocene to the present day (Poole & Robertson, 1998).

Low-temperature (U-Th)/He thermochronology on plutonic rocks from the Troodos Massif suggests an exhumation rate of 0.86 mm/yr with the onset of uplift at 6 ± 2 Ma (Morag et al., 2016). This rate broadly agrees with the uplift trajectory compiled from clast occurrences in the circum-Troodos sedimentary sequences (McCallum, 1989; Poole & Robertson, 1991, 1998; Rouchy et al., 2001; Stow et al., 1995).

6. Mechanistic Uplift Modeling

Explanation of the formation of the unique geometry of the Troodos Massif must address a number of key observations: (a) Uplift must occur within the well-constrained uplift trajectories from circum-Troodos sedimentary sequences (e.g., Follows, 1990; McCallum, 1989; Poole & Robertson, 1998; Robertson, 1977, 1998; Stow et al., 1995) and recent thermochronology (Morag et al., 2016); (b) Invoke a mechanism that explains the differential uplift between the exhumed Troodos Mantle Sequence atop Mount Olympus and the regionally uplifted mantle peridotites that underlie the remaining ocean crustal sequences; (c) Account for the subdivision of the Troodos Mantle Sequence into two distinct domains and their respective contrasting properties that has induced further uplift and exhumation of the Artemis domain relative to the Olympus domain. Here, we develop a one-dimensional uplift model for the Troodos Mantle Sequence to determine whether it is mechanistically possible to generate the observed ~2,000 m relief through a density contrast-driven isostatic response since ~5.5 Ma, whilst parameterizing for the subdivision of the Troodos Mantle Sequence.

6.1. Model Parameters

Using reasonable parameters for the Troodos ophiolite (Table 3), elevation is determined in a number of iterative steps by subtracting erosion from the isostatic uplift generated by an advancing one-dimension serpentinization front within a period of time, from an initial elevation of 0 m (Equation 1, Figure 7a, Table 3).

$$\text{Elevation} = \text{Uplift} - \text{Erosion} \quad (1)$$

Journal of Geophysical Research: Solid Earth 10.1029/2020JB021079

Table 3
Model Parameters for the Olympus and Artemis Domains Used in the Mechanistical Uplift Modeling

Symbol	Definition	Olympus domain parameters	Artemis domain parameters	Unit
S_D	Serpentinization front distance			m
S_r	Serpentinization front rate	(200, 1,000, 2,000, 3,000)	(600, 3,000, 6,000, 9,000)	m/Myr
H	Time period			Myr
	Time steps	10,000	2,000	
φ_D	Stretching distance			m
B	Stretching percentage	20% = 50% Serpentinization	40% = 100% Serpentinization	
D_D	Domain thickness/depth			m
U_t	Total uplift from isostatic response			m
ρ_M	Density of residual material	3,300 (background lithospheric mantle)	2,700 (Olympus)	kg/m^3
ρ_D	Domain density	2,700 (Olympus)	2,000 (Artemis)	kg/m^3
E_r	Erosion rate			m/Myr
ε_t	Erosion response time			Myr
τ_e	Bedrock erodibility coefficient	1.5×10^{-6}	6.4×10^{-6}	m
ω	Precipitation	910	910	mm/yr
E	Erosion			m

The serpentinizing front advances at an estimated average rate (S_r) for a given time period (η). This generates a depth (S_D) for the serpentinization front (Equation 2, Figure 7a).

$$S_D = S_r \times \eta \tag{2}$$

We assume that the advancing serpentinizing front occurs within a horizontally confined structure, advancing into background unserpentinized peridotite with a density of 3,300 kg/m^3. Serpentinization reactions reduce density and result in volume expansion. Assuming that the horizontally confined structure expands (Equation 3) in the vertical direction, the total percentage of volume expansion (β) is related to the total average serpentinization percentage above the advancing front. The rocks of the Olympus Domain are on average approximately ~50% serpentinized, and this produces a ~20% volume expansion (100% serpentinization results in ~40% bulk volume expansion).

$$\varphi_D = \left(\frac{S_D}{100}\right) \times \beta \tag{3}$$

The total depth of the expanded advanced serpentinizing front (φ_D) in a given time period added to the serpentinization front depth (S_D), yields the total depth (D_D) (Equation 4)

$$D_D = S_D + \varphi_D \tag{4}$$

D_D is then input into an isostatic calculation to determine the isostatic change in elevation over an increment of time, to the density difference between background ultramafic unserpentinized mantle (ρ_M) and a horizontally confined, vertical serpentinized body (ρ_D). The uplift due to isostatic response (U_t) of an advancing serpentinization front is equal to the total uplift (Equation 5) (Figure 7a).

$$U_t = \left(\frac{\rho_M - \rho_D}{\rho_M}\right) \times D_D \tag{5}$$

We then apply an erosional model (following e.g., Cao & Paterson, 2016; Lee et al., 2015; Simoes et al., 2010) to calculate the erosion rate (E_r) for a time period (Equation 6).

Journal of Geophysical Research: Solid Earth 10.1029/2020JB021079

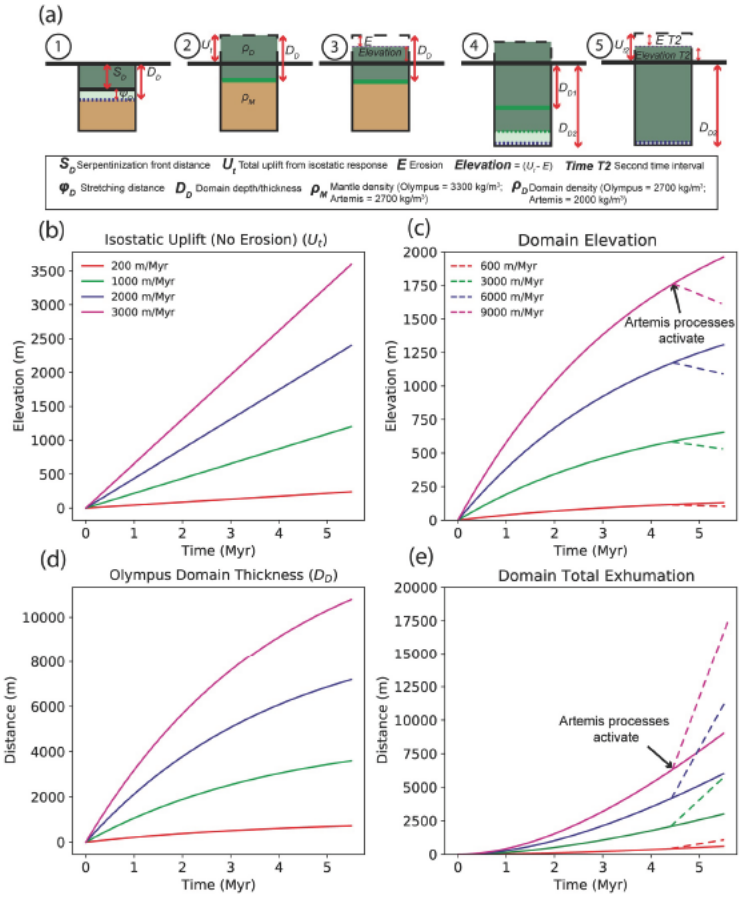

Figure 7. (a) Uplift model set up. One-dimensional horizontally confined model where elevation is determined by subtracting erosion from the isostatic uplift in response to an advancing average serpentinization transformation front. Model is repeated over a number of iterative steps from an initial elevation of 0 m for a total run time of 5.5 Myr. Differing parameters are utilized for each domain (see Table 3). (b) Olympus domain isostatic uplift output shown with no erosion applied. Output highlights the theoretical maximum surface uplift that can be generated through an advancing average serpentinization transformation front. (c) Olympus domain elevation model output shown, where differential erosional parameters are applied to the uplift model, generating an elevation value through subtracting erosion from surface uplift. Artemis domain total elevation output is also shown in dashed. Inflection point at 4.4 Myr highlights the change in parameterization from Olympus to Artemis (Table. 3). (d) Olympus domain evolving thickness output shown highlights the interplay between erosion and the advancing serpentinization front in producing the thickness of the domain. (e) Olympus domain exhumation total is shown along with the Artemis domain exhumation total (in dashed). Inflection point at 4.4 Myr represents the activation of Artemis parameters (see Table 3).

$$E_r = \frac{U_t}{\varepsilon_t} \tag{6}$$

$$\varepsilon_t = \frac{1}{\tau_e \times \omega} \tag{7}$$

$$E = E_r \times \eta \tag{8}$$

The erosion rate (E_r) is a function of the isostatic response uplift (U_t) and erosion response time (ε_t). The erosional response time is a function of the bedrock erodibility constant (τ_e) and average annual precipitation (ω) (Equation 7). By multiplying the erosion rate with the time period (η), the total erosion (E) for that time period can be calculated (Equation 8). Each step is repeated 10,000 times over a defined time period of 5.5 Myr.

6.1.1. Advancing Serpentinization Front Rates

A range of one-dimensional average advancing serpentinization front (S_r) rates are input into the Olympus mechanistical uplift model (Table 3) to determine the contribution of an advancing serpentinization front to uplift and unroofing of the Troodos Massif mantle peridotites. The range of Olympus domain one-dimensional serpentinization front advancement rates (S_r; 200–3,000 m/Myr) used in our model are broadly equivalent to serpentinization rates proposed with other serpentinization studies in seafloor settings (e.g., Lowell & Rona, 2002) and experimentally determined one-dimensional serpentinization hydration reaction "diffusion" rates that range between ~200 m/Myr and ~4,000 m/Myr (e.g., Lamadrid et al., 2017; Macdonald & Fyfe, 1985; Martin & Fyfe, 1970; McCollom et al., 2016). However, the rate of our advancing one-dimensional serpentinization front (S_r) is not strictly equivalent to an experimentally determined serpentinization diffusion rate because our simple uplift model does not explicitly consider fluid channeling or the spacing of cracks and channels.

In contrast, the Artemis domain does not express a simple progressive hydration/serpentinization style but coupled near-surficial to surficial deformation-alteration-recrystallization serpentinization processes. Surficial to near-surficial serpentinization rates are interpreted to be geologically rapid (e.g., Craw et al., 1987). Modeling of the interplay between chrysotile dissolution-recrystallization rates (e.g., Thom et al., 2013) and grain size in differing surficial (22°C), fluid-saturated pH conditions indicates that pH 8 a ~1 mm chrysotile particle would dissolve and recrystallize in ~20,000 years, whereas under the same conditions a ~1-m-sized particle size would take ~20 Ma (see supporting information). Consequently due to grain size reductions, coupled deformation-alteration-recrystallization mechanisms at surficial conditions within the Artemis domain are likely to occur at faster reaction rates than the hydration serpentinization style of the Olympus domain. This reflects the contrasting structural characteristics of each domain (Figure 5c) and is likely to continue to some degree at depth due to greater fracture density within the Artemis domain relative to the Olympus domain. To reflect this within the Artemis uplift model, the Artemis advancing transformation rate (S_r) is tripled relative to the Olympus domain.

6.1.2. Uplift Model Assumptions and Limitations

It is assumed that the isostatically uplifted Troodos ocean crust had a similar density and bedrock erodibility constant (τ_e) to partially serpentinized peridotites (2,700 kg/m^3). It is assumed that there is no "lag" time between the advance of the serpentinizing front and isostatic uplift. Within the model set-up, we assume a horizontally bound vertical structure, where the advancing serpentinization front and associated volume expansion occur only in the vertical direction. Although it is easier to conceptualize the model with fluid infiltration from the surface, the model is not reliant on whether the serpentinization fluid source is from above, below, or a combination of both since the mass-change outcome is the same in our one-dimensional setup. We assume that the advanced serpentinization front depth (S_D) is an average serpentinization percentage for the whole vertical structure. The model does not account for gravitational collapse. Nor does it account for thermo-mechanical boundary effects between the serpentinized portion and background unserpentinized mantle during exhumation/uplift. It is assumed that present-day precipitation levels of

910 mm/yr (Prodromos village, 1,400 m asl, Cyprus Department of Meteorology) are representative of rainfall throughout the model time frame. This may be an over-estimation as precipitation generally increases with elevation, and hence may have been lower during the initial stages of uplift. Although during the Plio-Pleistocene periods of greater humidity and precipitation levels than the present-day have been inferred from the relative abundance of sapropels (e.g., Poole & Robertson, 1998 and references therein). We propose a 1.1 Ma date (Mid Pleistocene) for the initiation of the Artemis domain alteration and deformation processes that must start some time between the initial exhumation and protrusion of ultramafic rocks in the Early Pleistocene and the end of the Pleistocene.

6.2. Uplift Modeling Results

6.2.1. Olympus Domain

A serpentinization transformation front advancing at a rate of 3,000 m/Myr will isostatically uplift rock a total of 3,600 m in 5.5 Myr, for a density contrast of 600 kg/m^3 (Figure 7b). Applying reasonable erosional parameters of 910 mm/yr precipitation and a bedrock erodibility of 1.5×10^{-6} m to the same uplift parameters (S_r = 3,000 m/Myr, $\Delta\rho$ = 600 kg/m^3) yields an elevation of ~1,950 m for the Olympus domain after 5.5 Myr (Figure 7c). Under the same model conditions, adjustment of the bedrock erodibility parameter from 1.5×10^{-6} m to 1×10^{-6} m and 2×10^{-6} m produces elevation values of ~2,350 and ~1,650 m respectively. Calculations of the evolving eroded total thickness (Figure 7d) and the total exhumation (Figure 7e) of the Olympus domain for different average advancing serpentinization front rates (S_r), suggests that up to ~9,000 m of material has been exhumed from the Olympus domain over 5.5 Myr.

6.2.2. Artemis Domain

To quantify the dynamic topography resulting from a secondary density contrast between the Artemis (2,000 kg/m^3) and Olympus (2,700 kg/m^3) domains, the elevation model is re-run using the Artemis model parameters (Table 3). After 4.4 Myr of the 5.5 Myr run time, the Artemis domain overprints the Olympus domain, generating a joint contribution to the uplift and differential exhumation of the Artemis domain. The advancing serpentinization front rate (S_r) of the Artemis domain is tripled. The bedrock erodibility constant (τ_e) is also increased to 6.4×10^{-6} m to account for the weak, friable, easily erodible material. Calculations using these parameters yield a lower elevation (~1,550 m) for the Artemis domain compared to the Olympus domain peak (1,952 m) (Figure 7c), in line with the current present elevations. Using the parameters applied, modeling suggests that ~17.5 km of material has been exhumed over 5.5 Myr period (Figure 7e and Table 3).

7. Discussion

7.1. Serpentinite Diapirism of Troodos Mantle Sequence

New measurements of the bulk densities of the Olympus and Artemis domains, and simple modeling indicate that mountains akin to Mount Olympus (~2,000 m elevation asl) can form within the required time constraints (~5.5 Myr; see supporting information) solely through serpentinization with the resultant density contrast causing isostatic uplift. Serpentinization alone is therefore mechanistically capable of producing the progressive uplift and exhumation that has culminated in the solitary, relatively high-altitude peak (1,952 m) of Mount Olympus, relative to the low to modest altitude of the sheeted dike complex (~1,000 m). We interpret the Olympus domain as a distinct serpentinite diapir that has resulted in the transportation and protrusion of mantle peridotites to 1,952 m asl above the regionally uplifted mantle peridotites that underlie the ophiolitic ocean crust. The minimum differential uplift of the Olympus diapir compared to the regionally uplifted "in-situ" Troodos ophiolite mantle peridotites can be estimated by considering the Cyprus Crustal Study Project CY-4 drill hole located near the village of Palaichori (~930 m asl) ~20 km east of Mount Olympus. With a total depth beneath the surface of 2,263 m, CY-4 penetrated sheeted dikes, gabbro, and lower crustal ultramafic cumulate rocks but did not reach tectonized upper mantle peridotites (Malpas et al., 1989). Assuming that the CY-4 drill hole would have intersected mantle peridotites at a depth of 2,500 m beneath the surface (1,600 m below sea level) the minimum required relative uplift is ~3,600 m.

We interpret the Artemis domain as a second, overprinting and distinct serpentinite diapir that has cannibalized the eastern portion of the Olympus diapir through coupled deformation-alteration-recrystallization processes to form a 100% serpentinized region (~1,949 ± 47 kg/m^3) with a large proportion of low-density breccia (1,568 ± 71 kg/m^3). Although the lower density of the Artemis diapir results in a greater amount of total isostatic uplift, its weak and easily erodible nature results in differential exhumation between both domains and a lower average elevation of the Artemis diapir (~1,550 m) compared to the Olympus diapir (>1,500–1,952 m).

Differences between the properties and characteristics of both diapiric boundaries, serpentinization extents, alteration mineralogy, deformation styles, geomorphology, density, and outcrop patterns indicate that the Artemis domain overprints and builds on pre-existing Olympus diapir serpentinization and uplift (Figure 2). This culminates in a distinct coupled serpentine deformation-alteration-recrystallization serpentinization style that is in direct contrast to the partial hydration serpentinization style of the Olympus diapir.

The initial localization of greater extents of serpentinization in the Artemis diapir must result from structural controls that have been obscured by on-going deformation as the Artemis diapir expands into the Olympus diapir. The high altitude of the Troodos Mountains and associated rainfall combined with strongly deformed rocks has enabled the incursion of meteoric fluids into the rocks results in increased serpentinization of the uplifted peridotites. An inevitable consequence of meteoric water incursion and serpentinization is the augmentation of a localized deformation-alteration-recrystallization positive-feedback mechanism that initiated the development of the overprinting Artemis diapir. These mechanisms induce the formation of the easily erodible rock, and consequently result in further uplift and exhumation relative to the Olympus diapir. By applying reasonable parameters to the uplift model, the total exhumation of the Artemis diapir is calculated to range between >3.6 and ~17.5 km (Figure 7e). Testing will require further detailed petrological and thermodynamic investigations.

There are clear geochemical differences between the rocks of the Olympus diapir and Artemis diapir. Previous oxygen and hydrogen stable isotope measurements (e.g., Heaton, 1976; Magaritz & Taylor, 1974; Nuriel et al., 2009) yield different measured values for the Olympus and Artemis diapirs (Figure 6c). Calculated oxygen and hydrogen serpentine stable isotope values in equilibrium with meteoric water at varying temperatures (Figure 6c) indicate that the Artemis diapir and portions of the Olympus diapir serpentinites equilibrated with low-temperature (~25°C–<100°C) meteoric water at or near the surface since the unroofing of mantle peridotites during the Early Pleistocene (Poole & Robertson, 1998; Wilson, 1959), and these reactions and exchanges are probably on-going. Serpentine hydrogen stable isotopes have been proposed to exchange with subsequent fluid episodes, potentially overprinting original values (e.g., Kyser & Kerrich, 1991; Kyser et al., 1999; Wenner, 1971). Since the proportions in the balance between oxygen and hydrogen in the fluid and rock are different, hydrogen is more likely to undergo post-formational isotopic exchange relative to oxygen; serpentine oxygen stable isotope values are likely to be more robust. The high $\delta^{18}O$ values of the Artemis diapir and portions of the Olympus diapir ($\delta^{18}O$ +10.3‰ to +14.1‰) suggest formation at low temperatures, likely with meteoric water (Figure 6c). Regardless of whether or not these values have been overprinted, they highlight that discreet portions of the Olympus and Artemis diapirs have likely interacted and exchanged with differing fluids. Our 1-D models are not sensitive to where fluid ingress and serpentinization occur and are consistent with a component of the uplift resulting from the focused upwelling into the overlying mantle wedge of hydrous fluids generated by the dewatering of partially subducted marine sediments and ocean lithosphere beneath the Troodos rocks, as has been proposed to have initially serpentinized the Troodos Mantle Sequence, inducing serpentinite diapirism (Gass, 1977; Moores & Vine, 1971; Robertson, 1977, 1998). Although there is strong evidence for two distinct textural and geochemical mantle domains (Batanova & Sobolev, 2000), direct evidence for the initial serpentinizing fluid remains elusive. Further geochemical and isotopic investigations are required to better constrain the sequence of fluid-rock exchanges that have occurred during the progressive serpentinization of the Troodos Mantle Sequence.

7.2. Previous Uplift Mechanisms Attributed to the Troodos Mantle Sequence

Previous studies, either do not or only partially satisfy the key criteria outlined in Section 6 necessary to explain the geometry of the Troodos Massif. Although there is compelling evidence in the Limassol

Forest Complex for the Cretaceous seafloor exhumation of mantle rocks (e.g., MacLeod, 1988, 1990; Murton, 1986), geological evidence for similar exposure of the Troodos Massif mantle rocks is less forthcoming. Models that suggest the preservation of Cretaceous seafloor ridge-related detachment faulting (e.g., Nuriel et al., 2009) and Cretaceous ridge-related serpentinite diapirism (e.g., Schuiling et al., 2011) are incompatible with uplift trajectories. These models propose that the exhumation of the Troodos ultramafic rocks occurred on the Cretaceous seafloor. This would require the preservation of original Cretaceous sea-floor relief through its progressive uplift from ocean depths to the current high elevation 1,952 m massif, but would also result in an inverted circum-Troodos sedimentary sequence, with the initial sequences rich in ultramafic materials as opposed to the basalts and diabase observed (Follows, 1990; McCallum et al., 1989; Rouchy et al., 2001; Stow et al., 1995; see supporting information).

Miocene to present-day convergence across the Cyprean subduction zone is also invoked as a mechanism for uplifting and exhuming the mantle peridotites that encompass Mount Olympus (Ring & Pantazides, 2019). These authors downplay the role of serpentinization in forming the Troodos Massif, and favor a west-east elongate doubly plunging anticline with a serpentinite core formed in response to gradual differential shortening. Differential uplift between the Troodos Mantle Sequence and the remaining ocean crustal sequences is proposed to result from the underthrusting of the Eratosthenes seamount (Ring & Pantazides, 2019). This proposed uplift mechanism presents the Troodos Mantle Sequence as a homogenous monolith and does not account for the long-standing subdivision into two separate discrete domains, including evidence that the peridotites from these domains originate from different mantle sources (Batanova & Sobolev, 2000).

7.3. A Unified Model for the Uplift of the Troodos Mantle Sequence

Initiation of significant uplift of the Troodos ophiolite is dated as latest Messinian to Early Pliocene (~5.5 Myr). Decoupling between the Olympus diapir and the regionally uplifted "in-situ" mantle peridotites of the Troodos ophiolite has resulted in at least >3,600 m of differential uplift, transporting mantle peridotites to 1,952 m absl (Figure 8). Unroofing and erosion of the first ultramafic clasts are interpreted to have occurred in the Early Pleistocene, suggesting significant peridotite relief has occurred since then (Figure 8). Once transported to high altitudes, increased rainfall results in the incursion of meteoric water (Figure 8), driving the coupling of deformation-alteration-recrystallization positive-feedback mechanisms of the intensely deformed Artemis diapir. The resulting lower density and easily erodible material induce a secondary decoupling that separates the lower density Artemis diapir from the Olympus diapir (Figure 8), in consequence, differential uplift and exhumation occurs between the Artemis diapir and the Olympus diapir.

7.4. Application of the Mechanistic Uplift Model to Other Settings

Here, we explore whether our simple 1-D mechanistic uplift model is unique to the Troodos Massif or whether it can be applied to a range of other terrestrial and submarine settings including St. Peter and St. Paul Rocks, New Idria Massif, California, Site 637 on the West Iberian Margin, and Macquarie Island.

7.4.1. St. Peter and St. Paul Rocks

The St. Peter and St. Paul Rocks are interpreted as a partially serpentinized serpentinite diapir (e.g., Campos et al., 2005, 2010). Recent interpretation of new bathymetry, seismic, and gravity data sets proposed that the St. Peter and St. Paul Rocks uplifted in response to a ~10 Myr period of transpression at the transform boundary (Maia et al., 2016). They conclude that the present convergence rates at stepovers and transpressive segments are sufficient to uplift the North Ridge Massif some ~3,500 m (Maia et al., 2016). However, a gravity anomaly on the southern flank of the massif indicates the presence of a large low-density layer. This is interpreted to be a ~25-km-thick zone of serpentinized mantle, the base of which approximately coincides with the estimated depth of the 500°C isotherm (Maia et al., 2016).

To establish whether isostatic uplift in response to partial serpentinization reactions can contribute to the overall uplift of the peridotite massif, we apply the mechanistic uplift model (with reasonable parameters; see supporting information) to the St. Peter and St. Paul Rocks. Calculations indicate that partial serpentinization (~40%) of a body in response to a serpentinization front advancing at an average rate of 2,000 m/Myr, will isostatically uplift rock a total of ~3,500 m in the required time frame (10 Myr; Maia et al., 2016),

Journal of Geophysical Research: Solid Earth 10.1029/2020JB021079

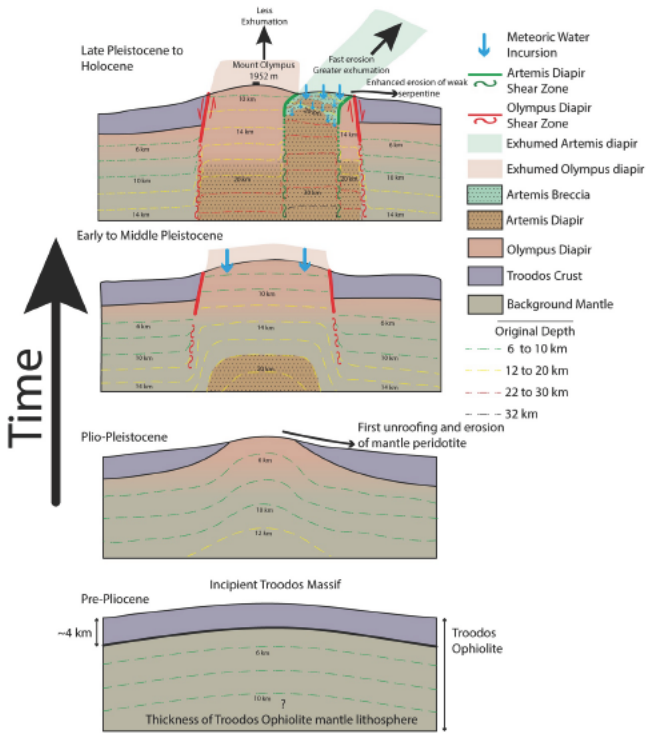

Figure 8. A schematic illustration of our uplift model for the Troodos Mantle Sequence Model highlights the temporal evolution within the Troodos Mantle Sequence culminating in differential serpentinite diapirism and exhumation resulting from contrasting serpentinization styles between both diapiric domains.

generating a body of moderate density (2,800 kg/m^3) that is ~23 km in total thickness (see supporting information), in broad agreement with published interpretation of the gravity data (Maia et al., 2016).

7.4.2. New Idria Serpentinite Diapir

The moderately elevated (1,605 m; prominence 1,061 m) New Idria serpentinite diapir is primarily composed of easily erodible, sheared and crushed, incohesive low-density serpentinite breccia (Coleman, 1996; Mumpton & Thompson, 1975). In addition to serpentine, blocks of eclogite are present that are interpreted to have been entrained during diapiric ascent (Tsujimori et al., 2007). Gravity measurements identify a −35 to −55 mGal negative Bouguer gravity anomaly and the New Idria serpentinite is interpreted to be a dome-like body that only extends to ~4 km depth (Byerly, 1966; McPhee et al., 2004). The gravity anomaly coincides with a strong magnetic signature (~210 nT; McPhee et al., 2004). The emergence of the New Idria serpentinite diapir is dated as Mid-Miocene (~12–~14 Ma) from the presences of detrital chrysotile serpentine in the Big Blue Formation (Casey & Dickinson, 1976; Coleman, 1996; Vermeesch et al., 2006) and continued serpentinite extrusion occurred throughout the Plio-Pleistocene (Coleman, 1996). Application

of the Artemis model parameters (Table 3) to the New Idria setting, suggests that an advancing serpentinization front of 3,000 m/Myr may isostatically produce and maintain an elevation of ~1,000 m in response to a ~4000-m-thick low-density body (see supporting information). These results are in agreement with geophysical constraints and suggest that isostatic uplift due to serpentinization may produce and maintain a serpentinite body of moderate elevation, coincidently generating significant differential uplift and exhumation relative to the surrounding area.

7.4.3. ODP Leg 103 Site 637

To the west of the Galicia Bank on the Iberian Margin, ODP Site 647 ("5100 m Hill") is a ~5-km-wide domal serpentinite protrusion, where strongly altered and completely serpentinized plagioclase-bearing subcontinental mantle rocks are uplifted some ~350 m above the surrounding seafloor (Boillot et al., 1988). Late Miocene sediments unconformably overlay, eroded strongly altered and brecciated serpentinized clasts that transition to strongly altered and brecciated serpentinites with increasing depth (Boillot et al., 1988; Evans & Baltuck, 1988). This exhumed peridotite is an elevated basement high, along an inferred ~70 km wide, ~250 km long peridotite ridge, organized into a series of broadly N-S orientated margin parallel segments, some of which extend over tens of kilometers, and generally denote the ocean-continental crust boundary (e.g., Beslier et al., 1993; Henning et al., 2004; Minshull et al., 2014; Whitmarsh et al., 1996). Recent three-dimensional imaging of serpentinized peridotite bodies along the West Iberian Margin shows that the volume of serpentinized peridotite is related to the amount of displacement along each fault, the implication being that serpentinization occurs when these large brittle normal faults are active (Bayrakci et al., 2016). In response to the penetration of seawater into the mantle along normal faults, isostatic uplift as a result of density reduction from serpentinization reactions is likely to have occurred. Strongly serpentinized (>75%) mantle peridotites are estimated from seismic data to occur on top of the basement with the extent of serpentinization decreasing to <25%–~2 km below (Minshull et al., 2014). The depth of the unaltered mantle is estimated at ~7.5 km below seafloor (Minshull et al., 2014). Lateral and vertical variations in the extent of serpentinization likely resulted in differing magnitudes of isostatic uplift. For example, if we assume the completely serpentinized peridotites recovered from Site 637 extend to ~2 km depth and have average bulk densities of 2,400 kg/m^3 and these rocks overlay a body of partly serpentinized peridotites of moderate density (2,900 kg/m^3) the resulting isostatic uplift due to serpentinization would be ~350 m. This amount of uplift is equivalent to the relative difference in elevation between the summit of Site 637 and the surrounding seafloor.

7.4.4. Macquarie Island

Macquarie Island is a small (34-km long, 5.5-km wide) subantarctic island that is broadly equidistant from Tasmania, New Zealand, and Antarctica (Selkirk et al., 1990) and is the only subaerial exposure of the Macquarie Ridge Complex, a region of shallow bathymetry along the Australian-Pacific plate boundary that runs 1,800 km from the southern extent of the Alpine Fault, New Zealand to the Indo-Pacific-Antarctic plate triple junction (Massell et al., 2000). Transpression along the Macquarie Island section of the Macquarie Ridge Complex is invoked to have uplifted and exposed a coherent section of ocean crust and associated upper mantle rocks (Selkirk et al., 1990). These rocks are in faulted contact with subhorizontal pillow lava flows that make up most of the island. The Finch-Langdon Fault that juxtaposes the lava flows and the titled but continuous upper mantle-lower crustal sequence has been interpreted to be an ocean ridge feature (Rivizzigno & Karson, 2004; Wertz et al., 2003). There is no metamorphic sole on Macquarie Island and nor does the geology present evidence for serpentinite diapirism (e.g., Goscombe & Everard, 1998).

Application of the Olympus domain mechanistic uplift model parameters of this study to this Macquarie Island setting suggests that ~400 m of uplift may be generated in response to an average serpentinization front rate of 3,000 m/Myr since the subaerial emergence of the island (~0.65 Ma; Adamson et al., 1996). Despite the extent of serpentinization and general structure of the rocks beneath Macquarie island being poorly constrained, these estimations suggest the resulting isostatic response may produce substantial uplift if localized serpentinization beneath the Macquarie island section of the Macquarie Ridge Complex has occurred. Although there may be other outcrops of serpentinized ultramafic rocks along the Macquarie Ridge Complex (e.g., Watkins & Gunn, 1971), serpentinization-induced isostatic uplift of Macquarie Island may be an additional contribution, overprinted onto the overall uplift trajectory of island, coincidentally generating the only sub-aerial portion along this transpressive plate boundary.

7.4.5. Wider Implications of the Mechanistic Uplift Model

Application of our 1-D mechanistic uplift model to other settings suggests that it may be applied universally across the spectrum of serpentinite diapirism occurrence. Calculations from previously reported examples of serpentinite diapirism and Macquarie Island suggest that the required amount of surface uplift to form their respective topographic relief, in the constrained timeframe, may be generated exclusively through serpentinization reactions. Manifestations of serpentinization may therefore synchronously induce isostatic uplift. In each of the serpentinized massif settings considered, the overall uplift budget is an interplay between the relative contributions of isostatic uplift and tectonic uplift. For example, for the New Idria Massif the isostatic contribution dominates the overall uplift budget (~4 mm/yr diapiric uplift rate vs. regional ~1 mm/yr tectonic uplift rate; Coleman, 1996; Page et al., 1998). In contrast, for the Macquarie Ridge dynamic tectonic uplift is the principal source of uplift with potentially a secondary minor component of isostatic uplift resulting from serpentinization reactions that have led to the exposure of Macquarie Island.

8. Conclusions

1. Contrasting serpentinization styles are manifest as two distinct serpentinite diapirs within the Troodos ophiolite: (a) a region where the partial hydration of primary minerals results in a strongly serpentinized yet competent and cohesive diapir of moderate density (2,686 ± 83 kg/m^3), here termed the Olympus diapir; and (b) the completely serpentinized Artemis diapir that is composed of an intensely deformed, weak and friable block-clast-breccia-gouge assemblage of low density (1,949 ± 47 kg/m^3) that results from the positive feedback between coupled deformation-alteration-recrystallization.
2. Density reduction and coincident volume expansion resulting from serpentinization reactions induce serpentinite diapirism combined with isostatic uplift transporting and protruding mantle peridotites to high altitude (1,952 m). Calculations from isostatic uplift and differential erosion modeling suggest that mountains akin to Mount Olympus (~2,000 m asl) may form exclusively through serpentinization within the required time frame (~5.5 Myr). The CY-4 drill hole geometry indicates that differential uplift of at least >3.6 km has occurred due to the decoupling between the Olympus diapir and the regional "in-situ" mantle peridotites.
3. The occurrence of mantle peridotites forming the highest elevations of the Troodos Mountains results in strong precipitation, leading to the ingression of meteoric water, as highlighted by oxygen and hydrogen stable isotope analyses. Activation of coupled mechanisms within the Artemis diapir form the low density (1,568 ± 71 kg/m^3), weak, serpentinite gouge end member; increasing the total exhumation (>3.6–~17.5 km) and localization of Artemis' deep materials (Batanova & Sobolev, 2000). Despite greater exhumation occurring within the Artemis diapir, the competent cohesive partially serpentinized peridotites of the Olympus diapir form the regional summit (Mount Olympus, 1,952 m) rather than the weaker deeper materials of the Artemis diapir.
4. Our 1-D mechanistic uplift model for the Troodos Massif is broadly applicable to a spectrum of other protrusions of serpentinized mantle peridotite. Isostatic uplift is an inevitable manifestation of serpentinization reactions that result in density reduction and concomitant volume expansion. For each serpentinized massif, the overall uplift budget will be a combination between the relative contributions of isostatic uplift and dynamic tectonic uplift that jointly contribute to the overall uplift and exposure of serpentinized massifs.

Acknowledgments
The authors gratefully thank the Geological Survey Department of Cyprus for their support (MoU/Ref. No. 05.26.001/5). The authors also thank Dan Doran and Matt Beverley-Smith at the University of Southampton for the preparation of thin sections. Aled D. Evans acknowledges a Natural Environmental Research Council–SPITFIRE CASE PhD award NE/L002531/1 (Natural History Museum CASE partner). Damon A. H. Teagle acknowledges a Royal Society Wolfson Research Merit Award (WM130051). We thank Alastair Robertson for discussions about the uplift and exposure of the Troodos mountains.

Data Availability Statement

All data used within this study are provided and cited accordingly. Previous oxygen and hydrogen stable isotope values are from Heaton (1976), Magaritz and Taylor (1974), and Nuriel et al. (2009).

References

Adamson, D. A., Selkirk, P. M., Price, D. M., Ward, N., & Selkirk, J. M. (1996). Pleistocene uplift and palaeoenvironments of Macquarie Island: Evidence from palaeobeaches and sedimentary deposits. *Papers and Proceedings of the Royal Society of Tasmania, 130*(2), 25–32. https://doi.org/10.26749/rstpp.130.2.25

Appendix B

Alt, J. C., & Shanks, W. C., III. (2006). Stable isotope compositions of serpentinite seamounts in the Mariana forearc: Serpentinization processes, fluid sources and sulfur metasomatism. *Earth and Planetary Science Letters, 242*(3–4), 272–285. https://doi.org/10.1016/j.epsl.2005.11.063

Aral, S. (1994). Characterization of spinel peridotites by olivine-spinel compositional relationships: Review and interpretation. *Chemical Geology, 113*(3–4), 191–204. https://doi.org/10.1016/0009-2541(94)90066-3

Batanova, V. G., & Sobolev, A. V. (2000). Compositional heterogeneity in subduction-related mantle peridotites, Troodos Massif, Cyprus. *Geology, 28*(1), 55–58. https://doi.org/10.1130/0091-7613(2000)028<0055:chisrm>2.3.co;2

Bayrakci, G., Minshull, T. A., Sawyer, D. S., Reston, T. J., Klaeschen, D., Papenberg, C., et al. (2016). Fault-controlled hydration of the upper mantle during continental rifting. *Nature Geoscience, 9*(5), 384–388. https://doi.org/10.1038/ngeo2671

Beslier, M. O., Ask, M., & Boillot, G. (1993). Ocean-continent boundary in the Iberia Abyssal Plain from multichannel seismic data. *Tectonophysics, 218*(4), 383–393. https://doi.org/10.1016/0040-1951(93)90327-g

Birch, F. (1961). The velocity of compressional waves in rocks to 10 kilobars: 2. *Journal of Geophysical Research, 66*(7), 2199–2224. https://doi.org/10.1029/jz066i007p02199

Birch, F. (1964). Density and composition of mantle and core. *Journal of Geophysical Research, 69*(20), 4377–4388. https://doi.org/10.1029/jz069i020p04377

Boillot, G., Girardeau, J., & Kornprobst, J. (1988). Rifting of the Galicia margin: Crustal thinning and emplacement of mantle rocks on the seafloor. In G. Boillot, E. L. Winterer, et al. (Eds.), *Proc. ODP, Sci. Results* (Vol. 103, pp. 741–756). College Station, Texas: Ocean Drilling Program. https://doi.org/10.2973/odp.proc.sr.103.179.1988

Boillot, G., Grimaud, S., Mauffret, A., Mougenot, D., Kornprobst, J., Mergoil-Daniel, J., & Torrent, G. (1980). Ocean-continent boundary off the Iberian margin: A serpentinite diapir west of the Galicia Bank. *Earth and Planetary Science Letters, 48*(1), 23–34. https://doi.org/10.1016/0012-821x(80)90166-1

Bonatti, E. (1976). Serpentinite protrusions in the oceanic crust. *Earth and Planetary Science Letters, 32*(2), 107–113. https://doi.org/10.1016/0012-821x(76)90048-0

Bonatti, E. (1978). Vertical tectonism in oceanic fracture zones. *Earth and Planetary Science Letters, 37*(3), 369–379. https://doi.org/10.1016/0012-821x(78)90052-3

Boronina, A., Balderer, W., Renard, P., & Stichler, W. (2005). Study of stable isotopes in the Kouris catchment (Cyprus) for the description of the regional groundwater flow. *Journal of Hydrology, 308*(1–4), 214–226. https://doi.org/10.1016/j.jhydrol.2004.11.001

Byerly, P. E. (1966). Interpretations of gravity data from the central Coast Ranges and San Joaquin Valley, California. *The Geological Society of America Bulletin, 77*(1), 83–94. https://doi.org/10.1130/0016-7606(1966)77[83:iogdft]2.0.co;2

Campos, T. F., Bezerra, F. H., Srivastava, N. K., Vieira, M. M., & Vita-Finzi, C. (2010). Holocene tectonic uplift of the St Peter and St Paul Rocks (Equatorial Atlantic) consistent with emplacement by extrusion. *Marine Geology, 271*(1–2), 177–186. https://doi.org/10.1016/j.margeo.2010.02.013

Campos, T. F., Neto, J. V., Srivastava, N. K., Petta, R. A., Hartmann, L. A., Moraes, J. F. S., et al. (2005). Saint Peter and Saint Paul's archipelago—Tectonic uplift of infra-crustal rocks in the Atlantic Ocean. *Geological and Paleontological Sites of Brazil*. Retrieved from http://sigep.cprm.gov.br/sitio002/sitio002english.pdf

Cao, W., & Paterson, S. (2016). A mass balance and isostasy model: Exploring the interplay between magmatism, deformation and surface erosion in continental arcs using central Sierra Nevada as a case study. *Geochemistry, Geophysics, Geosystems, 17*(6), 2194–2212. https://doi.org/10.1002/2015gc006229

Casey, T. A. L., & Dickinson, W. R. (1976). Sedimentary serpentinite of the Miocene Big Blue Formation near Cantua Creek, California. *AAPG-SEPM-SEG Pacific Sections Meeting, 60*(12), 2177. https://doi.org/10.1306/c1ea3ae1-16c9-11d7-8645000102c1865d

Coleman, R. G. (1996). New Idria serpentinite: A land management dilemma. *Environmental and Engineering Geoscience, 2*(1), 9–22. https://doi.org/10.2113/gseegeosci.ii.1.9

Craw, D., Landis, C. A., & Kelsey, P. I. (1987). Authigenic chrysotile formation in the matrix of Quaternary debris flows, northern Southland, New Zealand. *Clays and Clay Minerals, 35*(1), 43–52. https://doi.org/10.1346/CCMN.1987.0350106

Darwin, C. R. (1835). *Extracts from letters addressed to Professor Henslow by C. Darwin, Esq: Read at a meeting of the society on the 16th of November 1835*. University Press for the Cambridge Philosophical Society.

Dick, H. J., & Bullen, T. (1984). Chromian spinel as a petrogenetic indicator in abyssal and alpine-type peridotites and spatially associated lavas. *Contributions to Mineralogy and Petrology, 86*(1), 54–76. https://doi.org/10.1007/bf00373711

Dickinson, W. R. (1966). Table Mountain serpentinite extrusion in California Coast ranges. *Geological Society of America Bulletin, 77*(5), 451–472. https://doi.org/10.1130/0016-7606(1966)77[451:tmseic]2.0.co;2

Ergün, M., Okay, S., Sarı, C., Oral, E. Z., Ash, M., Hall, J., & Miller, H. (2005). Gravity anomalies of the Cyprus Arc and their tectonic implications. *Marine Geology, 221*(1–4), 349–358. https://doi.org/10.1016/j.margeo.2005.03.004

Evans, C. A., & Baltuck, M. (1988). Low-temperature alteration of peridotite, Hole 637A. In G. Boillot, E. L. Winterer, et al. (Eds.), *Proc. ODP, Sci. Results* (Vol. 103, pp. 235–239). College Station, Texas: Ocean Drilling Program. https://doi.org/10.2973/odp.proc.sr.103.139.1988

Feld, C., Mechie, J., Huebscher, C., Hall, J., Nicolaides, S., Gurbuz, C., et al. (2017). Crustal structure of the Eratosthenes Seamount, Cyprus and S. Turkey from an amphibian wide-angle seismic profile. *Tectonophysics, 700*, 32–59. https://doi.org/10.1016/j.tecto.2017.02.003

Follows, E. J. (1990). *Sedimentology and tectonic setting of Miocene reef and related sediments in Cyprus (PhD Thesis)*. University of Edinburgh.

Fossen, H., & Cavalcante, G. C. G. (2017). Shear zones—A review. *Earth-Science Reviews, 171*, 434–455. https://doi.org/10.1016/j.earscirev.2017.05.002

Fryer, P. (2012). Serpentinite mud volcanism: Observations, processes, and implications. *Annual Review of Marine Science, 4*, 345–373. https://doi.org/10.1146/annurev-marine-120710-100922

Fryer, P., Ambos, E. L., & Hussong, D. M. (1985). Origin and emplacement of Mariana forearc seamounts. *Geology, 13*(11), 774–777. https://doi.org/10.1130/0091-7613(1985)13<774:oaeomf>2.0.co;2

Fryer, P., Pearce, J. A., & Stokking, L. B. (1992). A synthesis of Leg 125 drilling of serpentine seamounts on the Mariana and Izu–Bonin forearcs. In P. Fryer, J. A. Pearce, L. B. Stokking, et al. (Eds.), *Proc. ODP, Sci. Results* (Vol. 125, pp. 445–485). College Station, Texas: Ocean Drilling Program. https://doi.org10.2973/odp.proc.sr.125.168.1992

Gass, I. G. (1968). Is the Troodos massif of Cyprus a fragment of Mesozoic ocean floor? *Nature, 220*(5162), 39–42. https://doi.org/10.1038/220039a0

Gass, I. G. (1977). *Origin and emplacement of ophiolites* (Vol. 7, pp. 72–76). London: Geological Society, Special Publications. https://doi.org/10.1144/gsl.sp.1977.007.01.07

Gass, I. G., & Masson-Smith, D. (1963). The geology and gravity anomalies of the Troodos Massif, Cyprus. *Philosophical Transactions of the Royal Society of London - Series A: Mathematical and Physical Sciences*, *255*(1060), 417–467. https://doi.org/10.1098/rspb.1963.003010.1098/rsta.1963.0009

Goscombe, B. D., & Everard, J. L. (1998). *1: 10000 geological map of Macquarie Island*. Mineral Resources Tasmania.

Hacker, B. R., Mosenfelder, J. L., & Gnos, E. (1996). Rapid emplacement of the Oman ophiolite: Thermal and geochronologic constraints. *Tectonics*, *15*(6), 1230–1247. https://doi.org/10.1029/96tc01973

Heaton, T. H. E. (1976). *Hydrogen and oxygen isotope study of the metamorphism and mineralisation of the Troodos Complex, Cyprus (PhD Thesis)*. University of Edinburgh.

Heaton, T. H. E., & Sheppard, S. M. F. (1977). *Hydrogen and oxygen isotope evidence for sea-water-hydrothermal alteration and ore deposition, Troodos Complex, Cyprus* (Vol. 7, pp. 42–57). London: Geological Society, Special Publications. https://doi.org/10.1144/gsl.sp.1977.007.01.05

Hekinian, R., Juteau, T., Gracia, E., Sichler, B., Sichel, S., Udintsev, G., et al. (2000). Submersible observations of Equatorial Atlantic Mantle: The St. Paul fracture zone region. *Marine Geophysical Researches*, *21*(6), 529–560. https://doi.org/10.1023/a:1004819701870

Henning, A. T., Sawyer, D. S., & Templeton, D. C. (2004). Exhumed upper mantle within the ocean-continent transition on the northern West Iberia margin: Evidence from prestack depth migration and total tectonic subsidence analyses. *Journal of Geophysical Research*, *109*(B5). https://doi.org/10.1029/2003jb002526

Hess, H. H. (1954). Geological hypotheses and the earth's crust under the oceans. *Proceedings of the Royal Society of London—Series A: Mathematical and Physical Sciences*, *222*, 341–348. https://doi.org/10.1098/rspa.1954.0077

Hyndman, R. D., & Drury, M. J. (1976). The physical properties of oceanic basement rocks from deep drilling on the Mid-Atlantic Ridge. *Journal of Geophysical Research*, *81*(23), 4042–4052. https://doi.org/10.1029/jb081i023p04042

Ishii, T., Robinson, P. T., Maekawa, H., & Fiske, R. (1992). Petrological studies of peridotites from diapiric serpentinite seamounts in the Izu-Ogasawara-Mariana forearc, Leg 125. In P. Fryer, J. A. Pearce, L. B. Stokking, et al. (Eds.), *Proc. ODP, Sci. Results* (Vol. 125, pp. 445–485). College Station, Texas: Ocean Drilling Program. https://doi.org/10.2973/odp.proc.sr.125.129.1992

Kelemen, P. B., Matter, J., Streit, E. E., Rudge, J. F., Curry, W. B., & Blusztajn, J. (2011). Rates and mechanisms of mineral carbonation in peridotite: Natural processes and recipes for enhanced, in situ CO_2 capture and storage. *Annual Review of Earth and Planetary Sciences*, *39*, 545–576. https://doi.org/10.1146/annurev-earth-092010-152509

Kil, Y., Lee, S. H., Park, M. H., & Wendlandt, R. F. (2010). Nature of serpentinization of ultramafic rocks from Hero Fracture Zone, Antarctic: Constraints from stable isotopes. *Marine Geology*, *274*(1–4), 43–49. https://doi.org/10.1016/j.margeo.2010.03.004

Kyser, T. K., & Kerrich, R. (1991). Retrograde exchange of hydrogen isotopes between hydrous minerals and water at low temperatures. In H. P. Taylor, J. R. O'Neil, & I. Kaplan (Eds.), *Stable Isotope Geochemistry: A Tribute to Samuel Epstein* (Vol. 3, pp. 409–424). Geochemical Society Special Publication.

Kyser, T. K., O'Hanley, D. S., & Wicks, F. J. (1999). The origin of fluids associated with serpentinization; evidence from stable-isotope compositions. *The Canadian Mineralogist*, *37*(1), 223–237.

Lamadrid, H. M., Rimstidt, J. D., Schwarzenbach, E. M., Klein, F., Ulrich, S., Dolocan, A., & Bodnar, R. J. (2017). Effect of water activity on rates of serpentinization of olivine. *Nature Communications*, *8*(1), 1–9. https://doi.org/10.1038/ncomms16107

Lee, C. T. A., Thurner, S., Paterson, S., & Cao, W. (2015). The rise and fall of continental arcs: Interplays between magmatism, uplift, weathering, and climate. *Earth and Planetary Science Letters*, *425*, 105–119. https://doi.org/10.1016/j.epsl.2015.05.045

Lowell, R. P., & Rona, P. A. (2002). Seafloor hydrothermal systems driven by the serpentinization of peridotite. *Geophysical Research Letters*, *29*(11). https://doi.org/10.1029/2001gl014411

Macdonald, A. H., & Fyfe, W. S. (1985). Rate of serpentinization in seafloor environments. *Tectonophysics*, *116*(1–2), 123–135. https://doi.org/10.1016/0040-1951(85)90225-2

Mackenzie, G. D., Maguire, P. K. H., Coogan, L. A., Khan, M. A., Eaton, M., & Petrides, G. (2006). Geophysical constraints on the crustal architecture of the Troodos ophiolite: Results from the IANGASS project. *Geophysical Journal International*, *167*(3), 1385–1401. https://doi.org/10.1111/j.1365-246x.2006.03144.x

MacLeod, C. J. (1988). *The tectonic evolution of the Eastern Limassol Forest Complex, Cyprus (PhD Thesis)*. The Open University.

MacLeod, C. J. (1990). Role of the Southern Troodos Transform Fault in the rotation of the Cyprus microplate: evidence from the Eastern Limassol Forest Complex. In J. Malpas, E. M. Moores, A. Panayiotou, & C. Xenophontos (Eds.), *Ophiolites: Ocean Crustal Analogues, Proc. Symp. "TROODOS 1987"* (pp. 75-85). Nicosia, Cyprus: Geological Survey Department.

Magaritz, M., & Taylor, H. P., Jr. (1974). Oxygen and hydrogen isotope studies of serpentinization in the Troodos ophiolite complex, Cyprus. *Earth and Planetary Science Letters*, *23*(1), 8–14. https://doi.org/10.1016/0012-821x(74)90023-5

Maia, M., Sichel, S., Briais, A., Brunelli, D., Ligi, M., Ferreira, N., et al. (2016). Extreme mantle uplift and exhumation along a transpressive transform fault. *Nature Geoscience*, *9*(8), 619–623. https://doi.org/10.1038/ngeo2759

Malpas, J., Robinson, P. T., & Salisbury, M. (1989). Geology and geophysics of borehole CY-4 of the Cyprus crustal study project, summary. In I. L. Gibson, J. Malpas, P. T. Robinson, & C. Xenophontos (Eds.), *Cyprus crustal study project Initial Rep. Hole CY-4* (pp. 381–393).

Martin, B., & Fyfe, W. S. (1970). Some experimental and theoretical observations on the kinetics of hydration reactions with particular reference to serpentinization. *Chemical Geology*, *6*, 185–202. https://doi.org/10.1016/0009-2541(70)90018-5

Masseli, C., Coffin, M. F., Mann, P., Mosher, S., Frohlich, C., Duncan, C. S., et al. (2000). Neotectonics of the Macquarie Ridge Complex, Australia-Pacific plate boundary. *Journal of Geophysical Research*, *105*(B6), 13457–13480. https://doi.org/10.1029/1999jb900408

McCallum, J. E. (1989). *Sedimentation and tectonics of the Plio-Pleistocene of Cyprus (PhD Thesis)*. University of Edinburgh.

McCollom, T. M., Klein, F., Robbins, M., Moskowitz, B., Berquó, T. S., Jöns, N., et al. (2016). Temperature trends for reaction rates, hydrogen generation, and partitioning of iron during experimental serpentinization of olivine. *Geochimica et Cosmochimica Acta*, *181*, 175–200. https://doi.org/10.1016/j.gca.2016.03.002

McPhee, D. K., Jachens, R. C., & Wentworth, C. M. (2004). Crustal structure across the San Andreas Fault at the SAFOD site from potential field and geologic studies. *Geophysical Research Letters*, *31*(12). https://doi.org/10.1029/2003gl019363

Melson, W. G., Hart, S. R., & Thompson, G. (1972). St. Paul's rocks, equatorial Atlantic: Petrogenesis, radiometric ages and implications on sea-floor spreading. In R. Shagam, R. B. Hargraves, W. J. Morgan, F. B. Van Houten, C. A. Burk, H. D. Holland, & L. C. Hollister (Eds.), *Studies in Earth and space sciences: A memoir in honor of Harry Hammond Hess* (Vol. 132, pp. 241–272). Geological Society of America. https://doi.org/10.1130/mem132-p241

Minshull, T. A., Dean, S. M., & Whitmarsh, R. B. (2014). The peridotite ridge province in the southern Iberia Abyssal Plain: Seismic constraints revisited. *Journal of Geophysical Research: Solid Earth*, *119*(3), 1580–1598. https://doi.org/10.1002/2014jb011011

Moore, D. E., & Rymer, M. J. (2007). Talc-bearing serpentinite and the creeping section of the San Andreas fault. *Nature*, *448*(7155), 795–797. https://doi.org/10.1038/nature06064

Appendix B

Moores, E. M., Robinson, P. T., Malpas, J., & Xenophontos, C. (1984). Model for the origin of the Troodos massif, Cyprus, and other mid-east ophiolites. *Geology*, *12*(8), 500–503. https://doi.org/10.1130/0091-7613(1984)12<500:mftoot>2.0.co;2
Moores, E. M., & Vine, F. J. (1971). The Troodos Massif, Cyprus and other ophiolites as oceanic crust: Evaluation and implications. *Philosophical Transactions of the Royal Society of London—Series A: Mathematical and Physical Sciences*, *268*(1192), 443–467. https://doi.org/10.1098/rsta.1971.0006
Morag, N., Haviv, I., & Katzir, Y. (2016). From ocean depths to mountain tops: Uplift of the Troodos ophiolite (Cyprus) constrained by low-temperature thermochronology and geomorphic analysis. *Tectonics*, *35*(3), 622–637. https://doi.org/10.1002/2015tc004069
Motti, M. J., Wheat, C. G., Fryer, P., Gharib, J., & Martin, J. B. (2004). Chemistry of springs across the Mariana forearc shows progressive devolatilization of the subducting plate. *Geochimica et Cosmochimica Acta*, *68*(23), 4915–4933. https://doi.org/10.1016/j.gca.2004.05.037
Mukasa, S. B., & Ludden, J. N. (1987). Uranium-lead isotopic ages of plagiogranites from the Troodos ophiolite, Cyprus, and their tectonic significance. *Geology*, *15*(9), 825–828. https://doi.org/10.1130/0091-7613(1987)15<825:ulaopf>2.0.co;2
Mumpton, F. A., & Thompson, C. S. (1975). Mineralogy and origin of the Coalinga asbestos deposit. *Clays and Clay Minerals*, *23*(2), 131–143. https://doi.org/10.1346/ccmn.1975.0230209
Murton, B. J. (1986). Anomalous oceanic lithosphere formed in a leaky transform fault: Evidence from the western Limassol Forest Complex, Cyprus. *Journal of the Geological Society*, *143*(5), 845–854. https://doi.org/10.1144/gsjgs.143.5.0845
Nuriel, P., Katzir, Y., Abelson, M., Valley, J. W., Matthews, A., Spicuzza, M. J., & Ayalon, A. (2009). Fault-related oceanic serpentinization in the Troodos ophiolite, Cyprus: Implications for a fossil oceanic core complex. *Earth and Planetary Science Letters*, *282*(1–4), 34–46. https://doi.org/10.1016/j.epsl.2009.02.029
Page, B. M., Coleman, R. G., & Thompson, G. A. (1998). Late Cenozoic tectonics of the central and southern Coast Ranges of California. *The Geological Society of America Bulletin*, *110*(7), 846–876. https://doi.org/10.1130/0016-7606(1998)110<0846:olctot>2.3.co;2
Parkinson, I. J., & Pearce, J. A. (1998). Peridotites from the Izu-Bonin-Mariana forearc (ODP Leg 125): Evidence for mantle melting and melt–mantle interaction in a supra-subduction zone setting. *Journal of Petrology*, *39*(9), 1577–1618. https://doi.org/10.1093/petroj/39.9.1577
Pearce, J. A., Lippard, S. J., & Roberts, S. (1984). *Characteristics and tectonic significance of supra-subduction zone ophiolites* (Vol. 16(1)pp. 77–94). London: Geological Society, Special Publications. https://doi.org/10.1144/gsl.sp.1984.016.01.06
Poole, A. J., & Robertson, A. H. F. (1991). Quaternary uplift and sea-level change at an active plate boundary, Cyprus. *Journal of the Geological Society*, *148*(5), 909–921. https://doi.org/10.1144/gsjgs.148.5.0909
Poole, A. J., & Robertson, A. H. F. (1998). Pleistocene fanglomerate deposition related to uplift of the Troodos Ophiolite, Cyprus. In A. H. F. Robertson, K.-C. Emeis, C. Richter, & A. Camerlenghi (Eds.), *Proc. ODP, Sci. Results* (Vol. 160, pp. 545–566). College Station, Texas: Ocean Drilling Program. https://doi.org/10.2973/odp.proc.sr.160.064.1998
Ramsay, J. (1980). Shear zone geometry: A review. *Journal of Structural Geology*, *2*(1–2), 83–99. https://doi.org/10.1016/0191-8141(80)90038-3
Ring, U., & Pantazides, H. (2019). The uplift of the Troodos Massif, Cyprus. *Tectonics*, *38*(8), 3124–3139. https://doi.org/10.1029/2019tc005514
Rivizzigno, P. A., & Karson, J. A. (2004). Structural expression of oblique seafloor spreading in the Macquarie Island Ophiolite. *Southern Ocean Geology*, *32*(2), 125–128. https://doi.org/10.1130/g19906.1
Robertson, A. H. F. (1977). Tertiary uplift history of the Troodos massif, Cyprus. *Geological Society of America Bulletin*, *88*(12), 1763–1772. https://doi.org/10.1130/0016-7606(1977)88<1763:tuhotT>2.0.co;2
Robertson, A. H. F. (1998). Tectonic significance of the Eratosthenes Seamount: A continental fragment in the process of collision with a subduction zone in the eastern Mediterranean (Ocean Drilling Program Leg 160). *Tectonophysics*, *298*(1–3), 63–82. https://doi.org/10.1016/s0040-1951(98)00178-4
Rooney, J. S., Tarling, M. S., Smith, S. A., & Gordon, K. C. (2018). Submicron Raman spectroscopy mapping of serpentinite fault rocks. *Journal of Raman Spectroscopy*, *49*(2), 279–286. https://doi.org/10.1002/jrs.5277
Rouchy, J. M., Orszag-Sperber, F., Blanc-Valleron, M. M., Pierre, C., Rivière, M., Combourieu-Nebout, N., & Panayides, I. (2001). Paleoenvironmental changes at the Messinian–Pliocene boundary in the eastern Mediterranean (southern Cyprus basins): Significance of the Messinian Lago-Mare. *Sedimentary Geology*, *145*(1–2), 93–117. https://doi.org/10.1016/s0037-0738(01)00126-9
Saccocia, P. J., Seewald, J. S., & Shanks, W. C., III. (2009). Oxygen and hydrogen isotope fractionation in serpentine-water and talc-water systems from 250 to 450 C, 50 MPa. *Geochimica et Cosmochimica Acta*, *73*(22), 6789–6804. https://doi.org/10.1016/j.gca.2009.07.036
Schuiling, R. D. (2011). Troodos: A giant serpentinite diapir. *International Journal of Geosciences*, *2*(2), 98–101. https://doi.org/10.4236/ijg.2011.22010
Searle, M., & Cox, J. (1999). Tectonic setting, origin, and obduction of the Oman ophiolite. *Geological Society of America Bulletin*, *111*(1), 104–122. https://doi.org/10.1130/0016-7606(1999)111<0104:tsoaoo>2.3.co;2
Selkirk, P., Seppelt, R., & Selkirk, D. (1990). *Subantarctic Macquarie Island: Environment and biology*. Cambridge University Press.
Shelton, A. W. (1993). Troodos revisited: The Mount Olympus gravity anomaly. *Geological Society, London, Special Publications* *76*(1), 197–212. https://doi.org/10.1144/gsl.sp.1993.076.01.09
Simoes, M., Braun, J., & Bonnet, S. (2010). Continental-scale erosion and transport laws: A new approach to quantitatively investigate macroscale landscapes and associated sediment fluxes over the geological past. *Geochemistry, Geophysics, Geosystems*, *11*(9). https://doi.org/10.1029/2010gc003121
Stow, D. A., Braakenburg, N. E., & Xenophontos, C. (1995). The Pissouri Basin fan-delta complex, southwestern Cyprus. *Sedimentary Geology*, *98*(1–4), 245–262. https://doi.org/10.1016/0037-0738(95)00035-7
Thom, J. G., Dipple, G. M., Power, I. M., & Harrison, A. L. (2013). Chrysotile dissolution rates: Implications for carbon sequestration. *Applied Geochemistry*, *35*, 244–254. https://doi.org/10.1016/J.APGEOCHEM.2013.04.016
Toft, P. B., Arkani-Hamed, J., & Haggerty, S. E. (1990). The effects of serpentinization on density and magnetic susceptibility: A petrophysical model. *Physics of the Earth and Planetary Interiors*, *65*(1–2), 137–157. https://doi.org/10.1016/0031-9201(90)90082-9
Tsujimori, T., Liou, J. G., Coleman, R. G., Cloos, M., Carlson, W. D., Gilbert, M. C., & Sorensen, S. S. (2007). *Finding of high-grade tectonic blocks from the New Idria serpentinite body, Diablo Range, California: Petrologic constraints on the tectonic evolution of an active serpentinite diapir*. Geological Society of America.
Vermeesch, P., Miller, D. D., Graham, S. A., De Grave, J., & McWilliams, M. O. (2006). Multimethod detrital thermochronology of the Great Valley Group near New Idria, California. *Geological Society of America Bulletin*, *118*(1–2), 210–218. https://doi.org/10.1130/b25797.1
Watkins, N. D., & Gunn, B. M. (1971). Petrology, geochemistry, and magnetic properties of some rocks dredged from the Macquarie ridge. *New Zealand Journal of Geology and Geophysics*, *14*(1), 153–168. https://doi.org/10.1080/00288306.1971.10422468
Wenner, D. B. (1971). *Hydrogen and oxygen isotopic studies of serpentinization of ultramafic rocks (PhD Thesis)*. California Institute of Technology.

Wenner, D. B., & Taylor, H. P. (1971). Temperatures of serpentinization of ultramafic rocks based on O^{18}/O^{16} fractionation between coexisting serpentine and magnetite. *Contributions to Mineralogy and Petrology*, *32*(3), 165–185. https://doi.org/10.1007/bf00643332

Wertz, K. L., Mosher, S., Daczko, N. R., & Coffin, M. F. (2003). Macquarie Island's Finch-Langdon fault: A ridge-transform inside-corner structure. *Geology*, *31*(8), 661–664. https://doi.org/10.1130/g19441.1

Whitmarsh, R.B., & Sawyer, D. S. (1996). The ocean/continent transition beneath the Iberia abyssal plain and continental-rifting to seafloor-spreading processes. In R. B. Whitmarsh, D. S. Sawyer, A. Klaus, & D. G. Masson (Eds.), *Proc. ODP, Sci. Results* (Vol. 149, pp. 713–733). College Station, Texas: Ocean Drilling Program. https://doi.org/10.2973/odp.proc.sr.149.249.1996

Wilson, R., & Ingham, F. (1959). *The geology of the Xeros-Troodos area (No. 1)*. Authority of the Government of Cyprus.

Zheng, Y. F. (1993). Calculation of oxygen isotope fractionation in hydroxyl-bearing silicates. *Earth and Planetary Science Letters*, *120*(3–4), 247–263. https://doi.org/10.1016/0012-821x(93)90243-3

Appendix C

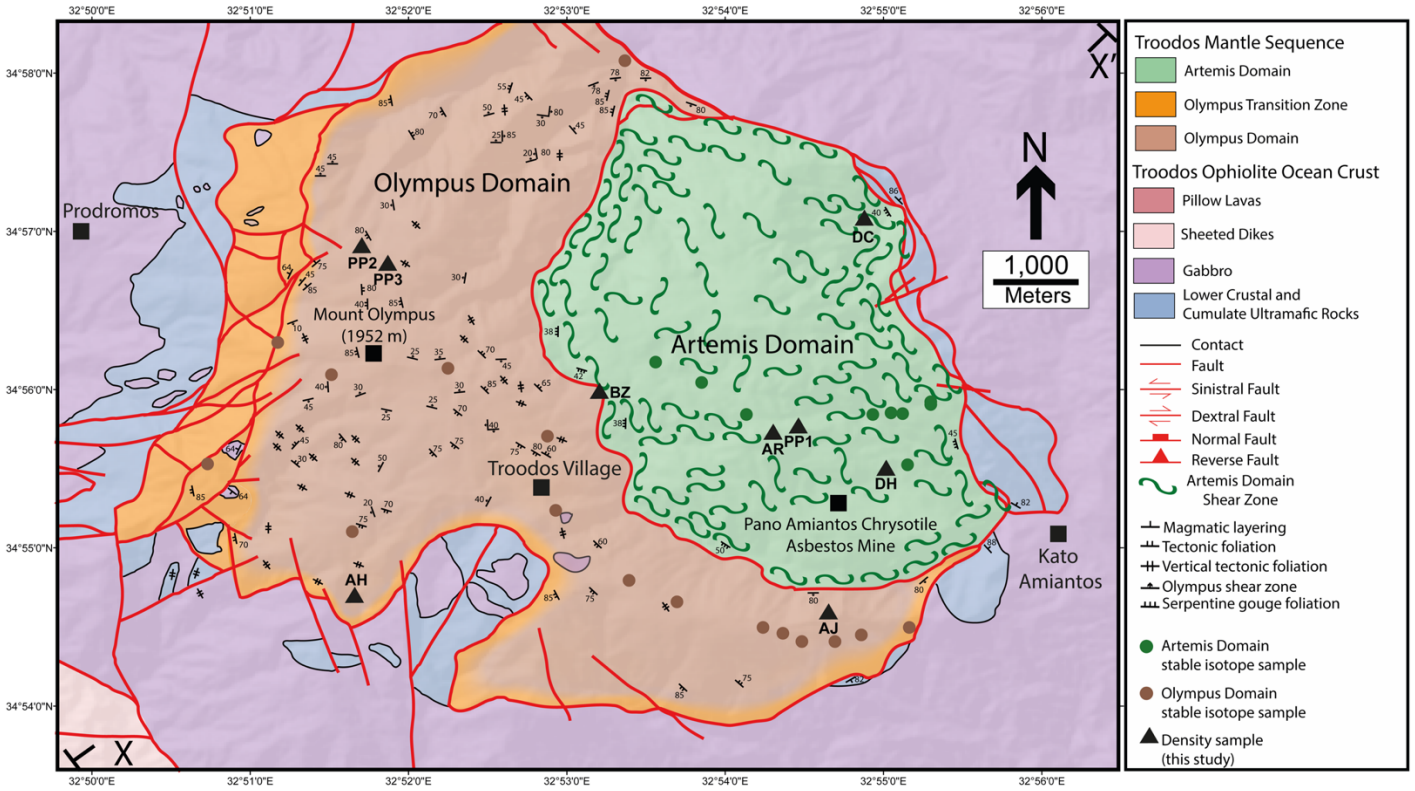

Supplementary Figure 1: Geological map of the Troodos Mantle Sequence. Mapped smaller bodies intercalated into the Olympus Transition Zone are only marked if >100 m in size. Bodies <100 m in size are absorbed into complex Olympus Transition Zone structural unit.

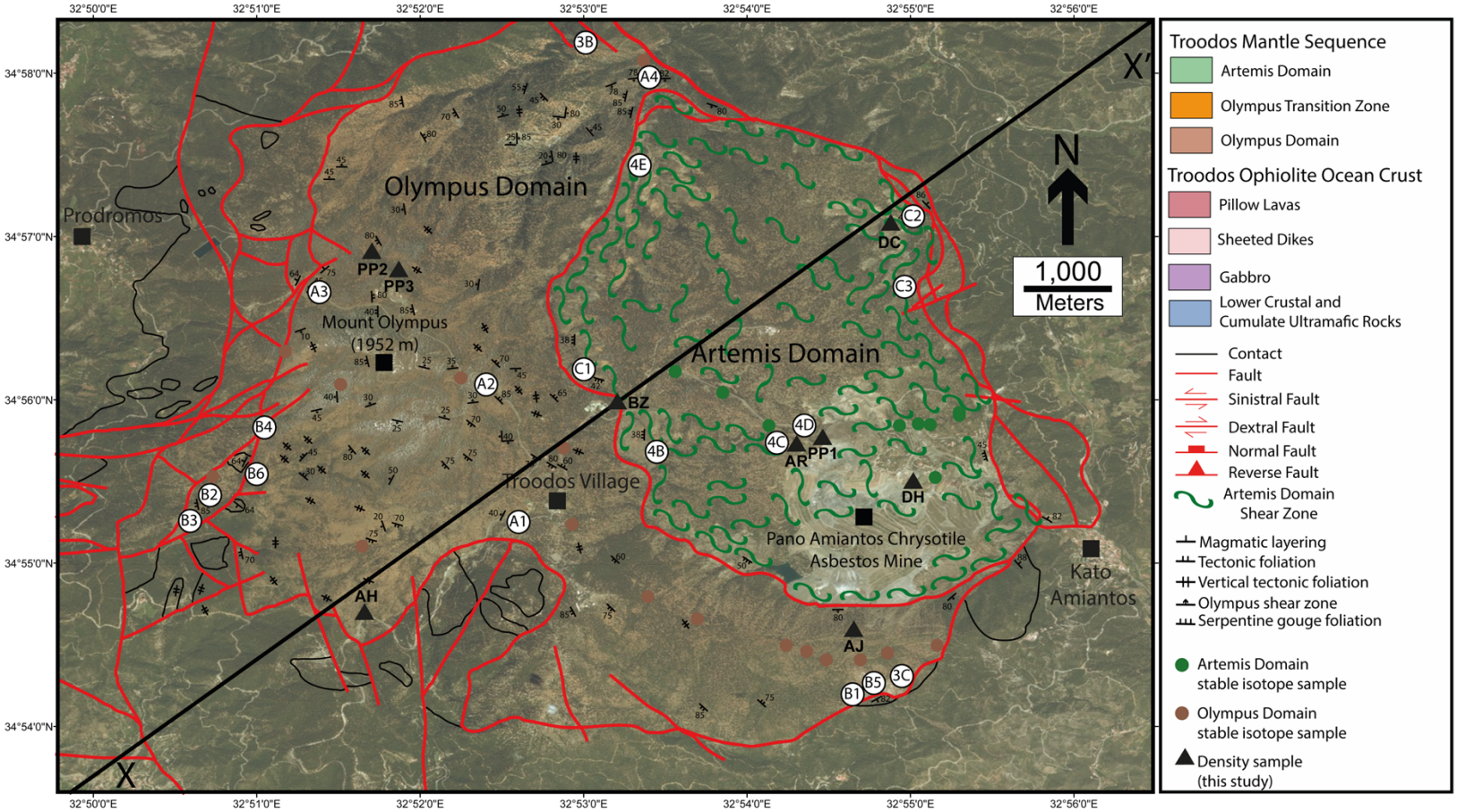

Supplementary Figure 2: Aerial imagery map of the Troodos Mantle Sequence with locations of field pictures from the paper and additional field pictures provided in the supplementary materials.

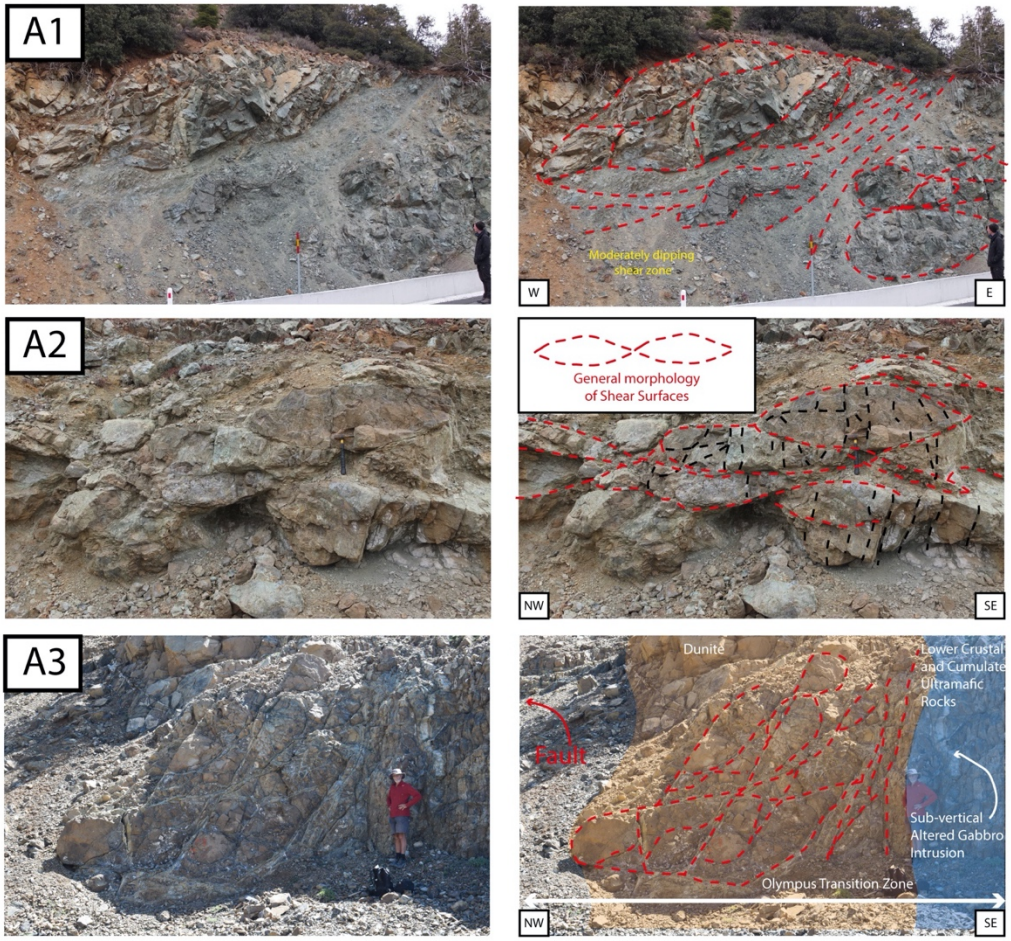
A1
Moderately dipping shear zone
W
E
A2
General morphology of Shear Surfaces
NW
SE
A3
Dunite
Lower Crustal and Cumulate Ultramafic Rocks
Fault
Sub-vertical Altered Gabbro Intrusion
Olympus Transition Zone
NW
SE

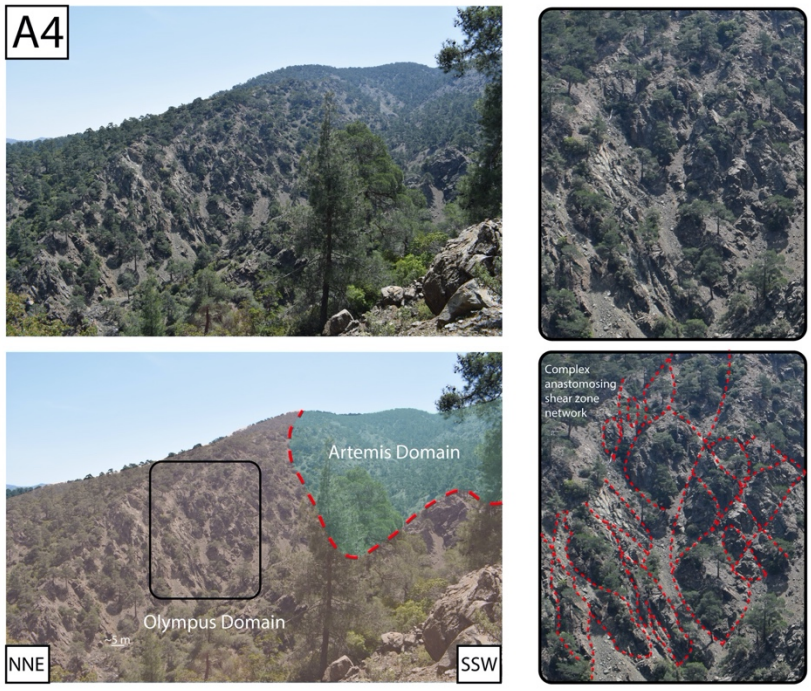
A4
Artemis Domain
Olympus Domain
NNE
SSW
Complex anastomosing shear zone network

Supplementary Figure 3: (A1) Unannotated and annotated field picture pair within the Olympus Domain. A moderately dipping brittle-plastic shear zone is shown. Deformation is concentrated within a zone ~1.5 m in thickness. S C fabrics are observed within the shear zone with competent lozenges exhibiting predominantly asymmetric morphologies. Outside of the main deformation band, shear surfaces separate the rock into separate generally underformed partially serpentinized lozenges of varying symmetries. Subsequent brittle fracturing has resulted in a complex extensional fracture (joint) pattern. Person for scale. (A2) Sub-horizontal conjugate brittle-plastic shear zone shown with generally symmetrical and undeformed lozenges forming in between the shear surfaces. These interconnected shear surfaces intersect at 120° (red lines) and are generally interpreted as examples of conjugate shear zones that have undergone coaxial deformation (e.g., Ramsay, 1980; Fossen and Cavalcante, 2017). The implication of the geometry is that the undeformed lozenges exhibit 'internal boudinage' (i.e., boudinage not related to competence contrasts; Ramsay, 1980) and in this case have extended in the ~horizontal direction and likely flattened in the ~vertical direction. Subsequent brittle fracturing (black lines) occurs within these undeformed, symmetrical, massive, partially serpentinized lozenges. These low-angle conjugate shears are prevalent in road cuttings on the road to the summit of Mount Olympus and are continuous over ~100 m in distance. Away from the summit the general dip angle of these conjugate shear zones increases from low angles (<30°) to moderate-high angles (~60° to <90°; A3), with a general increase in the asymmetry of the lozenges (e.g., A4). Hammer for scale. (A3) A shear zone array orientated at moderate dip angles is shown. Shear surfaces are generally orientated 120° and their geometries are more asymmetric relative to the lozenges of A2. Domain sub-division occurs where, within larger ~2 m lozenges, smaller lozenges are bounded by shear surfaces forming an intricated, anastomosing shear zone array across differing domain scales. Person for scale. (A4) Field picture of the Artemis / Olympus northern boundary. A complex high angle, ~NW dipping, shear zone array occurs. Asymmetric lozenge geometries occur, and shear surfaces are inferred across a range of scales (red lines), highlighting domain sub-division into increasing smaller asymmetric lozenges that are bounded by brittle-plastic shear surfaces. Despite the substantial internal deformation of the Olympus domain (A4), deformation within the Artemis domain is greater than the Olympus domain. Deformation within the Olympus domain results in a cohesive, blocky outcrop pattern, with development of serpentinite breccias localized to outcrop scales where strain has localised between less deformed lozenges (e.g., B4). In contrast, in the Artemis domain, entire hillslopes are composed of serpentinite breccia (e.g., C3).

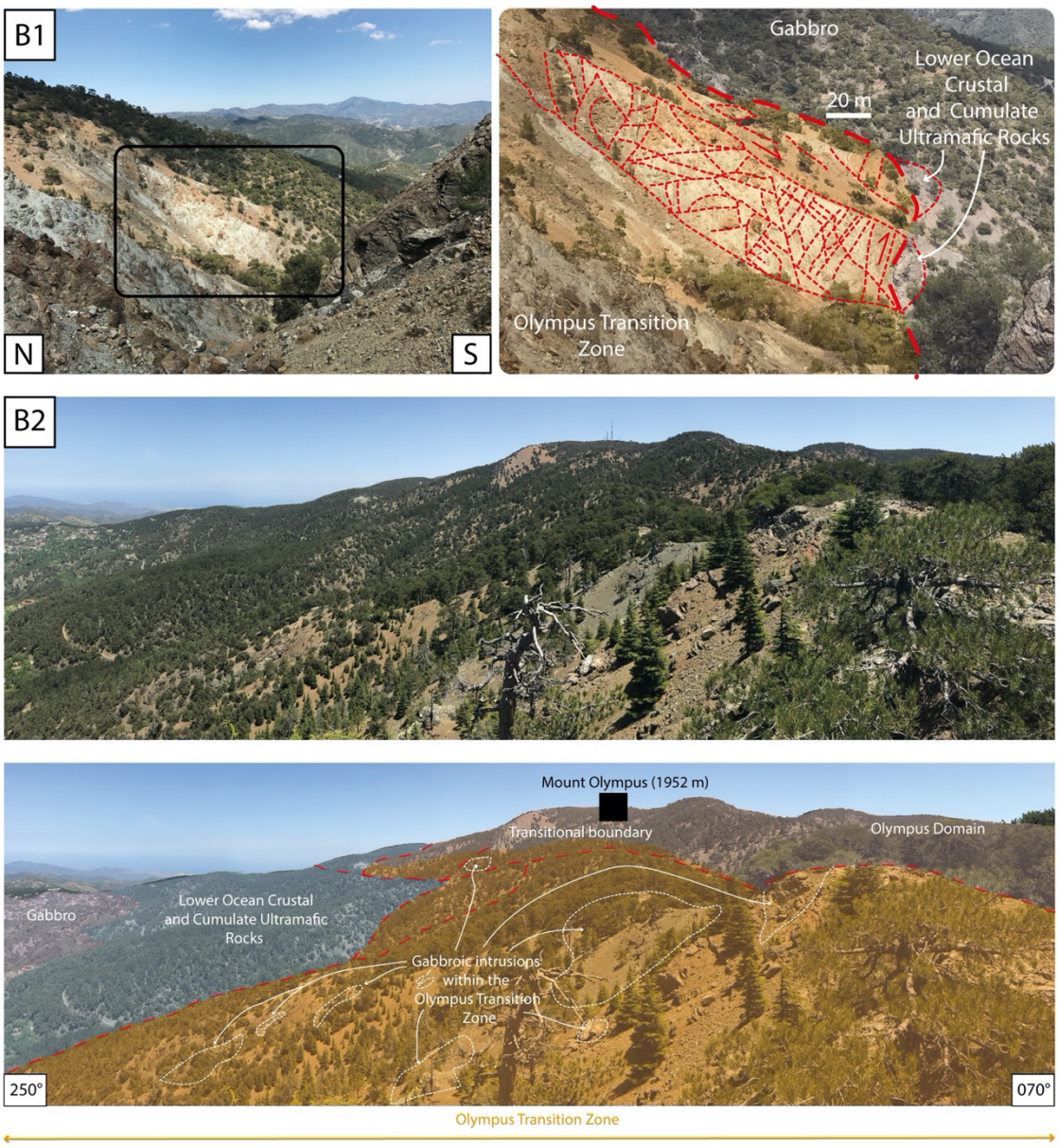
B1
N
S
Gabbro
20 m
Lower Ocean Crustal and Cumulate Ultramafic Rocks
Olympus Transition Zone
B2
Mount Olympus (1952 m)
Transitional boundary
Olympus Domain
Gabbro
Lower Ocean Crustal and Cumulate Ultramafic Rocks
Gabbroic intrusions within the Olympus Transition Zone
250°
070°
Olympus Transition Zone

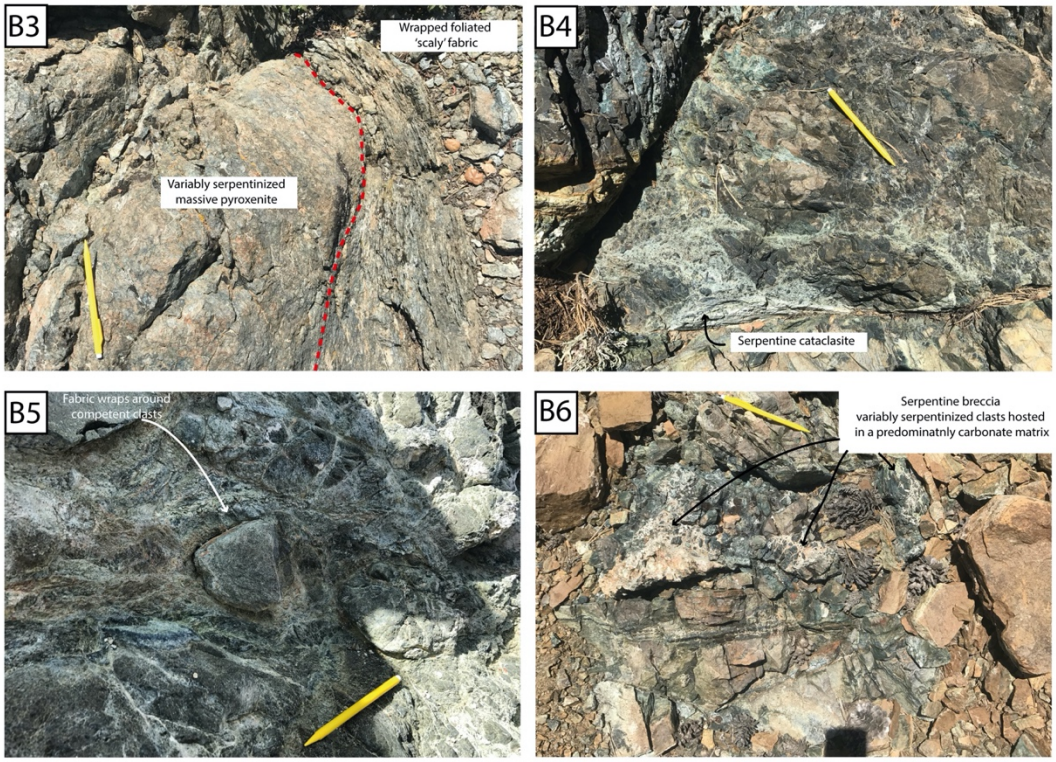

Supplementary Figure 4:

(B1) SE boundary between the Olympus Domain Transition Zone and lower ocean crust cumulate ultramafic rocks and gabbro. This boundary is interpreted as a complex fault zone composed (here at this locality) of primarily Olympus Domain dunites intercalated with lower ocean crust cumulate ultramafic rocks and gabbros. Discontinuous surfaces are inferred (red lines) and highlight a complex array of structures. The prime structure is the ~W-E orientated structure and is inferred as a high-angle reverse fault. The intensity of deformation varies spatially across the Olympus Transition Zone. The western margin of the uplifted mantle peridotites is less deformed (e.g., B2) relative to the intensely deformed SE portion (e.g., B1).

(B2) Field picture looking ~N towards the summit of Mount Olympus, highlighting the complex boundary between the differentially uplifted mantle peridotites and stratigraphically higher but topographically lower ocean crustal rocks. This differential uplift is evident and has been accommodated by a distributed ~500 m to ~1000 m wide zone of variable deformation presented here as the Olympus Transition Zone. The Olympus Transition Zone is a structural unit composed primarily of Olympus Domain dunites with of varying proportions of lower ocean crust cumulate ultramafic rocks and intrusive gabbroic bodies. A transition occurs within the Olympus Transition Zone from predominantly lower ocean crustal units with localized intercalated bodies of dunite and pyroxenite to predominantly Olympus Domain dunites with localized intercalated bodies of gabbro and lower ocean crustal mafic and ultramafic rocks.

Earlier mapping (Wilson, 1959) has inferred that the Previously, ~N-S orientated segment of this western boundary have been inferred as a continuous and conformable boundary with discontinuous oblique faults mapped as offsetting these otherwise conformable boundaries (e.g., Wilson, 1959). We propose that these ~N-S orientated contacts are not discrete lithological contacts but are discontinuous, and likely form part of a complex array of faults that have resulted in distributed deformation across the Olympus Transition Zone.

The western contact of the Olympus Transition Zone is inferred as a faulted contact and is generally denoted by: The occurrence of dunitic bodies; geomorphological changes such

as a break in slope and development of valley lows; a sharp reduction in the density of vegetation; and a change in the colour of float from white/grey to orange as highlighted in aerial photographs (Supp. Mat. Fig. 2). Whereas the eastern contact of the Olympus Transition Zone is transitional and is generally denoted as where outcrops are less deformed, generally massive, and composed of Olympus Domain partially serpentinized dunite and harzburgite.

(B3) A variably serpentinized massive pyroxenite body is wrapped by a matrix composed of a variably serpentinized foliated 'scaly' fabric.

(B4) Serpentine cataclasite located within the Olympus Transition Zone, composed of a cohesive cataclasite composed of variably serpentinized clasts hosted in a fine-grained comminuted serpentine gouge. This Olympus Transition Zone cataclasite is not equivalent to the Artemis serpentine breccia as it is cohesive and competent. The Olympus Transition Zone cataclasite is not ubiquitous, it is generally located where strain has localised between bodies of less deformed competent partially serpentinized peridotites.

(B5) A clast-breccia-gouge assemblage of the Olympus Transition Zone is shown. The assemblage is generally incohesive. The foliated gouge wraps around the competent undeformed clast.

(B6) Serpentine breccia located within the Olympus domain, nearby to the transitional boundary between the Olympus Transition Zone and the Olympus Domain. Deformation is expressed through brecciation with partially serpentinized angular clasts hosted in a predominantly carbonate matrix.

(B3-B6) This image plate highlights a general transition in deformation mechanisms from predominantly brittle-plastic shear zones that wrap around more massive and undeformed clasts (B3) to predominantly brittle deformation mechanisms generally cohesive cataclasis (B4) to then generally incohesive gouge and breccia development (B5) likely overprinting earlier brittle-ductile deformation similar to B3. Finally, an incohesive serpentinite breccia with a carbonate matrix and variably serpentinized clasts (B6). These rocks are likely recording the deformation resulting in the progressive exhumation of mantle peridotites.

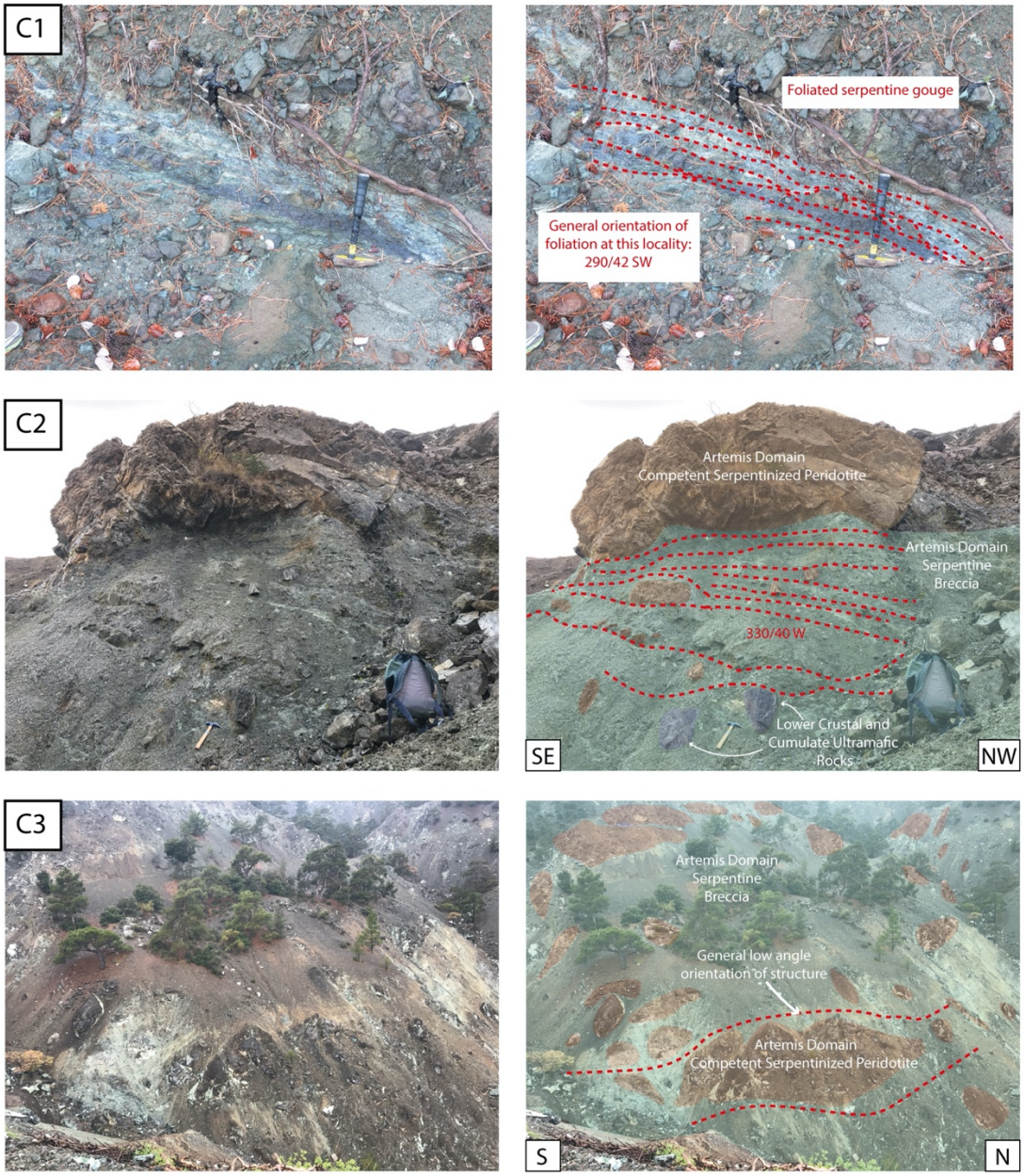

Supplementary Figure 5:

(C1) Foliated serpentine gouge orientated 290/42 SW at the C1 locality. Hammer for scale.

(C2) Typical Artemis domain block-clast-breccia-gouge assemblage with clasts of Competent Serpentinized Peridotite and Lower Crustal and Cumulate Ultramafic Rocks. Foliated gouge wraps around competent clasts. Hammer for scale.

(C3) NE boundary of the Artemis domain, highlights the chaotic nature of the Artemis domain. The general orientation of the structure is of a low dipping angle.

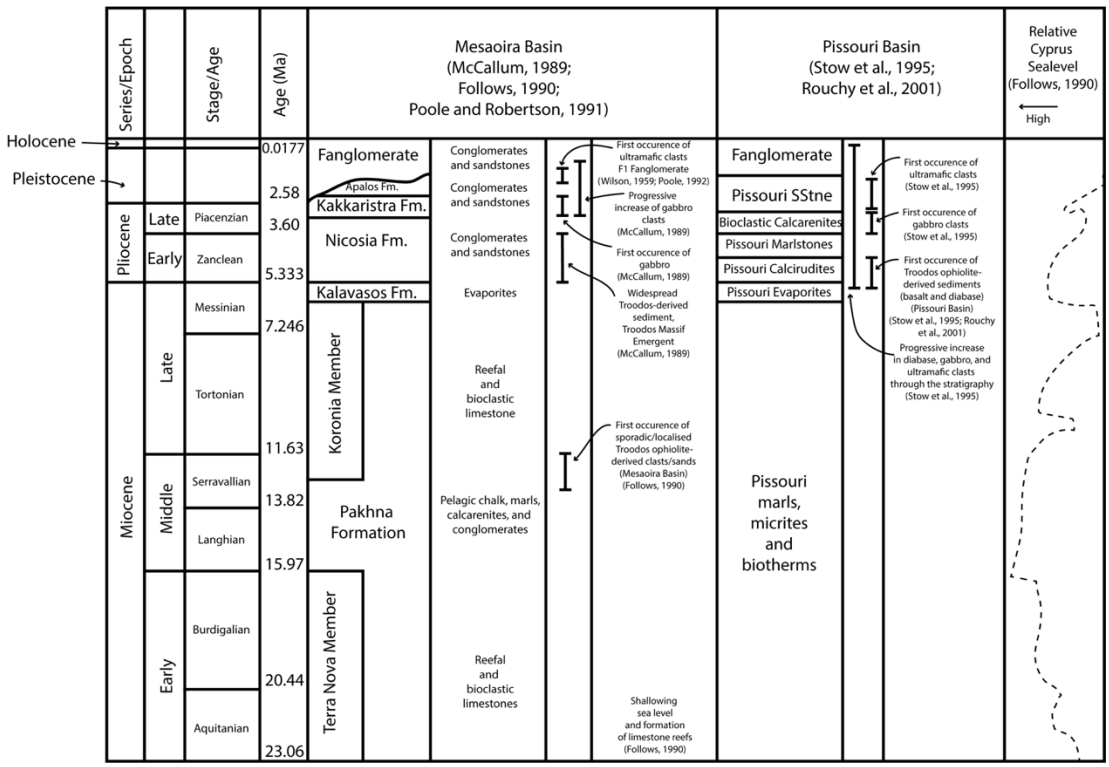

Supplementary Figure 6: Summary table of the circum-Troodos sedimentary sequence

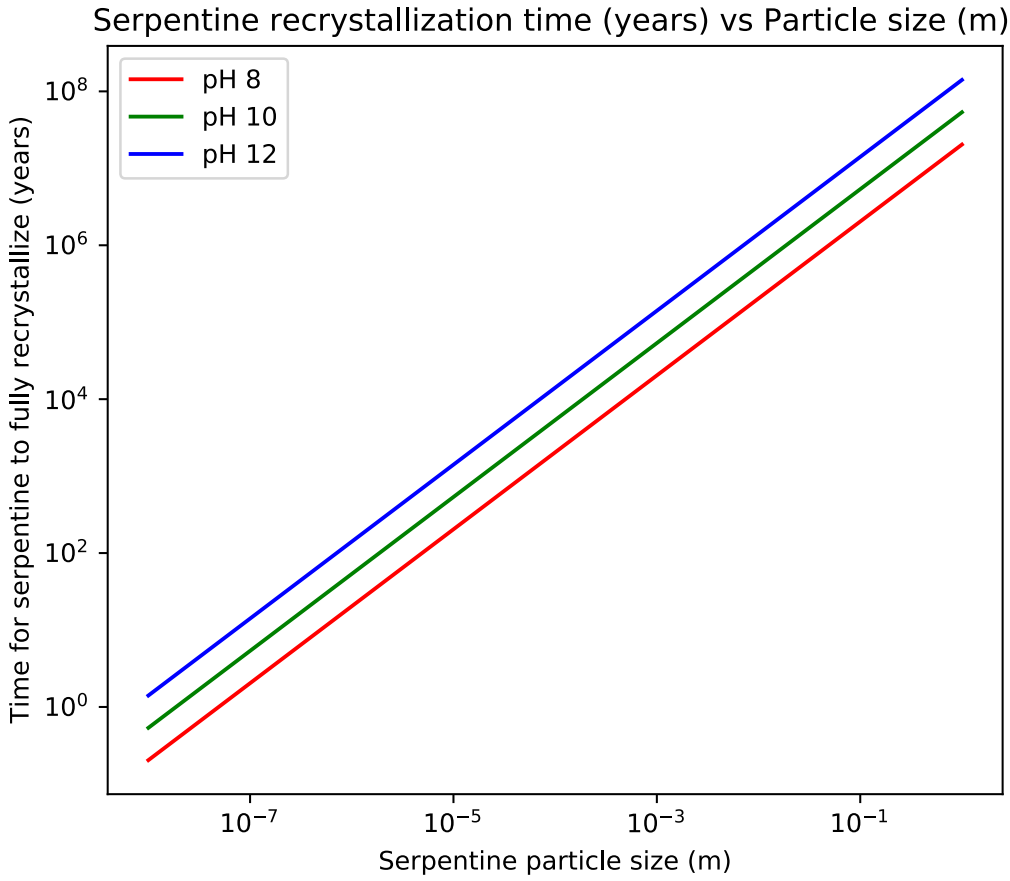

Supplementary Figure 7: Serpentine dissolution time vs particle size under varying pH conditions log-log plot (see main text for details). Serpentine dissolution rate from Thom et al., 2013.

Supplementary Table 1: Summary table of parameters utilised in the application of the mechanistic uplift model to other settings

Area	***St. Peter and St. Paul Rocks***	***Macquarie Island***	***ODP Leg 103 Site 637/'5100 m Hill'***	***New Idria Serpentinite***
Elevation High (m)	22 m asl	410 m asl	~-4948 m	1605 m asl
Surrounding Elevation (m)	~-4000 m	-	~-5300 m	~544 m asl
Parameters				
Time Period (Myr)	10	0.65	-	12
Diapir Density (kg/m3)	2800	2700	2400	2000
Mantle' Density (kg/m3)	3300	3300	2900	2700
Volume Expansion (%)	15	20	-	40
Bedrock Erodibility Constant (m)	-	0.0000015	-	0.0000064
Precipitation (m/yr)	-	0.98	-	0.64
Independent Constraints				
Uplift Rate	1.5 mm/yr (Campos et al., 2010)	0.8 mm/yr (avg.; Adamson et al., 1996)	-	1.7 to 4 mm/yr (Coleman, 1996)
Erosion Rate	-	0.1 mm/yr (coastal erosion; Smith and Bayliss-Smith, 1998)	-	4 mm/yr (Coleman, 1996)
Results				
Isostatic Uplift (Ut; No Erosion) (m)	~3500 m (2000 m/Myr)	~425 m (3000 m/Myr)	~350 m	~20000 m (3000 m/Myr)
Diapir Thickness (No Erosion) (m)	~23000 m (2000 m/Myr)	~2335 m (3000 m/Myr)	~2000 m	-
Elevation (m) (Erosion Applied)	-	~390 m (3000 m/Myr)	-	~1000 m (3000 m/Myr)
Additional Thickness (Dd; Erosion Applied)	-	~2150 m (3000 m/Myr)	-	-
Total Exhumation (Erosion Applied)	-	~185 m (3000 m/Myr)	-	~46000 m (3000 m/Myr)
Diapiric Mode	Isostatic Uplift	Isostatic Uplift	Serpentinite Extrusion	Serpentinite Extrusion
Troodos Massif Analogue	Olympus	Olympus	Artemis	Artemis

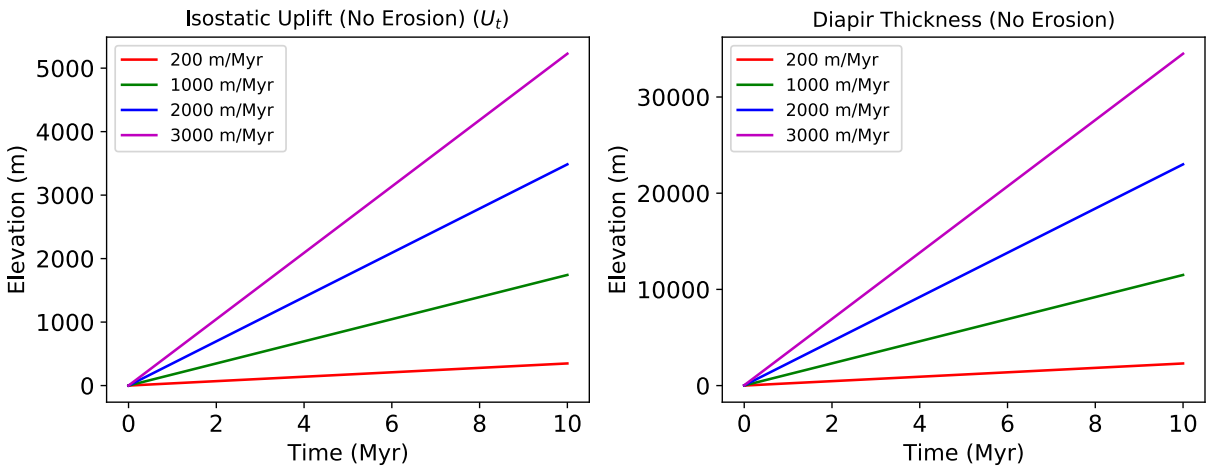

Supplementary Figure 8: Output from the mechanistic uplift model applied to the St. Peter and St. Paul Rocks

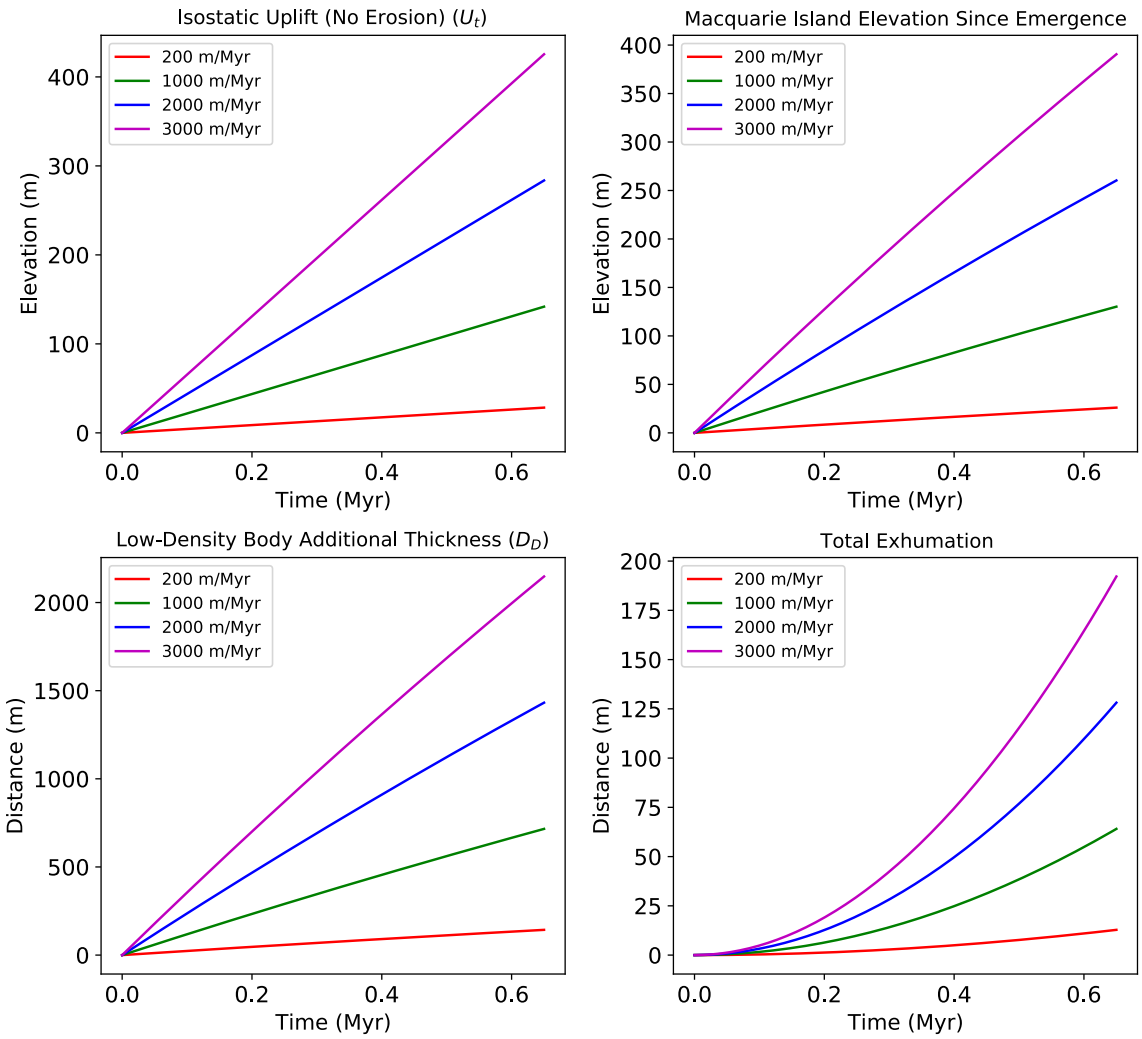

Supplementary Figure 9: Output from the mechanistic uplift model applied to Macquarie Island.

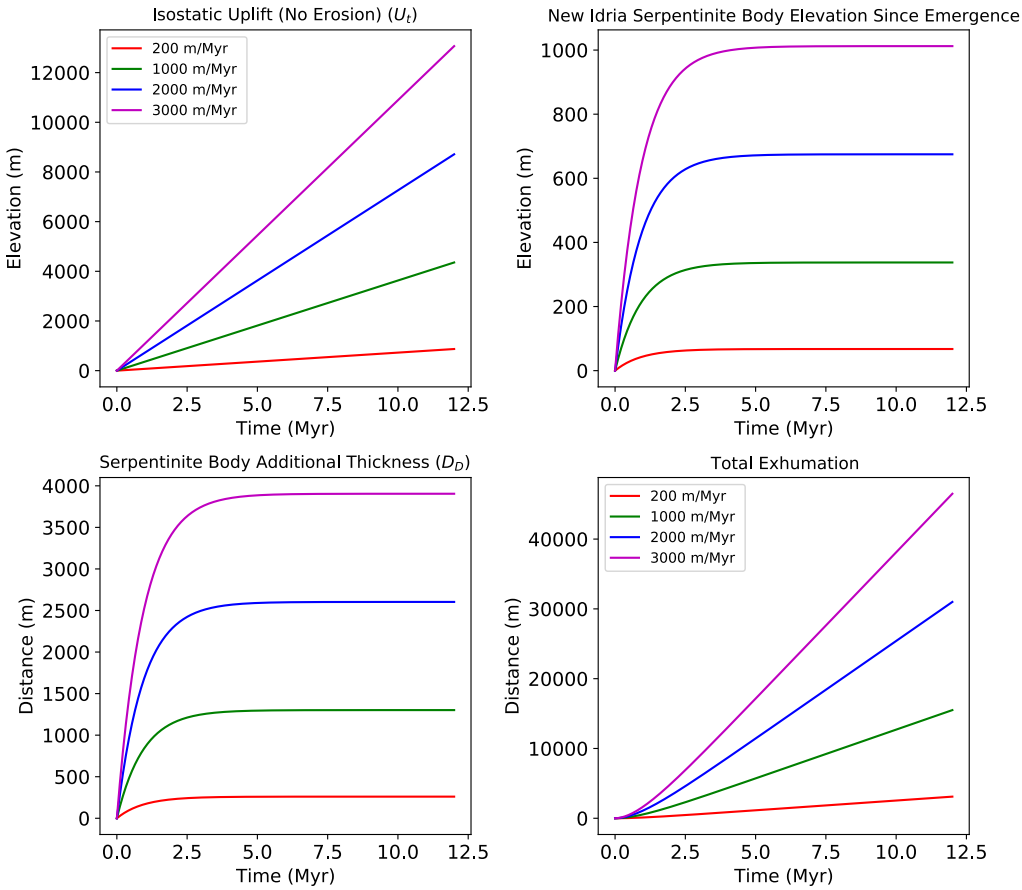

Supplementary Figure 10: Output from the mechanistic uplift model applied to the New Idria Serpentinite Diapir.

References

Adamson, D.A., Selkirk, P.M., Price, D.M., Ward, N., Selkirk, J.M., 1996. Pleistocene uplift and palaeoenvironments of Macquarie Island: evidence from palaeobeaches and sedimentary deposits. Pap. Proc. R. Soc. Tasman. 130, 25–32.

Agrinier, P., Cornen, G., and Beslier, M.-O., 1996. Mineralogical and oxygen isotopic features of serpentinites recovered from the ocean/continent transition in the Iberia Abyssal Plain. In Whitmarsh, R.B., Sawyer, D.S., Klaus, A., and Masson, D.G. (Eds.), Proc. ODP, Sci. Results, College Station, TX (Ocean Drilling Program), Vol. 149, 541–552.

Albers, E., Bach, W., Klein, F., Menzies, C.D., Lucassen, F., Teagle, D.A.H., 2019. Fluid--rock interactions in the shallow Mariana forearc: carbon cycling and redox conditions. Solid Earth 10, 907–930.

Albers, E., Bach, W., Pérez-Gussinyé, M., McCammon, C., Frederichs, T., 2021. Serpentinization-Driven H_2 Production From Continental Break-Up to Mid-Ocean Ridge Spreading: Unexpected High Rates at the West Iberia Margin. Front. Earth Sci. 9, 673063.

Albers, E., Kahl, W.-A., Beyer, L., Bach, W., 2020. Variant across-forearc compositions of slab-fluids recorded by serpentinites: Implications on the mobilization of FMEs from an active subduction zone (Mariana forearc). Lithos 364–365, 105525.

Allen, D.E., Seyfried, W.E., 2004. Serpentinization and heat generation: constraints from Lost City and Rainbow hydrothermal systems11Associate editor: J. C. Alt. Geochim. Cosmochim. Acta 68, 1347–1354.

Alt, J.C., 2003. Stable isotopic composition of upper oceanic crust formed at a fast spreading ridge, ODP Site 801. Geochem. Geophys. Geosyst. 4. https://doi.org/10.1029/2002gc000400

Alt, J.C., 1994. A sulfur isotopic profile through the troodos ophiolite, Cyprus: Primary composition and the effects of seawater hydrothermal alteration. Geochim. Cosmochim. Acta 58, 1825–1840.

Alt, J.C., Garrido, C.J., Shanks, W.C., Turchyn, A., Padrón-Navarta, J.A., López Sánchez-Vizcaíno, V., Gómez Pugnaire, M.T., Marchesi, C., 2012. Recycling of water, carbon, and sulfur during subduction of serpentinites: A stable isotope study of Cerro del Almirez, Spain. Earth Planet. Sci. Lett. 327–328, 50–60.

Alt, J.C., Laverne, C., Vanko, D.A., Tartarotti, P., Teagle, D.A.H., Bach, W., Zuleger, E., Erzinger, J., Honnorez, J., Pezard, P.A., Becker, K., Salisbury, M.H., and Wilkens, R.H., 1996. Hydrothermal alteration of a section of upper oceanic crust in the eastern equatorial Pacific: A synthesis of results from Site 504 (DSDP Legs 69, 70, and 83, and ODP Legs 111, 137, 140, and 148.) In Alt, J.C., Kinoshita, H., Stokking, L.B., and Michael, P.J. (Eds.), Proc. ODP, Sci. Results, College Station, TX (Ocean Drilling Program), Vol. 148, 417–434.

Alt, J.C., Schwarzenbach, E.M., Früh-Green, G.L., Shanks, W.C., Bernasconi, S.M., Garrido, C.J., Crispini, L., Gaggero, L., Padrón-Navarta, J.A., Marchesi, C., 2013. The role of serpentinites in cycling of carbon and sulfur: Seafloor serpentinization and subduction metamorphism. Lithos 178, 40–54.

References

Alt, J.C., Shanks, W.C., 2006. Stable isotope compositions of serpentinite seamounts in the Mariana forearc: Serpentinization processes, fluid sources and sulfur metasomatism. Earth Planet. Sci. Lett. 242, 272–285.

Alt, J.C., Shanks, W.C., III, 1998. Sulfur in serpentinized oceanic peridotites: Serpentinization processes and microbial sulfate reduction. J. Geophys. Res. 103, 9917–9929.

Alt, J.C., Teagle, D.A., 2000. Hydrothermal alteration and fluid fluxes in ophiolites and. Ophiolites and Oceanic Crust: New insights from field studies and the Ocean Drilling Program 349, 273.

Alt, J.C., Teagle, D.A.H., 2003. Hydrothermal alteration of upper oceanic crust formed at a fast-spreading ridge: mineral, chemical, and isotopic evidence from ODP Site 801. Chem. Geol. 201, 191–211.

Alt, J.C., Teagle, D.A.H., Brewer, T., Shanks, W.C., III, Halliday, A., 1998. Alteration and mineralization of an oceanic forearc and the ophiolite-ocean crust analogy. J. Geophys. Res. 103, 12365–12380.

Amalokwu, K.I., 2016. Saturation effects on frequency-dependent seismic anisotropy in fractured porous rocks. *PhD thesis,* University of Southampton.

Andreani, M., Escartin, J., Delacour, A., Ildefonse, B., Godard, M., Dyment, J., Fallick, A.E., Fouquet, Y., 2014. Tectonic structure, lithology, and hydrothermal signature of the Rainbow massif (Mid-Atlantic Ridge 36°14′N). Geochem. Geophys. Geosyst. 15, 3543–3571.

Andreani, M., Mével, C., Boullier, A.-M., Escartín, J., 2007. Dynamic control on serpentine crystallization in veins: Constraints on hydration processes in oceanic peridotites. Geochem. Geophys. Geosyst. 8. https://doi.org/10.1029/2006gc001373

Andrews, M.G., Jacobson, A.D., 2017. The radiogenic and stable Sr isotope geochemistry of basalt weathering in Iceland: role of hydrothermal calcite and implications for long-term climate regulation. Geochim. Cosmochim. Acta. 215, 247–262.

Arai, S., 1994. Characterization of spinel peridotites by olivine-spinel compositional relationships: Review and interpretation. Chem. Geol. 113, 191–204.

Arcis, H., Ferguson, J.P., Applegarth, L., Zimmerman, G.H., Tremaine, P.R., 2017. Ionization of boric acid in water from 298 K to 623 K by AC conductivity and Raman spectroscopy. J. Chem. Thermodyn. 106, 187–198.

Artiaga, D., García-Veigas, J., Cendón, D.I., Atalar, C., Gibert, L., 2021. The Messinian evaporites of the Mesaoria basin (North Cyprus): A discrepancy with the current chronostratigraphic understanding. Palaeogeogr. Palaeoclimatol. Palaeoecol. 584, 110681.

Bach, W., Garrido, C.J., Paulick, H., Harvey, J., Rosner, M., 2004. Seawater-peridotite interactions: First insights from ODP Leg 209, MAR 15°N. Geochem. Geophys. Geosyst. 5. https://doi.org/10.1029/2004gc000744

Bach, W., Paulick, H., Garrido, C.J., Ildefonse, B., Meurer, W.P., Humphris, S.E., 2006. Unraveling the sequence of serpentinization reactions: petrography, mineral chemistry, and petrophysics of serpentinites from MAR 15°N (ODP Leg 209, Site 1274). Geophys. Res. Lett. 33, L13306.

Bach, W., Peucker-Ehrenbrink, B., Hart, S.R., Blusztajn, J.S., 2003. Geochemistry of hydrothermally altered oceanic crust: DSDP/ODP Hole 504B - Implications for

seawater-crust exchange budgets and Sr- and Pb-isotopic evolution of the mantle. Geochem. Geophys. Geosyst. 4. https://doi.org/10.1029/2002gc000419

Barnes, I., Lamarche, V.C., Himmelberg, G., 1967. Geochemical evidence of present-day serpentinization. Science 156, 830–832.

Barnes, I., O'Neil, J.R., 1969. The Relationship between Fluids in Some Fresh Alpine-Type Ultramafics and Possible Modern Serpentinization, Western United States. GSA Bulletin 80, 1947–1960.

Barnes, I., O'Neil, J.R., Trescases, J.J., 1978. Present day serpentinization in New Caledonia, Oman and Yugoslavia. Geochim. Cosmochim. Acta 42, 144–145.

Barnes, J.D., Paulick, H., Sharp, Z.D., Bach, W., Beaudoin, G., 2009. Stable isotope (δ18O, δD, δ37Cl) evidence for multiple fluid histories in mid-Atlantic abyssal peridotites (ODP Leg 209). Lithos 110, 83–94.

Barnes, J.D., Sharp, Z.D., 2006. A chlorine isotope study of DSDP/ODP serpentinized ultramafic rocks: insights into the serpentinization process. Chem. Geol.

Batanova, V.G., Sobolev, A.V., 2000. Compositional heterogeneity in subduction-related mantle peridotites, Troodos massif, Cyprus. Geology 28, 55.

Bayrakci, G., Falcon-Suarez, I.H., Minshull, T.A., North, L., Barker, A., Zihlmann, B., Rouméjon, S., Best, A.I., 2018. Anisotropic Physical Properties of Mafic and Ultramafic Rocks From an Oceanic Core Complex. Geochem. Geophys. Geosyst. 19, 4366–4384.

Bayrakci, G., Minshull, T.A., Sawyer, D.S., Reston, T.J., Klaeschen, D., Papenberg, C., Ranero, C., Bull, J.M., Davy, R.G., Shillington, D.J., Perez-Gussinye, M., Morgan, J.K., 2016. Fault-controlled hydration of the upper mantle during continental rifting. Nat. Geosci. 9, 384–388.

Beard, J.S., Hopkinson, L., 2000. A fossil, serpentinization-related hydrothermal vent, Ocean Drilling Program Leg 173, Site 1068 (Iberia Abyssal Plain): Some aspects of mineral and fluid chemistry. J. Geophys. Res. 105, 16527–16539.

Benton, L.D., 1997. Origin and evolution of serpentine seamount fluids, Mariana and Izu-Bonin forearcs: Implications for the recycling of subducted material. The University of Tulsa, Ann Arbor, United States.

Benton, L.D., Ryan, J.G., Tera, F., 2001. Boron isotope systematics of slab fluids as inferred from a serpentine seamount, Mariana forearc. Earth Planet. Sci. Lett. 187, 273–282.

Beslier, M.-O., Ask, M., Boillot, G., 1993. Ocean-continent boundary in the Iberia Abyssal Plain from multichannel seismic data. Tectonophysics 218, 383–393.

Best, A.I., Sothcott, J., McCann, C., 2007. A laboratory study of seismic velocity and attenuation anisotropy in near-surface sedimentary rocks. Geophys. Prospect. 55, 609–625.

Bickford, M.E., Siegel, D.I., Mottl, M.J., Hill, B.M., Shosa, J., 2008. Strontium isotopic relations among pore fluids, serpentine matrix, and harzburgite clasts, South Chamorro Seamount, Mariana forearc. Chem. Geol. 256, 24–32.

Bickle, M.J., Teagle, D.A.H., 1992. Strontium alteration in the Troodos ophiolite: implications for fluid fluxes and geochemical transport in mid-ocean ridge hydrothermal systems. Earth Planet. Sci. Lett. 113, 219–237.

Birch, F., 1964. Density and composition of mantle and core. J. Geophys. Res. 69, 4377–4388.

Birch, F., 1961. The velocity of compressional waves in rocks to 10 kilobars: 2. J. Geophys. Res. 66, 2199–2224.

Birch, F., 1960. The velocity of compressional waves in rocks to 10 kilobars: 1. J. Geophys. Res. 65, 1083–1102.

Blackman, D.K., Cann, J.R., Janssen, B., Smith, D.K., 1998. Origin of extensional core complexes: Evidence from the Mid-Atlantic Ridge at Atlantis Fracture Zone. J. Geophys. Res. 103, 21315–21333.

Boillot, G., Grimaud, S., Mauffret, A., Mougenot, D., Kornprobst, J., Mergoil-Daniel, J., Torrent, G., 1980. Ocean-continent boundary off the Iberian margin: A serpentinite diapir west of the Galicia Bank. Earth Planet. Sci. Lett. 48, 23–34.

Boillot, G., Winterer, E.L., Meyer, A.W., et al., 1987. Proc. ODP, Init. Repts., College Station, TX (Ocean Drilling Program), Vol. 103.

Bonatti, E., 1978. Vertical tectonism in oceanic fracture zones. Earth Planet. Sci. Lett. 37, 369–379.

Bonatti, E., 1976. Serpentinite protrusions in the oceanic crust. Earth Planet. Sci. Lett. 32, 107–113.

Bonatti, E., Lawrence, J.R., Morandi, N., 1984. Serpentinization of oceanic peridotites: temperature dependence of mineralogy and boron content. Earth Planet. Sci. Lett. 70, 88–94.

Boronina, A., Balderer, W., Renard, P., Stichler, W., 2005. Study of stable isotopes in the Kouris catchment (Cyprus) for the description of the regional groundwater flow. J. Hydrol. 308, 214–226.

Boschetti, T., Etiope, G., Pennisi, M., Romain, M., Toscani, L., 2013. Boron, lithium and methane isotope composition of hyperalkaline waters (Northern Apennines, Italy): Terrestrial serpentinization or mixing with brine? Appl. Geochem. 32, 17–25.

Boschetti, T., Toscani, L., Iacumin, P., Selmo, E., 2017. Oxygen, Hydrogen, Boron and Lithium Isotope Data of a Natural Spring Water with an Extreme Composition: A Fluid from the Dehydrating Slab? Aquat. Geochem. 23, 299–313.

Boschi, C., Dini, A., Früh-Green, G.L., Kelley, D.S., 2008. Isotopic and element exchange during serpentinization and metasomatism at the Atlantis Massif (MAR 30°N): Insights from B and Sr isotope data. Geochim. Cosmochim. Acta 72, 1801–1823.

Bowers, T.S., 1989. Stable isotope signatures of water-rock interaction in mid-ocean ridge hydrothermal systems: Sulfur, oxygen, and hydrogen. J. Geophys. Res. 94, 5775.

Brace, W.F., Walsh, J.B., Frangos, W.T., 1968. Permeability of granite under high pressure. J. Geophys. Res. 73, 2225–2236.

Brazelton, W.J., Schrenk, M.O., Kelley, D.S., Baross, J.A., 2006. Methane- and sulfur-metabolizing microbial communities dominate the Lost City hydrothermal field ecosystem. Appl. Environ. Microbiol. 72, 6257–6270.

Brindley, G.W., Hayami, R., 1963. Kinetics and Mechanisms of Dehydration and Recrystallization of Serpentine—I. Clays Clay Miner. 12, 35–47.

Buchner, J., 2021a. UltraNest -- a robust, general purpose Bayesian inference engine. arXiv [stat.CO].

Buchner, J., 2021b. Nested Sampling Methods. arXiv [stat.CO].

Buchner, J., 2017. Collaborative Nested Sampling: Big Data vs. complex physical models. arXiv [stat.CO].

Buchner, J., 2014. A statistical test for Nested Sampling algorithms. arXiv [stat.CO].

Burke, W.H., Denison, R.E., Hetherington, E.A., Koepnick, R.B., Nelson, H.F., Otto, J.B., 1982. Variation of seawater 87Sr/86Sr throughout Phanerozoic time. Geology 10, 516–519.

Burkhard, D.J.M., O'Neil, J.R., 1988. Contrasting serpentinization processes in the eastern Central Alps. Contrib. Mineral. Petrol. 99, 498–506.

Byerlee, J., 1978. Friction of Rocks, in: Byerlee, J.D., Wyss, M. (Eds.), Rock Friction and Earthquake Prediction. Birkhäuser Basel, Basel, pp. 615–626.

Byerly, P.E., 1966. Interpretations of gravity data from the central Coast Ranges and San Joaquin Valley, California. Geol. Soc. Am. Bull. 77, 83–94.

Campbell, A.C., Edmond, J.M., 1989. Halide systematics of submarine hydrothermal vents. Nature 342, 168–170.

Campos, T.F.C., Bezerra, F.H.R., Srivastava, N.K., Vieira, M.M., Vita-Finzi, C., 2010. Holocene tectonic uplift of the St Peter and St Paul Rocks (Equatorial Atlantic) consistent with emplacement by extrusion. Mar. Geol. 271, 177–186.

Cann, J.R., Blackman, D.K., Smith, D.K., McAllister, E., Janssen, B., Mello, S., Avgerinos, E., Pascoe, A.R., Escartin, J., 1997. Corrugated slip surfaces formed at ridge–transform intersections on the Mid-Atlantic Ridge. Nature 385, 329–332.

Cannat, M., Fontaine, F., Escartín, J., 2010. Serpentinization and Associated Hydrogen and Methane Fluxes at Slow Spreading Ridges. Diversity of Hydrothermal Systems on Slow Spreading Ocean Ridges 241–264.

Cannat, M., Sauter, D., Mendel, V., Ruellan, E., Okino, K., Escartin, J., Combier, V., Baala, M., 2006. Modes of seafloor generation at a melt-poor ultraslow-spreading ridge. Geology 34, 605–608.

Cao, W., Paterson, S., 2016. A mass balance and isostasy model: Exploring the interplay between magmatism, deformation and surface erosion in continental arcs using central Sierra Nevada as a case study. Geochem. Geophys. Geosyst. 17, 2194–2212.

Carlson, R.L., Miller, D.J., 1997. A new assessment of the abundance of serpentinite in the oceanic crust. Geophys. Res. Lett. 24, 457–460.

Cartwright, I., Weaver, T.R., Fifield, L.K., 2006. Cl/Br ratios and environmental isotopes as indicators of recharge variability and groundwater flow: An example from the southeast Murray Basin, Australia. Chem. Geol. 231, 38–56.

Casey, T.A.L., Dickinson, W.R., 1976. Sedimentary serpentinite of the Miocene Big Blue Formation near Cantua Creek.

Chapman, H.J., Spooner, E.T.C., 1977. 87Sr enrichment of ophiolitic sulphide deposits in Cyprus confirms ore formation by circulating seawater. Earth Planet. Sci. Lett. 35, 71–78.

Charlou, J.L., Donval, J.P., Fouquet, Y., Jean-Baptiste, P., Holm, N., 2002. Geochemistry of high H2 and CH4 vent fluids issuing from ultramafic rocks at the Rainbow hydrothermal field (36 14′ N, MAR). Chem. Geol. 191, 345–359.

Chaussidon, M., Jambon, A., 1994. Boron content and isotopic composition of oceanic basalts: Geochemical and cosmochemical implications. Earth Planet. Sci. Lett. 121, 277–291.

Chavagnac, V., Monnin, C., Ceuleneer, G., Boulart, C., Hoareau, G., 2013. Characterization of hyperalkaline fluids produced by low-temperature serpentinization of mantle peridotites in the Oman and Ligurian ophiolites. Geochem. Geophys. Geosyst. 14, 2496–2522.

Christensen, N.I., 2004. Serpentinites, Peridotites, and Seismology. Int. Geol. Rev. 46, 795–816.

Christensen, N.I., 1972. The Abundance of Serpentinites in the Oceanic Crust. J. Geol. 80, 709–719.

Christensen, N.I., 1966. Elasticity of ultrabasic rocks. J. Geophys. Res. 71, 5921–5931.

Claypool, G.E., Holser, W.T., Kaplan, I.R., Sakai, H., Zak, I., 1980. The age curves of sulfur and oxygen isotopes in marine sulfate and their mutual interpretation. Chem. Geol. 28, 199–260.

Cleveland, W.S., 1979. Robust Locally Weighted Regression and Smoothing Scatterplots. J. Am. Stat. Assoc. 74, 829–836.

Clube, T.M.M., Creer, K.M., Robertson, A.H.F., 1985. Palaeorotation of the Troodos microplate, Cyprus. Nature 317, 522–525.

Clube, T.M.M., Robertson, A.H.F., 1986. The palaeorotation of the troodos microplate, cyprus, in the late mesozoic-early cenozoic plate tectonic framework of the Eastern Mediterranean. Surv. Geophys. 8, 375–437.

Coggon, R.M., Teagle, D.A.H., Smith-Duque, C.E., Alt, J.C., Cooper, M.J., 2010. Reconstructing past seawater Mg/Ca and Sr/Ca from mid-ocean ridge flank calcium carbonate veins. Science 327, 1114–1117.

Coleman, R.G., 1996. New Idria Serpentinite: A Land Management Dilemma. Environ. Eng. Geosci. II, 9–22.

Coleman, R.G., 1971. Plate tectonic emplacement of upper mantle peridotites along continental edges. J. Geophys. Res. 76, 1212–1222.

Coleman, R.G., Keith, T.E., 1971. A chemical study of serpentinization—Burro Mountain, California. J. Petrol. 12, 311–328.

Cooper, G.F., Macpherson, C.G., Blundy, J.D., Maunder, B., Allen, R.W., Goes, S., Collier, J.S., Bie, L., Harmon, N., Hicks, S.P., Iveson, A.A., Prytulak, J., Rietbrock, A., Rychert, C.A., Davidson, J.P., VoiLA team, 2020. Variable water input controls evolution of the Lesser Antilles volcanic arc. Nature 582, 525–529.

Cooperdock, E.H.G., Stockli, D.F., 2016. Unraveling alteration histories in serpentinites and associated ultramafic rocks with magnetite (U-Th)/He geochronology. Geology 44, 967–970.

Coulton, A.J., Harper, G.D., O'Hanley, D.S., 1995. Oceanic versus emplacement age serpentinization in the Josephine ophiolite: Implications for the nature of the Moho at intermediate and slow spreading ridges. J. Geophys. Res. 100, 22245–22260.

Courtier, A.M., Hart, D.J., and Christensen, N.I., 2004. Seismic properties of Leg 195 serpentinites and their geophysical implications. In Shinohara, M., Salisbury, M.H., and Richter, C. (Eds.), Proc. ODP, Sci. Results, College Station, TX (Ocean Drilling Program), Vol. 195, 1–12.

Craig, H., 1961. Isotopic Variations in Meteoric Waters. Science 133, 1702–1703.

Craw, D., Blattner, P., Landis, C.A., 1995. Stable isotopic signatures of authigenic minerals in a Holocene ophiolitic debris flow, Southland, New Zealand. Clay Miner. 30, 165–172.

Craw, D., Landis, C.A. and Kelsey, P.I., 1987. Authigenic chrysotile formation in the matrix of Quaternary debris flows, northern Southland, New Zealand. Clays and Clay Minerals, 35-1, 43-52.

Darwin, C.R. 1835. Extracts from Letters Addressed to Professor Henslow by C. Darwin, Esq: Read at a Meeting of the Society on the 16th of November 1835. University Press for the Cambridge Philosophical Society.

de Obeso, J.C., Kelemen, P.B., 2020. Major element mobility during serpentinization, oxidation and weathering of mantle peridotite at low temperatures. Philos. Trans. A Math. Phys. Eng. Sci. 378, 20180433.

de Obeso, J.C., Kelemen, P.B., 2018. Fluid rock interactions on residual mantle peridotites overlain by shallow oceanic limestones: Insights from Wadi Fins, Sultanate of Oman. Chem. Geol. 498, 139–149.

de Obeso, J.C., Santiago Ramos, D.P., Higgins, J.A., Kelemen, P.B., 2021. A mg isotopic perspective on the mobility of magnesium during serpentinization and carbonation of the Oman ophiolite. J. Geophys. Res. [Solid Earth] 126. https://doi.org/10.1029/2020jb020237

Decitre, S., Deloule, E., Reisberg, L., James, R., Agrinier, P., Mével, C., 2002. Behavior of Li and its isotopes during serpentinization of oceanic peridotites. Geochem. Geophys. Geosyst. 3, 1–20.

Deschamps, F., Godard, M., Guillot, S., Hattori, K., 2013. Geochemistry of subduction zone serpentinites: A review. Lithos 178, 96–127.

Dichicco, M.C., Laurita, S., Paternoster, M., Rizzo, G., Sinisi, R., Mongelli, G., 2015. Serpentinite Carbonation for CO2 Sequestration in the Southern Apennines: Preliminary Study. Energy Procedia 76, 477–486.

Dick, H.J.B., Bullen, T., 1984. Chromian spinel as a petrogenetic indicator in abyssal and alpine-type peridotites and spatially associated lavas. Contrib. Mineral. Petrol. 86, 54–76.

Dick, H.J.B., Lin, J., Schouten, H., 2003. An ultraslow-spreading class of ocean ridge. Nature 426, 405–412.

Dick, H.J.B., Tivey, M.A., Tucholke, B.E., 2008. Plutonic foundation of a slow-spreading ridge segment: Oceanic core complex at Kane Megamullion, 23°30′N, 45°20′W. Geochem. Geophys. Geosyst. 9. https://doi.org/10.1029/2007gc001645

Dickinson, W.R., 1966. Table Mountain Serpentinite Extrusion in California Coast Ranges. GSA Bulletin 77, 451–472.

Dickson, A.G., 1990. Thermodynamics of the dissociation of boric acid in synthetic seawater from 273.15 to 318.15 K. Deep Sea Res. A 37, 755–766.

Dickson, A.G., Sabine, C.L., Christian, J.R., 2007. Guide to best practices for ocean CO_2 measurements. North Pacific Marine Science Organization.

References

Ehlmann, B.L., Mustard, J.F., 2010. Geologic setting of serpentine deposits on Mars. Geophys. Res. Lett.

Ehlmann, B.L., Mustard, J.F., Swayze, G.A., Clark, R.N., Bishop, J.L., Poulet, F., Des Marais, D.J., Roach, L.H., Milliken, R.E., Wray, J.J., Barnouin-Jha, O., Murchie, S.L., 2009. Identification of hydrated silicate minerals on Mars using MRO-CRISM: Geologic context near Nili Fossae and implications for aqueous alteration. J. Geophys. Res. 114. https://doi.org/10.1029/2009je003339

Elderfield, H., Mills, R.A., Rudnicki, M.D., 1993. Geochemical and thermal fluxes, high-temperature venting and diffuse flow from mid-ocean ridge hydrothermal systems: the TAG hydrothermal field, Mid-Atlantic Ridge 26 N. Geological Society, London, Special Publications 76, 295–307.

Elliott, T., Plank, T., Zindler, A., White, W., Bourdon, B., 1997. Element transport from slab to volcanic front at the Mariana arc. J. Geophys. Res. 102, 14991–15019.

Ergün, M., Okay, S., Sari, C., Zafer Oral, E., Ash, M., Hall, J., Miller, H., 2005. Gravity anomalies of the Cyprus Arc and their tectonic implications. Mar. Geol. 221, 349–358.

Escartin, J., Hirth, G., Evans, B., 2001. Strength of slightly serpentinized peridotites: Implications for the tectonics of oceanic lithosphere. Geology.

Escartín, J., Hirth, G., Evans, B., 1997. Effects of serpentinization on the lithospheric strength and the style of normal faulting at slow-spreading ridges. Earth Planet. Sci. Lett. 151, 181–189.

Evans, A.D., Teagle, D.A.H., Craw, D., Henstock, T.J., Falcon-Suarez, I.H., 2021. Uplift and exposure of serpentinized massifs: Modeling differential serpentinite diapirism and exhumation of the troodos mantle sequence, Cyprus. J. Geophys. Res. [Solid Earth] 126. https://doi.org/10.1029/2020jb021079

Evans, B.W., 2004. The Serpentinite Multisystem Revisited: Chrysotile Is Metastable. Int. Geol. Rev. 46, 479–506.

Evans, C.A., and Baltuck, M., 1988. Low-temperature alteration of peridotite, Hole 637A. In Boillot, G., Winterer, E.L., et al., Proc. ODP, Sci. Results, College Station, TX (Ocean Drilling Program), Vol. 103, 235-239.

Evans, B.W., Hattori, K., Baronnet, A., 2013. Serpentinite: What, why, where? Elements 9, 99–106.

Evans, N.P., Turchyn, A.V., Gázquez, F., Bontognali, T.R.R., Chapman, H.J., Hodell, D.A., 2015. Coupled measurements of $\delta^{18}O$ and δD of hydration water and salinity of fluid inclusions in gypsum from the Messinian Yesares Member, Sorbas Basin (SE Spain). Earth Planet. Sci. Lett. 430, 499–510.

Falcon-Suarez, I., Bayrakci, G., Minshull, T.A., North, L.J., Best, A.I., Rouméjon, S., IODP Expedition 357 Science Party, 2017. Elastic and electrical properties and permeability of serpentinites from Atlantis Massif, Mid-Atlantic Ridge. Geophys. J. Int. 211, 686–699.

Falcon-Suarez, I., North, L., Amalokwu, K., Best, A., 2016. Integrated geophysical and hydromechanical assessment for CO_2 storage: shallow low permeable reservoir sandstones. Geophys. Prospect. 64, 828–847.

Feld, C., Mechie, J., Hübscher, C., Hall, J., Nicolaides, S., Gurbuz, C., Bauer, K., Louden, K., Weber, M., 2017. Crustal structure of the Eratosthenes Seamount, Cyprus and

S. Turkey from an amphibian wide-angle seismic profile. Tectonophysics 700–701, 32–59.

Flecker, R., Ellam, R.M., 2006. Identifying Late Miocene episodes of connection and isolation in the Mediterranean–Paratethyan realm using Sr isotopes. Sediment. Geol. 188–189, 189–203.

Florides, G.A., Pouloupatis, P.D., Kalogirou, S., Messaritis, V., Panayides, I., Zomeni, Z., Partasides, G., Lizides, A., Sophocleous, E., Koutsoumpas, K., 2011. The geothermal characteristics of the ground and the potential of using ground coupled heat pumps in Cyprus. Energy 36, 5027–5036.

Follows, E.J., 1990. Sedimentology and tectonic setting of Miocene reef and related sediments in Cyprus. University of Edinburgh.

Fonseca, R.O.C., Kirchenbaur, M., Ballhaus, C., Münker, C., Zirner, A., Gerdes, A., Heuser, A., Botcharnikov, R., Lenting, C., 2017. Fingerprinting fluid sources in Troodos ophiolite complex orbicular glasses using high spatial resolution isotope and trace element geochemistry. Geochim. Cosmochim. Acta 200, 145–166.

Fossen, H., Cavalcante, G.C.G., 2017. Shear zones--A review. Earth-Sci. Rev. 171, 434–455.

Foster, G.L., Pogge von Strandmann, P.A.E., Rae, J.W.B., 2010. Boron and magnesium isotopic composition of seawater. Geochem. Geophys. Geosyst. 11. https://doi.org/10.1029/2010gc003201

Francheteau, J., Armijo, R., Cheminée, J.L., Hekinian, R., Lonsdale, P., Blum, N., 1990. 1 Ma East Pacific Rise oceanic crust and uppermost mantle exposed by rifting in Hess Deep (equatorial Pacific Ocean). Earth Planet. Sci. Lett. 101, 281–295.

Francis, T.J.G., 1981. Serpentinization faults and their role in the tectonics of slow spreading ridges. J. Geophys. Res. 86, 11616.

Frost, B.R., Beard, J.S., 2007. On Silica Activity and Serpentinization. J. Petrol. 48, 1351–1368.

Früh-Green, G.L., Connolly, J.A.D., Plas, A., Kelley, D.S., Grobéty, B., 2004. Serpentinization of oceanic peridotites: Implications for geochemical cycles and biological activity, in: The Subseafloor Biosphere at Mid-Ocean Ridges, Geophysical Monograph. American Geophysical Union, Washington, D. C., pp. 119–136.

Früh-Green, G.L., Plas, A., and Lécuyer, C., 1996. Petrologic and stable isotope constraints on hydrothermal alteration and serpentinization of the EPR shallow mantle at Hess Deep (Site 895). *In* Mével, C., Gillis, K.M., Allan, J.F., and Meyer, P.S. (Eds.), *Proc. ODP, Sci. Results,* College Station, TX (Ocean Drilling Program), Vol. 147, 255–291.

Früh-Green, G.L., Weissert, H., Bernoulli, D., 1990. A multiple fluid history recorded in Alpine ophiolites. J. Geol. Soc. London 147, 959–970.

Fryer, P., Ambos, E.L., Hussong, D.M., 1985. Origin and emplacement of Mariana forearc seamounts. Geology 13, 774.

Fryer, P., Pearce, J.A. and Stokking, L.B., 1992. 36. A synthesis of Leg 125 drilling of serpentine seamounts on the Mariana and Izu–Bonin forearcs. In Proceedings of the Ocean Drilling Program, Scientific Results Vol. 125, 593-614.

References

Gale, A., Dalton, C.A., Langmuir, C.H., Su, Y., Schilling, J.-G., 2013. The mean composition of ocean ridge basalts. Geochem. Geophys. Geosyst. 14, 489–518.

Gamo, T., 1995. Wide variation of chemical characteristics of submarine hydrothermal fluids due to the secondary modification processes after high temperature water-rock interaction: a review. Biogeocheimical Processes and Ocean-Flux in the Western Pacific 425–451.

Gangjian, W., Jingxian, W., Ying, L., Ting, K., Zhongyuan, R., Jinlong, M., Yigang, X., 2013. Measurement on high-precision boron isotope of silicate materials by a single column purification method and MC-ICP-MS. J. Anal. At. Spectrom. 28, 606–612.

Gass, I.G., 1977. Origin and emplacement of ophiolites. Geological Society, London, Special Publications 7, 72–76.

Gass, I.G., 1968. Is the Troodos Massif of Cyprus a Fragment of Mesozoic Ocean Floor? Nature 220, 39–42.

Gass, I.G., 1960. The geology and mineral resources of the Dhali area. authority of the Government of Cyprus.

Gass, I.G., Cockbain, A.E., 1961. Notes on the occurrence of gypsum in Cyprus. HM Stationery Office.

Gass, I.G., Masson-Smith, D., 1963. The Geology and Gravity Anomalies of the Troodos Massif, Cyprus. Proceedings of the Royal Society B: Biological Sciences 157, 587–588.

Geilert, S., Grasse, P., Wallmann, K., Liebetrau, V., Menzies, C.D., 2020. Serpentine alteration as source of high dissolved silicon and elevated δ 30 Si values to the marine Si cycle. Nat. Commun. 11, 1–11.

Giampouras, M., Garrido, C.J., Zwicker, J., Vadillo, I., Smrzka, D., Bach, W., Peckmann, J., Jiménez, P., Benavente, J., García-Ruiz, J.M., 2019. Geochemistry and mineralogy of serpentinization-driven hyperalkaline springs in the Ronda peridotites. Lithos 350–351, 105215.

Gillis, K.M., Robinson, P.T., 1990. Patterns and processes of alteration in the lavas and dykes of the Troodos Ophiolite, Cyprus. J. Geophys. Res. 95, 21523.

Glein, C.R., Baross, J.A., Waite, J.H., 2015. The pH of Enceladus' ocean. Geochim. Cosmochim. Acta 162, 202–219.

Goldberg, D., and Zinszner, B., 1988. Acoustic properties of altered peridotite at Site 637 from laboratory and sonic waveform data. In Boillot, G., Winterer, E.L., et al., Proc. ODP, Sci. Results, College Station, TX (Ocean Drilling Program), Vol. 103, 269–276.

Goscombe, B.D., Everard, J.L., 1998. 1: 10000 Geological Map of Macquarie Island. Mineral Resources, Tasmania.

Govindaraju, K., 1995. 1995 working values with confidence limits for twenty-six CRPG, ANRT and IWG-GIT geostandards. Geostandards Newslett.: J. Geostandards Geoanalysis. https://doi.org/10.1111/j.1751-908X.1995.tb00164.x

Granot, R., 2016. Palaeozoic oceanic crust preserved beneath the eastern Mediterranean. Nat. Geosci. 9, 701–705.

Grevemeyer, I., Hayman, N.W., Peirce, C., Schwardt, M., Van Avendonk, H.J.A., Dannowski, A., Papenberg, C., 2018a. Episodic magmatism and serpentinized mantle exhumation at an ultraslow-spreading centre. Nat. Geosci. 11, 444–448.

Grevemeyer, I., Ranero, C.R., Ivandic, M., 2018b. Structure of oceanic crust and serpentinization at subduction trenches. Geosphere 14, 395–418.

Guillot, S., Hattori, K., 2013. Serpentinites: Essential roles in geodynamics, arc volcanism, sustainable development, and the origin of life. Elements 9, 95–98.

Guillot, S., Schwartz, S., Reynard, B., Agard, P., Prigent, C., 2015. Tectonic significance of serpentinites. Tectonophysics 646, 1–19.

Hacker, B.R., 2008. H_2O subduction beyond arcs. Geochem. Geophys. Geosyst. 9. https://doi.org/10.1029/2007GC001707

Hacker, B.R., Mosenfelder, J.L., Gnos, E., 1996. Rapid emplacement of the Oman ophiolite: Thermal and geochronologic constraints. Tectonics 15, 1230–1247.

Haggerty, J.A., and Chaudhuri, S., 1992. Strontium isotopic composition of the interstitial waters from Leg 125: Mariana and Bonin forearcs. In Fryer, P., Pearce, J.A., Stokking, L.B., et al., Proc. ODP, Sci. Results, College Station, TX (Ocean Drilling Program), Vol. 125, 397–400.

Harris, M., Coggon, R.M., Smith-Duque, C.E., 2015. Channelling of hydrothermal fluids during the accretion and evolution of the upper oceanic crust: Sr isotope evidence from ODP Hole 1256D. Earth Planet. Sci. Lett.

Hart, S.R., 1969. K, Rb, Cs contents and K/Rb, K/Cs ratios of fresh and altered submarine basalts. Earth Planet. Sci. Lett. 6, 295–303.

Harvey, J., Garrido, C.J., Savov, I., Agostini, S., Padrón-Navarta, A., Marchesi, C., López Sánchez-Vizcaíno, V., Gómez-Pugnaire, M.T., 2014. 11B-rich fluids in subduction zones: The role of antigorite dehydration in subducting slabs and boron isotope heterogeneity in the mantle. Chem. Geol. 376, 20–30.

Hatakeyama, K., Katayama, I., Abe, N., Okazaki, K., Michibayashi, K., the Oman Drilling Project Science Party, 2021. Effects of alteration and cracks on the seismic velocity structure of oceanic lithosphere inferred from ultrasonic measurements of mafic and ultramafic samples collected by the Oman drilling project. J. Geophys. Res. [Solid Earth] 126. https://doi.org/10.1029/2021jb021923

Hatakeyama, K., Katayama, I., Hirauchi, K.-I., Michibayashi, K., 2017. Mantle hydration along outer-rise faults inferred from serpentinite permeability. Sci. Rep. 7, 13870.

Hayes, G.P., Moore, G.L., Portner, D.E., Hearne, M., Flamme, H., Furtney, M., Smoczyk, G.M., 2018. Slab2, a comprehensive subduction zone geometry model. Science 362, 58–61.

Heaton, T.H.E., 1976. Hydrogen and oxygen isotope study of the metamorphism and mineralisation of the Troodos Complex, Cyprus. Ph.D. thesis, University of Edinburgh.

Heaton, T.H.E., Sheppard, S.M.F., 1977. Hydrogen and oxygen isotope evidence for sea-water-hydrothermal alteration and ore deposition, Troodos complex, Cyprus. Geological Society, London, Special Publications 7, 42–57.

Hekinian, R., Bideau, D., Francheteau, J., Cheminee, J.L., Armijo, R., Lonsdale, P., Blum, N., 1993. Petrology of the East Pacific Rise crust and upper mantle exposed in Hess deep (eastern equatorial Pacific). J. Geophys. Res. 98, 8069–8094.

Hekinian, R., Francheteau, J., Armijo, R., Cogné, J.P., Constantin, M., Girardeau, J., Hey, R., Naar, D.F., Searle, R., 1996. Petrology of the Easter microplate region in the South Pacific. J. Volcanol. Geotherm. Res. 72, 259–289.

Hekinian, R., Juteau, T., Gràcia, E., Sichler, B., Sichel, S., Udintsev, G., Apprioual, R., Ligi, M., 2000. Submersible observations of equatorial atlantic mantle: the St. Paul Fracture Zone region. Mar. Geophys. Res. 21, 529–560.

Hemming, N.G., Reeder, R.J., Hanson, G.N., 1995. Mineral-fluid partitioning and isotopic fractionation of boron in synthetic calcium carbonate. Geochim. Cosmochim. Acta 59, 371–379.

Henning, A.T., Sawyer, D.S., Templeton, D.C., 2004. Exhumed upper mantle within the ocean-continent transition on the northern West Iberia margin: Evidence from prestack depth migration and total tectonic subsidence analyses. J. Geophys. Res. 109. https://doi.org/10.1029/2003jb002526

Herzig, P.M., Friedrich, G.H., 1987. Sulphide mineralization, hydrothermal alteration and chemistry in the drill hole CY-2a, Agrokipia, Cyprus. Cyprus Crustal Study Project, Holes CY2-a and 2a, ed. PT Robinson, IL Gibson and A. Panayioutou 103–138.

Hess, H.H., 1954. Geological Hypotheses and the Earth's Crust under the Oceans. Proc. R. Soc. Lond. A Math. Phys. Sci. 222, 341–348.

Hickman, S., Zoback, M., Ellsworth, W., Boness, N., Malin, P., Roecker, S., Thurber, C., 2007. Structure and properties of the San Andreas Fault in central California: Recent results from the SAFOD experiment. Sci. Drill. 29–32.

Hilairet, N., Reynard, B., Wang, Y., Daniel, I., Merkel, S., Nishiyama, N., Petitgirard, S., 2007. High-pressure creep of serpentine, interseismic deformation, and initiation of subduction. Science 318, 1910–1913.

Hirth, G., 2002. Laboratory Constraints on the Rheology of the Upper Mantle. Rev. Mineral. Geochem. 51, 97–120.

Hirth, G., Guillot, S., 2013. Rheology and Tectonic Significance of Serpentinite. Elements 9, 107–113.

Hopkinson, L., Beard, J.S., Boulter, C.A., 2004. The hydrothermal plumbing of a serpentinite-hosted detachment: evidence from the West Iberia non-volcanic rifted continental margin. Mar. Geol. 204, 301–315.

Hostetler, P.B., Coleman, R.G., Mumpton, F.A., Evans, B.W., 1966. Brucite in alpine serpentinites. Am. Mineral. 51, 75–98.

Huang, R., Ding, X., Lin, C.-T., Zhan, W., Ling, M., 2018. Effect of saline fluids on chlorine incorporation in serpentine. Solid Earth Sciences 3, 61–66.

Hyndman, R.D., Drury, M.J., 1976. The physical properties of oceanic basement rocks from deep drilling on the Mid-Atlantic Ridge. J. Geophys. Res. 81, 4042–4052.

Hyndman, R.D., Peacock, S.M., 2003. Serpentinization of the forearc mantle. Earth Planet. Sci. Lett. 212, 417–432.

Hyndman, R.D., Yamano, M., Oleskevich, D.A., 1997. The seismogenic zone of subduction thrust faults. Island Arc 6, 244–260.

Ishibashi, J.-I., Tsunogai, U., Toki, T., Ebina, N., Gamo, T., Sano, Y., Masuda, H., Chiba, H., 2015. Chemical composition of hydrothermal fluids in the central and southern Mariana Trough backarc basin. Deep Sea Res. Part 2 Top. Stud. Oceanogr. 121, 126–136.

Ishikawa, T., Nakamura, E., 1992. Boron isotope geochemistry of the oceanic crust from DSDP/ODP Hole 504B. Geochim. Cosmochim. Acta 56, 1633–1639.

Ishii, T., Robinson, P.T., Maekawa, H., and Fiske, R., 1992. Petrological studies of peridotites from diapiric serpentinite seamounts in the Izu-Ogasawara-Mariana forearc, Leg 125. In Fryer, P., Pearce, J.A., Stokking, L.B., et al., Proc. ODP, Sci. Results, College Station, TX (Ocean Drilling Program), Vol. 125, 445–485.

Iturrino, G.J., Miller, D.J., and Christensen, N.I., 1996. Velocity behavior of lower crustal and upper mantle rocks from a fast-spreading ridge at Hess Deep. In Mével, C., Gillis, K.M., Allan, J.F., and Meyer, P.S. (Eds.), Proc. ODP, Sci. Results, College Station, TX (Ocean Drilling Program), Vol. 147, 417–440.

Jacobson, A.D., Grace Andrews, M., Lehn, G.O., Holmden, C., 2015. Silicate versus carbonate weathering in Iceland: New insights from Ca isotopes. Earth Planet. Sci. Lett. 416, 132–142.

James, R.H., Elderfield, H., Palmer, M.R., 1995. The chemistry of hydrothermal fluids from the Broken Spur site, 29°N Mid-Atlantic ridge. Geochim. Cosmochim. Acta 59, 651–659.

James, R.H., Green, D.R.H., Stock, M.J., Alker, B.J., Banerjee, N.R., Cole, C., German, C.R., Huvenne, V.A.I., Powell, A.M., Connelly, D.P., 2014. Composition of hydrothermal fluids and mineralogy of associated chimney material on the East Scotia Ridge back-arc spreading centre. Geochim. Cosmochim. Acta 139, 47–71.

Jamieson, H.E., Lyndon, J.A., 1987. Geochemistry of a fossil ore solution aquifer: Chemical exchange between rock and hydrothermal fluid recorded in the lower portion of research Drill Hole CY-2a, Agrokipia, Cyprus. Geol. Surv. Canada Paper 85–29.

Jochum, K.P., Nohl, U., Herwig, K., 2005. GeoReM: a new geochemical database for reference materials and isotopic standards. Geostand. Geoanal. Res. https://doi.org/10.1111/j.1751-908X.2005.tb00904.x

Jones, R.E., De Hoog, J.C.M., Kirstein, L.A., Kasemann, S.A., Hinton, R., Elliott, T., Litvak, V.D., 2014. Temporal variations in the influence of the subducting slab on Central Andean arc magmas: Evidence from boron isotope systematics. Earth Planet. Sci. Lett. 408, 390–401.

Jöns, N., Kahl, W.A., Bach, W., 2017. Reaction-induced porosity and onset of low-temperature carbonation in abyssal peridotites: Insights from 3D high-resolution microtomography. Lithos 268–271, 274–284.

Kahl, W.-A., Jöns, N., Bach, W., Klein, F., Alt, J.C., 2015. Ultramafic clasts from the South Chamorro serpentine mud volcano reveal a polyphase serpentinization history of the Mariana forearc mantle. Lithos 227, 1–20.

Kameda, J., Inoue, S., Tanikawa, W., Yamaguchi, A., Hamada, Y., Hashimoto, Y., Kimura, G., 2017. Alteration and dehydration of subducting oceanic crust within subduction zones: implications for décollement step-down and plate-boundary seismogenesis. Earth Planets Space 69, 1–15.

Karson, J.A., Klein, E.M., Hurst, S.D., Lee, C.E., Rivizzigno, P.A., Curewitz, D., Morris, A.R., Miller, D.J., Varga, R.G., Christeson, G.L., Cushman, B., O'Neill, J.M., Brophy, J.G., Gillis, K.M., Stewart, M.A., Sutton, A.L., 2002. Structure of uppermost fast-spread oceanic crust exposed at the Hess Deep Rift: Implications for subaxial processes at the East Pacific Rise. Geochem. Geophys. Geosyst. 3. https://doi.org/10.1029/2001gc000155

Katayama, I., Abe, N., Hatakeyama, K., Akamatsu, Y., Okazaki, K., Ulven, O.I., Hong, G., Zhu, W., Cordonnier, B., Michibayashi, K., Godard, M., Kelemen, P., the Oman Drilling Project Phase 2 Science Party, 2020. Permeability profiles across the crust-mantle sections in the Oman drilling project inferred from dry and wet resistivity data. J. Geophys. Res. [Solid Earth] 125. https://doi.org/10.1029/2019jb018698

Katayama, I., Terada, T., Okazaki, K., Tanikawa, W., 2012. Episodic tremor and slow slip potentially linked to permeability contrasts at the Moho. Nat. Geosci. 5, 731–734.

Kawahata, H., Scott, S.D., 1990. Strontium isotopes and water-rock interaction of the Agrokipia 'B'stockwork deposit in the Troodos ophiolite, Cyprus: a fossil subseafloor ore body. Geochem. J. 24, 349–356.

Kawano, S., Katayama, I., Okazaki, K., 2011. Permeability anisotropy of serpentinite and fluid pathways in a subduction zone. Geology 39, 939–942.

Keeling, C.D., 1958. The concentration and isotopic abundances of atmospheric carbon dioxide in rural areas. Geochim. Cosmochim. Acta 13, 322–334.

Kelemen, P.B., Hirth, G., 2012. Reaction-driven cracking during retrograde metamorphism: Olivine hydration and carbonation. Earth Planet. Sci. Lett. 345–348, 81–89.

Kelemen, P.B., Manning, C.E., 2015. Reevaluating carbon fluxes in subduction zones, what goes down, mostly comes up. Proc. Natl. Acad. Sci. U. S. A. 112, E3997-4006.

Kelemen, P.B., Matter, J., 2008. In situ carbonation of peridotite for CO2 storage. Proceedings of the National.

Kelemen, P.B., Matter, J., Streit, E.E., Rudge, J.F., Curry, W.B., Blusztajn, J., 2011. Rates and Mechanisms of Mineral Carbonation in Peridotite: Natural Processes and Recipes for Enhanced, in situ CO_2 Capture and Storage. Annu. Rev. Earth Planet. Sci. 39, 545–576.

Kelemen, P.B., Matter, J.M., Teagle, D.A.H., Coggon, J.A., Others, 2020. Oman Drilling Project: Scientific Drilling in the Samail Ophiolite, Sultanate of Oman. Proceedings of the Oman Drilling Project.

Kelley, D.S., Karson, J.A., Blackman, D.K., Früh-Green, G.L., Butterfield, D.A., Lilley, M.D., Olson, E.J., Schrenk, M.O., Roe, K.K., Lebon, G.T., Rivizzigno, P., Party, T.A.-60 S., 2001a. An off-axis hydrothermal vent field near the Mid-Atlantic Ridge at 30 degrees N. Nature 412, 145–149.

Kelley, D.S., Karson, J.A., Blackman, D.K., Früh-Green, G.L., Butterfield, D.A., Lilley, M.D., Olson, E.J., Schrenk, M.O., Roe, K.K., Lebon, G.T., Rivizzigno, P., Party, T.A.-60 S., 2001b. An off-axis hydrothermal vent field near the Mid-Atlantic Ridge at 30° N. Nature 412, 145–149.

Kempler, D., Ben-Avraham, Z., 1987. The tectonic evolution of the Cyprean Arc. Ann. Tecton. 1, 58-71.

Kerrick, D., 2002. Geology. Serpentinite seduction. Science.

Kil, Y., Lee, S.H., Park, M.H., Wendlandt, R.F., 2010. Nature of serpentinization of ultramafic rocks from Hero Fracture Zone, Antarctic: Constraints from stable isotopes. Mar. Geol. 274, 43–49.

Kimura, J.-I., Chang, Q., Ishikawa, T., Tsujimori, T., 2016. Influence of laser parameters on isotope fractionation and optimisation of lithium and boron isotope ratio measurements using laser ablation-multiple Faraday collector-inductively coupled plasma mass spectrometry. J. Anal. At. Spectrom. 31, 2305–2320.

Klein, F., Bach, W., Jöns, N., McCollom, T., Moskowitz, B., Berquó, T., 2009. Iron partitioning and hydrogen generation during serpentinization of abyssal peridotites from 15°N on the Mid-Atlantic Ridge. Geochim. Cosmochim. Acta 73, 6868–6893.

Klein, F., Bach, W., McCollom, T.M., 2013. Compositional controls on hydrogen generation during serpentinization of ultramafic rocks. Lithos 178, 55–69.

Klein, F., Humphris, S.E., Bach, W., 2020. Brucite formation and dissolution in oceanic serpentinite. Geochem. perspect. lett. 1–5.

Klein, F., Le Roux, V., 2020. Quantifying the volume increase and chemical exchange during serpentinization. Geology 48, 552–556.

Klein, F., Marschall, H.R., Bowring, S.A., Humphris, S.E., Horning, G., 2017. Mid-ocean Ridge Serpentinite in the Puerto Rico Trench: from Seafloor Spreading to Subduction. J. Petrol. 58, 1729–1754.

Knudsen, M., 1901. Hydrographische Tabellen. GEC Gad, Copenhagen, and Williams Norgate, London, pp. 63.

Kodolányi, J., Pettke, T., 2011. Loss of trace elements from serpentinites during fluid-assisted transformation of chrysotile to antigorite — An example from Guatemala. Chem. Geol. 284, 351–362.

Kodolányi, J., Pettke, T., Spandler, C., Kamber, B.S., Gméling, K., 2012. Geochemistry of Ocean Floor and Fore-arc Serpentinites: Constraints on the Ultramafic Input to Subduction Zones. J. Petrol. 53, 235–270.

Kounoudis, R., Bastow, I.D., Ogden, C.S., Goes, S., Jenkins, J., Grant, B., Braham, C., 2020. Seismic tomographic imaging of the Eastern Mediterranean mantle: Implications for terminal-stage subduction, the uplift of Anatolia, and the development of the north Anatolian fault. Geochem. Geophys. Geosyst. 21. https://doi.org/10.1029/2020gc009009

Kowalski, P.M., Wunder, B., 2018. Boron Isotope Fractionation Among Vapor–Liquids–Solids–Melts: Experiments and Atomistic Modeling, in: Marschall, H., Foster, G. (Eds.), Boron Isotopes: The Fifth Element. Springer International Publishing, Cham, pp. 33–69.

Kyser, T.K., Kerrich, R., 1991. Retrograde exchange of hydrogen between hydrous minerals and water at low temperatures. The Geochemical Society, Special Publication 409–422.

Kyser, T.K., O'Hanley, D.S., Wicks, F.J., 1999. The origin of fluids associated with serpentinization; evidence from stable-isotope compositions. Can. Mineral. 37, 223–237.

Ladegaard-Pedersen, P., Achilleos, M., Dörflinger, G., Frei, R., Kristiansen, K., Frei, K.M., 2020. A strontium isotope baseline of Cyprus. Assessing the use of soil leachates, plants, groundwater and surface water as proxies for the local range of bioavailable strontium isotope composition. Sci. Total Environ. 708, 134714.

Lamadrid, H.M., Rimstidt, J.D., Schwarzenbach, E.M., Klein, F., Ulrich, S., Dolocan, A., Bodnar, R.J., 2017. Effect of water activity on rates of serpentinization of olivine. Nat. Commun. 8, 16107.

Lang, S.Q., Brazelton, W.J., 2020. Habitability of the marine serpentinite subsurface: a case study of the Lost City hydrothermal field. Philos. Trans. A Math. Phys. Eng. Sci. 378, 20180429.

Lang, S.Q., Butterfield, D.A., Schulte, M., Kelley, D.S., 2010. Elevated concentrations of formate, acetate and dissolved organic carbon found at the Lost City hydrothermal field. et Cosmochimica Acta.

Lang, S.Q., Früh-Green, G.L., Bernasconi, S.M., Brazelton, W.J., Schrenk, M.O., McGonigle, J.M., 2018. Deeply-sourced formate fuels sulfate reducers but not methanogens at Lost City hydrothermal field. Sci. Rep. 8, 755.

Lang, S.Q., Lilley, M.D., Baumberger, T., Früh-Green, G.L., Walker, S.L., Brazelton, W.J., Kelley, D.S., Elend, M., Butterfield, D.A., Mau, A.J., 2021. Extensive decentralized hydrogen export from the Atlantis Massif. Geology 49, 851–856.

Lee, C.-T.A., Thurner, S., Paterson, S., Cao, W., 2015. The rise and fall of continental arcs: Interplays between magmatism, uplift, weathering, and climate. Earth Planet. Sci. Lett. 425, 105–119.

Leong, J.A.M., Howells, A.E., Robinson, K.J., Cox, A., Debes, R.V., II, Fecteau, K., Prapaipong, P., Shock, E.L., 2021. Theoretical predictions versus environmental observations on serpentinization fluids: Lessons from the samail ophiolite in Oman. J. Geophys. Res. [Solid Earth] 126. https://doi.org/10.1029/2020jb020756

Leong, J.A.M., Shock, E.L., 2020. Thermodynamic constraints on the geochemistry of low-temperature, continental, serpentinization-generated fluids. Am. J. Sci. 320, 185–235.

Liou, J.G., Hacker, B.R., Zhang, R.Y., 2000. Into the Forbidden Zone. Science 287, 1215–1216.

Liu, W.G., Xiao, Y.K., Peng, Z.C., An, Z.S., He, X.X., 2000. Boron concentration and isotopic composition of halite from experiments and salt lakes in the Qaidam Basin. Geochim. Cosmochim. Acta 64, 2177–2183.

Liu, Y., Tossell, J.A., 2005. Ab initio molecular orbital calculations for boron isotope fractionations on boric acids and borates. Geochim. Cosmochim. Acta 69, 3995–4006.

Lockwood, J.P., 1971. Sedimentary and Gravity-Slide Emplacement of Serpentinite. GSA Bulletin 82, 919–936.

Lowell, R.P., Rona, P.A., 2002. Seafloor hydrothermal systems driven by the serpentinization of peridotite. Geophys. Res. Lett. 29. https://doi.org/10.1029/2001gl014411

Macdonald, A.H., Fyfe, W.S., 1985. Rate of serpentinization in seafloor environments. Tectonophysics 116, 123–135.

Mackenzie, G.D., Maguire, P.K.H., Coogan, L.A., Khan, M.A., Eaton, M., Petrides, G., 2006. Geophysical constraints on the crustal architecture of the Troodos ophiolite: results from the IANGASS project. Geophys. J. Int. 167, 1385–1401.

MacLeod, C.J., 1988. The Tectonic Evolution of the Eastern Limassol Forest Complex, Cyprus. PhD thesis, Open University (United Kingdom).

MacLeod, C.J., Allerton, S., Gass, I.G., Xenophontos, C., 1990. Structure of a fossil ridge–transform intersection in the Troodos ophiolite. Nature 348, 717–720.

MacLeod, C.J., Escartín, J., Banerji, D., Banks, G.J., Gleeson, M., Irving, D.H.B., Lilly, R.M., McCaig, A.M., Niu, Y., Allerton, S., Smith, D.K., 2002. Direct geological evidence for oceanic detachment faulting: The Mid-Atlantic Ridge, 15°45′N. Geology 30, 879–882.

MacLeod, C.J., Murton, B.J., 1993. Structure and tectonic evolution of the Southern Troodos Transform Fault Zone, Cyprus. Geological Society, London, Special Publications 76, 141–176.

Magaritz, M., Taylor, H.P., 1976. Oxygen, hydrogen and carbon isotope studies of the franciscan formation, Coast Ranges, California. Geochim. Cosmochim. Acta 40, 215–234.

Magaritz, M., Taylor, H.P., 1974. Oxygen and hydrogen isotope studies of serpentinization in the Troodos ophiolite complex, Cyprus. Earth Planet. Sci. Lett. 23, 8–14.

Maia, M., Sichel, S., Briais, A., Brunelli, D., Ligi, M., Ferreira, N., Campos, T., Mougel, B., Brehme, I., Hémond, C., Motoki, A., Moura, D., Scalabrin, C., Pessanha, I., Alves, E., Ayres, A., Oliveira, P., 2016. Extreme mantle uplift and exhumation along a transpressive transform fault. Nat. Geosci. 9, 619–623.

Makarona, C., Nys, K., Claeys, P., 2012. Sr isotope analysis for the provenance study of ancient ceramics: An integrated approach, in: Proceeedings of the 39th International Symposium for Archaeometry.

Malpas, J., Robinson, P.T., Salisbury, M., 1989. Geology and geophysics of borehole CY-4 of the Cyprus crustal study project: summary. Natural Resources Canada/CMSS/Information Management. https://doi.org/10.4095/127341

Malvoisin, B., 2015. Mass transfer in the oceanic lithosphere: Serpentinization is not isochemical. Earth Planet. Sci. Lett. 430, 75–85.

Manzi, V., Lugli, S., Roveri, M., Dela Pierre, F., Gennari, R., Lozar, F., Natalicchio, M., Schreiber, B.C., Taviani, M., Turco, E., 2016. The Messinian salinity crisis in Cyprus: a further step towards a new stratigraphic framework for Eastern Mediterranean. Basin Res. 28, 207–236.

Marschall, H.R., Wanless, V.D., Shimizu, N., Pogge von Strandmann, P.A.E., Elliott, T., Monteleone, B.D., 2017. The boron and lithium isotopic composition of mid-ocean ridge basalts and the mantle. Geochim. Cosmochim. Acta 207, 102–138.

Martin, B., Fyfe, W.S., 1970. Some experimental and theoretical observations on the kinetics of hydration reactions with particular reference to serpentinization. Chem. Geol. 6, 185–202.

Martin, C., Flores, K.E., Harlow, G.E., 2016. Boron isotopic discrimination for subduction-related serpentinites. Geology 44. https://doi.org/10.1130/G38102.1

Martin, W., Baross, J., Kelley, D., Russell, M.J., 2008. Hydrothermal vents and the origin of life. Nat. Rev. Microbiol. 6, 805–814.

Massell, C., Coffin, M.F., Mann, P., Mosher, S., Frohlich, C., Duncan, C.S., Karner, G., Ramsay, D., Lebrun, J.-F., 2000. Neotectonics of the Macquarie Ridge Complex, Australia-Pacific plate boundary. J. Geophys. Res. 105, 13457–13480.

Matter, J.M., Kelemen, P.B., 2009. Permanent storage of carbon dioxide in geological reservoirs by mineral carbonation. Nat. Geosci. 2, 837–841.

Mattey, D., Lowry, D., Macpherson, C., 1994. Oxygen isotope composition of mantle peridotite. Earth Planet. Sci. Lett. 128, 231–241.

McArthur, J.M., Howarth, R.J., Shields, G.A., 2012. Strontium isotope stratigraphy. The geologic time scale.

McCaffrey, M.A., Lazar, B., Holland, H.D., 1987. The evaporation path of seawater and the coprecipitation of Br- and K+ with halite. J. Sediment. Petrol. 57, 928–938.

McCaig, A.M., Delacour, A., Fallick, A.E., Castelain, T., Früh-Green, G.L., 2010. Detachment fault control on hydrothermal circulation systems: Interpreting the subsurface beneath the TAG hydrothermal field using the isotopic and geological evolution of oceanic core complexes in the Atlantic, in: Geophysical Monograph Series, Geophysical Monograph. American Geophysical Union, Washington, D. C., pp. 207–239.

McCallum, J.E., 1989. Sedimentation and tectonics of the Plio-Pleistocene of Cyprus. Ph.D. thesis, University of Edinburgh.

McCann, C., Sothcott, J., 1992. Laboratory measurements of the seismic properties of sedimentary rocks. Geological Society, London, Special Publications 65, 285–297.

McCollom, T.M., Bach, W., 2009. Thermodynamic constraints on hydrogen generation during serpentinization of ultramafic rocks. Geochim. Cosmochim. Acta 73, 856–875.

McCollom, T.M., Klein, F., Robbins, M., Moskowitz, B., Berquó, T.S., Jöns, N., Bach, W., Templeton, A., 2016. Temperature trends for reaction rates, hydrogen generation, and partitioning of iron during experimental serpentinization of olivine. Geochim. Cosmochim. Acta 181, 175–200.

McCollom, T.M., Seewald, J.S., 2013. Serpentinites, Hydrogen, and Life. Elements 9, 129–134.

McCollom, T.M., Seewald, J.S., 2007. Abiotic synthesis of organic compounds in deep-sea hydrothermal environments. Chem. Rev. 107, 382–401.

McCulloch, M.T., Deckker, P.D., 1989. Sr isotope constraints on the Mediterranean environment at the end of the Messinian salinity crisis. Nature 342, 62–65.

McPhee, D.K., Jachens, R.C., Wentworth, C.M., 2004. Crustal structure across the San Andreas Fault at the SAFOD site from potential field and geologic studies. Geophys. Res. Lett. 31. https://doi.org/10.1029/2003gl019363

Melson, W.G., Hart, S.R. and Thompson, G., 1972. St. Paul's Rocks, Equatorial Atlantic: Petrogenesis, Radiometric Ages, and. Studies in Earth and Space Sciences: A Memoir in Honor of Harry Hammond Hess, 132, p.241.

Menzies, C.D., 2012. Fluid Flow Associated with the Alpine Fault, South Island, New Zealand. Phd thesis, University of Southampton.

Menzies, C.D., Price, R.E., Ryan, J., Sissmann, O., Takai, K., Wheat, C.G., 2022. Spatial variation of subduction zone fluids during progressive subduction: Insights from Serpentinite Mud Volcanoes. Geochim. Cosmochim. Acta 319, 118–134.

Merrill, G.P., 1899. III.—A Discussion on the Use of the Terms Rock-weathering, Serpentinization, and Hydrometamorphism. Geol. Mag. 6, 354–358.

Metwally, Y.M., Sondergeld, C.H., 2011. Measuring low permeabilities of gas-sands and shales using a pressure transmission technique. Int. J. Rock Mech. Min. Sci. 48, 1135–1144.

Mével, C., 2003. Serpentinization of abyssal peridotites at mid-ocean ridges. C. R. Geosci. 335, 825–852.

Michael, P.J., Langmuir, C.H., Dick, H.J.B., Snow, J.E., Goldstein, S.L., Graham, D.W., Lehnert, K., Kurras, G., Jokat, W., Mühe, R., Edmonds, H.N., 2003. Magmatic and amagmatic seafloor generation at the ultraslow-spreading Gakkel ridge, Arctic Ocean. Nature 423, 956–961.

Miller, D.J., and Christensen, N.I., 1997. Seismic velocities of lower crustal and upper mantle rocks from the slow-spreading Mid-Atlantic Ridge, south of the Kane Transform Zone (MARK). In Karson, J.A., Cannat, M., Miller, D.J., and Elthon, D. (Eds.), Proc. ODP, Sci. Results, College Station, TX (Ocean Drilling Program), Vol. 153, 437–454.

Millero, F.J., 2010. History of the equation of state of seawater. Oceanography 23, 18–33.

Millero, F.J., 1995. Thermodynamics of the carbon dioxide system in the oceans. Geochim. Cosmochim. Acta 59, 661–677.

Milliken, K.L., Lynch, F.L., and Seifert, K.E., 1996. Marine weathering of serpentinites and serpentinite breccias, Sites 897 and 899, Iberia Abyssal Plain. In Whitmarsh, R.B., Sawyer, D.S., Klaus, A., and Masson, D.G. (Eds.), Proc. ODP, Sci. Results, College Station, TX (Ocean Drilling Program), Vol. 149, 529–540.

Milliken, K.L., and Morgan, J.K., 1996. Chemical evidence for near-seafloor precipitation of calcite in serpentinites (Site 897) and serpentinite breccias (Site 899), Iberia Abyssal Plain. In Whitmarsh, R.B., Sawyer, D.S., Klaus, A., and Masson, D.G. (Eds.), Proc. ODP, Sci. Results, College Station, TX (Ocean Drilling Program), Vol. 149, 553–558.

Minshull, T.A., Dean, S.M., Whitmarsh, R.B., 2014. The peridotite ridge province in the southern Iberia Abyssal Plain: Seismic constraints revisited. J. Geophys. Res.

Miyashiro, A., 1973. The Troodos ophiolitic complex was probably formed in an island arc. Earth Planet. Sci. Lett. 19, 218–224.

Monnin, C., Chavagnac, V., Boulart, C., Ménez, B., Gérard, M., Gérard, E., Pisapia, C., Quéméneur, M., Erauso, G., Postec, A., Guentas-Dombrowski, L., Payri, C., Pelletier, B., 2014. Fluid chemistry of the low temperature hyperalkaline hydrothermal system of Prony Bay (New Caledonia). Biogeosciences 11, 5687–5706.

Moore, D.E., Lockner, D.A., 2013. Chemical controls on fault behavior: Weakening of serpentinite sheared against quartz-bearing rocks and its significance for fault creep in the San Andreas system. J. Geophys. Res. [Solid Earth] 118, 2558–2570.

Moore, D.E., Rymer, M.J., 2012. Correlation of clayey gouge in a surface exposure of serpentinite in the San Andreas Fault with gouge from the San Andreas Fault Observatory at Depth (SAFOD). J. Struct. Geol. 38, 51–60.

Moore, D.E., Rymer, M.J., 2007. Talc-bearing serpentinite and the creeping section of the San Andreas fault. Nature 448, 795–797.

Moores, E.M., Robinson, P.T., Malpas, J., Xenophonotos, C., 1984. Model for the origin of the Troodos massif, Cyprus, and other mideast ophiolites. Geology 12, 500–503.

Moores, E.M., Vine, F.J., 1971. The Troodos Massif, Cyprus and other Ophiolites as Oceanic Crust: Evaluation and Implications. Philosophical Transactions of the Royal Society A: Mathematical, Physical and Engineering Sciences 268, 443–467.

Morag, N., Haviv, I., Katzir, Y., 2016. From ocean depths to mountain tops: Uplift of the Troodos ophiolite (Cyprus) constrained by low-temperature thermochronology and geomorphic analysis. Tectonics 35, 622–637.

Morgan, P., 1973. Terrestrial hear flow studies in Cyprus and Kenya. PhD thesis, Imperial College London.

Morrow, C.A., Lockner, D.A., Moore, D.E., Hickman, S., 2014. Deep permeability of the San Andreas Fault from San Andreas Fault Observatory at Depth (SAFOD) core samples. J. Struct. Geol. 64, 99–114.

Morrow, C.A., Moore, D.E., Lockner, D.A., Bekins, B.A., 2019. Data report: permeability, porosity, and frictional strength of core samples from IODP Expedition 366 in the Mariana forearc. Proceedings of the International Ocean Discovery Program 366.

Mottl, M.J., Komor, S.C., Fryer, P., Moyer, C.L., 2003. Deep-slab fluids fuel extremophilicArchaeaon a Mariana forearc serpentinite mud volcano: Ocean Drilling Program Leg 195. Geochem. Geophys. Geosyst. 4. https://doi.org/10.1029/2003gc000588

Mottl, M.J., Wheat, C.G., Fryer, P., 2004a. Decarbonation, Serpentinization, Abiogenic Methane, and Extreme pH beneath the Mariana Forearc. pp. V13A-1441.

Mottl, M.J., Wheat, C.G., Fryer, P., Gharib, J., Martin, J.B., 2004b. Chemistry of springs across the Mariana forearc shows progressive devolatilization of the subducting plate. Geochim. Cosmochim. Acta 68, 4915–4933.

Mukasa, S.B., Ludden, J.N., 1987. Uranium-lead isotopic ages of plagiogranites from the Troodos ophiolite, Cyprus, and their tectonic significance. Geology 15, 825.

Müller, D.W., Mueller, P.A., 1991. Origin and age of the Mediterranean Messinian evaporites: implications from Sr isotopes. Earth Planet. Sci. Lett. 107, 1–12.

Müller, D.W., Mueller, P.A., and McKenzie, J.A., 1990. Strontium isotopic ratios as fluid tracers in Messinian evaporites of the Tyrrhenian Sea (western Mediterranean Sea). In Kastens, K.A., Mascle, J., et al., Proc. ODP, Sci. Results, College Station, TX (Ocean Drilling Program), Vol. 107, 603–614.

Müller, R.D., Sdrolias, M., Gaina, C., Roest, W.R., 2008. Age, spreading rates, and spreading asymmetry of the world's ocean crust. Geochem. Geophys. Geosyst. 9. https://doi.org/10.1029/2007gc001743

Mumpton, F.A., Thompson, C.S., 1975. Mineralogy and Origin of the Coalinga Asbestos Deposit. Clays Clay Miner. 23, 131–143.

Murton, B.J., 1986. Anomalous oceanic lithosphere formed in a leaky transform fault: evidence from the Western Limassol Forest Complex, Cyprus. J. Geol. Soc. London 143, 845–854.

Neal, C., Shand, P., 2002. Spring and surface water quality of the Cyprus ophiolites. Hydrol. Earth Syst. Sci. 6, 797–817.

Neal, C., Stanger, G., 1985. Past and Present Serpentinisation of Ultramafic Rocks, an Example From the Semail Ophiolite Nappe of Northern Oman, in: The Chemistry of Weathering. Springer Netherlands, Dordrecht, pp. 249–275.

Nielsen, S.G., Horner, T.J., Pryer, H.V., Blusztajn, J., Shu, Y., Kurz, M.D., Le Roux, V., 2018. Barium isotope evidence for pervasive sediment recycling in the upper mantle. Sci Adv 4, eaas8675.

Nielsen, S.G., Shu, Y., Auro, M., Yogodzinski, G., Shinjo, R., Plank, T., Kay, S.M., Horner, T.J., 2020. Barium isotope systematics of subduction zones. Geochim. Cosmochim. Acta 275, 1–18.

Niu, Y., 2004. Bulk-rock Major and Trace Element Compositions of Abyssal Peridotites: Implications for Mantle Melting, Melt Extraction and Post-melting Processes Beneath Mid-Ocean Ridges. J. Petrol. 45, 2423–2458.

North, L., Best, A.I., Sothcott, J., MacGregor, L., 2013. Laboratory determination of the full electrical resistivity tensor of heterogeneous carbonate rocks at elevated pressures. Geophys. Prospect. 61, 458–470.

Nuriel, P., Katzir, Y., Abelson, M., Valley, J.W., Matthews, A., Spicuzza, M.J., Ayalon, A., 2009. Fault-related oceanic serpentinization in the Troodos ophiolite, Cyprus: Implications for a fossil oceanic core complex. Earth Planet. Sci. Lett. 282, 34–46.

O'Hanley, D.S., 1991. Fault-related phenomena associated with hydration and serpentine recrystallization during serpentinization. Can. Mineral. 29, 21-35.

O'Hanley, D.S., Offler, R., 1992. Characterization of multiple serpentinization, Woodsreef, New South Wales. Can. Mineral. 30, 1113–1126.

O'Hanley, D.S., Schandl, E.S., Wicks, F.J., 1992. The origin of rodingites from Cassiar, British Columbia, and their use to estimate T and P(H_2O) during serpentinization. Geochim. Cosmochim. Acta 56, 97–108.

Pabst, S., Zack, T., Savov, I.P., Ludwig, T., Rost, D., Vicenzi, E.P., 2011. Evidence for boron incorporation into the serpentine crystal structure. Am. Mineral. 96, 1112–1119.

Pagani, M., Lemarchand, D., Spivack, A., Gaillardet, J., 2005. A critical evaluation of the boron isotope-pH proxy: The accuracy of ancient ocean pH estimates. Geochim. Cosmochim. Acta 69, 953–961.

Page, B.M., Coleman, R.G., Thompson, G.A., 1998. Late Cenozoic tectonics of the central and southern Coast Ranges of California. GSA Bulletin 110, 846–876.

Palandri, J.L., Reed, M.H., 2004. Geochemical models of metasomatism in ultramafic systems: Serpentinization, rodingitization, and sea floor carbonate chimney precipitation. Geochim. Cosmochim. Acta 68, 1115–1133.

Palme, H., O'Neill, H.S.C., 2014. 3.1 - Cosmochemical Estimates of Mantle Composition, in: Holland, H.D., Turekian, K.K. (Eds.), Treatise on Geochemistry (Second Edition). Elsevier, Oxford, pp. 1–39.

Palmer, M.R., 1996. Hydration and uplift of the oceanic crust on the Mid-Atlantic Ridge associated with hydrothermal activity: Evidence from boron isotopes. Geophys. Res. Lett. 23, 3479–3482.

Palmer, M.R., 1991. Boron isotope systematics of hydrothermal fluids and tourmalines: A synthesis. Chemical Geology: Isotope Geoscience section 94, 111–121.

Palmer, M.R., Edmond, J.M., 1989. Cesium and rubidium in submarine hydrothermal fluids: Evidence for recycling of alkali elements. Earth Planet. Sci. Lett. 95, 8–14.

Paris, G., Gaillardet, J., Louvat, P., 2010. Geological evolution of seawater boron isotopic composition recorded in evaporites. Geology 38, 1035–1038.

Park, J.-O., Takahata, N., Jamali Hondori, E., Yamaguchi, A., Kagoshima, T., Tsuru, T., Fujie, G., Sun, Y., Ashi, J., Yamano, M., Sano, Y., 2021. Mantle-derived helium released through the Japan trench bend-faults. Sci. Rep. 11, 12026.

Parkinson, I.J., Pearce, J.A., 1998. Peridotites from the Izu–Bonin–Mariana Forearc (ODP Leg 125): Evidence for Mantle Melting and Melt–Mantle Interaction in a Supra-Subduction Zone Setting. J. Petrol. 39, 1577–1618.

Patten, C.G.C., Pitcairn, I.K., Teagle, D.A.H., 2017. Hydrothermal mobilisation of Au and other metals in supra-subduction oceanic crust: Insights from the Troodos ophiolite. Ore Geol. Rev. 86, 487–508.

Peacock, S.A., 1990. Fluid processes in subduction zones. Science 248, 329–337.

Peacock, S.M., 1987. Serpentinization and infiltration metasomatism in the Trinity peridotite, Klamath province, northern California: implications for subduction zones. Contrib. Mineral. Petrol. 95, 55–70.

Pearce, J.A., Lippard, S.J., Roberts, S., 1984. Characteristics and tectonic significance of supra-subduction zone ophiolites. Geological Society, London.

Perrillat, J.-P., Daniel, I., Koga, K.T., Reynard, B., Cardon, H., Crichton, W.A., 2005. Kinetics of antigorite dehydration: A real-time X-ray diffraction study. Earth Planet. Sci. Lett. 236, 899–913.

Peters, D., Bretscher, A., John, T., Scambelluri, M., Pettke, T., 2017. Fluid-mobile elements in serpentinites: Constraints on serpentinisation environments and element cycling in subduction zones. Chem. Geol. 466, 654–666.

Peters, D., Pettke, T., John, T., Scambelluri, M., 2020. The role of brucite in water and element cycling during serpentinite subduction – Insights from Erro Tobbio (Liguria, Italy). Lithos 360–361, 105431.

Picazo, S., Manatschal, G., Cannat, M., Andréani, M., 2013. Deformation associated to exhumation of serpentinized mantle rocks in a fossil Ocean Continent Transition: The Totalp unit in SE Switzerland. Lithos 175–176, 255–271.

Plank, T., 2014. The Chemical Composition of Subducting Sediments, in: Holland, H.D., Turekian, K.K. (Eds.), Treatise on Geochemistry (Second Edition). Elsevier, Oxford, pp. 607–629.

Poole, A., and Robertson, A., 1998. Pleistocene fanglomerate deposition related to uplift of the Troodos Ophiolite, Cyprus. In Robertson, A.H.F., Emeis, K.-C., Richter, C., and Camerlenghi, A. (Eds.), Proc. ODP, Sci. Results, College Station, TX (Ocean Drilling Program), Vol. 160, 545–566.

Poole, A.J., Robertson, A.H.F., 1991. Quaternary uplift and sea-level change at an active plate boundary, Cyprus. J. Geol. Soc. London 148, 909–921.

Quandt, D., Micheuz, P., Kurz, W., Kluge, T., Boch, R., Hippler, D., Krenn, K., Hauzenberger, C.A., 2019. Geochemistry of vein calcites hosted in the Troodos pillow lavas and their implications for the timing and physicochemical environment of fracturing, fluid circulation, and vein mineral growth. Geochem. Geophys. Geosyst. 20, 5913–5938.

Rae, J.W.B., 2018. Boron Isotopes in Foraminifera: Systematics, Biomineralisation, and CO2 Reconstruction, in: Marschall, H., Foster, G. (Eds.), Boron Isotopes: The Fifth Element. Springer International Publishing, Cham, pp. 107–143.

Ramsay, J.G., 1980. Shear zone geometry: A review. J. Struct. Geol. 2, 83–99.

Ranero, C.R., Morgan, J.P., McIntosh, K., Reichert, C., 2003. Bending-related faulting and mantle serpentinization at the Middle America trench. Nature 425, 367–373.

Ranero, C.R., Sallarès, V., 2004. Geophysical evidence for hydration of the crust and mantle of the Nazca plate during bending at the north Chile trench. Geology 32, 549–552.

Rautenschlein, M., Jenner, G.A., Hertogen, J., Hofmann, A.W., Kerrich, R., Schmincke, H.U., White, W.M., 1985. Isotopic and trace element composition of volcanic glasses from the Akaki Canyon, Cyprus: implications for the origin of the Troodos ophiolite. Earth Planet. Sci. Lett. 75, 369–383.

Reiche, S., Hübscher, C., Ehrhardt, A., 2016. The impact of salt on the late Messinian to recent tectonostratigraphic evolution of the Cyprus subduction zone. Basin Res. 28, 569–597.

Ring, U., Pantazides, H., 2019. The uplift of the troodos massif, Cyprus. Tectonics 38, 3124–3139.

Rivizzigno, P.A., Karson, J.A., 2004. Structural expression of oblique seafloor spreading in the Macquarie Island ophiolite, Southern Ocean. Geology 32, 125–128.

Rizoulis, A., Milodowski, A.E., Morris, K., Lloyd, J.R., 2016. Bacterial Diversity in the Hyperalkaline Allas Springs (Cyprus), a Natural Analogue for Cementitious Radioactive Waste Repository. Geomicrobiol. J. 33, 73–84.

Roberts, S., Bach, W., Binns, R.A., Vanko, D.A., Yeats, C.J., Teagle, D.A.H., Blacklock, K., Blusztajn, J.S., Boyce, A.J., Cooper, M.J., Holland, N., McDonald, B., 2003. Contrasting evolution of hydrothermal fluids in the PACMANUS system, Manus Basin: The Sr and S isotope evidence. Geology 31, 805–808.

Robertson, A.H.F., 2007. Evidence of continental breakup from the Newfoundland rifted margin (Ocean Drilling Program Leg 210): Lower Cretaceous seafloor formed by exhumation of subcontinental mantle lithosphere, and the transition to seafloor spreading. *In* Tucholke, B.E., Sibuet, J.-C., and Klaus, A. (Eds.), *Proc. ODP, Sci. Results,* College Station, TX (Ocean Drilling Program), Vol. 210, 1–69.

Robertson, A. H. F., 1998a. Tectonic significance of the Eratosthenes Seamount: a continental fragment in the process of collision with a subduction zone in the eastern Mediterranean (Ocean Drilling Program Leg 160). Tectonophysics 298, 63–82.

Robertson, A.H.F., 1998b. Formation and destruction of the Eratosthenes Seamount, Eastern Mediterranean Sea, and implications for collisional processes. In Robertson, A.H.F., Emeis, K.-C., Richter, C., and Camerlenghi, A. (Eds.), Proc. ODP, Sci. Results, College Station, TX (Ocean Drilling Program), Vol. 160, 681–699.

Robertson, A.H.F., 1998c. Mesozoic–Tertiary tectonic evolution of the easternmost Mediterranean area: integration of marine and land evidence. In Robertson, A.H.F., Emeis, K.-C., Richter, C., and Camerlenghi, A. (Eds.), Proc. ODP, Sci. Results, College Station, TX (Ocean Drilling Program), Vol. 160, 723–782.

Robertson, A.H.F., 1977. Tertiary uplift history of the Troodos massif, Cyprus. GSA Bulletin 88, 1763–1772.

Robertson, A.H.F., Eaton, S., Follows, E.J., Payne, A.S., 1995. Depositional processes and basin analysis of Messinian evaporites in Cyprus. Terra Nova 7, 233–253.

Rollinson, H.R., 2014. Using stable isotope data, in: Using Geochemical Data. Routledge, pp. 292–341.

Rommel, U., Friedrichsen, H., Robinson, P.T., 1987. The alteration chemistry of CCSP hole CY-2a: A stable and radiogenic isotope study. Cyprus Crustal Study Project: Initial report, holes CY-2 and 2a: Geological Survey of Canada Paper 85–29.

Rooney, J.S., Tarling, M.S., Smith, S.A. and Gordon, K.C., 2018. Submicron Raman spectroscopy mapping of serpentinite fault rocks. Journal of Raman Spectroscopy, 49(2), pp.279-286.

Rose-Koga, E.F., Sheppard, S.M.F., Chaussidon, M., Carignan, J., 2006. Boron isotopic composition of atmospheric precipitations and liquid–vapour fractionations. Geochim. Cosmochim. Acta 70, 1603–1615.

Rouchy, J.M., Orszag-Sperber, F., Blanc-Valleron, M.-M., Pierre, C., Rivière, M., Combourieu-Nebout, N., Panayides, I., 2001. Paleoenvironmental changes at the Messinian–Pliocene boundary in the eastern Mediterranean (southern Cyprus basins): significance of the Messinian Lago-Mare. Sediment. Geol. 145, 93–117.

Rouméjon, S., Andreani, M., Früh-Green, G.L., 2019. Antigorite crystallization during oceanic retrograde serpentinization of abyssal peridotites. Contrib. Mineral. Petrol. 174, 1–25.

Roumejon, S., Cannat, M., Agrinier, P., Godard, M., Andreani, M., 2015. Serpentinization and fluid pathways in tectonically exhumed peridotites from the southwest Indian Ridge (62-65 E). J. Petrol. 56, 703–734.

Rouméjon, S., Früh-Green, G.L., Orcutt, B.N., 2018a. Alteration Heterogeneities in Peridotites Exhumed on the Southern Wall of the Atlantis Massif (IODP Expedition 357). J. Petrol. https://doi.org/10.1093/petrology/egy065

Rouméjon, S., Williams, M.J., Früh-Green, G.L., 2018b. In-situ oxygen isotope analyses in serpentine minerals: Constraints on serpentinization during tectonic exhumation at slow- and ultraslow-spreading ridges. Lithos 323, 156–173.

Roveri, M., Flecker, R., Krijgsman, W., Lofi, J., Lugli, S., Manzi, V., Sierro, F.J., Bertini, A., Camerlenghi, A., De Lange, G., Govers, R., Hilgen, F.J., Hübscher, C., Meijer, P.T., Stoica, M., 2014. The Messinian Salinity Crisis: Past and future of a great challenge for marine sciences. Mar. Geol. 352, 25–58.

Rumori, C., Mellini, M., Viti, C., 2004. Oriented, non-topotactic olivine→ serpentine replacement in mesh-textured, serpentinized peridotites. Eur. J. Mineral. 16, 731–741.

Russell, M.J., Hall, A.J., Martin, W., 2010. Serpentinization as a source of energy at the origin of life. Geobiology 8, 355–371.

Saccocia, P.J., Seewald, J.S., Shanks, W.C., 2009a. Oxygen and hydrogen isotope fractionation in serpentine–water and talc–water systems from 250 to 450°C, 50MPa. Geochim. Cosmochim. Acta 73, 6789–6804.

Saccocia, P.J., Seewald, J.S., Shanks, W.C., III, 2009b. Oxygen and hydrogen isotope fractionation in serpentine--water and talc--water systems from 250 to 450 C, 50 MPa. Geochim. Cosmochim. Acta 73, 6789–6804.

Safarov, J., Berndt, S., Millero, F., Feistel, R., Heintz, A., Hassel, E., 2012. (p,ρ,T) properties of seawater: Extensions to high salinities. Deep Sea Res. Part I 65, 146–156.

Safarov, J., Berndt, S., Millero, F.J., Feistel, R., Heintz, A., Hassel, E.P., 2013. (p,ρ,T) Properties of seawater at brackish salinities: Extensions to high temperatures and pressures. Deep Sea Res. Part I 78, 95–101.

Safarov, J., Millero, F., Feistel, R., Heintz, A., Hassel, E., 2009. Thermodynamic properties of standard seawater: extensions to high temperatures and pressures. Ocean Sci. 5, 235–246.

Saffer, D.M., Underwood, M.B., McKiernan, A.W., 2008. Evaluation of factors controlling smectite transformation and fluid production in subduction zones: Application to the Nankai Trough. Island Arc 17, 208–230.

Salters, V.J.M., Stracke, A., 2004. Composition of the depleted mantle. Geochem. Geophys. Geosyst. 5. https://doi.org/10.1029/2003gc000597

Savin, S.M., Lee, M., 1988. Isotopic studies of phyllosilicates. Rev. Mineral. Geochem. 19, 189–223.

Savov, I.P., Ryan, J.G., D'Antonio, M., Fryer, P., 2007. Shallow slab fluid release across and along the Mariana arc-basin system: Insights from geochemistry of serpentinized peridotites from the Mariana fore arc. J. Geophys. Res. 112. https://doi.org/10.1029/2006jb004749

Savov, I.P., Ryan, J.G., D'Antonio, M., Kelley, K., Mattie, P., 2005. Geochemistry of serpentinized peridotites from the Mariana Forearc Conical Seamount, ODP Leg 125: Implications for the elemental recycling at subduction zones. Geochem. Geophys. Geosyst. 6, 1–24.

Sawyer, D.S., Whitmarsh, R.B., Klaus, A., et al., 1994. Proc. ODP, Init. Repts, College Station, TX (Ocean Drilling Program), Vol. 149.

Schiffman, P., Smith, B.M., 1988. Petrology and oxygen isotope geochemistry of a fossil seawater hydrothermal system within the Solea graben, northern Troodos ophiolite, Cyprus. J. Geophys. Res. 93, 4612–4624.

Schildgen, T.F., Cosentino, D., Frijia, G., Castorina, F., Dudas, F.Ö., Iadanza, A., Sampalmieri, G., Cipollari, P., Caruso, A., Bowring, S.A., Strecker, M.R., 2014. Sea level and climate forcing of the Sr isotope composition of late Miocene Mediterranean marine basins. Geochem. Geophys. Geosyst. 15, 2964–2983.

Schmidt, K., Koschinsky, A., Garbe-Schönberg, D., de Carvalho, L.M., Seifert, R., 2007. Geochemistry of hydrothermal fluids from the ultramafic-hosted Logatchev hydrothermal field, 15°N on the Mid-Atlantic Ridge: Temporal and spatial investigation. Chem. Geol. 242, 1–21.

Schönfeld, J., Sirocko, F., Jørgensen, N.O., 1991. Oxygen isotope composition of Upper Cretaceous chalk at Lägerdorf (NW Germany): its original environmental signal and palaeotemperature interpretation. Cretaceous Res. 12, 27–46.

Schrenk, M.O., Brazelton, W.J., Lang, S.Q., 2013. Serpentinization, carbon, and deep life. Rev. Mineral. Geochem. 75, 575–606.

Schuiling, R.D., 2011. Troodos: A Giant Serpentinite Diapir. Int. j. geosci. 02, 98–101.

Schwartz, S., Guillot, S., Reynard, B., Lafay, R., Debret, B., Nicollet, C., Lanari, P., Auzende, A.L., 2013. Pressure–temperature estimates of the lizardite/antigorite transition in high pressure serpentinites. Lithos 178, 197–210.

Schwarzenbach, E.M., Früh-Green, G.L., Bernasconi, S.M., Alt, J.C., Shanks, W.C., III, Gaggero, L., Crispini, L., 2012. Sulfur geochemistry of peridotite-hosted hydrothermal systems: Comparing the Ligurian ophiolites with oceanic serpentinites. Geochim. Cosmochim. Acta 91, 283–305.

Scott, J.M., Smith, S.A.F., Tarling, M.S., le Roux, P.J., Harris, C., Hoffmann, J.E., Scherzer, S., Tulley, C.J., 2019. Element and Sr–O isotope redistribution across a plate boundary-scale crustal serpentinite mélange shear zone, and implications for the slab-mantle interface. Earth Planet. Sci. Lett. 522, 198–209.

Searle, M., Cox, J., 1999. Tectonic setting, origin, and obduction of the Oman ophiolite. GSA Bulletin 111, 104–122.

Selkirk, P., Seppelt, R., Selkirk, D., 1990. Subantarctic Macquarie Island: Environment and Biology. Cambridge University Press.

Seyfried, W.E., Janecky, D.R., Mottl, M.J., 1984. Alteration of the oceanic crust: Implications for geochemical cycles of lithium and boron. Geochim. Cosmochim. Acta 48, 557–569.

Sharp, Z.D., Barnes, J.D., 2004. Water-soluble chlorides in massive seafloor serpentinites: a source of chloride in subduction zones. Earth Planet. Sci. Lett. 226, 243–254.

Shelton, A.W., 1993. Troodos revisited: the Mount Olympus gravity anomaly. Geological Society, London, Special Publications 76, 197–212.

Sheppard, S.M.F., 1980. Isotopic evidence for the origins of water during metamorphic processes in oceanic crust and ophiolite complexes. Coll. int. C.N.R.S., 272, 135-147

Sheppard, S.M.F., Epstein, S., 1970. D/H and18O/16O ratios of minerals of possible mantle or lower crustal origin. Earth Planet. Sci. Lett. 9, 232–239.

Shipboard Scientific Party, 2004. Site 1277. In Tucholke, B.E., Sibuet, J.-C., Klaus, A., et al., Proc. ODP, Init. Repts., College Station, TX (Ocean Drilling Program), Vol. 210, 1–39.

Simoes, M., Braun, J., Bonnet, S., 2010. Continental-scale erosion and transport laws: A new approach to quantitatively investigate macroscale landscapes and associated sediment fluxes over the geological past. Geochem. Geophys. Geosyst. 11. https://doi.org/10.1029/2010gc003121

Skilling, J., 2004. Nested Sampling. AIP Conf. Proc. 735, 395–405.

Sleep, N.H., Meibom, A., Fridriksson, T., Coleman, R.G., Bird, D.K., 2004. H2-rich fluids from serpentinization: geochemical and biotic implications. Proc. Natl. Acad. Sci. U. S. A. 101, 12818–12823.

Smith, D.K., Cann, J.R., Escartín, J., 2006. Widespread active detachment faulting and core complex formation near 13 degrees N on the Mid-Atlantic Ridge. Nature 442, 440–443.

Smith, G.C., Vine, F.J., Robinson, P.T., Gibson, I.L., Panayiotou, A., 1989. The physical properties of diabases, gabbros and ultramafic rocks from CCSP drill hole CY-4 at Palekhori, Cyprus. Cyprus Crustal Study Project: Initial report, holes CY 4, 295–314.

Smith, H.J., Spivack, A.J., Staudigel, H., Hart, S.R., 1995. The boron isotopic composition of altered oceanic crust. Chem. Geol. 126, 119–135.

Smith, J.M.B., Bayliss-Smith, T.P., 1998. Kelp-plucking: coastal erosion facilitated by bull-kelp Durvillaea antarctica at subantarctic Macquarie Island. Antarct. Sci. 10, 431–438.

Snow, J.E., Dick, H.J.B., 1995. Pervasive magnesium loss by marine weathering of peridotite. Geochim. Cosmochim. Acta 59, 4219–4235.

Spivack, A.J., Edmond, J.M., 1987. Boron isotope exchange between seawater and the oceanic crust. Geochim. Cosmochim. Acta 51, 1033–1043.

Spivack, A.J., Palmer, M.R., Edmond, J.M., 1987. The sedimentary cycle of the boron isotopes. Geochim. Cosmochim. Acta 51, 1939–1949.

Spooner, E.T.C., Beckinsale, R.D., Fyfe, W.S., Smewing, J.D., 1974. O18 enriched ophiolitic metabasic rocks from E. Liguria (Italy), Pindos (Greece), and Troodos (Cyprus). Contrib. Mineral. Petrol. 47, 41–62.

Spooner, E.T.C., Chapman, H.J., Smewing, J.D., 1977. Strontium isotopic contamination and oxidation during ocean floor hydrothermal metamorphism of the ophiolitic rocks of the Troodos Massif, Cyprus. Geochim. Cosmochim. Acta 41, 873–890.

Standish, C.D., Chalk, T.B., Babila, T.L., Milton, J.A., Palmer, M.R., Foster, G.L., 2019. The effect of matrix interferences on in situ boron isotope analysis by laser ablation multi-collector inductively coupled plasma mass spectrometry. Rapid Commun. Mass Spectrom. 33, 959–968.

Staudigel, H., 2014. 4.16 - Chemical Fluxes from Hydrothermal Alteration of the Oceanic Crust, in: Holland, H.D., Turekian, K.K. (Eds.), Treatise on Geochemistry (Second Edition). Elsevier, Oxford, pp. 583–606.

Staudigel, H., Davies, G.R., Hart, S.R., Marchant, K.M., Smith, B.M., 1995. Large scale isotopic Sr, Nd and O isotopic anatomy of altered oceanic crust: DSDP/ODP sites417/418. Earth Planet. Sci. Lett. 130, 169–185.

Staudigel, H., Gillis, K.M., 1990. The timing of hydrothermal alteration in the Troodos Ophiolite, in Ophiolites: Oceanic Crustal Analogues: Proceedings of the Symposium Troodos 1987, ed. by J. Malpas, E. M. Moores, A. Panayiotou, and C. Xenophontos, Geol. Surv. Dep., Nicosia, Cyprus, pp. 665-672.

Stern, R.J., 2002. Subduction zones. Rev. Geophys. 40, 3-1-3–38.

Stesky, R.M., Brace, W.F., 1973. Electrical conductivity of serpentinized rocks to 6 kilobars. J. Geophys. Res. 78, 7614–7621.

Stow, D.A.V., Braakenburg, N.E., Xenophontos, C., 1995. The Pissouri Basin fan-delta complex, southwestern Cyprus. Sediment. Geol. 98, 245–262.

Su, C., Suarez, D.L., 2004. Boron release from weathering of illites, serpentine, shales, and illitic/palygorskitic soils. Soil Sci. Soc. Am. J. 68, 96–105.

Symeou, V., Homberg, C., Nader, F.H., Darnault, R., Lecomte, J.-C., Papadimitriou, N., 2018. Longitudinal and temporal evolution of the tectonic style along the Cyprus arc system, assessed through 2-D reflection seismic interpretation. Tectonics 37, 30–47.

Taylor, H.P., 1977. Water/rock interactions and the origin of H_2O in granitic batholiths: Thirtieth William Smith lecture. J. Geol. Soc. London 133, 509–558.

Teagle, D.A.H., Ildefonse, B., 2011. Journey to the mantle of the Earth. Nature 471, 437–439.

Teagle, D.A.H., Alt, J.C., Halliday, A.N., 1998a. Tracing the evolution of hydrothermal fluids in the upper oceanic crust: Sr-isotopic constraints from DSDP/ODP Holes 504B and 896A. Geological Society, London, Special Publications 148, 81–97.

Teagle, D.A.H., Alt, J.C., Halliday, A.N., 1998b. Tracing the chemical evolution of fluids during hydrothermal recharge: Constraints from anhydrite recovered in ODP Hole 504B. Earth Planet. Sci. Lett. 155, 167–182.

Tesei, T., Harbord, C.W.A., De Paola, N., Collettini, C., Viti, C., 2018. Friction of mineralogically controlled serpentinites and implications for fault weakness. J. Geophys. Res. [Solid Earth]. https://doi.org/10.1029/2018jb016058

Thayer, T.P., 1966. Serpentinization considered as a constant-volume metasomatic process. Am. Mineral. 51, 685–710.

Thom, J.G.M., Dipple, G.M., Power, I.M., Harrison, A.L., 2013. Chrysotile dissolution rates: Implications for carbon sequestration. Appl. Geochem. 35, 244–254.

Toft, P.B., Arkani-Hamed, J., Haggerty, S.E., 1990. The effects of serpentinization on density and magnetic susceptibility: a petrophysical model. Phys. Earth Planet. Inter. 65, 137–157.

Tsujimori, T., Liou, J.G., Coleman, R.G., Cloos, M., Carlson, W.D., Gilbert, M.C., 2007. Finding of high-grade tectonic blocks from the New Idria serpentinite body, Diablo Range, California: Petrologic constraints on the tectonic evolution of an active serpentinite diapir. Special Papers-Geological Society of America 419, 67–80.

Turchyn, A.V., Alt, J.C., Brown, S.T., DePaolo, D.J., Coggon, R.M., Chi, G., Bédard, J.H., Skulski, T., 2013. Reconstructing the oxygen isotope composition of late Cambrian and Cretaceous hydrothermal vent fluid. Geochim. Cosmochim. Acta 123, 440–458.

Turvey, C.C., Wilson, S.A., Hamilton, J.L., Tait, A.W., McCutcheon, J., Beinlich, A., Fallon, S.J., Dipple, G.M., Southam, G., 2018. Hydrotalcites and hydrated Mg-carbonates as carbon sinks in serpentinite mineral wastes from the Woodsreef chrysotile mine, New South Wales, Australia: Controls on carbonate mineralogy and efficiency of CO2 air capture in mine tailings. Int. J. Greenhouse Gas Control 79, 38–60.

Ulmer, P., Trommsdorff, V., 1995. Serpentine Stability to Mantle Depths and Subduction-Related Magmatism. Source: Science, New Series J. F. Bonaparte, in Actas II Cong. Arg. Pal. Bioestr. Buenos Aires Buenos Aires J. F. Bonaparte, Opera Lilloana A Geological Time Scale 268, 858–861.

Ulrich, M., Muñoz, M., Boulvais, P., Cathelineau, M., Cluzel, D., Guillot, S., Picard, C., 2020. Serpentinization of New Caledonia peridotites: from depth to (sub-)surface. Contrib. Mineral. Petrol. 175, 91.

Vengosh, A., De Lange, G.J., Starinsky, A., 1998. Boron isotope and geochemical evidence for the origin of Urania and Bannock brines at the eastern Mediterranean: effect of water-rock interactions. Geochim. Cosmochim. Acta 62, 3221–3228.

Vengosh, A., Kolodny, Y., Starinsky, A., Chivas, A.R., McCulloch, M.T., 1991. Coprecipitation and isotopic fractionation of boron in modern biogenic carbonates. Geochim. Cosmochim. Acta 55, 2901–2910.

Vermeesch, P., Miller, D.D., Graham, S.A., De Grave, J., McWilliams, M.O., 2006. Multimethod detrital thermochronology of the Great Valley Group near New Idria, California. GSA Bulletin 118, 210–218.

Vibetti, N.J., 1993. Chemical alteration trends, fluid inclusion patterns and stable isotope compositions in the plutonic sequence of the Troodos ophiolite, Cyprus. J. Afr. Earth. Sci. 17, 193–202.

Vibetti, N.J., 1987. A Study Of Deep Fluid Circulation In The Troodos Ophiolite, Cyprus. PhD thesis, Western University.

Vils, F., Tonarini, S., Kalt, A., Seitz, H.-M., 2009. Boron, lithium and strontium isotopes as tracers of seawater–serpentinite interaction at Mid-Atlantic ridge, ODP Leg 209. Earth Planet. Sci. Lett. 286, 414–425.

Viti, C., Collettini, C., Tesei, T., Tarling, M., Smith, S., 2018. Deformation Processes, Textural Evolution and Weakening in Retrograde Serpentinites. Minerals 8, 241.

Waite, J.H., Glein, C.R., Perryman, R.S., Teolis, B.D., Magee, B.A., Miller, G., Grimes, J., Perry, M.E., Miller, K.E., Bouquet, A., Lunine, J.I., Brockwell, T., Bolton, S.J., 2017. Cassini finds molecular hydrogen in the Enceladus plume: Evidence for hydrothermal processes. Science 356, 155–159.

Watkins, N.D., Gunn, B.M., 1971. Petrology, geochemistry, and magnetic properties of some rocks dredged from the Macquarie Ridge. N.Z. J. Geol. Geophys. 14, 153–168.

Watt, J.T., Ponce, D.A., Graymer, R.W., Jachens, R.C., Simpson, R.W., 2014. Subsurface geometry of the San Andreas-Calaveras fault junction: Influence of serpentinite and the Coast Range Ophiolite. Tectonics 33, 2025–2044.

Wdowinski, S., Ben-Avraham, Z., Arvidsson, R., Ekström, G., 2006. Seismotectonics of the Cyprian Arc. Geophys. J. Int. 164, 176–181.

Wenner, D.B., 1971. Hydrogen and oxygen isotopic studies of serpentinization of ultramafic rocks. PhD thesis, California Institute of Technology. https://doi.org/10.7907/KRKQ-4J37.

Wenner, D.B., Taylor, H.P., 1974. D/H and O18/O16 studies of serpentinization of ultramaflc rocks. Geochim. Cosmochim. Acta 38, 1255–1286.

Wenner, D.B., Taylor, H.P., 1973. Oxygen and hydrogen isotope studies of the serpentinization of ultramafic rocks in oceanic environments and continental ophiolite complexes. American Journal of Science. https://doi.org/10.2475/ajs.273.3.207

Wenner, D.B., Taylor, H.P., 1971. Temperatures of serpentinization of ultramafic rocks based on O18/O16 fractionation between coexisting serpentine and magnetite. Contrib. Mineral. Petrol. 32, 165–185.

Wertz, K.L., Mosher, S., Daczko, N.R., Coffin, M.F., 2003. Macquarie Island's Finch-Langdon fault: A ridge-transform inside-corner structure. Geology 31, 661–664.

Wheat, C.G., Seewald, J.S., Takai, K., 2020. Fluid transport and reaction processes within a serpentinite mud volcano: South Chamorro Seamount. Geochim. Cosmochim. Acta 269, 413–428.

Whitmarsh, R.B., Beslier, M.-O., Wallace, P.J., et al., 1998. Proc. ODP, Init. Repts., College Station, TX (Ocean Drilling Program), Vol. 173.

Whitmarsh, R.B., and Sawyer, D.S., 1996. The ocean/continent transition beneath the Iberia Abyssal Plain and continental-rifting to seafloor-spreading processes. In Whitmarsh, R.B., Sawyer, D.S., Klaus, A., and Masson, D.G. (Eds.), Proc. ODP, Sci. Results, College Station, TX (Ocean Drilling Program), Vol. 149, 713–733.

Whitmarsh, R. B., and D. S. Sawyer 1996. The ocean/continent transition beneath the Iberia abyssal plain and continental-rifting to seafloor-spreading processes, Proc. Ocean Drill. Prog. Sci. Results, Vol. 149, 713–732.

Wicks, F.J., O'Hanley, D.S., 1988. Serpentine minerals; structures and petrology. Rev. Mineral. Geochem. 19, 91–167.

Wicks, F.J., Plant, A.G., 1979. Electron microprobe and X-ray microbeam studies of serpentine textures. Can. Mineral. 17, 785–830.

Williams, L.B., Hervig, R.L., Holloway, J.R., Hutcheon, I., 2001. Boron isotope geochemistry during diagenesis. Part I. Experimental determination of fractionation during illitization of smectite. Geochim. Cosmochim. Acta 65, 1769–1782.

Wilson, R.A.M., 1959. The geology of the Xeros-Troodos area (No 1). Authority of the Government of Cyprus.

Woelki, D., Michael, P., Regelous, M., Haase, K., 2020. Enrichment of H2O and fluid-soluble trace elements in the Troodos Ophiolite: Evidence for a near-trench origin. Lithos 356–357, 105299.

Woelki, D., Regelous, M., Haase, K.M., Beier, C., 2019. Geochemical mapping of a paleo-subduction zone beneath the Troodos Ophiolite. Chem. Geol. 523, 1–8.

Wunder, B., Schreyer, W., 1997. Antigorite: High-pressure stability in the system MgO SiO2 H2O (MSH). Lithos 41, 213–227.

Yamaoka, K., Hong, E., Ishikawa, T., Gamo, T., Kawahata, H., 2015a. Boron isotope geochemistry of vent fluids from arc/back-arc seafloor hydrothermal systems in the western Pacific. Chem. Geol. 392, 9–18.

Yamaoka, K., Ishikawa, T., Matsubaya, O., Ishiyama, D., Nagaishi, K., Hiroyasu, Y., Chiba, H., Kawahata, H., 2012. Boron and oxygen isotope systematics for a complete section of oceanic crustal rocks in the Oman ophiolite. Geochim. Cosmochim. Acta 84, 543–559.

Yamaoka, K., Matsukura, S., Ishikawa, T., Kawahata, H., Böttcher, M.E., 2015b. Boron isotope systematics of a fossil hydrothermal system from the Troodos ophiolite, Cyprus: Water–rock interactions in the oceanic crust and subseafloor ore deposits. Chem. Geol. 396, 61–73.

Yeh, H.-W., 1980. D / H Ratios and late-stage dehydration of shales during burial. Geochim. Cosmochim. Acta 44, 341–352.

You, C.-F., Butterfield, D.A., Spivack, A.J., Gieskes, J.M., Gamo, T., Campbell, A.J., 1994. Boron and halide systematics in submarine hydrothermal systems: Effects of phase separation and sedimentary contributions. Earth Planet. Sci. Lett. 123, 227–238.

Zeebe, R.E., Wolf-Gladrow, D., 2001. CO2 in Seawater: Equilibrium, Kinetics, Isotopes. Gulf Professional Publishing.

Zheng, Y.-F., 1999. Oxygen isotope fractionation in carbonate and sulfate minerals. Geochem. J. 33, 109–126.

Zheng, Y.-F., 1993. Calculation of oxygen isotope fractionation in hydroxyl-bearing silicates. Earth Planet. Sci. Lett. 120, 247–263.